Development of novel chemical/biology approaches to elucidate the mechanism of T cell receptor signaling.

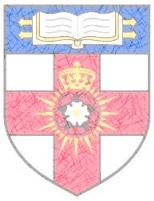

UNIVERSITY
OF LONDON

A thesis submitted in partial fulfilment of the requirements of the Degree of Doctor of Philosophy at the University of London
by

Yasel Fleitas

January 2020

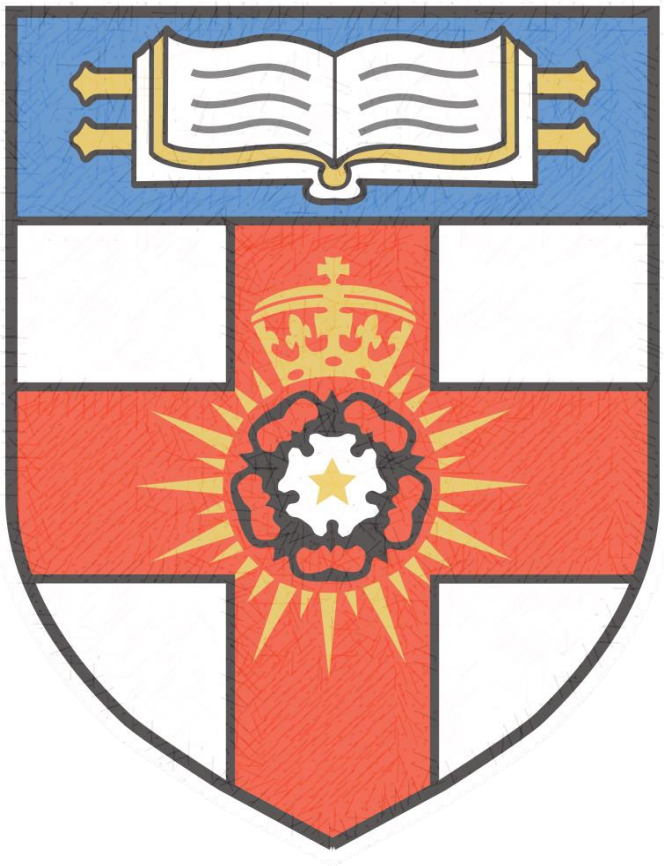

STATEMENT OF ORIGINALITY

I, Yasel Fleitas, confirm that the research included within this thesis is my own work or that where it has been carried out in collaboration with, or supported by others, that this is duly acknowledged below and my contribution indicated. Previously published material is also acknowledged below.

I attest that I have exercised reasonable care to ensure that the work is original and does not to the best of my knowledge break any UK law, infringe on any third party's copyright or other Intellectual Property Right, or contain any confidential material.

I accept that the College has the right to use plagiarism detection software to check the electronic version of this thesis.

I confirm that this thesis has not been previously submitted for the award of a degree by this or any other university.

The copyright of this thesis rests with the author and no quotation from it or information from it may be published without the prior consent of the author.

Signature:

Date:

ABSTRACT

A "chemical-biology" model has been created to study the mechanism of T cell receptor signaling. The T cell receptor (TCR) is a macromolecular complex that lies at the core of the activation, development and function of lymphocytes. Despite the large amount of data regarding the composition, structure and function of this receptor, there is no consensus about how TCR signaling is triggered after a stimulus. One hypothesis has proposed that initial signaling could proceed through an aggregation mechanism, in which multiple receptors copies cluster on the surface of the cellular membrane to promote signaling. To address this hypothesis we have designed a chemical approach based on a porphyrin-maleimide moiety as an aggregation reporter, the transmembrane region of a TCR, and phosphatidylcholine liposomes as model membranes. This system is free of all the complexities present in the natural cell membrane, i.e. proteins, lipid rafts, and carbohydrates. This will allow the study of the TCR aggregation phenomena itself, without the interference of other molecular elements. For the analysis of TCR aggregation we have conjugated of the porphyrin via the maleimide moiety with the thiol group of the cysteine present on the transmembrane peptide through the so-called "click reaction".

The starting point of this thesis has been the chemical synthesis of the porphyrin-maleimide probe. In order to define the best conditions to perform the conjugation reaction we achieved the labelling of some model thiols, e.g. N-acetylcysteine, γ-glutathione and a control peptide. In addition, we have optimized the methods to separate and identify the product of the labelling reaction by several analytical techniques. In conclusion, this chemi-

cal-biological model proved useful for the study of the aggregation of targets of biological relevance in hydrophobic environments.

The immunology studies carried out in the second part of this PhD project are focused on the role of the TCR in the development of the gamma delta (γδ) T cells. γδ T cells make rapid contributions to host defense of the host against invasive agents such as HIV, malaria, and tuberculosis, are also implicated in immunopathologies such as psoriasis and asthma. The ways in which these cells execute their function is through early provision of cytokines such as IFN-γ and IL-17. IFN-γ producers participate actively in anti-tumour activities while the IL-17 producers are involved in protection against extracellular bacteria and fungi. Interestingly, the capacity of these cells to produce cytokines is acquired while they are still in the thymus, without antigenic stimulation. This is in acute contrast with the acquisition of effector phenotypes by αβ T cells in secondary lymphoid organs in the immediate aftermath of an infection after the interaction with antigen presenting cells. The development of both αβ + γδ lineages is thought to proceed from a common thymic progenitor. Commitments to the γδ lineage require a strong signal delivered to the thymocytes through TCRγδ. However, it is also thought that TCRγδ signaling dictates thymic differentiation of γδ progenitors into one of two effector phenotypes: IFN-γ or IL-17 secreting cells. In our lab, we have developed a flow cytometry methodology that allows the visualization of these committed cells. One of the goals of this project is to understand the role of TCRγδ signaling in commitment of early γδ progenitors to distinct effector fates. We hypothesize that characteristics of the TCR, like CDR3 specificities, usage of particular TCR chains, or the interaction with TCR ligands could dictate commitment into a IFN-γ or IL-17 fate. To begin to address this we have cloned a TCRγδ from and IL-17 secreting γδ T cell, and have transduced it using a retroviral vector

into TCR-null $Rag2^{-/-}$ thymocytes. This has established an in vitro culture to further assess the TCRγδ characteristics that are required for the acquisition of γδ T cell effector fate.

A mi familia

Acknowledgements

I would like to thank my supervisors Dr Lilia Milanesi, Professor Daniel Pennington and Professor Marina Resmini for the opportunity to join their labs and for mentoring me throughout this unforgettable journey.

I would like to acknowledge my immense gratitude and respect for Nital who kindly taught me everything I need to know to carry on in the Immunology lab. Thank you for always being so lovely and patient, for your integrity and commitment to science, and for giving me so much in this journey. I am deeply grateful.

I am also very grateful to Stefania for her support in the project. Thank you for always being kind and cheerful. To Monica, Steve, Gerard, Delphine, Claire, Emma, Tony, Ana, Veronica, Juan, Paula, Sara, thank you for the chats, the laughs, and your patience.

I would also like to thank my colleagues from SBCS for all their help, support, advice and warmth. Angelo and Rosemary, having found you both is one of the luckiest things that happened to me. Thank you for bringing so much light to my life, and for inspiring me with your talent and personalities. I would also like to thank Cristiana for lending me a hand in the most critical moment of this project, you are a star. Thank you Anneta, Chiara, Giuseppe, Martina, Fosca, Gabriel, Lester, Soultana, Sidonie, Antonio, Shaima, Carmen, Giacomo, Luca, Giorgio, Mark, Pengfei, Qingyu, Charles, Jack, Agha for the great moments shared at SBCS and in the Senior Common Room. I am also thankful to have found such incredible people like Ankit, Giuseppe, Rossella and Shree, with whom I have learned much more than science, and having you around has enriched my life so much.

I would also like to take this opportunity to thank my friends, Bernabé and Humberto, for your long-standing friendship, for the encouragement, for the trust, and for your patience. I cannot say thank you enough! I am also grateful to Mirel, Sara, Mónica, Adriana, Yaima and Yoamna for being such great friends.

Pero sobre todo, quiero agradecer a mi familia. A mi Madre, que me ha dado todo a cambio de tan poco, gracias por tu amor constante, tu preocupación sin límites, tu entrega. A mi abuela por todo su amor, por ser mi primer ejemplo de disciplina, integridad y profesionalismo. A mi Padre, que me enseño que los sueños sí que se pueden convertir en realidad, siempre que se luche por ellos. A mis hermanas, Dianelys, Claudia y María por ser más y mejor de lo que cualquier hermano pudiera desear. A mi tía Ismarys, por supuesto, por ser fuente de inspiración y confidente, muchas gracias. A Pachi, por tu excelente y ardua labor de padre sustituto, muchas gracias.

Gracias Pit, por todo lo que me has dado durante estos cuatro años. Recorrer este camino contigo me ha transformado, me has enseñado más de lo que te puedes imaginar. Toalla!

TABLE OF CONTENTS

1 CHAPTER 1

1.1 INTRODUCTION.

1.1.1 Membrane Proteins

The cellular membrane is formed by a symmetrical two-layer structure of phospholipids where the polar heads (phosphates) are facing the exo and cytoplasmic sides while the hydrophobic core (fatty acid chains) are compacted in the interior (Figure 1-1).

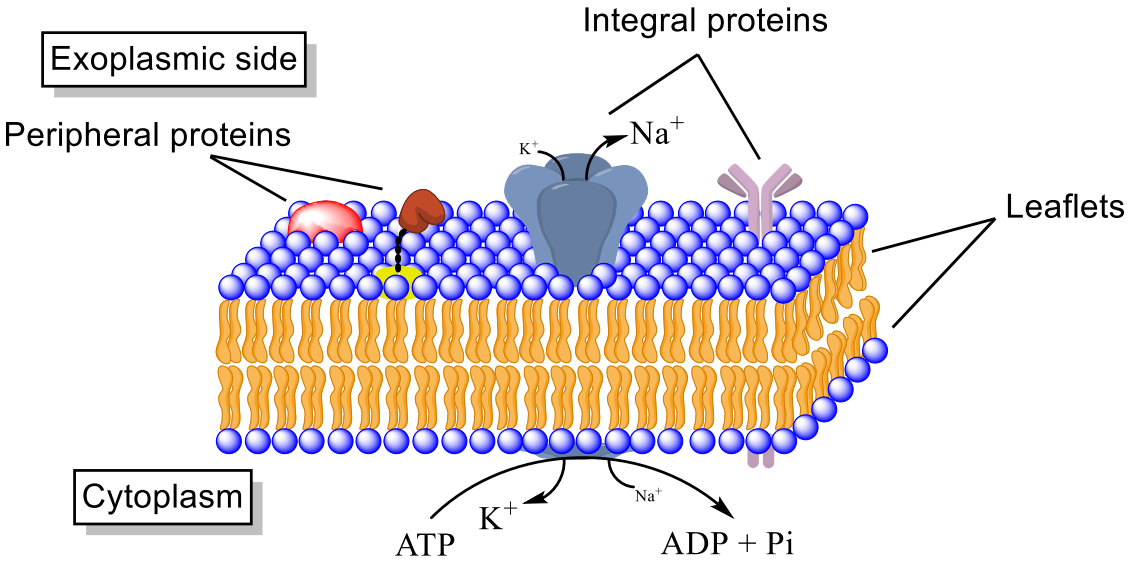

Figure 1-1. Schematic diagram of typical membrane with proteins embedded.

A myriad of different proteins associates with one or both leaflets enabling the membrane to carry out its particular activities. Based on the way in which the proteins interact with the membrane we can divide them into two major groups: peripheral and integral membrane proteins. The peripheral membrane proteins do not interact with the hydrophobic core of the membrane, instead, they associate with the polar heads or other integral proteins.

1.1.2 Integral Membrane Proteins

The integral membrane proteins (IMP) present one or more segments that are embedded in the lipid bilayer; they can span both leaflets or be anchored to only one. The IMPs that only interact with one leaflet are classified as "monotopic". A few of the best characterized monotopic proteins are enzymes involved in the metabolism of lipids, e.g. prostaglandin H_2, squalene-hopene cyclase, fatty acid amide hydrolase[4].

A special case of monotopic proteins is the glycosylphosphatidylinositol (GPI) anchored polypeptides. They are bound to the membrane by two or more lipid anchors. In humans, there are reported in literature around 150 GPI-anchored proteins, and they can function in different ways, such as receptors, adhesion molecules, enzymes, etc[5-7].

The most interesting group of IMPs contains one or more transmembrane (TM) domains that span the lipid bilayer. Depending on their topology these proteins can be classified as bitopic, politopic or oligomeric[4]. The bitopic proteins span the membrane one time, and based on their orientation can be subdivided in type I if the N-terminus is exposed to the extracellular side or type II when the C-terminus is facing outside. Politopic proteins or type III, have multiple segments spanning the membrane connected by loops. Several bitopic proteins get associated through their TM domains to form clusters, this configuration is denominated oligomeric or type IV (Figure 1-2).

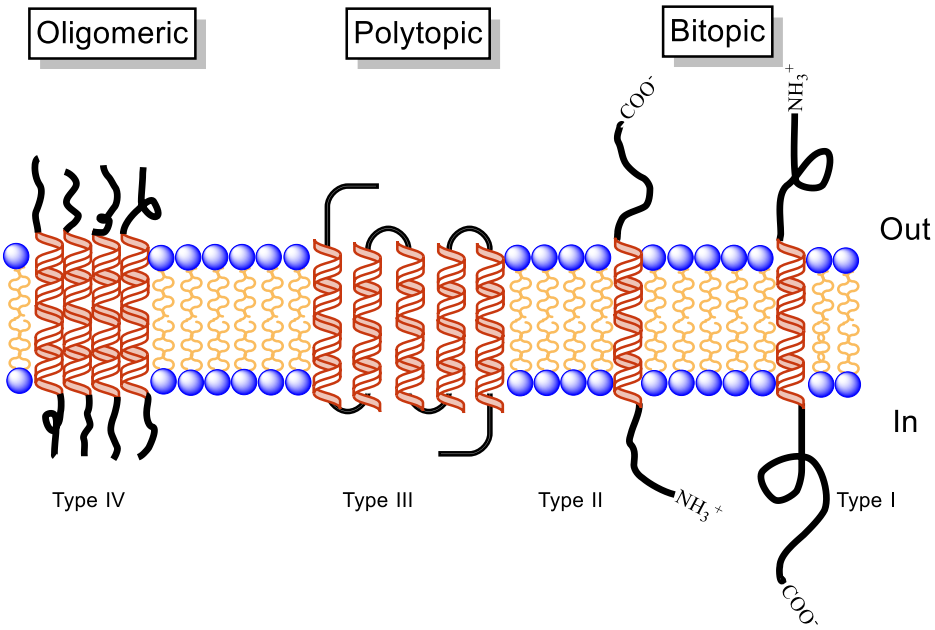

Figure 1-2. Schematic representation of the types of integral membrane proteins that cross the biological membrane.

1.1.3 Importance of Transmembrane Cell Signaling in Biology

Transmembrane cell signaling is a fundamental process in living organisms that is responsible, among others, to sense the changes in their environment. Many critical functions in cell biology are downstream transmembrane signaling events, i.e. development, differentiation, cell growth, immune response, apoptosis, among many others. Thorough comprehension of transmembrane signaling is crucial, due to its importance in cell fate decision and because its dysregulation is at the base of many diseases, i.e. autoimmune disorders, nervous malfunctions, and cancer.

A key aspect to understand the transmembrane signaling is the spatial organization of receptors in the membrane, in special the formation of clusters or oligomers of receptors. Some evidence suggests that formation of clusters of receptors is regulated by some molecular recognition events such as the assembly of neighboring lipids into rafts[8, 9], interaction with ligands[10, 11], and is stabilized by the cytoskeleton[12, 13].

While some receptors function as discreet assemblies in the membrane[14], some others function in aggregates. Of note, when the size of the assemblies is not determined they are known as clusters or oligomers[15]. In these clusters, the receptors are held by non-covalent interactions and they are in equilibrium with the non-clustered species. For example, it is well established that aggregates of neurotransmitter receptors are fundamental for the plasticity of neuronal synapsis[16]. Triller et al.[16] reported that in both, inhibitory and excitatory synapsis, receptors are bound to a subjacent meshwork of scaffolding proteins that stabilize them in the postsynaptic membrane. This receptor-scaffold interaction is transient, and the synaptic receptors are in equilibrium with a population of extra synaptic receptors.

The immunological synapse is another example where the formation of clusters follows the ligand binding[17]. Dustin at al.[18]proposed a model for the formation of the immunological synapse. In the model, engaging the major histocompatibility complex (MHC)-peptide complex by T cell receptors (TCR) induces a series of molecular recognition events that lead to formation of a stable synapse. The synapse area is characterized by two zones of assembly, the inner circle called the central supramolecular activation cluster (cSMAC) which concentrates most of TCR-MHC-peptide complex surrounded by the peripheral SMAC that is formed by integrins[19].

A similar study conducted by Munoz at al.[10] described how the interaction of TCR with MHC-peptide complex, induces clustering of surface CD38 and recruitment of intracellular pools of CD38 to the immunological synapse.

In summary, these studies illustrate how binding of ligands induces changes in the receptor that lead to clustering.

Another important component in the formation of clusters of receptors is the presence of lipid domains in the cell membrane called **lipid rafts**[20, 21]. Lipids rafts are nano-assemblies of cholesterol, sphingolipids and proteins in the outer leaflet of the membrane (Scheme 1-1). The packed association of saturated hydrocarbon chains of sphingolipid and cholesterol form a distinct liquid-ordered phase in the lipid bilayer that is dispersed in patches, in the liquid-disordered matrix of phospholipids[22-24]. These blocks of immiscible ordered lipids form platforms that can function in processes like membrane trafficking and signalling[25, 26]. Notwithstanding, the existence of lipid rafts is still controversial, mainly due to the difficulty to prove their existence on living cells[27].

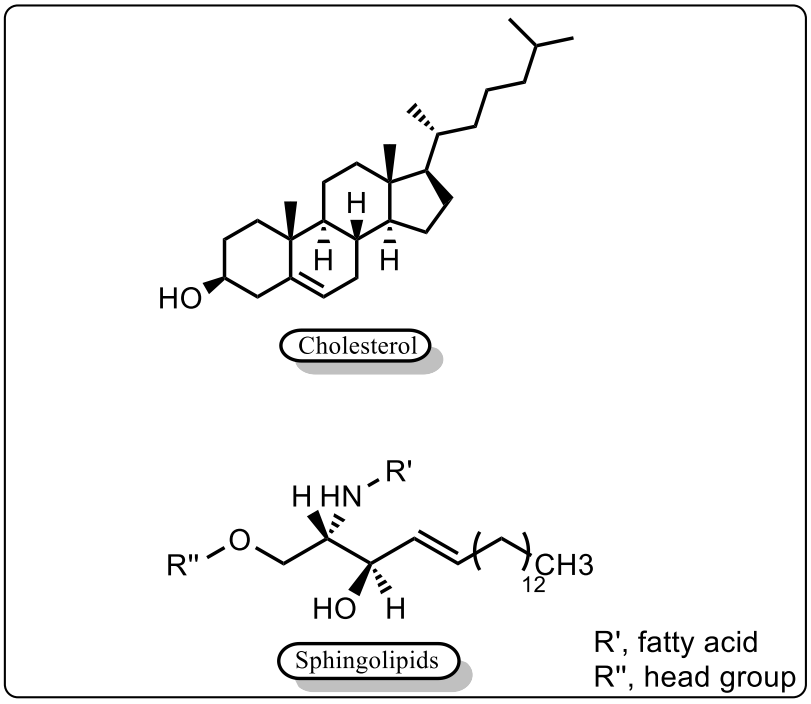

Scheme 1-1. Panel showing the main components of the lipid rafts in cell membranes.

Despite some sceptical opinions, the participation of lipid rafts in clustering during cell signaling is well established. For example, the activation mechanism of immunoglobulin E (IgE) signaling was described to involve aggregates of immunoglobulins in lipid rafts. This signaling pathway is activated when the monomeric Fc epsilon receptor (FcRεI) is bound to the Fc region of an IgE (Figure 1-3). Fc receptor is a complex of four subunits (tetramer), α, β, and two γ[28]. The alpha subunit binds IgE, while the other three subunits contain the immunoreceptor tyrosine-based activation motifs (ITAMs) that participate in signal transduction. During allergic response, the FcRεI-IgE bound complex is crosslinked by oligomeric antigens triggering the activation of the receptor. Activation recruits the double acylated non-receptor Src-like tyrosine kinase Fyn that in turn phosphorylates the ITAMs initiating the signaling cascade by joining the Syk/Zap-70 through their phosphotyrosine residues[29, 30]. Finally, downstream of this signaling cascade is the increase of the intracellular calcium levels near the membrane, which in turn induces release of histamine from their granules. One of the first experimental observations in favor of raft associated signaling of immunoglobulins came from the fact that in steady state the FcRεI was soluble in Triton X-100, but after activation the receptor became insoluble, suggesting their incorporation on lipid insulates[30]. Another hint on the lipid raft-mediated activation was that after treatment with Methyl-β-Cyclodextrin, which depleted the cholesterol concentration of the cell, the IgE signaling was abolished[29].

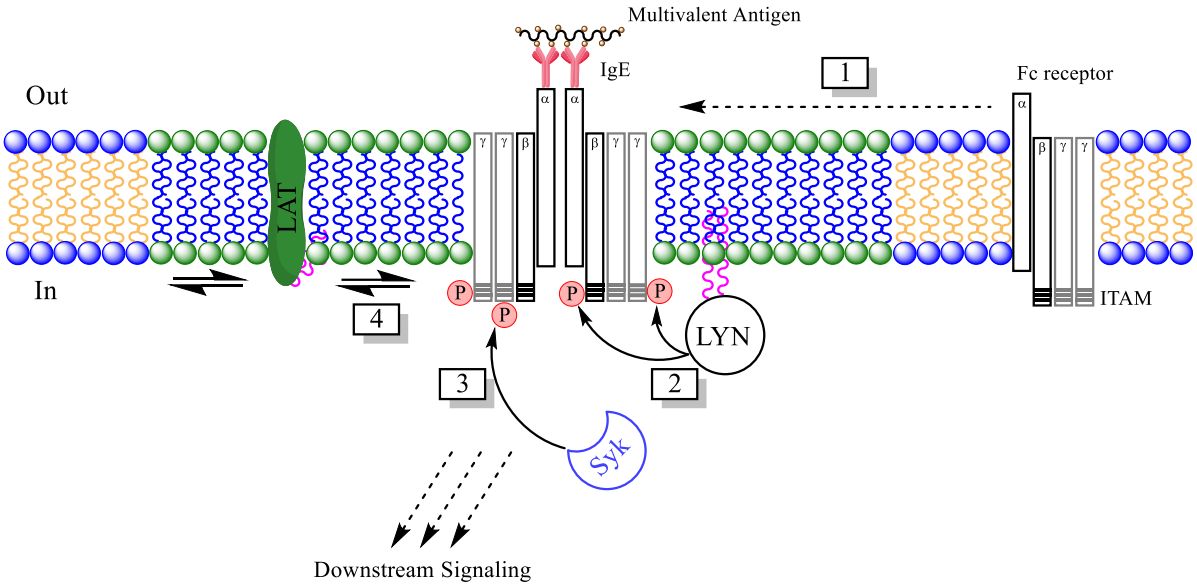

Figure 1-3. Initial signaling events in rafts for the IgE receptor (FcεRI). The likely sequence of key events is illustrated numerically. 1. Ligand induced dimerization of the receptor and association with the lipid rafts. 2. Phosphorylation of the ITAMs in the immunoreceptor by the Src-family kinases LYN. 3. The phosphorylated ITAMs act as a membrane-docking site for the cytoplasmic kinase Syk. 4. Recruitment and activation of the adaptor protein LAT and further cascade that leads to the down-stream signaling events. Immunoreceptor tyrosine-based activation motifs (ITAMs), Tyrosine protein kinases (Syk and LYN), linker for activation of T cells (LAT), Immunoglobulin E (IgE), fragment crystallizable region receptor (Fc receptor).

More experimental evidence that suggests participation of lipid rafts in cell-signaling comes from the work of Roy et al on Ras-GTPase signaling proteins[31]. There are three isoforms of Ras. H-Ras and K-Ras isoforms are identical in their aminoacid sequence and have a carboxy-terminal prenylated sequence CAAX but while the isoform K-Ras has a polybasic region that target the protein towards the plasma membrane, the H-Ras isoform is palmytoilated, which probably direct this isoform to lipid rafts. In a very clever experiment, they produced a dominant-negative mutant for the protein caveolin. Caveolin is the main structural component of caveolae, which are small invaginations of the plasma membrane that plays an important role in the trafficking of cholesterol towards the plasma. In addition, it was suggested that caveolin participates in signaling transduction events. In this study, they

observed that activation of Raf mediated by H-Ras was inhibited, while activation of Raf by K-Ras isoform was not affected. This outcome was reproduced when they treated cells with Methyl-β-Cyclodextrin, which depleted cholesterol from the cell membrane as mentioned before. The explanation given to these observations was that the absence of caveolin in the mutants could reduce the cholesterol levels in the plasma membrane and this could affect the number of lipid rafts present on the cell membrane. This could explain why the activation of Raf mediated by H-Ras was prohibited.

1.1.4 Background on transmembrane receptors that transmit signal via discreet self-assemblies.

In this section, we will introduce some examples of receptors that form discreet assemblies by non-covalent interactions in response to an intracellular or an extracellular event, such as ligand binding. The key characteristic of these self-assemblies is that they are of a known stoichiometry regardless of ligand type. Below, we will present some examples with different types of ligands, such as small molecule for G-coupled receptors, receptor on another membrane for gap junction and single or multivalent ligand for Bacterial chemotaxis.

1.1.4.1 G-coupled protein receptors (GPCRs)

The G-coupled protein receptors (GPCRs) constitute one of the largest family of cell surface receptors[32]. Structurally, each GPCRs is an integral membrane protein constituted by seven transmembrane domains[33], an extracellular amino-terminal end and a cytoplasmic carboxy-terminal tail (see Figure 1-4). The transduction unit is formed by the trimeric ($\alpha\beta\gamma$) G-protein and an effector component. The mechanism of action can be briefly described as follows: after ligand binding the receptor suffers an allosteric change that leads to release of GDP and binding of GTP to the γ-subunit. This association destabilizes the trimeric complex and produces the dissociation of the GTP-α subunits from the $\beta\gamma$ dimer. This "activated" form of the receptor interacts with the effector component through the G_α subunit or $G_{\beta\gamma}$ dimer. Hydrolysis of GTP linked to G_α leads to the production of GDP, which is carried out by an intrinsic hydrolase activity of the G_α-subunit, switching off the receptor.

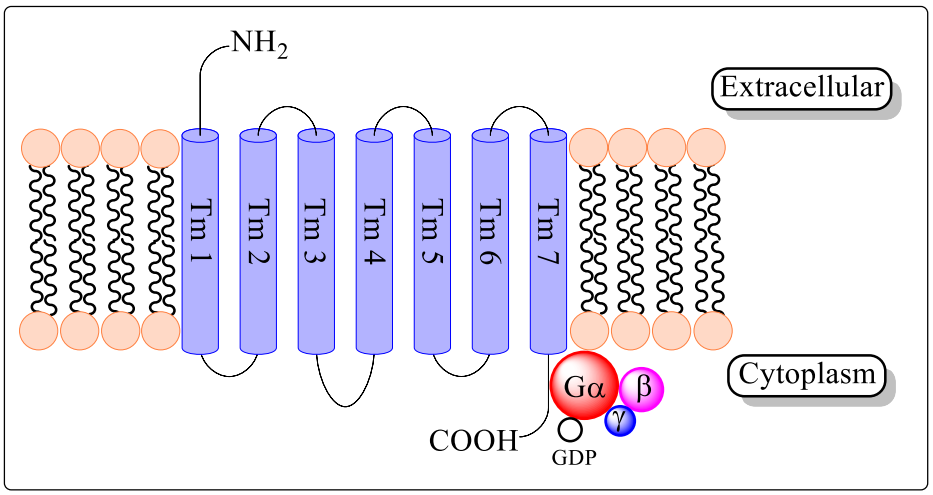

Figure 1-4 Schematic diagram of the structure of the GPCR receptor. It consists of seven trans-membrane domains, three extracellular loops and three intracellular loops with an N-terminus outside and a C-terminus inside. The membrane-bound heterotrimeric G protein complex is composed of three subunits: alpha (Gα), beta (β), and gamma (γ). The Gα subunit associated to GDP is in the inactive state. GDP, Guanosine diphosphate

Receptor dimerization have been proposed as a key aspect of the activity of GPCRs. One of the more interesting observations in support of GPCR receptor dimerization come from studies with the GPCR $GABA_B$ receptor[34].It has been shown that co-expression of two isoforms of $GABA_B$ receptor, $GABA_BR_1$ and $GABA_BR_2$, is necessary for formation of a functional GABA receptor on the cell surface[34-36].

More experimental evidence suggesting the importance of receptor dimerization is the study conducted by Benkiran et al.[37]. Working with a truncated form of the chemokine receptor CCR5 (CCR5Δ32), they showed that co-expression of this truncated form with the wild type counterpart produced intracellular retention of the heterodimer. The dominant-negative retention effect was associated with the slower onset of AIDS in patients that were heterozygous for this mutation.

1.1.4.2 Connexins gap-junction

Gap junctions are plasma membrane structures that mediate translocation of small molecules and ions between adjacent cells[38]. Gap-junctions are constituted by several members of integral membrane proteins denominated connexins[39]. Briefly, a connexin is a protein that spans the cellular membrane four times and contains both the amino and carboxyl-terminus in the cytoplasmic space. This protein oligomerizes intracellularly into **hexamers** to form the so-called connexons that insert into the plasma membrane. Each connexon pairs with their counterpart in the neighboring cell to form an intercellular channel. These channels aggregate to form the gap-junctions[40] (Figure 1-5).

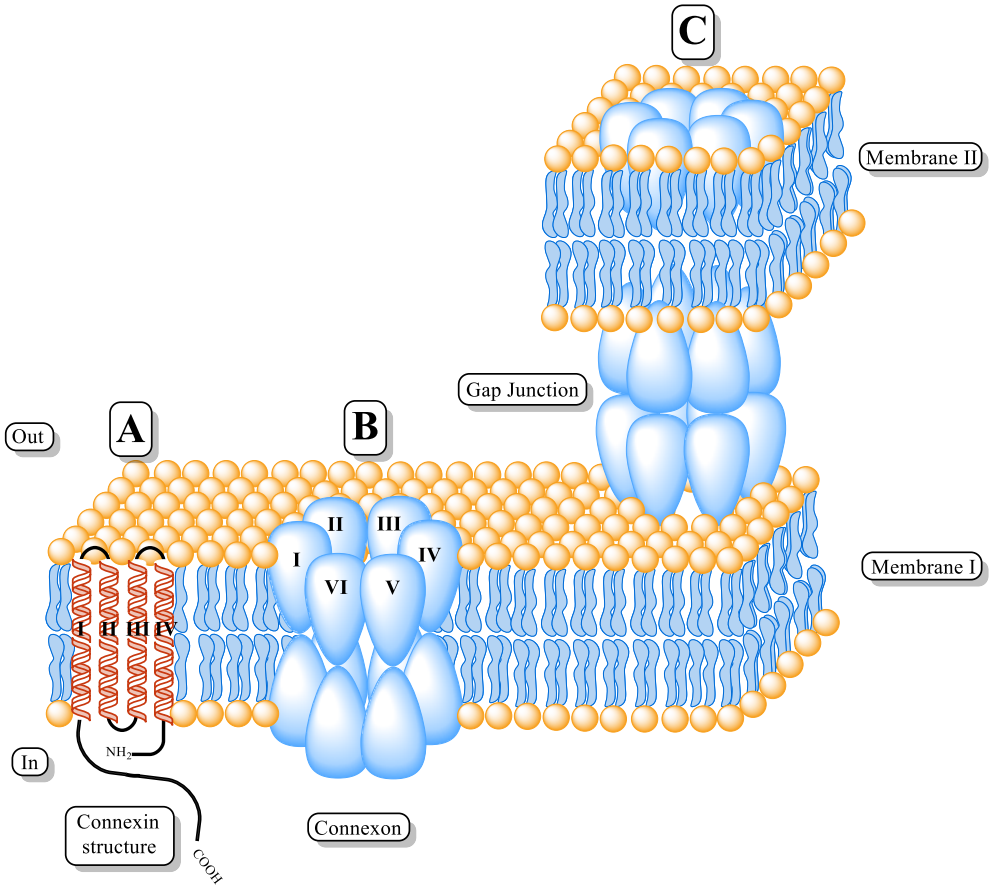

Figure 1-5. Diagram showing a gap junction and its principal elements. A) Structure of the connexin. B) Connexon, hexamer constituted by 6 connexins. C) Representation of the Gap-Junction.

The intercellular channels or gap junction have been described in many important cellular processes. For example, as mentioned before they allow the cell–cell diffusion of ions and small molecules between interacting cells[38]. In addition, the ionic conductance of these channels permits the rapid intercellular spread of action potentials in excitable cells, such as heart cells[41] and neurons[42].

1.1.4.3 Bacterial Chemotaxis

Bacterial migration in response to chemical gradients is a well-described phenomenon reported in the literature[43-46]. During chemotaxis, chemoattractants such as amino acids and sugars, or chemorepellent, are recognized by specific chemoreceptors present in the bacterial plasma membrane and promote the flagellar response[47]. The molecular events that control bacteria chemotaxis have been well investigated and provide a good model to study receptor mediated responses[48]. For example, ligand binding induces the clustering of chemoreceptors in the plasma membrane which generate the signal transduction.

In addition, some studies have reported the important role of ligand valency in the clustering of chemoreceptors. Ligand valency can be defined as the number of biologically active epitopes -sites- that a multivalent ligand have for the union with the chemoreceptor. In an elegant study, Gestwicky et al. chemo-stimulated the E.coli strain with galactose bearing-ligands of different valency, i.e. a fixed number of galactose tethered to a backbone. Their results provided evidence that ligands with different valency differentially cluster the chemo-receptors. This suggests that multivalent ligands bearing several sites of union can influence chemotactic responses by changing the extent of cell surface chemoreceptor clustering[49] (Figure1-6).

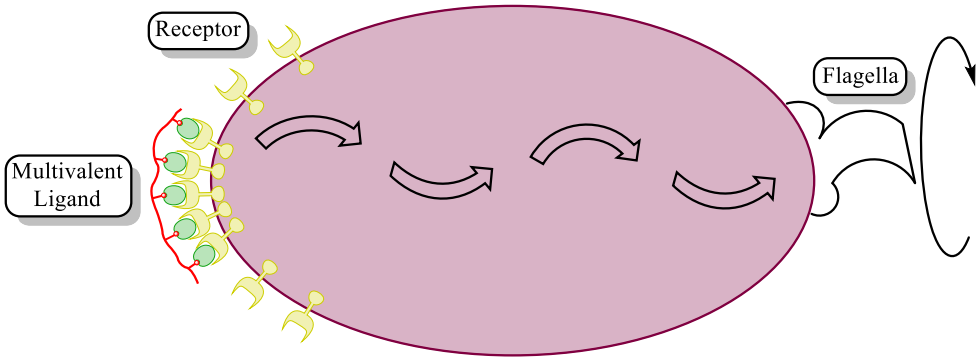

Figure 1-6. Model of receptor clustering by multivalent ligand.

1.1.5 Transmembrane receptors that transmit signal via Non-discreet self-assemblies.

In this section, we will briefly introduce some examples of receptors that signal via non-discreet assemblies. By non-discreet assemblies, we mean clusters of receptors with unknown stoichiometry linked by non-covalent interactions.

1.1.5.1 Ras proteins

The first example to illustrate the importance of membrane association and clustering of receptors in signaling transduction comes from the Ras superfamily. As mentioned in section 1.1.3, Ras is a family of related proteins that are widely expressed in several tissues and organs. Ras proteins are monomeric, low molecular weight GTPases[50], that adopt their active state when complexed with guanosine triphosphate (GTP). After binding guanosine diphosphate (GDP) they switch off to the inactive mode. Ras proteins are very important in cellular processes such as signal transduction, cell growth, cell differentiation, and cancer. Particular attention in the literature was directed towards the three isoforms of Ras: H, N and K. All three exert their biological and oncogenic functions from the inner leaflet of the plasma membrane[51]. To be target and bind the membrane, Ras proteins are post-transcriptionally modified by covalent insertion of lipid groups[52]. There are experimental data from in vitro and in vivo studies that have shown the ability of these lipidated proteins to form fluid microdomains. It has being proposed that self-association of Ras proteins in small domains shortens the time for the receptor to meet other molecules, thus speeding up signaling processes. In addition, it has being suggested that these nanoclusters are also sensitive to lower signaling inputs. The anchor motif is located in the three isoforms at the C-terminus, with a common S-farnesylcysteine carboxymethyl ester functioning in conjunction with one or two

adjacent S-palmitoylcysteine residues in N and H-Ras, and with a polybasic domain in K-Ras[53] (Figure 1-7). It is believed that S-palmytoylation directs N and H-Ras towards lipid microdomains also called lipid rafts, whereas the isoprenyl moiety has affinity for the non-raft portions of the plasma membrane. It is important to mention that both, lipids and C-terminus peptides are crucial for clustering and signaling of the Ras family[50].

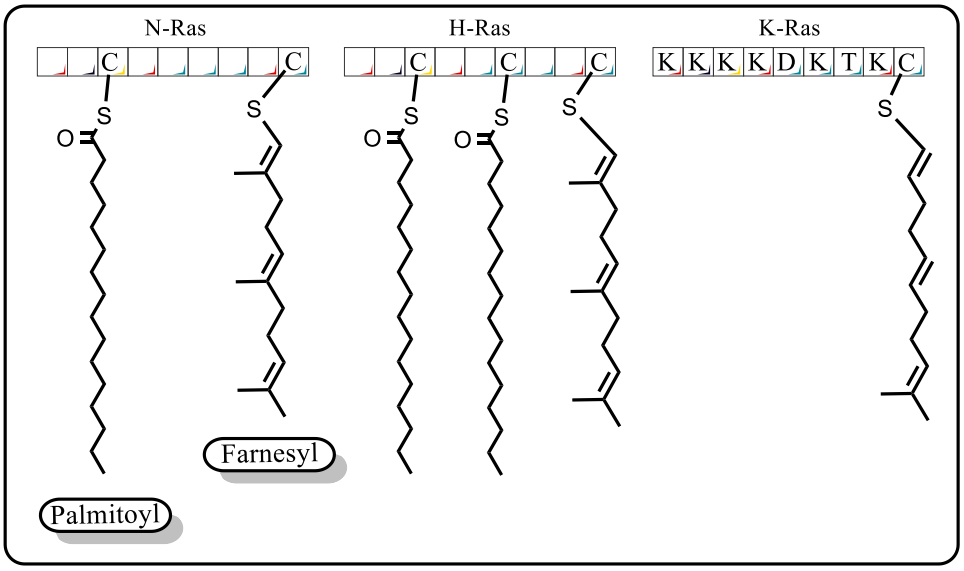

Figure 1-7. Scheme depicting the C-terminal lipidation motifs for N, H and K-Ras proteins. One palmitoyl and farnesyl anchor groups are known to be present in N-Ras; two palmitoyl and one farnesyl anchors in H-Ras, while in K-Ras a polybasic region rich in lysine's (K) and a farnesyl group are found.

1.1.5.2 SNARE protein complex

The SNAREs proteins are large complex proteins, more than 60 in mammalian cells, that play an important role in membrane fusion processes[54]. The most studied SNARE proteins are those responsible for docking the synaptic vesicle with the presynaptic membrane during neuronal exocytosis. Briefly, this complex is constituted by three proteins located in two different membranes: synaptobrevin, also denominated VAMP (vesicle-associated membrane protein) located in the vesicle membrane, and syntaxin along with synaptosomal nerve-associated protein 25 (SNAP 25) located in the plasma membrane of the presynaptic neuron. It has been described that membrane fusion progresses through formation of a four-helix bundle known as a "core complex": one helix from syntaxin and synaptobrevin, and two helices from SNAP 25[55] (Figure 1-8). It has been shown by several authors that SNARE residing in the plasma membrane i.e. syntaxin, form microclusters that are critical in the fusion events. The study of Tamm et al. is of particular interest for us because they use an in vitro model close to our experimental design, but with a different fusion reporter and proteins to study the effect of the lipid membrane composition on the oligomerization of the syntaxin[56]. This paper will be discussed in depth later on, however, their results suggest that formation and stability of these oligomeric assemblies are dependent on the cholesterol concentration and is negatively affected by the presence of anionic lipids like: 1-palmitoyl-2-oleoylphosphatidylserine (POPS), and phosphatidylinositolphosphate (PIPs). In addition, some studies[57-59] suggest that the transmembrane region of the SNARE proteins is also involved in the formation of assemblies. e.g. mutagenesis of syntaxin transmembrane region affects exocytosis[59].

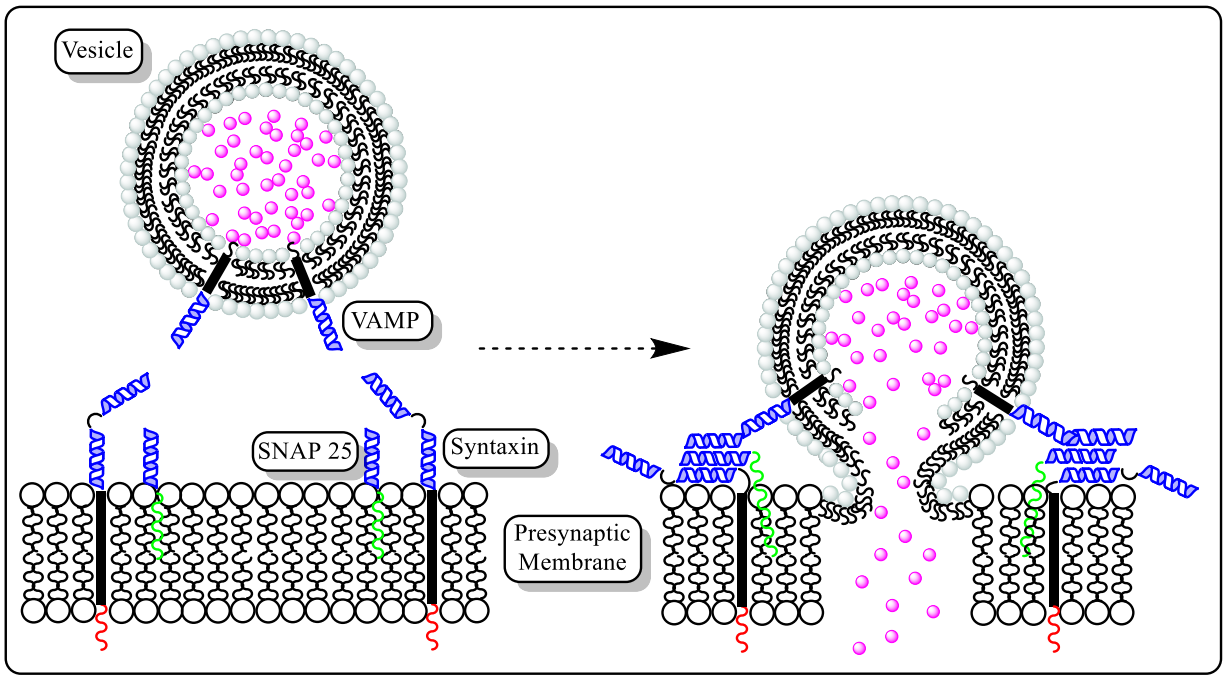

Figure 1-8. Molecular model of the membrane fusion and vesicle exocytosis. Syntaxin and SNAP 25 are located in the presynaptic membrane whereas the syneptobrevisn (VAMP) is located in the vesicle membrane. After association of the helices during the formation of the SNARE core the membranes are fused and the neurotransmitter is released to the synaptic cleft, VAMP (vesicle-associated membrane protein).

1.1.5.3 Adhesion proteins

Cell adhesion molecules are a family of proteins that mediate contacts between cells[60]. They participate in a wide range of cellular processes such as differentiation of cell structures during development, tissue formation, and immune response, etc.

Adhesion molecules share a characteristic structure made up of an extracellular portion constituted by several domains and responsible for the interaction with other adhesion molecules in *cis* (same membrane) or *trans* (different membrane) and the transmembrane segment that anchors the protein to the cellular surface[61] (Figure 1-9).

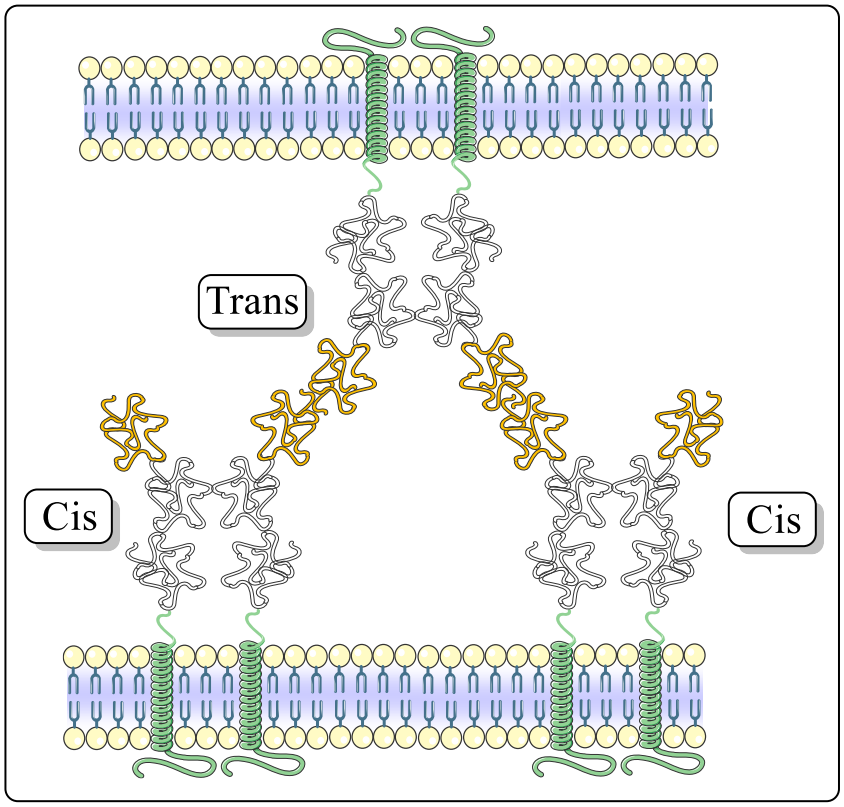

Figure 1-9. Schematic of interacting cadherin in membranes. The pictures shows the Cis-interaction of cadherins embedded in the same membrane to form a dimer through one of their Ig-like domains (Grey). The trans-interaction trough the Ig-like domains (yellow) in cadherins located different membranes is also illustrated. Ig, immunoblogulin.

Some studies with the crystal structure of cadherins have revealed that the *trans* binding interaction are weak reflected by its *Kd* in the range 20-100 μM[62]. Cadherins englobe a large Ca^{2+}-dependent superfamily of cell surface adhesion protein receptors that contain an extracellular region, also called ectodomain, composed of a tandem of immunoglobulin (Ig)-like domains followed by a transmembrane region that spans the bilayer one time and the C-terminal intracellular region that contains binding sites for other proteins. Immunoglobulin-like domains are a type of motif found in many proteins. They are composed of around 125 amino acids that are organized in two β-sheets, each one made up of approximately 7-9 anti-parallel β-strands.

Ben-Shaul et al. investigated the aggregation of cadherins on cell surfaces, and their results suggested that weak *trans* binding capacity of the monomeric cadherins can be enhanced by their clustering on the cell surface[63] (Figure 1-10).

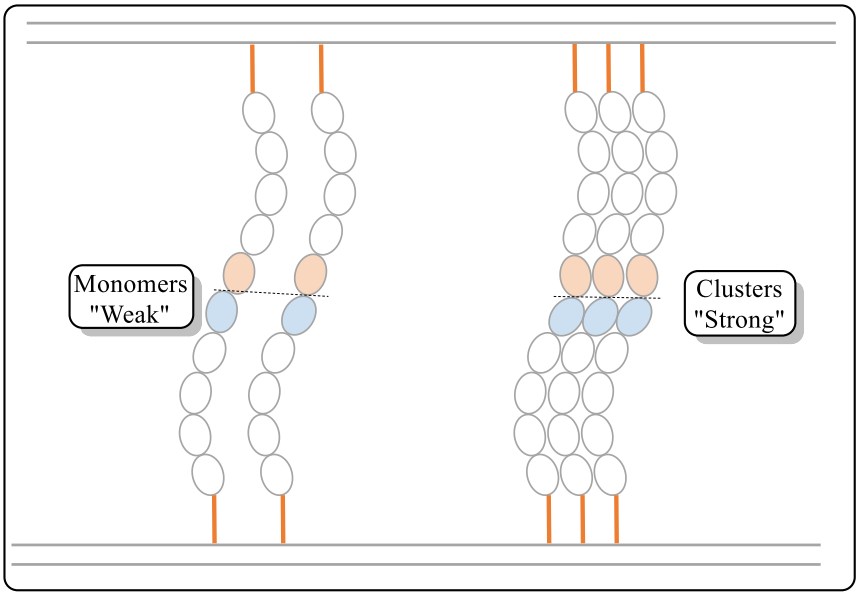

Figure 1-10. Illustration of two interacting cadherins in apposed cell membranes. The clustering of the cadherins enhances the adhesion of the cells to form tight junctions, while the association of the monomeric cadherins does not increase cellular adhesion.

1.1.6 The TCR

The T cell receptor (TCR) is a molecular dimer present in all T lymphocytes. This receptor is crucial for development, survival and differentiation of T lymphocytes[64]. It also plays a key role in antigen recognition and activation of T cells that leads to the immune response.

1.1.7 TCR structure

Structurally, TCR consist of a heterodimer of two integral membrane proteins, denoted α and β, covalently linked by a disulfide bond[65, 66] (Figure 1-11). There is another type of TCR, found in a small percentage of T lymphocytes that is made of a γ and δ chains[67]. Each α and β or γ and δ chain consists of one Ig-like N-terminal variable (V) domain, one Ig-like constant (C) domain, a hydrophobic transmembrane segment (TM) and a short cytoplasmic region. The extracellular part of the αβ (γδ) TCR is structurally similar to the antigen-binding fragment (Fab) of an immunoglobulin molecule.

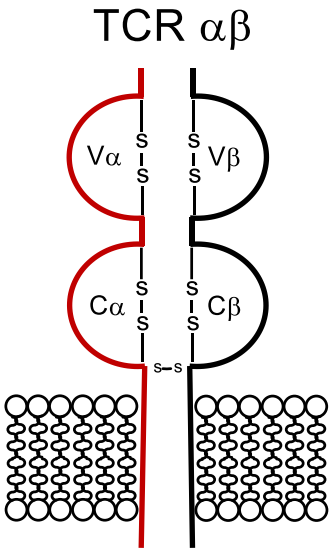

Figure 1-11. TCRαβ receptor molecule. The immunoglobulin domain are represented with disulfide bridges.

1.1.8 TCR - CD3 Complex

The TCR αβ (γδ) heterodimer is associated non-covalently with the CD3 and ζ proteins in the surface of lymphocytes. Once the receptor recognizes the antigen during the immunological synapse, these associated proteins transduce the signal that lead to T cell activation[18]. CD3 molecules consist of three integral proteins that are denominated CD3ε, δ and γ[66]. CD3 proteins and ζ are the same in all T cells subtypes regardless of specificity, which reinforce their role in signaling and not in recognition (Figure 1-12).

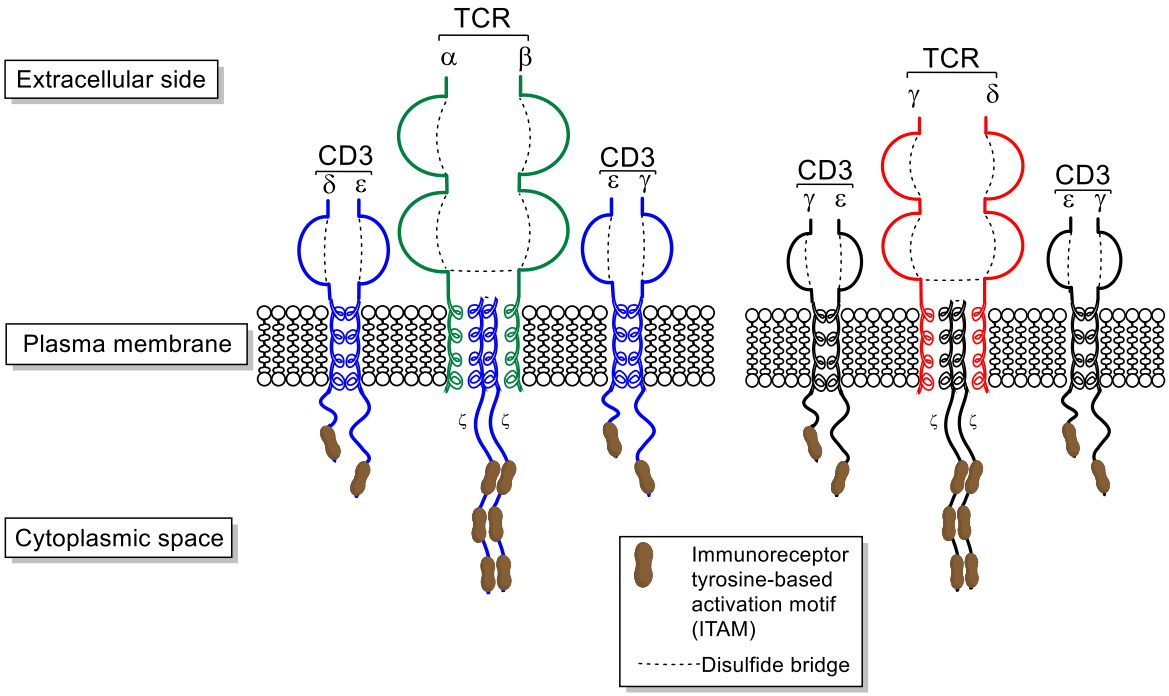

Figure 1-12. TCR-CD3 complex structure. Figure shows the organization of the TCRαβ together with the signaling subunits CD3γε, CD3δε, and the ζζ. Also represented are the TCRγδ, with the signaling subunits CD3γε repeated and the homodimer ζζ. The TCR and CD3 subunits consist of an immunoglobulin domain exposed to extracellular media, followed by a short stalk region that connects with the transmembrane domain, and finish in the cytoplasmic portion that contains the ITAMS.

The cytoplasmic regions of CD3 ε, δ and γ proteins vary between 40 to 81 amino acids residues, and each of these domains has a conserved characteristic amino acid sequence fundamental for the signaling called the immunoreceptor tyrosine-based activation motif (ITAM)[68]. Each ITAM contains two copies of the following sequence: tyrosine-X-X-leucine/isoleucine, separated by six to eight amino acid residues from the next one. The ITAMs plays an important role in signaling by the TCR complex. The other protein, ζ, has an extracellular portion about nine amino acids long and a long intracellular chain that contains three ITAMs. All the proteins mentioned above are indispensable and sufficient for the expression of TCR in the lymphocyte surface in the absence of any other T cell-specific protein[69].

The organization of the four dimeric molecules within the membrane follows a specific pattern[70]. The lysine in the position 10 of the transmembrane segment of the TCRα chain interact with the two glutamic acid residues on the CD3δε forming a three helix complex[71]. The specific mutation of the lysine 10 residue for alanine abolishes completely the expression of the complex in the cellular surface[69]. Similar studies demonstrated that assembly of the CD3γε occurs through interaction of an aspartic and glutamic residues with lysine at position nine in the TCRβ chain. Interaction of the last dimer ζζ occurs between two aspartic acids and an arginine residue at position 5 in the TCRα chain. In summary, the organization of these subunits in the membrane is based on the interaction of three pair of polar residues located in the transmembrane domain of TCR-CD3 complex (Figure 1-13).

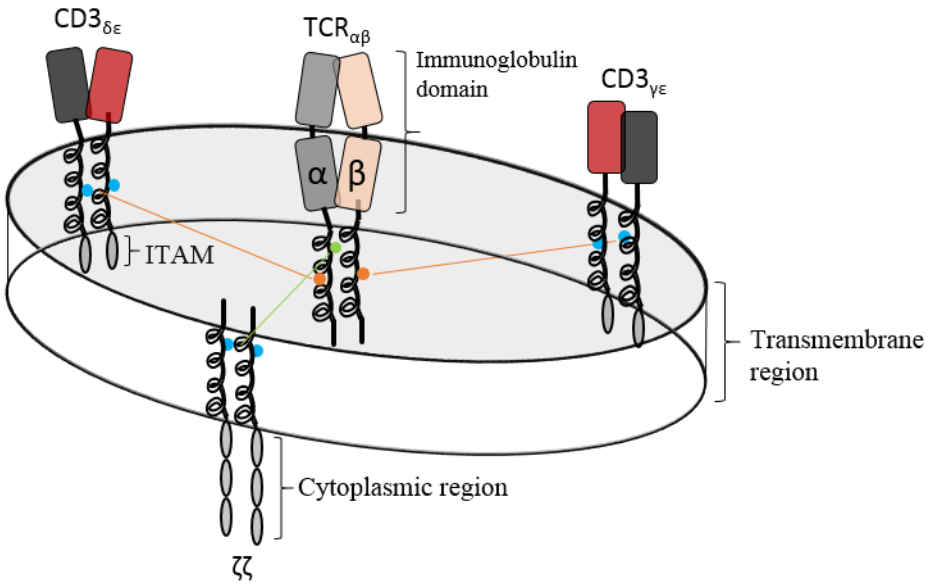

Figure 1-13. Organization of the TCR – CD3 complex assembly based on the interaction of three pairs of ionizable TM residues. (D) ● aspartic acid, (E) ● : glutamic acid, ● (K): lysine, ● (R): arginine, α: alpha chain of the TCR, β: beta chain of the TCR, ζ: zeta chain. Source: (Matthew E, 2007)

In addition, Call et al.[72] showed that a tetracysteine motif in the membrane-proximal stalk region, defined as the sequence that spans from the transmembrane peptide until the first Ig-like motive- of CD3γε or CD3δε dimers is an important structural element in their assembly with TCR. They observed that a TCRα mutant lacking the entire Ig domain is capable of assembling with CD3δ. These results suggest that interactions among the membrane-proximal segments, and not the variable or constant Ig-domains, might be involved in assembly of TCRα with CD3δε. This also indicates that ligand binding, which involves necessarily the variable Ig-like domain, is not essential for receptor assembly.

1.1.9 TCR assembly and Signal Transduction

There is controversy regarding the natural state of the heterodimer TCR in the plasma membrane, in particular whether it is found as a monomer or, on the contrary, as a cluster of receptors. There are experimentally based papers that suggest either one or the other theory (cluster[73-75] or monomeric[76-78]). However, it is clear that ligand-induced clustering is an important event in early stages of T cell activation and clustering is important to initiate signaling in TCRαβ T cells[79, 80]. Kupfer et al. observed that clustering of multiple copies of TCR-CD3 complex in the lymphocyte surface is crucial to form the supramolecular activation complex[81]. Fluorescence imaging studies showed that antigen-dependent formation of TCR microclusters is concomitant with T cell activation and contribute to the immunological synapse with the antigen presenting cell[82, 83].

Notwithstanding, Davis et al.[84] argued that the TCR does not form clusters. Their evidence is based on a special technique called bioluminescence resonance energy transfer (BRET). Briefly, BRET is an analytical technique that involves the energy transfer between a bioluminescent donor and a fluorescent acceptor without the necessity of fluorescence excitation. It has been widely used in studies of protein-protein interaction. The investigation of Davis et al. indicates that exclusively monomeric or monovalent membrane proteins are likely to drive receptor triggering in T cells, offering a simplified structural framework for understanding receptor triggering[84]. Is important to mention that studies of TCR assembly and triggering are very difficult in biological systems, mainly due to the intrinsic complexity of cells.

Several models[85] have been proposed to explain how the TCR is triggered, in other words, how the ligand binding (agonist peptide-major histocompatibility complex MHC) produce the biochemical changes in the cytoplasmic tail of the CD3 molecules (phosphorylation) that leads to cell activation (Figure 1-14).

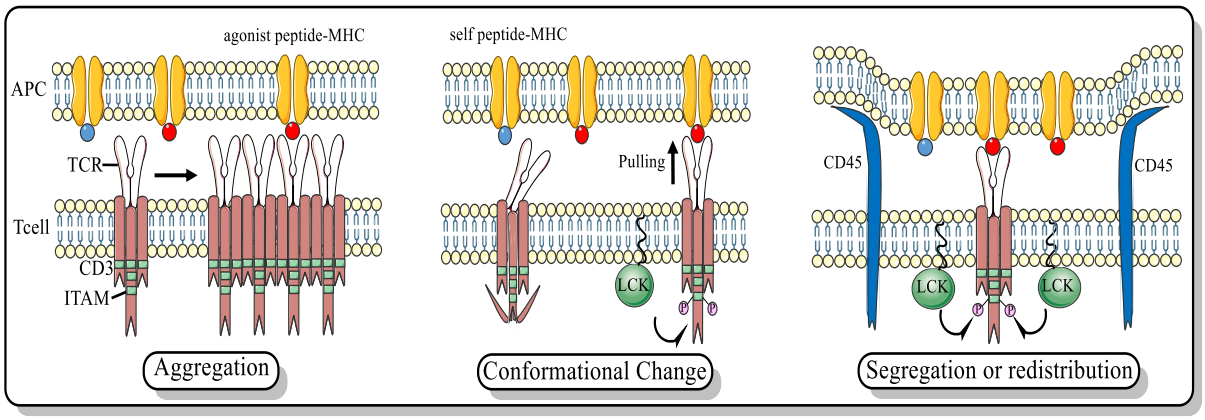

Figure 1-14. Mechanism of TCR triggering. Illustration of three models: aggregation, conformational change and segregation or redistribution. In the aggregation model the binding of the receptor to a high affinity agonist peptide-MHC induces the clustering of second receptors. In the conformational change model, the binding of the agonist peptide-MHC induces a conformational change in the TCR-CD3 complex, such as exposure of the cytoplasmic ITAMs that becomes accessible to the phosphorylation by kinases like LCK. In the third model, the binding of the TCR to the peptide–MHC ligand traps the TCR–CD3 complex in close-contact zones, segregating it from the inhibitory tyrosine phosphatase CD45, and leading to the steady phosphorylation of TCR–CD3 ITAMs by kinases like LCK.

1.1.9.1 Conformational changes

This model proposes that ligand binding induces a conformational change in the TCR that triggers the response. Some particular mechanisms have being invoked in support to this model, i.e. changes in the TCR ectodomains, CD3 ectodomains, and CD3 cytoplasmic regions. However, since the structure of the intact TCR-CD3 complex is not yet resolved, those currently proposed models cannot really address how the ligand binding promote any conformational change in the TCR-CD3 complex.

1.1.9.2 Segregation-redistribution

In this model, the ligand binding induces segregation or redistribution of TCR-CD3 complex with respect to other membrane bound proteins. The TCR-CD3 complex is inserted in the membrane together with other proteins that enhance signaling (like the tyrosine kinase LCK) and molecules that inhibit the signal transduction (such as the tyrosine phosphatase CD45). Experimental evidence[86] suggests that in resting T cells signaling enhancing molecules are constitutively active but their action are counteracted by the presence of phosphatases. Clearly, any event that interrupts this balance will conduct to the increment of the phosphorylation of TCR-CD3 ITAMS, thus to TCR signaling. One way in, which this balance could be altered, is by redistributing the TCR-CD3 complex, for example by separating LCK and CD45 in the membrane surface.

1.1.9.3 Aggregation

The aggregation model had been proposed a long time ago to explain the TCR triggering mechanism. According to this model, aggregation of TCR molecules follows ligand engagement and can lead to trans-phosphorylation of ITAMS in the second receptors by the LCK protein in close proximity. However, some other mechanisms can be found in the literature that account for the triggering within the aggregation model. Some experimental data in support of this mechanism showed that forced aggregation of TCR by soluble antibodies or using multimeric peptide-MHC complexes is sufficient to initiate triggering. In fact, Eisen at al[87], provided evidence that a single peptide-MHC molecule can elicit cytolitic response in T cells. More experimental evidence in support of the aggregation mechanism comes from the work of Irving et al. They showed that T cells expressing the CD4 co-receptor respond with transient signaling to even a single agonist peptide-MHC ligand, and that organization of the molecules in the area of contact between the T cell and antigen presenting cell (APC) adopt their characteristic immunological synapse when about ten agonist peptides are present. They suggest the formation of dimers or aggregates of TCRs leads to activation of the TCR and that the CD4 co-receptor plays an important role in the aggregation process[88].

The inspiration of this project is based on the work of Pennington and colleagues[89] towards elucidating the structural and signaling requirements of TCRγδ in thymocyte development. Their approach was based in the construction of two sets of truncated forms of the TCRγδ receptor (Figure 1-15): the first set lacks the variable regions that include the complementarity-determining regions (CDR), involved in ligand recognition by analogy with the TCRαβ. The second set of truncated receptors lacked both the variable and the constant domains.

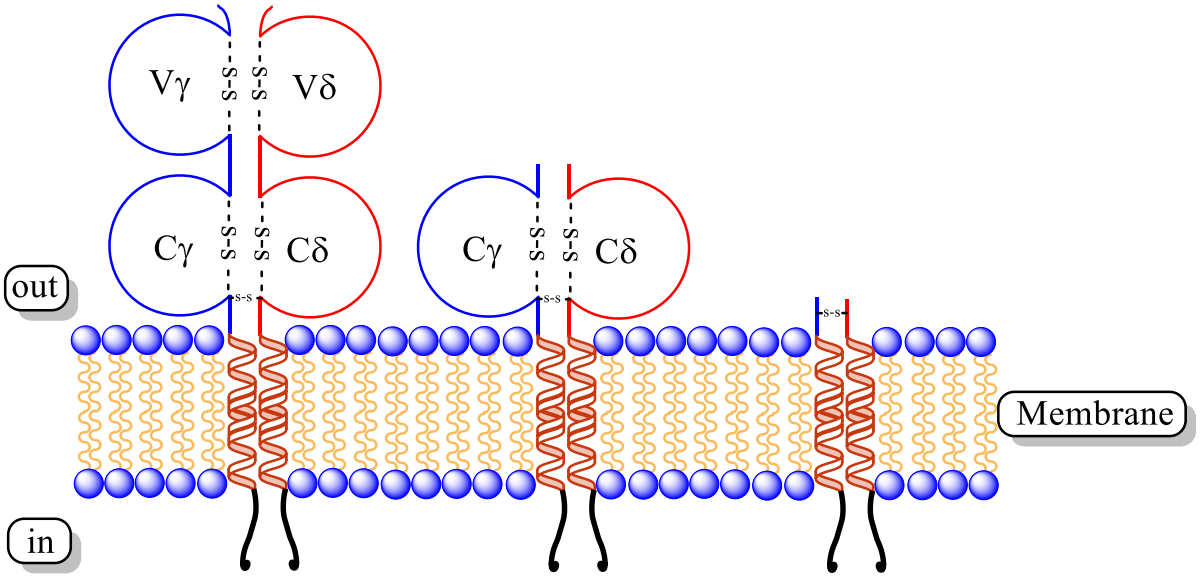

Figure 1-15. Truncated TCRγδ receptors. Figure show the full-length receptor and the truncated forms lacking one or all the Ig domains (Vγ, Vδ, Cγ, and Cδ) with the disulfide bonds indicated.

These truncated forms of the receptor were expressed in immature thymocyte progenitors and the development was analyzed. Interestingly, their results demonstrated that truncated TCRγδ that lacked both the Vγ and Vδ, or that lacked all the extracellular Ig-domains are able to initiate signaling in immature progenitors. They concluded that in early progenitors signaling initiation is independent of ligand binding. In addition, they also demonstrated that signaling initiation was not mediated by oligomerization of the extracellular Ig-domains of the TCR as previously proposed by other authors. Based on this result we decided to investigate how the TCR signal initiation occurs in the absence of any ligand binding.

To address this question we will center our attention in the aggregation mechanism, due to the interest of this thesis in the study of clustering of receptors in model membranes.

To answer this question we set the hypothesis that TCR undergoes aggregation through the transmembrane peptide in a ligand independent manner. By clustering, the receptors are able to concentrate some key molecules e.g. Lck, that enhance phosphorylation of the CD3 ITAMs and triggers signaling initiation. We also hypothesize that the lipid composition of the membrane of early T cell progenitors play a critical role in the clustering of receptors.

1.1.10 Difficulties in the study of receptor clustering.

The cellular membrane is a dynamic structure with many levels of structural complexity[90]. Fujiwara et al. have proposed a mechanism for signal transduction in the plasma membrane that involves three hierarchical stages. The first stage is the membrane compartments, composed of patches of membrane underpinned by the cytosqueleton, interacting with the cytoplasmic tails of the integral membrane proteins. Lipid rafts make the second stage in the organization, which depends of the lipid composition of the membrane. The third level involves the smallest domains constituted by transient aggregates of membrane associated proteins or integral membrane complexes.

It is easy to envisage how complex it is to study the clustering phenomena in such a complex and dynamic system as the cell, where factors like lipid composition, intracellular and intercellular binding events, cytoskeleton interaction and many other parameters can be affecting the clustering of receptors. In addition, it is also very difficult to dissect systematically all these factors in order to understand their contribution to the clustering. Therefore, the use of model membranes, like lipid vesicles, constitute a good approach to focus our attention in determine if ***spontaneous*** clustering of receptors can occur within a simplified lipid environment devoid of the typical complexity of biological membranes.

1.1.11 Synthetic approaches to study receptor clustering in lipid membranes

As mentioned before, given the inherent complexity of biological membranes we have decided to use structurally and compositionally simplified model membranes, i.e. lipid vesicles. The principal advantage of such model systems is that they lack all the complexity of the plasma membrane, i.e. integral membrane proteins, glycolipids, etc. that could interfere with the clustering process. However, it is important to mention that such a reductionist model has the disadvantage to simplify in-extremis the clustering process, eliminating the contributions that other biochemical elements can play in vivo. In the following paragraph, I will described the lipid vesicles, also denominated Liposomes, as these are the model membranes relevant for our study.

1.1.11.1.1 Composition

Liposomes are artificially prepared vesicles consisting of lipid bilayers dissolved in a polar solvent[91]. They are formed when amphiphilic lipids such as phospholipids are dispersed in an aqueous solution[92]. Phospholipids are composed by two long hydrophobic chains joined to a phosphate group by a glycerol linker, forming a head to tail like molecule (Scheme 1.2).

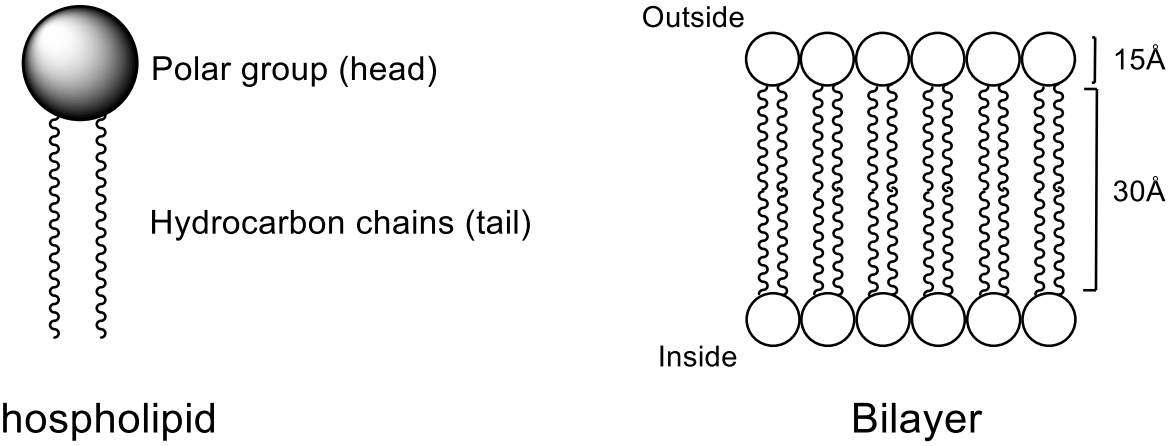

Scheme 1-2. General representation of the phospholipid structure, showing the phosphate group in blue (head), and the aliphatic chains (tail). The scheme also shows how the phospholipids arranged together to form the bilayer, exposing the polar heads to the aqueous solution while the lipids packed internally.

When phospholipids are dissolved in aqueous solutions, they tend to self-assemble acquiring a conformation in which the hydrophobic tails pack together avoiding contact with water molecules, shielded by the hydrophilic phosphate groups that stay exposed to the polar environment. During this rearrangement, phospholipids can adopt, among others, a spherical shape, which corresponds to one of the most entropically favorable conformations[93, 94]. In this process, part of the aqueous solution is trapped in the internal cavity of liposomes, making them ideal vehicles for any kind of hydrophilic compounds dissolved on the media[95, 96]. On the other hand, the bilayer itself can be a carrier for any type of hydrophobic molecule as well (Figure 1-16).

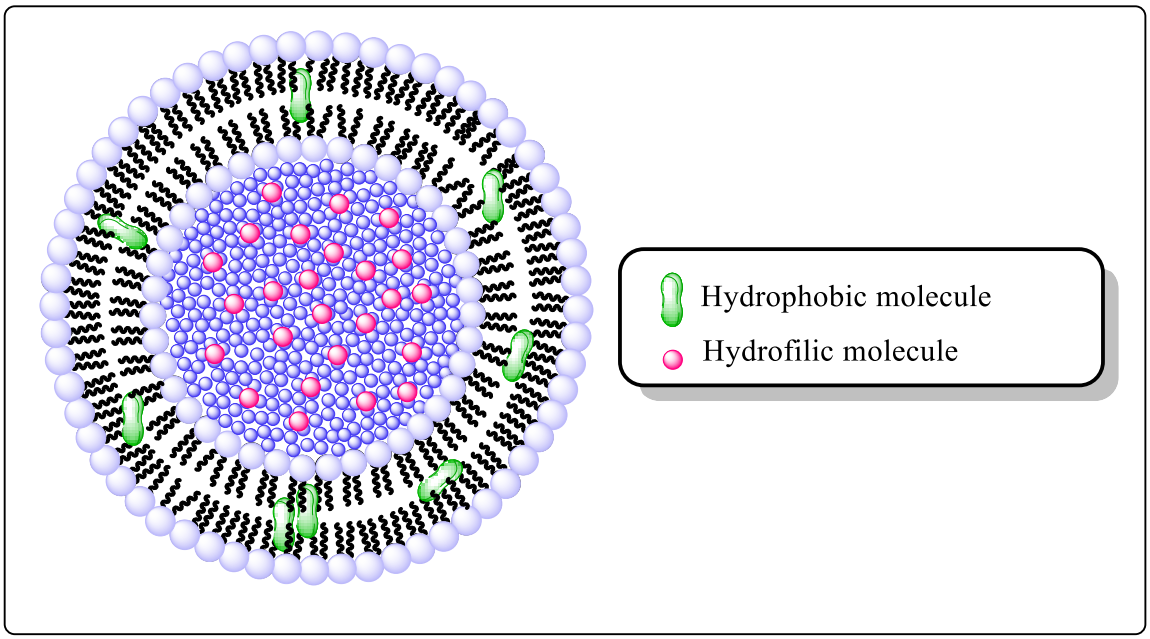

Figure 1-16. Schematic representation of liposome with hydrophilic and hydrophobic molecules trapped in their respective part of the structure. Orange: hydrophobic substance; Pink: hydrophilic compound.

1.1.11.1.2 Types of liposomes

Liposomes can be classified attending to the size of the vesicles, lamellarity, or number of layers that are present in the vesicle into[97] (Figure 1-17):

a. Small unilamellar vesicles (SUV): 20–100 nm
b. Large unilamellar vesicles (LUV): > 100 nm
c. Giant unilamellar vesicles (GUV): > 1000 nm
d. Oligolamellar vesicles (OLV): 100–500 nm
e. Multilamellar vesicles (MLV): > 500 nm

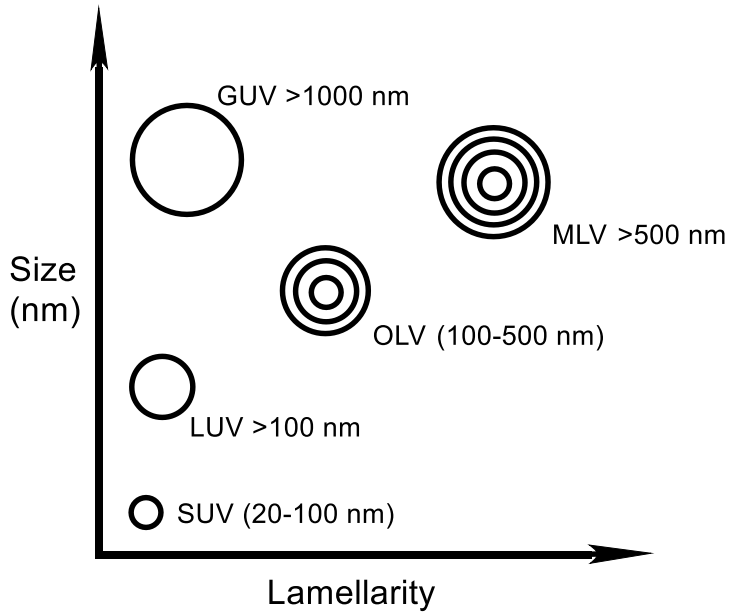

Figure 1-17. Classification of liposomes based on the size and lamellarity.

1.1.11.1.3 Methods of preparation

There are four methods of liposome preparation[94]. The difference between them is based mainly in the way the lipids are dried from the organic solvent in which they are dissolved. For the purpose of this thesis I focus mainly in the classical technique also known as Bangham method[98]: In here, the phospholipid of interest is dissolved in an organic solvent. The solvent is then removed by rota-evaporation under reduced pressure leaving a thin film of the phospholipid attached to the vial wall. Then, an aqueous solution or buffer is added to the vial and the thin film is re-suspended with vigorous agitation.

This method of preparation is very easy to handle but produce a very heterogeneous population of multilamellar liposomes with different sizes. To homogenize the previous liposome mixture a few techniques are implemented. i.e. sonication to produce SUV, or extrusion through a polycarbonate membrane to render LUV liposomes[99, 100].

The extrusion technique (Figure 1-18) is a very straightforward method to produce LUV liposomes with similar size range. By means of a mini-extruder consisting of a stainless steel cylinder bearing the mechanism that contains the polycarbonate membrane and two gas-tight syringes by transferring mechanically the solution multiple times from one syringe to the other obtain in a good quality and high efficiency the desired mixture of liposomes. However, the size of the pore in the polycarbonate membrane is of the utmost importance, due to the fact that only membranes with a pore size $\leq$ 0.2μm will yield the desired LUV liposomes[101].

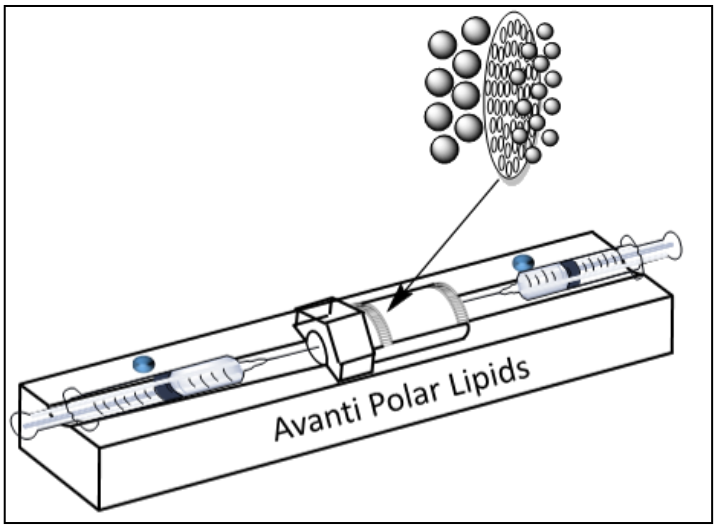

Figure 1-18. Mini-extruder instrument used for the production of the LUV liposomes. Marked with an arrow is the location of the polycarbonate membrane where the extrusion of the crude vesicles takes place.

1.1.11.1.4 Applications of Liposomes

Liposomes have been extensively used since their discovery by Bangham in the 1960's[102]. In the pharmaceutical field, liposomes have being used as systemic and topical drug delivery systems. In this regards, Rowland et al. have shown that liposomes can be used to transport encapsulated drugs through the gastrointestinal tract[103]. Dapergolas et al. published results pointing towards the suitability of liposomes as candidates for oral delivery of peptides, i.e. insulin and proteins[104].

Alving et al. have described the usage of liposomes as carriers of antigens and adjuvants in the development of vaccines[105, 106]. The first liposomal vaccine against hepatitis A was approved in Europe[107] in the 1990's.

In cosmetics[94], the exploitation of the liposomes has grown since the late 1980's. The capacity of the liposomes to retain water molecules in their interior is a major advantage to deliver hydration to the skin and combat dryness, which is one of the causes of ageing of the skin. Products such as Capture by Cristian Dior, Efect du Soleil by L'Oréal and Future Perfect Skin Gel by Estée Lauder are based on liposomes carrying different ingredients like: Vitamin E, A, cerebroside, ceramide, tanning agents, etc.

Another important application of liposomes is in the agro-food industry. The liposomes can be prepared with pesticides, fungicides or herbicides that can have a prolonged action time. By adding some components to the liposome membrane we can make it sticky thus, staying attached to the plant for a longer time delivering the active compound[108].

1.1.12 Biomimetic models

In this section, we will describe some examples of systems where synthetic approaches have been employed to study the clustering of proteins. Depending on the components, these systems can be synthetic when all the components are chemically synthetize or biomimetic. The biomimetic systems usually contains a biological molecule, as a protein or peptide.

1.1.12.1 Synthetic models

Tomas et al.[109] with the aim to study the relationship between embedded-receptor clustering and binding of ligands in the absence of any multivalence, developed a synthetic system based on a zinc-metalloporphyrin molecule as a model of membrane receptor, soluble nitrogen-containing molecules as ligands, and unilamellar liposomes as model membranes. (Scheme 1-3). When studying the binding of ligands to membrane embedded receptor, most of the published studies assume that ligand binding is based on: 1) the effect of the membrane-water interface in the binding affinity of the ligands, 2) the effect of the membrane-embedded receptor on the multivalent effect of the ligand. Working with monovalent ligands, Tomas et al. demonstrated that in fact a cooperative effect between the binding of monovalent ligands and the clustering of membrane-embedded receptors exists, that is only evident when the receptors are in-membrane and most important that is not dependent of any multivalent effect.

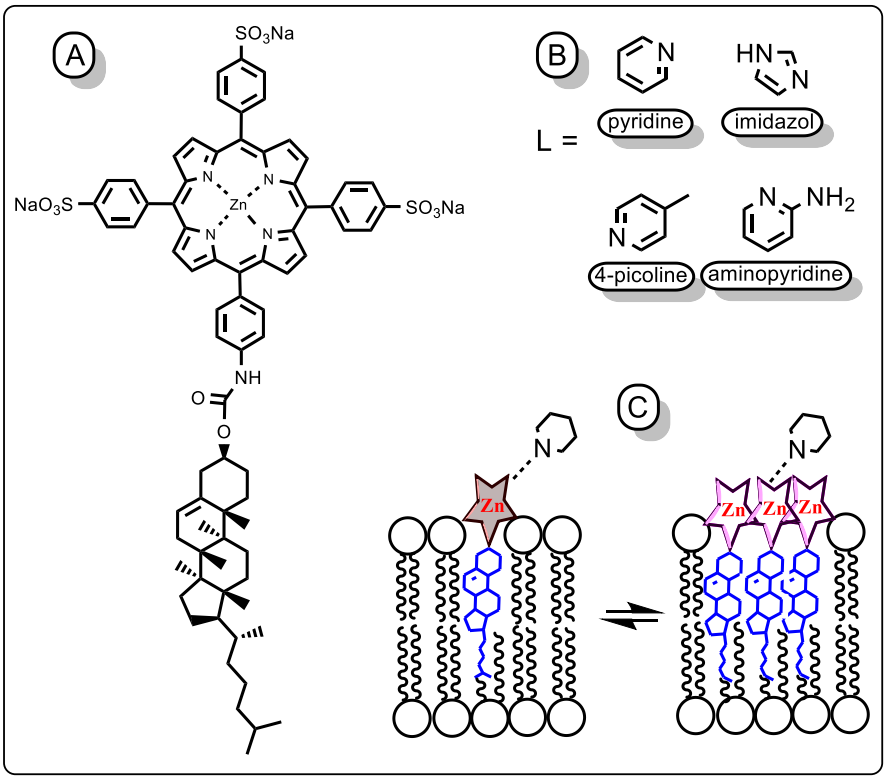

Scheme 1-3. Porphyrin cholesteryl receptor and N-bearing ligands used in the study of Tomas et al. A) Chemical structure of the receptor. B) Chemical structure of some of the ligands used in the study. C) Representation of the equilibrium of membrane-embedded receptor with a ligand L. The change in colour represents the ability of the porphyrin to report on clustering.

For the sake of clarity, we will describe briefly the synthetic approach used in this work to the reader; also because it was the model for the design of our experimental approach in this study. To generate an amphiphilic membrane embedded-receptor Tomas et al[110] linked a cholesterol molecule to the zinc-metalloporphyrin (Scheme 1-3, A). Cholesterol is an important constituent of biomembranes. The porphyrin contains three ionized sulfonate groups that force the porphyrin head group towards the water media, and adopting a perpendicular position in respect to the plane of the membrane, as observed previously[111]. The zinc atom provides the receptor the capacity to form complexes with nitrogen bearing ligands that have

moderate stability in aqueous media. In addition, the porphyrin is the clustering reporter due to its spectroscopic properties being different for the monomer and the aggregate forms.

This chemical approach was used to study clustering of embedded receptor in model membranes, and in particular, how ligand binding modulates clustering. The authors concluded that a cooperative effect between ligand binding and receptor clustering exists. They observed that ligand binding was able to modulate clustering of receptors. Moreover, they also reported that clusters of receptors showed different affinity towards ligands in solution, compared to the monomers. However, this phenomenon was not obvious when both the ligand and receptor were in solution. Of note, they proposed a model to analyse the receptor clustering i.e. a binding-clustering thermodynamic cycle that in principle could be extended to any other system formed by a ligand and a membrane embedded receptor, like our biomimetic model. This study also demonstrated how simplified synthetic models can be used to address complex biological events.

As a second example of a synthetic model we would like to present the work done by Clayden et al.[112] In a recent study, they reported the design and synthesis of a photo responsive helical molecule that can be inserted in the membrane bilayer to study the changes in its conformation when photo-stimulated. The aim of this study was to create a synthetic analog of the membrane-spanning segment of a protein conjugated with a molecule that can be used to track conformational changes in-membrane to study the effect of the phospholipid bilayer over the conformational changes of membrane-embedded molecules. The helical molecule or foldamer[113] is a synthetic polymeric molecule with a known conformational state built from oligomers of 2-aminoisobutyric acid (Aib). This foldamer shows a strong preference for the helix conformation and can adopt alternatively two different modes, the left-handed or the

right-handed sense. To the foldamer, they linked covalently an azobenzene[114] motif that is known to show reversible conformational changes driven by the light. The stimulation of the azobenzene at a certain wavelength triggered a conformational change that induced a change in the geometry of the foldamer that was tracked by proton magnetic resonance spectroscopy (^{1}H-NMR), which is a technique that helps to determine the chemical structure of the molecules. Briefly, with the ^{1}H-NMR we can identify the proton framework of an organic compound and from here elucidate its entire structure, in conjunction with other analytical techniques such as mass-spectrometry and infrared spectroscopy. Their results showed that indeed it is possible to modify the conformation of this foldamer embedded in the lipid bilayer after being photo-stimulated, replicating the results observed for these molecules in solution. Most interesting, this work also demonstrates that simplified synthetic models can be design to mimic essential process, such as conformational changes of proteins that are embedded in lipid bilayer, that are not normally achievable in the more complex biological systems.

In a different study conducted by Clayden et al.[115] they designed, synthetize and characterized probes of bis(pyrene) to report conformational changes in membrane embedded foldamer. The bys (pyrene) probe was designed to be able to distinguish between each of the conformers, left-handed (M) or right-handed (P) of the helix (Figure 1-19). As mentioned in the previous example, the foldamer is made of α-aminoisobutyric acid (Aib) peptide. The use of the pyrene as a fluorescence reporter of conformational changes is based on its capacity to show different emission spectra in the monomer and the dimer states (excimer). The excimer emission is observed when two pyrenes are close together as shown in Figure 1-19. In this study, they observed that this reporter successfully allowed the investigation of how the chirality of phospholipids affected the conformation of the foldamer embedded in the bilayer.

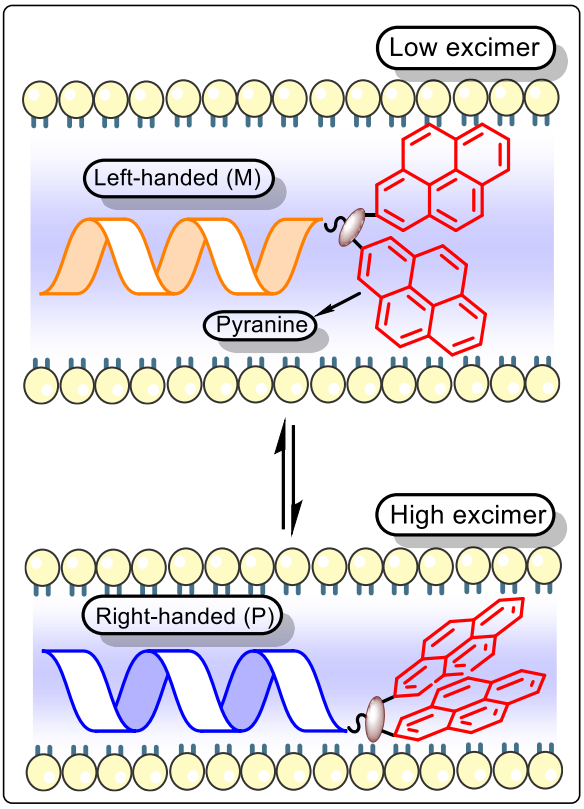

Figure 1-19. Schematic representation of bis (pyrene) probe attached to M and P conformers, showing the change in the relative position of the fluorescence probe in each conformational position.

1.1.12.2 Semisynthetic models

In this section, we would like to present three published examples of semisynthetic models used in the study of protein clustering and membrane fusion.

1.1.12.2.1 N-Ras

The first study consists of the work developed by Winter et al.[52] With the aim to explore the insertion and partitioning of the protein N-Ras in model membranes, they synthetized in solid phase a lipid modified peptide containing farnesyl and palmytoil anchors, which are known to drive protein insertion in membranes[50]. This lipidated-peptide was further modified to have in the N-terminus a maleimidocaproic acid, and in the C-terminus the boron-dipyrromethene (BODIPY-FL) label, a fluorescent dye. In a similar approach to our project, the maleimide-peptide was tethered to N-Ras through a cysteine exposed on the protein surface. The addition of the sulfhydryl group to the maleimide function is shown in Figure 1-20. The model membrane was prepared from a binary phospholipid mixture of 1-palmitoyl-2-oleoylphosphatidylcholine (POPC), sphingomyelin and varying levels of cholesterol which is known to produce lipid microdomains with two fluid phases, liquid disordered (l_d) and liquid-ordered (l_o) in giant vesicles[116] (see section 1.1.11.1.2). Their results provide evidence that partitioning of N-Ras occurs preferentially into the liquid disordered (l_d) lipid domains, concomitant with faster kinetics of incorporation into the fluid lipid bilayers. In addition, they detected that a large proportion of lipidated N-Ras locates at the interface of the l_d/l_o phases leading to a decrease in the tension localized in the two phases boundary. They suggested that this interfacial adsorption effect could be the vehicle for clustering of signalling proteins in membranes.

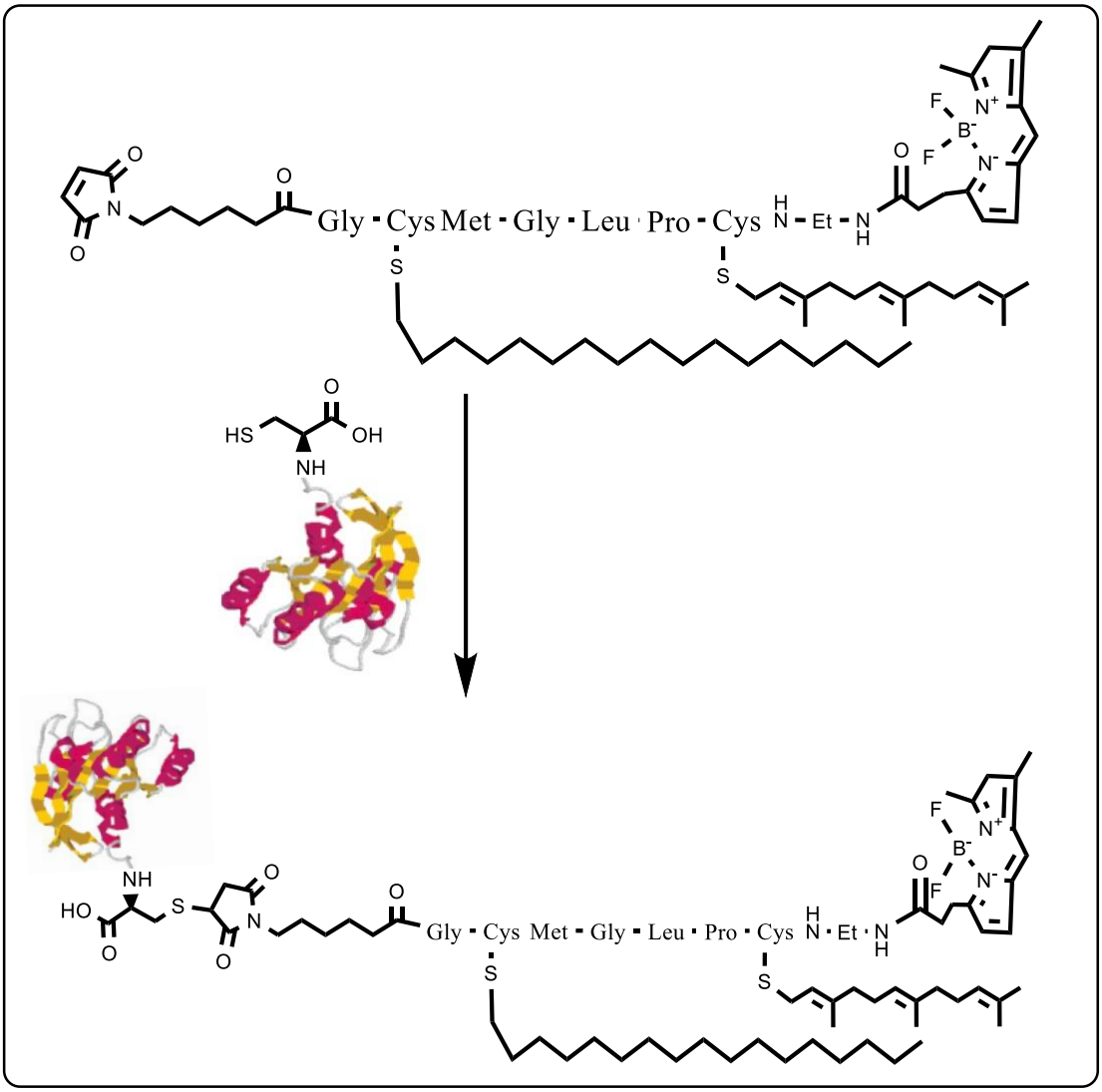

Figure 1-20. Schematic representation of the labeling reaction between the semisynthetic Ras protein with the C-terminal peptide containing the palmitoyl and farnesyl anchors. The C terminal peptide is labeled with the BODI-PY fluorescent dye. It was introduced by a Michael addition between the surface accessible cysteine (181) and the maleimide function introduced in the peptide as shown by Winter et al.

1.1.12.2.2 Study on the effect of cholesterol and phosphatidylinositol 4,5-bisphosphate PI(4,5)P_2 over the syntaxin clustering.

Tamm et al[56] aimed to study the molecular mechanisms of cholesterol and phosphoinositide's mediated syntaxin (Syx) clustering. As mentioned in the section 1.1.5.2 the SNARE complex is a molecular machinery that governs membrane fusion in neuronal synapsis through the participation of syntaxin-1A, SNAP-25 in the presynaptic membrane and synaptobrevin in the synaptic vesicle. There is ample evidence regarding the key role of syntaxin in the SNARE acceptor complex in interaction with the SNAP-25. However, the dynamics and equilibrium of the interaction of Syx-SNAP-25 is poorly understood. It has been shown that Syx oligomerization is dependent on the cholesterol concentration in several cell types. The importance in the clustering process of the residues located in the N-terminal segment of the SNARE domain was also explored. However, the authors of this study also believed that the polybasic region of approximately 10 residues that connect the SNARE motif with the transmembrane segment and the presence of anionic lipids is very important in the clustering process. Moreover, previous studies have demonstrated, that phosphatidylinositol 4,5-bisphosphate (PI (4,5) P_2) interacts with Syx electrostatically, disrupting the syntaxin clusters. To understand the molecular events that control the interaction between Syx and anionic lipids they created a semisynthetic model of Syx coupled to a fluorescence cluster reporter and a model membrane composed of POPC/POPS/phosphoinositides and cholesterol. To generate the fluorescently labelled protein, they expressed the Syx protein with an extra cysteine in the C-terminal. The fluorescent tag, Alexa Fluor 647, contains the maleimide function that will react with the reduced cysteine for the addition of the tag. Of note, to check the orientation of the modified-protein in the proteoliposomes they used the trypsin digestion and

subsequent SDS-PAGE, observing that approximately 90% of the inserted protein was in the right orientation with the N-terminus exposed to the extra-liposomal side and the C-terminus with the fluorophore towards the lumen. The insertion efficiency of the protein was determined by fluorescence spectroscopy in samples of liposomes solubilized with detergents. Clustering-dispersion studies were conducted following the self-quenching of the fluorescence probe (Figure 1-21).

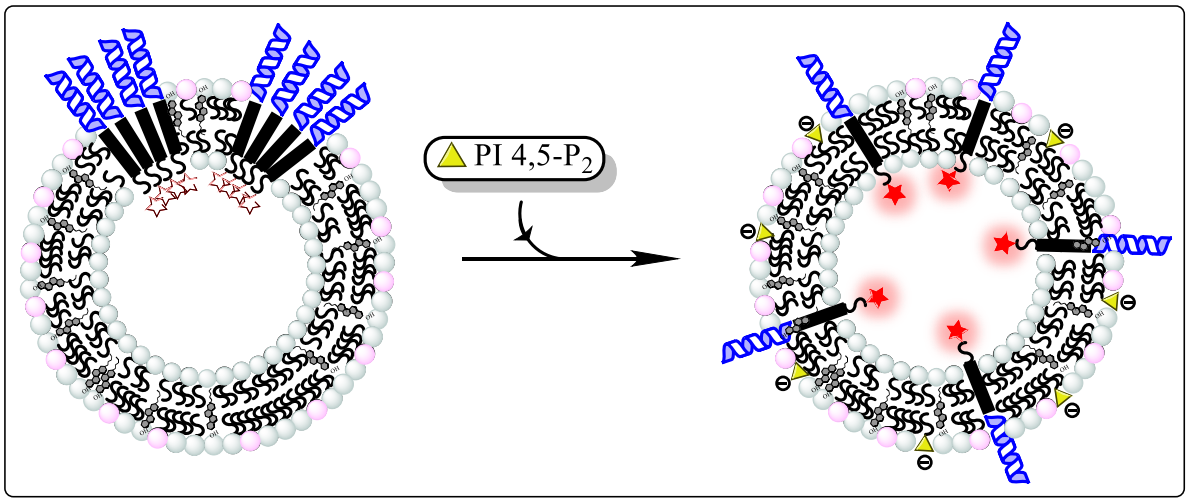

Figure 1-21. Cartoon model depicting how the cholesterol-dependent clustering of syntaxin-1A is reduced by the presence of anionic lipids, such as phosphatidylinositol 4,5-bisphosphate (PI (4,5) P_2). The disaggregation of the syntaxin-1A is followed by the weakening in the self-quenching of the Alexa-Fluor 647 attached to the Sintaxin-1A.

The results of this study showed that all types of phosphatidylinositol (PI) disrupted the clusters of syntaxin. This result suggested that syntaxin disruption was not selective towards a particular PI member. Moreover, they observed that after formation of Syx clusters the protein SNAP-25 was not able to bind it anymore. By contrast, when Syx was in the monomeric form the SNAP-25 was able to bind it and the union precluded formation of new clusters. They concluded that syntaxin-1A and synaptobrevin both interacted directly with PI (4,5) P_2 and that this interaction activates fusion.

2 CHAPTER 2

2.1 **INTRODUCTION.**

In this chapter we will describe the synthesis of the maleimide-porphyrin derivative (Scheme 2-1), and the reason why we choose this molecule as the target compound.

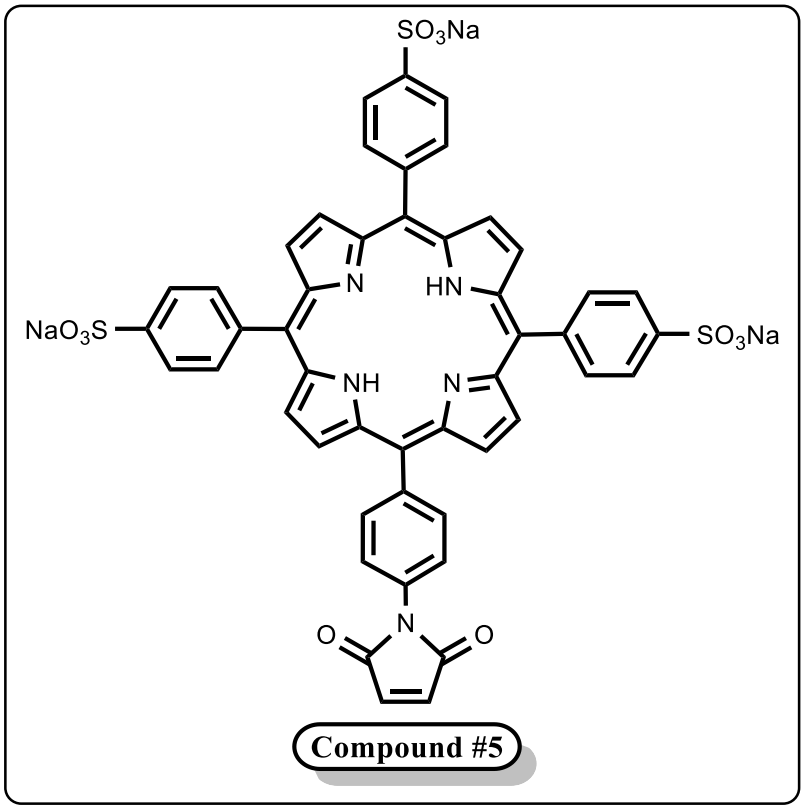

Scheme 2-1. Maleimide – porphyrin derivative (compound #5). Target molecule of this doctoral thesis.

2.2 OBJECTIVES

One of the main objectives of this work was the synthesis in four steps of the compound 5-(4-maleimide-phenyl)-10, 15, 20-tris (4-sulfonatophenyl) porphyrin. The interest in the synthesis of this compound was based on two major characteristics:

1. The property of porphyrin macrocycle to respond upon aggregation displaying different optical signatures, with the traces belonging to the monomer and aggregate clearly differentiated. This application of porphyrins is based on previous work by Tomas and Milanesi[109]. As they demonstrated, the porphyrin group showed distinct optical properties when it formed aggregates at the lipid/water interface (see Introduction, Section 1.1.12.1).
2. The possibility to link the hydrophobic peptide through a Michael addition reaction between the sulfhydryl group in the flanking cysteine of the peptide and the maleimide function. As explained in Chapter 4 section 4.2.1, the hydrophobic peptide contains the amino acid sequence of the transmembrane segment of Vγ7Jγ1Cγ1 TCR chain. In this study, we aim to elucidate the aggregation capacity of the transmembrane peptide inserted in model lipid vesicles. We hope this approach will provide some preliminary results on the self-assembling capacity of the TM peptide. This might help to elucidate some key aspects of the signaling mechanism of T cell receptor. The rationale in support of this approach is based on the work reported by Pennington's group discussed in the Introduction, Section 1.1.9.3.

These properties will be used in the construction of a chemical model that might provide a better understanding of the mechanism of T cell receptor signaling in model lipid bilayers, which is the major objective of the first part of this thesis.

2.3 **PORPHYRINS**

The porphyrins are a group of heterocyclic and aromatic compounds constituted by carbon, hydrogen and nitrogen. The structure of porphyrins was elucidated by Hans Fischer in 1927[117]. Porphine is the simplest molecular member of the group, and was very important because its ring system is the fundamental ring system of all porphyrins. It is composed by 24 atoms arranged in a macrocycle; the macrocycle is formed by four pyrroles rings linked by four methine bridges (Scheme 2-2).

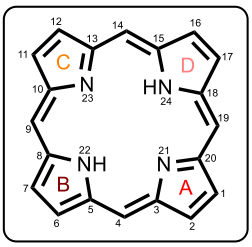

Scheme 2-2. Porphyrin macrocycle

This macrocycle is susceptible to several modifications. The flexibility in the number of substitutions produces a vast repertoire of different physical and chemical properties that confer great interest to the porphyrin family. The macrocycle can bear additions in the β position of the pyrrole ring to render porphyrins similar to those found in nature. Moreover, it is also possible to add some substituents in the δ positions in the methine bridges –the so called meso-substituted porphyrins- and this product, by contrast, does not have an analog in biological systems. Based on these two types of substitutions porphyrins can be classified and

studied in two main groups: the β-pyrrole substituted and the meso-substituted poprhyrins (Scheme 2-3).

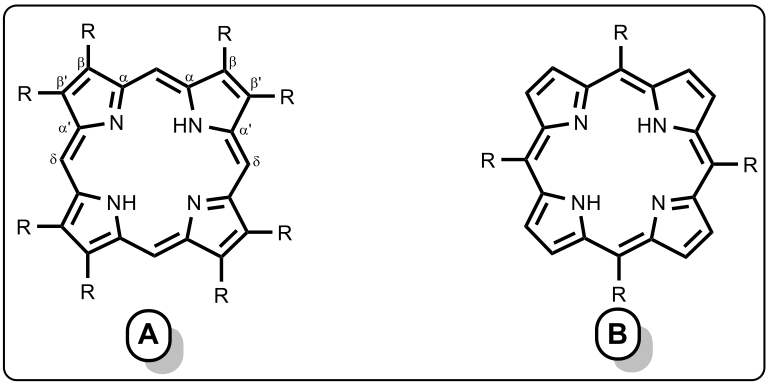

Scheme 2-3. Types of porhyrines. (A) β-pyrrol subsituted. (B) meso-substituted.

The family of porphyrins has been much studied due to its electronic and optical properties as explained in chapter one. One of the major strengths of porphyrins reside in their flexibility towards modification. This advantage allows the introduction of many substituents in the macrocycle, with the concomitant variation in its general properties. These modifications can be used to tune porphyrins in different ways. Due to its almost limitless capacity of modification, porphyrins can be used in multiple applications e.g.: as sensors[118], catalysts[119], solar cells[120], medicine due to their antitumor and radiosensitizing effects on cancer cells[121], and in photodynamic therapy[122].

2.3.1 The meso-substituted porphyrins

The first synthesis of this type of porphyrin was reported by Rothemund in 1935[123]. Reacting pyrrole in a saturated solution of acetaldehyde in methanol heated in a sealed tube at 85-90°C produced the α,β,γ,δ-tetramethylporphin. The same author published works in the synthesis of other meso-tetrasubstitutedporphyrins[124]. The synthesis of the α,β,γ,δ-tetraphenhylporphin (TPP) was first described for Rothemund in 1941[125].

He condensed pyrrole and benzaldehyde in pyridine solution, in sealed tubes at 220°C for forty-eight hours. The product crystallized from the solution in the form of lustrous deep blue needles crystals (Scheme 2-4).

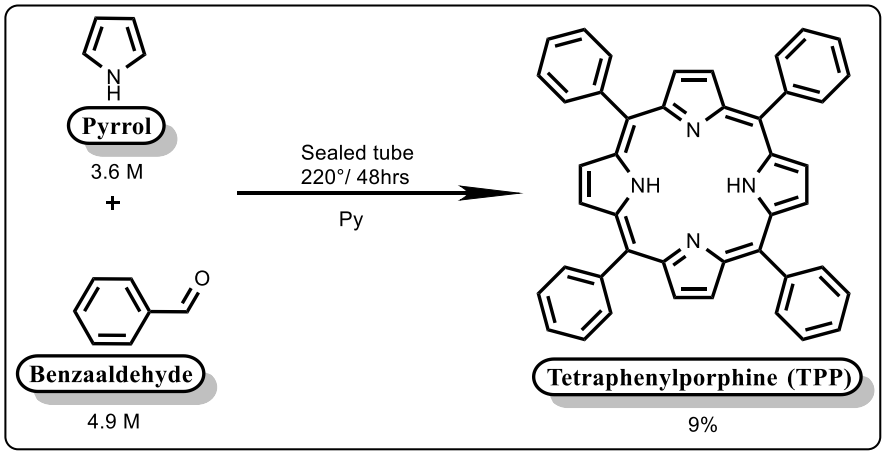

Scheme 2-4. First synthesis of the α,β,γ,δ-tetraphenhylporphin (Rothemund's synthesis)

The TPP is a commercially available reagent today, very important in the synthesis of many porphyrin derivatives, specially nitrosilated, and sulfonated porphyrins.

2.3.2 Background to the nitration of the meso-tetraphenylporphyrin.

Interest in the production of asymmetrically functionalized aryl-porphyrins has led to extensive research. The use of this type of aromatic substitution is very useful in order to produce posterior modifications in the porphyrins that will allow the covalent incorporation of porphyrins into macromolecules, e.g.: monoclonal antibodies[126], nucleic acids[127], polymers[128], etc. One of the many problems related with this reaction is that any peripheral functionalization of the porphyrin with electrophiles or radicals led to the modification of the macrocycle at either the meso or the β-pyrrole carbons[129]. The only exception known to this outcome is the electrophilic reaction with sulfuric where the aryl group is attacked without the parallel substitution of the macrocycle[130, 131].

The first synthetic routes found in the literature to prepare the compound 5-(4-Nitrophenyl)-10, 15, 20-tryphenylporphyrin (Scheme 2-5) are all derived from Rothemund's condensation and were associated with a very low yield production (<5%)[128, 132-134].

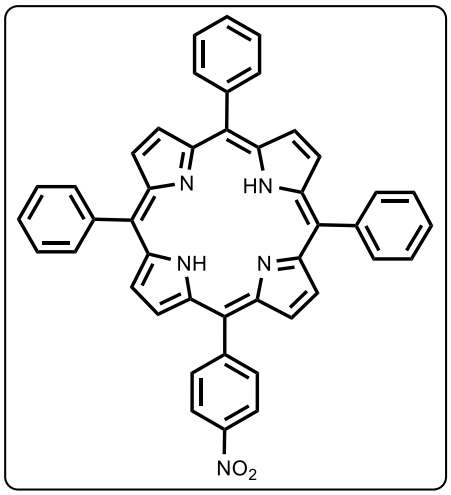

Scheme 2-5. Compound 5-(4-Nitrophenyl)-10, 15, 20-tryphenylporphyrin.

However, in 1989 the group of Kochany et al[129] published a procedure to produce the controllable and highly regiospecific nitration of tetraarylporphyrins. When a chloroform solution of tetraphenylporphyrin (TPP) was treated with excess fuming nitric acid the selective and stepwise nitration of the aryl groups at the para position occurred. The yield of the reaction was good (yield = 55%) although the dinitro-TPP side-product was also found, but in a much lower yield (7%). Use of chloroform proved very appropriate for the selectivity of the mononitration although other solvents such as methylene chloride had been tested. Although the use of a large excess of oxidant can result in damage to the macrocycle producing its degradation. This procedure had been optimized by our group to achieve the mononitration of the TPP with a better yield and a reduction in the reaction time of nearly five-fold (66%, 25 min vs 55%, 120 min).

2.3.3 Background to the reduction reaction of the mono-nitrophenylporphyrin.

There are a few methods in the literature describing the reduction reaction of nitro-porphyrin derivatives to render the amino products. The group of Dr Kochany describe a method of reduction based on the modification of Hasegawa's procedure[128]. This procedure is used in our synthesis and will be explained in detail in the experimental section of this chapter (Scheme 2-6)

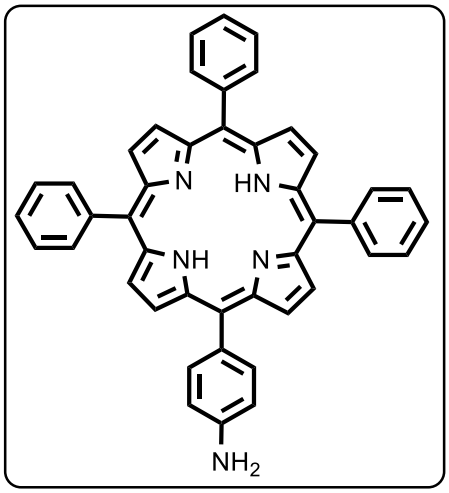

Scheme 2-6. Compound #5-(4-Aminoophenyl)-10, 15, 20-tryphenylporphyrin.

In June 2017, shortly after we had already completed successfully the synthesis of the target molecule (Compound #5) in quantities sufficient for our experiments, a new procedure for the reduction of nitroarenes was published. Royo et al. described the use of a nickel–NHC (N-heterocyclic carbene) complex in conjunction with phenylsilane as a reducing agent of nitroarenes[135] (Scheme 2-7). Their results showed that reduction is chemoselective towards the nitroarenes and tolerant with a wide range of functional groups like halogens, cyano, hydroxyl, ketone, amide, methoxy, and ester groups, likewise the reduction with tin chloride and hydrochloric acid. However, in terms of yield, their procedure showed an improvement

in the conversion of the Cu^{II} β-nitroporphyrin of ninety-four per cent (94%), while the conversion in the reduction of the mono-nitrophenylporphyrin was seventy-four per cent (74%). Unfortunately, the duration of the reaction stated in this protocol is longer compared to our reaction time (15 hours vs 3 hours). Hence, this catalyzed reaction, is a good alternative to the canonical reduction with tin chloride and hydrochloric acid, based on the better yield reported in spite of the long reaction time. From the point of view of Health and Safety, it is also recommendable especially when taking into consideration the high toxicity associated with the use of tin salts.

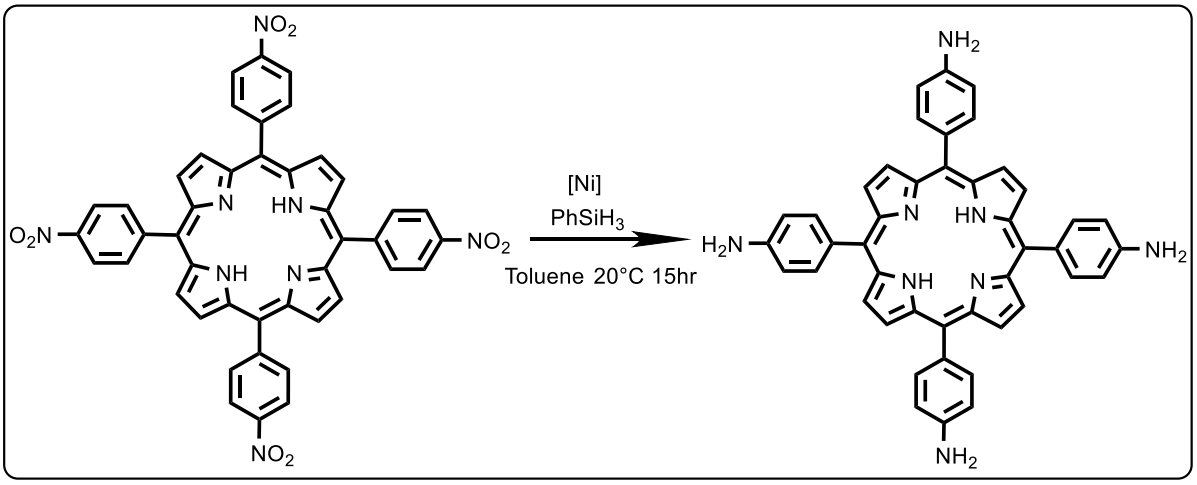

Scheme 2-7. Reduction of 5,10,15,20-tetra-(nitrophenyl)porphyrin (TNPP).

2.3.4 Background to the sulfonation of tetraphenylporphyrin.

Functionalization of porphyrins by adding different groups to the macrocycle is a way to produce a huge amount of new compounds that will be otherwise difficult to synthetize with de novo routes. There are a few methods in the literature regarding the electrophilic and/or nucleophilic substitutions in the meso or the β-pyrroles positions dependable on the different conditions of reactions and the steric hindrance present in the molecules[136-138].

In porphyrins with the meso-positions available, the sulfonation occurred preferentially at the β pyrrole carbons[139]. By contrast, in meso-tetraarylporphyrins (Scheme 2-3) the sulfonation occurred preferentially at the meso-aryl groups[129, 140]. The reaction of tetraphenylporphyrin (TPP) with sulfuric acid produces substitution in the para-positions of aryl groups and no substitution at the β-pyrrole carbons. The extension of sulfonation in TPP is variable as shown in Scheme 2-8[141].

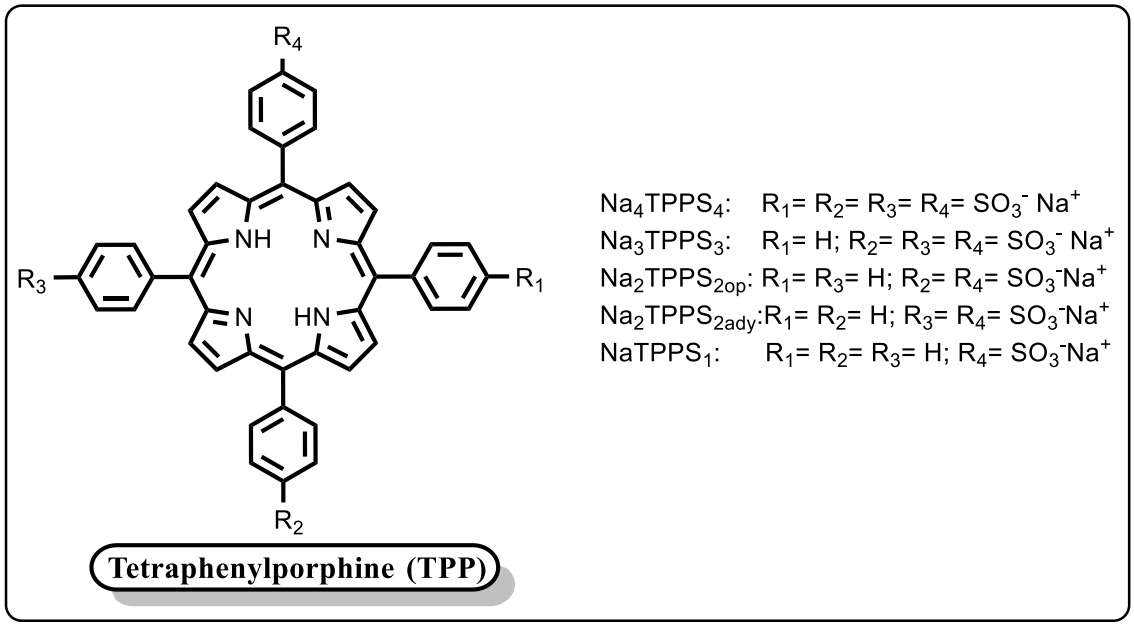

Scheme 2-8. Sulfonated porphyrins after the reaction of TPP with H_2SO_4 conc.

2.3.5 Background to the reaction with maleic acid imides (maleimides)

Maleimides are derivative compounds from the reaction of maleic anhydride with ammonia or any amine (Scheme 2-9).

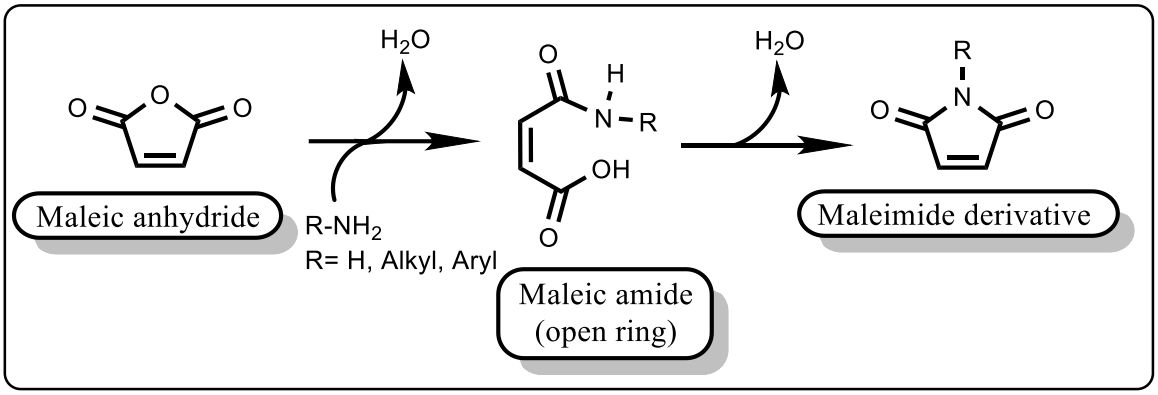

Scheme 2-9. Synthesis of the maleimide derivate.

In 1948, Friedman et al[142] studying the antimitotic effect of maleic acid and similar compounds determined the existence of a certain parallelism between the mitotic inhibition and -SH uptake. In 1955, Gregory et al[143] studied the reaction of N-ethylmaleimide with sulfhydryl groups and concluded that the rate of the reaction was a function of the pH. The reaction performed at a pH close to neutrality (6.7 to 7.5) was enhanced while in the basic range hydrolysis of maleimide competes with the sulfhydryl's addition reaction. These initial experiments demonstrated that the double bond in maleimides can undergo an alkylation reaction with sulfhydryl groups to form stable thioether bonds at neutral pH (Scheme 2-10). Maleimides can also react with amino groups of peptides, with imidazole group of histidine[144], and with α-amino of amino acids[145], but the rate of reaction at neutrality is 1000 times slower than the reaction with the sulfhydryl group[146]. Due to the presence of the thiol group in some rare aminoacids, and the fact that we can introduce them via synthesis or by

recombination technology in target proteins, their reaction with maleimides have become widely used in the construction of bio-conjugates, e.g. as a crosslinker[147].

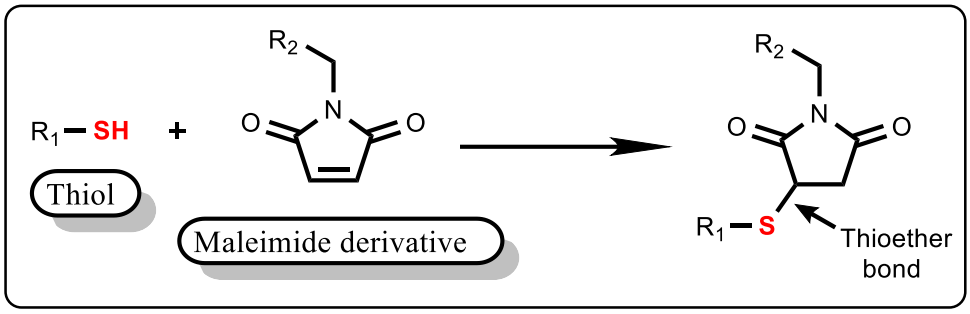

Scheme 2-10. Generic reaction between the sulfhydryl group and maleimide to form a thioether bond.

The maleimide group can also suffer hydrolysis to become unreactive. This reaction also occurs after coupling of sulfhydryl groups. The opening of the ring is proportional to the basic strength of the solution, higher pH correlates with faster hydrolysis, and is also subjected to the type of chemical group that might be attached to the maleimide function. For example, some groups can provide an increase in the stability of the maleimide towards hydrolysis e.g. the cyclohexane ring of the succinimidyl 4-[N-maleimidomethyl] cyclohexane-1-carboxylate (SMCC)[146].

2.4 RESULTS AND DISCUSSION

2.4.1 Synthesis of 5-(4-Nitrophenyl)-10, 15, 20 try-phenylporphyrin (Compound #2)

For the synthesis of compound #2 we followed the method described by Kochany et al.[129]. However, this methodology was optimized in order to improve the velocity of the reaction, the yield, and purification step. (Scheme. 2-11)

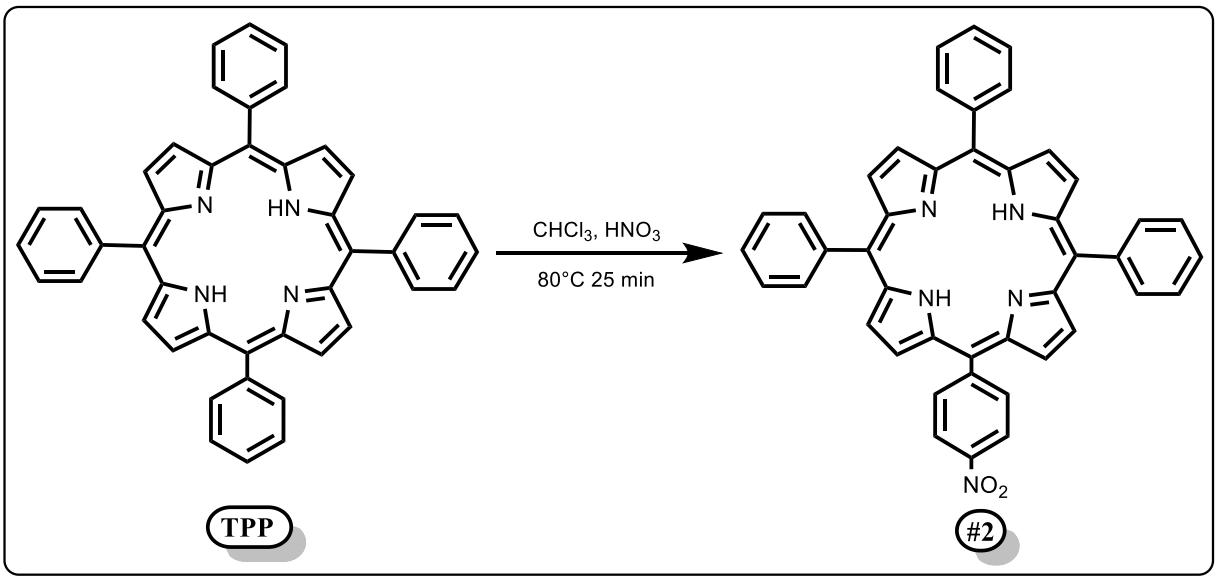

Scheme 2-11. Synthesis of compound #2

In this reaction one of the phenyl groups of the TPP undergo an electrophilic attack from the nitric acid with the substitution of one of the aromatic hydrogens in the *para*-position with a nitro group ($-NO_2$).

One of the optimizations that we had introduced in the protocol was the increase of temperature of reaction from 5 to 60^{o}C, compared with the published protocol[148]. In this way, we could speed up the formation of the mononitro porphyrin.

However, due to the lack of selectivity in the nitration of the para positions of the tetraphenylporhyrin, this increment in temperature was problematic because it produced rather quickly the non-desired di, tri or tetra-nitroporphyrin derivative. To overcome this problem, we monitored the reaction via thin layer chromatography (TLC) regularly (every 5 minutes) until we detected the second spot on the plate. Immediately after, the reaction was quenched by cooling down the mixture. Following this procedure, we were able to obtain a better yield in the formation of the mono-nitroporphyrin with a considerable reduction in the reaction time (66% 25 min vs 55% 120 min).

Due to similarities in the molecular structure of the products in the crude, and the small differences in polarity, we observed very subtle variation in retention factor, hence, the separation of the mono from the dinitro-porphyrin derivative was very difficult when we used chloroform ($CHCl_3$) as recommended in the original protocol. To improve the outcome of the purification we performed several trials with different combinations of solvents (see below). We found out that isocratic elution of the mixture using petroleum ether, ethylacetate, and methanol (97:2:1) produced best separation and yield. (Figure 2-1, Table 2-1). Miss Priya Limbu, one master student in our group, working on the same purification, employed gradient elution starting from 30% chloroform in petroleum ether and finishing with 40% chloroform. Her results showed a low yield (28%) with this elution method.

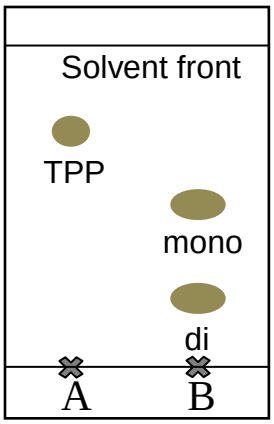

Figure 2-1. TLC showing the migration of tetraphenylporphyrin (A), mono-nitroporphyrin, and dinitroporphyrin compounds (B).

Compound	$R_{f(97:2:1)}$	$R_{f(CHCl_3)}$	$R_{f(DCM)}$
Tetraphenylporphyrin (TPP)	0.83	0.92	0.91
Mono-nitroporphyrin (#2)	0.60	0.90	0.87
Di-nitroporphyrin	0.26	0.87	0.85

Table 2-1. Calculated R_f values for the reaction crude eluted with petroleum ether, ethyl acetate, and methanol (97:2:1), chloroform ($CHCl_3$), and dichloromethane (DCM).

The ^{1}H-NMR spectrum recorded for the compound #2 is in agreement with the published data[129]. The chemical shift and the calculated integrals are in accordance with the structure and the twenty-nine hydrogens presents in the purified mono-nitroporphyrin (Figure 2-2). Twenty-seven of these protons showed resonances in the aromatic region of the spectra. Starting from the most downfield proton we found a doublet at 8.81 ppm with an integral value of two that corresponds to the proton **a** of the β-pyrrole ring. At 8.79 ppm we have a singlet with an integral value of four that correspond to the four protons assigned as **b** in the β-pyrrole ring. The next resonances appear at 8.67 ppm and belong to protons assigned as **c** at the β carbon of the pyrrole ring. The next doublet at 8.56 ppm and integral value of two

corresponds to the protons **d**; they are located in the *ortho*-position, adjacent to the nitro function. The protons **e** in the *meta*-position appeared at 8.33 ppm and the integral value correspond to two protons. Protons **f** in the *ortho*-positions of the three peripheral phenyl group appear as a multiplet in the region 8.27- 8.18 ppm with an integral that corresponds to six protons. Protons in the *meta/para*-position of the three phenyl rings assigned as **g** + **h** appears as a multiplet from 7.89 – 7.70 ppm; the integral showed a value that corresponds to nine protons.

The last two protons correspond to the NH pyrrole inside the macrocycle. The negative value of the chemical shift -2.76 ppm is due to these protons being heavily shielded by the porphyrin electronic cloud, and the integral value corresponds to two protons. As this compound had already been synthetized, and the introduction of nitro group had been well characterized by ^{1}H NMR; we considered this analysis to be sufficient to ascertain the successful substitution.

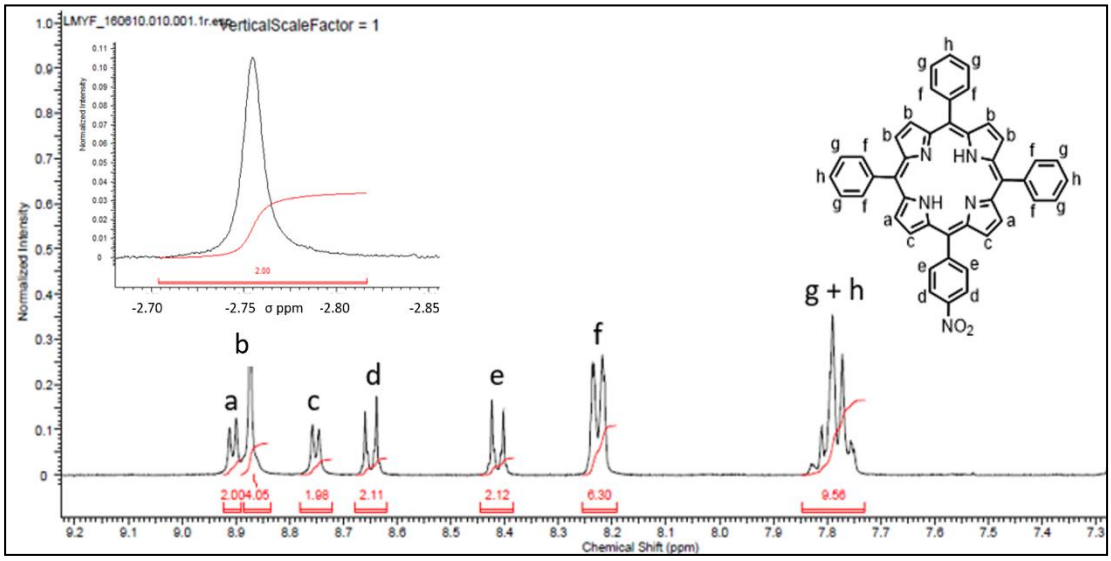

Figure 2-2. ^{1}H NMR (400 MHz, CDCl3) spectrum of the 5-(4-Nitrophenyl)-10, 15, 20-tryphenylporphyrin (Compound #2) at 25°C.

2.4.2 Synthesis of 5-(4-Aminophenyl)-10, 15, 20 try-phenylporphyrine (Compound #3)

The next step in the synthesis was the reduction of the nitro function to an amino group. This reaction was also optimized relative to the published protocol[148] by changing the temperature from 60°C to 80°C and extending the time of reaction from one to three hours. The desired product was extracted with dichloromethane and washed with sodium hydroxide to adjust the pH to 8. One of the problems, not reported in the original protocol, that we found after the addition of dichloromethane was the formation of a thick emulsion that was destroyed by adding brine to the separation funnel. Once the emulsion was removed, the organic phase was collected and dried over magnesium sulfate. After the evaporation of the solvent, we obtained a purple sparkly powder with a yield of 71%, comparable with the yield in the published protocol (Scheme 2-12)

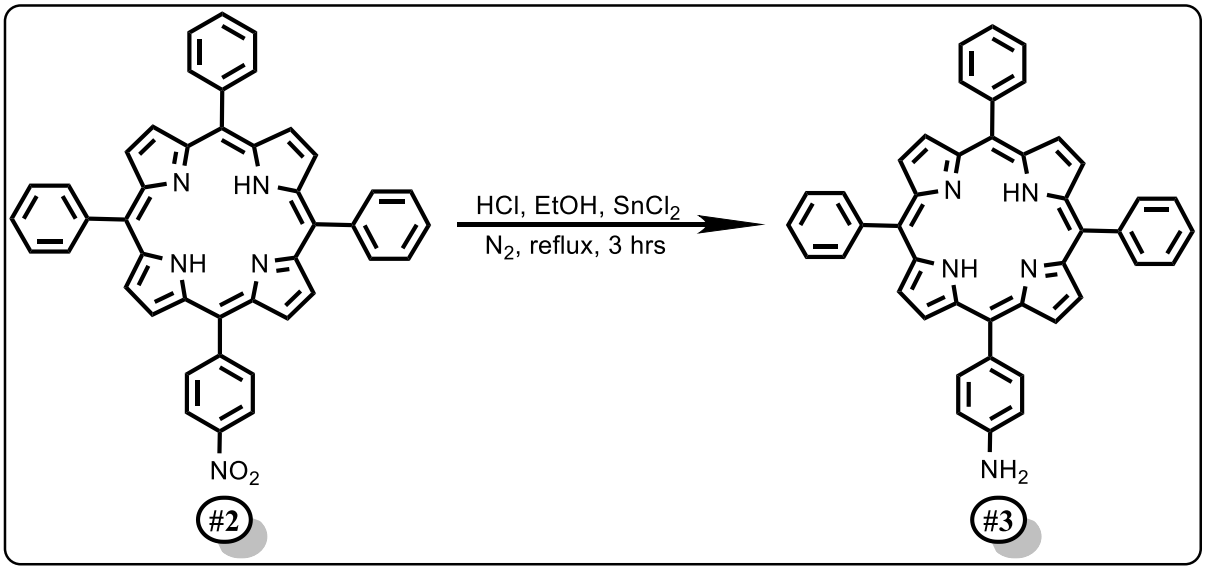

Scheme 2-12. Synthesis of compound #3.

The reaction was monitored by thin layer chromatography. The solvent tried as mobile phase, that had produced the best resolution was a mixture of ethyl acetate and petroleum ether (20:80). The results of the TLC showed that our product was of sufficient purity to carry out the next step of the reaction as only one spot was observed in the TLC plate with complete clearance of the starting material. This was a considerable advantage relative to the published protocol (Figure 2-3, Table 2-2) because in the original procedure they performed a column chromatography to purify the product. In our procedure, we did not need to perform column chromatography, and this translated into direct savings of time and resources i.e. solvents, silica.

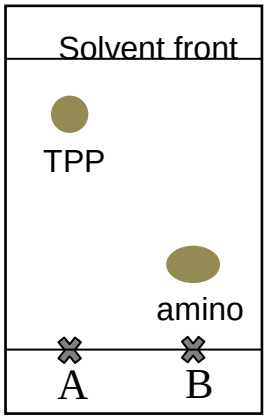

Figure 2-3. TLC showing the migration of tetraphenylporphyrin (A), and 5-(4-Aminophenyl)-10, 15, 20 tryphenylporphyrine (B).

Compound	**R_f**
Tetraphenylporphyrin (TPP)	0.79
5-(4-Aminophenyl)-10, 15, 20 tryphenylporphyrine (#3)	0.22

Table 2-2. Calculated R_f values for the TPP and 5-(4-Aminophenyl)-10, 15, 20 tryphenylporphyrine (#3) eluted with petroleum ether and ethyl acetate (80:20).

The ^{1}H-NMR spectrum for this compound is identical to the one described in the literature[148] (Figure 2-4). However, due to presence of the new amino group, there are new resonances. The doublet at 8.03 ppm corresponds to the protons **d**, located in *meta*-position in respect to the 4-aminophenyl function. Another doublet detected at 7.10 ppm with an integral value of two corresponds to the protons labelled **f**, located in the *ortho*-position next to the amino group. As expected, the chemical shifts of these two protons appear upfield in comparison with the protons **d** in the same position on the compound #2 (Figure 2-2). The reason being is most probably due to the electron donor effect of the amino group. Its influence over the closest protons in *ortho* will increase the electronic density on the vicinity of these protons and generate a magnetic field that will be opposed directly to the magnetic field applied externally by the nuclear magnetic resonance. This produced a shift on the resonance of these two protons towards the upfield regions of the scale. A broad singlet was recorded at 4.06 ppm, which corresponds to the protons of the amino function, and had an integral value of two, as expected.

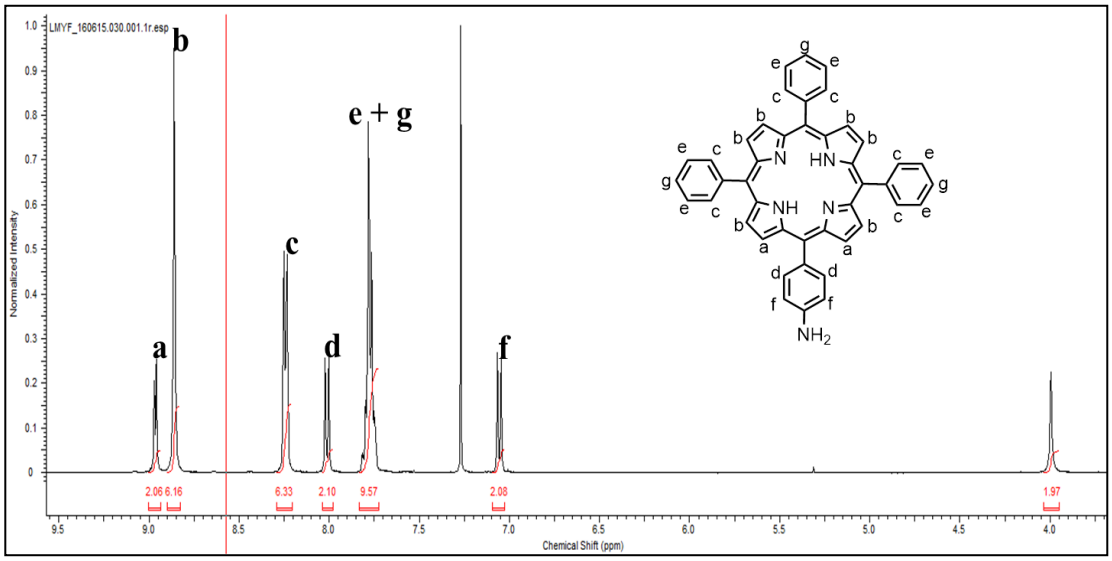

Figure 2-4. ^{1}H NMR (400 MHz, DMSO-d6) spectrum of the 5-(4-Aminophenyl)-10, 15, 20-tryphenylporphyrin (Compound #3) at 25°C.

2.4.3 Synthesis of 5-(4-Aminophenyl)-10, 15, 20 tris (4 - sulfonatophenyl) – porphyrin, Trisodium Salt (Compound #4)

The main objective for introducing three sulfonate functions into the porphyrin is to make this molecule soluble in aqueous solutions. As discussed before about the electrophilic aromatic substitution (S_EAr), this reaction occurs preferentially over the *para* positions of the three meso phenyl groups with no substitution in the β-pyrrole carbons of the macrocycle (Scheme 2-13).

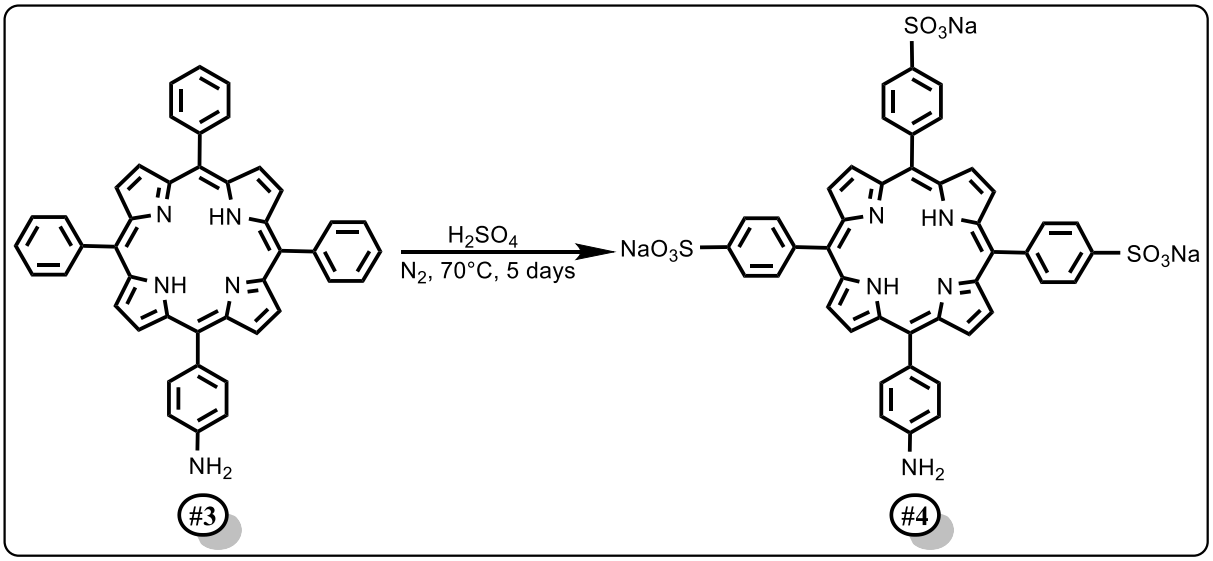

Scheme 2-13. Synthesis of compound #4.

The synthesis was carried out at 70°C under nitrogen atmosphere for five days. After completion the sulfuric acid was quenched by adding sodium hydroxide 10 M. Given the large amount of sodium sulfate that was generated it took considerable time to remove all the salt from the mixture. Despite the good quality of the NMR spectrum the mass of sample recovered of the product was greater than 100% suggesting that salts were still present. The good quality of the NMR spectrum was explained because the sodium sulfate does not have

protons, so cannot produce any signal in the ^{1}H-NMR spectrum. As this issue was not described, it was decided to speed up the separation by introducing a centrifugation step. In the separation, the fact that sodium sulfate was not soluble in methanol unlike the sodium porphyrinate was very helpful. Centrifugation was performed in small volumes to achieve the best possible separation although the procedure required significant time. Finally, a filtration over celite was done to remove fine particles of salt that remain in suspension followed by a final centrifugation step. Methanol was eliminated by rota-evaporation to produce a green-brown porphyrinate with a yield of 86%.

The ^{1}H-NMR spectrum of the product was in agreement with the published spectrum[148] (Figure 2-5). The relevant chemical shift changes are those related with the hydrogens in the positions *ortho/meta* respecting the sulfonic groups. A doublet at 8.18 ppm with an integral value of six corresponds to the **c** protons in the *ortho*-position of the 4-sulfonatopenyl rings. A doublet at 8.05 ppm corresponds to protons **d**, located in *meta*-position in respect to the 4-sulfonatophenyl function.

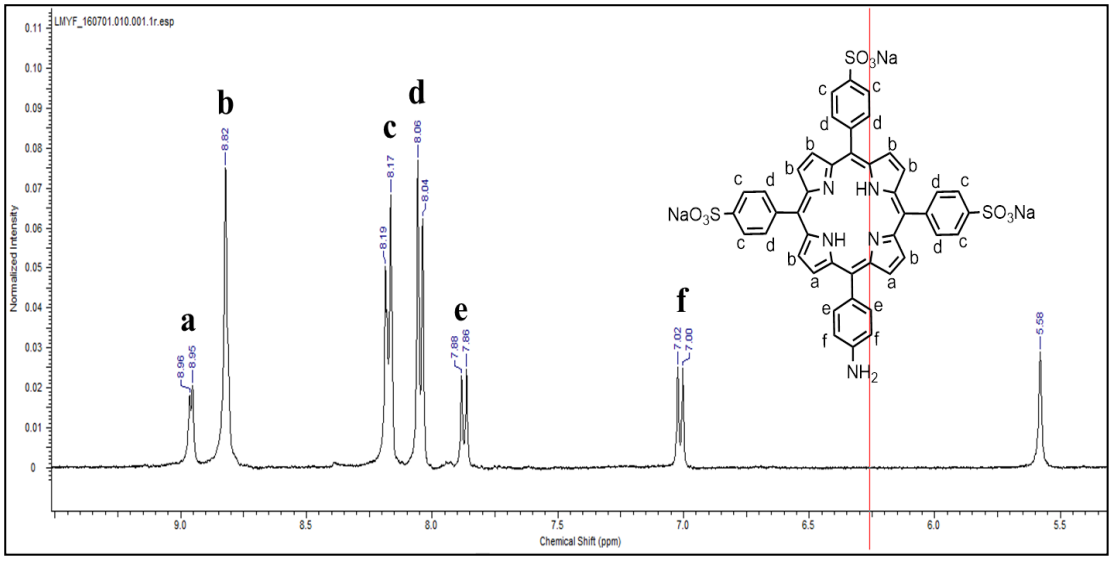

Figure 2-5. ^{1}H NMR (400 MHz, DMSO-d6) spectrum of the 5-(4-Aminophenyl)-10, 15, 20 tris (4 - sulfonatophenyl) – porphyrin, Trisodium Salt (Compound #4) at 25°C.

The heavily shielded protons inside the macrocycle are shifted from -2.76ppm as seen in the mononitro and amino tetraphenylporphyrin to -2.86ppm in the trisulfonatophenylpoprhyrin. This observed change in the chemical shift was unexpected, because the introduction of three electron-withdrawing groups should render unshielded pyrrole protons, with a downfield shift in the resonances (see Figure 2-6).

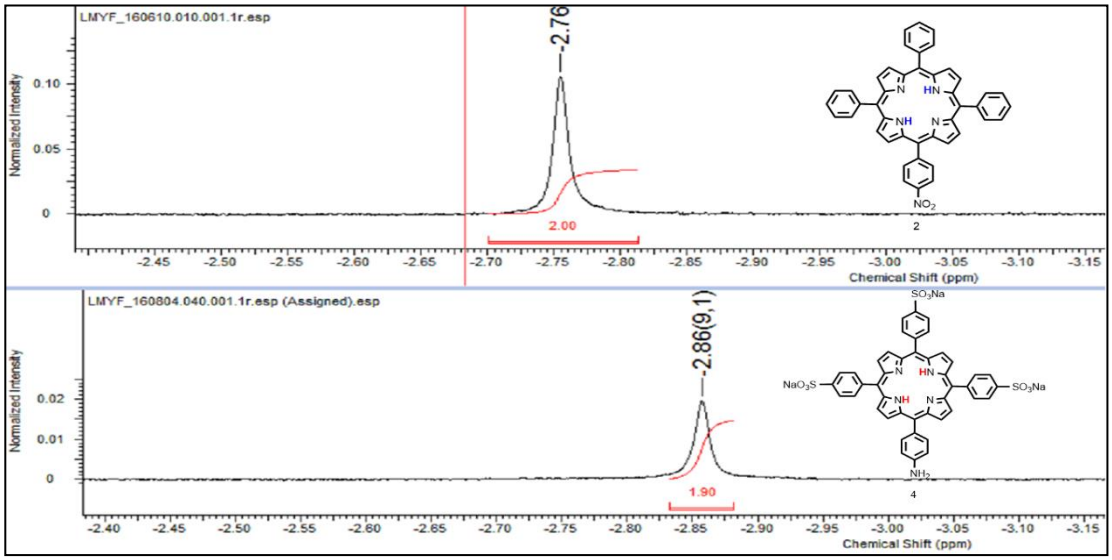

Figure 2-6. ^{1}H NMR (400 MHz, DMSO-d6) spectra showing the negative chemical shift of the protons in the pyrroles of the compound #2 (blue protons) and the compound #4 (red protons), at 25°C.

2.4.4 Synthesis of 5-(4-maleimide)-10, 15, 20 tris (4 - sulfonatophenyl) – porphyrin, tetrabutylammonium salt (Compound #5)

Synthesis of compound #5 was carried out in two consecutive steps: A) reaction with maleic anhydride to produce maleic amide derivative (open ring), B) closure of ring to produce the maleimide function, compound #5 (Scheme 2-14).

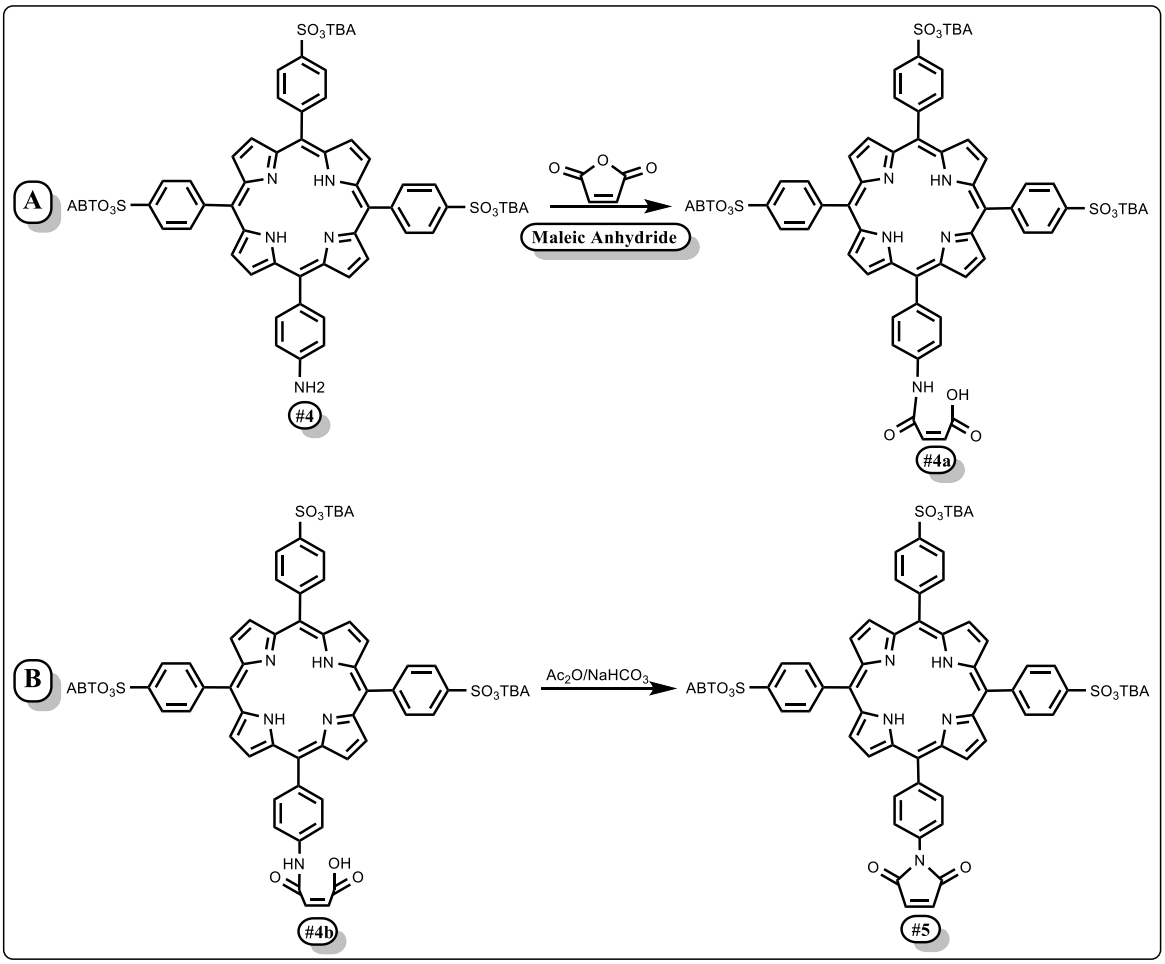

Scheme 2-14. Synthesis in two steps of the compound #5. A) Reaction with the maleic anhydride to produce the maleic amide (open ring); B) closure of the ring to produce the maleimide derivative in the presence of acetic anhydride and sodium bicarbonate (closure of the ring). TBA state for tetrabutylammonium.

To accomplish step A, compound #4 needed to be soluble in organic solvent, but the sodium salt form of compound #4 is only soluble in aqueous media. Therefore, the reaction involved initially the conversion of the trisodium salt form into the tetrabutylammonium salt by several washes with dichloromethane containing the tetrabutylammonium bromide. This is a common method to change polarity of porphyrin salts[149]. The procedure is rather quick, as soon as the conversion takes place compound #4 started to be solubilized in the organic phase, which was evident due to the transfer of the deep green color from the aqueous to the organic phase. The yield of the conversion was 93.3%. The conversion was followed by ^{1}H-NMR (Figure 2-7).

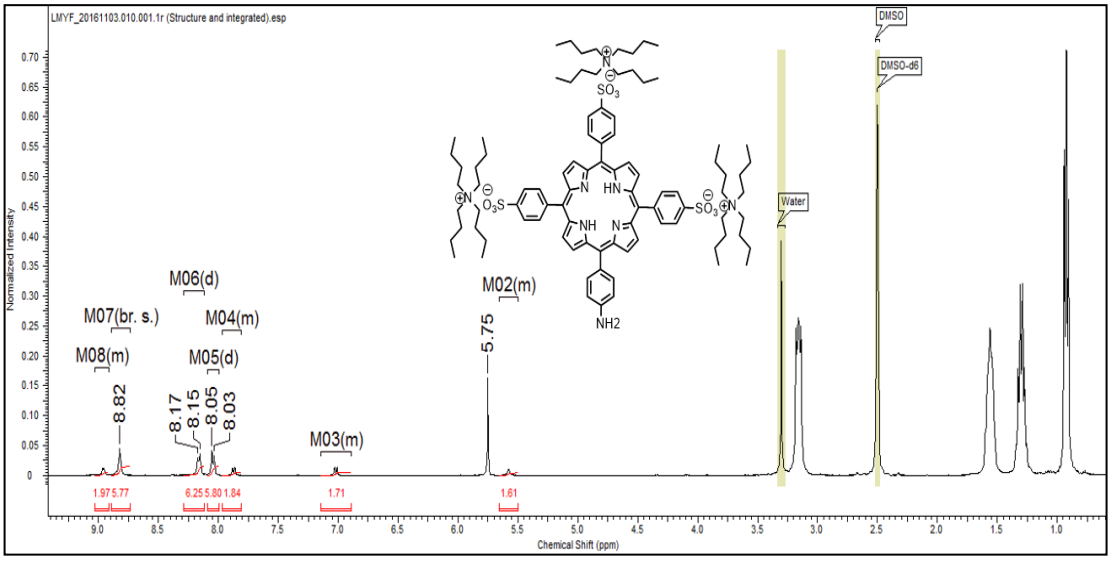

Figure 2-7. ^{1}H NMR (400 MHz, DMSO-d6) spectrum of mixture reaction after the conversion of the sodium for the tetrabutylammonium bromide salt, at 25°C.

Evaporation of dichloromethane under vacuum yielded the tetrabutylammonium salt as an oily brown product. This product was dissolved in dry solvent to avoid its reactivity with traces of water.

The reason being was that the closure of the ring is a dehydration reaction that will not proceed if traces of water are present in the media. In fact, we found that the reaction needed to be repeated several times because the automated drying solvent system of the department was not working properly and there were traces of water in the acetonitrile. This required a further step whereby we re-distilled the acetonitrile using calcium hydride as the drying agent. After stopping the reaction, we performed the analysis of the crude product by nuclear magnetic resonance.

The ^{1}H-NMR spectrum of the crude product showed 30 protons in the aromatic region (Figure 2-8). The spectrum showed a singlet at 10.92ppm that corresponds to proton **i** in the carboxylic group with an integral of one. A doublet at 6.72 ppm represents the protons **g/h.**

These signals were very important because they can be used to ascertain that the reaction had progressed successfully. Compared with the NMR spectrum of compound #4 (see Figure 2-7) it was clear that appearance of these two doublets were new, because in the region around 6.5 ppm in compound #4 there are no signals. The next doublet at 6.45 ppm with an integral value of one corresponds to proton **g/h** on the maleic amide. These two doublets were found at the position expected for olefin protons, and had the expected multiplicity and integral value. A singlet at 5.77 ppm with an integral value of 0.32 we suggest corresponds to proton **j** of the amide nitrogen. Moreover, we observed in the spectrum one signal at 6.27 ppm with an integral value of two that could belong to the maleic anhydride that is in excess

in the reaction mixture. No ^{1}H-NMR spectrum has previously been published for this compound, since in the original protocol they did not isolate it[150].

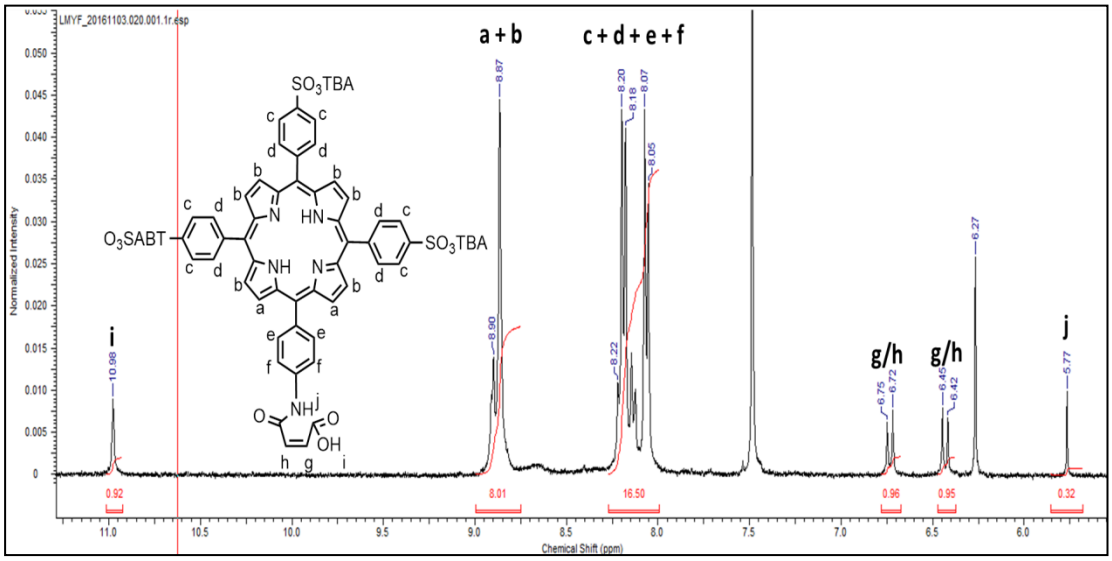

Figure 2-8. ^{1}H NMR (400 MHz, DMSO-d6) spectrum of the maleic amide (open ring), tetrabutylammonium salt (Compound #4*) at 25°C. The TBA state for tetrabutylammonium group.

The next step was the condensation reaction to produce the ring yield the maleimide derivative (see Scheme 2-14 B). The reaction is usually carried out in a mixture of acetic anhydride and sodium bicarbonate with the removal of the acetic anhydride under alkaline conditions[150]. The product was obtained in the form of tetrabutylammonium salt with 24% yield. As we needed the product to be water soluble, we performed ionic exchange chromatography to replace the tetrabutylammonium cation for sodium[151] (see Experimental Section 2.5.2.5). The product was characterized by resonance magnetic spectroscopy and mass spectrophotometry (see Figures 6-1, 2 and 3 in Appendix).

The ^{1}H-NMR spectrum showed in the aromatic region a total of 28 protons (Figure 2-9). From the analysis of the spectrum, it was clear that the doublets **g/h** are no longer present (see Figure 2-8)**.** The singlet at 7.36 ppm with an integral of two was assigned to the protons

g, which corresponded to the maleimide protons. Of note, the resonances of the maleimides attached to aromatic systems are located around 7.00 ppm[150]. Compound #5 is a molecule that possess one plane of symmetry, which means that protons in the same environment or equivalent appeared at the same chemical shift, as is the case.

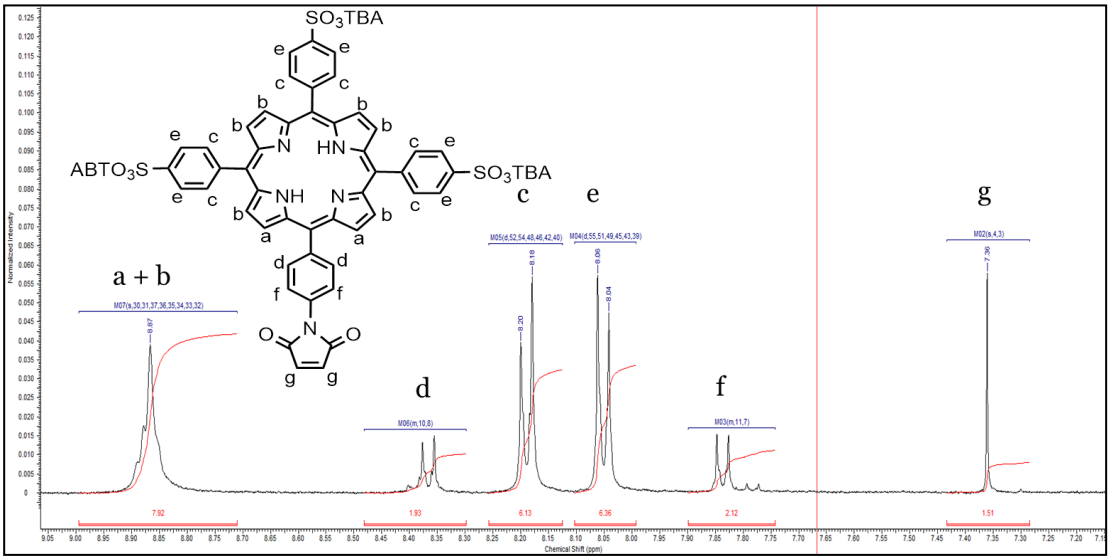

Figure 2-9. 1H NMR (400 MHz, DMSO-d6) spectrum of the maleimide tetrabutylammonium salt (close ring), (Compound #5) at 25°C. TBA; tetrabutylammonium cation.

To ascertain whether we removed the tetrabutylammonium cation entirely we analyzed by NMR compound #5 before and after the ion exchange chromatography. Comparison of the spectrum with another of tetrabutylammonium bromide in deuterated methanol revealed that exchange was accomplished successfully (Figure 2-10 and 2-11). Of note, Dowex Marathon proved to be efficient only when was used fresh. However, we did try the exchange using a regenerated resin that we obtained by doing three washes with hydrochloric acid (0.1 M) followed by deionized water, then sodium hydroxide (0.1 M) followed by deionized water. The result clearly demonstrated that use of new resin provides a better outcome with a 90% yield.

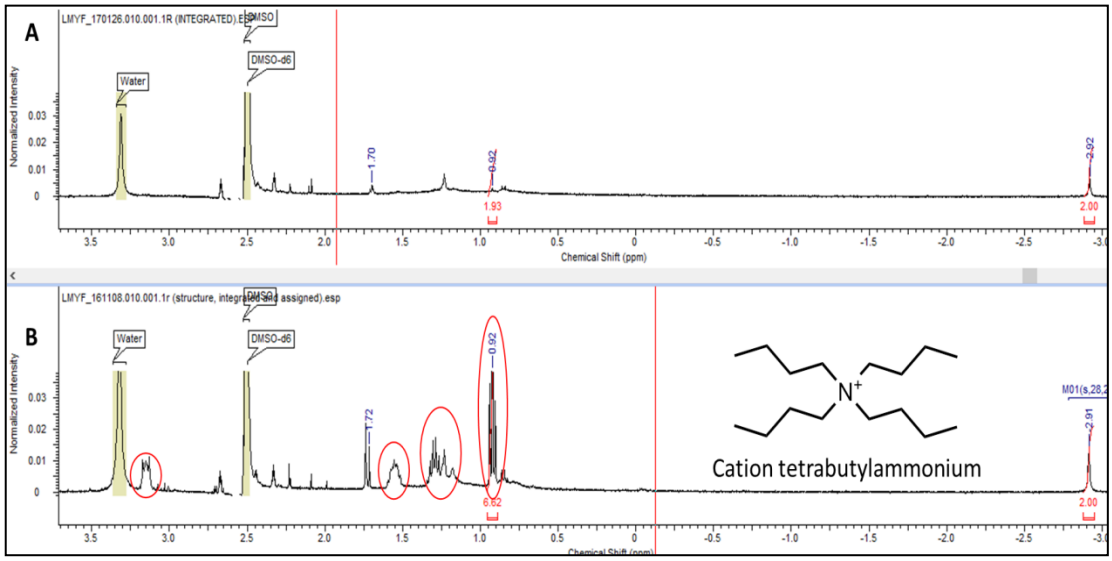

Figure 2-11. ^{1}H NMR spectra at 25 °C (400 MHz, DMSO-d6) of Compound #5 after (A) and before (B) the ionic exchange chromatography. Circled in red are the signals corresponding to the tetrabutylammonium cation.

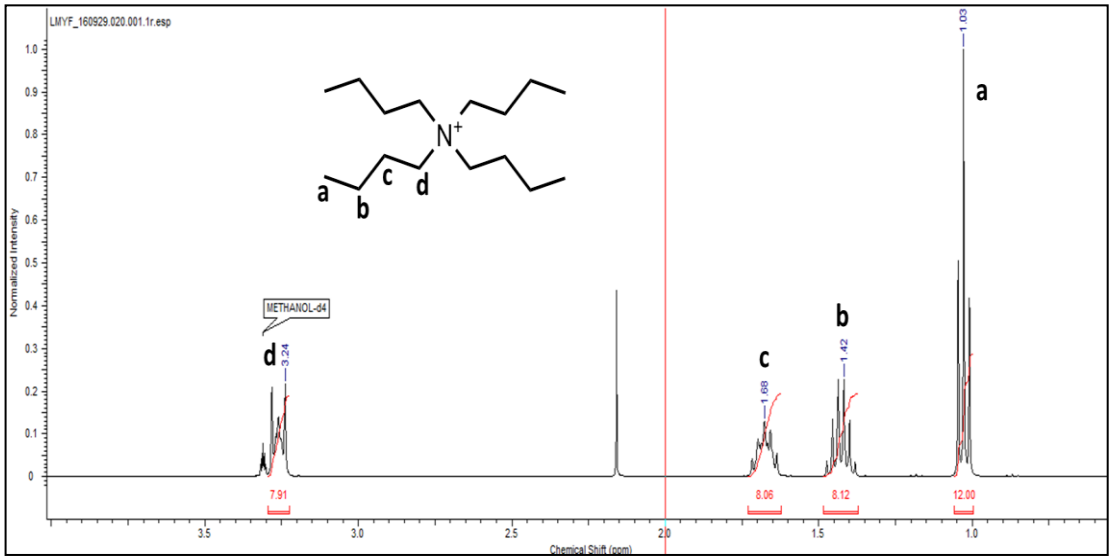

Figure 2-10. ^{1}H NMR (400 MHz, MeOD) spectrum of the tetrabutylammonium bromide at 25 °C.

2.4.5 Summary

We have successfully achieved the synthesis of the 5-(4-maleimide)-10, 15, 20 tris (4 - sulfonatophenyl) – porphyrin, trisodium salt) (Compound #5). The analysis by mass spectrophotometry and proton nuclear magnetic resonance (see appendix) showed the compound #5 was obtained with 90% yield. The reaction protocol was improved in several aspects compared to the original method. For example, the rise in the temperature in the nitration of the porphyrin sped up the reaction from 120 min to 25 min. In addition, the introduction of the isocratic elution with a mixture of petroleum ether, ethylacetate, and methanol (97:2:1) considerably improved the separation of side products and the yield of mononitro-porphyrin. Moreover, during the processing of the sulfonation reaction to isolate the porphyrin lots of sodium sulfate was generated. The solubilization of the porphyrin in methanol and the introduction of a centrifugation step proved very helpful, as sodium sulfate was very difficult to remove and time consuming when we followed the initial protocol. To remove the tetrabutylammonium cation an ionic exchange chromatography was performed using a Dowex Marathon resin with 90% yield[151].

2.5 EXPERIMENTAL SECTION

2.5.1 Solvents and Reagents

The chloroform (Fisher) for the synthesis was used without any previous treatment. For the liquid chromatography petroleum ether, ethyl acetate, and methanol (Fisher) were used with analytical grade purity and without further treatment. The acetonitrile (Fisher) for the synthesis of the compound #5 was refluxed with calcium hydride for 2 hours to remove water. Then the dry acetonitrile was distilled to separate it from the by-products of the reflux reaction, and was kept in a dark glass sealed bottle. The acetic anhydride (Alfa Aesar) for the synthesis was used without any further treatment as well as the dichloromethane (Fisher) for the synthesis. Deionized water was obtained from water purifier purelab option (ELGA).

Nitric acid (69%, BDH), sulfuric acid (98%, BDH), hydrochloric acid (35%, BDH), ethanol, and inorganic salts used for the synthesis were of analytical grade purity. For the synthesis of compound #2 we used tetraphenylporphyrin (TPP) (> 99%, Merck). For the synthesis of compound #5 we employed tetrabutylammonium bromide (TBA) (> 98%, Merck), and maleic anhydride (> 99%, Merck).

The deuterated solvents for the ^{1}H-NMR analysis were deuterium oxide (D_2O) (isotopic purity 99.9%, Merck), deuterochloroform (CD_3Cl) (99.96 %, Merck), dimethyl sulfoxide, (d_6-DMSO) from Eurisotop.

All the reactions were performed under nitrogen atmosphere and with permanent stirring unless otherwise stated.

2.5.2 Synthesis, purification and characterization of the porphyrins.

2.5.2.1 Synthesis of the of 5-(4-Nitrophenyl)-10, 15, 20 triphenylporphyrin (Compound #2)

Tetraphenylporphyrin (1.0 g, 1.63 mmol) was dissolved in 80 mL of chloroform. Nitric acid (11.2 g, 178 mmol, sp gr = 1.4 g/cm^3) was added to the stirred solution of porphyrin and the mixture was heated at 60°C for 25 minutes. The reaction was monitored at intervals by TLC to insure total conversion of starting material (R_f = 0.83) to product (R_f = 0.6) by using petroleum ether, ethyl acetate, methanol (97:2:1) in pre-coated aluminum-backed silica gel plates. When dinitro-porphyrin derivatives were detected the (R_f = 0.26) the reaction was stopped and cooled down. The dark green solution was extracted with 3 x 120 mL portions of a saturated solution of sodium carbonate and brine. The addition of this basic solution changes the color of the mixture from dark green to purple. The organic layer was extracted and dried over magnesium sulfate and filtered. The chloroform was removed under reduced pressure to obtain purple sparkle crystals. The solid was suspended in 5 ml of chloroform and loaded into the silica column (50 cm x 4 cm). Fractions containing only the mononitro derivative (compound #2) were combined, giving mono (nitropheny1) triphenylporphyrin in 66% yield (0.7 g, 1.07 mmol): ^{1}H NMR (400 MHz, $CDCl_3$) 8.81 (2H, d, J = 4.80 Hz, β-pyrrole), 8.79 (4H, s, β-pyrrole), 8.67 (2H, d, J = 5.00 Hz, β-prrrole), 8.56 (2H, d, J = 8.72 Hz, nitrophenyl), 8.33 (2H, d, J = 8.59 Hz, nitrophenyl), 8.27-8.18 (6H, m, *ortho* triphenyl), 7.89-7.70 (9H, m, *meta/para* phenyl), -2.76 (2H, s, NH of pyrrole).

2.5.2.2 Synthesis of 5-(4-Aminophenyl)-10, 15, 20 triphenylporphyrin (Compound #3)

The (nitrophenyl)-triphenylporphyrin (220 mg, 0.334 mmol) was dissolved in 20 mL of concentrated hydrogen chloride. Tin (II) chloride dehydrate (0.630 g, 3.34 mmol) was added to the solution and the reaction was heated for three hours at 80°C. The reaction was cooled down and mixed with dichloromethane (50.0 mL), which solubilized the product and produced two phases. The green suspension was washed with 1 M sodium hydroxide (4 x 50.0 mL), which transformed the porphyrin solution to purple. The dichloromethane was separated and dried over magnesium sulfate, filtered and evaporated under reduced pressure to produce the desired (aminophenyl)-triphenylporphyrin (250 mg, 0.40 mmol) which was obtained in a 72% yield. ^{1}H NMR (400 MHz, d_6-DMSO) 8.97 (2H, d, J = 4.50 Hz, β-pyrrole), 8.86 (6H, s, β-pyrrole), 8.29-8.21 (6H, m, *ortho* triphenyl), 8.03 (2H, d, J = 8.00 Hz, 4-aminophenyl), 7.84-7.72 (9H, m, *meta/para* triphenyl), 7.10 (2H, d, J = 8.10 Hz, 4-aminophenyl), 4.06 (2H, br s, amino), -2.72 (2H, s, NH of pyrrole).

2.5.2.3 Synthesis of 5-(4-Aminophenyl)-10, 15, 20 tris (4 - sulfonatophenyl) – porphyrin, Trisodium Salt (Compound #4)

(Aminophenyl)-triphenylporphyrin (250 mg, 0.40 mmol) was dissolved in 54 mL of concentrated sulfuric acid (98%, BDH, reagent grade) and heated at 75°C with stirring under nitrogen atmosphere for five days. The dark green solution was cooled down and neutralized with a saturated solution of sodium carbonate in an ice bath. The deprotonation of the mixture was established when the solution turned purple. Methanol was added then to the mixture to induce the precipitation of the sodium sulfate salt. The salt was vacuum filtered, and the remaining fine salt was centrifuged at 4000 rpm for twenty five minutes. The solution was then filtered, and evaporated under reduced pressure to give the green-brown desired trisulfonate-triphenylpoprhyrin (320 mg, 0.35 mmol) with a yield 86%. ^{1}H NMR (400 MHz, d_6-DMSO) 8.95 (2H, d, J = 4.14 Hz, β-pyrrole), 8.84 (6H, s, β-pyrrole), 8.18 (6H, d, J = 7.98 Hz, 4-sulfonatephenyl), 8.05 (6H, d, J = 7.98 Hz, 4-sulfonatephenyl), 7.89 (2H, d, J = 7.98 Hz, 4-aminophenyl), 7.03 (2H, d, J = 8.28 Hz, 4-aminophenyl).

2.5.2.4 Synthesis of 5-(4-maleimide)-10, 15, 20 tris (4 - sulfonatophenyl) – porphyrin, tetrabutylammonium salt (Compound #5)

5-(4-Aminophenyl)-10, 15, 20 tris (4 - sulfonatophenyl) – porphyrin, trisodium Salt (Compound #4) (320 mg, 0.35 mmol) was dissolved in 15 mL of deionized water and washed (3 x 20 mL) of a solution of dichloromethane containing tetrabutylammonium bromide (690 mg, 2.2 mmol). The organic fractions were collected and pooled together. The green color confirmed the presence of the porphyrinate. The dichloromethane was evaporated under reduced pressure to produce a brown oily product. The oily product was dissolved in 10 mL of dry acetonitrile and maleic anhydride (89 mg, 0.9 mmol) was added to the mixture, and the reaction was then refluxed for five hours. The reaction was cooled down and the solvent was rota-evaporated. The crude was then re-dissolved in 2 mL of acetic anhydride (Alfa Aesar, reagent grade), and sodium bicarbonate (76 mg, 0.9 mmol) was added to the mixture. The reaction was heated at 80°C for one and a half hour. Then the mixture was cooled down and dissolved in 50 mL of chloroform; the organic phase was washed (3 x 50 mL) with deionized water. The chloroform was dried over magnesium sulfate anhydrous, filtered and removed under reduced pressure to produce the desired product (190 mg, 0.11 mmol) with 25% yield. ^{1}H-NMR (400 MHz, d_6-DMSO) 8.93 (brs, 4H), 8.82 (brs, 4H), 8.31 (m, 8H), 8.22 (d, J=8.1 Hz, 6H), 7.78 (d, J=8.4 Hz, 2H), 7.02 (s, 2H), 3.30 (m, 24H), 1.68 (m, 24H), 1.45 (m, 24H), 1.04 (t, J=7.6 Hz, 36H). MS (positive) calculated. 949.1 $[M+H]^+$, found 950.2.

2.5.2.5 Ionic exchange of tetrabutylammonium cation for sodium in the compound #5

A Luer Lock, non-jacketed (1.5 cm × 30 cm) column was packed with 40-60 g of dry Dowex previously left in water for 1 hour. The stationary phase was washed with deionized water three times with the column volume (56 mL). The tetrabutylammonium salt of compound #5 (190 mg, 0.11 mmol), was dissolved in 6 mL of deionized water and loaded into the column. The elution of the compound 5 is very fast, less than 2 min. The fractions containing the colored compound 5 were pooled together and freeze/dried to render a brown cottony product (110 mg, 0.10 mmol) with a 90% of yield.

2.5.3 Chromatographic techniques

The thin layer chromatography was performed on coated aluminum-backed silica gel 60, layer thickness 200 µm, particle size of 10-12 µm, with two inorganic fluorescent indicators for UV detection of colorless substances (F_{254}, Merck)

Column chromatography was performed with silica gel for flash chromatography from VWR, SiO_2 (60 A CC, 40-60 µm, 230-240 *mesh*, SDS). For the ionic exchange chromatography the matrix used was Dowex Marathon C sodium form, 20-50 *mesh* (Merck). The UV monitoring of TLC was performed with UVGL-58 handheld UV lamp (UVP) with visualization under UV light ($\lambda = 254$ nm).

2.5.4 Instruments

Proton Nuclear Magnetic Resonance (^{1}H-NMR): The ^{1}H-NMR was performed on the departmental Nuclear Magnetic Resonance (NMR) service. The spectra were recorded on the Bruker 400 MHz spectrometers (Avance and Avance III). The description of the peaks is as follows: singlet (s), doublet (d), triplet (t), multiplet (m), broad (br). The coupling constants are reported in hertz (Hz), the chemical shift (δ) in parts per million (ppm).

Mass Spectrometry: Mass spectrometry was performed using an Agilent LC-MS, comprising an 1100 Series LC and SL Ion Trap MSD, located in the analytical service of SBCS.

Rotary evaporator: The removal of the solvents under reduced pressure was performed with a Hei-VAP Model rota-evaporator. The instruments include an integrated vacuum control, and a temperature accurate bath set on 40°C.

Freeze Dryer: The freeze/drying of the samples was performed with a Labconco Freezone Freeze Dry System.

3 CHAPTER 3

In this chapter, we will determine the chemical conditions to perform and to follow up to completion the labeling of the hydrophobic peptide in the membrane of liposomes (Figure 3-1).

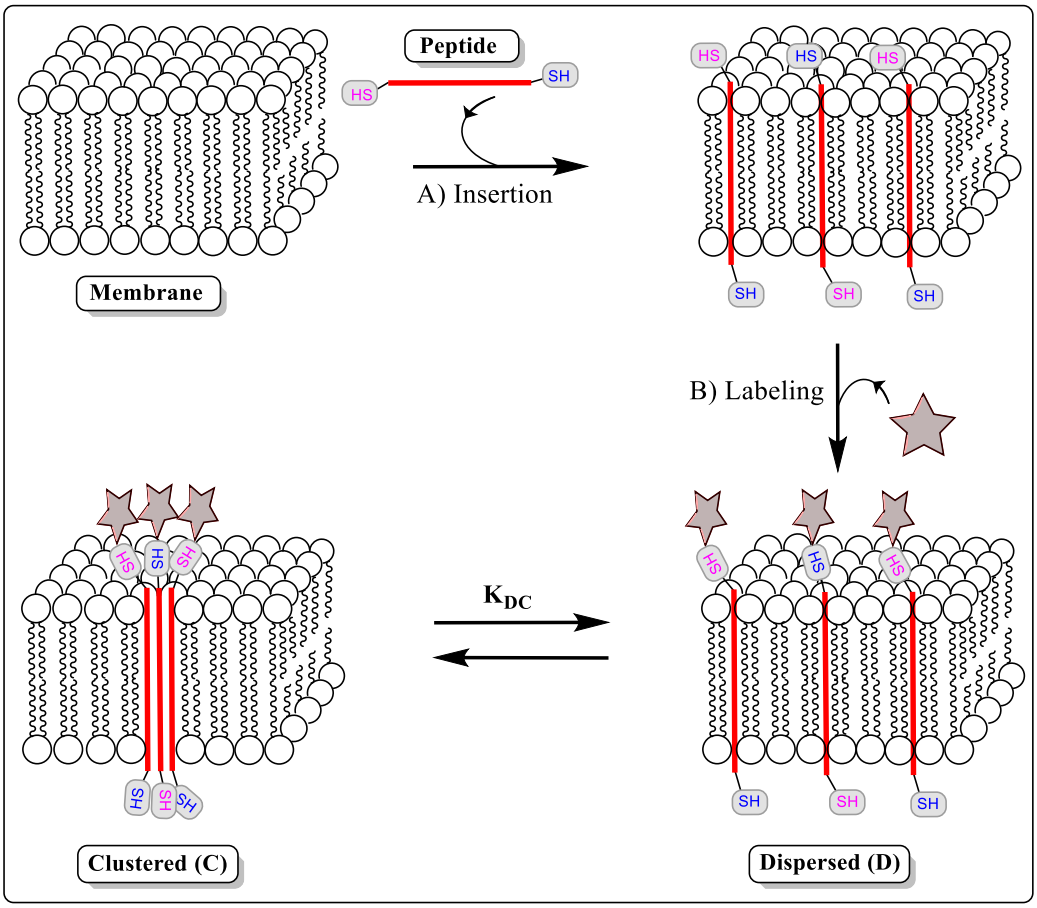

Figure 3-1. Graphic depiction of the steps involved in the labelling of the full-length transmembrane peptide. A) Solubilization of the peptide through insertion in the lipid bilayers. B) Addition of the maleimide –derivative and reaction with the external nucleophilic groups. C) Equilibrium established between the dispersed and the clustered forms of the peptide in the lipid vesicles. Peptide sequence: Ac-CWQDKNDVLQLQFTITSAYYTYLLLLLKSVIYLAIISFSLLRRTSVC-NH

Due to lack of information regarding the conditions to perform the labelling of the hydrophobic peptide in lipid membranes, and taking into consideration the starting material is limited and expensive, we decided to start our study by using model thiols like N-acetylcysteine, γ-glutathione, and 1-hexadecanothiol. These model thiols contain the same nucleophilic group as our hydrophobic peptide which can be used to follow up their reactivity with 5-(4-maleimide)-10, 15, 20 tris (4 - sulfonatophenyl)–porphyrin (compound #5), which is our clustering reporter (Scheme 3-1). Another desirable feature of these model thiols is that are easy to manipulate in the laboratory and less expensive.

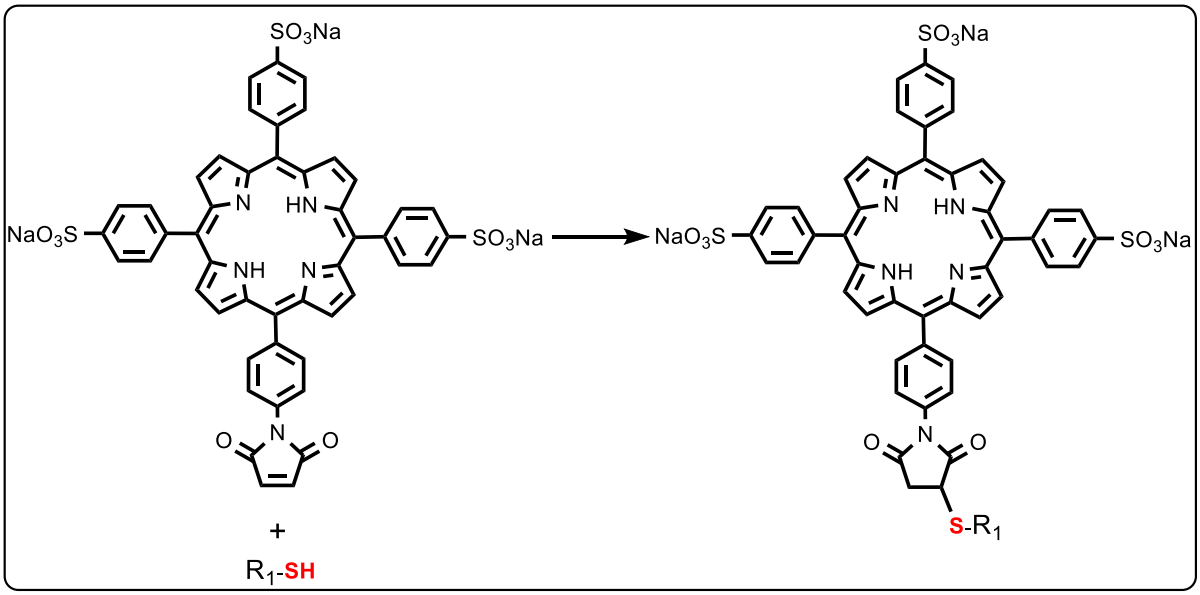

Scheme 3-1. Reaction of the compound #5 with a generic thiol to render the addition of the thiolate to the double bond of the maleimide with the formation of the thioether bond. R_1: alkyl, aryl substituent.

3.1 **OBJECTIVE**

The objective of this chapter is to study the chemical properties of the compound 5-(4-maleimide-phenyl)-10, 15, 20-tris (4-sulfonatophenyl) porphyrin in terms of reactivity towards model thiols, that have the same nucleophilic group as the hydrophobic peptide and are smaller in size, easier to manipulate, and less expensive. In order to achieve the labeling of the porphyrin-maleimide derivative we need to meet some requirements:

1. The sulfhydryl group (SH) on the model thiols needs to be in the reduced state to be able to react as a nucleophile.

2. The maleimide group in the porphyrin derivative needs to be stable under the conditions used to perform the labelling reaction.

3. We need to be able to follow up and quantify the reaction between the porphyrin derivative and the model thiols.

4. We need to determine to what extent the presence of lipids can affect the chemistry of the labelling reaction since the goal is to label the hydrophobic peptide solubilized in the membrane of the liposomes.

In this chapter, we will describe the experiments done to address the points 1 to 3.

3.2 INTRODUCTION

3.2.1 Thiol detection

3.2.1.1 Ellman's reagent (Aromatic disulfide)

The chromogenic compound 5,5'-dithiobis-(2-nitrobenzoic acid) (DTNB) is the most employed reagent in the stoichiometrically quantification of thiols[152]. The reagent has a disulfide bond that is highly oxidizing, that react with free thiolates present in solution to yield a yellow anion 5-thio-2-nitrobenzoic acid (TNB)[153] (Scheme 3-2). The TNB anion is a very good leaving group because the electronegative nitro group and the conjugated aromatic system help to stabilize the thiolate anion; the pKa value of the thiol is 4.5[153]. DTNB reacts irreversibly to produce one TNB anion per thiol oxidized. In this reaction, the absorbance of the TNB anion can be used as an indirect measure of the number of reacted sulfhydryl groups[154]. While DTNB absorbs weakly at 412nm, the TNB anion absorbs with an extinction coefficient (ε) equal to 14,150 $M^{-1}cm^{-1}$ at pH 7.2[153]. The TNB absorption is very sensitive to changes in the ionic strength or the pH. The molar extinction coefficient is stable from pH 6 to pH 9.5. However, over pH 7, the DTNB is sensitive to hydrolysis, so special attention must be taken. Of note, under pH 6, TNB becomes protonated which highly affects the absorption of light[155]. In addition, alkylating agents can react with TNB suppressing the absorption; this property, for instance, has been used to determine the concentration of such reagents in solution[156].

DTNB is an excellent reagent for the quantification of small thiols, and is particularly useful in determination of thiol concentration in stock solutions, such as N-acetylcysteine, glutathione, phosphines, L-cysteine ethyl ester, and dithiothreitol[157]. For example, when us-

ing a high molar excess of Ellman's reagent in a buffer solution at pH around 7.3 the reaction is complete in approximately one minute.

One of the disadvantages of the DTNB is the limited sensitivity of the reagent to the nanomolar scale, which means that detection of thiols in very diluted protein solutions could be problematic[156]. However, detection in the micromolar scale is achievable, and since we will use at least 10 µM of the hydrophobic peptide, the use of DTNB for the quantification of free thiol in our peptide will be feasible.

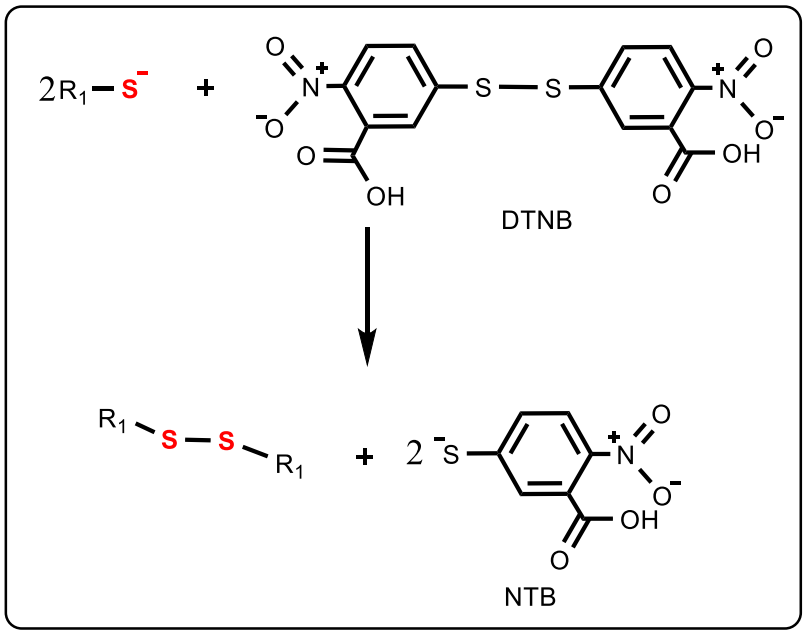

Scheme 3-2. Reaction of DTNB with free thiol to form stoichiometrically the colored anion TNB. R_1: alkyl, aryl substituent

Thiols in aqueous solution can suffer oxidation to yield the disulfide[158]. This species is unable to act as a nucleophile, hence, cannot be used in the labeling reaction. To overcome this difficulty, there are two alternatives:

1. Prepare the peptide solution stock in a reduced atmosphere.

2. Add a reducing agent to the peptide solution before the labelling reaction.

The first option requires the use of costly equipment i.e. hypoxic chamber; necessity of specialized training, and is time consuming. The alternative, instead, is more feasible in the lab, and it is widely described in the literature. Notwithstanding, to be able to employ these reagents we have to make sure they are compatible with maleimide chemistry. In addition, we might need to test the ability of these compounds to permeabilize the lipid bilayer, as we may not want to generate a reduced atmosphere inside the liposomes.

In the next paragraph, we will summarize the main characteristics of maleimide chemistry described in the literature. In the results and discussion section, we will show the experiments we performed towards the identification of conditions to achieve the labeling reaction of model thiols with compound #5 in the presence of these reducing agents.

3.2.2 Maleimides

The maleimides are exceptionally good reagents for the selective modification, quantitation and analysis of compounds that contain free thiols (Scheme 3-3).

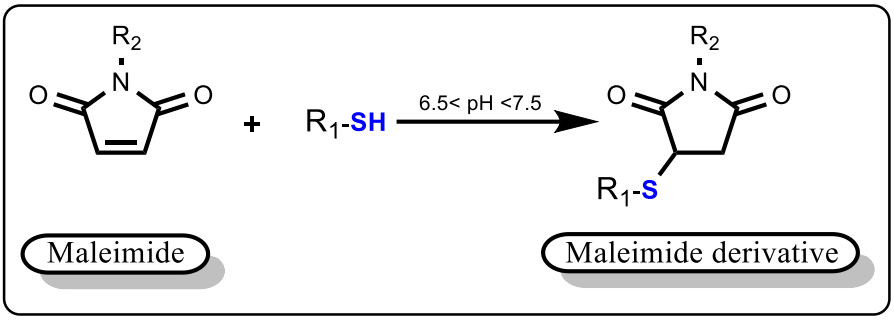

Scheme 3-3. Reaction of a maleimide with a thiol. R2: alkyl, aryl substituent.

The chemistry of maleimides is well known nowadays. They selectively react with sulfhydryl groups, in the so called "click reaction" in aqueous media at a pH near neutrality to form a stable thioether, following a Michael addition mechanism[159] . The thiolate anion is a reactive nucleophile that attacks the α, β- unsaturated carbon of the maleimide to produce a new thioether (S-C) bond. The rate of reaction is closely dependent on the thiol deprotonation, thus on the pH of the reaction. In addition, the stability of maleimide is dependent on the pH. Some studies with the N-ethylmaleimide (NEM)[159-161] showed that this compound was stable at pH < 6, whereas at pH = 7 the half-life was approximately 45hrs and at pH > 9.0 was less than 1hr. The instability of maleimide is due to hydrolysis of the ring at basic pH leading to formation of maleamic acid and the concomitant loss of reactivity[143, 162]. Some thiol adduct maleimides e.g. N-acetylcysteine-N-ethylmaleimide, can suffer intramolecular transamidation at pH values above 9[144].A recent study by Baldwin et al.[163] described that succinimides-aromatic thiols can suffer retro Michael-type addition reaction under conditions

of high reduction potential, and are easily cleaved by exogenous thiols like glutathione. Moreover, Beutler et al.[164] observed slow regeneration of thiol in adducts of glutathione and N-ethylmaleimide between pH 7 and 9 (Scheme 3-4).

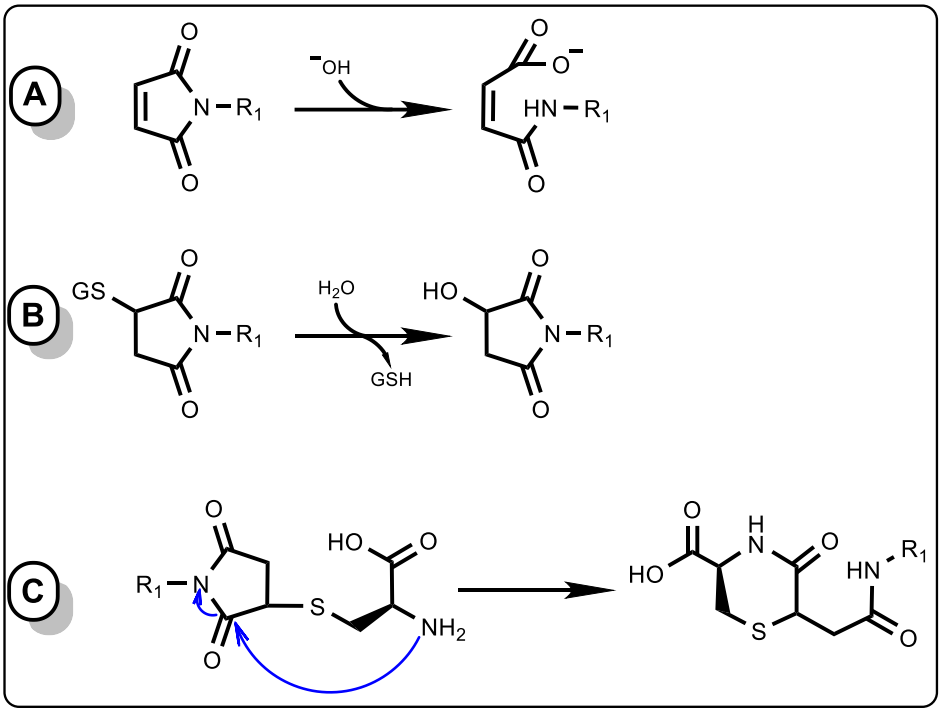

Scheme 3-4. Common reactions involving maleimides. (A) Alkaline hydrolysis of maleimides. (B) Hydrolysis of the adduct glutathione with maleimide to render the free thiol. (C) Transamidation reaction involving the adduct of cysteine and N-ethylmaleimide.

Despite these reports in the chemistry of maleimides, they are still one of the best alkylating reagents compared with others, such as as iodoacetic (IAA) and iodoacetamide (IAM). For example at pH = 7 the alkylation rate of some thiols like TNB with NEM are 85 and 20-fold faster than with IAA and IAM, respectively[156]. The superior reactivity of maleimides has been studied in alkylation of protein thiols[165-168]. Keillor et al.[161] showed that N-arylmaleimides at neutral pH are stable enough to undergo conjugation reaction, because addition of the thiol is faster than hydrolysis of the maleimide ring. Of note, maleimides are small, uncharged molecules that can react with thiols even in hydrophobic environment.

3.2.3 Model thiols for this study

The model thiols used in our experiments were N-acetylcysteine and glutathione as examples of hydrophilic thiols and 1-hexadecanothiol as hydrophobic.

3.2.3.1 N-acetylcysteine (NAC)

N-acetylcysteine (Scheme 3-5) is a cysteine derivative thiol of biological importance, e.g. has being used largely as a therapeutic drug against toxic overdoses of acetaminophen[169]. It is a small molecule, economically accessible, with a pKa = 9.52, very close to the pKa of many protein thiols[170]. Reaction of NAC with bis-maleimides has been studied in the context of the synthesis of low molecular weight hydrogelators[150].

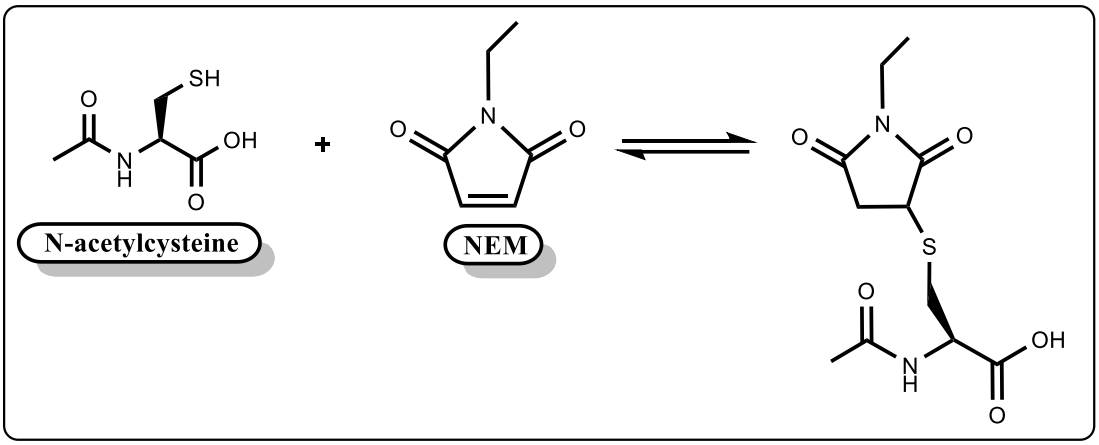

Scheme 3-5. Reaction of NEM with NAC to form the thiol-maleimide adduct.

3.2.3.2 γ-Glutathione (Glu)

Glutathione is a cysteine containing tripeptide (Scheme 3-6) formed by γ-L-glutamyl-L-cystenyl-glycine that plays a very important role in the intracellular redox state of the cells[171]. The reason why we chose this molecule in our experiments was because it is slightly longer than the NAC, and chemically closer to the peptide that we intend to use in this study. In addition, the adduct of glutathione and compound #5 might be easier to separate by HPLC than the adduct of the compound #5 and the NAC (see Results).

Interest on the glutathione as model thiol is based on its reactivity towards maleimides which is based on the presence of a cysteine with a pKa = 9.63 similar to that showed by NAC[172]. Formation of the adduct when combined with NEM at pH 7,2 is completed in less than 5 min[164]. The mechanism of the reaction is the Michael addition.

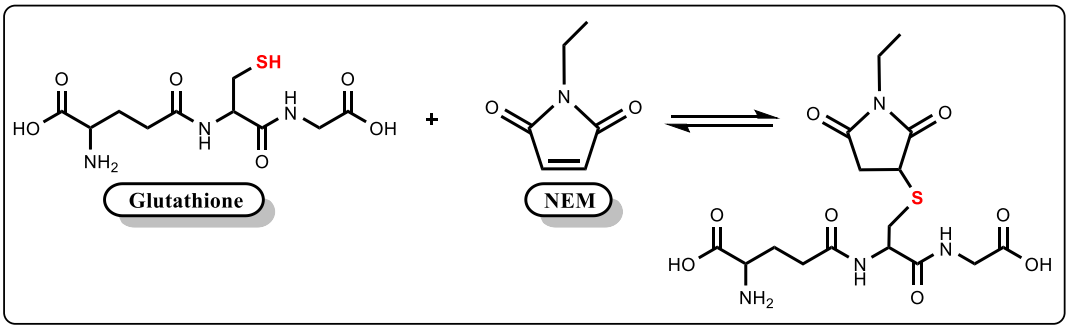

Scheme 3-6. Reaction of NEM with GSH to form the thiol-maleimide adduct.

3.2.3.3 1-Hexadecanethiol (1-Hex)

1-Hexadecanethiol is a hydrophobic thiol with global formula $CH_3(CH_2)_{14}CH_2SH$ that we used in our experiments in order to study the reaction between the compound #5 and a hydrophobic thiol, similar to the peptide (Scheme 3-7).

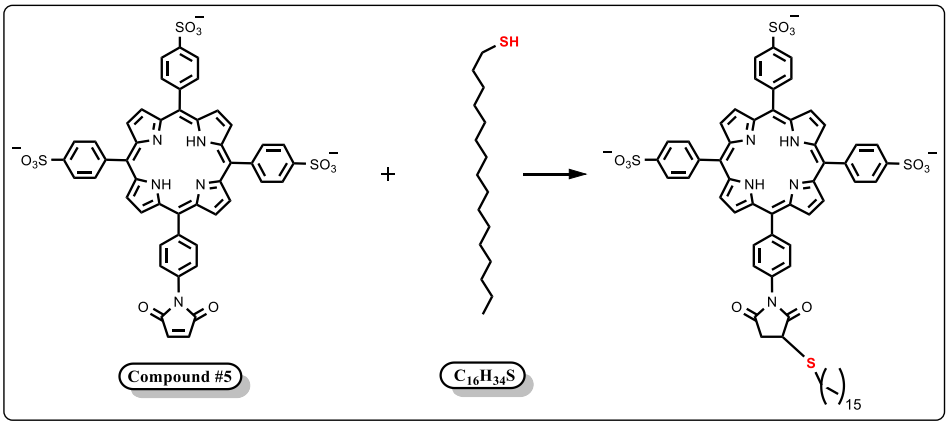

Scheme 3-7. Reaction of 1-hexadecanethiol with compound #5 to form the thiol-maleimide adduct.

The aim of this experiment was to elucidate the conditions to carry out the reaction between the hydrophobic thiol and compound #5 in the presence of liposomes. The reaction was followed up by UV-vis spectroscopy and HPLC. This experiment might provide some preliminary data before the approach to the reaction with the hydrophobic full-length transmembrane peptide. However, we found several problems working with this hydrophobic thiol: first, it was very difficult to handle and to solubilize it in aqueous solutions; second, the amount of reduced thiol was considerably low, which made the reaction with maleimides very difficult as mentioned before (see Results and Discussion).

3.2.4 Reducing agents

The experiments to check the status of the reduced thiol in the model compounds and the control peptide (see Results and Discussion) showed that a fraction of the thiol had been oxidized to disulfide. This phenomenon is a typical reaction of thiols present in peptides and proteins, in fact, many of the labelling reactions that involved biological thiol as reagents need to be carried out in the presence of reducing agents. Therefore, to achieve successfully the labelling of compound #5 we must first accomplish the reduction of the thiols present in the peptides[173]. There are a few methodologies reported in the literature to achieve complete labeling of maleimide-containing reactants with reducing agents:

1. The reducing agents are removed prior to the addition of the maleimide-containing reactant via column chromatography[56].
2. The thiol and the reducing agent are added first, then the maleimide reactant is added in 10-fold excess to be later on separated by column chromatography[174].
3. There are some procedures described in the literature in which the labeling is compatible with the presence of some reducing agents like phosphines[56].

In the next section, we will summarize the benefits and disadvantages of the reducing agents that we decided to use in this study for the labeling of the compound #5 with the model thiols.

3.2.4.1 Thiol-based reductants

Some of the most common reducing agents found in the literature are themselves thiols. In particular, dithiothreitol (DTT) and mercaptoethanol (ME) (Scheme 3-8) are two of the most common reagents used for reduction of biological disulfides.

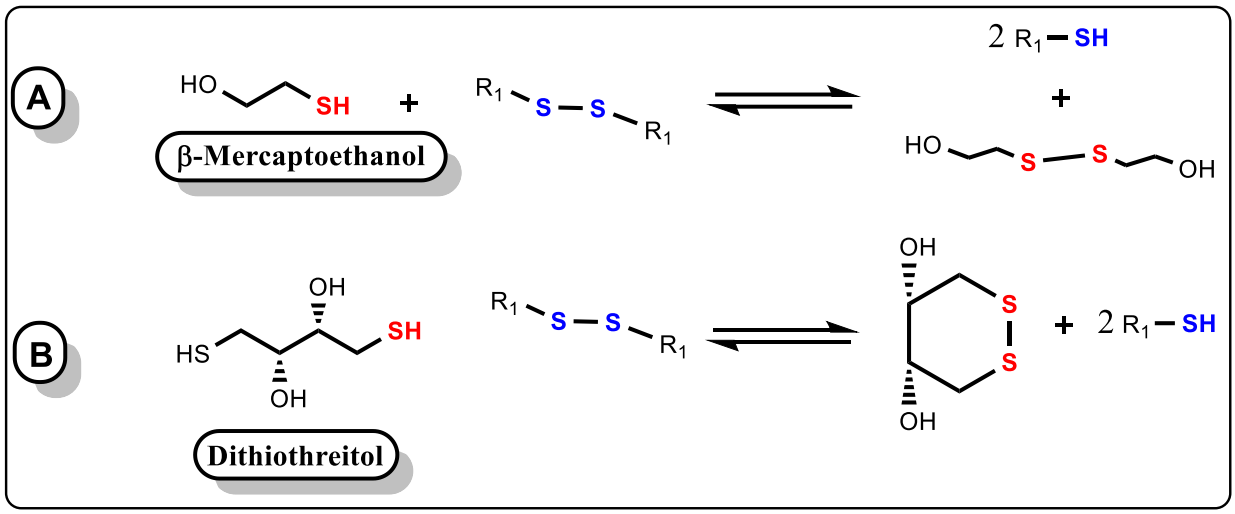

Scheme 3-8. Reduction of disulfides. A) β-mercaptoethanol (β-ME), B) dithiothreitol (DTT).

One of the advantages of this type of reductant is the high degree of specificity they show against disulfides[175] with little reactivity towards other functional groups in proteins or peptides. Moreover, due to these reagents being soluble in water we could use them to perform our labelling reaction in phosphate buffer. However, the main disadvantage of these thiol-containing reductants is that they will compete with the thiol present in the peptide for the thiol reactive reagent i.e. maleimides or iodoacetamide derivatives[156]. To overcome this, the most common methodology is to separate the DTT from the proteins or peptides prior to the addition of the maleimide reagent by column chromatography or reverse phase chromatography[56, 167, 168]. An alternative procedure could be to add an excess of the maleimides reagent to alkylate all the thiols present in solution and then use HPLC to separate the labeled

compound from the side products[174]. However, the best option for us would be to use a reducing agent that would be compatible with the labeling reaction, because in this way we could avoid any extra purification step or wastage of compound #5, which is hard to produce. Another problem associated with the use of these reagents is that they can easily cross the lipid membrane generating a reduced environment in both the inner and outer membrane compartments, i.e. inside and outside of the liposomes[156, 176, 177] as illustrated in Figure 3-2. The ability of DTT and ME to permeabilize the lipid membrane represents a problem in our study because we want to mimic as close as possible the natural arrangement of the transmembrane peptide in the biological membrane. In this regard, the TCR receptor complex is stabilized by the presence of extracellular disulfide bonds between cysteine residues present in the short sequence immediately after the transmembrane peptide region of both TCRγ and TCRδ chains. Thus, in the design of our peptide, we have kept carefully this cysteine in order to allow formation of this disulfide bond and the concomitant stabilization of the transmembrane peptide clusters. Phosphines are reducing agents that seem a good alternative to overcome this problem because they are highly polar compounds that do not permeate membranes, thus keeping the reduced environment restricted to the outer space of the lipid vesicles[156, 177].

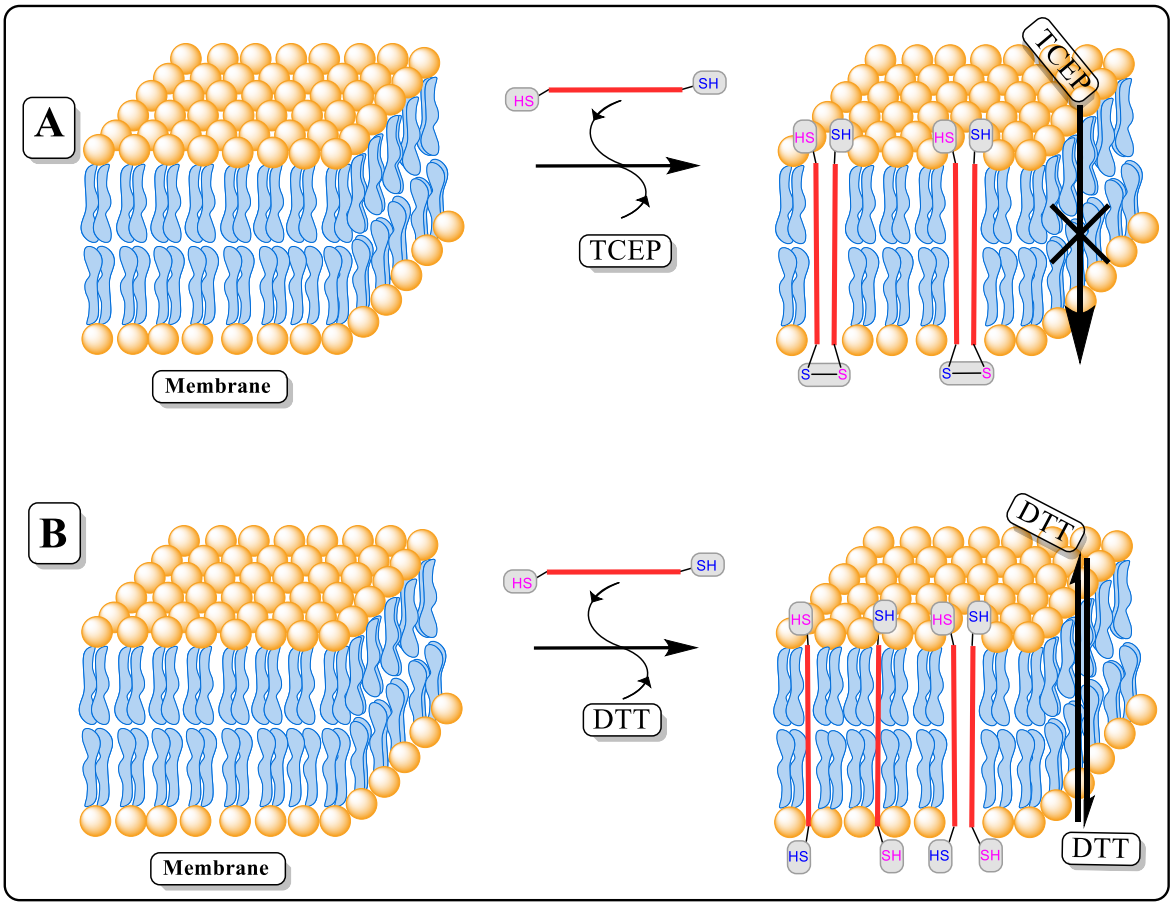

Figure 3-2. Illustration of the ability of the reducing agents used in this study to cross the bi-layer and the effect on the clustering of the full-length transmembrane peptides. A) TCEP is restricted to the outer space. B) DTT can permeate the membrane of the liposomes, reducing the disulfide bonds that could stabilize the clusters of peptides.

3.2.4.2 Phosphines

Trialkylphosphines, and especially Tris-2-carboxyethylphosphine (TCEP), reduce disulfides to free thiols. In the first step, phosphine is the nucleophile that attacks the disulfide bond to form a phosphonium salt (limiting step) and liberate the first thiol. The second step is rapid hydrolysis to produce the second thiol and phosphine oxide (Scheme 3-9). Oxidation of phosphine is irreversible; hence, it is not able to further participate in another reduction reaction. Phosphines, like thiol-containing reductants, are highly specific reducing disulfides with little reactivity towards other groups present in peptides[178]. In addition, TCEP is soluble in water, and negatively charged which makes its permeation through hydrophobic lipid membranes difficult[177]. It is also very efficient, reducing low molecular weight thiols and disulfides exposed in the surface of proteins[156], and a much more potent reductant than dithiothreitol at pH < 8 due to the pKa of the phosphine being 7.6, and is also more stable at pH values higher than 7.5[157]. Some published protocols suggest that TCEP is compatible with maleimide-thiol chemistry[159, 179-181]. A recent article by Bowman et al. described the role of phosphines as catalysts in nucleophilic thiol-Michael addition reactions[182].

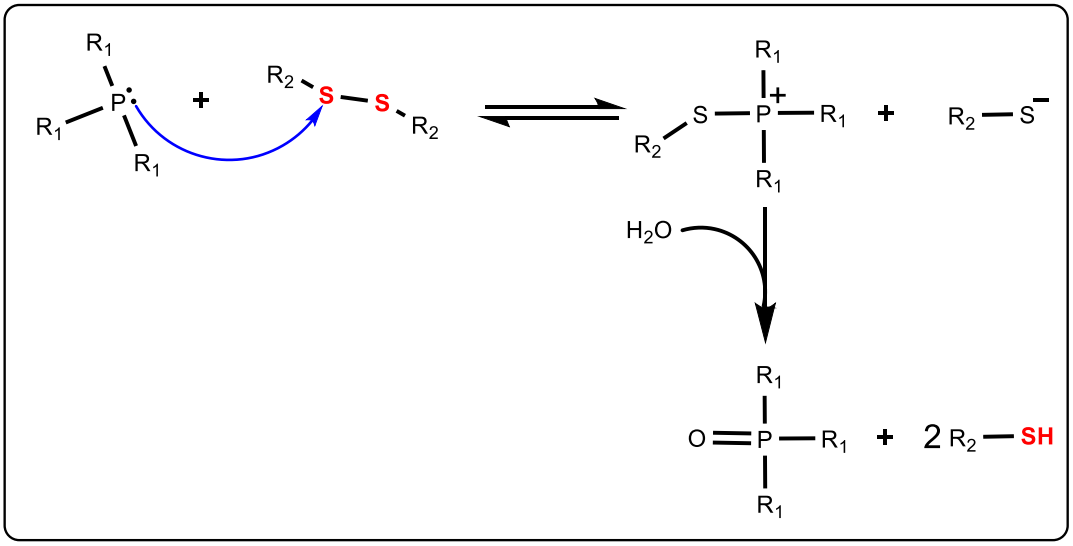

Scheme 3-9. General mechanism proposed for the reduction of disulfides by trialkylphosphines.

3.2.4.2.1 Sodium dithionite

Dithionite has been extensively used for the reduction of disulfides in proteins and peptides.[183, 184] The reaction must be carried out in basic solution to avoid decomposition by hydrolysis of dithionite ion in acid solutions[185]. The reactions can be carried out in water but sodium bicarbonate must be added to keep the solution basic thus avoiding the decomposition of the reagent as mentioned before. The dithionite ion can dissociate to a radical ion, and in the equilibria both species can act as reducing agents[186] (Scheme 3-10). Some reports have described that sodium dithionite can permeate biological membranes[187]. However, there is not much literature available describing the reaction of sodium dithionite in the reduction of disulfides[183, 188].

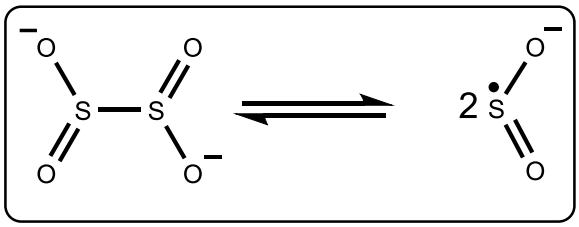

Scheme 3-10. Dissociation of the sodium dithionite anion.

3.3 RESULTS AND DISCUSSION

3.3.1 Quantification of free thiol in NAC with DTNB test.

The aim of this experiment was to determine the minimum amount of reduced N-acetylcysteine that we could quantify with the DTNB reagent. To achieve this, we prepared a stock solution of 2.5 µM of the model thiol NAC. Since the concentration of the hydrophobic peptide in our experiment will be 10 µM, this concentration would be appropriate to demonstrate the effectiveness of the DTNB in measuring the amount of free thiols in the micromolar scale.

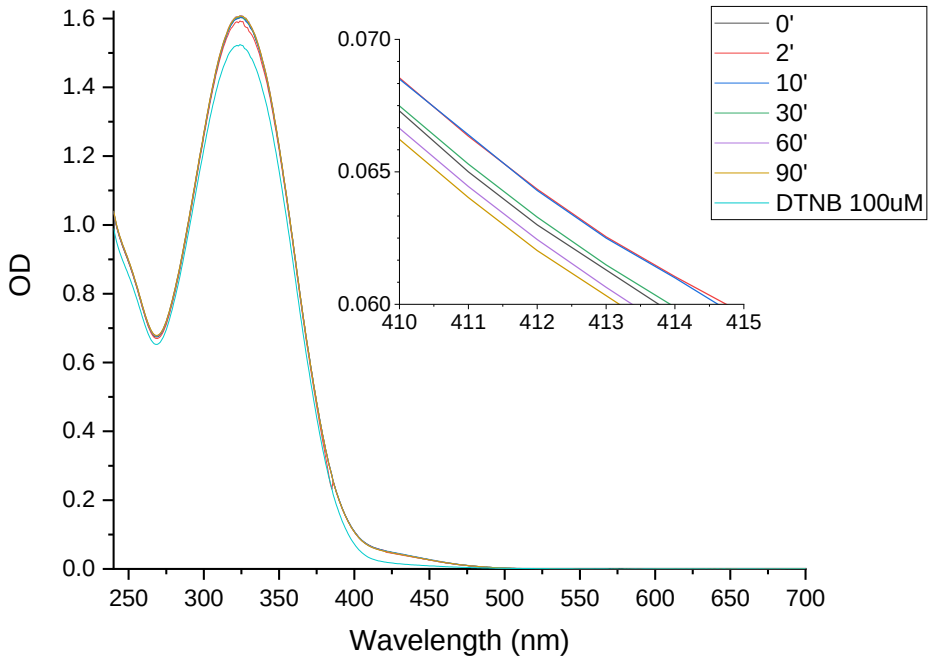

Figure 3-3. DTNB reaction to quantify the concentration of free thiol in a solution of 2.5 µM of NAC. The inset shows the changes in the absorbance at 412 nm. The reaction reach completion after 2 min.

Figure 3-3 shows the results obtained. The spectra of the reaction mixture between the DTNB (100 µM) and NAC (2.5 µM) in PB pH 7.2 were recorded at 0, 2, 10, 30, 60, 90 minutes after addition of DTNB. The inset shows an enlargement in the range 400-420 (the TNB^{-2} species is known to show a maximum absorbance at 412 nm, see Section 3.2.1.1). From the inset graph, it is also possible to see the reaction took approximately 2 min to complete (red line) and the stability of TNB^{-2} in solution started to decrease after 30 min. A graphic representation of absorbance at 412 nm versus time confirmed the reaction was completed at 2 min, noted by the location of A_{max} at this time point (Figure 3-4).

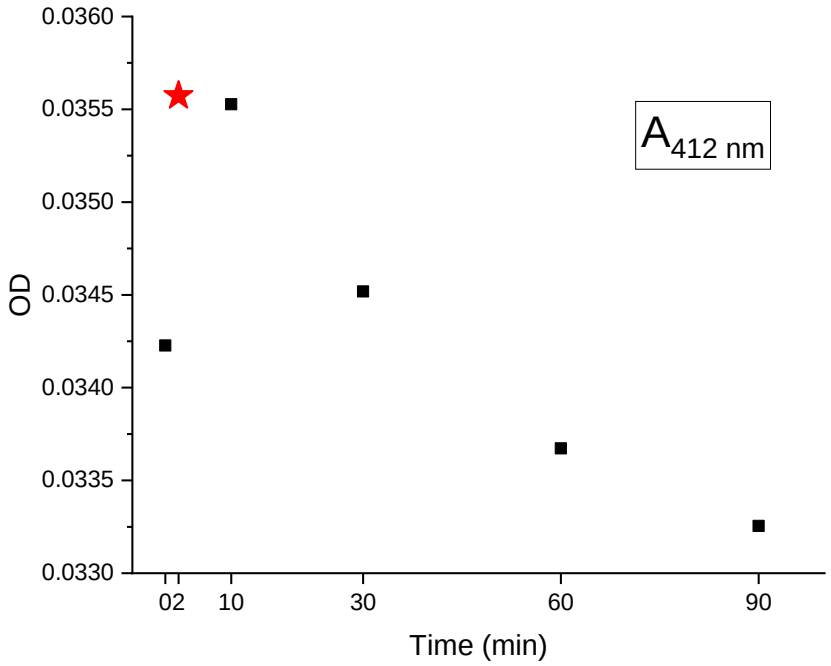

Figure 3-4. Plot of absorbance (412 nm) versus time. The red start corresponds to the time point when the [TNB^{2-}] is maximum therefore the reaction is completed.

Quantification of the reduced NAC was performed with the Lambert-Beer law, based on the extinction coefficient of the TNB^{-2} species in PB pH 7.2, which was 14600 $M^{-1}cm^{-1}$ (Table 3-1).

Time (min)	A_{412}	Path cm	ε $M^{-1}cm^{-1}$	[SH] µM
0	0.0342	1	14600	2.34
2	0.0355	1		2.43
10	0.0355	1		2.43
30	0.0345	1		2.36
60	0.0336	1		2.30
90	0.0332	1		2.27

Table 3-1. Quantification of the amount of free thiol in a solution of 2.5 µM NAC with the Lambert-Beer law.

3.3.2 Quantification of free thiol in peptide control with DTNB test.

Prior to performing the reaction between compound #5 and the full-length transmembrane peptide, we decide to establish the chemistry with a surrogated peptide (control peptide). The control peptide is an oligopeptide of 16 residues, Ac-CWQDKNDVLQLQFTIT-NH2, which is actually contained in the full-length peptide. This control peptide contains one cysteine at the amino terminal end, which is the nucleophilic group. We used the tryptophan adjacent to that cysteine with the intention to use its fluorescence properties as an insertion reporter[189]. We might be able to follow the insertion and the orientation of the peptide in the lipid membrane by analyzing the changes in the fluorescence pattern of the tryptophan[190].

We quantified the fraction of reduced peptide in a fresh sample, prepared from the lyophilized stock of the starting material kept at -20 ^{o}C. We also explored the rate of oxidation in aqueous solution with the DTNB test in a sample of 10 µM of peptide in PB pH 7.2 (Figure 3-5). This experiment is critical in order to define the conditions to perform the labeling reaction i.e. the necessity of a reducing agent. The results showed that at time point 0, 26% of the peptide control was already oxidized.

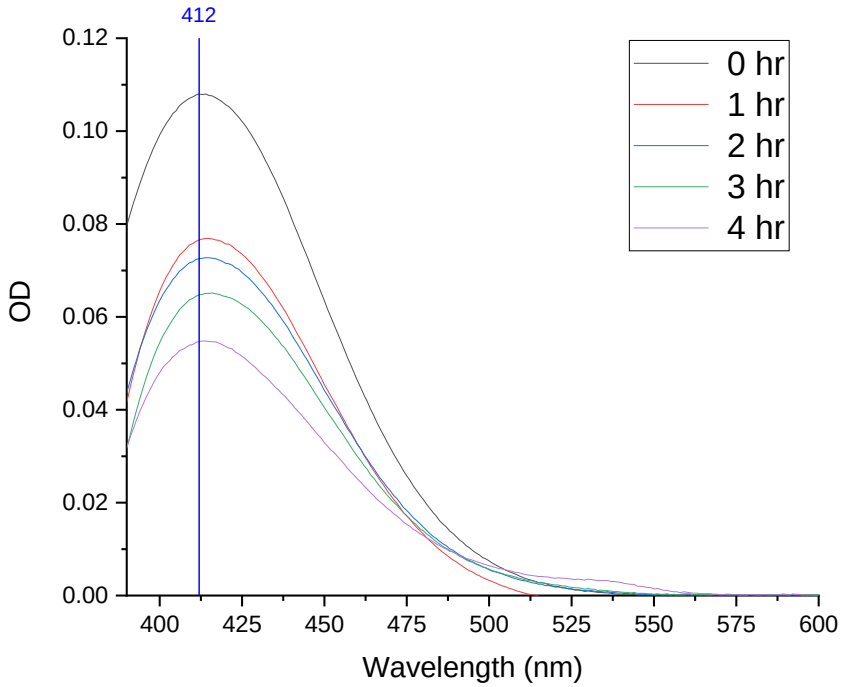

Figure 3-5. DTNB test to quantify the fraction of reduced peptide control and the rate of oxidation in a sample of 10 µM peptide containing 3.3% DMSO in PB. UV-vis traces were recorded every hour in a 4 hours kinetic study.

The kinetics of the oxidation reaction was followed by UV-vis and the analysis of the traces showed that oxidation of the peptide progressed quickly from around 50% at 1 hr to 62.6 % at 4 hrs (Table 3-2).

Time (hr)	A_{412}	ε $M^{-1}cm^{-1}$	[SH] µM
0	0.1079	14600	7.39
1	0.0765		5.24
2	0.0725		4.96
3	0.0647		4.43
4	0.0547		3.74

Table 3-2. . Quantification of the fraction of reduced thiol in a solution of 10 µM of peptide control in PB (+ 3.3% DMSO).

In summary, this experiment demonstrated the necessity of using a reducing agent to keep the peptide in the reduced form before the labeling reaction with compound #5. This is especially important in reactions that require a long set up because the results showed that after 1 hour of incubation, half of the thiol in solution was already oxidized.

3.3.3 Quantification of free thiol in 1-Hexadecanethiol with DTNB test

Here, we aimed to determine the fraction of non-oxidized thiol that was reduced in a solution of 10 µM of 1-hexadecanethiol in PB before the labeling reaction with compound #5. Additionally, we decided also to explore the conditions to perform the DTNB test with this hydrophobic thiol, which is similar to the full-length transmembrane peptide. Analysis of the data (Figure 3-6) (Table 3-3) showed that the reaction with DTNB was considerably slower when compared with NAC. Possibly, due to the hydrophobic nature of 1-hexadecanethiol it tended to form micelles in aqueous solution. We suspect this might restrict the access of the DTNB reagent to the thiol group. The table also showed that after 180 minutes around 14% of the thiol was oxidized to disulfide.

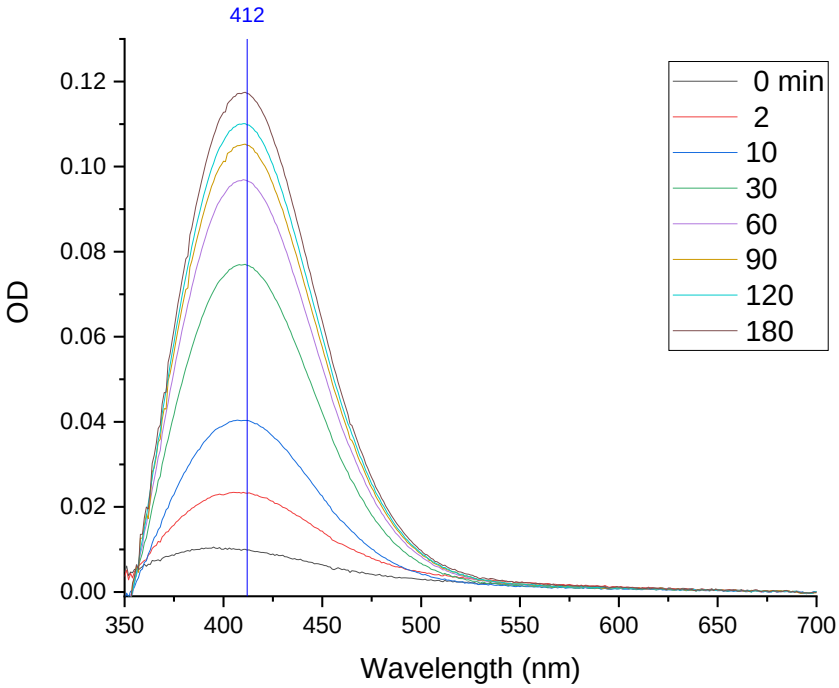

Figure 3-6. DTNB test to quantify the fraction of reduced 1-hexadecanethiol and the rate of oxidation in a sample of 10 µM 1-Hex containing 3.3% DMSO in PB. UV-vis traces were recorded as indicated in the legend.

Time (min)	A_{412}	ε ($M^{-1}cm^{-1}$) pH 7.2	[1-Hex]µM
0	0.0098	14600	0.7
2	0.0232		1.6
10	0.0403		2.8
30	0.0767		5.3
60	0.0966		6.6
90	0.1050		7.2
120	0.1098		7.5
180	0.1172		8.0

Table 3-3. Quantification of the amount of free thiol in a solution of 10 µM of 1-Hexadecanethiol.

Figure 3-7 showed how after 120 min the reaction approximate to the plateau, which indicates that DTNB had reacted with all the reduced thiol available in solution.

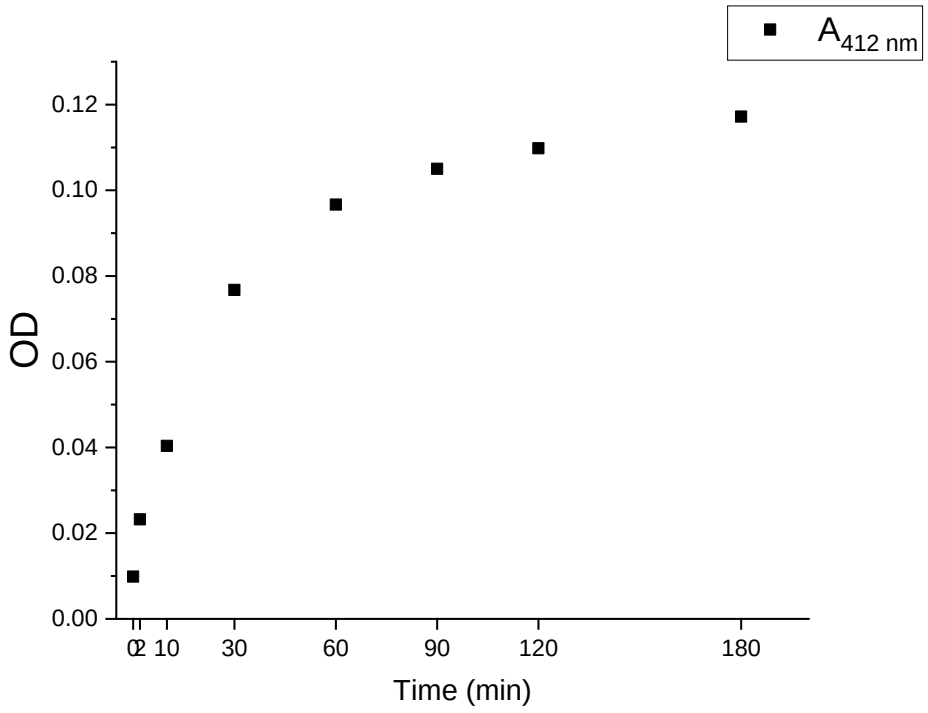

Figure 3-7. Graphic representation of the absorbance at 412 nm versus time in the reaction of the DTNB with the 1-hexadecanethiol. The graph shows that after the 120 min the reaction reach the plateau.

In conclusion, the DTNB reaction with 1-Hexadecanothiol (1-Hex) is slower than the reaction with the peptide control, probably due to the hydrophobic nature of 1-Hex and the formation of aggregates in PB, although this is just speculation that needs to be further investigated. In the time period tested in this experiment, we could determine that after 180 minutes ~14% of the thiol was oxidized. However, the oxidation rate of 1-Hex was slower when compared with the control peptide, which suggests the necessity to reduce the thiols in a previous step, before to proceed to the labelling reaction with compound #5.

3.3.4 Quantification of free thiol in the full-length peptide with DTNB test

Similar to the experiment described in section 3.3.2, we decided to quantify the amount of reduced thiol and the rate of oxidation for the full-length transmembrane peptide. Briefly, the full-length transmembrane peptide is composed of 47 residues and contain two cysteines towards both ends of the peptide. A sample containing 10 μM of the full-length peptide and 3.3% DMSO was prepared in PB. The stock solution was freshly prepared in DMSO immediately before from a lyophilized stock of peptide kept at -20 ºC. Figure 3-8 shows the results obtained in the reaction with DTNB (100 μM) over a time period of 5 hrs.

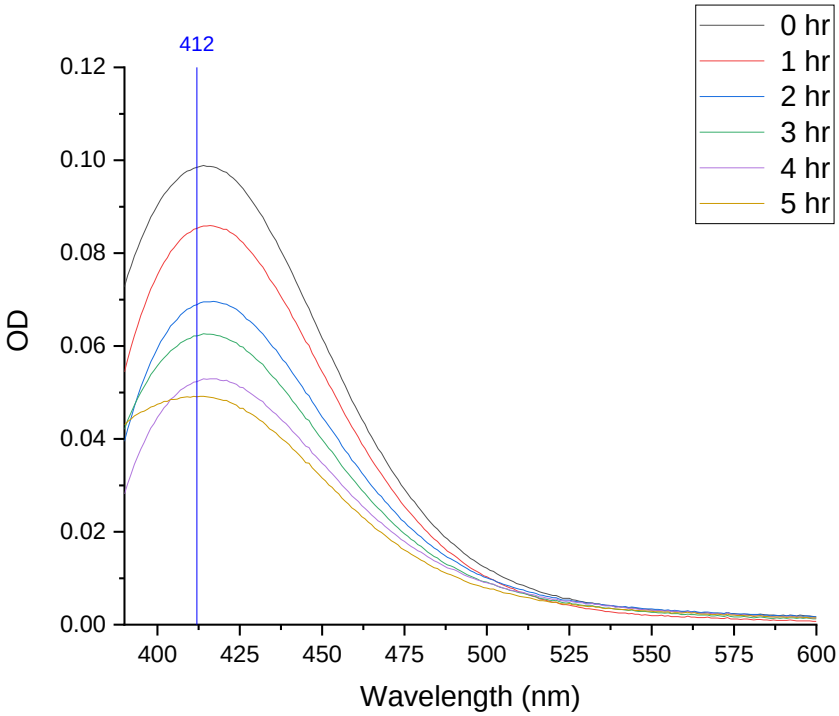

Figure 3-8. UV-vis spectra collected from the DTNB test to quantify the fraction of reduced full-length transmembrane peptide control and the rate of oxidation in a sample of 10 μM peptide containing 3.3% DMSO in PB.

The data from the kinetic study in Table 3-4 reveal that at time 0 approximately 32% of the full-length-peptide was already oxidized. In addition, and similar to the results observed for the control peptide (Section 3.3.2) the rate of oxidation increased proportionally with time, hence, after 5 hrs of incubation approximately 66% of the peptide was oxidized.

Time (hr)	A_{412}	ε $M^{-1}cm^{-1}$	[SH] μM	Percentage
0	0.0985	14600	6.7	67.4
1	0.0853		5.8	58.4
2	0.0689		4.7	47.2
3	0.0622		4.3	42.6
4	0.0523		3.6	35.8
5	0.0491		3.4	33.6

Table 3-4. Quantification of the amount of free thiol in a solution of 10 μM of the full-length transmembrane peptide.

It is important to mention that we found difficulties in solubilizing the full-length transmembrane peptide in solvents other than DMSO. To test the possibility that a fraction of the full-length peptide had precipitated in the actual sample prepared in PB, therefore altering the real thiol concentration, we decided to measure the peptide concentration by reading the absorbance at 280 nm (see Figure 6-5 in Appendix). The results showed the concentration of the peptide was approximately 10.1 μM immediately after the preparation of the sample. Moreover, we also observed that it was stable after 1 hour (9.8 μM) hence, demonstrating that the peptide did not precipitate in the sample.

In summary, this experiment showed that to work with the full-length peptide it is necessary to add a reducing agent to ensure that all the thiol is reduced, in order to successfully achieve the labelling reaction with compound #5.

3.3.5 Determination of the extinction coefficient (ε) of compound #5 in PB.

We then decided to determine the extinction coefficient of compound #5 in phosphate buffer. Using a geometric dilution method (see Experimental Section) we performed a titration of compound #5 in 15 samples with increasing concentration of porphyrin. From the fitting of the experimental data, i.e. absorbance at the maximum wavelength (413 nm) against the concentration of compound #5, it was possible to calculate the extinction coefficient in PB 100 mM pH 7.2 at RT based on the application of the Lambert-Beer Law (Figure 3-9). The fitting gave a value for the extinction coefficient of compound #5 in PB at RT equal to 218200$M^{-1}cm^{-1}$. This value was used in all the following experiments.

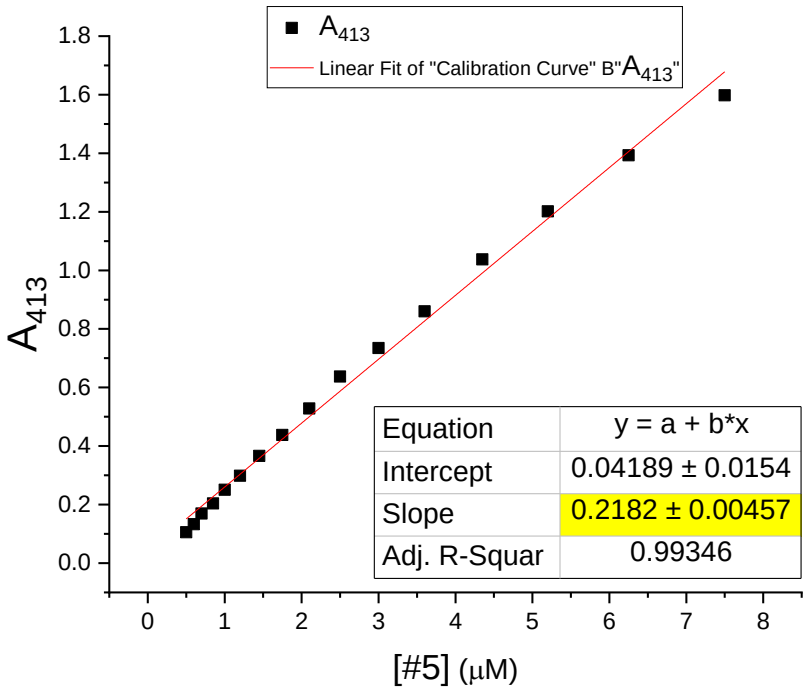

Figure 3-9. Lambert-Beer Law fit to determine the extinction coefficient, ε($M^{-1}cm^{-1}$), of compound #5 at 413 nm.

3.3.6 Reaction of N-acetylcysteine with 5-(4-maleimide)-10, 15, 20 tris (4 - sulfonatophenyl)–porphyrin (Compound #5).

Taking advantage of the optical properties of the porphyrin moiety, it was used in UV-vis spectroscopy experiments to follow the reaction with the model thiol N-acetylcysteine (Scheme 3-11).

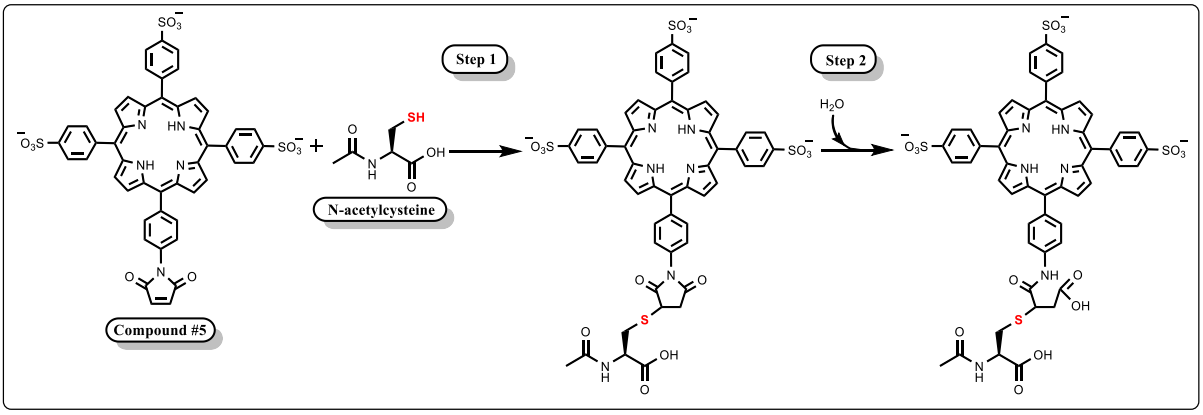

Scheme 3-11. Reaction of Compound #5 with NAC. Step 1: synthesis of the adduct maleimide-NAC, Step 2: hydrolysis of the maleimide.

Thanks to the high extinction coefficient of compound #5 (218200$M^{-1}cm^{-1}$) it was possible to follow the reaction with compound #5 in the low micromolar regions.

In the experiment, NAC was added in 2000-fold excess compared to the compound #5 to force completion and the reaction was followed by recording the UV-vis spectra for 100 minutes immediately after addition of NAC with 5 minute intervals between measurements. Traces are shown in Figure 3-10.

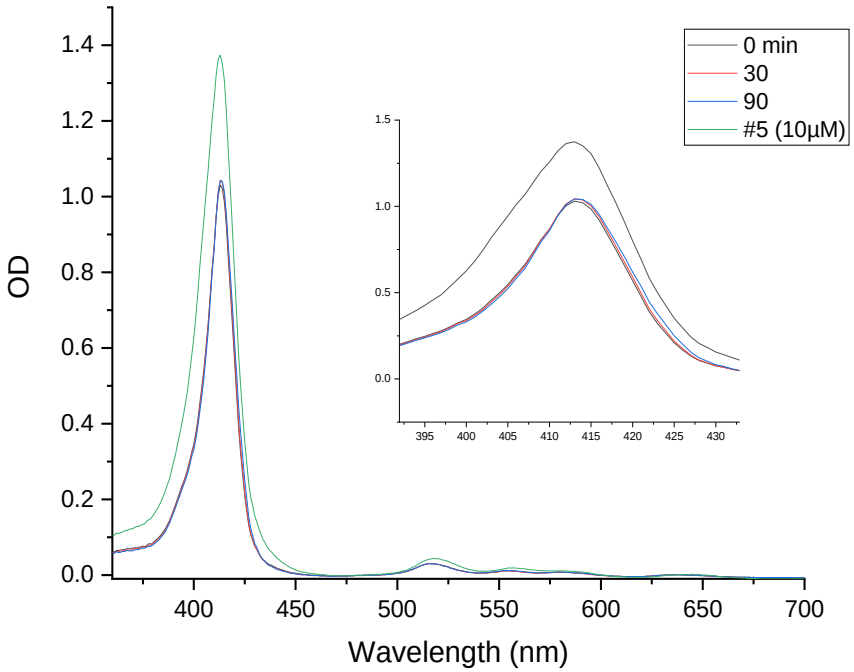

Figure 3-10. UV-vis traces from the reaction mixture of compound #5 (10 µM) and NAC (20 mM) in PB. The traces were collected at 0, 30, and 90 minutes.

Spectra showed no major differences between them, and the position of the λ_{max} was observed at 413 nm in each case. This result suggests that reaction of NAC and compound #5 cannot be followed by UV-vis spectroscopy. We hypothesize the reason being is that NAC is a small molecule unlikely to produce a big impact in the absorbance of the porphyrin macrocycle. Moreover, its position is too far from the porphyrin moiety to generate any major perturbation in the electronic distribution of the macrocycle. Moreover, we think the hypochromic effect observed in those traces recorded after the addition of NAC when compared with the trace of compound #5, might be due to a dilution effect.

However, to rule out the possibility that compound #5 in the stock solution has suffered hydrolysis and therefore became unable to react with the NAC, we collected an NMR spectrum of the stock solution to evaluate the integrity of the maleimide moiety (Figure 3-11).

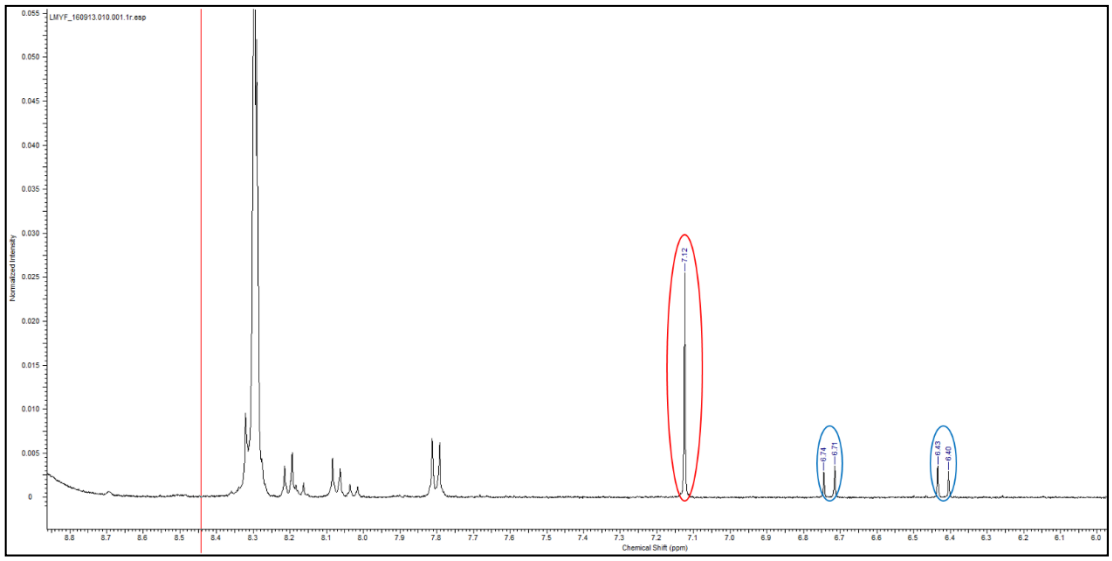

Figure 3-11. ^{1}H NMR spectrum (400 MHz, MeOD) of compound #5 stock solution at 25 °C in methanol. Circled in red the singlet belonging to the maleimide group, in blue, the two doublets showing some methanolysis of the maleimide function.

The ^{1}H-NMR spectrum shows a singlet at 7.12 ppm belonging to the maleimide (see Chapter 2). There are also two set of doublets at 6.71 and 6.43 ppm, which belong to protons **g/h** of the open ring (Scheme 3-12), respectively. From the integral ratios, we quantified the concentration of both species, hydrolyzed and non-hydrolyzed in the stock solution. The predominant species was the non-hydrolyzed maleimide (67.5 %), while the remaining 32.5% represented the hydrolyzed maleimide.

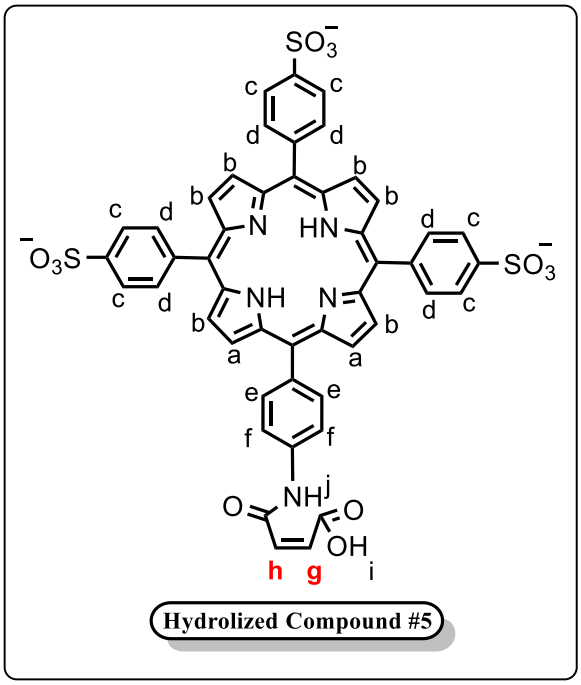

Scheme 3-12. Panel showing the chemical structure of the hydrolyzed compound #5. The proton g and h produce the doublets observed in the NMR spectra at 6.71 and 6.43 ppm, respectively.

Based on the results we concluded that the reactive maleimide was the predominant form in the stock solution, hence, most likely the reaction with the NAC to produce the adduct #5-NAC was successful, although we could not follow it by UV-vis spectroscopy.

As mentioned before, due to subtle changes in the electronic configuration of the macrocycle between compound #5 and adduct 5-NAC, the reaction cannot be tracked by changes in the UV-vis spectra. Therefore, we decided to go further and explore whether the hydrolysis of the adduct might have yielded any changes in the molecule that could be traceable by UV-vis spectroscopy. To study this hypothesis, we left the mixture over a period of 24 hours at room temperature to induce the hydrolysis of the maleimide. We recorded the UV-vis spectra over a 20 hour period with an interval of 1 hour between measurements (Figure 3-12).

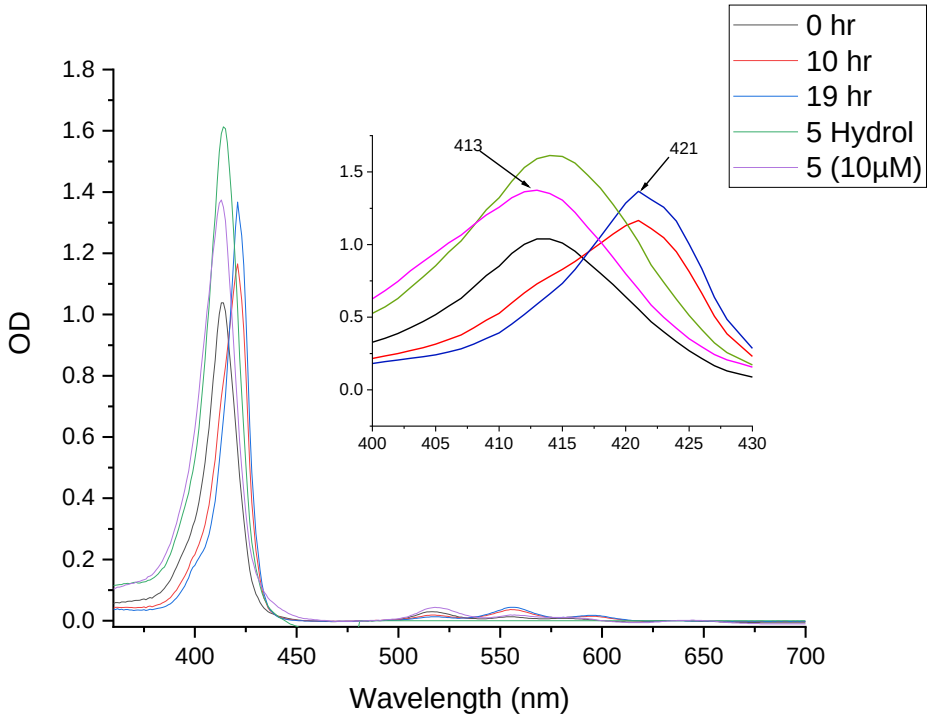

Figure 3-12. UV-vis traces of the compound #5 (10 μM), hydrolyzed compound #5, and the adduct compound #5 N-acetylcysteine recorded in PB at 0, 10, and 19 hours after the beginning of the reaction. The inset graph illustrates the bathochromic shift of the λ_{max} of the Soret band.

Interestingly, the spectra showed a bathochromic shift in the λ_{max} of the Soret band from 413 to 421 nm coupled with a hypochromic effect for the trace at time point 0 hr. By contrast, a visible hyperchromic effect was observed for the traces at 10 and 19 hrs. Presumably, the changes in the intensity can be explained by aggregation of the porphyrin-adduct in the cuvette. In addition, aggregation might induce the participation of free monomer in solution which could explain why the intensity of the band at 413 nm also decreases with time. The formation of the aggregates could be followed by changes observed in the new Soret band at maximum of 421 nm.

3.3.7 Reaction of γ-Glutathione with 5-(4-maleimide)-10, 15, 20 tris (4 - sulfonatophenyl) – porphyrin (Compound #5).

In order to test whether the addition of a longer thiol relative of NAC would produce significant changes in the UV-vis spectra of the adduct with compound #5, we decided to use a different model thiol: γ-glutathione (Scheme 3-13). The rationale behind this new approach was based on the fact that glutathione is a peptide, like the transmembrane segment that we will employ in our chemical model. However, glutathione is quite different in size and polarity when compared to the hydrophobic peptide.

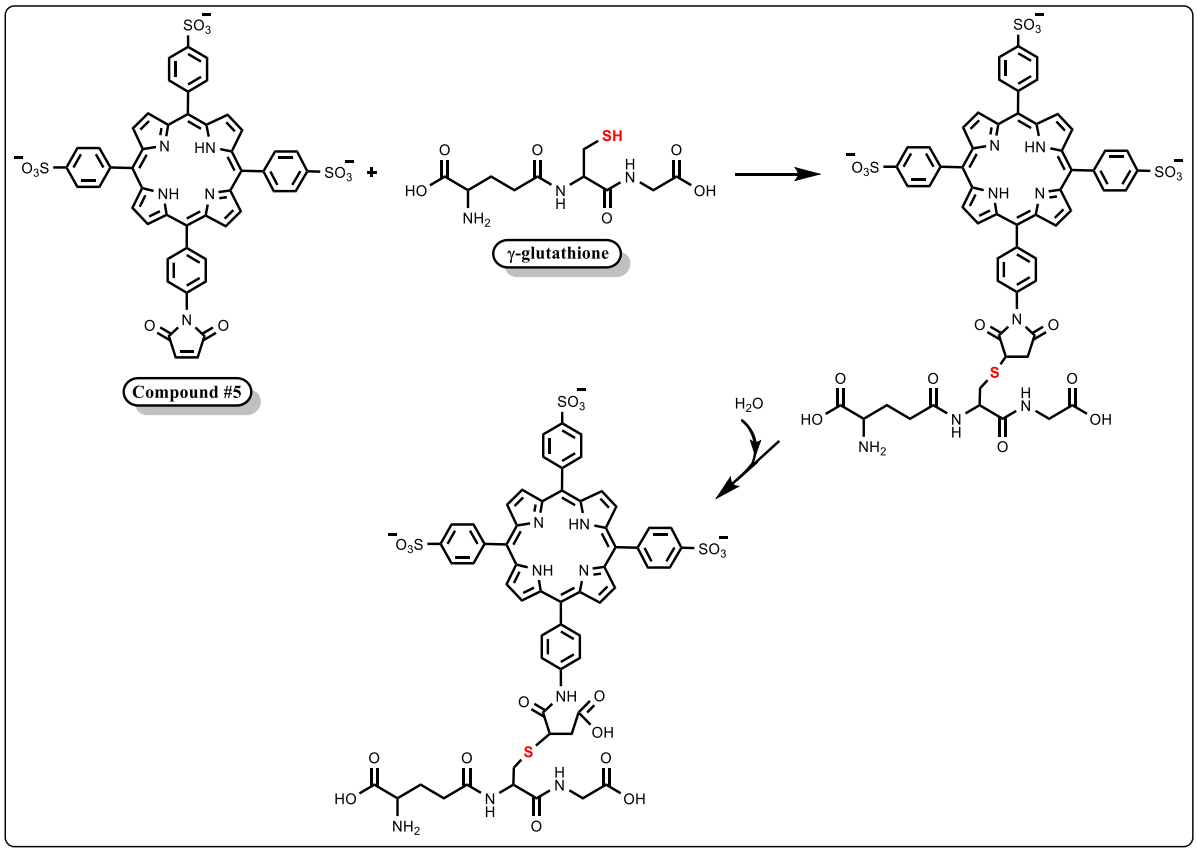

Scheme 3-13. Reaction of Compound #5 with γ-glutathione. Step 1: synthesis of the adduct maleimide- γ-glutathione, Step 2: adduct hydrolysis with opening of the maleimide ring.

To study the reaction with the γ-glutathione and compound #5, a solution of porphyrin (10 µM) was prepared and the UV-vis spectrum recorded. Immediately after we added the reduced glutathione to reach 10 mM in the cuvette, we mixed and recorded the traces up to 45 minutes with 5 minute intervals in between measurements (Figure 3-13).

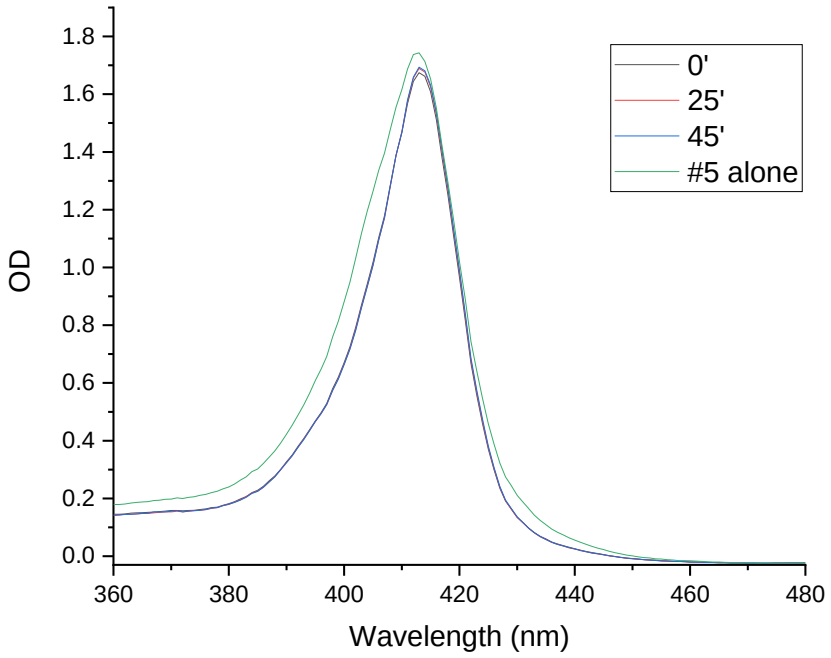

Figure 3-13. UV-vis traces from the reaction mixture of compound #5 (10 µM) and NAC (10 mM) in PB. The traces were collected at 0, 25, and 45 minutes.

Spectra of compound #5 alone and those recorded at 0, 25, and 45 minutes after initiated the reaction showed no great differences in the position of the λ_{max} (413 nm) or in absorption intensity of the Soret band. Moreover, no changes in the extinction coefficient at 413 nm were noted. The glutathione, similar to NAC, most probably did not introduce any disturbance in the electronic density of the porphyrin macrocycle that could produce a major

change in the spectroscopic properties of the chromophore. Following the same rationale as described in the section 3.3.6 we decided to explore the effect of the hydrolysis over the spectroscopic properties of the porphyrin. To tackle this we extended the measurements for another 20 hours, recording traces every hour. We took special attention to avoid the photolysis of the sample in the cuvette (see Experimental Section).

Figure 3-14 shows UV-vis traces taken at time 0, 10, and 19 hours compared to those of compound #5 non-hydrolyzed, and hydrolyzed. Analysis of the spectra showed that there was a bathochromic shift combined with a hypochromic effect in the traces that corresponded to the adduct porphyrin-glutathione and the hydrolyzed compound #5. However, we do not know how to explain this observation but we suggest that presumably this could be due to aggregation of porphyrin monomers. If this was the case, then we could also add that the spectroscopic data suggest that the adduct glutathione-porphyrin is less biased towards aggregation than the adduct of 5- N-acetylcysteine.

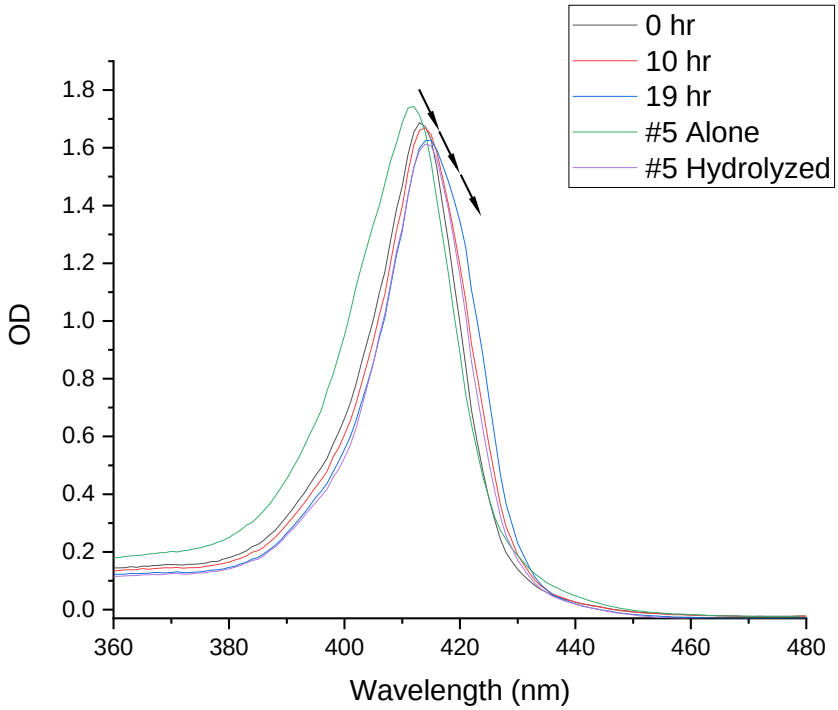

Figure 3-14. UV-vis traces of compound #5 (10 µM), hydrolyzed compound #5, and the adduct compound #5-γ-gluthathione recorded in PB at 0, 10, and 19 hours after the beginning of the reaction. The direction of the arrows illustrates the changes in the Soret band.

In summary, from this experiment we could not determine any spectroscopic changes in the porphyrin traces that were indicative of the formation of the adduct compound #5-γ-gluthathione. However, if our hypothesis is correct, the glutathione seems to have a negative effect over the aggregation of the porphyrin in solution, presumably by affecting the nucleation of the monomers, which has been reported previously as the limiting step in the aggregation of porphyrins[191].

3.3.8 Interaction of tris (2-carboxyethyl)phosphine (TCEP) with 5-(4-maleimide)-10, 15, 20 tris (4 - sulfona-tophenyl)–porphyrin (Compound #5).

The aim of this experiment was to study by NMR whether the reducing agent TCEP reacts with compound #5. Since the NMR spectrum of TCEP (Figure 3-15) does not show any signal above 5.0 ppm, where most of all the signals of compound #5 are located, NMR spectroscopy could be used to follow the reaction. To answer this question we prepared two samples from a unique stock, one containing compound #5 only, and the second containing compound #5 (0.5 mM) plus a 10-fold excess of TCEP (5 mM), both in deuterated methanol. Interestingly, after the addition of TCEP to the solution of compound #5, we observed immediately the formation of a precipitate, with colour change from purple to green. To elucidate whether all the porphyrin in the sample containing TCEP had precipitated we performed the analysis by NMR, at 0, 1, 2, 3, 4, 48, and 72 hours. The sample containing only compound #5 was also analysed. Figures 3-15, 16, and 17 show the ^{1}H-NMR spectra recorded at 0 and 48 hours, respectively.

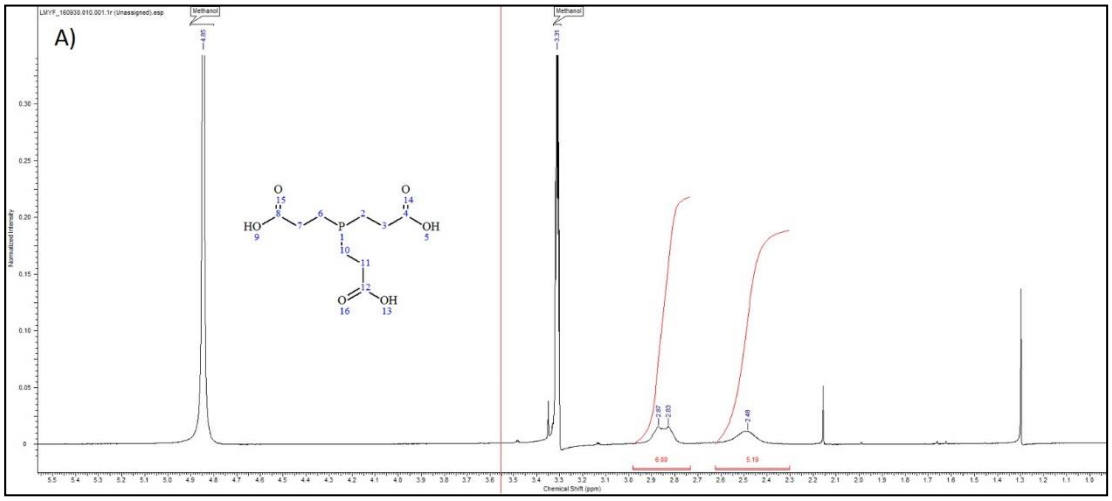

Figure 3-15. ^{1}H NMR spectra (400 MHz) of the solution stock of TCEP at 25 °C. A) in deuterated methanol.

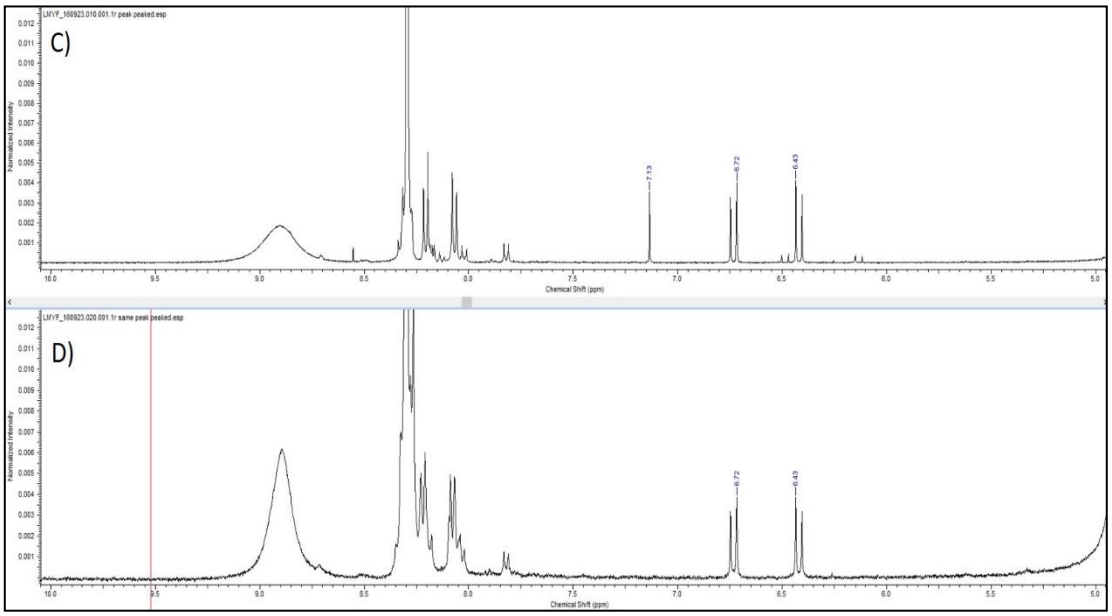

Figure 3-16. ^{1}H NMR spectra (400 MHz, MeOD). C) Compound #5 alone. D) Compound #5 after the addition of the TCEP at 0 hrs.

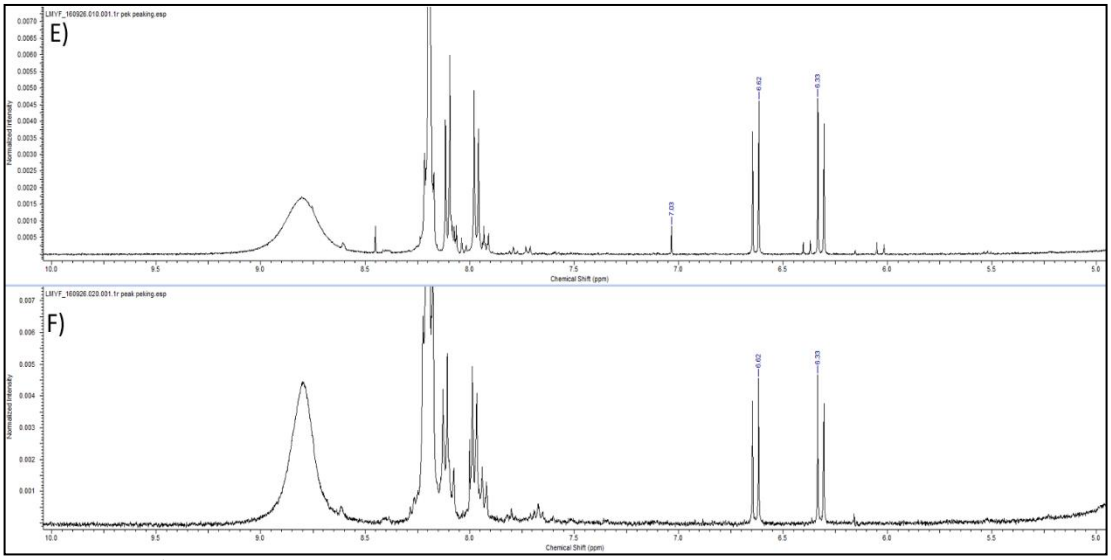

Figure 3-17. ^{1}H NMR spectra (400 MHz, MeOD). E) Compound #5 alone. F) Compound #5 after the addition of the TCEP at 48 hrs.

Figure 3-16 shows the ^{1}H NMR spectrum at 0 hrs. After addition of TCEP the signal belonging to maleimide at 7.13 ppm immediately disappeared. This result suggests that upon interaction between TCEP and compound #5 an insoluble product was formed, and this solid product was not visible by ^{1}H-NMR. Another possible explanation is that TCEP reduces the double bond of the maleimide. However, in this case we should have observed two doublets from the maleimide protons, which in fact we did not see in the spectra, but this could occur in the case of a non-covalent interaction. During the course of this study we found a recent paper that indeed confirmed that TCEP reacts with maleimides under the conditions normally used in the bio-conjugation reactions to form the TCEP-maleimide adduct[192].

To continue exploring this reaction we decided to analyze the sample after 48 hrs incubation. Figure 3-17 shows that in the sample of compound #5 alone the singlet at 7.03 ppm was still present although the intensity was clearly lower, presumably due to the methanolysis of a large fraction of compound #5. However, in the sample containing the TCEP the signal belonging to the maleimide was absent, as it was before.

These results showed that despite some porphyrin precipitate after the addition of the TCEP, probably due to aggregation of the monomers triggered by the protonation of the pyrrole nitrogen, some porphyrin remains in solution as we can actually see it in the NMR analysis. However, upon addition of TCEP the characteristic singlet from the maleimide at 7.13 ppm disappeared. The absence of the expected doublets from the succinimide ring was explained satisfactorily by the formation of the double bond (P=C) between TCEP and the maleimide, to form an ylene as shown in Scheme 3-14.

To understand the reactivity of the TCEP towards maleimide we set up the reaction of TCEP with a model maleimide called N-ethylmaleimide (Scheme 3-14). The reaction was followed by NMR sprectroscopy.

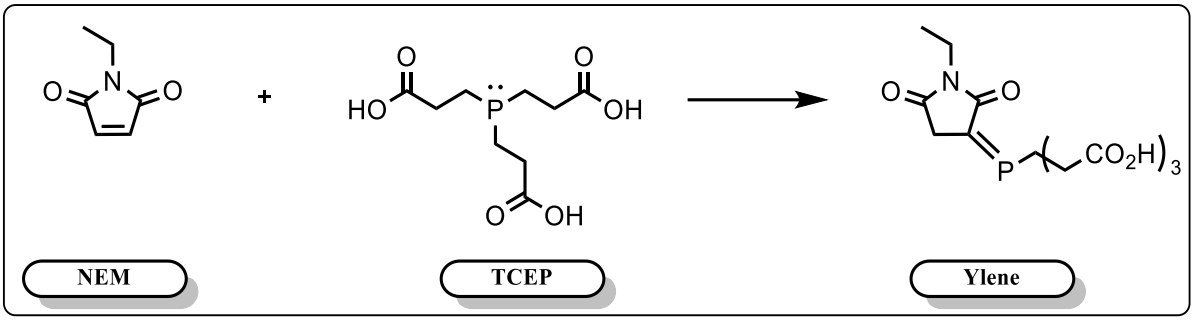

Scheme 3-14. Reaction of TCEP and NEM in 0.1 M phosphate buffer pH 7, RT, to render the adduct TCEP-NEM (4-ylene).

Figure 3-18 illustrates the ^{1}H NMR spectrum of the product the reaction between NEM and TCEP and the assignment of each signal to their corresponding protons in the molecule.

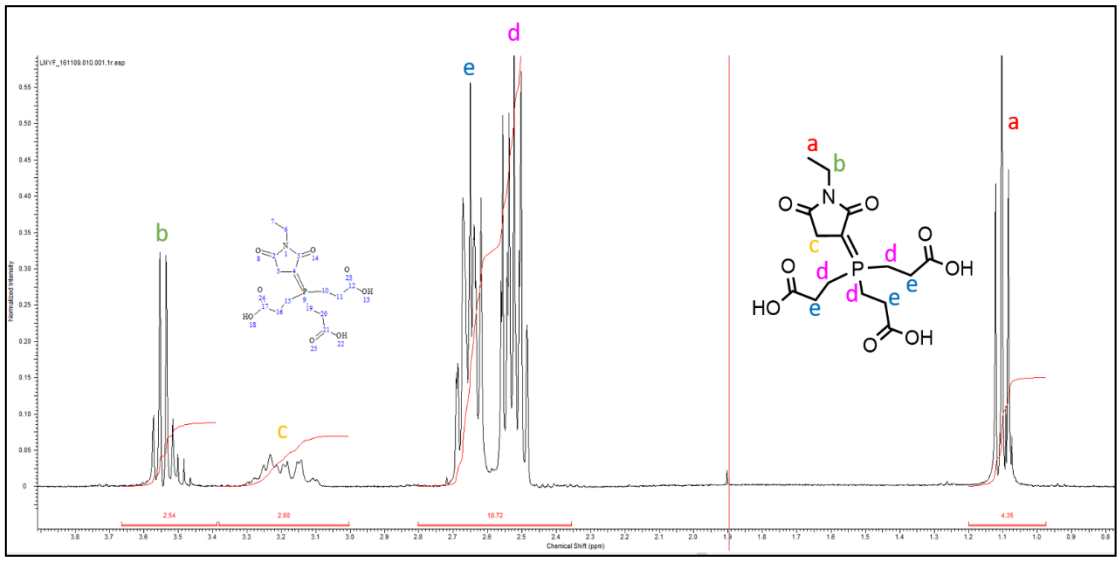

Figure 3-18. ^{1}H NMR (400 MHz, D_2O) spectrum of NEM-TCEP adduct.

Importantly, the multiplet at 3.2 ppm corresponds to the two protons ***c*** in the succinimide ring. From the analysis of the integrals, 89.3% of NEM reacted with the TCEP, leaving only 10.7 % of NEM available for the labeling reaction with the thiol.

To investigate whether the unexpected precipitation of the porphyrin in methanol after adding the TCEP was due to acidification we decided to perform the reaction in a mix of phosphate buffer pH 7.2 and methanol. Before the sample preparation, we tested whether the methanol/phosphate buffer mixture does not alter the solubility of the phosphate buffer salt.

	Methanol (ml)	1	2	3	4	5	6	7	8	9
PB Buffer (ml)		↓								
9	→	S								
8			S							
7				S						
6					S					
5						S				
4							S			
3								S		
2									S	
1										S

Table 3-5. Mix of methanol and phosphate buffer to study the solubility of the phosphate salt. S) completely soluble.

Table 3-5 shows that for all the ratios tested the phosphate salt was completely soluble. Therefore, we proceed to study the reaction with TCEP. To this end, we prepared three working solutions with the following composition: 1) 25% MeOD: 75% PB, 2) 50% MeOD: 50% PB, and 3) 75% MeOD: 25% PB and a final concentration of compound #5 equal to 5 mM (Figure 3-19).

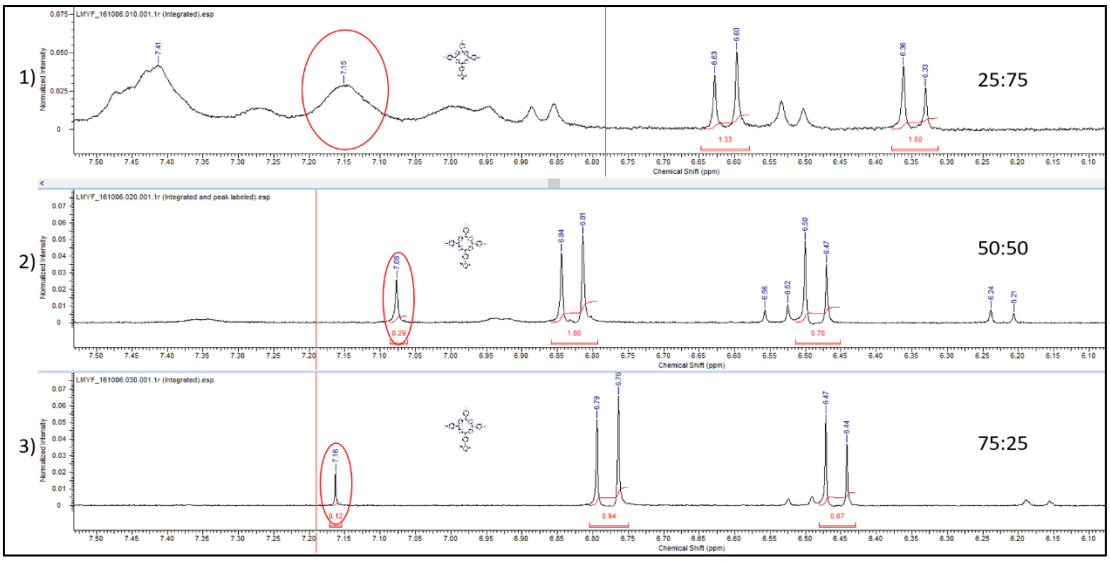

Figure 3-19. ^{1}H NMR (400 MHz, MeOD) spectra of three solutions of compound #5 at 25 °C. 1) 25% MeOD: 75% PB, 2) 50% MeOD: 50% PB, and 3) 75% MeOD: 25% PB. Circled in red the singlet belonging to the maleimide group.

From the integral ratios of the peaks located at 7.16 ppm, approximately 30% correspond to compound #5 and 70% to hydrolyzed maleimide. The resolution of the peaks in the spectrum of 25MeOD: 75PB solution was poor compared with the other two spectra. To each solution we added TCEP to reach a final concentration of 5 mM. The samples were mixed and no change in color or precipitation was observed. Immediately after we recorded the ^{1}H-NMR spectra (Figure 3-20).

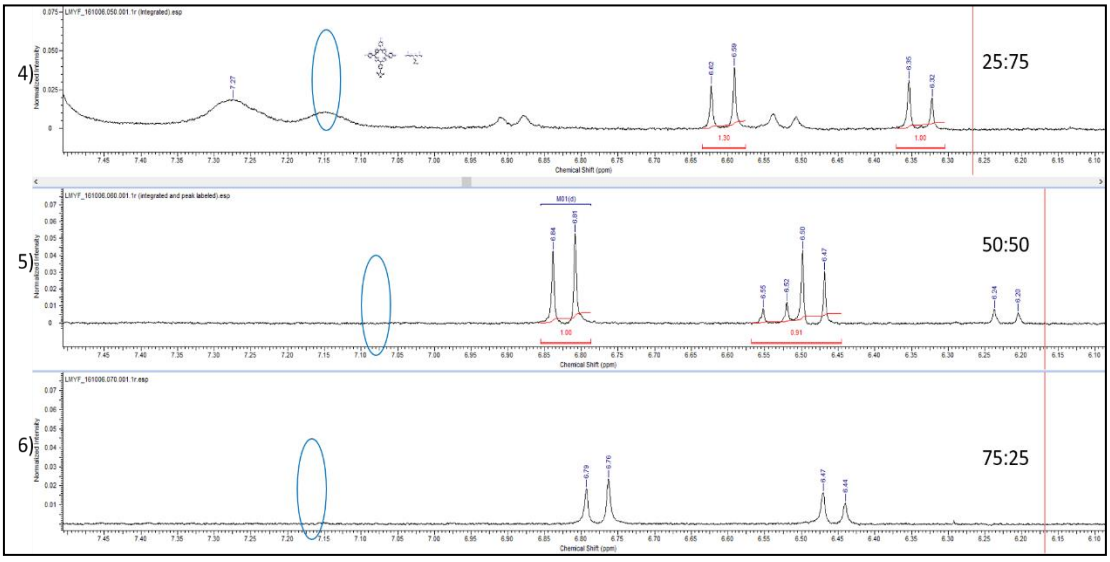

Figure 3-20. ^{1}H NMR (400 MHz, MeOD) spectra of three solutions of compound #5 + TCEP at 25 °C. 4) 25% MeOD: 75% PB, 5) 50% MeOD: 50% PB, and 6) 75% MeOD: 25% PB. Circled in blue is the area where the peak belonging to the maleimide group is missing.

These results demonstrated that the maleimide reacted with TCEP under the conditions used. The three samples were centrifuged to precipitate any possible particles in suspension, but no solid residue was observed. Absence of any precipitate or change in color ruled out the possibility that any physical phenomena, like aggregation or precipitation were the cause of absence of the maleimide peak in the ^{1}H NMR spectra.

In order to further study this reaction we performed another experiment. Here, we used a stock solution of TCEP prepared in PB pH 7. The aim of this experiment was to ensure there was no acidification of the reaction mixture after the addition of TCEP. The reason being is that due to the high acidity of the stock solution of TCEP, we suspect this could overcome the buffering capacity of the PB pH 7.2, therefore, changing drastically the pH in the reaction mixture upon addition. The compound #5 stock was freshly prepared in MeOD. A sample containing the porphyrin (5 μM) was analyzed by H-NMR and UV-vis spectroscopies. Immediately after we added the solution of TCEP to reach a final concentration of 5 mM. No change in color or formation of any precipitate in the NMR tube was observed. Then we recorded the NMR and the UV-vis spectra again (Figures 3-21 and 3-22).

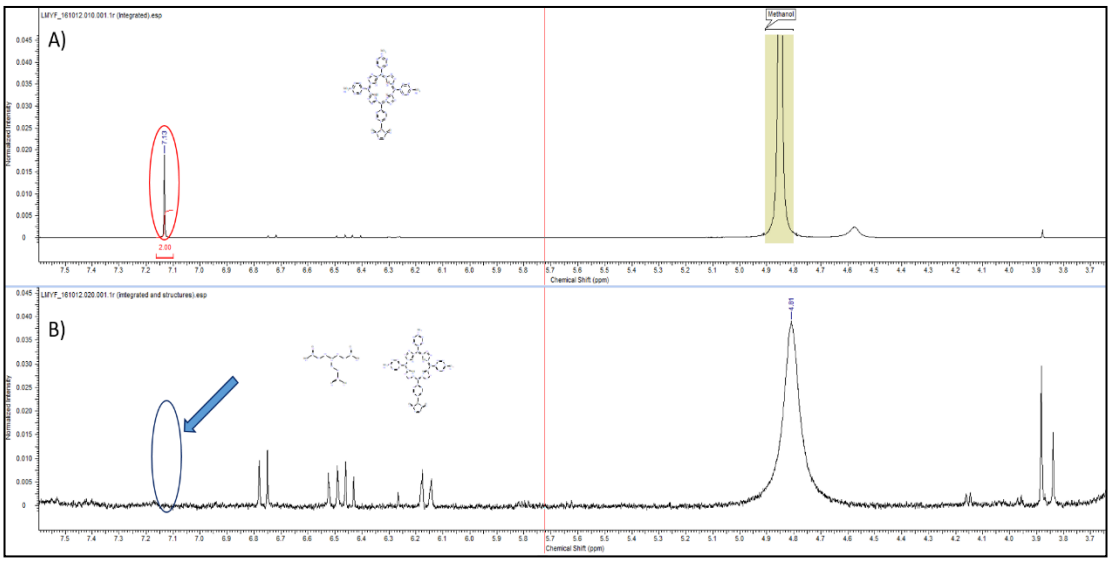

Figure 3-21. ^{1}H NMR (400 MHz, MeOD) spectra of two samples. A) 5 mM of compound #5 alone; B) 5 mM of compound #5 + 5mM TCEP at 25°C. Circled in red is the peak belonging to the protons in the maleimide group; circled in blue and pointed with an arrow is the chemical shift where the peak belonging to the maleimide group is missing.

From Figure 3-21 it is clear that initially the maleimide functional group was present in the porphyrin solution, however after addition of TCEP the signal disappeared, most probably due to reaction of the maleimide with the reducing agent.

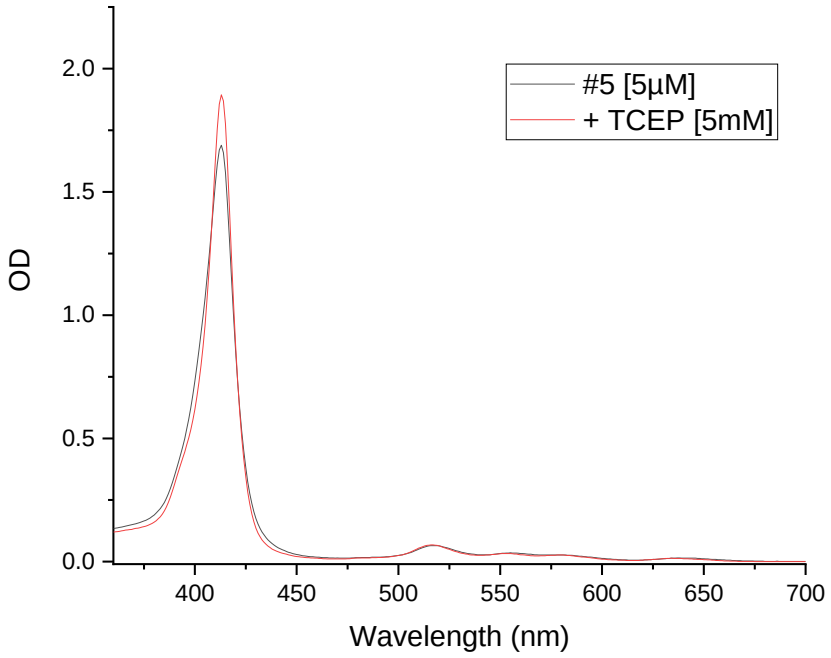

Figure 3-22. UV-vis trace of compound #5 (5 µM) in PB (100 mM) pH 7.2 and the compound #5 + TCEP (5 mM).

Figure 3-22 shows the UV-vis traces of both samples. No major differences can be identified which makes clear that the best way to follow up the reactivity of the maleimide double bond is by using ^{1}H-NMR spectroscopy rather than UV-vis spectroscopy.

3.3.9 Study the reactivity of tris (2-carboxyethyl)phosphine (TCEP) with N-Ethylmaleimide (NEM).

To elucidate the nature of the interaction between TCEP and the maleimide derivative, we decided to perform a control experiment with TCEP and the model maleimide NEM. The spectrum of a solution of NEM (5 mM) in PB 100 mM pH 6 containing 10% of D_2O was recorded, and immediately after we added TCEP (5 mM) to the NMR tube and recorded the spectrum again (Figure 3-23). The spectrum of TCEP (5 mM) alone in DMSO was also recorded (see Figure 6-6 in Appendix).

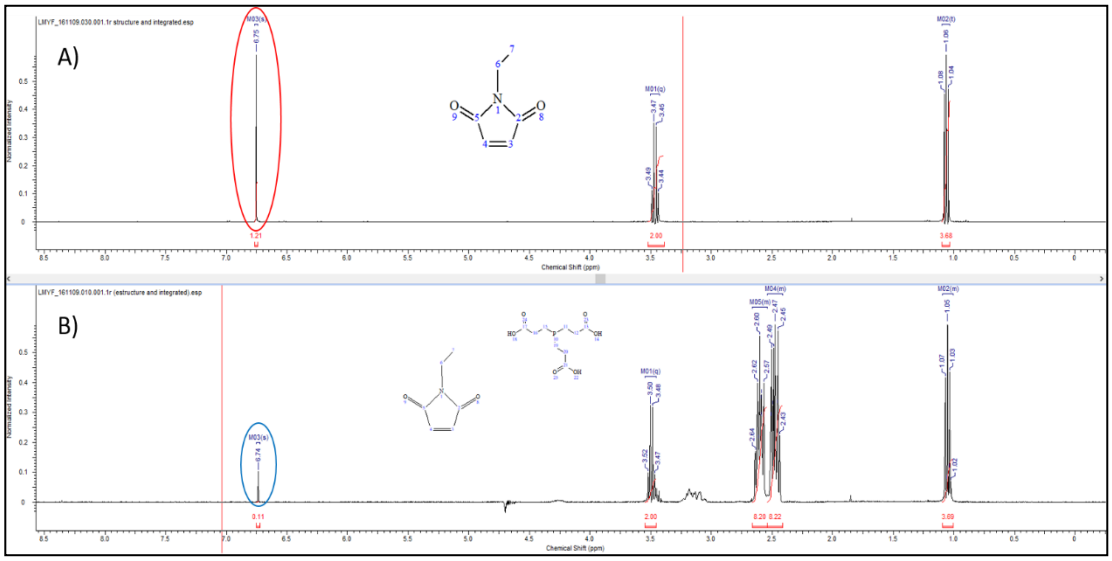

Figure 3-23. ^{1}H NMR (400 MHz, D_2O) spectra of the two samples. A) 5 mM of NEM alone; B) 5 mM of NEM + TCEP at 25 °C. Circled in red is the integrated peak belonging to the hydrogens of the double bond (between C_4 and C_3); circled in blue is the same peak after the addition of the TCEP.

As illustrated by the ^{1}H-NMR spectra, the singlet at position 6.75 ppm with an integral of 1.21 that corresponds to the two protons in NEM, was reduced after addition of TCEP. Integration of the peak after addtition of TCEP was equal to 0.11, which means that more than 85% of the maleimide reacted with the TCEP reagent. This result confirmed the previous observation in section 3.3.8 and proved that TCEP reacts with the double bond of the maleimide.

In addition to the H-NMR spectra, we analyzed the reaction by UV-vis spectroscopy. As shown in Figure 3-24, the double bond in NEM absorbs in the UV region of the spectra with the maximum wavelength located near 304 nm (black line). TCEP, on the contrary, does not absorb in this region, as shown by the red line. After addition of TCEP stock solution to the NEM the intensity of the band at 304 nm clearly decreases with no change in the spectral position of the $\lambda_{max.}$. Due to the stock of TCEP being 40-fold excess compared to NEM, we added a very small volume to reach the final concentration, in such a way that any dilution effect was minimal. In conclusion, TCEP reacts with NEM, with the double bond integrity of the maleimide compromised.

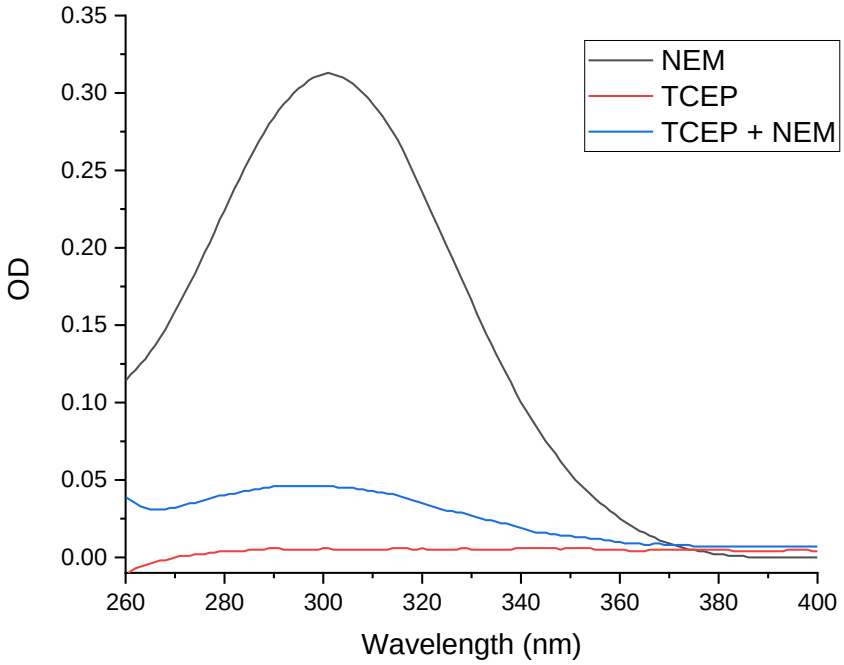

Figure 3-24. UV-vis spectra of NEM (0.5 mM) in PB (100 mM) pH 6.0 and mixture of NEM + TCEP.

3.3.10 Study of the reactivity of N-Ethylmaleimide (NEM) with N-acetylcysteine (NAC) in the presence of tris (2-carboxyethyl) phosphine (TCEP).

The previous experiments have shown that TCEP reacts with the maleimide ring present in both, compound #5 and NEM. This observation suggests that we will need to remove any reducing agent remaining in solution after the reduction of the thiol peptide, otherwise it will compete with the peptide for the maleimide moiety. We decided to test with a model thiol, like NAC, to what extent the labeling reaction was achievable in the presence of TCEP. To this end, we prepared a solution of NEM (1 mM) in PB pH 6 with 10%D_2O and recorded the ^{1}H-NMR spectrum. Immediately after, we added the volume of NAC to reach a final concentration of 2 mM, and recorded the^{1}H-NMR spectrum (Figure 3-25). This first reaction was a control that we used as a reference when analyzing the reaction between NEM and NAC in the presence of TCEP.

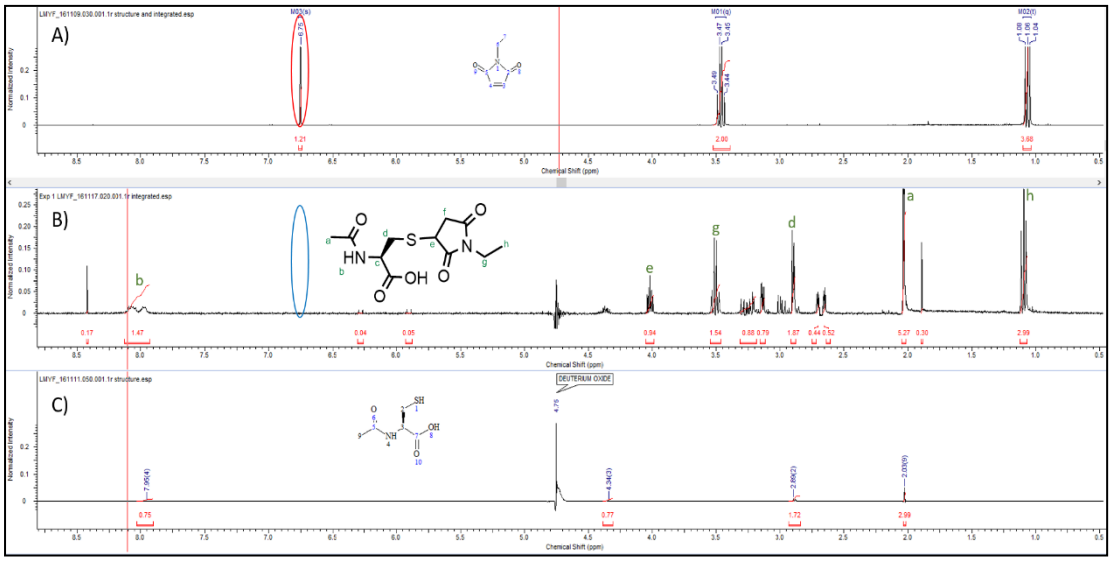

Figure 3-25. ^{1}H NMR (400 MHz, D_2O) spectra A) 5 mM of NEM alone; B) 1 mM of NEM + 2 mM NAC; C) 2 mM of NAC at 25 °C. Circled in red is the integrated peak belonging to the proton of double bond (between C_4 and C_3); circled in blue is shown the disappearance of the peak after the reaction.

After the reaction with NAC the peak belonging to the maleimide double bond disappears, which means the reaction was achieved. When we moved upfield in the chemical shift (ppm) scale, we could detect a new set of peaks in the region 2.5-4.5 ppm. The integrals and assignment of protons of this product were in agreement with the published data for the adduct NEM-NAC[150].

For the second reaction we prepared a mixture of NAC and 2-fold excess of TCEP. This mixture was added to a fresh solution of NEM in PB pH 6 and the ^{1}H-NMR spectra recorded before and after the addition of the mixture (Figure 3-26).

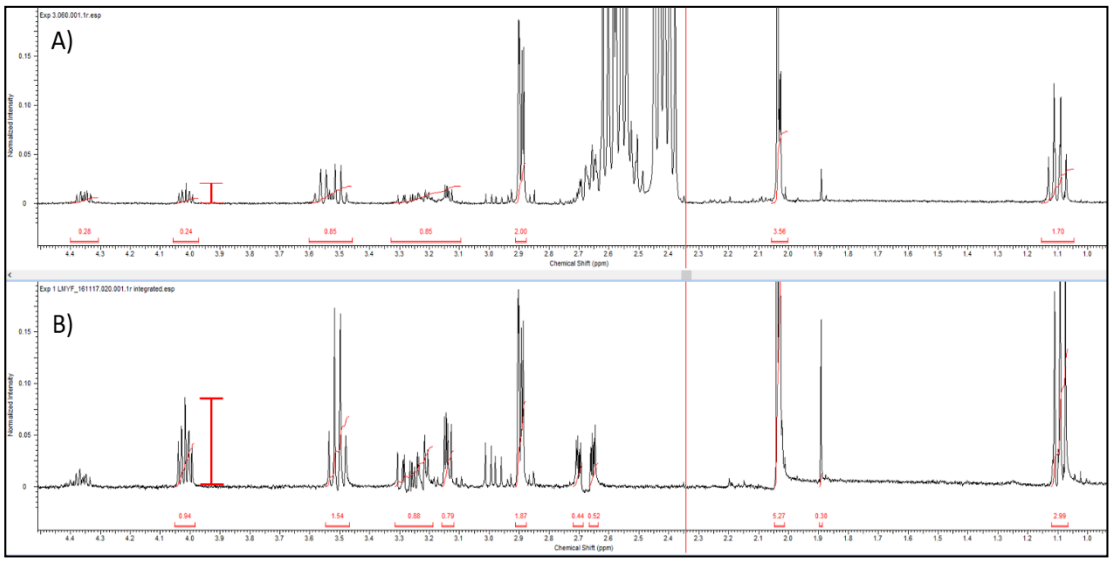

Figure 3-26. ^{1}H NMR (400 MHz, D_2O) spectra. A) 1 mM of NEM plus 2.5 mM NAC and 5 mM TCEP; B) 1 mM of NEM + 2 mM of NAC at 25 °C.

From the comparison of the spectra (Figure 3-26, Panel A and B) it is obvious that the reaction of NEM and NAC in the presence of TCEP occurred. However, analysis of the integrals showed that formation of the adduct NEM-NAC reached approximately 75% in the reaction without TCEP (Figure 3-26, Panel B). Whereas, in the presence of TCEP, the formation of the adduct NEM-NAC was around 25% (Figure 3-26, Panel A).

In summary, although it is possible to achieve the labeling reaction in one-step with TCEP present, it is evident that TCEP will affect extensively the extension of the labeling reaction due to its high reactivity towards the maleimide function. We could overcome this problem by adding Compound #5 in excess in relation to both the thiol and the TCEP. However, due to the limited amount of Compound #5 synthetized, we discarded this alternative. Instead, we decided that the best way to proceed was to separate the TCEP from the reduced thiol before the labeling reaction with Compound #5.

3.3.11 Study of the reactivity of N-Ethylmaleimide (NEM) with N-acetylcysteine (NAC) in the presence of sodium dithionite.

Because TCEP, showed some cross reactivity with the maleimide, we decided to test sodium dithionite as a potential reducing agent. We followed an approach similar to that described in section 3.3.10. We began by performing the same control experiment with NEM and NAC (Figure 3-25, Panel A and C). Sodium dithionite does not show any NMR signal and therefore was ideal to follow the reaction between the peptide and the maleimide by ^{1}H-NMR spectroscopy. We recorded the ^{1}H-NMR spectrum of a solution of NEM in PB pH 6, and immediately after added the sodium dithionite in 10-fold excess (Figure 3-27).

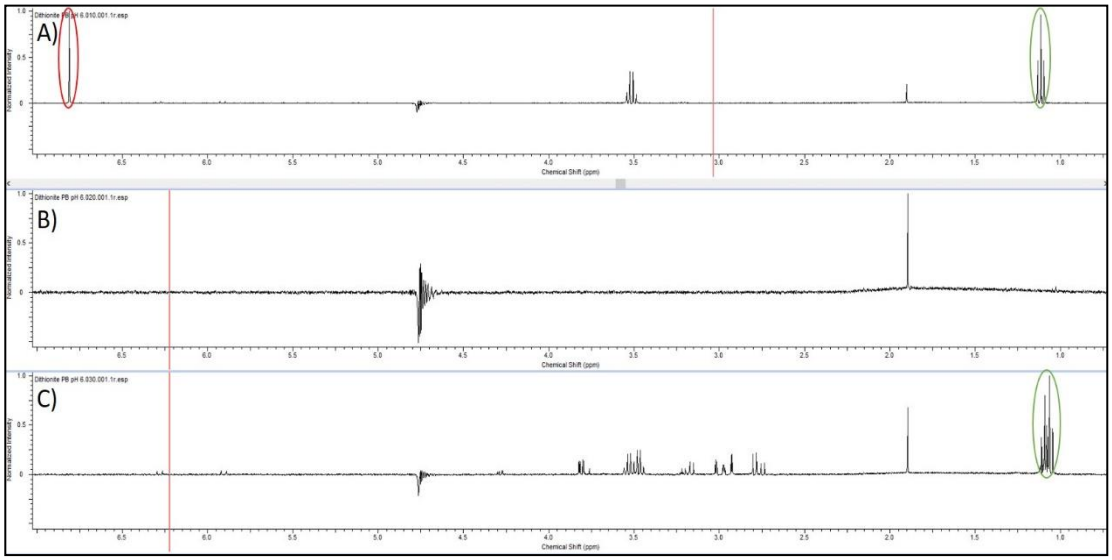

Figure 3-27. ^{1}H NMR (400 MHz, D_2O) spectra. A) 1 mM of NEM alone; B) 10 mM of $Na_2S_2O_4$; C) 1 mM of NEM + 10 mM $Na_2S_2O_4$ at 25 °C. Circled in red is the peak belonging to the protons of double bond (between C_4 and C_3); circled in green is the change from a triplet to a multiplet in the NEM after the addition of sodium dithionite.

The analysis of the spectra showed that the peak of the maleimide at 6.82 ppm disappears after addition of sodium dithionite. Moreover, the triplet at position 1.11 ppm belonging to the CH_3 on the NEM changed to a multiplet. There was also a new set of peaks in the range 2.7 – 4 ppm. Sodium dithionite appears to reduce the NEM, presumably the carbonyl groups and the double bond. These results indicate that the use of the sodium dithionite is not suitable for the one pot labelling reaction with Compound #5.

The second step in the control experiment was the addition of the mixture NAC + sodium dithionite to the solution of NEM in PB pH 6 to explore whether the labeling reaction will be faster than the reaction with sodium dithionite. To this end, we prepared a solution containing NAC and sodium dithionite in 2-fold excess and followed the same procedure described for the labelling of NEM in the presence of TCEP (Section 3.3.10). The mixture was incubated for 15 minutes to allow the reduction of NAC. Afterwards, we added the solution of NEM and recorded the ^{1}H-NMR spectrum shown in Figure 3-28.

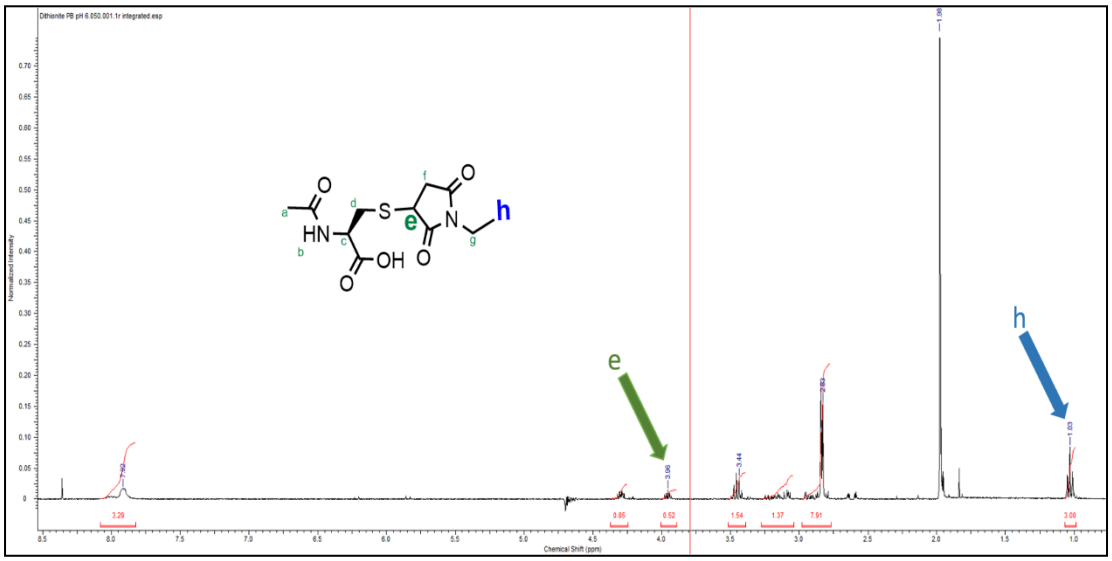

Figure 3-28. ^{1}H NMR (400 MHz, D_2O) spectrum of the reaction product of NEM+NAC in the presence of $Na_2S_2O_4$ at 25 °C. The green arrow indicates the multiplet belonging to the proton e in the adduct NEM+NAC, while the blue the arrow shows the peak belonging to the intact CH_3 in the NEM.

The reaction of NEM with NAC in the presence of sodium dithionite was successful as is evident by the presence of the multiplet at 3.96 ppm which was assigned to proton *e*, therefore indicative of formation of the adduct NEM+NAC. Moreover, the presence of the intact triplet at position 1.03 ppm belonging to protons *h* in the NEM+NAC adduct suggests that reduction of NEM by sodium dithionite is incomplete in the presence of NAC despite the fact we used sodium dithionite in excess (see Experimental Section 3.5.12).

In conclusion, the sodium dithionite also reacts with the double bond of the maleimide. Therefore, it is clear that we need to remove the reducing agent to avoid competition for the maleimide during the labeling reaction with the peptide.

3.3.12 HPLC analysis.

One of the analytical techniques that we also used in our experiments was the Reverse Phase High Pressure Liquid Chromatography (RP-HPLC). The main objective of its application was:

1. Identify the retention times (RT) of the different species involved in the labeling reaction with model thiols and Compound #5.
2. Follow and quantify the extent of the labeling reaction.

3.3.12.1 **Study to define whether it is possible to detect micromolar concentrations of Compound #5 by HPLC.**

The aim of this experiment was to determine whether the analysis of a range of ten solutions of compound #5 on the micromolar scale was feasible by RP-HPLC. This study was very important, as the labeling reaction of the peptide with compound #5 would be carried out using micromolar quantities of both reagents. To pursue this aim we prepared by serial dilution 10 samples of compound #5 ranging from 50 to 2 µM and injected each one into the RP-HPLC column. The detection was carried out with a UV-vis lamp at 430 nm.

Figure 3-29 illustrates the traces of eight injections of Compound #5 into the RP-HPLC column. The traces belonging to the sample at 5 and 6 µM concentrations are not included due to inaccuracies in their retention time as a consequence of the manual injection of the sample.

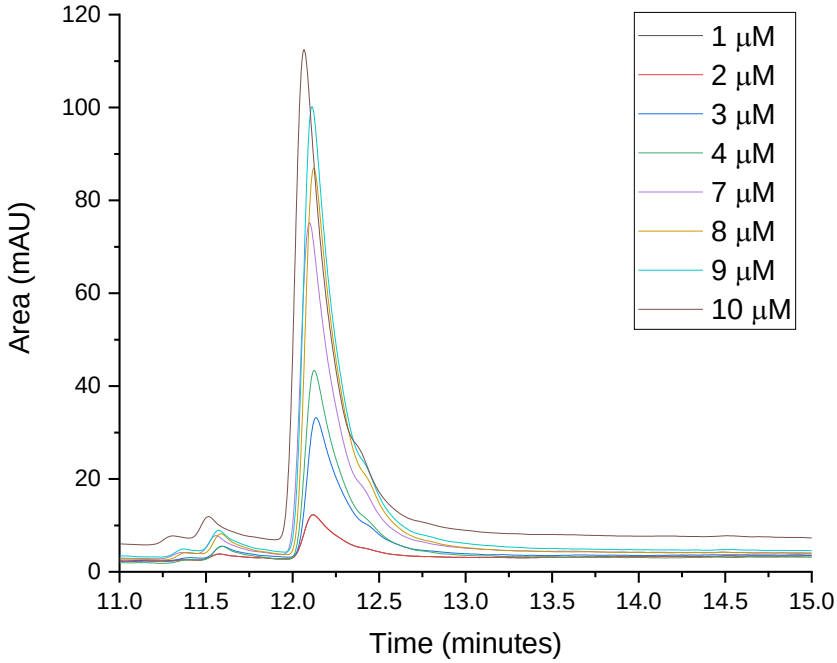

Figure 3-29. HPLC traces belonging to samples of compounds ranging from 1-10 μM. Samples were injected in PB and detected at 430 nm.

The representation of the data as peak area versus concentration of compound #5 shown in Figure 3-30, demonstrates nicely how the increment in the concentration of the compound #5 correlates linearly with the increment of the peak area, which is directly proportional to the amount of porphyrin in the sample.

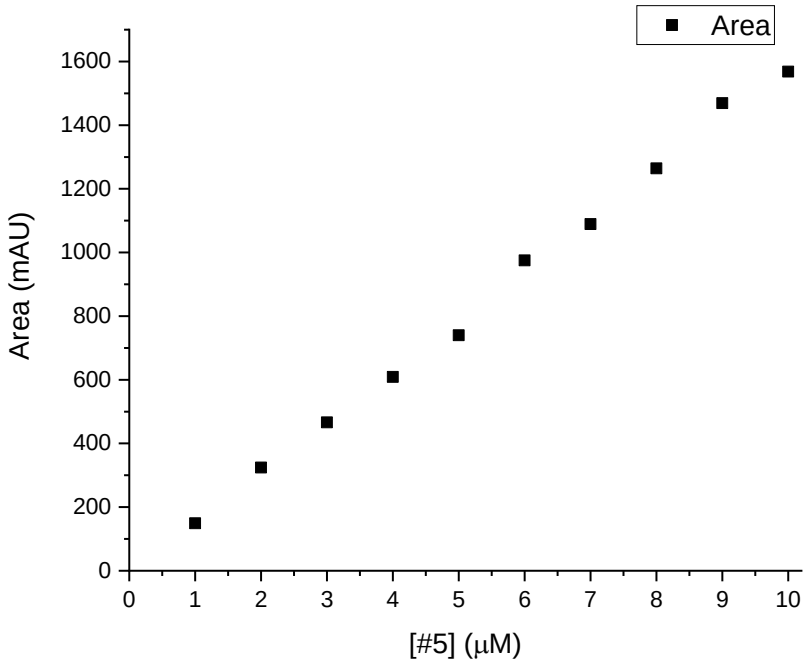

Figure 3-30. Plot of the Area of the peaks (mAU) vs [5] uM.

From this experiment, we concluded that RP-HPLC was a suitable analytical technique for the detection of micromolar concentrations of compound #5. Of note, as shown in Figure 3-30 we were able to detect concentrations of porphyrin as low as 1 μM.

3.3.12.2 Following the reaction of compound #5 with N-acetylcysteine (NAC) and γ-glutathione (Glu).

The labeling reaction of model thiols NAC (10 mM) and Glu (10 mM) with compound #5 (195 μM) was followed by RP-HPLC. Figure 3-31 show that separation of the unreacted compound #5, hydrolyzed compound #5, and the adduct thiol-compound #5 is achievable. From the retention times of the adduct thiol-compound #5 for N-acetylcysteine (11.5 min) and γ-glutathione (10.9 min) it is evident that a better separation is achieved with the largest thiol i.e. glutathione.

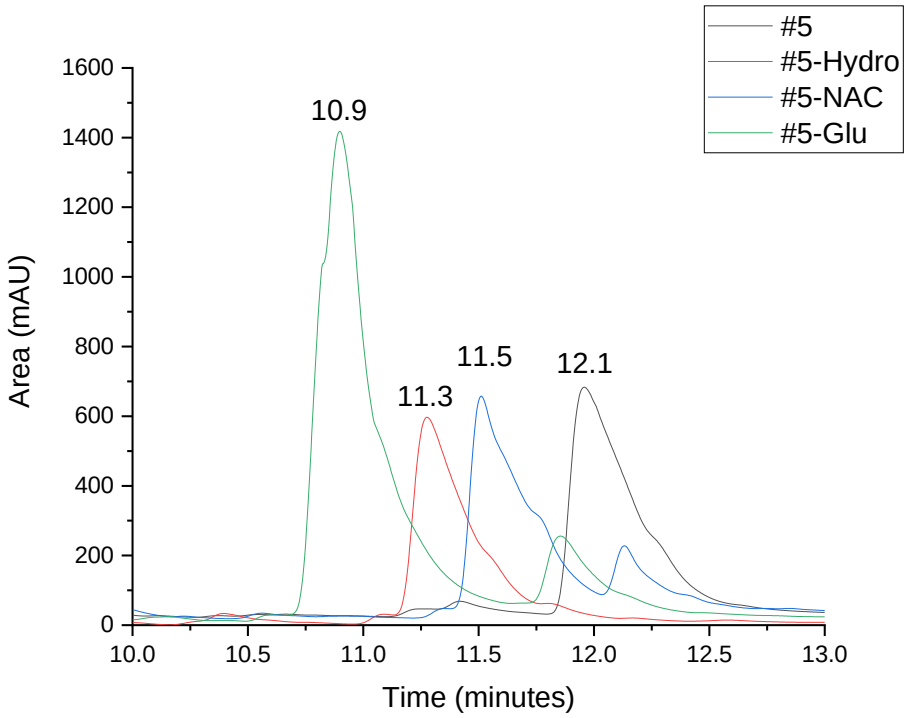

Figure 3-31. RP-HPLC traces showing the retention times of compound #5, compound #5 hydrolyzed, the adduct of compound 5 and NAC, and 5-Glu. Abbreviations: NAC: N-acetylcysteine, Glu: γ-Glutathione, 5-Hydro: Compound 5 hydrolyzed. Detection lamp at 430 nm.

In conclusion, from the analysis of the chromatogram we determined that for the reaction of compound #5 with NAC, 77.9% of compound #5 reacted with N-acetylcysteine, while the remaining 22.1% remain unreacted. When we looked at the reaction with γ-glutathione, we determined that approximately 84% of compound #5 reacted with the thiol to produce the adduct, while ~16 % remain unreacted. Quantification of the reaction was carried out using the integral of the peaks in each chromatogram automatically calculated by the Agilent Software.

3.3.12.3 Following the reaction of compound #5 with 1-Hexadecanethiol (1-Hex).

The labeling reaction of compound #5 (100 μM) with the hydrophobic compound 1-hexadecanethiol (50 μM) was followed by RP-HPLC. Due to the strong hydrophobic interaction of this long thiol with the C18 matrix of the column, we decided to perform the separation with a less hydrophobic column, i.e. C5, and increased hydrophobicity of the mobile phase to shorten the elution time (see Experimental Section) (Figure 3-32).

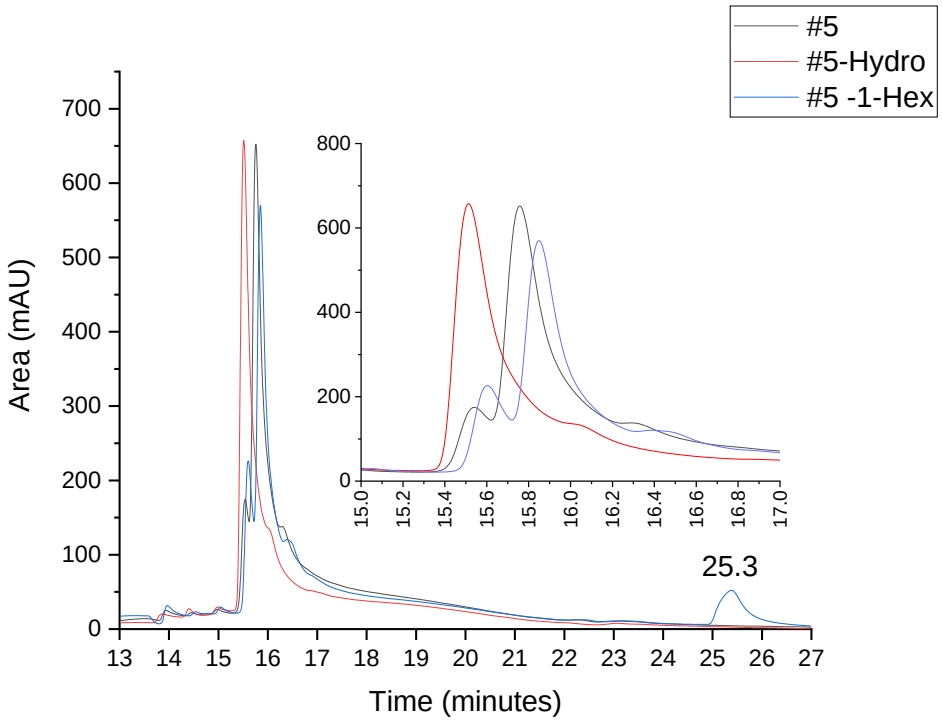

Figure 3-32. RP-HPLC traces. The inset graph illustrates the retention times of compound #5, compound #5 hydrolyzed, compound #5-1-hexadecanethiol adduct. Abbreviations: 1-Hex: 1-hexadecanethiol, #5-Hydro: Compound #5 hydrolyzed.

As shown in Figure 3-32 we successfully achieved the reaction and most importantly we found optimal conditions to separate the 5-1-hexadecanethiol adduct. From the area of the peaks we determined that ~10 % of compound #5 reacted with 1-hexadecanethiol, whereas the remaining ~90% was a mixture of unreacted and hydrolyzed compound #5.

3.4 SUMMARY

In this chapter, we described the work done with Compound #5 and model thiols such as N-acetylcysteine, γ-glutathione and 1-hexadecanethiol towards the identification of the conditions needed to perform the labeling reaction. In addition, we demonstrated the difficulties found in the work with thiols, especially their high susceptibility to oxidation in aqueous solution. Due to the necessity to work with the reduced thiol to achieve the labeling reaction we explored different reducing agents as potential candidates e.g. TCEP and sodium dithionite. Our results demonstrated that both reducing agents cross-react with the maleimide group. Therefore, achieving the labeling reaction in one pot, as was our initial approach is not possible. Instead, we need to introduce a further step in which we separate the reducing agent before the addition of compound #5 to the reduced peptide. We will design further experiments to address this problem. Moreover, in this section we also showed how we successfully tracked the reaction of compound #5 and model thiols such as N-acetylcysteine, γ-glutathione and 1-hexadecanethiol by RP-HPLC. Indeed, in here we demonstrated that RP-HPLC is sensitive enough to detect, qualitativly and quantitativly, micromolar concentrations of the 5-thiol adduct. These results are very important as they suggest we will be able to follow the labelling reaction with the transmembrane peptide in a similar way.

3.5 EXPERIMENTAL SECTION

3.5.1 Solvents and Reagents

The methanol (Fisher) for the preparation of the stock of the compound #5 was of analytical grade. Deionized water was obtained from water purifier purelab option (ELGA).

N-ethylmaleimide (NEM), N-acetylcysteine (NAC), tris (2-carboxyethyl)phosphine (TCEP), γ-Glutathione, sodium dithionite, and the sodium borohydride were purchased from Sigma-Aldrich with analytical grade purity. The inorganic salt, sodium phosphate monobasic dihydrate used in the preparation of the buffer was also of analytical grade purity.

The deuterated solvents for the ^{1}H-NMR analysis were deuterium oxide (D_2O) (isotopic purity 99.9%, Merck), tetradeuteromethanol (CD_3OD) (99.96 %, Merck), dimethyl sulfoxide (d_6-DMSO) from Eurisotop.

The stock of 10 mM DTNB (0.05 mmol, 0.02 g) was prepared in 5 ml of acetonitrile. To solubilize the DTNB the solution was sonicated for 30 min. Mr (DTNB) = 396.35g/mol.

The stock of 10 mM of 1-Hexadecanothiol (0.0153 ml, 0.0129 g). was prepared in 5 ml of acetonitrile. Mr (1-hexadecanothiol) = 258.51 g/mol, d = 0.84 g/ml.

The stock of 250 μM of peptide control (5×10^{-7} mol, 0.001 g) was prepared in 2 ml DMSO. Mr (Peptide control) = 1993.3 g/mol.

The stock of 90 μM of full-length transmembrane peptide (1.79×10^{-7} mol, 0.001 g) was prepared in 2 ml of DMSO. Mr (Full-length peptide) = 5559.6 g/mol. All the reactions were performed at room temperature on the bench.

3.5.2 Quantification of free thiol in NAC with the DTNB test.

To a 3 ml quartz cuvette were added in the following order:

- 2 ml of PB pH 7.2
- 2 µl of NAC stock (5 mM) $[NAC]_{final}$ = 2.5 µM
- 20 µl of DTNB (10 mM) $[DTNB]_{final}$ = 100 µM

The solution was gently shaken and UV spectra at 240-700 nm were recorded immediately and after intervals of 2, 10, 30, 60 and 90 minutes between each scan. A control sample without the addition of thiol and DTNB was used as a reference (Figure 3-3).

3.5.3 Quantification of free thiol in the 1-Hexadecanethiol with the DTNB test

To a 3 ml quartz cuvette were added in the following order:

- 3 ml of PB pH 7.2
- 3 µl of 1-Hexadecanethiol stock (10mM) $[1\text{-Hexdecanethiol}]_{final}$ = 10 µM
- 30 µl of DTNB (10mM) $[DTNB]_{final}$ = 100 µM

The solution was gently shaken and UV spectra at 240-700 nm were recorded immediately and after intervals of 2, 10, 30, 60, 90, 120, and 180 minutes between each scan. A control sample without the addition of thiol and DTNB was used as a reference (Figure 3-6).

3.5.4 Quantification of free thiol in the peptide control with the DTNB test.

To a 1 ml quartz cuvette were added in the following order:

- 1 ml of PB pH 7.2
- 40 μl from the 250 μM Peptide control (0.5 μmol, 0.001 g) stock freshly prepared in 2 ml DMSO. $[\text{Peptide Control}]_{final} = 10\ \mu M$
- 20 μl of DTNB (10 mM) $[\text{DTNB}]_{final} = 100\ \mu M$

The solution was gently shaken and UV spectra at 240-700 nm were recorded immediately and after intervals of 1, 2, 3 and 4 hours between each scan. A control sample without the addition of peptide and DTNB was used as a reference (Figure 3-5).

To determine the concentration of the peptide control in the sample solution I record the UV spectrum before the addition of the DTNB was recorded. For correction of the absorption due to the DMSO, a sample containing 3.3% of DMSO was prepared by mixing 33 μl of DMSO and 967 μl of PB pH 7.2 (see Figure 3-33). For the determination of the concentration of peptide control we measured the absorbance at 280 nm with the extinction coefficient of 5810 $mol^{-1}cm^{-1}$.

3.5.5 Quantification of free thiol in the full-length peptide with the DTNB test

To a 1 ml quartz cuvette were added in the following order:

- 890 ml of PB pH 7.2
- 110 μl from the 90 μM Full Peptide control (1.79×10^{-7} mol, 0.001 g) stock freshly prepared in 2 ml DMSO. $[\text{Peptide Control}]_{final} = 10\ \mu M$
- 20 μl of DTNB (10 mM) $[\text{DTNB}]_{final} = 100\ \mu M$

The solution was gently shaken and UV spectra at 240-700 nm were recorded immediately and after intervals of 0, 1, 2, 3, 4, and 5 hours between each scan. A control sample without the addition of peptide and DTNB was used as a reference (Figure 3-8).

To determine the concentration of the peptide control in the sample solution the UV spectrum before the addition of the DTNB was recorded. For the correction of the absorption due to the DMSO, a sample containing 3.3% of DMSO was prepared by mixing 233 μl of DMSO and 6767 μl of PB pH 7.2 (see Figure 3-34). For determination of the concentration, the absorbance at 280 nm, with an extinction coefficient of 11050 $mol^{-1}cm^{-1}$, immediately and after 1 hr was used.

3.5.6 Determination of the extinction coefficient (ε) of compound #5 in PB.

To determine the extinction coefficient from a 5 mM stock solution of compound #5, 600 µl working solution of 0.15 mM in PB 100 mM pH 7.2 was prepared. As summarized in Table 3-6 dilution of samples P0 to P15 was performed. These samples were further diluted 1:200 to produce the final samples D0 to D15. The traces were recorded with a Perkin Elmer UV-vis spectrophotometer in the range $240 < \lambda < 700$ nm, with an increment of 1 nm.

Volume (µl)	[5] (µM)	Sample Name		Sample Name	[5]FINAL (µM)	Vol Cuvette
600	150	P0	50µl +950 µl buffer	D0	7.5	1ml
500 P0 + 100 buffer	125	P1	50µl +950 µl buffer	D1	6.25	
500 P1 + 100 buffer	104	P2	50µl +950 µl buffer	D2	5.2	
500 P2 + 100 buffer	87	P3	50µl +950 µl buffer	D3	4.35	
500 P3 + 100 buffer	72	P4	50µl +950 µl buffer	D4	3.6	
500 P4 + 100 buffer	60	P5	50µl +950 µl buffer	D5	3	
500 P5 + 100 buffer	50	P6	50µl +950 µl buffer	D6	2.5	
500 P6 + 100 buffer	42	P7	50µl +950 µl buffer	D7	2.1	
500 P7 + 100 buffer	35	P8	50µl +950 µl buffer	D8	1.75	
500 P8 + 100 buffer	29	P9	50µl +950 µl buffer	D9	1.45	
500 P9 + 100 buffer	24	P10	50µl +950 µl buffer	D10	1.2	
500 P10 + 100 buffer	20	P11	50µl +950 µl buffer	D11	1	
500 P11 + 100 buffer	17	P12	50µl +950 µl buffer	D12	0.85	
500 P12 + 100 buffer	14	P13	50µl +950 µl buffer	D13	0.7	
500 P13 + 100 buffer	12	P14	50µl +950 µl buffer	D14	0.6	
500 P14 + 100 buffer	10	P15	50µl +950 µl buffer	D15	0.5	

Table 3-6. Protocol for the titration of the compound #5 in PB pH 7.2 to determine the extinction coefficient.

3.5.7 Reaction of N-acetylcysteine with #5-(4-maleimide)-10, 15, 20 tris (4 - sulfonatophenyl)–porphyrin (compound #5).

The first step was the preparation of a stock solution of compound #5 (0.01 M) in methanol. From this stock a working solution (10 µM, 2 ml) in PB pH 7.2 was prepared. The solution was split into two vials containing 1 ml each. The first vial label P1 only contained compound #5; to the second vial, labelled as P2, added 250 µl from a stock solution of NAC (100 mM) was added to reach a final concentration of 20 mM in the cuvette. Before the addition of the NAC to the P2 vial, the UV-vis spectrum was recorded in the range 388-460 nm. After the addition of NAC, both samples were loaded into the spectrophotometer. The spectra were recorded using the multisampler option. The program was set up as follows: absorbance ranges 388-460 nm, number of cycles: 20, interval: 5 minutes. The first position in the carrousel was left empty to avoid the photolysis of the sample by the constant irradiation of the beam in the periods between readings. Once the first round of measurements was completed, measurements were repeated increasing the interval to one hour with the same number of cycles.

3.5.8 Reaction of γ-Glutathione with #5-(4-maleimide)-10, 15, 20 tris (4 - sulfonatophenyl)–porphyrin (compound #5).

Glutathione reduced (0.15 mmol) stock solution (100 mM, 1.5 ml) was prepared in PB 100 mM pH 7.2. From the stock of compound #5 (10 mM) prepared previously 1 µl was pipetted into 1000 µl of PB 100 mM pH 7.2 to prepare a solution of 10 µM. The absorbance of this solution was recorded using the same set up as described in the section 3.5.7. Then, 100 µl of the glutathione reduced stock solution were added to the cuvette to reach a final concentration in the cuvette of 10 mM. The content was carefully mixed and the absorbance was recorded under the same conditions. Once all the cycles were finished a new round of measurements were recorded using a one-hour interval over 20 cycles.

3.5.9 Interaction of tris (2-carboxyethyl)phosphine (TCEP) with 5-(4-maleimide)-10, 15, 20 tris (4 - sulfonatophenyl)–porphyrin (compound #5).

A stock solution of tris (2-carboxyethyl)phosphine (TCEP) (0.05 mmol) in deuterated methanol was prepared initially. A solution of compound #5 (0.5 mM) was prepared and further split into two separate samples. To one of these samples the stock solution of TCEP (100 mM) was added to reach a final concentration of 5 mM, with the immediate formation of a green precipitate in the NMR tube and change of color in the solution from purple to green. ^{1}H-NMR spectra of both samples were recorded and repeated every 1 hour for 5 hours. Once the acquisitions were finished the samples were left at room temperature and spectra recorded again at 24 and 48 hours. The spectrum of a solution of TCEP (10 mM) in deuterated methanol and dimethyl sulfoxide (DMSO) was also recorded in order to perform the analysis.

To find the best conditions to perform the ^{1}H-NMR analysis of compound #5 in the presence of TCEP it was decided to buffer the mixture to keep the pH stable around 7.2. Before the preparation of the samples an investigation of whether or not the methanol/PB mixture affected the solubility of the inorganic salt with the concomitant destruction of the buffer capacity was performed. To achieve this, we prepared a solution of PB 50 mM pH 7.2 and mixed with methanol in nine different ratios: buffer:methanol, 1:9, 2:8, 3:7, 4:6, 5:5, 6:4, 7:3, 8:2, 9:1. Each mixture was agitated, and left at room temperature for several hours and examined for the formation of any precipitate or turbidity in the vial.

A stock of compound #5 was prepared (50 mM, 210 µl) in MeOD. From this stock were prepared three samples (700 µl) with the ratios of deuterated methanol: PB as follows: 25:75, 50:50, 75:25 (Table 3-7). Once all the samples were prepared the NMR spectra were recorded using the water suppression mode option.

Solution	ratio MeOD:PB	V(MeOD) µl	V(Stock 5) µl	V(PB)µl
1	25:75	105	70	525
2	50:50	280	70	350
3	75:25	455	70	175

Table 3-7. Mixtures of methanol and phosphate buffer used in the study of the interaction of compound #5 and TCEP by ^{1}H-NMR spectroscopy.

3.5.10 Study the reactivity of tris (2-carboxyethyl) phosphine (TCEP) with N-Ethylmaleimide (NEM).

Three stock solutions were prepared of NAC (100 mM), NEM (100 mM), TCEP (200 mM) in PB pH 6.0 (Table 3-8).

Stock solutions (PB pH6)	MW (g/mol)	C (mmol)	m (mg)	V (ml)
NAC	163.19	100	32.6	2.00
TCEP	286.65	200	114.6	2.00
NEM	125.13	100	25	2.00

Table 3-8. Details of the reagents used in the preparation of the three stock solutions.

A solution of NEM (5 mM, 700 µl) was prepared from the previous stock and the ^{1}H-NMR spectra recorded. Immediately after 17.5 µl from the stock solution of TCEP was added to the NMR tube to reach a final concentration of 5 mM. The mixture was mixed and the ^{1}H-NMR spectrum recorded using the watergate gradient mode (Table 3-9).

Reagent	Cstock (mmol)	C_{NMR} (mmol)	Vstock (µl)	V D_2O (µl)	V PB pH6 (µl)	V_{NMR} (µl)
NMR Tube				70	577.5	700
TCEP	200	5	17.5			
NEM	100	5	35			

Table 3-9. Details of the reagents used in the preparation of the NMR samples.

The samples for the UV-vis experiments were collected from the NMR tubes after the recording of the spectra (Table 3-10). The UV-vis trace of the NEM (0.5 mM), was recorded first, followed by the trace of the mixture TCEP+NEM, and the trace of the TCEP alone (Table 3-11). The parameters of the instruments were: wavelength: 700 – 200 nm, scan speed: 600 nm/min, sampling interval: 1.00 nm.

NMR Sample	[NMR tube] (mM)	[Cuvette] (mM)	V PB pH 6 (µL)	V NMR tube (µL)	DF
NEM	5	0.5	900	100	10
TCEP + NEM	N/A		900	100	10

Table 3-10. Details of the reagents used in the preparation of the samples for the UV-vis experiments.

NMR Sample	[stock] (mM)	[Cuvette] (mM)	V PB pH 6 (µL)	V stock (µL)
TCEP	200	0.5	997.5	2.5

Table 3-11.Details of the reagents used in the preparation of the samples for the UV-vis experiments.

3.5.11 Study of the reactivity of N-Ethylmaleimide (NEM) with N-acetylcysteine (NAC) in the presence of tris (2-carboxyethyl)phosphine (TCEP).

3.5.11.1 Reaction between NEM and NAC:

To a glass vial were added 623 µl of PB 100 mM pH 6.0, followed by 70 µl of D_2O. Afterwards 7 µl was added from the stock of NEM (see Table 3-12). The mixture was mixed and transferred into an NMR tube to record the ^{1}H-NMR spectrum using the watergate gradient mode. Once the spectrum was recorded the contents of the NMR tube were transferred to a new glass vial and 14 µl of the stock of NAC was added to reach 2 mM in the NMR tube, we mixed the mixture, checked the pH with paper strips and transferred the contents into the same NMR tube to record the spectrum again.

NMR sample	Cstock (mM)	C_{NMR} (mM)	Vstock (µl)	V D_2O (µl)	V PB pH6 (µl)	V_{NMR} (µl)
NMR Tube				70	623	700
NEM	100	1	7			
NAC	100	2	14			

Table 3-12. Details of the reagents used in the preparation of the samples for the NMR experiments.

3.5.11.2 Reaction between NEM and NAC in presence of TCEP:

To a glass vial were added 623 µl of PB 100 mM pH 6.0, followed by 70 µl of D_2O. Afterwards, 7 µl from the stock solution of NEM were added (see Table 3-13). The mixture was mixed and transferred into an NMR tube to record the ^{1}H-NMR spectrum. Once the spectrum was recorded the contents of the NMR tube were transferred to a new glass vial. From the stock of NAC (100 mM) and TCEP (191 mM) a working solution was prepared by mixing 20 µl of both into an Eppendorf tube to produce a solution of NAC (50 mM) and TCEP (95.5 mM). From this working solution 36 µl were added to the vial containing the NEM solution. The mixture was mixed and immediately after transferred to an NMR tube and the spectrum recorded.

NMR sample	Cstock (mM)	C_{NMR} (mM)	Vstock (µl)	V D_2O (µl)	V PB pH6 (µl)	V_{NMR} (µl)
NMR Tube				70	623	700
NEM	100	1	7			
TCEP + NAC	95.5 + 50	5 + 2.6	36			

Table 3-13. Details of the reagents used in the preparation of the samples for the NMR experiments.

3.5.12 Study of the reactivity of N-Ethylmaleimide (NEM) with N-acetylcysteine (NAC) in the presence of sodium dithionite.

The solution stock of the sodium dithionite 100 mM (85 % purity) was prepared by weighing 24.7 mg and dissolved in 1 ml of PB 100 mM pH 6. The first experiment was the recording of the sodium dithionite spectrum by ^{1}H-NMR using the watergate gradient mode (see Table 3-14).

NMR sample	Cstock (mM)	C_{NMR} (mM)	Vstock (µl)	V D_2O (µl)	V PB pH6 (µl)	V_{NMR} (µl)
NMR Tube						
Dithionite	100	10	70	70	560	700

Table 3-14. Details of the reagents used in the preparation of the samples for the NMR experiments.

For the second experiment we prepared a solution of NEM 1 mM in PB 100 mM pH 6 with 10% D_2O and recorded the NMR spectrum. To this solution 70µl from the sodium dithionite stock was added to reach a final concentration of 10 mM. Afterwards, the solution was transferred to the NMR tube and the spectrum recorded (see Table 3-15).

NMR sample	Cstock (mM)	C_{NMR} (mM)	Vstock (µl)	V D_2O (µl)	V PB pH6 (µl)	V_{NMR} (µl)
NMR Tube						
NEM	100	1	7	70	623	700
Dithionite	100	10	70			

Table 3-15. Details of the reagents used in the preparation of the samples for the NMR experiments.

For the third experiment a solution of NEM (1mM) in PB 100 mM pH 6 was prepared and NMR spectrum recorded. A solution of NAC (25 mM) and sodium dithionite (50 mM) was prepared from the initial stock of both reagents. This solution was mixed and an aliquot was removed and added to the NEM (1 mM) to reach final concentrations of NAC and sodium dithionite of 10 and 5 mM respectively. Immediately after the solution was transferred into an NMR tube and the ^{1}H-NMR spectrum recorded (see Table 3-16).

NMR sample	**Cstock (mM)**	**C_{NMR} (mM)**	**Vstock (µl)**	**V D_2O (µl)**	**V PB pH6 (µl)**	**V_{NMR} (µl)**
NMR Tube				70	623	700
NEM	100	1	7			700
Dithionite+NAC	25 + 50	10 + 5	140			

Table 3-16. Details of the reagents used in the preparation of the samples for the NMR experiments.

3.5.13 HPLC analysis.

3.5.13.1 Reaction of compound #5 and N-acetylcysteine

Compound #5 (0.004 g, 0.0039 mmol) solution was prepared from frozen aliquots. N-acetylcysteine (0.00326 g, 0.02 mmol) stock solution was prepared fresh PB 100 mM pH 7.2. The reaction mixture was prepared by adding N-acetylcysteine to the solution of compound #5 (100 μM), mixed and injected in to the RP-HPLC immediately. Column (Phenomenex Jupiter C18, 250mm) Manual injection of 20 μl, λ = 430 nm, flow 1 ml/min, eluting with 0.1% TFA/MeCN and 0.1% TFA/H2O with the following gradi-ent: 0-20 min, 0-100% MeCN, 20-22 min, 100-100% MeCN, 22-23 min, 100-0% MeCN, 23-25 min, 0-0% MeCN.

3.5.13.2 Reaction of compound #5 and γ-glutathione

Compound #5 (0.004 g, 0.0039 mmol) solution was prepared from frozen aliquots. The γ-glutathione (0.00878 g, 0.0285 mmol) stock solution was prepared fresh in PB 100 mM pH 7.2. The reaction mixture was prepared by adding the γ-glutathione to the solution of compound 5 (100 μM), vortexed and injected in to the RP-HPLC immediately. Column (Phenomenex Jupiter 5u C18, 300A) Manual injection of 20 μl, λ = 430 nm, flow 1 ml/min, eluting with 0.1% TFA/MeCN and 0.1% TFA/H2O with the following gradi-ent: 0-20 min, 0-100% MeCN, 20-22 min, 100-100% MeCN, 22-23 min, 100-0% MeCN, 23-25 min, 0-0% MeCN.

3.5.13.3 Reaction of compound #5 and 1-Hexadecanothiol

The compound #5 (0.004 g, 0.0039 mmol) solution was pre-pared from frozen aliquots. The 1-Hexadecanothiol (15.3 μl, 0.005 mmol) stock solution was prepared fresh in ethanol. The reaction mixture was prepared by adding the 1-hexadecanothiol (50 μM) to the solution of compound 5 (100 μM), mixed and injected in to the RP-HPLC immediately. Column (Phenomenex Jupiter 5u C5, 300A) Manual injection of 20 μl, λ = 430 nm, flow 0.5 ml/min, eluting with 0.1% TFA/2IPA:1MeCN and 0.1% TFA/H_2O with the following gradient: 0-20 min, 0-100% 2IPA:1MeCN, 20-40 min, 100-100% 2IPA:1MeCN, 40-42 min, 100-0% 2IPA:1MeCN, 42-45 min, 0-0% 2IPA:1MeCN.

3.5.14 Instruments

Proton Nuclear Magnetic Resonance (^{1}H-NMR): ^{1}H-NMR spectroscopy was performed on the departmental Nuclear Magnetic Resonance (NMR) service. The spectra were recorded on Bruker 400 MHz spectrometers (Avance and Avance III). The description of the peaks is as follows: singlet (s), doublet (d), triplet (t), multiplet (m), broad (br). The coupling constants are reported in hertz (Hz), the chemical shift (δ) in parts per million (ppm).

UV-vis Spectrophotometry: The UV-vis spectra for all experiments were carried on the departmental Perkin Elmer Lambda 35, UV/VIS Spectrometer. The cuvettes for all the measurements were polystyrene and disposable with a pathlength of 1 cm and a volume capacity of 2.5 ml.

pH-meter: The pH measurements were taken with a Mettler Toledo pH-meter with a glass electrode (InLab Ultra-Micro, Electrolyte Friscolyl) pH 1…11.0, 80 ^{o}C. All the readings were performed at room temperature. The pH-meter was calibrated before each measurement with standard solutions at pH 4 and 7 respectively.

RP-HPLC: The RP-HPLC was performed using a Varian Prepstar pump with autosampler and fraction collector. The stationary phase column was a Jupiter 4u Proteo 90A AXIA with a packed prep column (250 x 21.2 mm).

All the measurements were recorded at RT, with no further treatment of the samples.

4 CHAPTER 4

4.1 INTRODUCTION AND OBJECTIVES

The aim of this chapter is to explore tools and analytical methods required to determine the extent of aggregation of the TCR transmembrane peptide. To accomplish this aim we need to design and synthetize peptide sequences that are biologically relevant, meaning they need to resemble the natural TCR transmembrane sequence. These peptides need also to have the reactivity required for the labelling reaction with compound #5. In other words, to have the thiol group incorporated to allow for covalent attachment to the porphyrin moiety of Compound #5 via the maleimide-thiol chemistry that we studied in Chapter 3 with small thiols rather than peptides. The approach is shown in Figure 4-1.

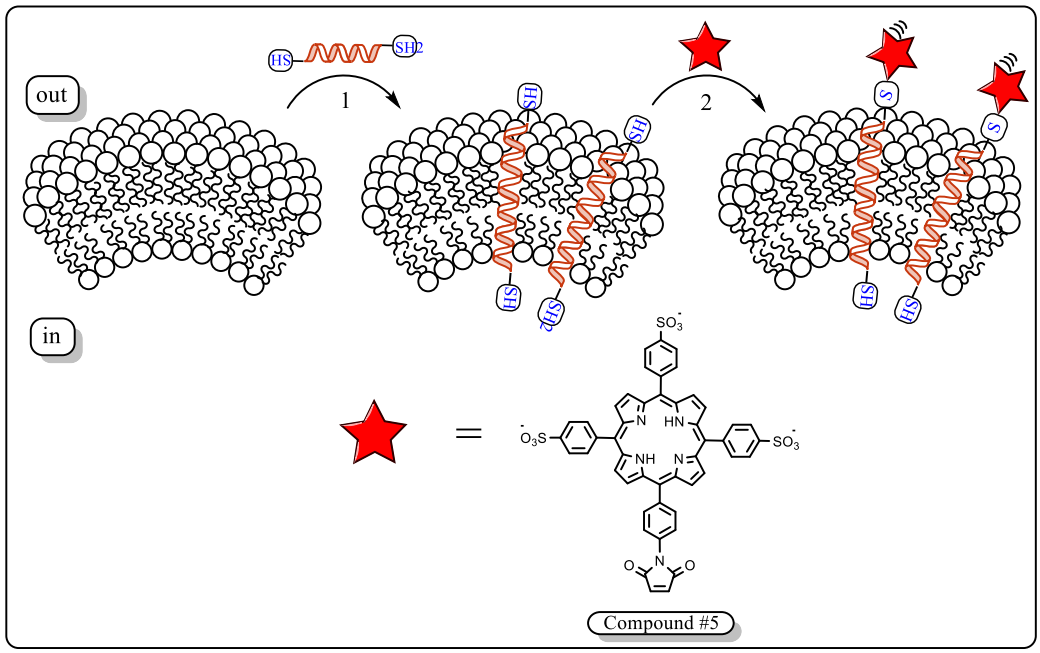

Figure 4-1. Schematic representation of the approach used in this study. Step 1 represents the random insertion of the full-transmembrane peptide into the lipid vesicles to form the proteoliposomes, with 50% distribution of the peptide in both possible orientation. Step 2, illustrates the labeling of the proteoliposomes in the external thiol with a representation of the chemical structure of compound #5.

For the sake of clarity, we will call the liposomes containing the porphyrin labelled peptides, proteoliposomes. A robust methodology for the preparation of the proteoliposomes must allow the measuring of peptide aggregation within the membrane by following the spectroscopy changes of the porphyrin moiety (UV-vis absorbance and/or fluorescence) at different concentrations of peptide within the membrane. In other words, we will aim to prepare proteoliposomes containing different ratios of peptide-porphyrin to lipids and we expect that the spectroscopic properties of the porphyrin will change for those ratios in which peptide clustering takes places. The rational for these experiments and the methodologies to detect and analyze clustering have been already developed and tested on a system made purely of synthetic molecules, i.e. a receptor made of a porphyrin head connected to a cholesteryl tail (Figure 4-2). The model system and the analytical methods used to determine the equilibrium constant of clustered and dispersed receptor (K_{DC} in Fig 4.2) are described in section 1.1.12.1 of the introduction chapter of this thesis.

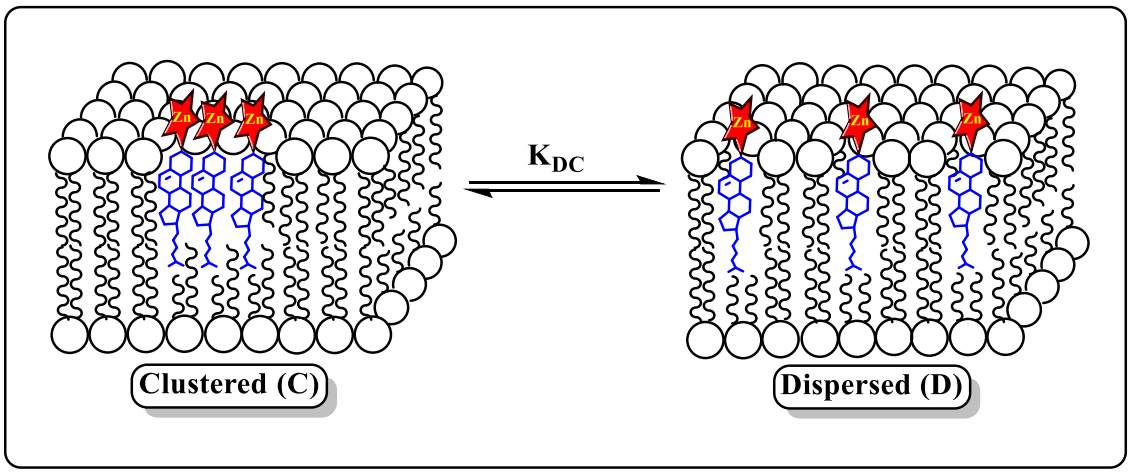

Figure 4-2. Scheme showing the distribution of a porphyrin-cholesteryl based fluorescent probe on the outer leaflet of the lipid bilayer. They represent either the clustered form (C) or the dispersed form (D).

In our approach, we aim to build up a similar system and use a similar analysis for the clustering-disperse equilibria of the TCR transmembrane peptides (Figure 4-3).

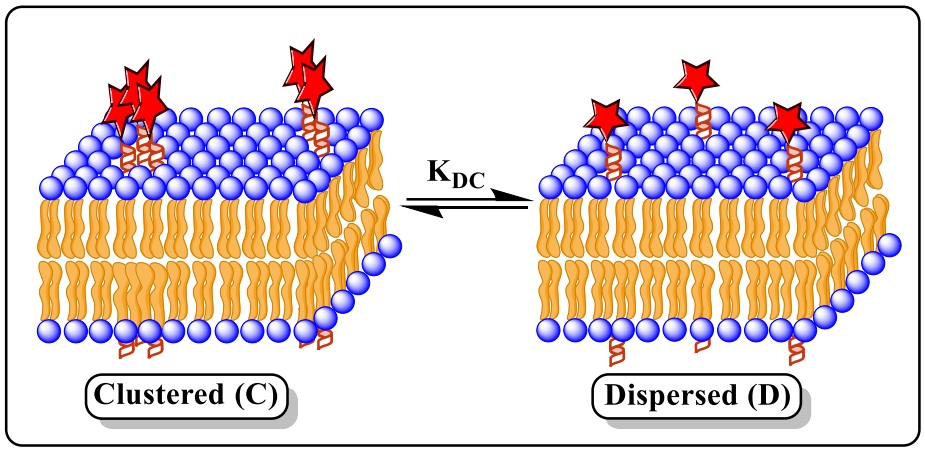

Figure 4-3. Scheme showing the distribution of a porphyrin-peptide based fluorescent probe on the outer leaflet of the lipid bilayer. They represent either the clustered form (C) or the dispersed form (D).

The objectives of this chapter are to set up the experimental conditions to construct the proteoliposomes and follow up quantitatively the peptide aggregation with the porphyrin cluster reporter. Specifically:

1. To design and synthetize TCR transmembrane peptides sequences that can be used to build up the proteoliposomes
2. To design and set up experiments for the analysis of the interaction between such peptides and lipid vesicles (in the absence of any added porphyrin)
3. To determine any interaction between the porphyrin and the lipids vesicles in the absence of peptides.
4. To investigate methodologies for the chemical attachment (labeling reaction) of Compound #5 to the lipid vesicles containing the peptides (Figure 4-1).

4.2 RESULTS AND DISCUSSION

4.2.1 Design and synthesis of the transmembrane peptides

For the design of the synthetic peptide we used the primary structure of the TCRVγ7 (Figure 4-4) based on previous work described by Pennington et al[193] and summarized in section 1.1.9.3 of the introduction chapter. Their results demonstrated that TCR assembly and signaling initiation in early progenitors do not require the extracellular domains of the receptor. Therefore, presumably the signaling initiation is not a consequence of ligand engagement or aggregation of the receptor through the extracellular immunoglobulin domains. Instead, they suggest that simply the expression on the cell surface of the appropriate TCR transmembrane chains might be enough to promote initiation of signaling.

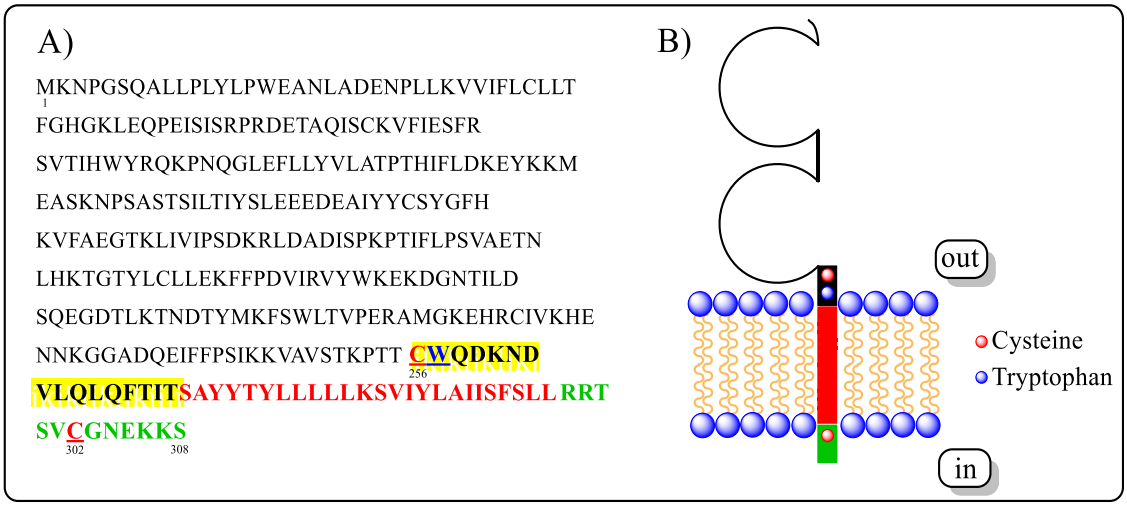

Figure 4-4. A) Representation of the primary structure of the TCRVγ7. Letters in bold represent the sequence of the full-length transmembrane peptide used in this study. Black for the extracellular region containing the cysteine (red) and the tryptophan (blue) residues. In red the transmembrane region, and in green the cytoplasmic sequence of the receptor, containing the cysteine (red) important in our study. B) Schematic representation of the TCRVγ7 chain, in black, red and green are illustrated the residues that composed the full-transmembrane peptide synthetized in our study. Represented with their natural orientation are the cysteines and the tryptophan, red and blue dots, respectively. The control peptide sequence is represented in bold black letters and highlighted in yellow.

The designed peptide has sixteen residues from the stalk region, twenty-five residues from the transmembrane domain, and a short sequence of six aminoacids coming from the cytoplasmic region of the TCRVγ7 (Table 4-1 and Figure 4-4 B). The transmembrane region with 25 hydrophobic amino acids is long enough to span the hydrophobic interior of the bi-layer –approximately 30 Å- according to the characteristic 1.5 Å of helical rise per residue[194]. This means that after insertion in the lipid bilayer of the vesicles the peptide will have two cysteines located at both ends facing the aqueous solutions outside and inside of the liposome bilayer. One important question to answer is how the peptide will be oriented in the bilayer after insertion. We hypothesize that orientation can be random, with a 50% of probability of finding the N-terminus lying outside against 50% of chances to found it in the internal cavity of the liposome. However, some studies in the field suggest that orientation of lipophilic peptides is not completely random and there is a preferential orientation depending on the intrinsic chemical and physical properties of the peptide and lipid composition of the in vitro system. For example, the electrostatic interactions of the polar heads of phospholipids can interplay with the charged groups in the peptide driving the special orientation of C-terminus over N-terminus, as the peptide approaches the membrane[195]; whilst the hydrophobic interactions between the phospholipids and the peptide will drive the insertion of the peptide in the membrane. In our system, to explore the interaction and location of the lipophilic peptide with the lipid bilayer, i.e. insertion and orientation, we will use the optical properties of the tryptophan, which is naturally present in the peptide sequence. Tryptophan fluorescence is a common tool to monitor changes in the conformation- folded or unfolded- of proteins and help to make inferences about the local structure and polar environments[189]. For example, Mingarro et al. recently reported that the presence of aromatic amino acids, i.e. tryptophan or tyrosine

in transmembrane helices is biased. The author observed they are mostly found towards the end of the TM helix (between the hydrophobic core and the bulk water solution) suggesting that at this position the aromatic residues may serve as anchors for the TM helix in the lipid bilayer. Of note, the naturally occurring tryptophan in our peptide is located towards the C-terminus of the peptide, and next to the cysteine that will participate in the labelling reaction with the porphyrin.

In another seminal study, Costa et al.[196] investigating the interaction of carrier proteins, like human serum albumin (HSA) and β- lactoglobulin (βLG) with meso-tetrakis (p-sulfonatophenyl) porphyrin sodium salt (TSPP), which is very similar to compound #5 used in this thesis (Scheme 4-1), described the binding characteristics of TSPP by absorption, and fluorescence.

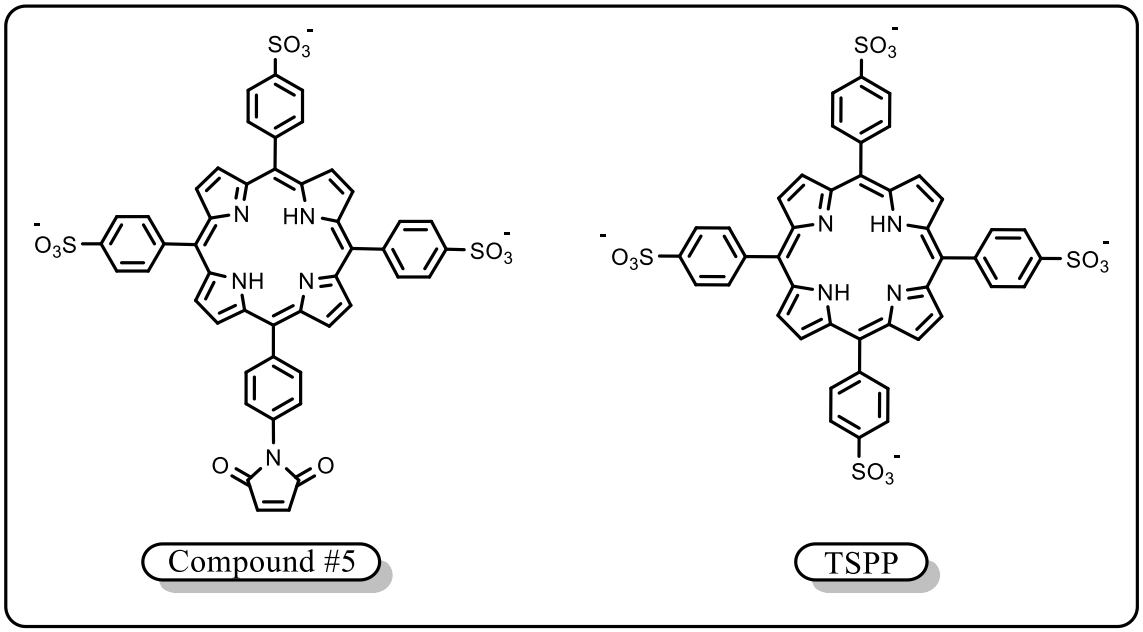

Scheme 4-1. Panel showing the similarities found in the chemical structures of compound #5 and the meso-tetrakis (p-sulfonatophenyl) porphyrin (TSPP) used in the Costa et al.study[196].

Based on previous observations[197] that addition of ligands to proteins can produce quenching of the intrinsic tryptophan fluorescence Costa and colleagues[196] reported that addition of 2-30 μM of TSPP to HSA resulted in concentration-dependent quenching of tryptophan fluorescence. Because there is an important overlap between the tryptophan emission and the TSPP absorption spectrum, they hypothesized that quenching was due to an energy transfer mechanism. Moreover, they also observed a red shift in the tryptophan fluorescence (from 334 to 338 nm) upon addition of TSPP. Costa[196] attributed this shift to the changes in the polar environment of the residue probably due to conformational changes in the protein produced by binding of porphyrin. By analogy, we hypothesize that the presence of the porphyrin moiety near the tryptophan in our peptide will have a quenching effect over its fluorescence as previously described by Costa et al[196]. We expect to see quenching and/or a shifting of the maximum absortion in the fluorescence spectra of tryptophan upon binding to compound #5 in a similar way to that reported by Costa et al. This spectroscopic data could provide information regarding the insertion and orientation of the peptide in the lipid bilayer of vesicles.

In the design of the peptide, we maintained two cysteines residues, C_{256} and C_{302} (see Figure 4-4), which are naturally present in the primary structure of the full-length TCRVγ7 receptor. Of the two cysteines, the residue C_{256} has an important role in the structure of the receptor because it links together the heterodimer through a disulphide bond with a second cysteine located in the TCRδ chain[69]. These cysteines are also convenient for the chemistry because the sulfhydryl functional group will be the nucleophile in the labelling reaction with the maleimide group (see Figure 4-5). The reader is refered to Chapter 3 where the reactivity of Compound #5 towards some model thiols, i.e. N-acetylcysteine and γ-glutathione is de-

scribed as well as experiments that aimed to determine the optimal conditions to perform the labelling reaction before the work with the more expensive and valuable peptide.

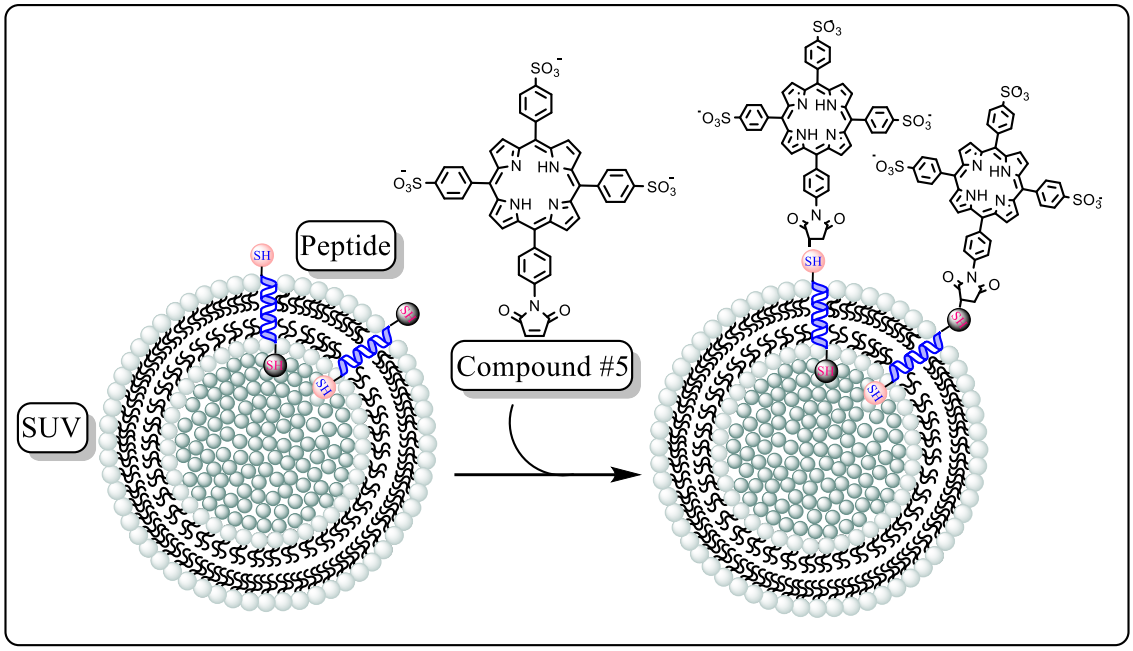

Figure 4-5. Schematic representation of the labelling reaction. In the cartoon, compound #5 is mixed with the proteoliposomes (LUV + Peptide). As illustrated, the labeling reaction is restricted to the external thiols, due to compound #5 being incapable of crossing the lipid membrane based on the presence of three negatively charged sulfonate groups. The peptides are represented in both possible orientations.

4.2.1.1 Control peptide

In order to establish the chemistry of the labelling reaction, we decided to proceed with the synthesis of a smaller peptide. This small peptide is in fact contained in the full-length peptide but unlike its counterpart is less hydrophobic. Chemically, the control peptide is made of 16 amino acids, represented in black color as the extracellular bit of the full-length peptide, and contains one thiol in its sequence (see Figure 4-4 B). Although it is less lipophilic than the full-length peptide, because of its smaller size and content of hydrophobic residues e.g. lack the transmembrane sequence, it is still lipophilic enough to interact with the lipid membranes of the vesicles as shown by its grand average of hydropathicity index (GRAVI) equal to -0.35. Negative GRAVY values indicate that the peptide is non-polar[198]. Due to its short length (16 residues) it is unlikely that it can span the lipid membrane[199] We have denominated this small peptide the **control peptide**. The reason for the usage of the control peptide is to build up a system stripped of all the complexity of the full-length peptide such as, poor solubility, two reactive thiol groups, with which we can study the chemistry of the labeling reaction. By beginning to explore the labeling reaction with the control peptide and Compound #5 we expect to obtain an insight into the conditions that must be set to perform and analyze the reaction of Compound #5 with the more complex full-length peptide.

As mentioned before, in the design of the peptides the presence of the amino acid tryptophan (W) is also very important. The tryptophan fluorescence is sensitive to the polarity of its local environment[189]. Some studies have shown that tryptophan emission maximum (λ_{max}) changes depending on the polarity of the surrounding i.e. hydrophilic vs hydrophobic[200-202]. Some authors have determined that in hydrophobic environments such as the membrane interior, tryptophan has a fluorescence emission maximum at λ_{max} <330 nm

(blue), while in polar environments the maximum is shifted towards λ_{max} >330 nm (red). Indeed, one way to determine binding of peptides to lipid bilayers of large unilamellar vesicles (LUV) is to measure the affinity (binding constant) of the peptide in the presence of increasing concentration of lipids by monitoring the changes in the tryptophan fluorescence spectra upon addition of LUV[203]. These kind of experiments were conducted for both, the full-length and the control peptides, to assess the fluorescence read out of the tryptophan in the control peptide that cannot cross the membrane and in the full-length peptide that presumably will span the lipid membrane. The reader can find these data reported in section 4.2.2.

Notwithstanding, changes in tryptophan fluorescence alone might not be sufficient to determine the relative orientation of the peptide in the lipid bilayer. Two orientations, shown in Figure 4-6 A are possible in LUV, as they do not have the biological machinery that ensure the correct orientation and insertion of peptides in cell membranes. When the full-length peptide is in the correct biological orientation, the single tryptophan faces the aqueous environment on the outer leaflet. This tryptophan is also adjacent to the cysteine that will be used in the labelling reaction with the porphyrin. If such a reaction happens, the porphyrin will be close to the tryptophan and we expect this will induce quenching of the tryptophan fluorescence (Figure 4-6 B) as reported in the work of Costa et al.[196] that we have summarized in paragraph 4 section 4.2.1.

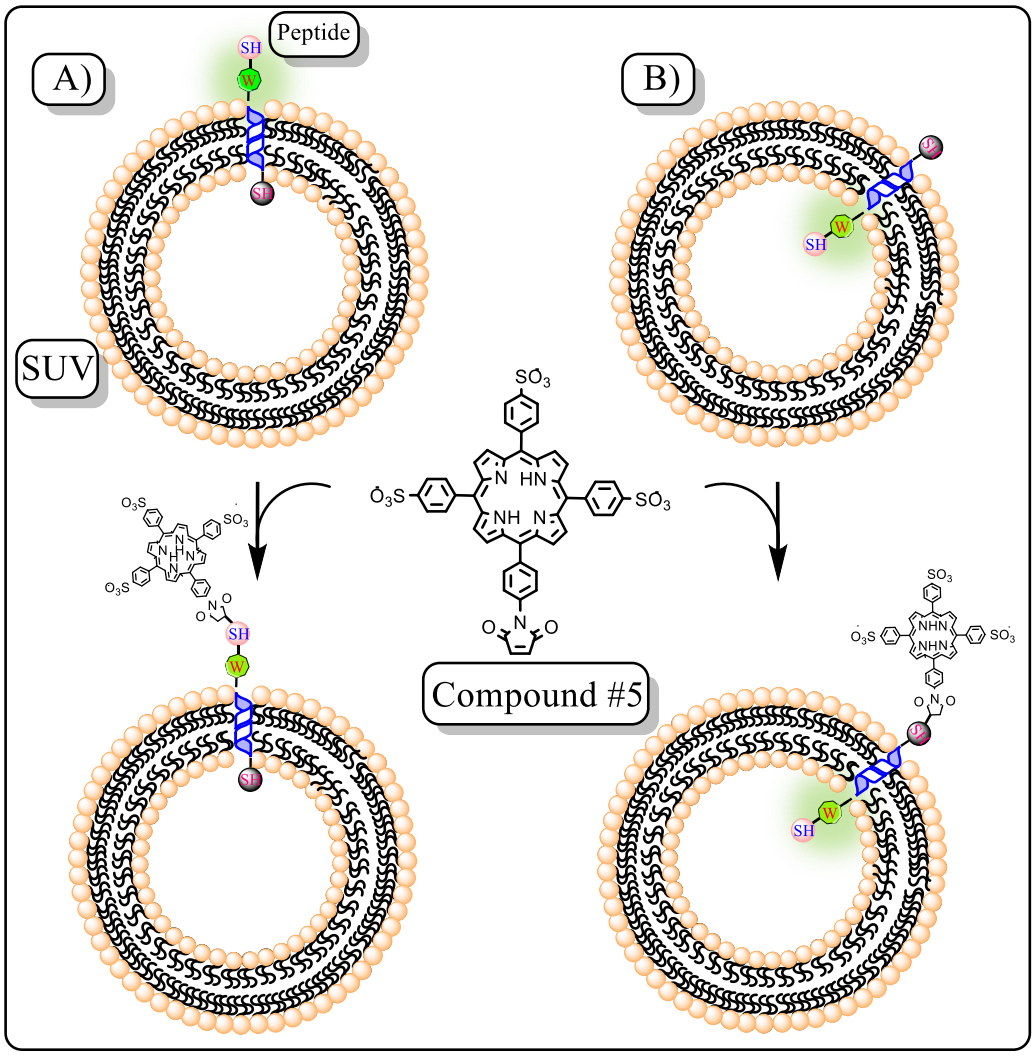

Figure 4-6. Schematic of the two possible membrane orientations of the full-length peptide showing the different orientations for the single tryptophan residue (W). A) Tryptophan exposed to outer leaflet and in close proximity to porphyrin, which might induce quenching. B) Tryptophan exposed to inner aqueous cavity, which is not accessible to porphyrin leading to full fluorescence as indicated by the green halo.

4.2.1.2 Method used for the preparation of LUV

There are different methods for the preparation of lipid vesicles, some of the most common methods are described in the Introduction chapter of this thesis. In our work, we have used the extrusion method for the preparation of the liposomes (see Figure 4-7).

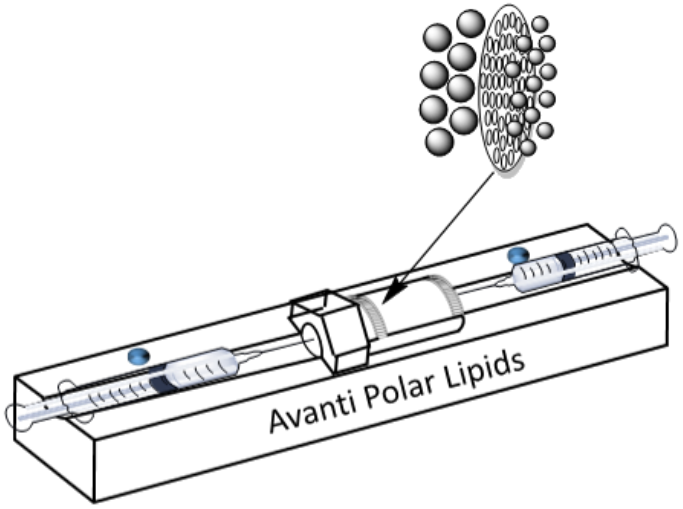

Figure 4-7. Mini-extruder instrument used for the production of the LUV liposomes. Marked with an arrow is the location of the polycarbonate membrane where the extrusion of the crude vesicles takes place.

All the LUV vesicles used in this work were prepared by extrusion of a stock solution of phosphatidylcholine (PC) in ethanol. The PC was the choice of preference because it is a neutral lipid present in natural biomembranes. In addition, it is readily available for the production of vesicles and inexpensive. The PC-ethanol mixture was loaded into a glass vial and then the ethanol was evaporated by flushing with nitrogen gas until a white dry film of PC was formed on the wall of the vial. Upon-dryness, the film was re-suspended in phosphate buffer solution by mixing and further sonicated for one minute to destroy the foam and air bubbles in the solution. A milky appearance is a good sign of successful preparation. Immediately after, the solution is loaded into one of the gas chambers of the mini-extruder. Then

the extrusion takes place by transferring the PC solution from one gas chamber to the other for a minimum of thirty times. In the production of LUV's we used filters of polycarbonate with 100 nm of pore size. This allows for the production of a homogenous lipid vesicle solution with a desirable size, small enough for in-solution measurements and sufficiently stable to stand for the duration of the experiments. For the purpose of this thesis we will use the term LUV predominantly, however lipid vesicle and liposome can be found and they must be taken as interchangeable.

4.2.1.3 Analysis of LUV using UV/Vis spectroscopy

Light scattering is the physical process by which light is forced to deviate its path due to some uniformities in the media it passes through. In our studies with LUV vesicles in solution, wavelength-dependent scattering of light was observed, the extent of which depended on the size of the lipid vesicle used. In fact, we used 100 nm vesicles because the scattering can be corrected, allowing us the use of in-solution measurements by traditional spectroscopic techniques such as UV-vis and fluorescence. Regarding the stability of the lipid vesicle, it has been shown that smaller vesicles i.e. LUV, about 20 – 50 nm in size, possess high curvature that induces structural tension and less stability, therefore we decided to use LUVs with less surface curvature and greater stability[204]. A common way to correct the contribution of the wavelength-dependent scattering of light in the samples is by subtracting the scattering spectrum obtained from control samples containing only lipid vesicles to the optical measures from the experiments where the proteoliposomes are present. Whenever we performed experiments containing PC vesicles and porphyrin, peptide, or both we also determined the scattering of the vesicles alone. In our experiments, the concentration of PC in the vesicles was between 0.1 mM and 10 mM. These spectra were consistently subtracted from

the traces of the samples i.e. containing porphyrin, peptide, or both to eliminate the contribution of the PC (see Figure 6-10 in Appendix).

Figure 4-8 shows that increase in light scattering is proportional to the concentration of the PC in the vesicles.

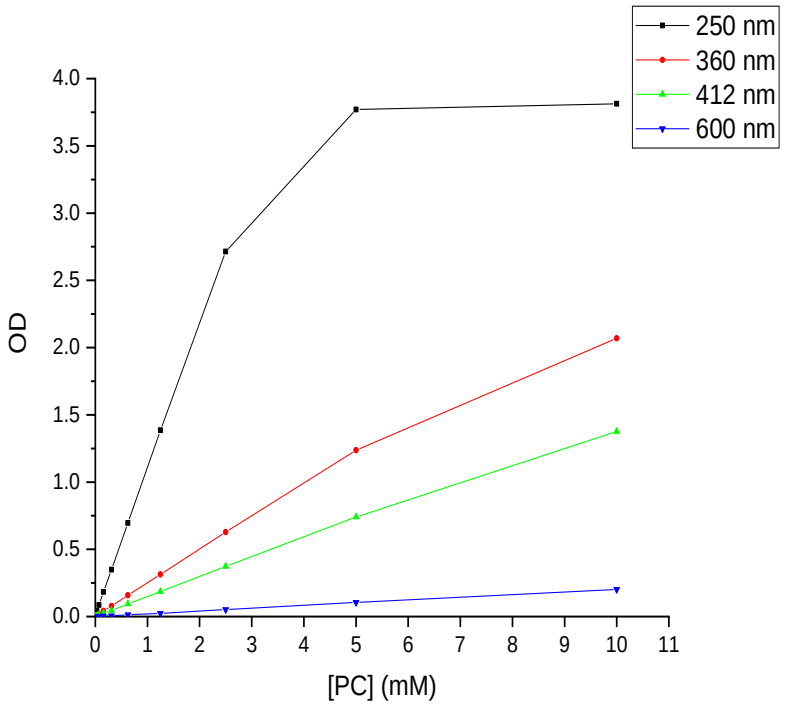

Figure 4-8. Plot of optical density against concentration of PC (mM) (See appendix) at four different wavelengths indicated in the legend.

In addition, we also subtracted the contribution of the phosphate buffer. For the entire LUV samples the spectra of the phosphate buffer was recorded and subtracted using raw spectral data rather than automatic instrument subtraction. A further correction was applied for the position of the baseline when it was necessary to compare multiple spectra with different positions of the baseline. This correction was applied using raw spectral data rather than the instrumental function as follows: the first 12 wavelengths (700 – 688 nm) were used

to calculate the average. This average was subtracted from each spectroscopic read-out obtained from the instrument. This methodology was followed consistently as a pre-processing technique for the removal of backgrounds noise in all the experiments discussed in this chapter.

4.2.1.4 Basic Theory for the Determination of Equilibrium Association Constants (Only 1:1 System)

In this section, we will describe briefly the basic theory and the methodology employed to quantify the interaction between the LUV with both peptides and compound #5. As described by Thordarson el al.[205] the most common method to quantify the complexation in supramolecular chemistry is the **titration**. In general, titration is a powerful analytical technique in which one component (ligand) is added to a solution of a second component (receptor) and the change of a physical property i.e. absorbance or fluorescence intensity that is sensitive to the molecular interaction is recorded. The information obtained from the titration is then plotted on a graph and the titration curve, also known as binding isotherm, is then fitted to a binding model using appropriate software to calculate the binding constant which is also referred as association constant (*Ka*).

In this thesis all the titration data were fitted using the simplest association model, i.e. a straightforward 1:1 model, which assumes that only two species are important in the binding equilibrium. The equation used for the fitting of the data was obtained from the 1:1 binding equilibrium (0):

$$[L] + [R] \overset{Ka}{\leftrightarrow} [RL] \qquad (0)$$

As follows:

$$K = \frac{[RL]}{[R][L]} \qquad (1)$$

$$[R]_0 = [R] + [RL] \qquad (2)$$

$$[L]_0 = [L] + [RL] \qquad (3)$$

Where equation 2 and 3 represents the mass balance for the 1:1 binding model. Due to fact that the concentrations of free ligand [L] and free receptor [R] cannot be directly measured we will use these three equations 1, 2 and 3 to write the concentration of the complex [RL] as a function of the known total concentration $[R]_0$ and $[L]_0$:

$$K = \frac{[RL]}{([R]_0 - [RL])([L]_0 - [RL])} \qquad (4)$$

$$K = \frac{[RL]}{[RL]^2 - [RL][R]_0 - [RL][L]_0 - [R]_0[L]_0} \qquad (5)$$

$$K = \frac{[RL]}{[RL]^2 - [RL]([R]_0 + [L]_0) + [R]_0[L]_0} \qquad (6)$$

$$[RL]^2 - [RL]([R]_0 + [L]_0) + [R]_0[L]_0 = \frac{[RL]}{K} \qquad (7)$$

$$[RL]^2 - [RL]([R]_0 + [L]_0) + [R]_0[L]_0 - \frac{[RL]}{K} = 0 \qquad (8)$$

$$[RL]^2 - [RL]\left([R]_0 + [L]_0 + \frac{1}{K}\right) + [R]_0[L]_0 = 0 \qquad (9)$$

$$[RL] = \frac{[R]_0 + [L]_0 - \frac{1}{K} - \sqrt{\left([R]_0 + [L]_0 + \frac{1}{K}\right)^2 - 4[R]_0[L]_0}}{2} \qquad (10)$$

The relationship between [RL] and the absorbance, assuming [L] does not absorb at the wavelength under study can be written as:

$$A = \varepsilon_R[R] + \varepsilon_{RL}[RL] \qquad (11)$$

If we substitute eq., 2 in 11 we obtain,

$$A = \varepsilon_R([R]_0 - [RL]) + \varepsilon_{RL}[RL] \qquad (12)$$

$$A = \varepsilon_R[R]_0 + (\varepsilon_{RL}\text{-}\varepsilon_R)[RL] \qquad (13)$$

$$A = \varepsilon_R[R]_0 + \Delta\varepsilon[RL] \qquad (14)$$

If we now substitute eq. 10 in eq. 14

$$A = \varepsilon_R[R]_0 + \Delta\varepsilon\frac{[R]_0 - [L]_0 + \frac{1}{K} - \sqrt{([R]_0 + [L]_0 + \frac{1}{K})^2 - 4[R]_0[L]_0}}{2} \qquad (15)$$

Where A is the absorbance and εR, the extinction coefficient of Compound #5.

From equation 15 it is possible to describe the expected changes in the spectroscopic properties of the titration experiment from two known parameters ($[R]_0$ and $[L]_0$) and two unknown parameters ($\Delta\varepsilon$ and K). In practice, the last two parameters can be obtained by non-linear regression analysis from the titration data. In this thesis, we have inputted a version of equation 15 in the software Origin Pro and used its fitting routine procedure to calculate the value of K. The estimate of good fitting is given by the error parameter embedded in the Origin software. (see Experimental Section for details).

The choice of UV-vis spectroscopy as the technique to monitor the titration experiments is subject to the availability of a good chromophore. In our system, this condition was successfully fulfilled with compound #5. Porphyrins are excellent chromophores with an intense absorption in the UV-vis range. This capacity makes it possible to use them in concentrations as low as sub-micromolar range, allowing the determination of association constants as high as 10^9 M^{-1}. However, in the selection of the concentrations, we must ensure that the absorption of the porphyrin and the complex porphyrin-lipids lie within the limits of the Lambert-Beer law ($A<1$). Additionally, it is desirable if the ligand [L] -lipids- does not have any absorption in the region of interest, as this simplifies the system considerably. In our particular system, the lipid vesicles did not absorb light in the wavelength range of interest in the porphyrin spectra. Although some wavelength dependent scattering of light was observed and further corrected as described in previous section 4.2.1.3.

4.2.2 Fluorescence Experiments

In this section, we will report the experiments that we performed to explore whether the full-length transmembrane peptide was inserted in the LUV and the orientation of the single tryptophan relative to the lipid bilayer as shown in Figure 4-9.

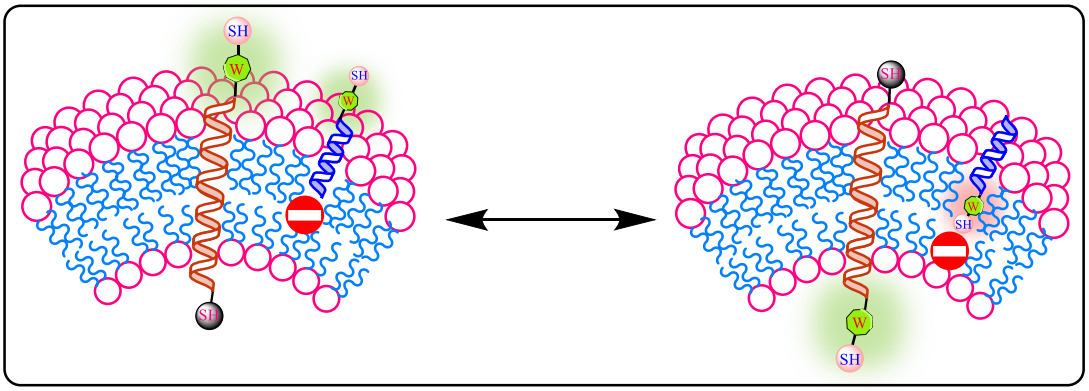

Figure 4-9. Schematic of the two possible membrane orientations of the full-length peptide and the control peptide in the lipid vesicle. As illustrated, the peptide control is unable to span the lipid membrane, and the fluorescence of the tryptophan residue embedded in the lipid bilayer should be different from the fluorescence of the residue when exposed to bulk aqueous solution.

4.2.2.1 Tryptophan–LUV Titrations

The aim of these experiments was to determine the association constant of both the transmembrane and control peptide to LUV. Changes in the fluorescence of single tryptophan in peptide have been used to determine binding of such peptides to LUV, where the strength of such interactions is indicative of peptide insertion[203, 206, 207]. Because the control peptide lacks the sequence for membrane insertion, it is reasonable to expect that any difference in binding association to LUV between the two peptides might be indicative of membrane insertion (see Figure 4-9). Typically, the association constant, which is a measure of peptide-membrane binding, is obtained by titration methods.

The titration was carried out keeping constant the concentration of the peptide against 12 solutions of liposomes containing increasing concentrations of PC. The selection of the peptide concentration for this experiment was 6 μM. This is the lowest concentration that gives a good fluorescence spectrum and was selected taking into consideration that in the titration experiment the peptide-lipid interaction could quench the fluorescence of the tryptophan. The twelve point titration was repeated three times. LUVs with increasing concentrations of PC (0-3 mM) were prepared by the extrusion method as discussed in sections 1.1.11.1.3 and 4.2.1.2. The sensitivity of the fluorescence titration technique allows for the determination of association constant as high as 10^{6} [205].

In order to prepare a working solution of tryptophan at 6 μM it was necessary to prepare a concentrated stock solution, but this proved to be challenging, due to the poor solubility. Both peptides proved to be insoluble at a concentration of 250 μM in the following solvents: 100 mM phosphate buffer pH 7.2, and acetonitrile, which was indicative of their amphiphilic character and was somewhat unexpected for the control peptide, as it is more hydrophilic.

In addition, dithiothreitol was added to all solutions at a concentration 100-fold higher than the peptide to keep the cysteines in the reduced state during the titration experiment thus preventing the oxidation of the peptides, which does occur in time as was shown in sections 3.3.2 and 3.3.4 of Chapter 3. To determine the concentration of the peptides in solution we used the Von Hippel method[208]. The method reported an equation that allows the calculation of the extinction coefficient of any protein/peptide based on the presence of three amino acids: cysteine, tyrosine, and tryptophan, due to these residues being the only ones that contribute to the absorbance of the protein/peptide in the range of 270-280 nm. Based on their

work, we calculated the extinction coefficient of the peptide control as 5810 $M^{-1}cm^{-1}$ and the full-length peptide as 11050 $M^{-1}cm^{-1}$.

4.2.2.2 Determination of the fluorescence spectra of both peptides in the absence of lipids

As shown in Chapter #3 and mentioned in section 1.2.7 a fraction of the peptide was already oxidized, or does it quickly in solution; therefore, the concentration of DTT was 100-fold higher than the peptide. Representative spectra of three different experiments are shown in Figure 4-10. The spectra for both peptides are very similar in terms of range of lambda max (approx. 350 nm) and intensity, the bathochromic shift (7 nm) observed in the maximum for the control peptide is also expected given that this peptide is more polar than the full-length peptide.

The objective of this experiment was to record the fluorescence spectra of both peptides in the absence of lipids. Due to the poor solubility of both peptides in aqueous buffer the stock solutions of both peptides were prepared in dimethylsulfoxide. Due to the necessity of keeping the amount of non-aqueous solvent as low as possible (as this might damage the LUV) the samples used in the fluorescence measurements contained ~3.3% of dimethylsulfoxide in phosphate buffer pH 7.2 and dithiothreitol (100-fold excess compared to peptide). The excitation wavelength selected was 295 nm because using an excitation wavelength shorter than 295 nm will result in excitation of other aromatic aminoacids (tyrosine, phenylalanine), which may obscure the shape of tryptophan's emission spectra, and the fluorescence emission was recorded from 300 – 600 nm (Figure 4-10).

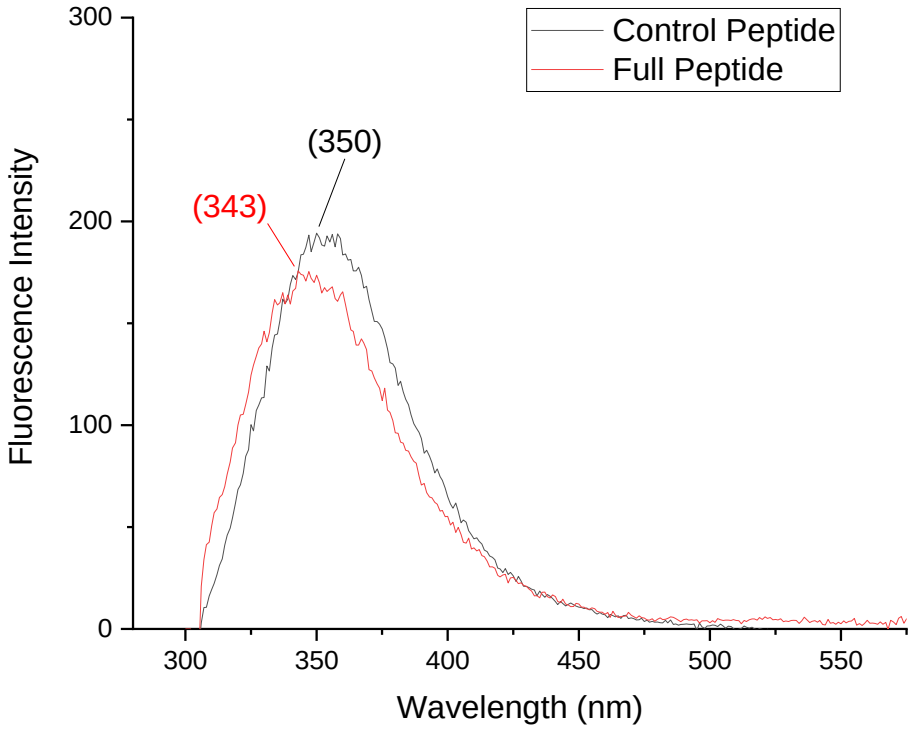

Figure 4-10. Fluorescence spectra of both peptides (6 μM) in the absence of lipids. The samples were prepared in PB pH 7.2 with 3.3% DMSO and 600 μM DTT.

4.2.2.3 Titrations of both peptides

The aim of this experiment was to explore whether we could follow the insertion of the peptides, and possibly their orientation in the lipid vesicles by studying the changes in the fluorescence properties of the tryptophan, i.e. wavelength of maximum emission (λ_{max}), emission intensity at λ_{max}. Previous studies[190] have described that the fluorescence of tryptophan is solvatochromic, showing a strong correlation between its fluorescence and the polarity of the solvent that surround the residue (see section 4.2.1.1). However, is important to mention that only the full-length transmembrane peptide contains the domain that will allow membrane insertion and spanning, while the control peptide-lacks the transmembrane domain and therefore cannot cross the membrane (Table 4-1).

Regarding the methodology followed for the peptide insertion, we found two methods described in the literature[203, 209, 210]. In the first method, the stock solution of lipid and peptide is mixed to achieve the desired ratio lipid/peptide. The solvent is then evaporated and the lipid/peptide film re-hydrated with the appropriate buffer to produce the lipid vesicles with the peptide inserted. In the second method, that the hydrophobic peptide is combined with preformed lipid vesicles. Due to the lipophilic nature of the peptide, we expect it will insert spontaneously in the lipid membrane the second method was adopted. The reason why we discarded the first method is due to the possibility that with the extrusion method the peptide conformation result damage. In fact, in this method, often detergents are used to preserve the peptide conformation, and these detergents might interfere with the measurements we want to make, i.e. peptide in-membrane aggregation. In contrast, for the second method, given the hydrophobicity of the full-length peptide, it will likely incorporate spontaneously in the membrane of the vesicles. However, the insertion can take some time; therefore, we equili-

brate the peptide-lipid vesicles mixture for 1 hour to allow the quantitative insertion of the peptides into the liposomes.

As mentioned in sections 4.2.1 and 4.2.2, both peptides, the full-length transmembrane and the control peptides are highly hydrophobic, constituted by 47 and 16 aminoacids, respectively. Both peptides contain tryptophan as a reporter residue and cysteines for the labeling reaction with Compound #5 (see Table 4-1).

Peptide	Sequence	AA	PI	E $M^{-1}cm^{-1}$	MW gM^{-1}	GRAVI
Control	Ac-CWQDKNDVLQLQFTIT-NH2	16	4.2	5690	1993.2	-0.35
Full-length	Ac-CWQDKNDVLQLQFTITSAYYTYLLLLLKSVI-YLAIISFSLLRRTSVC-NH2	47	8.7	11050	5559.6	0.68

Table 4-1. The sequence of the control and the full-length peptide as well as the main parameters calculated by ExPASy, Abb: AA: aminoacids, PI: isoelectric point, E: extinction coefficient, MW: molecular weight, GRAVI: grand average of hydropathicity.

Based on the methodology described in section 4.2.2.1, we perform both titrations by keeping constant the peptides at 6 μM in phosphate buffer plus ~3.3% dimethylsulfoxide and 600 μM of dithiothreitol against twelve solutions of liposomes of increasing lipid concentrations (0-3 mM) (Figure 4-11).

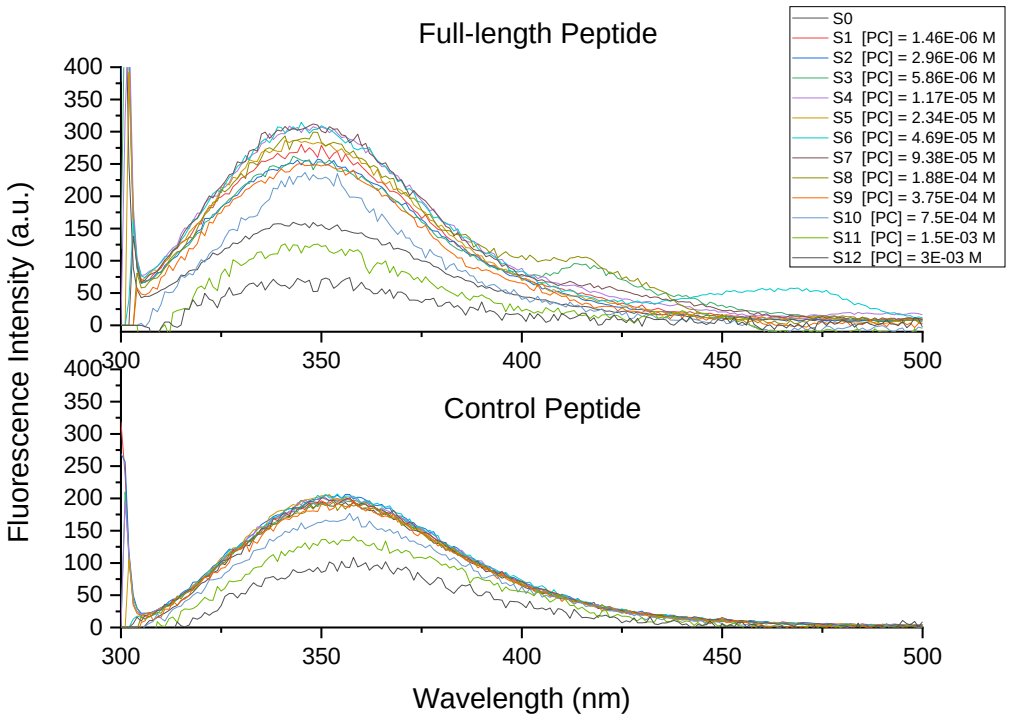

Figure 4-11. Fluorescence spectra of control and full-length peptide with vesicle lipids of increasing PC concentration. The twelve point titration samples contained 3.3% DMSO and 600 μM of DTT.

Fluorescence measurements were corrected by blank measurements of vesicles without peptides as shown in the Figure 4-12.

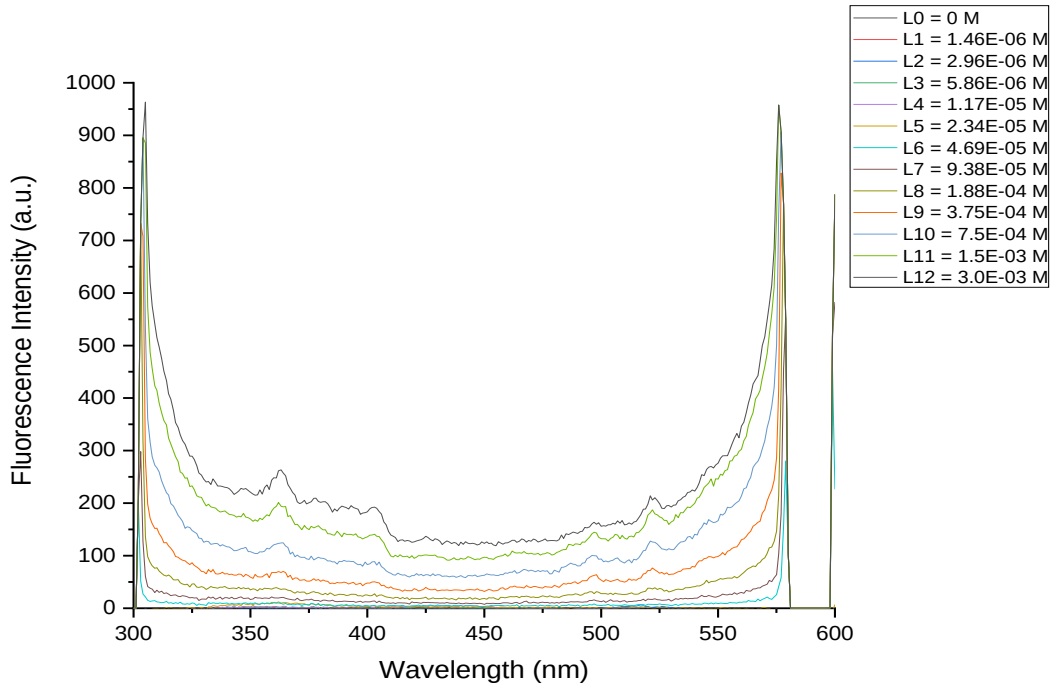

Figure 4-12. Fluorescence spectra of twelve solutions of liposomes in PB pH 7.2 at increasing concentration of PC as indicated in the legend. (λexc: 295 nm).

For the correction, we prepared 12 solutions of liposomes with increasing concentration of lipids (0-3 mM) in PB pH 7.2 without peptides, dithiothreitol or dimethyl sulfoxide. The fluorescence spectrum of each solution of PC was then subtracted from that of each sample containing the corresponding peptide as mentioned in section 4.2.1.3.

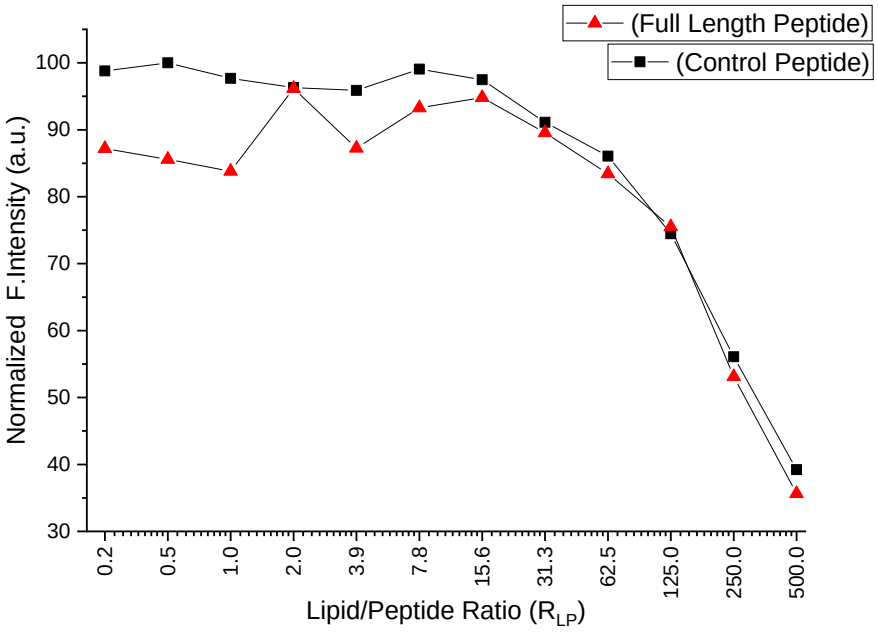

Figure 4-13. Normalized fluorescence emission of tryptophan at 350 nm as a function of the molar ratio of phosphatidylcholine to peptide for the control and the full-length transmembrane peptides. The data represented are mean values obtained in at least two independent experiments.

To better visualize the dependence of the fluorescence intensity changes with lipid concentration, the normalized fluorescence intensity at 350 nm was represented as a function of the molar ratio of the phosphatidylcholine lipid to peptide (R_{LP}). The data represented in the Figure 4-13 are the mean values of two independent sets of experiments (See raw data in Appendix, Figure 6-7).

The plot of normalized fluorescence against phosphatidylcholine lipid to peptide ratio, shows that the intensity of fluorescence emission at 350 nm is constant up to R_{LP} = 15.6 and then decreases with the increasing of the lipid concentration. This suggests that addition of tryptophan containing peptides to neutrally charged lipid vesicles, affect the fluorescence of tryptophan in different ways depending on the polarity and net charge of the peptide and amino acid residues near to the tryptophan. For relatively short peptides, it has been observed that tryptophan fluorescence increases with increasing concentration of lipid whilst if the neighboring aminoacids are charged there are no significant changes in the fluorescence emission[203, 206, 207]. For both our peptides, we observed a quenching of the fluorescence intensity with increasing lipid concentration which might indicate that tryptophan experiences a more polar environment upon addition of lipid vesicles. A possible explanation is that for both peptides the tryptophan is near to the QDKN sequence that contains polar amino acids (charged and hydrogen bonding prone)[211]. Within this polar environment, the tryptophan might be position at the lipid water interface and this environment would be more polar than the membrane interior. In addition, both peptides tend to aggregate in PB, therefore it is possible that in the aggregates the tryptophan fluorescence is higher (i.e. in hydrophobic environments the tryptophan fluorescence is higher) than at the lipid/water interface. In other words, that upon addition of lipids vesicles the tryptophan prefers to lay in the more polar environment of the lipid/water interface. If this is the case then the data might also suggest that both peptides are oriented similarly to their orientation in biological membranes (i.e. with the N-terminus facing the outer water environment). Therefore, even if the data for both peptides are very similar and therefore cannot be used as an indication that the full-length

peptide is spanning the membrane relative to the control peptide, they are promising in terms of orientation of the peptide relative to the lipid bilayer.

However, to lend support to this explanation, further experiments with external tryptophan quenchers were carried out.

In conclusion, from these titrations, we could not record any relevant difference in the fluorescence read-out of the peptide control compared to the full-length peptide. Therefore, monitoring the changes in the spectroscopic features of the intrinsic tryptophan in both peptides did not help to elucidate whether the full-length peptide was spanning the vesicle bilayer when compared to the control peptide. Notwithstanding, the small absolute red shift of the maximum emission wavelength observed in the titration suggests that this tryptophan is located near the membrane/buffer interface. This might indicate that both peptides are oriented with the N-terminus facing the bulk solution in a similar position with respect to their natural orientation.

However, it is evident from the fluorescence data that the emission of the tryptophan was particularly weak in our experimental conditions, limiting the scope of our conclusions. In the light of these results, we decided to explore another method to unravel the peptide orientation, i.e. fluorescence quenching techniques. We think that quenching experiments might be a good approach to explore the insertion and orientation of the peptides in the lipid vesicles. The rationale of these experiments will be discussed in detail in the next section.

4.2.2.4 Determination of the optimal conditions to quench the fluorescence of the compound #5.

In order to be able to understand how both, the full-length and the control peptide are oriented in the membrane of the vesicles we decided to use a fluorescence quenching technique. This method uses a fluorophore quencher. A quencher is a compound that when added to a fluorophore either reduces the fluorescence intensity or quenches it completely.

The rationale to carry out this experiment is based on the assumption that if we mix the peptide and the lipid vesicles following the methodology described in the section 4.2.2.1, the peptides can be inserted in the membrane, randomly distributed as discussed in section 4.2.2. These proteoliposomes can be labelled at both ends of the full length-peptide facing the aqueous media, assuming the orientation of the peptide is 50:50 meaning that half of the peptide will be oriented with the N- terminus facing the outer leaflet of the lipid vesicles while the other half will be exposing the C-terminus as shown in Figure 4-14. The labeling will be performed by the addition of excess compound #5, in a similar way as described in Chapter 3 section 3.3.12.2. Taking into consideration that compound #5 is unable to cross the lipid bilayer, after washing the excess of porphyrin by gel permeation chromatography we will end with proteoliposomes labelled in the outer leaflet of the membrane, with the N or C-termini labelled depending on the peptide orientation relative to the bilayer (three possible scenarios depicted in Figure 4-14). Therefore in the outer leaflet, the labelling will results in the tryptophan and porphyrin being in close proximity, which we expect will induce a quenching of the tryptophan fluorescence. This hypothesis is supported by the work described by Costa et al.[196] summarized in section 4.2.1.

Therefore, after the excitation of tryptophan at 295 nm the fluorescence recorded will come presumably from the tryptophan facing the internal cavity of the liposomes. In this way, we might be able to identify the relative orientation of the peptide in our system.

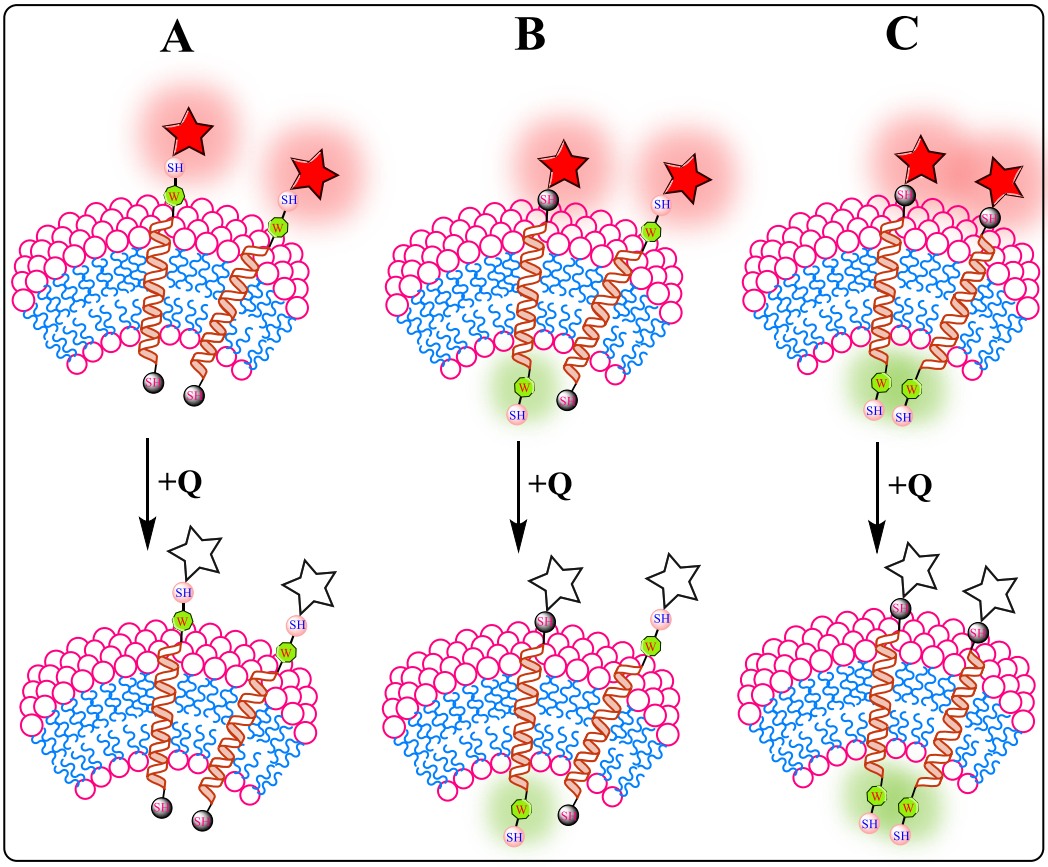

Figure 4-14. Schematic of the three possible membrane orientations of the full-length peptide with different quenching extents (A–C). A) The peptides are oriented with the tryptophan residues next to the outer leaflet. B) The conformation of the peptides is 50:50 randomly distributed. C) Both peptides present the tryptophan residue located in the internal cavity of the liposomes. As illustrated, the reaction with the porphyrin might quench the fluorescence of the tryptophan only when the peptide is oriented with the N-terminus towards the bulk aqueous solution. Upon addition of the quencher (Q) all the fluorescence from the porphyrin moiety will be quenched; therefore, the only fluorescence registered should come from the tryptophan residues lying in the interior of the liposomes.

However, to make sure the porphyrin does not contribute to the fluorescence we will add an external quencher that is unable to cross the membrane. In this way, any fluorescence must come presumably from the tryptophan facing the internal cavity of the liposome. This approach offers a qualitative way to follow the orientation of the peptides. However, the fluorescence measurements will be coupled with high pressure liquid chromatography (HPLC) to determine the yield of the labeled peptide.

Due to the need to find a porphyrin quencher that does not cross the lipid membrane, as a starting point we tried the molecules p-Xylene –bis-(N-pyridinium bromide) and 1,1′-diheptyl-4,4′-bipyridinium dibromide, based on a previous work by Miss Rimsha, an MSc student in our group.

Briefly, the aim of her project was to synthetize a fluorescent probe (POC16), to explore the extent of lipid aggregation in model membranes. To this end, the fluorescent probe POC16, made of a pyranine hydrophilic head group and a C16 hydrocarbon chain was synthetized (see Figure 4-15). To explore whether there was a preferential distribution of the fluorescent probe between the inner or the outer leaflets she performed some experiments with two fluorescent quenchers, p-Xylene –bis-(N-pyridinium bromide) (DPX) and 1,1′-diheptyl-4,4′-bipyridinium dibromide (DPB) (see Figure 4-15). Her results showed that both compounds were able to quench the pyranine fluorescence in the presence of lipid vesicles composed of phosphatidylcholine with 100 nm diameter and that both quenchers were membrane impermeable. Moreover, her experimental data demonstrated that DPB was a better quencher of the pyranine probe both in solution and in the presence of lipids.

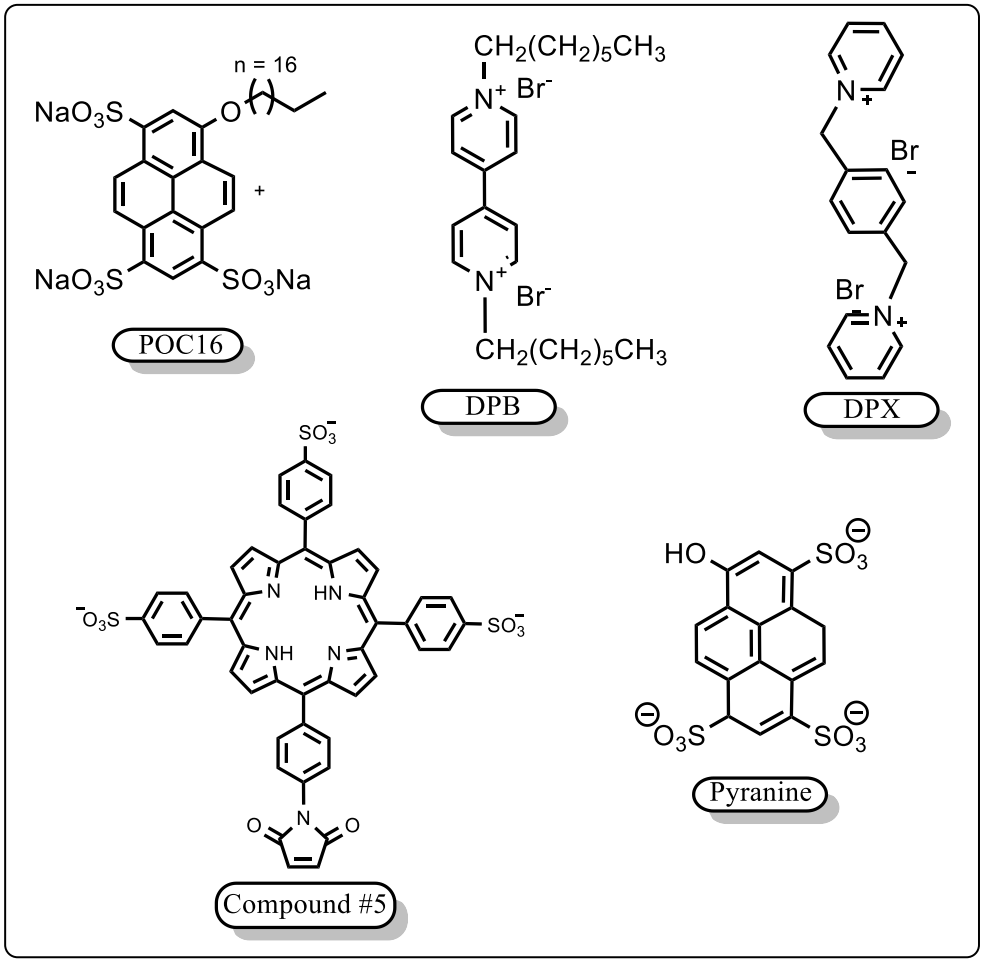

Figure 4-15. Scheme showing the chemical structure of POC16, DPB, DPX, compound #5, and pyranine.

Based on these preliminary results and the fact that both pyranine and Compound #5 are made of an aromatic core and contain three negatively charged sulfonate groups, we thought that it might be possible to use these quenchers to quench the fluorescence of Compound #5.

To address this, the initial experiment was to determine the concentration of DPX needed to quench the fluorescence of compound #5 without lipids. A solution of compound #5 (0.2 μM) was excited at 413 nm, corresponding to the maximum absorption of the Soret band, and the fluorescence emission was recorded between 430-900 nm (Figure 4-16 B). The fluorescence spectra showed two intense bands with maxima at 645 and 705 nm. After adding small volumes of the stock solution of DPX we detected a decrease in the fluorescence emission of compound #5 from 100% to 48.6%. Figure 4-17 show how as the concentration of DPX increased, the fluorescence of the Compound #5 is quenched until it reaches a plateau, where further addition of DPX does not quench the fluorescence any further. From the results, we determined that with 16.6 mM of DPX we reached the plateau with a quenching efficiency of approximately 51.4 % of the total fluorescence of Compound #5 in solution.

Based on the results with DPB and pyranine (Figure 4-15), we decided to also explore this quencher with Compound #5. Interestingly, it is also reported in the literature as an efficient quencher of the tetrakis (4-carboxyphenyl)porphyrin[212]. In fact, the structure of DPB, containing two long alkyl chains suggests a better interaction with the amphiphilic compound #5. Albeit, the presence of the polar charges in the molecule will preclude the quencher from crossing the lipid membrane as demonstrated by Miss Rimsha Anjum (Unpublished data).

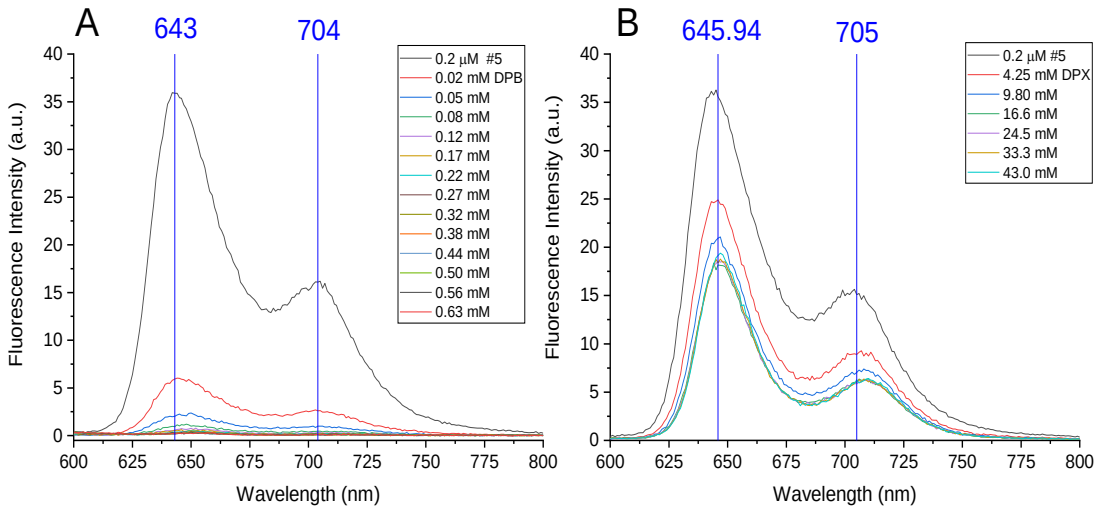

Figure 4-16. Effect of quenching by the molecules used in this study on Compound #5. (A) The observed fluorescence intensity of compound #5 decreases with increasing concentration of DPB. (B) The observed fluorescence intensity of compound #5 decreases with increasing concentration of DPX.

Following the same protocol as discussed above we added small aliquots of DPB to a solution of compound #5 (0.2 µM). Figure 4-17 shows the same trend in the quenching of the fluorescence as observed with DPX. We determined that 0.44 mM of DPB was the concentration at which the fluorescence quenching curve reach the plateau, therefore subsequent additions of the quencher do not improve the quenching of Compound #5 fluorescence in solution. It was quite evident from the Figure 4-17 that lower concentrations of DPB produce a higher fluorescence quenching of Compound #5 than DPX. Although, in both cases the fluorescence quenching was never 100%.

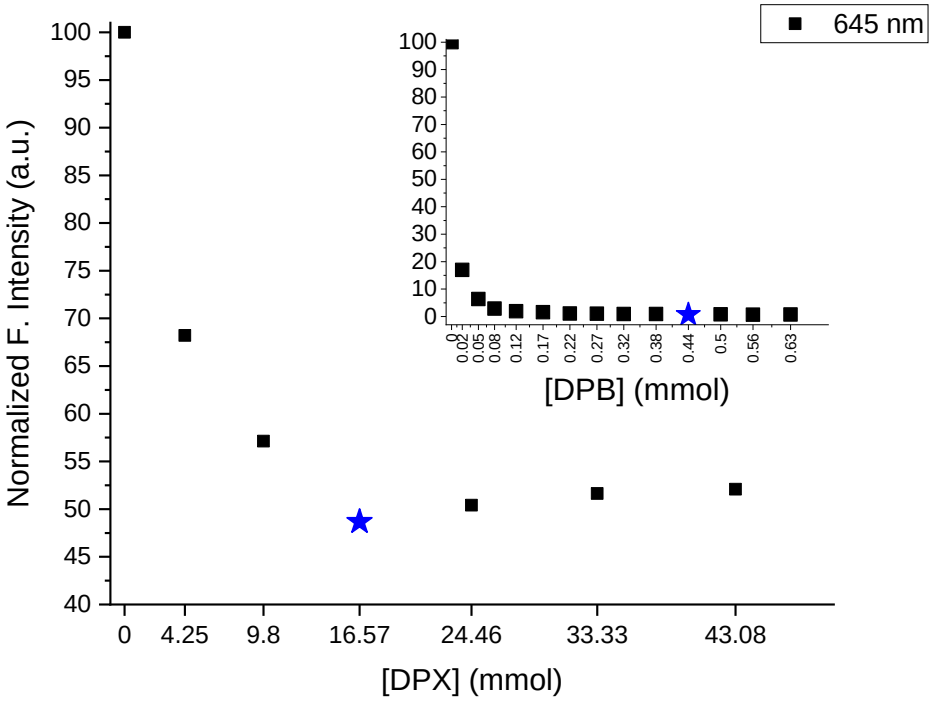

Figure 4-17. Dynamic fluorescence quenching of the compound #5 at increasing concentration of DPX (λem = 645 nm). For the sake of comparison, the inset graph represents the fluorescence quenching by DPB on compound #5.

In conclusion, we determined that the best quencher of the fluorescence of Compound #5 in solution was DPB. It was found that 0.44 mM of DPB was able to quench up to 99% of the fluorescence of compound#5 in PB 100 mM pH 7.2. Although these results are promising further experiments have to be done to explore the quenching ability of DPB on Compound #5 in the presence of lipid vesicles as it might be the case that more hydrophobic environments can have an impact on the quenching ability of DPB. However, experimental data from Miss Rimsha conducted with POC16 in the presence of lipid vesicles showed that DPB was still an efficient quencher of the POC16 fluorescence.

4.2.3 Studies of tetrasulphonate porphyrin binding to LUV

In this section, we will describe the experiments done to explore the interaction of Compound #5 with lipid vesicles in the absence of peptides. These experiments will provide some preliminary data that are necessary before we address the more complex experiment of aggregation of the transmembrane peptide with Compound #5 as a clustering reporter. We plan to begin with the insertion of the peptides in the lipid vesicles freshly prepared. The following step will be the adding of excess Compound #5 to force the equilibrium towards the reaction with cysteines. As discussed in section 3.2.4 in Chapter 3 we need to use excess DTT to keep the sulfhydryl groups in the reduced state, to be available to react with the porphyrin. Afterwards, we will remove the excess of Compound #5 and DTT in solution. Achieving the maximum separation possible of the unreacted compound #5 from the labelled lipid vesicles is critical to accurately evaluate the extension of the peptide aggregation. The reason being is free porphyrin in solution will interfere with the read-out of bound Compound #5. To determine qualitatively and presumably quantitatively the extent of the labelling reaction we will destroy the liposomes with a detergent e.g. Triton and the mixture will be analyzed by HPLC. Based on the different retention times between the labelled and unlabeled peptides we expect to quantify the extent of the reaction, and possibly the amount of any unreacted porphyrin. The general steps briefly described above are represented in Figure 4-18.

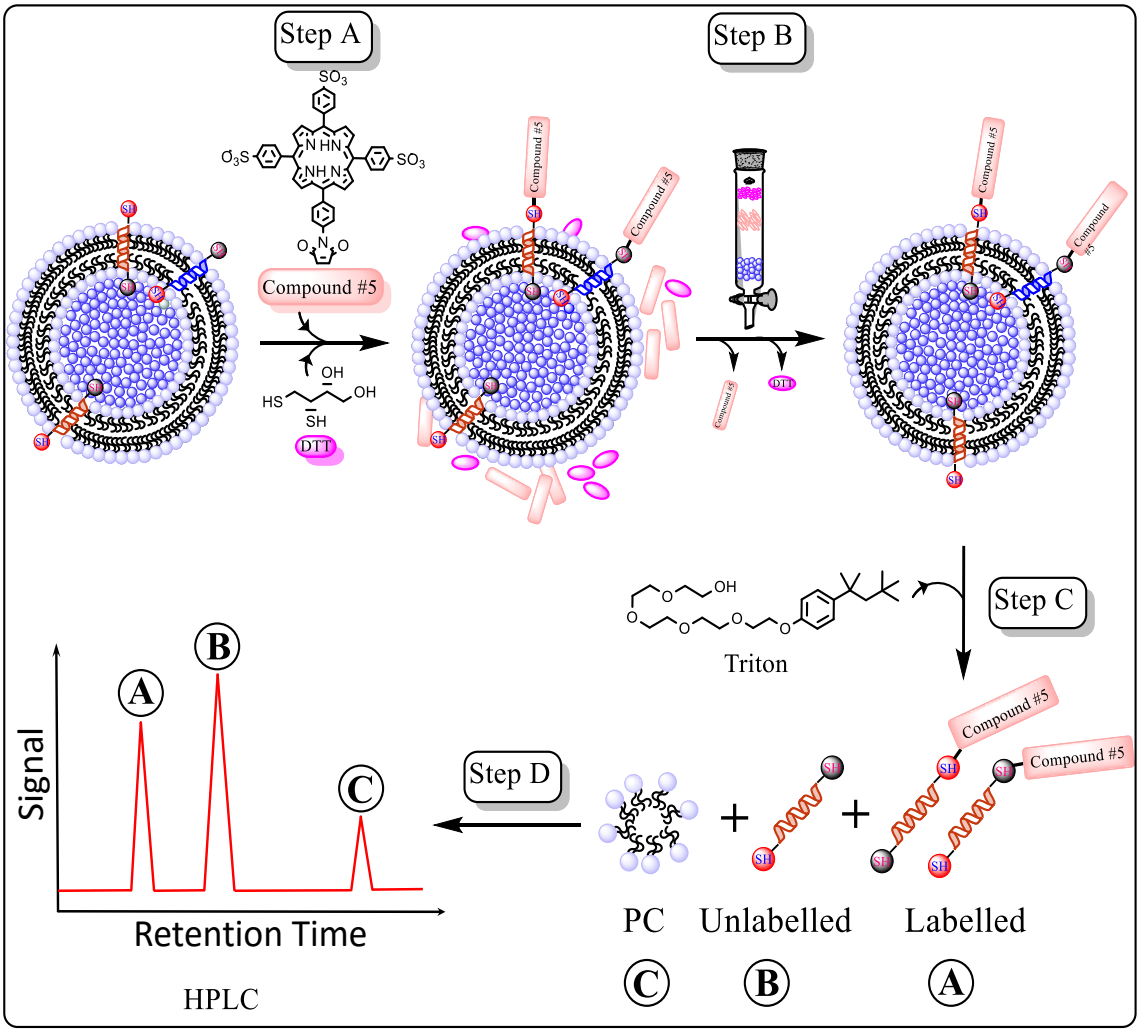

Figure 4-18. Schematic representation of all the general steps envisaged in this study to achieve the chemical (labeling) reaction. Step A) Labeling of the proteoliposomes with excess of compound #5 in the presence of reducing agent DTT. Step B) Removal of the unreacted porphyrin and DTT by GPC. Step C) Release of the labeled and non-labelled forms of the peptides by solubilization of the lipid vesicles with TX-100 (Triton). Step D) Qualitative and quantitative analysis of the labeling reaction by RP-HPLC.

4.2.4 Effect of phosphatidylcholine liposome on the optical properties of compound #5.

As we want to use compound #5 as a reporter of clustering, the first thing we set out on was to determine the interaction of #5 with LUV in the absence of any peptide. UV-vis spectroscopy was the method of choice because the spectroscopic signature of the porphyrin combined with a high extinction coefficient allow for determination of clustering constants in the low micromolar region (Figure 4-19). To begin, we determined the extinction coefficient of compound #5 in PB to be 218200 $M^{-1}cm^{-1}$ which was in the range expected for tetrasulfonate porphyrins in phosphate buffer pH 7.2 at 25 ^{o}C[213].

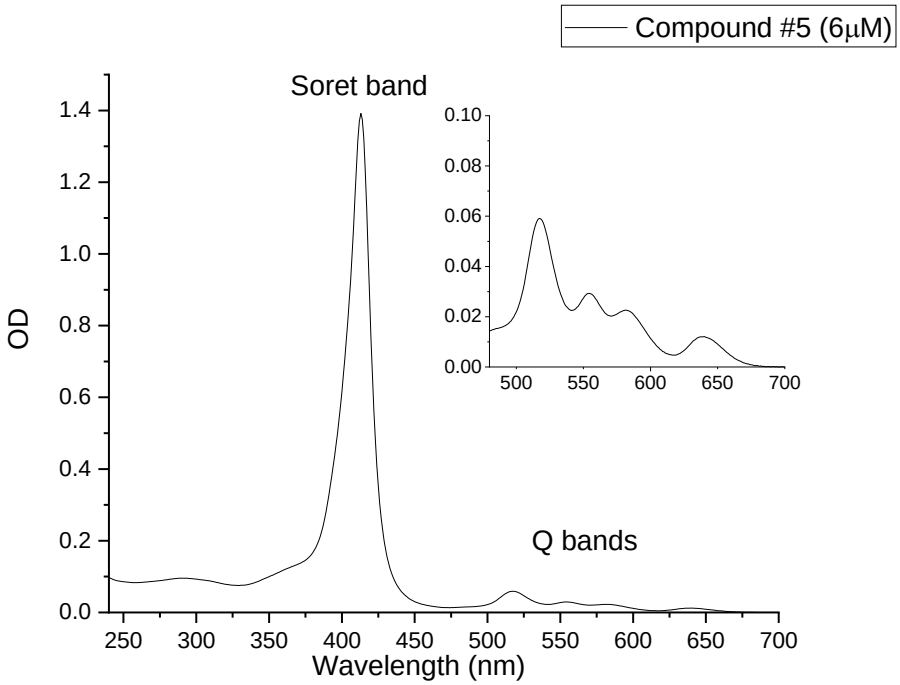

Figure 4-19. UV-vis spectrum of the tetrasulfonate porphryrin with the two characteristic regions of the porphyrin spectrum showing the Soret band in the near ultraviolet and the Q bands in the visible range. The inset graph shows the Q bands enlarged (480 -700 nm).

To assess whether the optical properties, i.e. extinction coefficient of compound #5 will change in the presence of phosphatidylcholine liposomes we prepared 4 solutions of compound #5 at 2, 3, 4, and 5 µM with PC liposomes at 2 mM. The high concentration of PC was selected to evaluate the effect of lipids over the spectroscopic properties of compound #5 (Figure 4-20) (See raw data in Appendix, Figure 6-8).

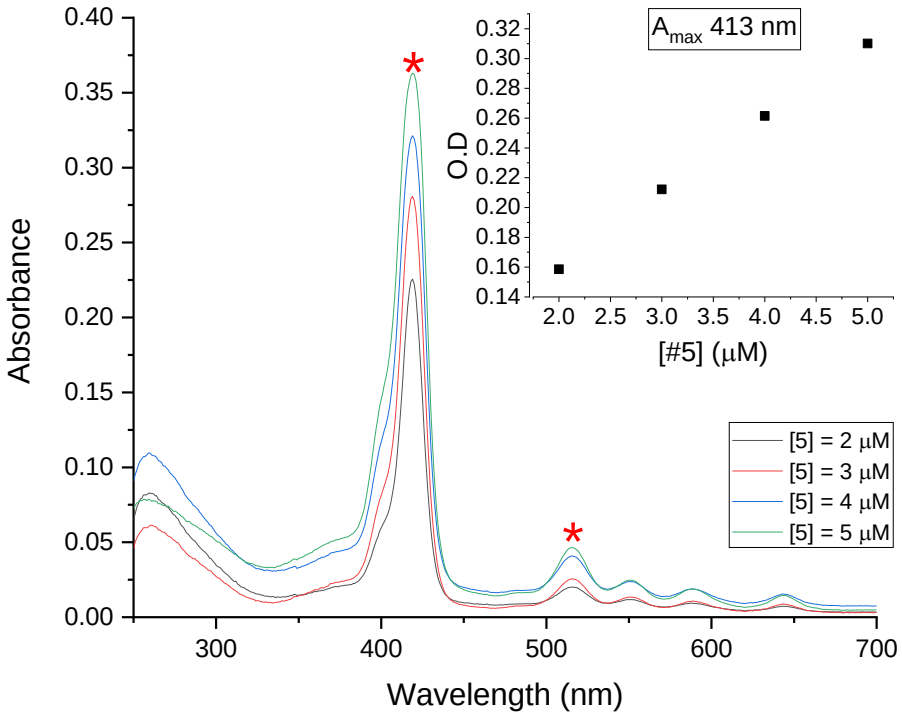

Figure 4-20. (2, 3, 4, 5 µM) in PB solvent. The spectra were corrected for LUV light scattering of the liposomes (2 mM PC).The Soret and Q band are highlighted with a star. Inset: plot of absorbance at the maximum wavelength of Soret band (413 nm) versus nominal concentration.

The goodness of the scattering correction was qualitatively assessed by plotting the increase in the maximum intensity of the Soret band (λ_{max}= 413 nm) versus the nominal concentration of compound #5. It can be seen that the relationship is linear (see Figure 4-20 inset) which indicates that the scattering effect was subtracted correctly from each sample.

However, the most important issue here was to determine whether the lipids affect the UV-vis spectra of #5. We addressed this question by comparing the spectra of #5 in PB solvent and in solution with 2 mM PC as shown in Figure 4-21.

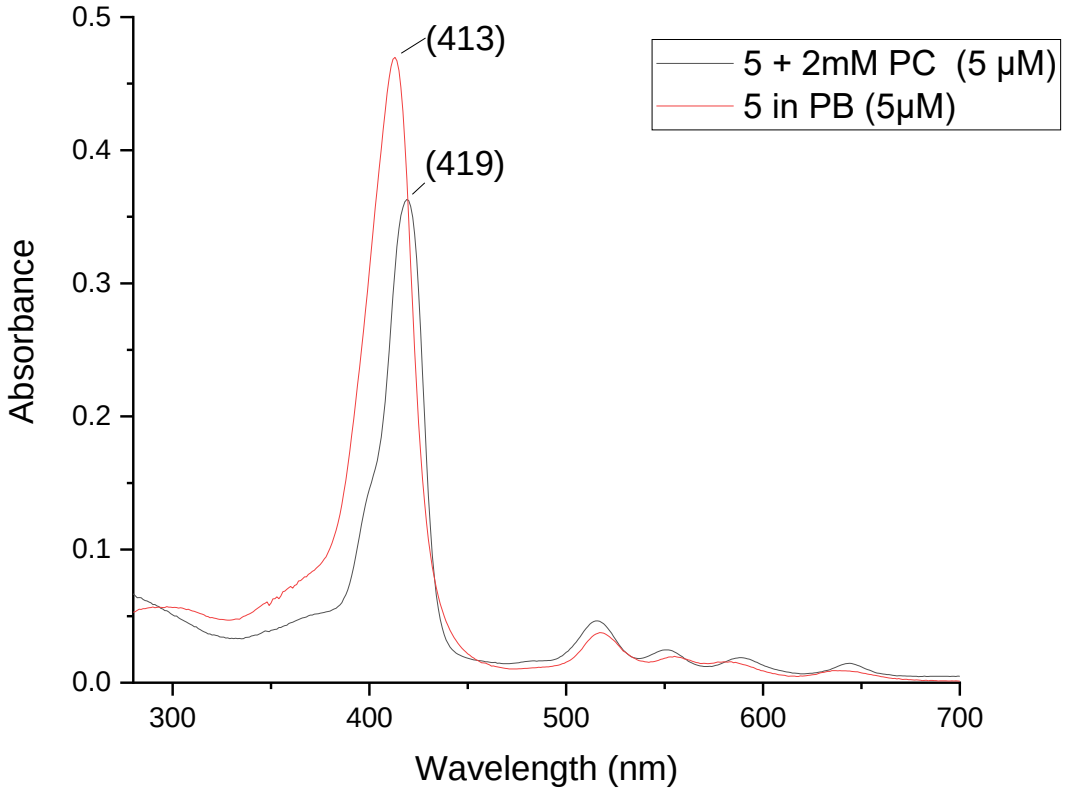

Figure 4-21. The bathochromic shift in the Soret band of compound #5 by increasing the hydrophobicity of the solvent (2 mM PC). The spectra also show the dependence between the intensity of absorption of the Soret band and the polarity of the solvent.

It can be seen that:

- the maximum of absorbance of the Soret band displayed a bathochromic shift of 6 nm, from 413 to 419 nm, in the presence of LUV (Table 4-2).

-the intensity at the maximum wavelength of the Soret band is reduced by 23.4% (Table 4-2).

Sample	λ_{MAX}	Abs (λ_{MAX})
#5 + PC (5µM)	419	0.36
#5 alone (5µM)	413	0.47

Table 4-2. Spectral position of the Soret band and the intensity at λmax for compound #5 in PB and in the presence of 2 mM PC.

We suggest that the changes in the spectroscopic properties of the porphyrin induced by LUV might be due to a binding event between compound #5 and the lipid vesicles. Both traces were recorded in PB 100 mM pH 7.2.

4.2.5 Titration of compound #5 with PC liposomes to study the effect of the lipids over the spectroscopic properties (binding).

To explain the results observed in the previous section we performed a titration of compound #5 with increasing concentrations of phosphatidylcholine liposomes according to the general protocol described in section 4.2.1.4 and in the experimental section. Briefly, in all solutions the concentration of Compound #5 was constant at 1.5 μM, whereas the phosphatidylcholine increased from 0 to 3.0 mM. Twelve solutions of phosphatidylcholine were prepared and added to Compound #5. The solvent was phosphate buffer at pH 7.2. The recorded spectra, corrected for the scattering of the lipids, are shown in Figure 4-22 (raw, uncorrected spectra are shown in the Appendix, Figure 6-9).

The starting point of the titration, called S0, is a solution of compound #5 in PB at pH 7.2 without lipids. The spectrum of this solution showed the typical porphyrin Soret band with the maximum located at 413 nm. Addition of Compound #5 to the first titration point, corresponding to the lowest phosphatidylcholine concentration (1.46 μM), did not produce any change in the spectral position of the Soret band (λmax = 413 nm). However, there was an increase in the band intensity of approximately 18.3%. At intermediate concentrations of PC, between 1.46 μM and 5.86 μM, there was no increase in the intensity of the Soret band nor change in the spectral position (λmax = 413 nm) (S1-S4). At higher concentrations of PC (2.34×10^{-5} to 3.0×10^{-3} M) (S5 - S12), the Soret band undergoes a bathochromic shift (413 to 419 nm) with a concomitant increase in the absorption intensity. At the maximum phosphatidylcholine concentration (3 mM), the band (λ_{max} = 413 nm) disappeared. Consistent with the conversion of one species of porphyrin into another there is one isosbestic point in

the Soret band around 415 nm. Isosbestic points observed in UV-vis spectra of titrations are usually indicative of formation of a binding complex[205].

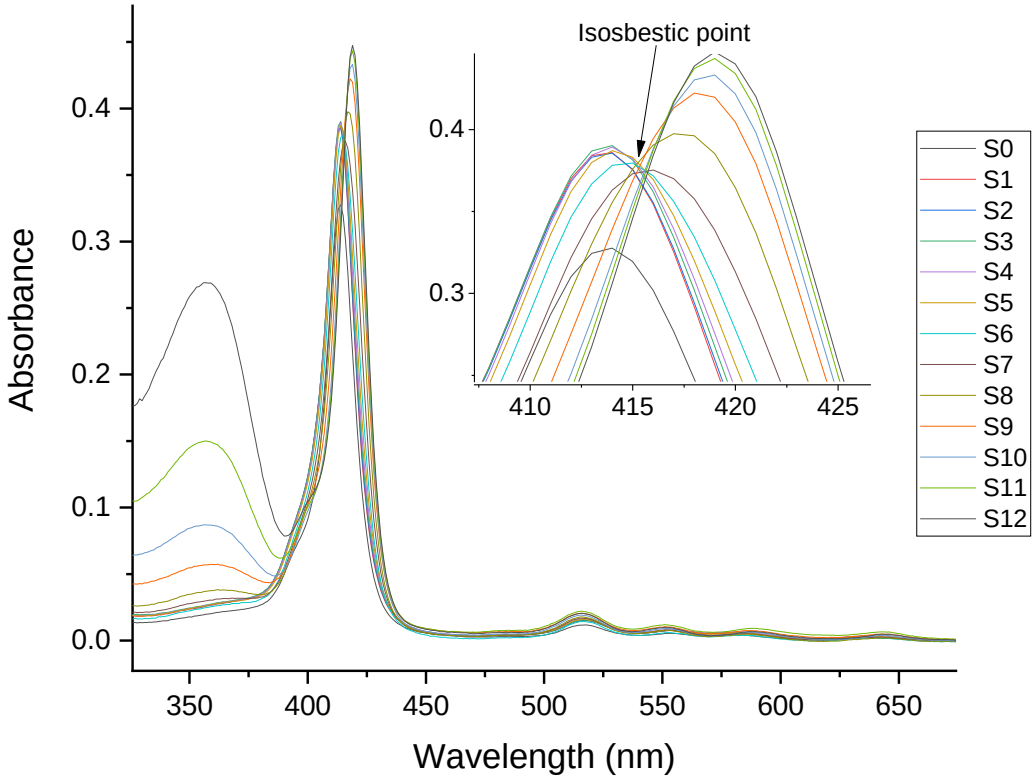

Figure 4-22. Curves obtained by titrating 1.5 μM of compound #5 with 12-solutions of PC liposomes (1.46 μM to 3 mM). Transition from the free monomer to the binding complex is accompanied by a batho-chromic shift in the absorption maximum (413 to 419 nm). The pres-ence of one isosbestic point in the region 410-425 nm is also evidence of the existence of a binding complex.

To explore the spectral changes at the different titration points we performed further analysis at the wavelength of the maximum for three of the spectra (S12, S5, S3). The maxi-mum for each spectrum was determined by subtracting the spectral data of the starting point of the titration (S0). A plot of absorbance at the maximum changes at 413, 419 and 421 nm as a function of PC concentration can be seen in Figure 4-23.

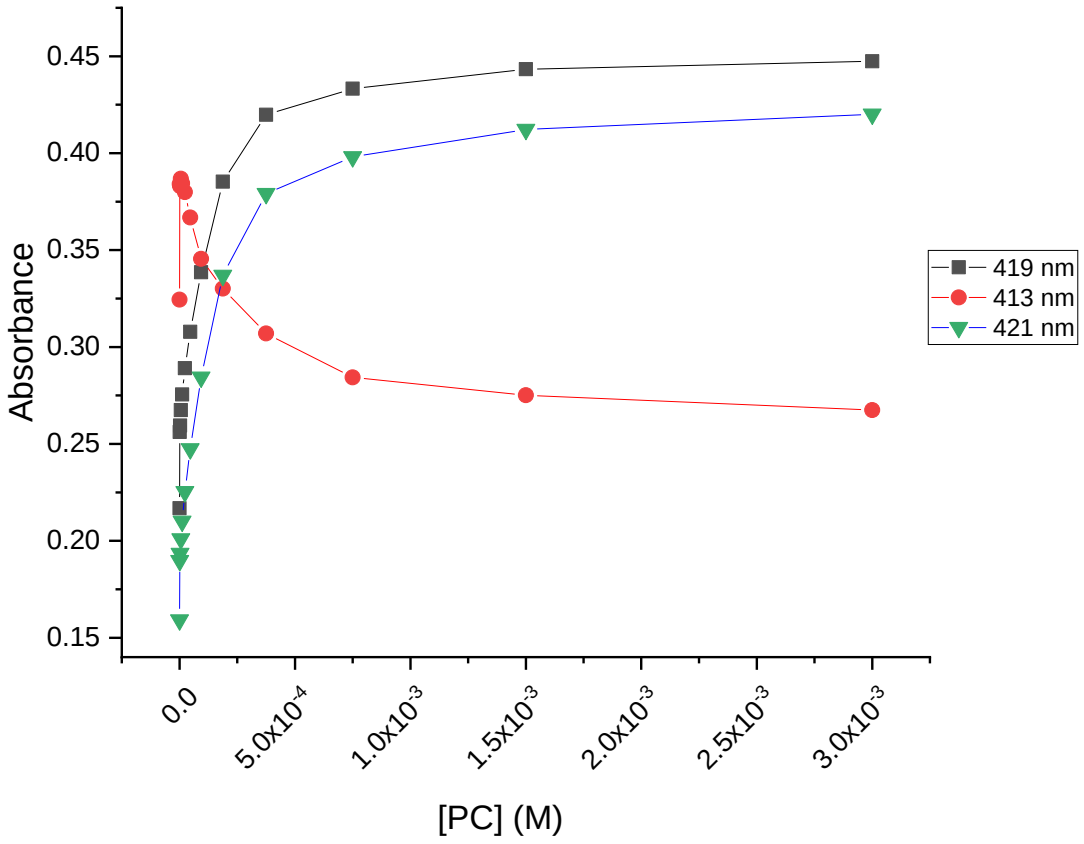

Figure 4-23. Absorption intensity of compound #5 (1.5 μM) vs increasing concentration of phosphatidylcholine (0 – 3 mM) at λ= 413, 419, 421 nm.

Figure 4-23 showed that two chemically distinct species are present in solution. These species showed a distinct spectral position and different intensities for their Soret band absorption maxima. At 413 nm (Figure 4-23, red line) compound #5 (unbound) in the absence of liposomes is the only component present in solution (λmax = 413 nm). The other component is only present upon addition of lipid vesicles. The second component appears in the first titration point, which corresponds to the lowest phosphatidylcholine concentration (1.46 μM). As shown in Fig 4.23 red line, addition is followed by an increase in the Soret band intensity at 413 nm of 18.4%, which is constant up to the fourth titration point (1.17 μM) after

which the intensity decreases whilst a new band at 419 nm is formed (Figure 4-23, black line). The 419 nm band showed an increment in the intensity of absorption that correlates with the increase of the PC concentration.

We think the increase of intensity in the Soret band at first titration point (1.46 μM) is due to complete solubilization of porphyrin #5 which is not 100% soluble in aqueous solvent and it is a well-known phenomenon observed with amphiphilic porphyrins[110]. The disappearance of the 413 nm band and the appearance of the 419 nm band follow the same trend, this and the presence of one isosbestic point suggests that two species are present throughout the titration as mentioned before, i.e. the free porphyrin and the porphyrin-vesicle complex.

Therefore we decided to plot the traces at 419 and 421 nm showed in Figure 4-23 and fitted them using a binding isotherm. We assumed here a simple 1:1 binding equilibrium with porphyrin as one species and phosphatidylcholine lipids as the second species.

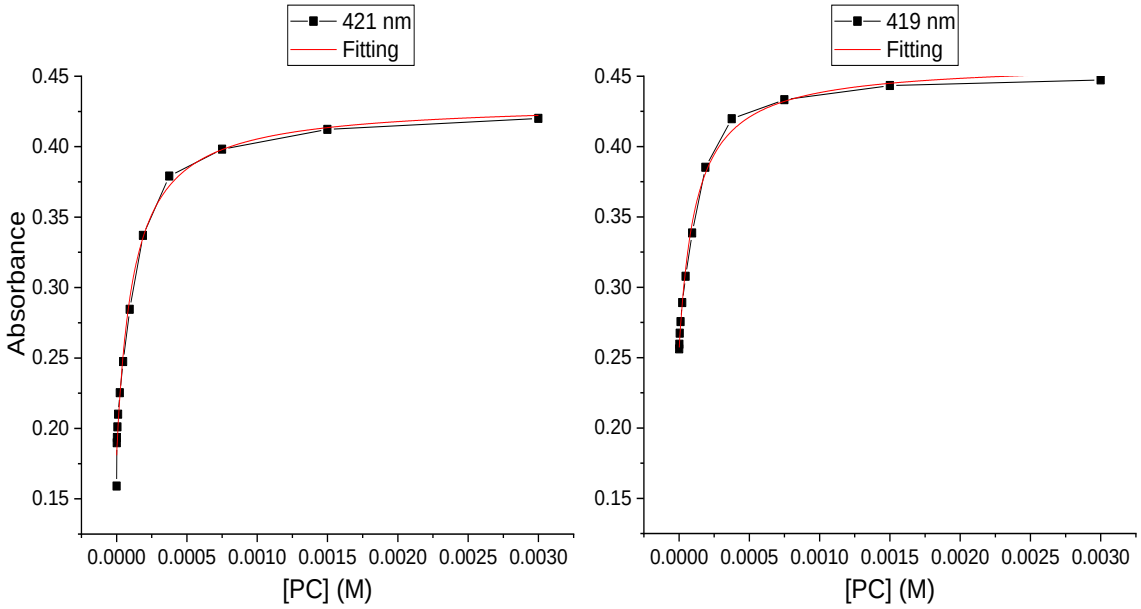

Figure 4-24. Experimental and best fitted curves of 1:1 binding model at 419 and 421 nm of the titration experiments of constant porphyrin (1.5 μM) and 12 solution of lipid vesicles with increasing concentration of phosphatidylcholine (1.4610^{-6} – 3.010^{-3} M). The binding constants were calculated from equation 15 in section 4.2.1.4.

The binding constants were obtained from equation 15 (see Section 4.2.1.4) after the fitting of the UV-vis data and are reported in Table 4-3.

***Ka* (419 nm) M^{-1}**	***Ka* (421 nm) M^{-1}**
8577±759	8602±1090

Table 4-3. Binding constant (*Ka*) and error, calculated using equation (15), from the fitting of the UV-vis data at 419 and 421 nm.

4.2.6 Separation of the compound #5 from PC liposomes by GPC column.

As mentioned in the introduction (see Section 4.2.3), for labelling peptides compound #5 will be use at least 10-fold in excess (100 μM) compared with the amount of peptide (10 μM). This excess of porphyrin will ensure that all the peptide available will react, by forcing the equilibrium towards the formation of the adduct porphyrin-peptide. However, to guarantee that all the spectroscopic data used in determination of the clustering is produced by the compound #5 –peptide adduct we need to remove all the unreacted porphyrin from the system. Obviously, any excess of porphyrin will contribute to the absorbance and fluorescence in a similar way as the target adduct compound #5-peptide. This interference will be directly proportional to the amount of unbound compound #5 present in the system and will affect negatively the accuracy in the determination of the clustering constant.

As shown in Figure 4-18 step B, the reaction between LUV containing peptide and #5 will require removal of excess porphyrin. From the inverse of the binding constant determined in section 4.2.5 for binding complex compound #5-phosphatidylcholine we calculated the dissociation constant, Kd = 117 μM. The dissociation constant is usually used to indicate the strength of binding, thus, presumably we have around 50% porphyrin bound at 117 μM.

To perform the separation we decided to use the gel permeation chromatography method (GPC)[214, 215]. GPC is a chromatographic technique that allows the separation of individual components in the sample based on their differential size. Briefly, the sample of interest is dissolved in a mobile phase that is forced to pass through the stationary phase, usually porous gels beads packed into a column. The smaller components of the sample are trapped in the adsorbent bed, thus taking more time to pass through the column. By contrast, the larg-

est particles, i.e. lipid vesicles, cannot traverse the porous column easily and will pass through quickly, eluting first.

It has been shown that Sepharose 4B (see Solution and Reagents section) is the best matrix that allows the separation of 100 nm sized vesicles from small molecules, therefore a column packed with that matrix was prepared[110, 216].

Based on the binding studies in section 4.2.5 that showed a relatively strong degree of interaction (Ka = 8577 M^{-1}, Kd = 117 μM) in the sense that at 100 μM of Compound #5 we expect to find ~50% of the porphyrin bound to the phosphatidylcholine we decided to perform a GPC column separation to remove the excess of porphyrin. Briefly, we prepared a sample containing phosphatidylcholine vesicles (10 mM) and 100 μM Compound #5, we left it for 30 minutes at room temperature and then we proceed to inject the mixture into the GPC column.

To determine how much porphyrin was effectively removed from the vesicles we pooled the collected fractions containing the liposomes. Fractions were easily identified due to the turbidity; we also collected the fractions immediately before and after the appearance of turbidity to ensure full recovery of lipid vesicles.

The determination of the amount of porphyrin bound to the lipid vesicles was calculated by UV-vis spectroscopy at 413 nm. The spectra were corrected for the scattering of lipid vesicles and the dilution factor was determined by measuring the volume of the pool fractions containing the liposomes-porphyrin mixture. Of note, the volume of lipid-porphyrin mixture loaded on the column was also determined. The calculated amount of bound porphyrin was 22.3 μM. In summary, we were able to remove with this method around 77.7% of the total porphyrin added to the sample (Figure 4-25).

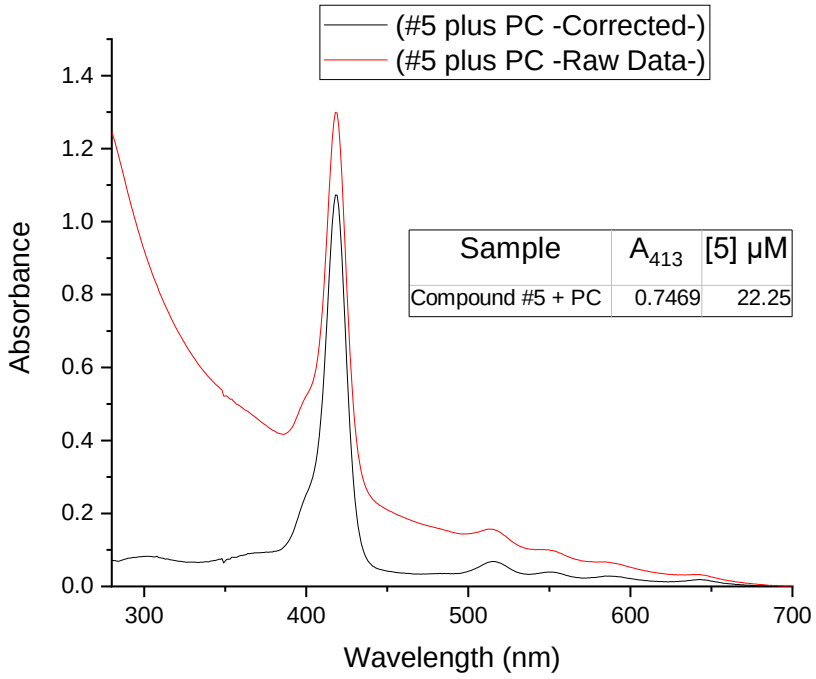

Figure 4-25. Plot showing the UV-vis traces –corrected for light scattering and Raw data-collected from the pooled fractions of lipid vesicles containing compound #5. The inset table shows the value of the maximum absorbance (λmax 413 nm) used to calculate the concentration of the compound #5 bound to the vesicles.

Despite achieving a good separation of porphyrin from the liposomes with one GPC column (~78%) the remaining porphyrin (~22%) was still too high. The minimum amount of unreacted porphyrin that can be tolerated should not exceed 3% of the total porphyrin (100 μM), otherwise, the unbound porphyrin will interfere with the measurement of the clustering based on the relative values of association constants, i.e. 8577 M^{-1} for compound #5. Therefore, we decided to add γ-glutathione (GSH) to the mixture of compound #5 and liposomes to improve the separation. Figure 4-28 shows graphically the aim of this experiment.

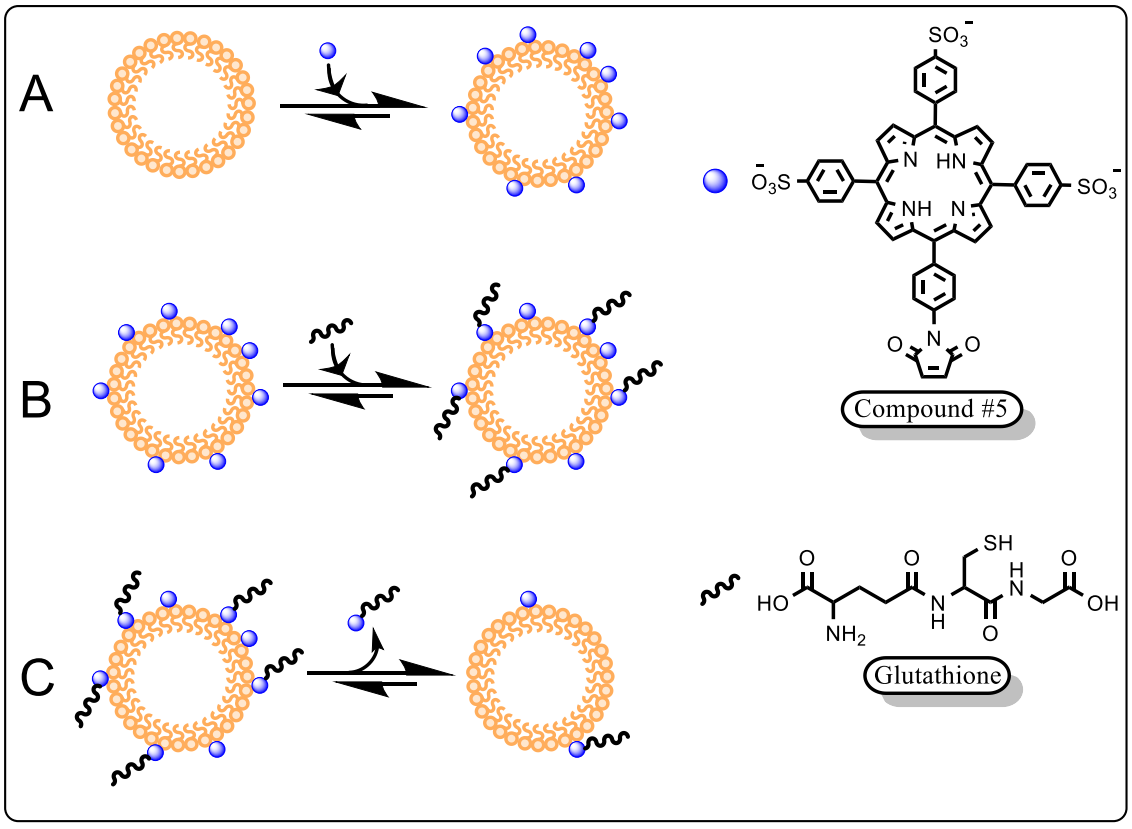

Figure 4-26. Schematic representation of the equilibrium established during the separation of compound #5 from the liposomes by the GPC column. A) Addition of compound #5 and binding to the lipid surface. B) Addition of reduced hydrophilic glutathione to the mixture LUV + #5 and reaction of #5 with the glutathione. C) The more polar adduct compound #5-gluthathione is now more susceptible to be detached from the hydrophobic surface of liposomes facilitating the clearance of unreacted porphyrin.

γ-glutathione is a hydrophilic small tripeptide, composed of glycine, cysteine, and glutamic acid, of biological relevance (see Chapter #3, section 3.2.3.2). As we showed in Chapter #3, section 3.3.12.2 the adduct compound #5-gluthathione is more hydrophilic than Compound #5 alone as demonstrated by its shorter retention time of ~10.9 minutes against 12.1 minutes, in reverse-phase high pressure liquid chromatography (RP-HPLC) (Scheme 4-2).

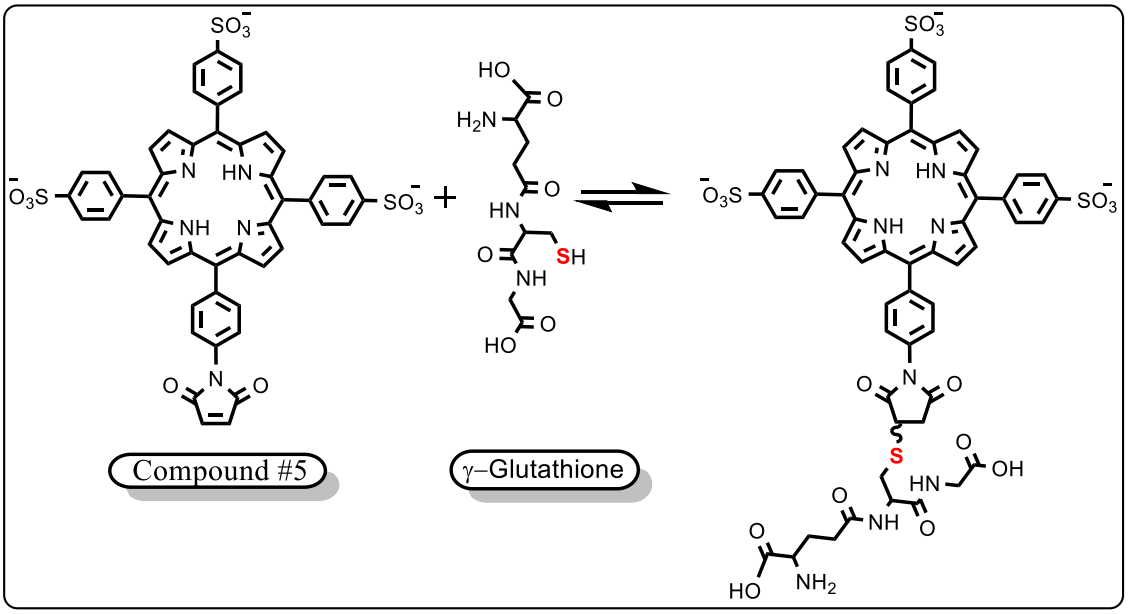

Scheme 4-2. Chemical structure of the compound #5, γ-glutathione and the adduct compound#5-gluthathione used in this study.

Based on this result, we decided to perform the reaction between the maleimide-porphyrin and the glutathione to increase the polarity of the porphyrin. Presumably, the more polar adduct Compound #5-gluthathione will have less affinity for the phosphatidylcholine lipid vesicle, therefore we expect to remove more porphyrin.

Figure 4-27 shows how the separation was in fact improved. We were able to remove up to 93% of the total porphyrin present with ~7 μM of unreacted bound porphyrin.

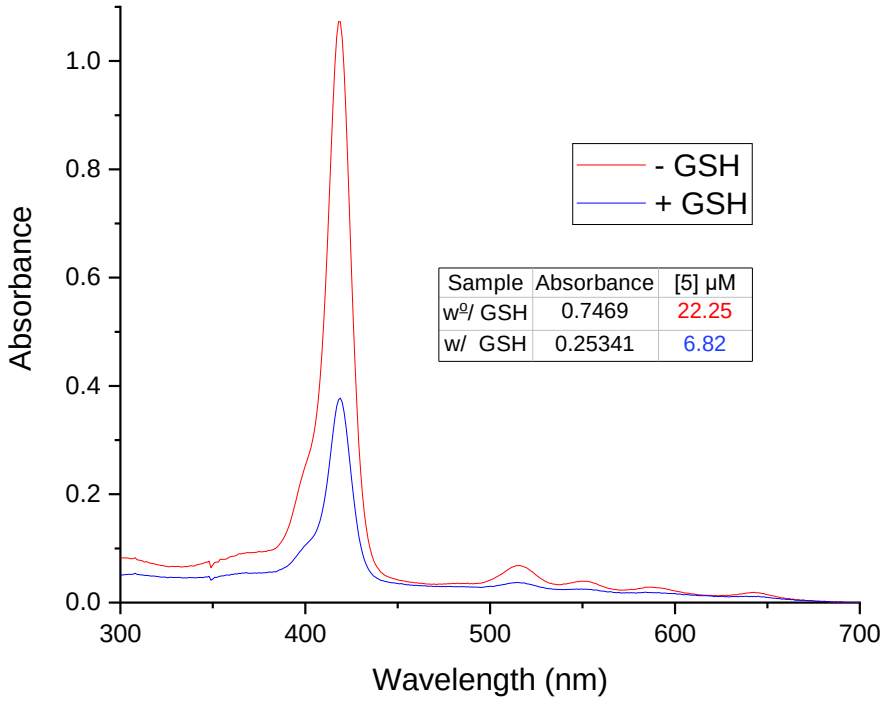

Figure 4-27. Plot showing the UV-vis traces of the fraction of porphyrin bound to the liposomes in the two experiments, without GSH and with GSH. The inset table shows the value of the maximum absorbance (λmax = 413 nm) and the concentration of compound #5 bound to the lipid vesicles.

As mentioned before the limit of unreacted porphyrin tolerated in the lipid vesicles cannot exceed 3.0 μM. Thus, we needed to implement a different method to improve the previous results. Following the same principle as described above, with GSH included, we decided to run the GPC and three washes with a concentrator device.

With the GPC column, we removed the huge excess of porphyrin present in the mixture as shown in the previous experiment. The fractions collected from the column were further diluted with 20 ml of PBS containing GSH (1 mM) to wash the liposomes. The mixture was then concentrated to approximately 500 µl using a Vivaspin concentrator. This is a disposable ultrafiltration device designed for the concentration of aqueous and biological samples. Each concentrator contains a molecular weight cut off (MWCO) membrane (50000 PES), that allows the selective filtration of molecules smaller than the membrane cut off, while retaining those molecules with molecular weight above the MWCO. The membrane is placed in a vertical chamber that provides high-speed concentration, with low fouling, even with particle-laden solutions and is illustrated in Figure 4-28.

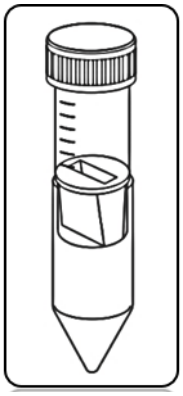

Figure 4-28. Vivaspin concentrator of 20 ml capacity used in this study.

However, in order to improve the separation the incubation with GSH was extended to one hour. The reason being was to force the reaction of compound #5 with the GSH, therefore removing more porphyrin from the liposomes by forcing the binding equilibrium towards the dissociation from the vesicles.

Figure 4-29 shows the results obtained in the separation of the porphyrin with one GPC column and three washes with the 20 Vivaspin concentrator. After the third concentration step we achieved the removal of 98.2% of the total porphyrin added (100 μM).

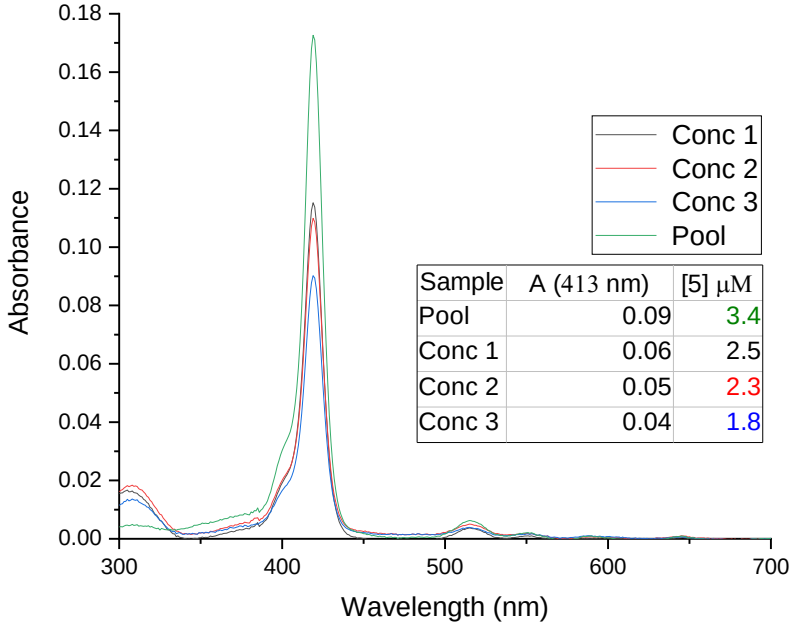

Sample	A (413 nm)	[5] μM
Pool	0.09	3.4
Conc 1	0.06	2.5
Conc 2	0.05	2.3
Conc 3	0.04	1.8

Figure 4-29. UV-vis curves showing the amount of porphyrin bound to the liposomes after the first gel permeation chromatography (Pool I), and the three steps of dilution and concentration (Conc. 1, 2, 3). The inset table shows the values of the absorbance at 413 nm and the concentrations of the porphyrin bound to the liposomes.

In conclusion, with the introduction of the concentration step using a 20 ml capacity dispositive we were able to remove up to ~98% of free porphyrin from liposomes. The remaining ~2% of compound #5 was within the acceptable range (less than 3.0 μM) that can be tolerated in the measuring of clustering.

4.2.7 Study of LUV solubilisation by Triton-X and its effect on porphyrin optical properties.

We next went on to determine the conditions to destroy the liposomes by measuring the scattering of the light in a solution of 1, 2.5, and 5 mM PC liposomes by UV-vis spectroscopy. Triton X-100 (Scheme 4-3) is one of the most common detergents to solubilize membranes in the laboratory and recover any component assembled in membrane[217, 218].

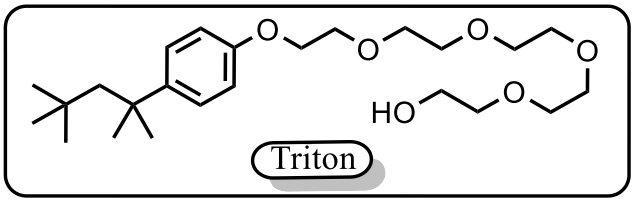

Scheme 4-3. Panel showing the chemical structure of Triton X-100 (TX-100).

TX-100 is usually considered a fast solubilizing detergent that can easily flip from the outer to the inner monolayer causing a rapid solubilization[219-221], but its surfactant function depends both on temperature[222] and the lipid phase[223]. The solubilization mechanism proposed by Goñi et al.[221] is described in Figure 4-30.

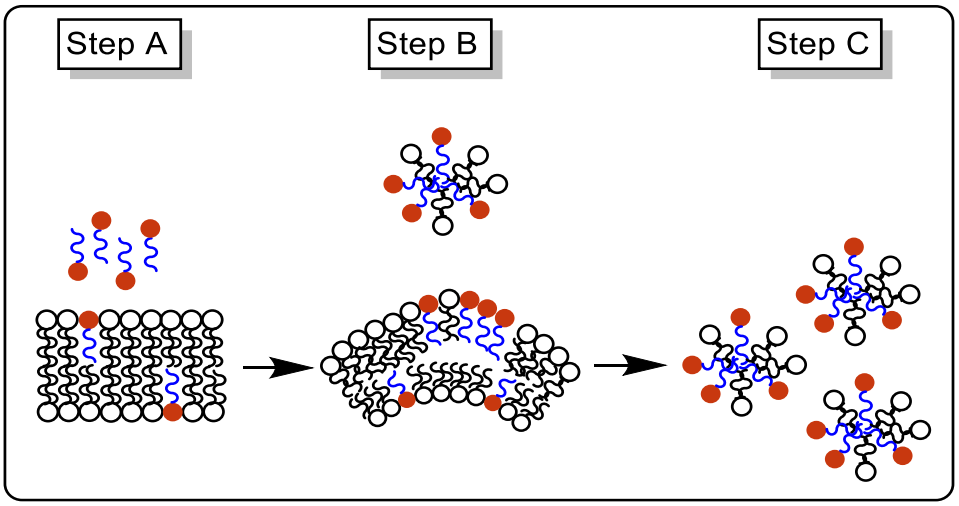

Figure 4-30. Illustration of the solubilization mechanism. The detergent molecules approach the lipid bilayer (step A). Formation of mixed lipid/detergent aggregates (step B). Dissociation of the whole bilayer into mixed micelles (step C).

Since we will perform the labeling reaction of Compound #5 with peptide in the presence of lipids, we need to define the conditions to get rid of the liposomes and liberate the thiol-5 adduct to be quantified by HPLC and spectrophotometry. This experiment will help to elucidate and optimize the method for the reaction with the transmembrane peptide.

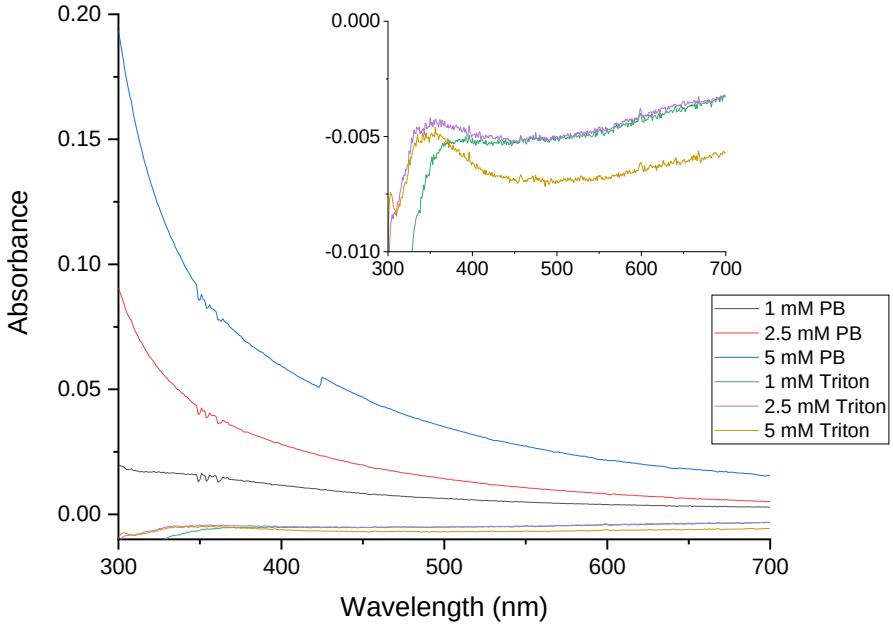

Figure 4-31 Solution of liposomes with 1, 2.5, 5 mM PC in PB and Triton X-100, respectively. The inset shows how in the region (300-700 nm) the light scattering disappears when the liposomes are treated with TX-100.

In conclusion, a solution of 75 mM of TX-100 was able to solubilize the lipid vesicles at 1, 2.5, and 5 mM PC in PB. Figure 4-31 shows the UV-vis traces recorded for each solution of liposomes at 1, 2.5, and 5 mM without TX-100 with the typical slope increase due to the light scattering of the lipid vesicles. As shown in the inset, after addition of TX-100, the light scattering disappears due to full solubilization, or destruction, of the lipid vesicles.

4.2.8 Reaction of compound #5 and the peptide control follow by HPLC.

Reverse Phase High Performance Liquid Chromatography (RP-HPLC) is a technique in analytical chemistry that permits separation, analysis and quantification of components in a complex mixture. In this technique, the stationary phase is a non-polar matrix and the mobile phase a mix of two solvents, usually water in combination with a less polar solvent, such as methanol, acetonitrile, etc. In RP-HPLC, the sample is first injected into the system and with the help of two pumps is forced to flow into the column. Once the sample enters in contact with the stationary phase, the less polar molecules will be retained in the column longer, due to hydrophobic interaction with the matrix, while more polar molecules will elute earlier. Playing with the polarity of the mobile phase and the flow rate, the user can modify the retention times of the different components in the mixture.

To analyze the reaction with compound #5 (see Figure 4-18, section 4.2.3) we decided to begin studying the reaction with the control peptide. The reason being is the control peptide is less hydrophobic than the full-length transmembrane peptide and contains only one thiol. Hence, the control peptide will presumably be easier to establish the conditions to achieve a successful separation. Our first aim was to determine the retention time of all the species involved in the reaction. For example, compound #5 and hydrolyzed compound #5 which is a non-reactive species were investigated in the Chapter 3, section 3.3.12. In addition the retention time of reduced peptide control, and the compound #5-peptide control adduct will be determined.

However, we will also determine the retention time of the oxidized control peptide. Although the reaction will be carried out in the presence of 1, 4-dithiothreitol and presumably, no oxidized peptide will be present, by knowing the retention time of the oxidized form we will make sure the control peptide has been reduced to the reactive form.

The first sets of measurements were performed with a C18 column to determine the retention time of the fresh peptide control. A C18 column contains an alkyl chain of 18 carbons tethered to the stationary phase of the column, granting a better hydrophobicity to the matrix and allowing the best retention times in the separation. To begin, we injected three solutions of 250, 100 and 10 μM of the peptide control dissolved in dimethylsulfoxide, respectively. Figure 4-32 shows the chromatogram for the three samples. The run time was 15 min, flow rate 1 ml/min, and the solvents were acetonitrile (0.1% trifluoroacetic acid)/water (0.1% trifluoroacetic acid). The detector lamp was set at 280nm, due to the presence of tryptophan in the peptide control.

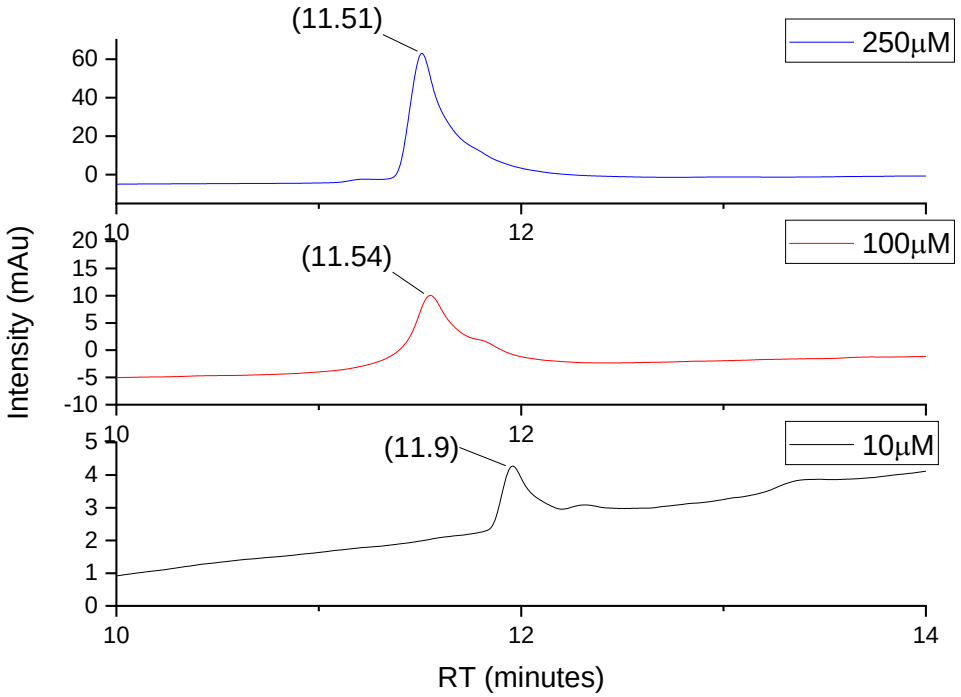

Figure 4-32. HPLC traces of three solutions of the peptide control at 10, 100, and 250 μM. Run time 15 min, λ = 280 nm, MeCN/Water (0.1% TFA), 0-15 min, 0-90% MeCN

From these injections, we determined the retention time of the peptide control around 11.5 minutes. In addition, we proved that RP-HPLC is also sensitive enough to detect concentrations of peptide control as low as 10 μM.

Based on these results we concluded that it was possible to follow the disappearance of peptide should the labeling reaction occur from starting concentrations as low as 10 μM. Importantly, the results reported in Figure 4-32 were run with the same mobile phase used previously for the separation of compound #5 and hydrolyzed compound #5 (see Chapter #3, section 3.3.12).

We decided then to determine the retention time of the peptide control under the same parameters used for the identification of the retention time of compound #5, i.e. run time 25 min, flow rate 1 ml/min, acetonitrile (0.1% trifluoroacetic acid)/water (0.1% trifluoroacetic acid). Here, as mentioned before, the detector was set at 280 nm due to the presence of aromatic tryptophan. The aim of this experiment was to use a separation method that presumably could be used in the detection of all the components present in the reaction mixture. Figure 4-33 shows the retention time of the peptide control was around 14.7 minutes.

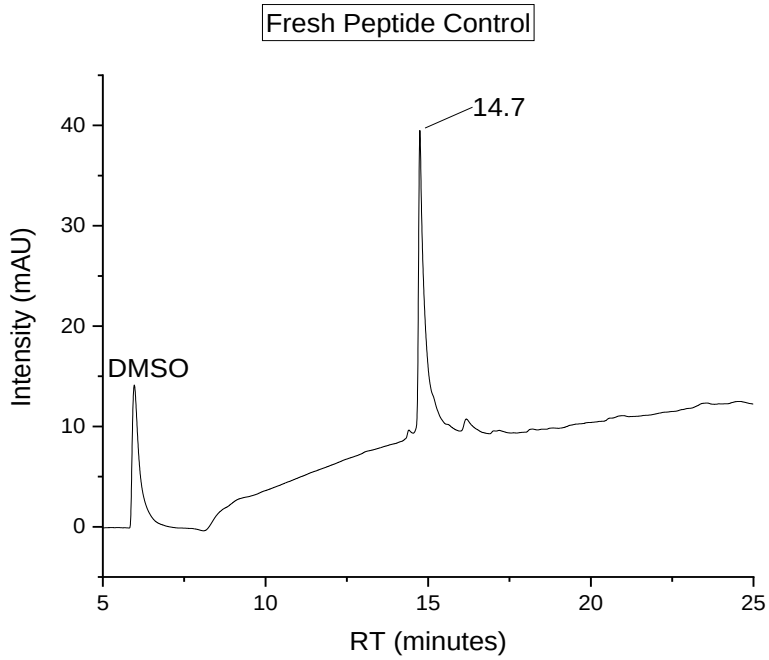

Figure 4-33. Chromatogram of 100 μM of fresh peptide control injected in the RP-HPLC. The peaks labeled at 14.7 minutes belong to the reduced form of the control peptide. The first peak in the figure represents the DMSO that absorbs at 280 nm.

The injection (100 μM) was prepared from a stock of 250 μM of the peptide control in dimethylsulfoxide from the lyophilized starting material kept at -20 ºC to avoid oxidation. All the injections of the peptide control were made from the stock in dimethylsulfoxide due to the poor solubility of the peptide control in phosphate buffer pH 7.2. From here onward, all injections done were made applying the separation parameters mentioned before.

To determine the retention times of the oxidized forms of the peptide control we prepared a sample of 100 μM from a stock of peptide control in dimethylsulfoxide that presumably contained an important fraction of oxidized peptide control. In fact, in section 3.3.2 of Chapter 3 we demonstrated that 30% of the peptide control was oxidized in a fresh stock in phosphate buffer pH 7.2 at 0 minutes, and more than 50% of peptide control was oxidized after 4 hours.

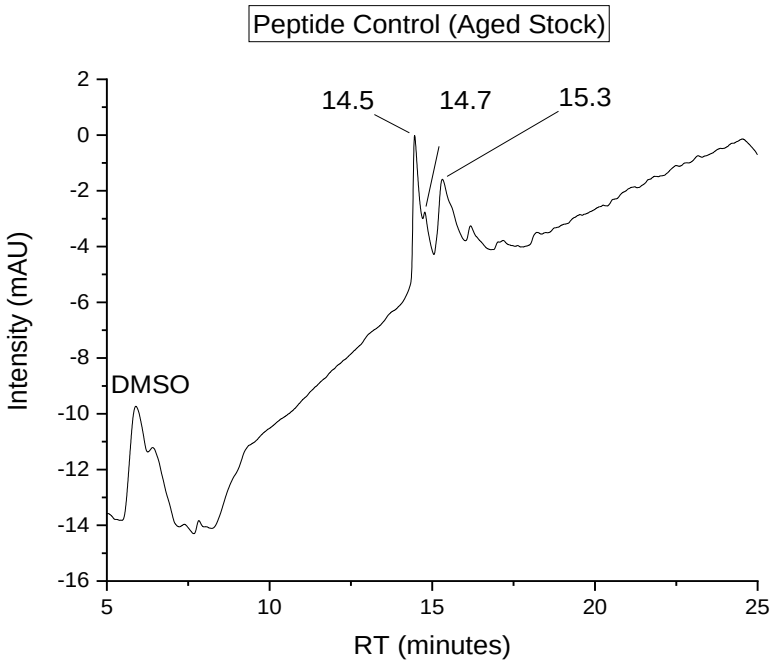

Figure 4-34. Chromatogram of 100 μM of an old stock of the peptide control showing three peaks at 14.5, 15.3 and 16.2 minutes. The first peak belongs to DMSO.

Analysis of the chromatogram showed there were three species present in the sample prepared from the old stock of the peptide control in dimethylsulfoxide. The first species eluted at 14.5 minutes and represented around 40% of the total sample. The next signal was recorded at 14.7 minutes and corresponded to the reduced form of the peptide control (17%). The last peak recorded at 15.3 minutes represented the 43% of the remaining peptide control. The calculation of the percentages was obtained from the integral of the peaks automatically calculated from Agilent Software.

Interestingly, instead of the two peaks expected, one for the reduced and one for the oxidized form of the peptide control, we recorded three peaks. A possible explanation for this observation could be the presence of two forms of the oxidized control peptide instead of one. In fact, in the literature the cyclization of the peptides is described. We hypothesized the species eluted at 14.5 minutes, very close in retention time to the reduced form of the peptide control -probably just a different conformation of the peptide- could be a cyclic form of the peptide but this is just a speculation that needs to be further demonstrated. The other species (R_T=15.3 minutes) we think could belong to two peptides linked by the disulfide bridge; the higher hydrophobicity of this species could explain the long retention time in the column.

The retention time of the reacting species i.e. compound #5 (as determined in Chapter #3 section 3.3.12), and the peptide control (as previously shown) is sufficiently distant to allow the study of the labeling reaction via RP-HPLC.

The first reaction followed by RP-HPLC was compound #5 (250 μM) and the fresh peptide control (10 μM) in PB pH 7.2 (Figure 4-35). The reaction was left for 30 minutes at RT and no reducing agent was added because the stock was freshly prepared from a lyophilized aliquot of the peptide control kept at -20ºC (See Data in Chapter #3 section 3.3.2 for the oxidation status of the peptide control in phosphate buffer pH 7.2 at time zero).

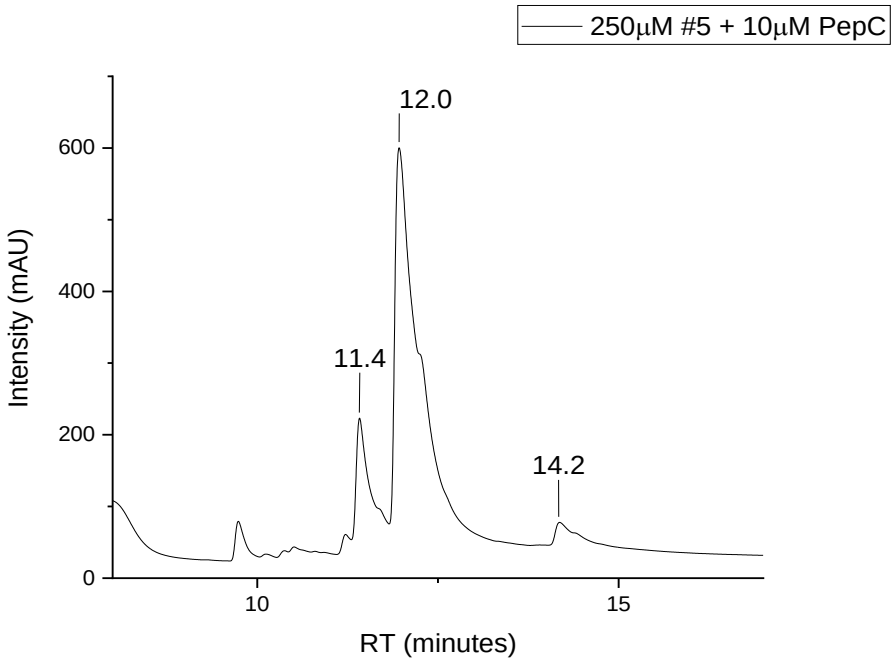

Figure 4-35. Chromatogram illustrating the peaks obtained in the reaction between 250 μM of compound #5 and 10 μM of the peptide control in PB 100 mM pH 7.2. Labeled peaks at RT: 11.4, 12, 14.2 minutes, they correspond to the hydrolyzed compound #5, the unreacted compound #5, and #5-peptide control adduct, respectively.

The separation was followed by the absorbance of the porphyrin at 430 nm. In this way, we make sure that all the signals recorded come from the different species of the compound #5 in the mixture. The first signal recorded in the chromatogram was the peak at 11.4 minutes, which corresponded, as previously shown, to the hydrolyzed form of compound #5.

The following signal at 12.0 min belonged to the unreacted compound #5. We suggest the peak with a retention time of 14.2 minutes represents the compound #5-peptide control adduct. From the chromatogram, using the integrals of the peaks for each signal we determined that approximately 4% of the porphyrin reacted with the peptide control, which means that all the peptide control (10 μM) reacted with compound #5 (250 μM), as 10 μM is the 4% of 250μM. From this experiment, we concluded that it is possible to follow up quantitatively the labeling reaction via RP-HPLC.

Although the reaction with thiol and maleimide is really fast, and the control peptide freshly prepared shows little oxidation; the fact is that after 1 hour approximately 50% of the control peptide is oxidized (Chapter #3 section 3.3.2). Therefore, we decided to test the reaction in the presence of the reducing agent γ–glutathione. γ–glutathione was introduced previously in this chapter in section 4.2.6; we just want to point out here that it is a small peptide of biological relevance that is widely used as a reducing agent. In this reaction, equimolar solutions of peptide control (20 μM) and glutathione (20 μM) were mixed and incubated for 15 minutes. Then, a solution of compound #5 (50 μM) 2.5 times in excess was added taking into consideration that both, the unreacted glutathione and the reduced peptide control can react with the maleimide group of compound #5. The reaction was injected at time 0 and after 30 minutes of incubation and the detector was set at 430 nm (Figure 4-36).

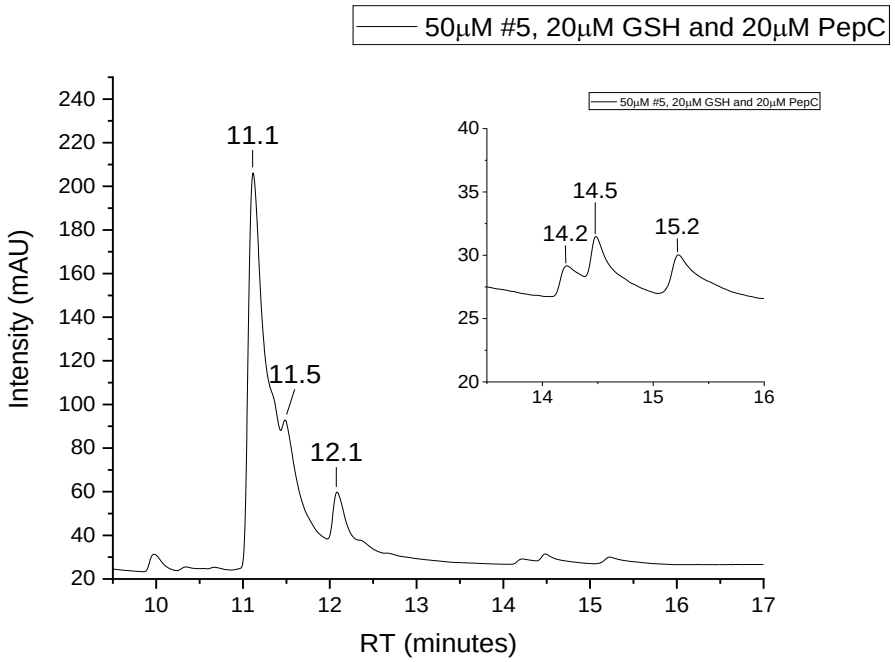

Figure 4-36. Chromatogram illustrating the peaks obtained in the reaction between 50 μM of compound #5 and 20 μM of the peptide control in the presence of 20 μM γ–glutathione. The peaks at RT: 11.1, 11.5, 12.1, 14.2, 14.5 and 15.2 minutes, correspond to #5-gluthathion adduct, compound #5 hydrolyzed, compound #5 unreacted, #5-peptide control adduct, and two unidentified peaks.

From the previous determination of the retention time of adduct Compound #5-gluthathione (Chapter 3, section 3.3.12.2) we assigned the first peak recorded at 11.1 minutes to the adduct #5-gluthathion. Based on the integral of the peaks retrieved from the chromatogram, we determined the percentages of each peak, by dividing the integral of each peak by the total area obtained from the sum of the integrals that were assigned to the porphyrin species. In this way, we determined that the peak at 11.1 minutes represented ~62% of the total compound #5 used in the reaction. The following peak (11.5 minutes) belonged to the Compound #5 hydrolyzed (24%) and the next peak at 12.1 minutes to the unreacted Compound #5 (10%). The peak at 14.2 minutes constituted ~ 1% of the total Compound #5 and represented

the adduct #5-peptide control. The peaks at 14.5 and 15.2 minutes, respectively, could represent the existence of some conformations of the reduced peptide control that reacted with the porphyrin. This suggestion implied the peptide control had available thiol groups to react with the maleimide function. From the analysis of these data, we concluded that glutathione competed with the peptide control in the reaction with Compound #5. These results reinforce the idea of the necessity to reduce the peptide control in a step before the labeling reaction. We think that separation of the reducing agent from the control peptide via GPC column separation or even HPLC before the labelling reaction would be a good approach to increase the yield of the reaction.

We moved forward and decided to test the reaction in the presence of an alternative reducing agent. As we had performed the reaction with TCEP (2-carboxyethyl-phosphine) (see Chapter 3, section 3.3.8) we decided to test this compound instead. As mentioned before, TCEP is a well know reducing agent of thiols, especially used in proteomics for the reduction of cysteines in peptides and proteins[156]. For the reaction 10 μM of peptide control was mixed with 50 μM of TCEP to ensure full reduction of the peptide control. To this mixture, we added the solution of compound #5 to reach 100 μM. Compound #5 was added in excess to make sure the peptide control reacts with the porphyrin. As previously shown in Chapter 3 section 3.3.8, TCEP reacts with the maleimide group of Compound #5. The reaction was injected into the RP-HPLC at time 0 and 30 minutes after incubation to qualitatively evaluate the kinetics of the reaction (Figure 4-37).

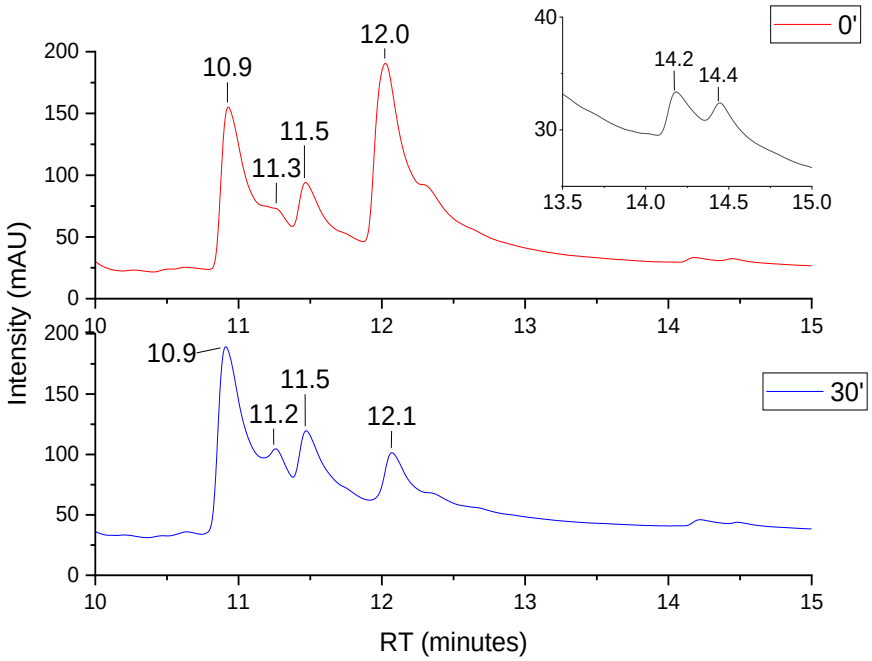

Figure 4-37. Chromatograms of reaction of compound #5 and peptide control in the presence of TCEP. The graphic above represents the reaction recorded at time 0; while the chromatogram below the reaction after 30 minutes. The inset graph shows the two small peaks belonging to the product of compound #5 and the peptide control.

At time 0, we determined that 51% of Compound #5 remained unreacted (RT = 12 min), whereas 13% corresponded to the hydrolyzed form of #5. The peak at 10.9 min was assigned to the #5-TCEP adduct, based on the high polarity of this complex we expect it to elute first. The peaks at 11.5, and 12.0 minutes, which were previously identified, will be described later here. There was also a small peak at 11.3 min that we assigned to the hydrolyzed #5-TCEP adduct. In the inset graphic, we showed the adduct of #5-peptide control recorded at 14.2 min, which represented ~1.5% of compound #5 available. The peak at 14.4 min accounts for 1% of the total #5. At 30 min, compound #5 present in the mixture diminished to 15% and the hydrolyzed #5 increased to 22.1%. The peak at 10.9 min that corresponds to the #5-TCEP adduct increased to 46% as well as the hydrolyzed form of the adduct that

reached 14%. The signal belonging to the #5-peptide control adduct increased to 1.5%, while the peak at 14.4 min did not show any appreciable change.

In conclusion, we could detect the presence of the compound #5-peptide control adduct in the presence of the reducing agent TCEP at 14.2 min. However, the reaction of compound #5 with the TCEP is considerably fast and competes with the peptide control in adduct formation. This data reinforce the idea of performing the reduction of the sulfhydryl group in a previous step, with the elimination of the reducing agent before the labelling reaction.

In summary, although we could detect #5-peptide control adduct in the one pot reaction with both γ-glutathione and 2-carboxyethyl-phosphine (TCEP) by RP-HPLC, the results shown in here suggest that the separation of the reducing agent before the labeling reaction is advisable in order to avoid competition for the maleimide moiety and improve the yield of the product.

4.3 CONCLUSIONS AND FUTURE WORK

The first part of this thesis aimed to develop a chemical biology approach to elucidate the mechanism of T cell receptor (TCR) signaling. We pursued to create an uncomplicated system constituted by a cluster reporter (porphyrin) and a model membrane (PC vesicles) to study in detail the aggregation of the TCR transmembrane peptide. The below point summarize the main accomplishments of the first part of this thesis:

a) The synthesis of the cluster reporter (5-(4-maleimide)-10, 15, 20 tris (4 - sulfonatophenyl) – porphyrin, trisodium salt) (Compound #5) was successfully achieved with optimization of the original method.
b) Successful determination of the extinction coefficient of the Compound#5.
c) Reaction of the Compound #5 and model thiols e.g. N-acetylcysteine, and glutathione was successfully achieved in order to determine the chemistry to perform the labeling reaction with the transmembrane peptide.
d) Interaction studies of the Compound #5 and PC vesicles with determination of binding parameters was achieved.
e) Separation of the compound #5 from PC vesicles by GPC was successfully achieved.
f) Determination of the optimal conditions to quench the fluorescence of the compound #5 was accomplished.
g) Successful reaction between the Compound #5 and the peptide control to form the adduct 5-peptide control was achieved.

This preliminary study have shown interesting results. However, there remains much work to be done on the construction of the chemical model to address the TCR signaling mechanism. One of the major achievements of this project was to synthetize the cluster reporter and to test the conditions to satisfactorily perform the labeling reaction. However, because the complexity of the chemical system require many optimizations and the time available was limited we were unable to test the aggregation of the full-length transmembrane peptide in the phosphatidylcholine vesicles. Therefore, future work could aim to:

1. Test the aggregation properties of the full-length transmembrane peptide based on the preliminary results achieved in this thesis.
2. Redesign the composition of the artificial membrane to introduce major structural lipids present in eukaryotic membranes, particularly in lymphocytes, such as phosphatidylcholine, phosphatidylethanolamine, phosphatidylserine, phosphatidylinositol, and phosphatidic acid.
3. Include the transmembrane peptide of the TCRδ chain may be particularly important as the TCRγδ receptor is a heterodimer.
4. Achieve the reduction of the sulfhydryl group is critical to ensure the labeling reaction with the maleimide moiety of the porphyrin reporter, therefore finding appropriate reducing agents will be very useful and require more study.

4.4 EXPERIMENTAL SECTION

4.4.1 Solutions and Reagents

The ethanol (Fisher) for the preparation of the liposomes was of analytical grade. De-ionized water was obtained from water purifier purelab instrument (ELGA).

The L-α-phosphatidylcholine (PC) from egg yolk was from Avanti Polar lipids, Inc. The γ-glutathione, 1, 4-dithiothreitol (DTT), tris (2-carboxyethyl) phosphine (TCEP), was purchased from Sigma-Aldrich with analytical grade purity. The inorganic salt, sodium phosphate monobasic dihydrate used in the preparation of the buffer was also of analytical grade purity. The matrix for the GPC column was Sepharose 4B (4B200), 45-165 μm bead diameter, 30,000-50,000 Da fractionation range (Dextranus).

The control peptide and full-length peptide were purchased from PeptideSynthetics.

All the reactions were performed at room temperature on the bench.

4.4.1.1 Compound #5 stock solution

The stock solution of compound #5 (P1) (1015.96 g/mol) [5] = 5 mM was prepared in PB 100 mM pH 7.2 and aliquoted in several tubes (50 μl) and stored at -20 °C. The aliquots were defrosted one by one. The aliquot on use was frozen back until needed again.

4.4.1.2 Phosphate Buffer

For the preparation of the phosphate buffer 100 mM pH 7.2. 12.0 gr of sodium mono-basic phosphate salt (119.98 g/mol) was dissolved in 500 μl of distilled water. This solution was treated with sodium hydroxide (10 M) to adjust the pH to 7.2. The solution was then

topped up with distilled water to reach a final volume of 1 L. The buffer phosphate was kept in a fridge at 4 °C.

4.4.1.3 γ-Glutathione stock solution

A fresh preparation of the GSH (307.32 g/mol) stock was carried out for every reaction. As 30% of the glutathione in the stock was already oxidized, determined with the DTNB test, the amount of GSH was adjusted to correct for this. 8.78 mg of reduced GSH was dissolved in 2 ml of PB 100 mM pH 7.2 to produce a solution of [GSH] = 10 mM.

4.4.1.4 Preparation of the stock of 1, 4-dithiothreitol (DTT)

The stock of DTT was prepared by weighting 1.29 mg (8.4×10^{-6} mol) of solid DTT in 7 ml of PB 100 mM pH 7.2, the final concentration 0.0012 M. The pH was checked to be seven.

4.4.1.5 Control peptide solution stock

The control peptide stock (1.00 mg, 5.0×10^{-7} mol) was prepared in DMSO to a final concentration of 250 μM. From this stock two new stocks of 12 μM were prepared by dilution (V_f = 6 ml) in PB 100 mM pH 7.2 and in DTT 1.2 mM.

4.4.1.6 Full-length peptide solution stock

The full-length peptide stock (1.20 mg, 2.15×10^{-7} mol) was prepared in 0.5 ml of DMSO to a final concentration of 359 μM. From this stock two new stocks of 12 μM were prepared by dilution (Vf = 6 ml) in PB 100 mM pH 7.2 and in DTT 1.2 mM.

4.4.2 Determination of the light scattering of the phosphatidylcholine liposomes.

A film of 10 mM PC was prepared by pipetting 1.85 ml of 6.5 mM stock solution of the PC in ethanol. The ethanol was evaporated under nitrogen until a dry white layer was observed on the walls of the vial. The film was re-suspended in 1.2 ml of PB 100 pH 7.2, with 1-minute mix and sonication. The milky solution was loaded in the extruder and extruded 25 times. From the extrusion, 1 ml of liposomes was recovered and the UV-vis spectrum recorded in the range 240-700 nm. The buffer PB 100mM pH 7.2 UV-vis spectrum was also recorded. Afterwards, the cuvette was washed and dried. The rest of the solutions were prepared in the cuvette by diluting the solution of the extruded liposomes by 50% with PB and up to 100 μM PC. After the addition of the buffer every sample was carefully mixed and immediately introduced in the instrument and recorded. The cuvette was carefully washed and dried in between all the measurements. The final concentrations prepared for these experiments were: 5, 2.5, 1.25, 0.62, 0.31, 0.15, 0.07, 0.03, 0.01 mM.

4.4.3 Solubilization of the liposomes with Triton X-100.

To Triton X-100 (1 g, 1.54 mmol) 20 ml of phosphate buffer 100 mM, pH 7.2 were added to prepare a 75 mM solution of Triton X-100. The solution was stirred until the Triton was completely dissolved. A fresh solution of 10 mM PC liposome (as described before) was prepared and from this stock were made six working solutions at 5, 2.5, 1 mM in PB or Triton (Tables 4-4, 4-5, 4-6) were made. Each working solution was homogenized and immediately after the measurements of the light scattering was done by UV-vis spectroscopy. The absorbance of 1 ml of PB 100 mM was measured and used as blank. The determinations of the absorbance spectra of all the sample solutions were performed quickly with a wash/dry step intercalated between measurements. The spectrophotometer was set up to record the spectrum between 240-700 nm with baseline correction.

A (Stock PC (mM)	[PC] (mM)	VA (µl)	V PB (µl)
6.5	10	1.85	1200

Table 4-4. Details of the reagents used in the preparation of the working stock solution of PC.

[PC] (mM)	VA 10mM (µl)	V PB (µl)
5	500	500
2.5	250	750
1	100	900

Table 4-5. Details of the reagents used in the preparation of the three working solution 5, 2.5, 1 mM PC in PB.

[PC] (mM)	VA 10mM (µl)	V TRITON (µl)
5	500	500
2.5	250	750
1	100	900

Table 4-6. Details of the reagents used in the preparation of the three working solution 5, 2.5, 1 mM PC in Triton X-100.

4.4.4 Effect of the phosphatidylcholine liposome in the optical properties of the compound #5.

Fresh solution of liposomes of 10 mM PC were prepared by extrusion as described in the previous pages. An aliquot of the compound #5 (3.9 mM) was thawed and diluted 1:100 with 100 mM PB pH 7.2 to prepare a working solution of final concentration 39 μM. For the preparation of the samples PB 100 mM pH 7.2 was added to each tube previously labelled. Afterwards we added the amount of the working stock of 5 (39 μM) to have the solutions of 2, 3, 4, 5 μM, and each solution was carefully mixed. Finally, we added the volume of the liposomes to achieve the final concentration of 2 mM in each solution. The samples were mixed and ready for the UV-vis (Table 4-7).

The UV-vis measurements were recorded in a Cary Agilent brand Spectrophotometer. The quartz cuvette was filled with 1 ml of sample solution and recorded in the region 240 – 700 nm with baseline correction against the buffer phosphate. The cuvette was cleaned and dried between measurements.

[#5] (μM)	[PC] (mM)	V PC 10mM (μl)	V Stock 5 (μl)	V PB (μl)
2	2	200	51.3	748.7
3	2	200	76.9	723.1
4	2	200	102.6	697.4
5	2	200	128.2	671.8

Table 4-7. Volumes of the solutions used in the preparation of the four working stocks at 2, 3, 4, 5 μM of the compound #5 and 2 mM of PC liposomes.

4.4.5 Effect that Triton X-100 has over the optical properties of the compound #5.

A fresh stock of PC liposomes 10 mM PC was prepared in PB 100 mM pH 7.2 by extrusion. The working solution (39 µM) of compound #5 was prepared by 1:100 dilution of freeze aliquot (A1) (3.9 mM). These two stocks were used to prepare two sets of experiments in which three samples of PC liposomes at 0.5, 1.0, and 2.0 where mixed with the compound #5 to reach a final concentration of 5 µM. The first the experiemnt was prepared with PB 100 mM pH 7.2, while the second experiment was prepared with Triton X-100. The preparation of the samples were as follows: first the PB/Triton X-100 was added to the tube, immediately after the volume of stock solution of compound #5 was added to reach 5 µM. The mixture was stirred and then PC liposomes were added and mixed. UV-vis spectra were recorded using a quartz cuvette of 1 cm path length, range $240 < \lambda < 700$ nm, and baseline against air (Tables 4-8 and 4-9).

[PC] (mM)	[#5] (µM)	V stock #5 (39 µM)	V stock (10mM PC)	V PB
0.5	5	128.2	50	821.8
1	5	128.2	100	771.8
2	5	128.2	200	671.8

Table 4-8. Details of the volumes used for the preparation of the three samples of 0.5, 1.0, and 2.0 mM PC in PB at a constant concentration of the compound #5.

[PC] (mM)	[#5] (µM)	V stock #5 (39 µM)	V stock (10mM PC)	V TRITON
0.5	5	128.2	50	821.8
1	5	128.2	100	771.8
2	5	128.2	200	671.8

Table 4-9 Details of the volumes used for the preparation of the three samples of 0.5, 1.0, and 2.0 mM PC in Triton X-100 at a constant concentration of the compound #5.

4.4.6 Titration of the compound #5 with PC liposomes to study the effect of the lipids over the spectroscopic properties.

For the titration experiment, the stock solution of the porphyrin control (PS) was prepared from the stock P1 (5 mM) by dilution in PB 100 mM pH 7.2 to a final concentration [PS] = 3 μM], V_f = 7 ml. Since all PS had the same concentration, 7 ml was prepared as final volume to have enough material for all the titration samples (500 μl per titration sample plus one extra 500 μl accounting for transfer loses).

The liposomes were prepared by extrusion from the freeze stock of PC in ethanol (see previous chapter). After the extrusion, 1.2 ml of 6.0 x 10^{-3} M PC liposomes was obtained. By serial dilutions mixing 600 μl of PB 100mM pH 7.2 with 600 μl of LS samples starting from L12 and repeating down to LS1 collection of samples (LS) were prepared to combine with the porphyrin stock and generate the target samples (S) to be used for the titration experiment.

For the preparation of the titration samples (S) 500 μl of the lipid sample LS was mixed with 500 μl of the porphyrin sample (PS) to generate 1000 μl of (S) (Table 4-11).

For the calculation of the absorbance (A) initial guesses for Δε and K, where Δε is the variation of the extinction coefficient of the free porphyrin and the complex #5 plus phosphatidylcholine and K is the binding constant. This theoretical absorbance (A_T) was then compared with the experimental absorbance (A_E). The values of Δε and K were adjusted with the parameter R_0 (Initial concentration of porphyrin) fixed (1.5 x 10^{-6} M) until a good fitting was obtained (Table 4-10).

Fitting 419nm

Model	bindingequilibrium (User)
Equation	eR*Ro+(eRL-eR)*(Ro+Lo+1/K-sqrt((Ro+Lo+1/K)^2-4*Ro*Lo))/2
Plot	Absorbance
eR	169786.24069 ± 1857.61536
eRL	306529.4753 ± 2481.44969
K	8577.38708 ± 759.05679
Ro	1.5E-6 ± 0
Reduced Chi-Sqr	2.41967E-5
R-Square (COD)	0.99669
Adj. R-Square	0.99595

Fitting 421nm

Model	bindingequilibrium (User)
Equation	eR*Ro+(eRL-eR)*(Ro+Lo+1/K-sqrt((Ro+Lo+1/K)^2-4*Ro*Lo))/2
Plot	Absorbance
eR	120639.79367 ± 2965.01302
eRL	287718.3949 ± 4511.02125
K	8602.2378 ± 1090.44864
Ro	1.5E-6 ± 0
Reduced Chi-Sqr	8.13558E-5
R-Square (COD)	0.99258
Adj. R-Square	0.99109

Table 4-10. Binding constant and other parameters calculated from the 1:1 binding model from the fitting of the UV-vis data entering the initial concentration of the free porphyrin as fixed parameter. eR, extinction coefficient of the free porphyrin; eRL, extinction coefficient of complex #5 and lipids; K, binding constant; Ro, initial concentration of the porphyrin.

Sample	$[L_{Final}]$ / M	$[Peptide_{Final}]$ / M	Liposome Stock	$[L_{Initial}]$ / M	Porphyrin stock	$[P_{Initial}]$ / M
S0	0	1.5E-06	LS0	0	PS0	3E-06
S1	1.46E-06	1.5E-06	LS1	2.93E-06	PS1	3E-06
S2	2.93E-06	1.5E-06	LS2	5.86E-06	PS2	3E-06
S3	5.86E-06	1.5E-06	LS3	1.17E-05	PS3	3E-06
S4	1.17E-05	1.5E-06	LS4	2.34E-05	PS4	3E-06
S5	2.34E-05	1.5E-06	LS5	4.69E-05	PS5	3E-06
S6	4.69E-05	1.5E-06	LS6	9.38E-05	PS6	3E-06
S7	9.38E-05	1.5E-06	LS7	1.88E-04	PS7	3E-06
S8	1.88E-04	1.5E-06	LS8	3.75E-04	PS8	3E-06
S9	3.75E-04	1.5E-06	LS9	7.50E-04	PS9	3E-06
S10	7.50E-04	1.5E-06	LS10	1.50E-03	PS10	3E-06
S11	1.50E-03	1.5E-06	LS11	3.00E-03	PS11	3E-06
S12	3.00E-03	1.5E-06	LS12	6.00E-03	PS12	3E-06

Table 4-11. Serial dilution used in the preparation of the samples LS. Started with 1200 µl of L12 and generating LS11 by mixing 600 µl of LS12 + 600 µl of PB buffer. This was repeated down to LS1. LS0 was only buffer. The PS solutions had the same concentration of the porphyrin ($3x\ 10^{-6}$ M). The PS stock solution was prepared as follows: 500 µl for each one of the 13 samples and an extra 500 µl that account for loses for a total volume of 7 ml. The working solution was prepared by mixing 500 µL of LS and 500 µL of PS, which generated a 1000 µl of the target sample (S).

4.4.7 Determination of the optimal conditions to quench the fluorescence of the compound #5.

4.4.7.1 P-Xylene –bis-(N-pyridinium bromide) (DPX)

DPX (26 mg) was weighed out and dissolved in 125 µl of phosphate buffer (100 mM, pH 7.2) to produce a final stock of 500 mM. A stock of compound #5 (50 µM) was prepared in PB 100 mM pH 7.2 from a frozen stock of compound #5 (5 mM) (10 µl of #5 in 990 µl of PB). The previous stock was used to prepare the working solution (1 ml, 0.2 µM) in PB 100mM pH 7.2. The fluorescence emission of this sample was recorded and immediately after, 700 µl were withdrawn from the cuvette and the addition of DPX started (Table 4-12). After each addition, the solution was mixed and the fluorescence intensity recorded. The excitation wavelength ($\lambda = 413$ nm), emission $430 < \lambda < 600$.

Measure	[5] µM	n (DPX)	Vcuv (µl)	V [0.5M DPX]	[DPX] mM
1	0.2	0.000003	706	6	4.25
2	0.2	0.000007	714	8	9.80
3	0.2	0.000012	724	10	16.57
4	0.2	0.000018	736	12	24.46
5	0.2	0.000025	750	14	33.33
6	0.2	0.000033	766	16	43.08
7	0.2	0.000042	784	18	53.57
8	0.2	0.000052	804	20	64.68
9	0.2	0.000063	826	22	76.27
10	0.2	0.000075	850	24	88.24
11	0.2	0.000088	876	26	100.46
12	0.2	0.000102	904	28	112.83
13	0.2	0.000117	934	30	125.27
14	0.2	0.000133	966	32	137.68
15	0.2	0.00015	1000	34	150.00
16	0.2	0.000168	1036	36	162.16
17	0.2	0.000187	1074	38	174.12
18	0.2	0.000207	1114	40	185.82
19	0.2	0.000228	1156	42	197.23
20	0.2	0.00025	1200	44	208.33

Table 4-12. Volume of the stock of DPX (0.5 M) that were added to quench the fluorescence of compound #5. In the far right column is shown the final concentration of DPX in the reaction cuvette.

4.4.7.2 1,1′-Diheptyl-4,4′-bipyridinium dibromide (DPB)

Initially a 50 mM stock was made by weighing out DPB (25.7 mg) and dissolving in 1 ml of phosphate buffer (100 mM, pH 7.2), however 0.5 mM was required for the experiments so this stock was simply diluted 10 fold in PB. The procedure was similar to the one described for the DPX (Table 4-13). The concentration of the DPB stock was 0.0025 M in PB 100 mM pH 7.2.

Measure	[5] µM	n (DPB)	Vcuv (µl)	V [0.0025M DPB]	[DPB] mM
1	0.2	0.000000015	706	6	0.02
2	0.2	0.000000035	714	8	0.05
3	0.2	0.00000006	724	10	0.08
4	0.2	0.00000009	736	12	0.12
5	0.2	0.000000125	750	14	0.17
6	0.2	0.000000165	766	16	0.22
7	0.2	0.00000021	784	18	0.27
8	0.2	0.00000026	804	20	0.32
9	0.2	0.000000315	826	22	0.38
10	0.2	0.000000375	850	24	0.44
11	0.2	0.00000044	876	26	0.50
12	0.2	0.00000051	904	28	0.56
13	0.2	0.000000585	934	30	0.63
14	0.2	0.000000665	966	32	0.69
15	0.2	0.00000075	1000	34	0.75
16	0.2	0.00000084	1036	36	0.81
17	0.2	0.000000935	1074	38	0.87
18	0.2	0.000001035	1114	40	0.93
19	0.2	0.00000114	1156	42	0.99
20	0.2	0.00000125	1200	44	1.04

Table 4-13. Volume of the stock of DPB (0.0025 M) that were added to the cuvette to quench the fluorescence of the compound #5. In the far right column is shown the final concentration of DPX in the reaction cuvette after the addition of each aliquot.

4.4.8 Separation of the compound #5 from PC liposomes by GPC column.

4.4.8.1 One GPC column with γ-glutathione

1 ml of liposomes [PC] = 10 mM were prepared. 10 μl of stock solution of [5] = 5 mM was added to this solution to reach a final concentration of 100 μM. The sample was split into two vials PCI and PCII (470 μl). The first vial (PC I) was mixed and incubated for 15 minutes in the dark. 50 μl of the sample PC I was diluted 1:100 with PB 100 mM pH 7.2 and the absorption spectrum was recorded (250-700 nm). The remaining volume (400 μl) was loaded into the column matrix (see Solutions and Reagents), and the fractions were collected immediately. In total 20 fractions were collected from which the fractions 9, 10, 11 and 12 appeared turbid. To monitor the separation the fractions 8-13 were separated and the UV-vis spectra measured. From the light scattering of each fraction collected and the porphyrin signal the targets fractions (9-12) were identified. Finally, the fractions 9-12 were pooled together (Pool) and the absorbance recorded for analysis.

The second aliquot (PC II) was treated with fresh GSH stock (10 mM) to achieve a final concentration of 1mM. The sample was mixed and incubated 15 minutes in the dark. 400 μl of PC II were loaded in a clean column and the collection of the fractions started immediately. 20 fractions were collected from which the turbids (9-12) were poold together and analyzed by UV-vis spectroscopy (Pool + GSH).

4.4.8.2 Two consecutive GPC columns with an intercalated concentration step.

A fresh solution of liposomes was prepared [PC] = 10 mM as previously described. A 500 μl aliquot was separated and combined with compound 5 to get [5] = 100 μM. Afterwards, the GSH was added to reach [GSH] = 1 mM. The mixture was mixed and incubated in the dark for 1 hour. After the incubation period the mixture was loaded into the column and the fractions collection started immediately. The turbid fractions were isolated, combined together (Pool I), the final volume of the pool was measured and the UV-vis spectrum was recorded. Using a concentrator (Vivaspin 500), the pool I solution was concentrated by centrifuging the liposomes 30' at 13000 RPM. After each 10 min the centrifuge was stopped and the sample mixed by gentle pipetting the solution to avoid sedimentation of the liposomes and help the centrifugation process. Once the remaining volume was between 100 -500 μl the centrifugation was stopped. The concentrated solution was added to a cleaned second GPC column and the collection was repeated as previously described. The turbid fractions were once more combined (Pool II), the volume was measured with precision using a cylinder (5 ml) and the UV-vis spectrum recorded for analysis (200-700 nm).

4.4.8.3 One GPC column plus three concentration/dilution steps.

Compound #5 was added to a fresh solution of liposomes [PC] = 10 mM to reach a final concentration of [5] = 100 μM. The sample was incubated for 1 hour in the dark. From the solution were withdrawn 20 μl and further diluted (1:100) to be used as a reference to check the efficiency of the separation (precolumn). After the incubation GSH was added to the sample to reach a final concentration of [GSH] = 1 mM. An aliquot of solution was separated, diluted (1:100), and the UV-vis spectra recorded (+GSH). 500 μl were loaded into the column and the collection of the fractions started as described in the sections above. The turbid fractions were collected together (Pool), the volume was measured with a cylinder (5 ml), and the UV-vis spectrum was recorded. Before loading into the concentrator GSH was added to the Pool to reach a final concentration of [GSH] = 1 mM and was incubated for 15 minutes. The concentrator was loaded, the volume brought up to 20 ml and then centrifuged for 15' at 3 rcg. Once the volume was reduced to approximately 4 ml (identified with a marking in the concentrator tube) the concentrated solution (Conc 1) was mixed with GSH as described above to reach [GSH] = 1 mM, mixed and top it up with phosphate buffer up to 20 ml. The last steps were repeated twice, to achieve the concentrated solutions (Conc 2 and Conc 3). Finally, the traces were collected and analyzed by UV-vis spectroscopy.

4.4.8.4 Labelling of the full-length peptide with the compound 5 in the presence of liposomes and excess removal by GPC.

The working solution (10μM, 3ml) was prepared from a previous stock solution of the full-length peptide (359 μM) in PB 100 mM pH 7.2. An aliquot from this solution was withdrawn and quantified by UV-vis spectroscopy using a Perkin Elmer spectrophotometer, range 200-700 nm (4.05 μM). A concentrated solution of DTT (0.0015 g, 9.72 μmol) was prepared in 1 ml vial. From this stock solution an aliquot was added to the stock of full-length peptide to reach 100 μM of DTT. The liposomes [PC] = 10 mM were freshly prepared as described before and further diluted with 780 μl of PB 100 mM pH 7.2 100 μl. This solution was combined with 100 μl of stock solution of full-length peptide and DTT and incubated for 10 min. Once the incubation period finished 20 μl of P1 was added and the mixture was incubated for 15 minutes. 10 μl of this solution were diluted with 990 μl (1:100) of phosphate buffer, and the UV-vis spectra recorded (Rxn Mixture). The mixture was loaded into the Vivaspin PES MWCO 50.000 concentrator and centrifuged for 15 minutes at 4.4 RPG. 1 ml of the filtrate solution was withdrawn and the UV-vis spectrum recorded (filtrate). The content of the concentrator was collected back (V = 640 μl) and 500 μl were loaded into a fresh and clean GPC column. The turbid fractions were collected together, the volume measured with a cylinder (1.6 ml), and the UV-vis spectrum recorded (Pool). A new concentrator was used to load the pool fraction and then centrifuged for 15’ at 4.4 RPG. When the volume was reduced to approximately 1 ml (identified with a marking in the concentrator tube), the concentrated solution was collected and the UV-vis spectrum recorded (Conc 1). Finally, the traces were combined and analyzed using the Origin Pro 8b software.

4.4.9 Experiments with the Control Peptide.

4.4.9.1 Determination of the fluorescence spectra of the peptide control

A 1:2 dilution of the peptide control 12 μM was prepared with PB 100 mM pH 7.2. Immediately after the pH was checked (pH = 7) and the fluorescence cuvette was we filled with 1 ml of peptide control solution. This sample was used to record the fluorescence spectrum with medium and high photomultiplier tube voltage (PMT) to determine the best conditions to perform the fluorescence experiments. A second solution of the peptide control containing DTT (600 μM) was prepared and the fluorescence spectrum recorded. For the measures the instrument was setup as follows: start 300 nm and stop 600 nm, Ex wavelength 295 nm, ex lit 5nm, em lit 5nm, scan rate 600 nm/min, PMT voltage, high. The traces were collected and analyzed using the software Origin Pro 8b.

4.4.9.2 Titration of the Peptide Control

For the titration experiment, the stock solution of the peptide control (PS) was prepared by dilution of a stock solution (250 μM) in PB 100mM pH 7.2 to reach a final concentration of [Peptide control = 1.20 x 10^{-5} M], V_f = 7 ml.

Liposomes were prepared by extrusion from the stock solution of PC in ethanol (see Section 3.3.2). 1.2 ml of 6.0 x 10^{-3} M PC liposomes were prepared by extrusion and further diluted with PB 100 mM pH 7.2 to generate the samples (LS). LS samples were combined with the stock solution of peptide control to generate the target samples (S) that were used in the titration experiment (Table 4-14).

Sample	$[L_{Final}]$ / M	$[Peptide_{Final}]$ / M	Liposomes Stock	$[L_{Initial}]$ / M	Peptide Stock	$[Peptide_{Initial}]$ / M
S0	0	6.00E-06	LS0	0	PS0	1.20E-05
S1	1.46E-06	6.00E-06	LS1	2.93E-06	PS1	1.20E-05
S2	2.93E-06	6.00E-06	LS2	5.86E-06	PS2	1.20E-05
S3	5.86E-06	6.00E-06	LS3	1.17E-05	PS3	1.20E-05
S4	1.17E-05	6.00E-06	LS4	2.34E-05	PS4	1.20E-05
S5	2.34E-05	6.00E-06	LS5	4.69E-05	PS5	1.20E-05
S6	4.69E-05	6.00E-06	LS6	9.38E-05	PS6	1.20E-05
S7	9.38E-05	6.00E-06	LS7	1.88E-04	PS7	1.20E-05
S8	1.88E-04	6.00E-06	LS8	3.75E-04	PS8	1.20E-05
S9	3.75E-04	6.00E-06	LS9	7.50E-04	PS9	1.20E-05
S10	7.50E-04	6.00E-06	LS10	1.50E-03	PS10	1.20E-05
S11	1.50E-03	6.00E-06	LS11	3.00E-03	PS11	1.20E-05
S12	3.00E-03	6.00E-06	LS12	6.00E-03	PS12	1.20E-05

Table 4-14 Serial dilution used in the preparation of the samples LS. LS11 was generated by mixing 600 μl of LS12 + 600 μl of PB buffer. This operation was repeated down to LS1. LS0 was only buffer. The PS solutions had all the same concentration of control peptide (1.2 x 10^{-5}). The PS stock was prepared using 500 μl for each titration sample and and 500 μl extra accountin for loses for a total volume of 7 ml. The target samples (S) were prepared by mixing 500 μL of LS with 500 μL of PS.

4.4.9.3 Determination of the liposomes fluorescence

Determination of the liposome fluorescence was performed following the same procedure described in section 4.4.9.1. In here, the preparation of the target samples (S) was as follows: 500µl of liposomes (LS) was mixed with 500 µl of PB 100 mM pH 7.2. The fluorescence spectrum was recorded immediately after the preparation of the samples was completed.

4.4.9.4 Titration of the Full Length Peptide.

The preparation of the stock solution of the full-length peptide is described in the section 4.4.1.6. The dilutions carried out for the preparation of the samples is described in Table 4-11.

4.4.10 Reaction of compound #5 and the peptide control follow by HPLC.

4.4.10.1 Determining the retention time of the peptide control

The determination of the peptide control by RP-HPLC was carried out with three solutions of 10, 100 and 250 μM. The working solutions were prepared by dilution with DMSO of a fresh stock solution of peptide control 250 μM (1.18 mg, 5.9 x 10^{-7} M). Each solution was manually injected into the RP-HPLC. The column was (Phenomenex Jupiter C18, 250mm) Manual injection of 20 μl, λ = 280 nm, flow 1 ml/min, eluting with 0.1% TFA/MeCN and 0.1% TFA/H2O with the following gradient: 0-15 min, 0-90% MeCN.

The retention time of the peptide control was determined under the same conditions used to identify the retention time of compound #5. A solution of 100 μM of peptide control freshly prepared in DMSO was injected. The column was (Phenomenex Jupiter C18, 250mm) Manual injection of 20 μl, λ = 280 nm, flow 1 ml/min, eluting with 0.1% TFA/MeCN and 0.1% TFA/H2O with the following gradient: 0-20 min, 0-100% MeCN, 20-22 min, 100-100% MeCN, 22-23 min, 100-0% MeCN, 23-25 min, 0-0% MeCN.

The retention time of the peptide control oxidized was determined injecting an old stock solution of the peptide control (250 μM) using the same method described in the previous paragraph.

4.4.10.2 Reaction of compound #5 and peptide control

A peptide control stock solution (250 μM) was prepared weighing 1.0 mg of peptide control dissolved in 2 ml of DMSO. Compound #5 solution was prepared from the frozen aliquot (5mM) (A1). The reaction mixture was prepared by diluting 25 μl of A1 stock with 455 μl of PB. Afterwards, 20μl of the peptide control stock solution was added to the solution of compound #5 and mixed thoroughly. The reaction mixture was incubated for 30 minutes in the dark and then injected in RP-HPLC column (Phenomenex Jupiter C18, 250mm). Manual injection of 20 μl, λ = 430 nm, flow 1 ml/min, eluting with 0.1% TFA/MeCN and 0.1% TFA/H2O with the following gradient: 0-20 min, 0-100% MeCN, 20-22 min, 100-100% MeCN, 22-23 min, 100-0% MeCN, 23-25 min, 0-0% MeCN.

4.4.10.3 Reaction of compound #5 and peptide control in the presence of GSH

A γ-glutathione stock solution of 10 mM (6.015 mg) was prepared in 2 ml of fresh phosphate buffer. The peptide control aliquot was taken from the stock (250 μM) as described in the previous paragraph. A solution of 20 μM of peptide control and 20 μM of GSH was prepared in 1 ml PB 100 mM pH 7.2. The solution was mixed and incubated for 15 minutes to ensure reduction of the sulfhydryl's group. Afterwards, 10 μl from the stock solution of the compound #5 (A1) (5mM) was added to reach a final concentration of [#5] = 50 μM. The reaction was injected into the RP-HPLC column (Phenomenex Jupiter C18, 250mm). Manual injection of 20 μl, λ = 430 nm, flow 1 ml/min, eluting with 0.1% TFA/MeCN and 0.1% TFA/H2O with the following gradient: 0-20 min, 0-100% MeCN, 20-22 min, 100-100% MeCN, 22-23 min, 100-0% MeCN, 23-25 min, 0-0% MeCN.

4.4.10.4 Reaction of compound #5 and peptide control in the presence of TCEP

A TCEP stock solution of 44 mM (10 mg) was prepared in 1 ml of fresh phosphate buffer 100 mM pH 7.2. The peptide control aliquot was taken from the stock solution (250 μM) described in the previous paragraph. A solution of 10 μM of peptide control and 50 μM of TCEP was prepared with 1 ml of PB 100 mM pH 7.2. The solution was mixed and incubated for 15 minutes to allow reduction of the sulfhydryl moiety. To this solution was added 20 μl from the compound #5 stock solution (A1) (5mM) to reach a final concentration of [#5] = 100 μM. The reaction was injected at time 0 and after 30 minutes incubation into the RP-HPLC column (Phenomenex Jupiter C18, 250mm). Manual injection of 20 μl, λ = 430 nm, flow 1 ml/min, eluting with 0.1% TFA/MeCN and 0.1% TFA/H2O with the following gradient: 0-20 min, 0-100% MeCN, 20-22 min, 100-100% MeCN, 22-23 min, 100-0% MeCN, 23-25 min, 0-0% MeCN.

4.4.11 Instruments

Balances: The preparation of all stock solutions, buffers, and samples, was done with the MS-TS Precision Balance with Draft Shield (Mettler Toledo).

UV-vis Spectrophotometry: The UV-vis spectra for all these experiments were measured on the departmental Perkin Elmer Lambda 35, UV/VIS Spectrometer. The cuvettes for all the measurements were polystyrene and disposable with a path-length of 1 cm and a volume capacity of 2.5 ml.

pH-meter: The pH measurements were taken with a Mettler Toledo pH-meter with a glass electrode (InLab Ultra-Micro, Electrolyte Friscolyl) pH 1…11.0, 80 ^{o}C. All the readings were performed at room temperature. The pH-meter was calibrated before each measurement with standard solutions at pH 4 and 7 respectively.

RP-HPLC: The RP-HPLC was performed using a Varian Prepstar pump with autosampler and fraction collector. The stationary phase column was a Jupiter 4u Proteo 90A AXIA with a packed prep column (250 x 21.2 mm).

Fluorescence Spectrophotometer: The fluorescence spectra were recorded with the departmental Agilent Cary Eclipse fluorescence spectrophotometer. The cuvettes for all the measure were disposable with a length-path of 1 cm and 2.5 ml capacity. The data was analyzed with the software Agilent Cary WinFLR.

All the measurements were recorded at RT, with no further treatment of the samples.

5 CHAPTER 5

5.1 INTRODUCTION

The immune system is a highly complex biological machinery that has evolved to identify and destroy harmful foreign challenges, for example, bacteria, viruses and parasites that can cause disease. In complex organisms, the immune system is further subdivided in two subsystems: the innate and the adaptive immune system.

5.1.1 Innate and Adaptive Immunity

The innate immune system constitutes the early line of defense against pathogens. It consists of cellular and biochemical host defense mechanisms that are ready before any infectious challenges and that respond rapidly after the invasion. The components of the innate immune system include physical and chemical barriers, such as epithelial surfaces; phagocytic cells e.g. neutrophils and macrophages, dendritic cells, and natural killer (NK) cells; blood proteins such as the complement system, and messenger proteins called cytokines. The main function of the innate immune system is to control the early stages of infection by recognizing structures that are common to groups of pathogens, known as pathogen associated molecular patterns (PAMPs)[224, 225].

In contrast to the innate immune system, adaptive immunity developed much later in evolution, around 360 million years ago in jawed vertebrates[65]. The main characteristics of the adaptive system is the capacity to recognize many different molecules and the ability to "remember" repeated exposures to the same pathogen. The adaptive system can be subdivided in two main arms: humoral immunity and cell-mediated immunity[226]. Humoral immunity is mediated by soluble proteins called antibodies secreted by B-lymphocytes, while cell-

mediated immunity is driven by the T cells. Both the innate and the adaptive immune systems are components of an integrated system that provides defense to the host (Figure 5-1).

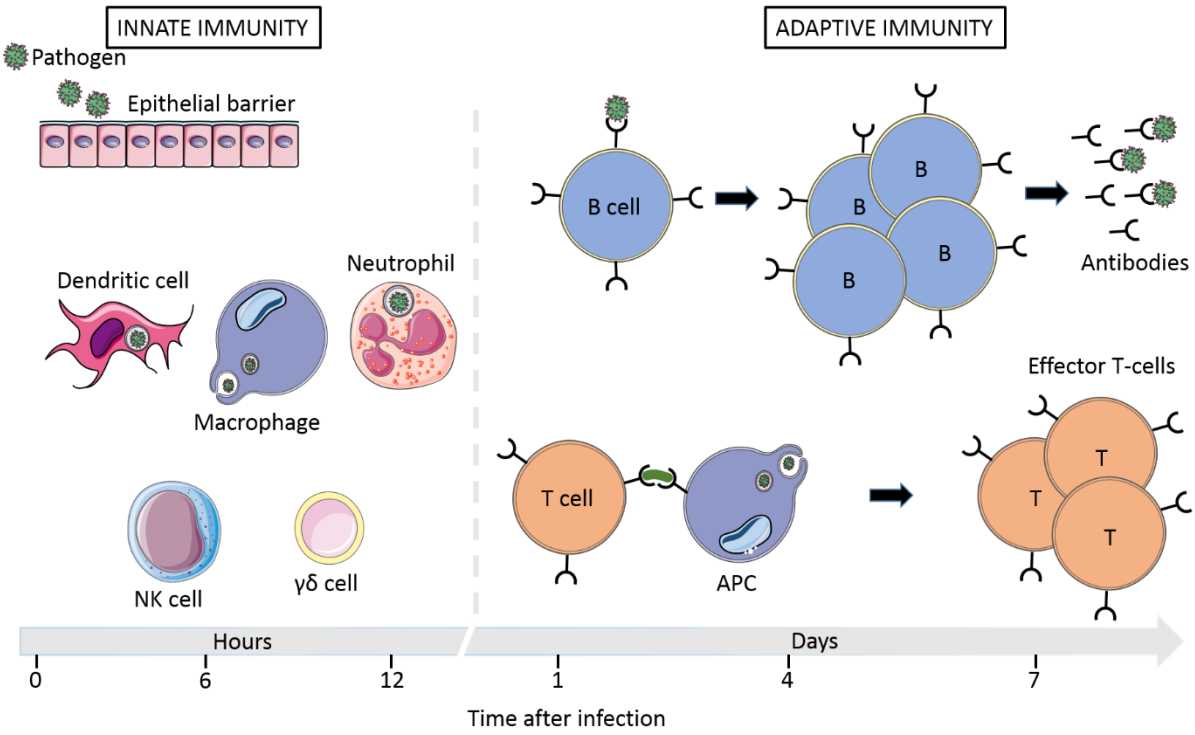

Figure 5-1. The mechanisms of innate immunity provide the initial defense against infections. Adaptive immune responses develop later and consist of activation of lymphocytes. The kinetics of the innate and adaptive immune responses are approximations and may vary in different infections. APC, antigen-presenting cell.

5.1.2 T cells

All blood cells are derived from pluripotent stem cells, also denominated hematopoietic stem cells (HSCs), in the bone marrow. HSCs mature into common lymphoid progenitors (CLP) that give rise to myeloid and lymphoid progenitors[65]. T cell precursors travel from the bone marrow to the thymus where they complete their maturation to become mature T cells[227].

T cells are one of the main components of the adaptive immune system. T cells consist of a group of functionally diverse cells such as, helper T cells, cytotoxic T cells, regulatory T cells, and natural killer T (NKT) cells. The majority of T cells developing in the thymus are αβ T cells, but a small population γδ T cells[227].

The work presented in this chapter focuses mainly on γδ T cell biology and therefore, this introduction will review the state of the art in the development, effector subsets and function of murine γδ T cells.

5.1.3 γδ T Cells

γδ T cells appeared in evolution around 450 million years ago with the emergence of jawed vertebrates[228]. They develop in the thymus together with αβ T cells, however they express a T cell receptor (for TCR structure see Section 1.1.6) consisting of a TCR-γ and TCR-δ chain[229,67].

γδ T cells represent approximately 1-5% of murine peripheral T cells. Unlike αβ T cells, γδ T cells can mature in the absence of MHC-I and II, and β2m, because they do not follow the same stages of thymic selection or peripheral activation[230, 231]. Instead, they express innate-like receptors, e.g. NKG2D and TLRs, which allows them to respond early after pathogen invasion in an innate-like manner[232].

5.1.3.1 Anatomical location of γδ T cells

γδ T cells are predominantly tissue-associated lymphocytes, where anatomical localization and function correlates with the expression of TCRγδ that include specific TCRγ/TCRδ combination, and that often have limited diversity[233, 234]. For example, the mouse epidermis harbours a population of γδ T cells expressing a Vγ5Vδ1 TCR, which morphologically resembles a dendritic cell, thus are known as dendritic epidermal T cells (DETCs). These cells are thought to participate in epidermal skin homeostasis through the secretion of cytokines and other factors like keratinocyte growth factor (KGF) and insulin-like growth factor 1 (IGF-1)[235].

The uterus, tongue[236], lung[237], liver[238] and dermis[239] of the mouse contain a population of γδ T cells expressing a Vγ6Vδ1 TCRγδ and are restricted to the production of IL-17.

γδ NKT cells expressing a Vγ1Vδ6 TCRγδ are mainly localized in the liver and spleen, and secrete predominantly IFN- γ and IL-4[240, 241].

Cells containing Vγ1 and Vγ4 TCR chains are preferentially found circulating in the blood and residing in secondary lymphoid organs[242] (Table 5-1). Interestingly, recent studies have shown that Vγ4$^+$ γδ T cells are a heterogeneous pool of effector cells with the capacity to produce either IL-17 or IFN-γ[243, 244].

Vγ-Usage		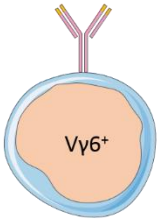	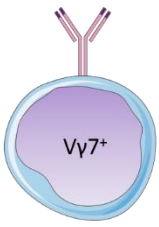	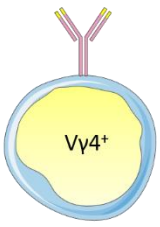	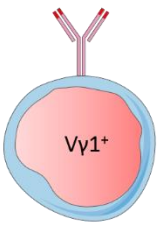
Anatomical Location	Skin epidermis	Genital tract Tongue Peritoneal Cavity Lung Dermis Liver	Intestinal mucosa	Lymph nodes Spleen Dermis Liver	Lymph nodes Spleen Liver

Table 5-1. Vγ-usage correlates with the anatomical localization of murine peripheral γδ T cells. Vγ5$^+$ lymphocytes preferentially located in the skin epidermis, while Vγ6$^+$ cells are preferentially located in the dermis, lung, peritoneal cavity, tongue and lining the genital tract. Vγ7$^+$ cells migrate to the intestinal mucosa and the pool of Vγ4$^+$, Vγ2$^+$ and Vγ1$^+$ are found mainly circulating in the blood and populating secondary lymphoid organs i.e. spleen and lymph nodes.

5.1.3.2 γδ T cell effector subsets

As shown in section 5.1.3.1 murine peripheral γδ cells can be segregated into several subsets based on their usage of certain TCRγ variable regions i.e. Vγ1$^+$, Vγ2$^+$, Vγ4$^+$, Vγ5$^+$, Vγ6$^+$, Vγ7$^+$. For the sake of clarity, the Tonegawa nomenclature for Vγ and Vδ usage will be followed in this chapter[245]. The mouse TCRγ locus comprises four clusters of V, J and C regions containing seven V segments (V1 to V7), four J segments (J1 to J4) and four C regions (C1 to C4)[3]. Each cluster has a C region, one J segment, and from one to four V segments as shown in Figure 5-2. However, the V3-J3-C3 cluster is believed to be non-functional in most mouse strains[246].

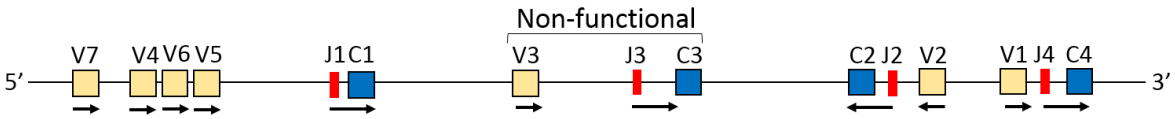

Figure 5-2. Schematic representation of the TCRγ locus in the mouse. The arrows indicate the transcriptional orientation. Three of the clusters are functional: C1 cluster, C2 cluster (orientation inverted) and C4 cluster. The C3 cluster is non-functional. The variable regions are represented with yellow boxes, the joining region with red boxes and the constant segments by blue boxes. Figure adapted from Pereira et al[3].

Unlike TCRγ, the TCRδ locus consists of six variable segments, two diversity segments, two joining regions and one constant region. Due to its location within the TCRα locus, the TCRδ locus is excised after the successful rearrangement of the TCRα chain, preventing the expression of any γδ receptor in lymphocytes that are already committed to αβ lineage[247].

5.1.3.3 γδ T cell effector function

γδ effector subsets execute their function in their anatomical places through the production of cytokines[248]. It has been observed that Vγ5$^+$ DETCs secrete abundant IFN- γ[249], and IL-13[250] but not IL-17. Similarly, Vγ7$^+$ γδ cells homing to the intestinal mucosa have the potential to produce IFN-γ after interaction with butyrophilin-like 1 (Btnl1) expressing epithelial cells in the intestine[1]. This early provision of IFN-γ is believed to defend the host against viral infections e.g. cytomegalovirus infections in fetuses and infants[251, 252], and also plays an important role in tumor surveillance. It has been reported in the literature that γδ T cells are one of the first sources of IFN-γ in the context of tumor immunity, being able to recognize stress molecules, e.g. Rae-1 and ULBP-1 expressed by tumor cells in mice and humans, respectively[232, 253].

In contrast to IFN-γ producers, Vγ6$^+$ γδ T cells are restricted to the production of IL-17[1]. As shown in Table 5-1, these cells are found mainly in the tongue, peritoneal cavity, dermis, and lung. IL-17 producers provide rapid responses against intracellular and extracellular pathogens by recruiting neutrophils and monocytes to the site of infection[254]. King et al. have reported that IL-17 secreting γδ intraepithelial lymphocytes (IELs) have a protective effect in mouse lungs after infection with Nocardia asteroids, a gram-positive bacteria[255]. In addition, other groups have confirmed the important role of the γδ17 effector cells during the early phase of the immune response against Mycobaterium[256], Listeria[238], and E.Coli[257].

The Vγ4$^+$, Vγ1$^+$, and Vγ2$^+$ pool of γδ T cells have the potential to secrete either IFN-γ or IL-17, but barely both simultaneously[244]. They are found predominantly in secondary lymphoid organs, the liver and circulating in the blood[1] (Table 5-2).

Interestingly, Prinz et al.[258] recently reported a Vγ4$^{(+)}$ Vδ5$^{(+)}$ population of γδ cells restricted to the γδ17 effector subset. As mentioned before, the pool of Vγ4$^{(+)}$ γδ T cells is heterogeneous with cells able to secrete either IFN-γ or IL-17[243]. With the aim of understanding the relationship between the Vγ4$^{(+)}$ TCR and Vγ4$^{(+)}$ effector function, Prinz and colleagues performed high resolution sequencing analysis of the mouse TCRγδ with special focus on the Vγ4$^{(+)}$ TCR[258]. They discovered an invariant subset of innate γδ T cells with a TCR composed of Vγ4Jγ1 motif paired with a germline rearranged Vδ5Dδ2Jδ1 within the Vγ4^{+} population that developed in the foetal or perinatal thymus. This innate-like γδ T cell subset was found mainly among the CCR6^{+} CD27^{-} γδ T cells that are characterized as IL-17 producers[244, 259]. Moreover, they identified that the Vδ5^{+} CDR3 amino acid motif ASGYIGGIRATDKLV was principally, but not exclusively, restricted to CCR6^{+} CD27^{-}Vγ4^{+} γδ T cells. Single cell analysis of the corresponding TCRVγ4 chain in cells bearing the Vδ5Dδ2Jδ1 rearrangement revealed that seven cells share the Vγ4 CDR3 sequence SYGLYSSGFHKV. Based on these observations they suggested that the foetal thymus contained a pool of IL-17 producing γδ T cells with a TCR composed of a germline-rearranged Vδ5Dδ2Jδ1 and a canonical Vγ4Jγ1 motif[258]. This TCR is the focus of this work.

Murine peripheral γδ subsets					
Type of cell	Vγ-usage	Cytokines produced	Type of cell	Vγ-usage	Cytokines produced
	Vγ5⁺Vδ1⁺	IFN-γ IL-13		Vγ4⁺	IFN-γ IL-17A
	Vγ6⁺Vδ1⁺	IL-17A IL-22		Vγ7⁺	IFN-γ
	Vγ4⁺Vδ5⁺	IL-17A		Vγ1⁺ / Vγ2⁺	IFN-γ IL-17A

Table 5-2. Terminally differentiated murine peripheral γδ T cell subsets can be classified by the Vγ- usage and the secretion of the cytokines such as IL-17 or IFN-γ. However, other cytokines like IL-13 and IL-22 can be produced alongside. DETC: dendritic epidermal T cells.

5.1.4 Overview of the developmental stages of murine thymocyte development

As mentioned in section 5.1.2, T cell precursors formed in the bone marrow migrate to the thymus to continue their maturation. These early thymic precursors are denominated double negative (DN) thymocytes because they do not express the CD4/CD8 co-receptors (See Figure 5-3). The developmental progression of DN thymocytes in the thymus can be characterized by the expression of CD44 (phagocyte glycoprotein-1), CD25 (IL-2 receptor α chain) and c-Kit (stem cell factor receptor) as described by Godfrey at al[260]. DN thymocytes progress through four stages of development, namely DN1 to DN4 where: **DN1** thymocytes are defined by the expression $CD44^{+}CD25^{-}c\text{-}Kit^{+}$, **DN2** cells are $CD44^{+}CD25^{+}c\text{-}Kit^{+}$, **DN3** cell $CD44^{-}CD25^{+}c\text{-}Kit^{-}$ and, **DN4** cells are $CD44^{-}CD25^{-}c\text{-}Kit^{-}$.

The identity and differentiation potential of the DN1 subset is not fully understood. For example, it is not clear whether early thymic precursors can give rise to all lymphoid and myeloid cells or is restricted to T and NK cells[2, 261]. Despite these fundamental gaps in our knowledge of the biology of these early progenitors, it is quite clear that full commitment to the T cell lineage requires Notch-1 signalling in early thymic precursors[262, 263]. Notch-1 is a transmembrane receptor expressed in progenitor cells. It associates with the transmembrane ligands Delta-like 1 (DL1), DL3, and DL4 expressed in neighbouring cells. The interaction leads to the cleavage of the intracellular domain of Notch, which migrates to the nucleus where it acts as a transcription factor of some key genes in T cell lineage commitment, e.g. recombination-activating gene-1 (RAG-1)[2]. Schmitt et al[264] have shown that Notch-1 signalling is required to maintain progression from the DN1 to DN3 stages during T cell lineage development.

The progression to the DN2 stage is characterised by upregulation of CD25 and intense proliferation[265]. DN2 cells are first detected in the mouse foetal thymus at embryonic day 13.5 (E13.5). These cells start to express RAG-1 and RAG-2 genes, fundamental for TCR rearrangement, as well as genes involved in TCR and pre-TCR complex formation[266, 267].

The DN3 cell population can be detected around day E14.5, and are fully committed to the T lineage as they can only differentiate into αβ or γδ T cells[268]. At this stage, the thymocytes that have rearranged a functional TCRγ and TCRδ chain and are able to express the TCRγδ complex at the cell surface will be committed to the γδ lineage.

Those cells that produce a functional TCRβ chain start to express a surrogate receptor denominated pre-TCR[269]. The pre-TCR is expressed at the cell surface with CD3 molecules and is required for the transition of DN3 thymocytes through the "β-selection" checkpoint[270, 271]. Pre-TCR signalling promotes down-regulation of CD25, cell survival, proliferation, and further differentiation beyond the DN3 stage[269].

DN4 cells can be detected in the mouse foetal thymus around E14.5. Before their progression to the $CD4^+CD8^+$ double positive (DP) stage, the thymocytes enter an intermediate stage known as the "immature single positive" (ISP) characterized by the expression of the CD8 co-receptor[272]. Afterwards, thymocytes upregulate the co-receptor CD4 to become "double positive" (DP). These double positive cells represent the majority of cells in the thymus[273]. TCRα rearrangements are initiated and completed during the DP stage. The TCRβ chain will then form TCRαβ heterodimers with the TCRα chain and with CD3 molecules[69]. Cells that express a TCRαβ complex that is able to recognize an MHC-self-antigen complex

presented by thymic epithelial cells are positively selected, i.e. cells survive and continue their maturation towards the single positive (SP) stage. However, thymocytes that express a TCRαβ with high affinity for the self peptide-MHC complex will enter apoptosis to avoid autoreactive responses in the periphery in a process denominated negative selection[274].

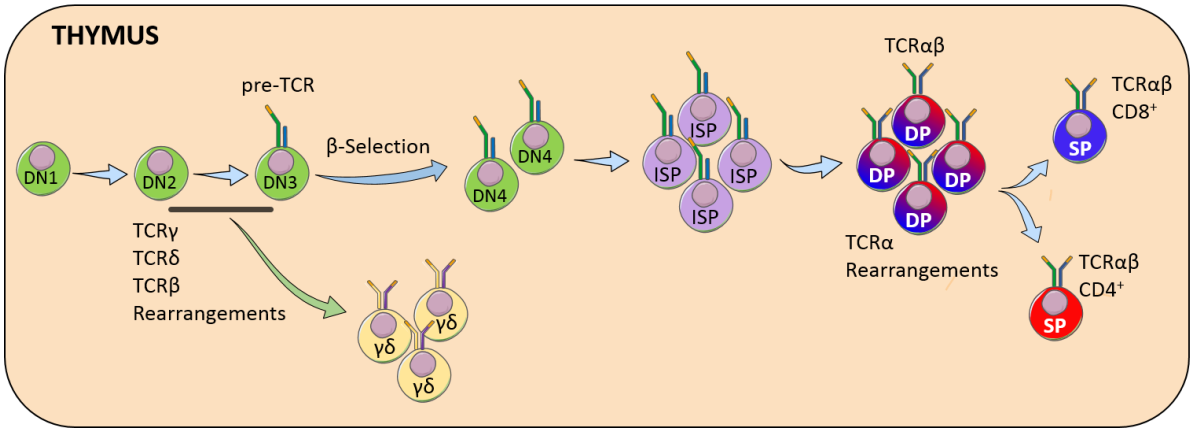

Figure 5-3. Graphic representation of the different stages of thymocyte development in the murine thymus. The double negative thymocytes (DN) progress through a number of stages during their thymic maturation that culminate in the development of the γδ T cells, CD4+ and CD8+ αβ T cells. DP, double positive; ISP, immature single positive; SP, single positive.

5.1.5 Murine γδ T cell development

5.1.5.1 Models for γδ lineage commitment

Double negative thymocytes that successfully rearrange and express the γδ TCR are capable of developing along the γδ T cell lineage at some point between the DN2 and DN3 stage of development[275] (See Figure 5-3). However, the specific branch-point where this fate decision occurs and the molecular mechanisms involved in lineage fate commitment are poorly understood[276]. Notwithstanding, three models have been proposed to-date: the instructional model[277, 278], the stochastic model[279] and the signal strength model[280].

5.1.5.1.1 Instructional model

In the instructional model, the γδ versus αβ cell fate decision is dictated by expression of a certain TCR, and the qualitatively different signals they transmit. In other words, DN cells that express a γδ TCR will commit to the γδ lineage, while those expressing the pre-TCR will be diverted towards the αβ lineage. The initial proposal of this model was based on the experimental observation that γδ cells develop early in ontogeny (E14.5)[277]. It was suggested that only those cells that failed to rearrange and produce a functional γδ TCR would then attempt the rearrangement of the TCRα and TCRβ chains.

However, the discovery of the pre-TCR led to the reformulation of this model. The revised model stated that TCRβ, TCRγ, and TCRδ would undergo rearrangements simultaneously[281]. If the loci rearranged first were TCRγ and TCRδ, the cell would commit to the γδ lineage, whereas if TCRβ is rearranged first then the DN cell will become an αβ T cell.

Fehling et al[269] challenged this model in their work with mice deficient in TCRβ/pTα, in which they observed that TCRγδ was driving limited development of αβ committed DP

thymocytes as well as γδ T cells. Similarly, the work published by Bruno et al[282] with transgenic mice where early expression of TCRαβ promoted development of γδ-like T cells demonstrate the necessity to formulate a model that better explained these observations.

5.1.5.1.2 The stochastic model

The stochastic model proposes that early double negative thymocytes do not possess the same potential to develop towards the αβ or γδ lineage, arguing that pre-existing factors bias the thymocytes towards one lineage or the other[279]. For this model, the expression of a particular TCR is just concomitant to the pre-commitment to a specific lineage. In support of this model are the observations of Raulet et al[279] showing that while all DN1 cells express similar levels of IL-7 receptor α chain (IL-7Rα), DN2 thymocytes show heterogeneous expression. Most striking is the observation that IL-7Rα $^{(-)}$ DN2 thymocytes appeared to be diverted towards the αβ lineage, while IL-7Rα$^{(+)}$ cells preferentially developed as γδ T cells[279]. Other experimental evidence suggests that the transcription factor SRY-box-containing gene 13 (Sox13) is required for γδ but not αβ commitment[283]. The authors found that Sox13 is expressed in only 45% of DN2 thymocytes, and correlated with the expression of IL-7Rα[283]. In addition, mice deficient in Sox13 showed normal αβ T cell development in comparison with γδ T cells that were reduced by more than 50%[283]. Moreover, overexpression of Sox13 was shown to compromise the normal development of αβ cells when compared with γδ T cells, suggesting that expression of Sox13 in combination with IL-7Rα in DN2 cells pre-selects these progenitors towards the γδ lineage. In contrast to the previous observation, the studies conducted by Gray et al[284] with a spontaneous mutant for Sox13 demonstrated that this transcription factor was not necessary for γδ commitment. Instead, it was important for the development and function of the Vγ4^{+} subset of γδ T cells in particular.

5.1.5.1.3 The signal strength model

The “signal-strength” model is the latest model to explain αβ versus γδ lineage commitment. This model states that lineage commitment is determined by the strength of signal delivered by the TCR (TCRγδ or pre-TCR) in early progenitors. Specifically, the model suggests that strong TCR signals promote the development of γδ cells, whereas weak TCR signals favour progression into the αβ lineage as illustrated in Figure 5-4.

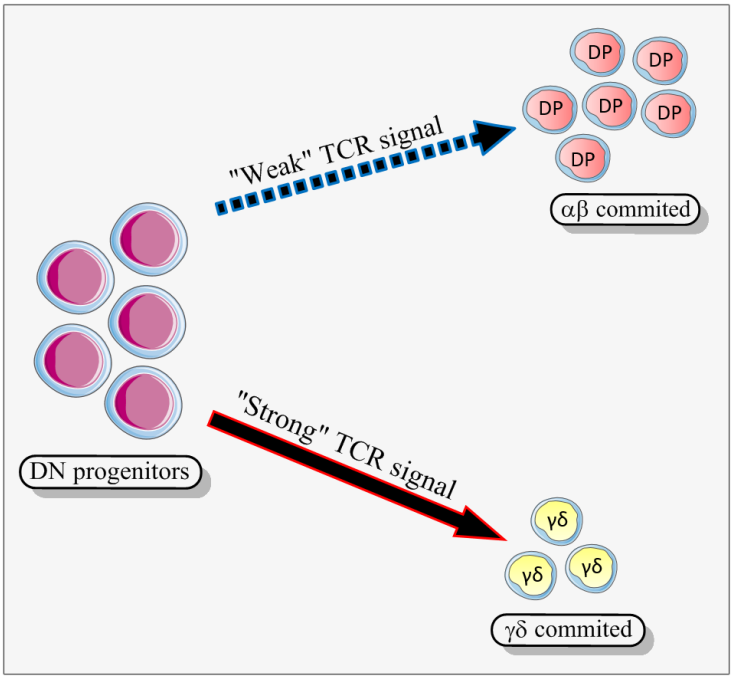

Figure 5-4. The “signal-strength” model of γδ versus αβ lineage commitment. The model proposes that fate commitment is dictated by the strength of signal delivered from the TCR. Strong TCR signals favor the development of γδ cells whereas weak TCR signals promote progression into the αβ lineage (illustrated by the DP cells). DN, double negative; DP, double positive.

In support of this model, Hayes et al[285]showed that the expression of a single TCRγδ (TCR-Vγ6Jγ1Cγ1-Vδ1Dδ1Jδ2Cδ1) transgene was capable of driving both γδ and DP development. Interestingly, surface expression levels of the TCRγδ were lower on DP thymocytes, compared with γδ T cells, suggesting that lower level of receptor expression promotes the

development of DP cells. To further understand the influence of TCR surface abundance on αβ versus γδ lineage fate commitment they used a further transgenic mouse model (TCRγδ Tg TCR-$\zeta^{+/-}$) where the TCR expressed is the TCR-Vγ6Jγ1Cγ1-Vδ1Dδ1Jδ2Cδ1 and one of the TCRζ alleles have been inactivated ($\zeta^{+/-}$). These transgenic mice expressed fifty percent less TCR on the cell surface than their wild-type counterparts, TCRγδ Tg TCR-$\zeta^{+/+}$ mice[286]. Analysis showed that this reduction correlated with an increase in the total number of DP cells and a decrease in γδ thymocytes. Introduction of a full-length TCRζ transgene reduced the number of DP cells and restored γδ thymocytes. The authors concluded that increasing the density of TCR expression correlates with increased signal strength and commitment to the γδ lineage. Conversely, a low density of TCR is translated into weak signal strength and this in turn favours the commitment of the progenitors towards the αβ lineage.

More recently, Zarin et al.[287] showed that $Rag2^{(-/-)}$ DN cells expressing both the pre-TCR and TCRγδ developed along the γδ pathway, down regulating CD24 expression, and up-regulating CD73. However, in the absence of inhibitor of DNA-binding 3 expression (ID3) γδ-expressing cells showed a reduced propensity to commit towards the γδ fate. Importantly, differentiation along the γδ lineage was restored by pre-TCR co-expression, which induced greater down-regulation of CD24 and higher levels of CD73.

Altogether, these findings reinforce the view that the cumulative signal strength received by developing DN cells serves to dictate lineage choice (αβ versus γδ) and not the type of receptor itself.

5.1.5.2 Waves of γδ T cell development

γδ T cell development starts at the foetal stage and progresses in waves that correlate with usage of particular Vγ chains[245] (Figure 5-5). The first wave of cells are $V\gamma5^+$ at day E13 until E17 that migrate to the skin epidermis[248]. The following wave that spans from the E14 to around birth, generates IL-17-producers that consist predominantly of $V\gamma6^+$ cells that migrate to the dermis, tongue and genital tract[242]. The next wave generates $V\gamma1^+$ and $V\gamma4^+$ cells from E16 onward, which populate the lymph nodes, dermis, peritoneal cavity and lungs. Near birth, $V\gamma7^+$ cells are generated which migrate to the gut[242]. There is limited explanation for these organized waves of development at the moment. However, Xiong et al[275] have proposed that the pattern of sequential γδ cell development is associated with the germline transcription and rearrangement program of the TCRγ locus.

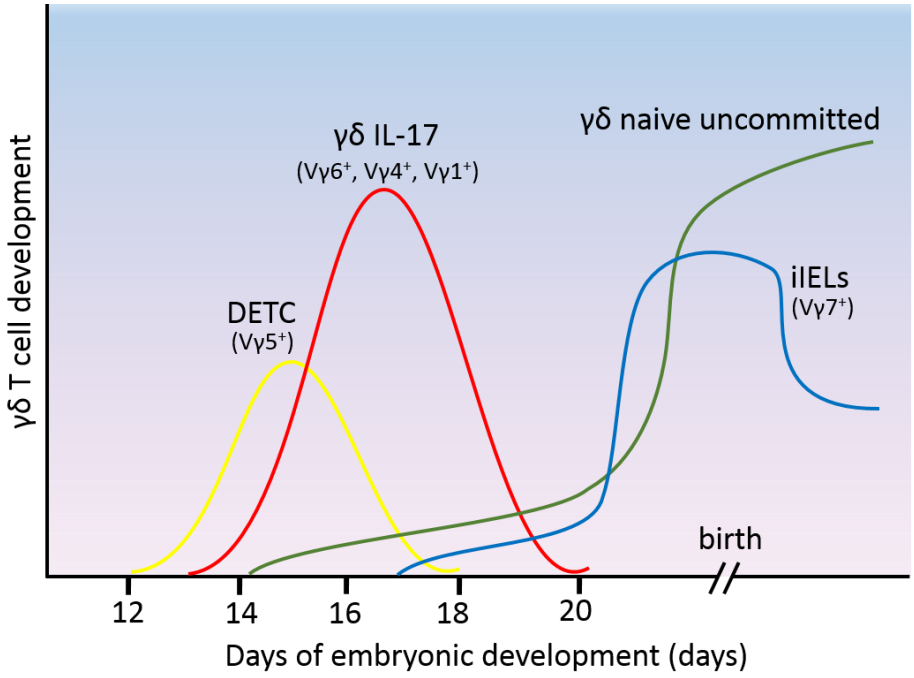

Figure 5-5. Development of murine γδ T cells. The figure shows how different functional subsets of γδ T cells develop during ontogeny to populate different anatomical locations. The waves of development correlate with the usage of a specific Vγ chain. Dendritic epidermal T cells (DETC), intestinal intraepithelial lymphocytes (iIELs).

5.1.6 Assessment of γδ T cell development

The developmental stages of γδ T cell maturation can be identified by flow cytometry using the markers CD25, CD24, CD44 and CD45RB (Figure 5-6 A and B). The first γδ thymic progenitors which are characterized by double expression of $CD24^{(+)}$ and $CD25^{(+)}$ can be detected in E14 thymic lobes[1]. Consensus holds that signaling through the TCRγδ promotes the downregulation of CD25 and induces an increase in the surface expression of TCRγδ[288]. In the next step of development the $CD24^{(+)}$ $CD25^{(-)}$ population downregulates expression of CD24. This suggests a developmental progression in the early γδ progenitors of $CD24^{(+)}$ $CD25^{(+)}$ to $CD24^{(+)}$ $CD25^{(-)}$ to $CD24^{(-)}$ $CD25^{(-)}$ [1]. It is around the latter stage that immature γδ cells commit to effector fate i.e. the ability to produce either IFN-γ or IL-17[244] (Figure 5-6 B).

To identify γδ cells that are committed towards one of these two cytokine secreting pathways our lab (Sumaria et al[1]) developed a flow cytometry methodology (Figure 5-6 A). The staining strategy is based on the use of CD24, CD25, CD44 and CD45RB antibodies that segregate $CD24^{(-)}$ γδ T cells into two clearly different developmental pathways: $CD44^{(+)}$ $CD45RB^{(-)}$ thymocytes are committed to secrete IL-17, whereas $CD44^{(-)}$ $CD45RB^{(+)}$ are committed to the production of IFNγ. For the sake of clarity, we will use the terminology a, b, c, and d to denominate the subsets $CD44^{(-)}CD45RB^{(-)}$, $CD44^{(-)}CD45RB^{(+)}$, $CD44^{(+)}CD45RB^{(+)}$, and $CD44^{(+)}CD45RB^{(-)}$, respectively. Notably, $CD44^{(-)}$ $CD45RB^{(-)}$ (a) thymocytes have the potential to give rise to all other subsets (b, c, and d).

One of the advantages of this methodology is that cells remain alive after analysis for further analysis, an option that is precluded in the traditional fix/perm techniques where cells dye after intracellular staining for cytokines.

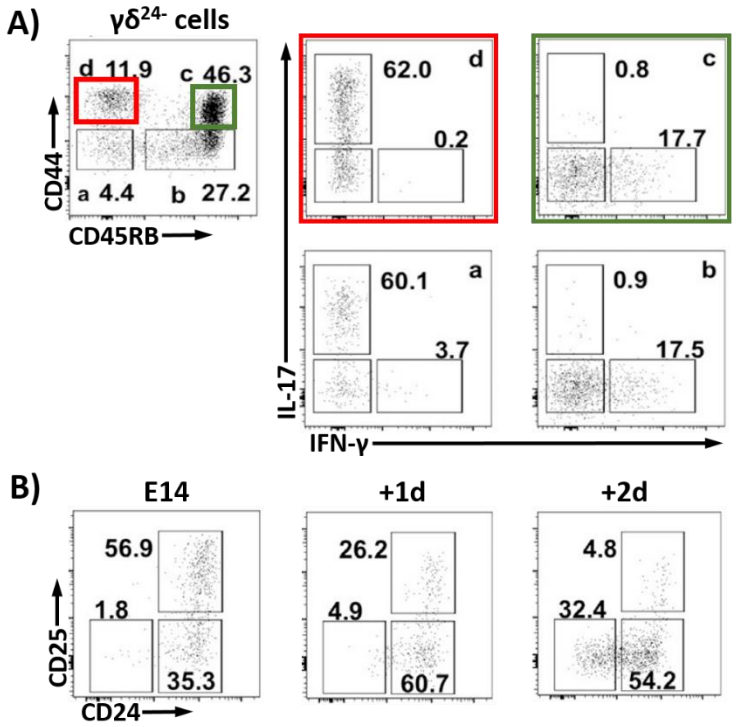

Figure 5-6. **Methodology to identify γδ thymocytes committed toward one of two effector phenotypes, IFN-γ or IL-17**. **A)** Mature γδ T cells ($CD24^-$) can be assessed using CD44 and CD45RB and four distinct populations can be identified; $CD44^-CD45RB^-$ (a) are the early mature subset and have the potential to develop into either effector phenotype. $CD44^-CD45RB^+$ (b) and $CD44^+CD45RB^+$ (c) (green gate) are committed to the secretion of IFN-γ. $CD44^+CD45RB^-$ (d) (red gate) develop towards the IL-17 producer subtype. **B)** γδ maturation assessed by the expression of CD24 and CD25 in E14 thymocytes, or thymocytes isolated after 1 or 2 days FTOC culture. Figure adapted from Sumaria et al.[1]. CD, cluster of differentiation; FTOC, fetal thymic organ culture.

5.1.7 The role of TCRγδ in γδ T cell development and commitment to effector phenotypes

As mentioned in section 5.1.5.1 surface expression of TCRγδ on DN3 thymocytes is a key event for commitment to the γδ lineage[288]. The generation of a strong signal from TCRγδ in DN can be the result of higher expression of receptors on the cell surface, by comparison with the scant amount of pre-TCR expressed. However, the most plausible cause of a strong signal generated by TCRγδ is ligand (binding by analogy with αβ cell development). For example, the absence of MHC-II has a profound impact on the generation of $CD4^{(+)}$ αβ T cells leading to impaired T cell mediated immunity[289]. Notwithstanding, the small number of TCRγδ ligands so far identified has made the demonstration of this hypothesis difficult. Furthermore, it was observed that γδ T cells also acquire their effector function while residing in the thymus i.e. IL-17 or IFN-γ secretion capacity. In summary, γδ lineage commitment and acquisition of effector function have both been postulated to depend on the signal strength delivered by TCRγδ (strong versus weak), and this may correlate with ligand-dependent versus ligand-independent signal initiation (See Figure 5-7). In the next section some experimental evidence in support of both hypotheses is presented.

5.1.7.1 Ligand independent signaling

Evidence of ligand independent signaling through TCRγδ was presented by Jensen and colleagues[290] who showed in vitro that TCRδ oligomerization was mediated by the interaction of the Ig-like variable domains. However, work carried out by our lab[291] and discussed in section 1.1.9.3 in Chapter 1 of this thesis, provides experimental evidence that challenges the oligomerization theory. These experimental data suggest that signal initiation in DN thymocytes, although ligand-independent is rather a consequence of successful pairing of TCR chains at the cell surface, and the strength of signal transmitted through the TCR is simply correlated to the abundance of TCR on the cell surface.

5.1.7.2 Ligand dependent signaling

As mentioned above (Section 5.1.7), the identification of TCRγδ ligands has been very limited; therefore, it is uncertain whether γδ progenitors require ligand interactions during their development and acquisition of effector function. Despite that, some experimental evidence supports the ligand engagement hypothesis these studies are discussed in this section but it should be emphasized that this is a field under active investigation.

5.1.7.2.1 Vγ5$^{(+)}$ Vδ1$^{(+)}$ dendritic epidermal γδ T cells (DETC)

Strong support for the engagement of ligands in the development of γδ T cells comes from studies on the development of DETCs. A seminal observation in the FVB sub-strain of mice (FVB-Tac) revealed that they had very few Vγ5$^{(+)}$ Vδ1$^{(+)}$ skin homing γδ T cells, and impaired development of Vγ5$^{(+)}$ Vδ1$^{(+)}$ thymocytes even though other subsets of γδ cells developed normally[292]. In contrast to FVB-Tac, the FVB-Jax mice had normal thymic development and skin migration of Vγ5$^{(+)}$ Vδ1$^{(+)}$ thymocytes[292]. Interestingly, the transfer of FVB-Tac thymocytes to the thymic stroma of FVB-Jax mice rescued the development of Vγ5$^{(+)}$ Vδ1$^{(+)}$ T cells. Conversely, the culture of FVB-Jax thymocytes on the stroma of FVB-Tac thymuses abolished the development of the Vγ5$^{(+)}$ Vδ1$^{(+)}$ T cells. These experiments illustrate the important role of the thymic stroma in the development of the Vγ5$^{(+)}$ Vδ1$^{(+)}$ subset. Further analysis demonstrated that the thymic stroma of FVB-Tac mice is deficient for the immunoglobulin-like membrane protein Skint-1 (selection and upkeep of intraepithelial T cells 1)[293]. It was also demonstrated that this protein is normally expressed in the thymus as well as the skin epithelium, therefore it was concluded that Skint-1 is indispensable for the positive selection of Vγ5$^{(+)}$ Vδ1$^{(+)}$ T cells in the thymus[294]. In addition, transgenic expression of Skint-1 expressed from a β-actin promoter, with the mature protein tagged with an amino-terminal FLAG epitope that allowed its detection, fully rescued Vγ5$^{(+)}$ Vδ1$^{(+)}$ DETC maturation in FVB-Tac mice[293]. The same study demonstrated that Skint-1 is mainly expressed by medullary thymic epithelial cells (mTECs). However, there is no evidence to demonstrate that the TCR is the direct target of the Skint-1 protein. Therefore, further studies are required to elucidate the target of Skint-1 and its particular role in the development of Vγ5$^{(+)}$ Vδ1$^{(+)}$ DETCs.

5.1.7.2.2 T10/T22 specific γδ T cells

Ligand dependent signaling has also been investigated in relation to the non-classical MHC-Ib molecules T10 and T22. Briefly, T10 and T22 proteins are encoded in the thymic leukemia antigen (TL) locus and share approximately ninety-four percent sequence similarity[295]. These molecules were first described for their capacity to bind to the G8 and KN6 γδ T cell hybridomas[296]. It was also demonstrated that T10/T22 pair with β2-microglobulin (β2m), similar to the MHC-I, but are not engaged in antigen presentation functions[297].

Development of γδ T cells that engage T10 and T22 is still unclear. Studies have used two TCRγδ transgenic models, TCR-Vγ2Jγ1Cγ1-Vα11DδJδ1Cδ1 (**G8**) and, TCR-Vγ4Jγ1Cγ1-Vδ5DδJδ1Cδ1 (**KN6**) and both have been introduced transfected onto the C57BL/6 background (expresses both T10 and T22), BALBc (only express T10) or β2m deficient mice (absent for T10 and T22) to assess development of γδ T10/T22 specific γδ T cells[298, 299].

Dent et al.[299] used the G8 model to study the development of this repertoire in the presence or absence of the T22 ligand. They observed that G8 γδ T cells were able to develop in the absence of T22 ligand, but they were scant in the periphery of T22-positive mice. They concluded that the absence of G8 cells in the periphery of T22-positive mice was the result of negative selection of these transgenic thymocytes in a similar way to negative selection of the self-reactive thymocytes.

In a different study Pereira et al.[300] crossed KN6 transgenic mice with β2m$^{(-/-)}$ mice. They reported that KN6 γδ cells were not detected in the thymus or the spleen of these mice in the absence of both T10 and T22, suggesting that the interaction with these MHC-Ib molecules was required for the development of KN6 γδ T cells.

In a further study Schweighoffer et al.[271] showed that the number of mature G8 γδ T cells in β2m$^{(-/-)}$ mice was normal, contradicting a requirement for T10/T22 ligand interaction during γδ thymic development. The experimental data presented in these different studies showed little agreement about the requirement for ligand recognition in the development of γδ T cells.

Despite the lack of consensus on the role of T10/T22 in γδ T cell development, some interesting observations using a tetramer of the T22 protein showed that in WT mice there is a fraction of γδ cells reactive to T22[297]. Experiments conducted with T22-reactive γδ T cells from thymus, spleen and epithelial tissue from C57BL/6 and β2m$^{(-/-)}$ mice showed that the proportion of T22-specific γδ T cells was similar regardless of the genetic background[290]. Further analysis of phosphorylated ERK (pERK) which is a signaling molecule involved in TCR signal transduction and CD5, an indicator of TCR signal strength, revealed no differences between T22-specific γδ thymocytes from the C57BL/6 and β2m$^{(-/-)}$ backgrounds[301, 302]. These results demonstrated that the T22 ligand is not essential for the development of T22-reactive γδ T cells. Therefore, assuming that these cells are not binding a different ligand, the authors concluded that thymic γδ T cell development could take place in the absence of ligand interactions.

Further analysis of T22 tetramer positive γδ T cells revealed that those cells coming from the β2m$^{(-/-)}$ mice acquired a "naïve phenotype" characterized by expression of CD44^{low} and CD122^{low}, while T22 positive γδ T cells from C57BL/6 mice were CD44^{Hi} CD122^{Hi} [290]. Moreover, Jensen et al[290] discovered that upon TCR triggering the "antigen naïve" γδ cells (CD44^{low} CD122^{low}) secreted IL-17 whereas "antigen experienced" γδ cells, (CD44^{Hi} CD122^{Hi}) secreted IFN-γ.

Thus, they concluded that in the thymus, TCRγδ signal initiation can occur in a lig-and-independent manner, similar to the pre-TCR, and that the thymic microenvironment seems to play an important role in the acquisition of γδ effector function[290].

5.1.7.2.3 Strong TCRγδ signaling prohibits development of all IL-17A secreting γδ T cells

Recently, our laboratory provided important observations regarding the role of TCRγδ signaling in the acquisition of γδ effector function[1]. As mentioned before, in section 5.1.7.2.2, general opinion considered that strong signals through the TCRγδ favored γδ T cell commitment to secretion of IFN-γ[290]. In agreement with this hypothesis, the addition of anti-TCRδ antibody (GL3) which has been reported to promote strong signaling through TCRγδ[303], to 7-day foetal thymic organ cultures (FTOC) of E15 thymic lobes, reduced the generation of IL-17 committed γδ T cells but increased the generation of $CD44^{(+)}$ $CD45^{(+)}$ γδ cells (the IFN- γ committed subset)[1]. In addition, cells committed to the IFN-γ pathway showed an increase in expression of CD73, a surface marker that correlates with strong TCRγδ signals as reported previously[1, 304].

To assess the effect of a weak signal through TCRγδ, a small molecule inhibitor targeting the Extracellular Signal–Regulated Kinases (ERK) pathway was added to 7-day FTOC. ERK is involved in the signaling cascade downstream of TCRγδ[301, 302, 305]. The results showed that inhibition of ERK increased the development of IL-17-producing γδ T cells subset when compared with control cultures.

Based on these results it was concluded that modulation of signal strength delivered by TCRγδ, i.e. a strong signal generated by crosslinking the receptor with antibody, or a weak signal obtained through inhibition of the ERK protein, fundamentally influenced the development of IL-17 committed γδ T cells. This is consistent with the hypothesis that a strong TCRγδ signal is not compatible with the development of IL-17 producing γδ T cells[1].

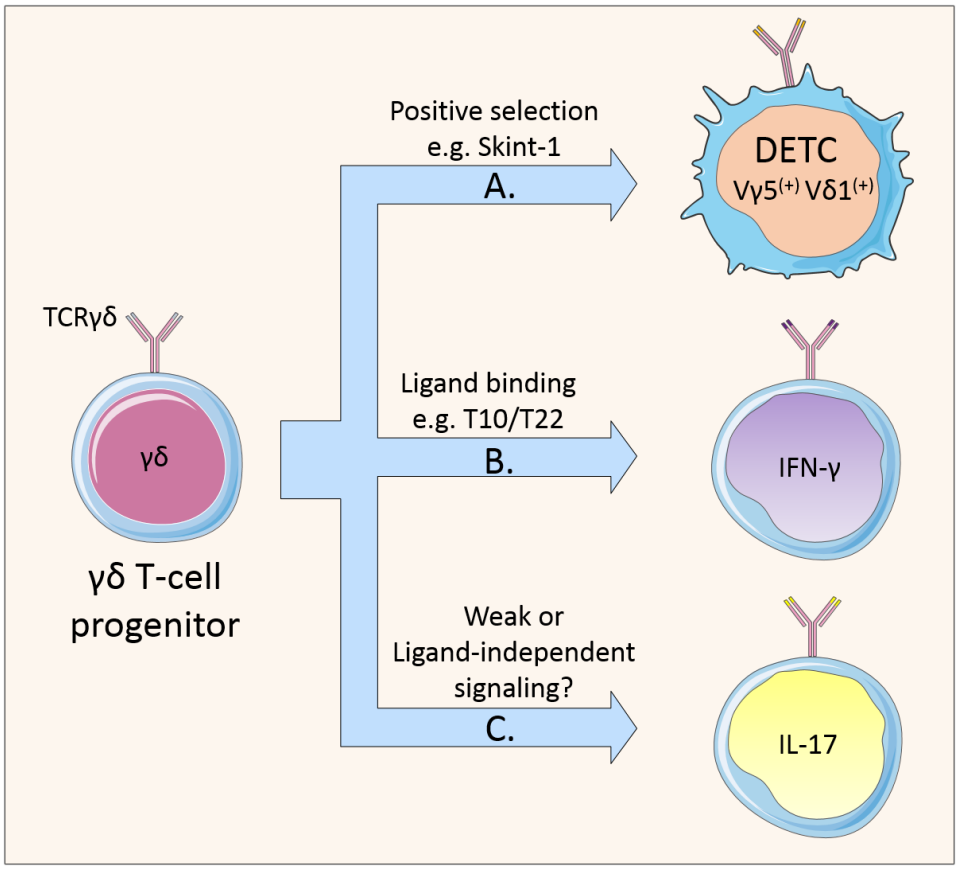

Figure 5-7. Schematic representation of the role of TCRγδ in γδ T cell development and acquisition of effector function. **(A)** The development of $V\gamma5^{(+)}$ $V\delta1^{(+)}$ DETCs and their migration to the skin epidermis is dependent on the Skint-1 protein. **(B)** T22-specific γδ T cells that develop in the presence of the T22 ligand acquire the IFN-γ secretion phenotype. **(C)** T22-specific γδ T cells that develop in the absence of their cognate ligand acquire an IL-17-secreting phenotype. Manipulation of signal strength delivered by the TCRγδ shows that a strong signal prohibits the development of IL-17-secreting γδ T cells. DETC, dendritic epidermal T cells; Skint-1, selection and upkeep of intraepithelial T cells.

5.2 Summary

γδ T cells are important components of the immune system, with the capacity to respond quickly to various challenges e.g. Malaria, HIV, tuberculosis, tumors, etc. They are regarded as one of the earliest sources of the proinflammatory cytokines IL-17 and IFN-γ in many diseases. Unlike their αβ T cell counterparts, γδ cells do not need peripheral activation to acquire their effector phenotype. Instead, they attain the capacity to secrete IL-17 or IFN-γ while still developing in the thymus; therefore, they are considered a "developmentally preprogrammed" subset of T cells. However, the precise role of TCRγδ in the differentiation of γδ progenitors towards the two effector subsets remains unclear. Preliminary data have shown that strong TCRγδ signaling seems to drive the development of IFNγ-committed γδ T cells, while IL-17 commitment requires weak TCRγδ signaling or perhaps a ligand-independent event[1]. In fact, it has been described that some subsets of γδ T cells characterized by certain Vγ usage are predominantly represented in one or the other effector subset i.e. $V\gamma5^+$ in the IFN-γ pathway, $V\gamma6^+$ in the IL-17 pathway, while some Vγ subsets are more heterogeneous and can be found in both effector groups such as $V\gamma4^+$ γδ T cells (IL-17 and IFN-γ). To that end, the second part of this PhD project aimed to establish a system to begin to clarify the role of TCRγδ in the development and acquisition of γδ T cell effector function.

5.2.1 Statement of the Problem

Specifically, this section of the thesis has attempted to address whether features of the TCRγδ directly dictate the effector fate of developing γδ progenitors. Simply put, it tries to answer the question, "Do γδ progenitors all adopt the same effector fate if they all express the same TCRγδ?", and if so, "What features of the TCRγδ dictate this effect on developmental potential?".

5.2.2 Hypothesis

We hypothesize that features of TCRγδ (e.g. CDR3 specificities, Vγ usage) directly dictate the thymic differentiation of γδ progenitors towards distinct effector phenotypes.

5.2.3 Aim

The initial aims of this project were to clone and express a specific TCRγδ in early thymic progenitors, thus establishing a system to study how TCRγδ instructs thymic progenitors towards the acquisition of γδ T cell effector fates.

5.2.4 Project Plan

We will first identify and clone a TCRγδ containing the Vγ4Jγ1-Vδ5Dδ2Jδ1 chains into a retroviral vector so that this TCR can be transduced into $Rag2^{(-/-)}$ E14 or E15 thymocytes. This TCRγδ is restricted to the $CCR6^{+}$ $CD27^{-}$ IL-17-producing γδ T cell subset as described in section 5.1.3.3[258]. The transduced thymocytes will be cultured for 7-10 days on the bone-marrow derived preadipocyte cell line (OP9DL1 cells) that allows their normal development *in vitro*. Afterwards, we will assess development of γδ thymocytes by flow cytometry. Moreover, γδ fate commitment will be evaluated using the methodology described by Sumaria et al[1]. Briefly, $CD44^{+}CD45RB^{-}$ cells are committed to the IL-17 effector pathway

and $CD44^{+}CD45RB^{+}$ cells to the IFN-γ secreting pathway (see Figure 5-6). If TCRγδ is selecting γδ progenitors towards certain effector fates we expect to see that transduced Vγ4Jγ1-Vδ5Dδ2Jδ1 cells all develop toward an IL-17 secreting effector fate ($CD44^{+}CD45RB^{-}$) (see Appendix).

5.3 METHODS

5.3.1 MOLECULAR BIOLOGY

5.3.1.1 Gel electrophoresis

Gel electrophoresis was used for the separation, visualization and isolation of polymerase chain reaction (PCR) products and the restriction enzymes digestion products. Agarose (Sigma, DNase and RNase free) was dissolved in TAE 1X buffer solution and the Gel Red Nucleic Acid Stain (BIOTIUM) was added to stain and visualize the DNA products.

The PCR products were run at 1% Agarose at 100 V for 60 minutes. For the visualization and isolation of the digested plasmids and the subsequent cloning reaction 0.7% Agarose gel was prepared. The reaction mixture ran at 100 V for 90 minutes.

To load the samples on the wells the 6X TriTrack gel loading dye (ThermoScientific) was used. To determine the size of the DNA samples in every run a 100 bp quick purple load DNA ladder (BioLabs) was added to the first well.

5.3.1.2 DNA gel extraction

For the extraction of the DNA products, the gel was excised with sterile scalpels under a UV lamp and the gel fragments were digested following the instructions provided with the Monarch Gel Extraction Kit (BioLabs, lot 0081804). The DNA was eluted with 30 μl of the elution buffer provided in the kit previously warmed up to 50 °C. The sample was kept at -20 °C until needed.

5.3.1.3 Plasmid DNA isolation

5.3.1.3.1 Maxiprep

To obtain enough plasmids for the molecular biology work, 100 ml of Luria-Bertani (LB) broth containing the appropriate antibiotic was inoculated with 5 ml of the bacterial culture (chemically competent DH5α strain) and left shaking overnight at 37°C. The following day the bacterial culture was pelleted and treated with the Plasmid Maxi Kit (Qiagen) to isolate the plasmids. The DNA was extracted in 50 µl of nuclease-free distilled water and stored at -20 °C until needed. The concentration and grade of purity was determined with the nanodrop spectrophotometer ND-100 at 260 nm (Labtech).

5.3.1.4 Restriction Enzymes

Restriction enzymes were used for the double digestion of plasmids with 1 µg of DNA (Table 5-3). The enzymatic reaction conditions were as follows: 1 µl of the restriction enzyme, 5 µl of 10X NEBuffer, (*x)* µl of nuclease-free water to complete 50 µl of total volume. The reaction was incubated for 15 minutes at 37°C, and inactivated at 65°C for 20 min. Table 1 shows summarises the enzymes used in this thesis. All restriction enzymes used in this study were purchased from New England BioLabs.

Enzyme	Restriction Site	Buffer
Age-HF	5' A^CCGGT 3' 3' TGGCC^A 5'	CutSmart
PacI	5' TTAAT^TAA 3' 3' AAT^TAATT 5'	CutSmart
PvuI	5' CGAT^CG 3' 3' GC^TAGC 5'	NEBuffer 3.1
PflMI	5' CCANNNN^NTGG3' 3' GGTN^NNNNACC 5'	NEBuffer 3.1
BamHI-HF	5' G^GATCC 3' 3' CCTAG^G 5'	CutSmart
XhoI	5' C^TCGAG 3' 3' GAGCT^C 5'	CutSmart
MluI	5' A^CGCGT 3' 3' TGCGC^A 5'	NEBuffer 3.1

Table 5-3. List of the restriction enzymes, along with their respective restriction site and the buffer used in each reaction.

5.3.1.5 Polymerase Chain Reaction (PCR)

Polymerase chain reaction is a powerful technique in molecular biology that allows the production of many copies of a target DNA sequence. However, in this thesis, the PCR reaction was also used to engineer the single TCRVγ4 and TCRVδ5 chains to produce the bicistronic construct Vγ4-2A-Vδ5 (Table 5-4).

The primers were manually designed and synthesis was performed by Eurofins Genomics (See Tables 5-5 and 5-6). The PCR polymerase used in this study was the Thermo Scientific Phusion High-Fidelity DNA Polymerase. The Phusion DNA Polymerase possesses the following activities: 5′→3′ DNA polymerase activity and 3′→5′ exonuclease activity. It generates blunt ends in the amplification products that allow the posterior cloning of the product into the pCR-Blunt II-TOPO vector.

Reagent	Volume (µl)
Template cDNA	x
HF Buffer	4
dNTP mix (2.5mM)	2
Forward primer (2.5pmol/µl)	1
Reverse primer (2.5pmol/µl)	1
Phusion polymerase	0.15
ddH_2O	x
Total Volume	20

Temperature/ °C	Time / Cycles	
98	30	
98	10	30x
TM	30	
72	30	
72	5 min	

Table 5-4. PCR components and PCR programme used to construct the TCRVγ4Jγ1 and the TCRVδ5Dδ2Jδ1 chains. Phusion enzyme and HF buffer were purchased from Thermos Scientific and dNTPs from Takara Bio-Clontech.

The melting temperatures for each set of primers used in this study were provided by Eurofins. To estimate the annealing temperature of each pair of primer the online tool (https://tmcalculator.neb.com) was used, with a primer concentration of 2.5 pmol/µl. However, in order to find the optimum conditions for each reaction, a gradient PCR was performed with every pair of primers. For the gradient PCR, the temperature chosen was ± 5°C of the lowest Tm provided from the NEB Tm calculator tool. All the reactions were performed in 0.2 ml 8 strip PCR tubes individually attached with domed caps (StarLab). The PCR reactions were run in a BioRad thermal cycler.

5.3.1.6 Primers

The primers used in the construction of the TCRγδ receptor in this study are presented in the following tables.

Primer	Sequence (5'→3')	Tm °C
Fp1γ	GACAAAAGGCTTGATGCAGACATTTCCCCCAAG	71
Rp2γ	CATGGGACCGGGGTTTTCTTCCACGTCTCCTGCTTGCTTTAACAG	
Fp3γ	CAACCTGAAATATCAATTTCCAGAGCAAG	60
Rp4γ	CTTGGGGGAAATGTCTGCATCAAGCCTTTTGTCTGCAGAGGGAATTACTATGAGCTTAGTTCC	
SPfg1	CTC**GGATCC**ACTATGAAGAACCCTGGCTCACAAG	72
SPrg2	CTTGCTCTGGAAATTGATATTTCAGGTTGTCCAAATGTCAAGAGGCATAAG	

Table 5-5. Details of oligonucleotide primers designed to generate TCRγ chain. Nucleotides in red correspond to overhanging sequences. Underlined nucleotides correspond to the restriction site sequence for BamHI. F, forward primer; R, reverse primer.

Primer	Sequence 5'-3'	Details	Tm (°C)
Fp1δ	AGCCAGCCTCCGGCCAAACCATCTG		69
Rp2δ	CTCTAGATGCATGCTCGAGCG	Contain the restriction site for XhoI (sequence underlined)	59
Fp3δ	TGCATCACGCTGACCCAGAGCTCCACT		69
Rp4δ	GATGGTTTGGCCGGAGGCTGGCTCCTT-GGTTCCACAGTCACTTGGGTT	Overhanging sequence in red is complementary to Fp1δ (will be joined to the 5'-3' chain)	62
Fp7δ	GGAGACGTGGAA-GAAAACCCCGGTCCCATGATTGTT-GCCGCGACCCTTACCCTTCTG	Overhanging sequence in red is complementary to Rp2γ (will be joined to the 3'-5' chain) to joing the TCRγ - P2A with the TCRδ construct.)	68
Rp6δ	AGTGGAGCTCTGGGTCAGCGTGATGCACAG-CACATCCTTGTAGGCAAACAGAAGG	Overhanging sequence in red is complementary to Fp3δ (will be joined to the 5'-3' chain)	76
Fp9δ	GTGGCAATGAGAAGAAATCCGGCTCCGGAGC-CACGAACTTCTCTCTGTTAAAGCAAGCAGGA-GACGTGGAAGAAAACCCCGGTCCCATGATT-GTTGCCGCGACCCTTACCCTTCTG	Overhanging sequence in red is complementary to Rp2γ (will be joined to the 3'-5' chain) to joing the TCRγ - P2A with the TCRδ construct.	>72

Table 5-6. Details of oligonucleotide primers designed to generate TCRδ chain. Nucleotides in red correspond to overhanging sequences. Underline nucleotides correspond to the restriction site sequence for BamHI and XhoI. F, forward primer; R, reverse primer.

5.3.2 CLONING

5.3.2.1 Cloning into pCR-Blunt II TOPO

The blunt topo vector provides an easy and fast way to insert blunt-end PCR fragments into plasmid vectors. The vector is linearized and contains a DNA topoisomerase I covalently bound to the 3' end of each DNA strand, providing a direct insertion into the vector. Furthermore, the plasmid contains the lethal E.Coli gene *ccdB* fused to the C-terminus of the LacZα fragment, which permits only positive recombinants to grow upon transformation. In addition, the plasmid contains resistance genes for Kanamycin and Zeocyn for positive selection of the transformants (Figure 5-8).

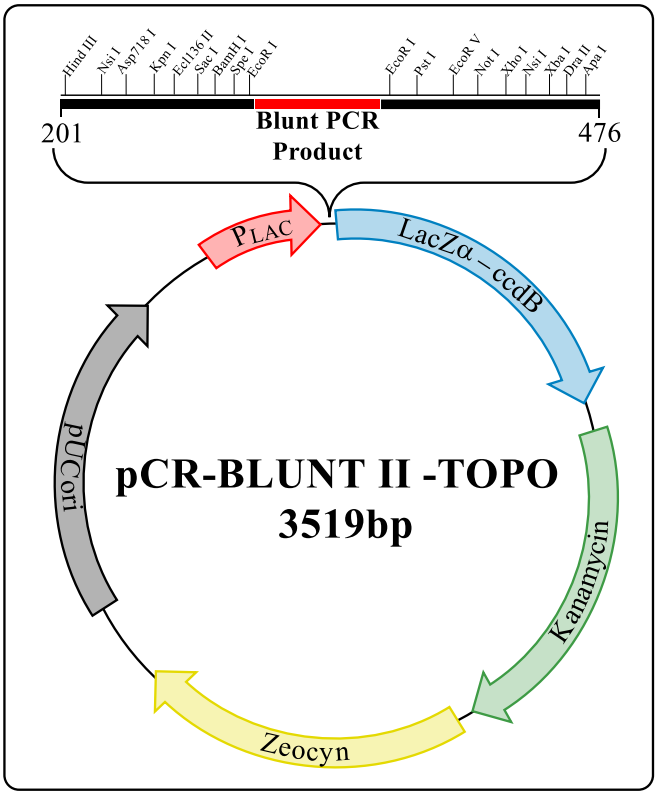

Figure 5-8. pCR-Blunt II TOPO vector map the multiple cloning site. Plac is the lac promoter that is separated from the lethal lacZ-ccdB gene fusion by the multiple cloning site. pUC ori is the origin of replication of the plasmid. The Kanamycin and Zeocyn resistance genes allows for positive selection of transformed bacteria on Kanamycin/Zeocyn containing

The blunt ended PCR fragments were amplified using the Thermo Scientific Phusion High-Fidelity DNA Polymerase, isolated with the agarose gel electrophoresis and extracted from the gel with the Monarch DNA gel extraction Kit (NEB #T1020). The cloning reaction was performed with a 10:1 molar ratio of insert to vector as recommended in the reaction kit. The cloning reaction was set up as shown in Table 5-7.

Reagent	Volume (µl)
Fresh PCR product	4
Salt solution	1
Water	0
pCRII-Blunt-TOPO	1
Total Volume	6

Table 5-7. Components used in the cloning reaction of the blunt PCR fragment into the pCR II TOPO Blunt vector Invitrogen.

The reaction was incubated at 22-23 ^{o}C (room temperature) for about 5 minutes before proceeding with transformation of the DH5α competent cells. 2 µl of the cloning reaction was added to 50 µl of the DH5α competent cells on ice and incubated for 15 minutes. The cells were then heat-shocked for 45 seconds at 42^{o}C and then transferred quickly into ice for another 15 minutes. After incubation, 200 µl of LB medium without antibiotics were added to the transformed cells and the vial was shaken for 1 hour at 37 ^{o}C. 2 µl, 20 µl and the rest of the transformation reaction was plated into three LB Agar plates containing kanamycin (50 µg/ml). The plates were incubated overnight at 37^{o}C. Positive transformants were analysed by restriction digestion (EcoR I) and sent to Sources Biosciences to be sequenced (SP6 priming site).

5.3.2.2 Cloning into pLZRS-IRES-eGFP (pLZ) retroviral vectors

The pLZRS-IRES-eGFP (pLZ) vector[306] is a retroviral vector that possess two long terminal repeats (LTRs) flanking the multiple cloning site (MCS) (Figure 5-9). Downstream of the multiple cloning site and between the two LTRs there is an internal ribosomal entry site (IRES) followed by a reporter gene, enhanced Green Fluorescent Protein (eGFP). The IRES lies downstream of the insert, and allows the translation of the insert and of the eGFP into two individual proteins. Upstream of the MCS is a packaging signal (Ψ) for packaging of the plasmid into virus particles. The pLZ vector contains Ampicillin and Puromycin resistance genes for selection of positive bacterial transformants and transfected phoenix cells, respectively.

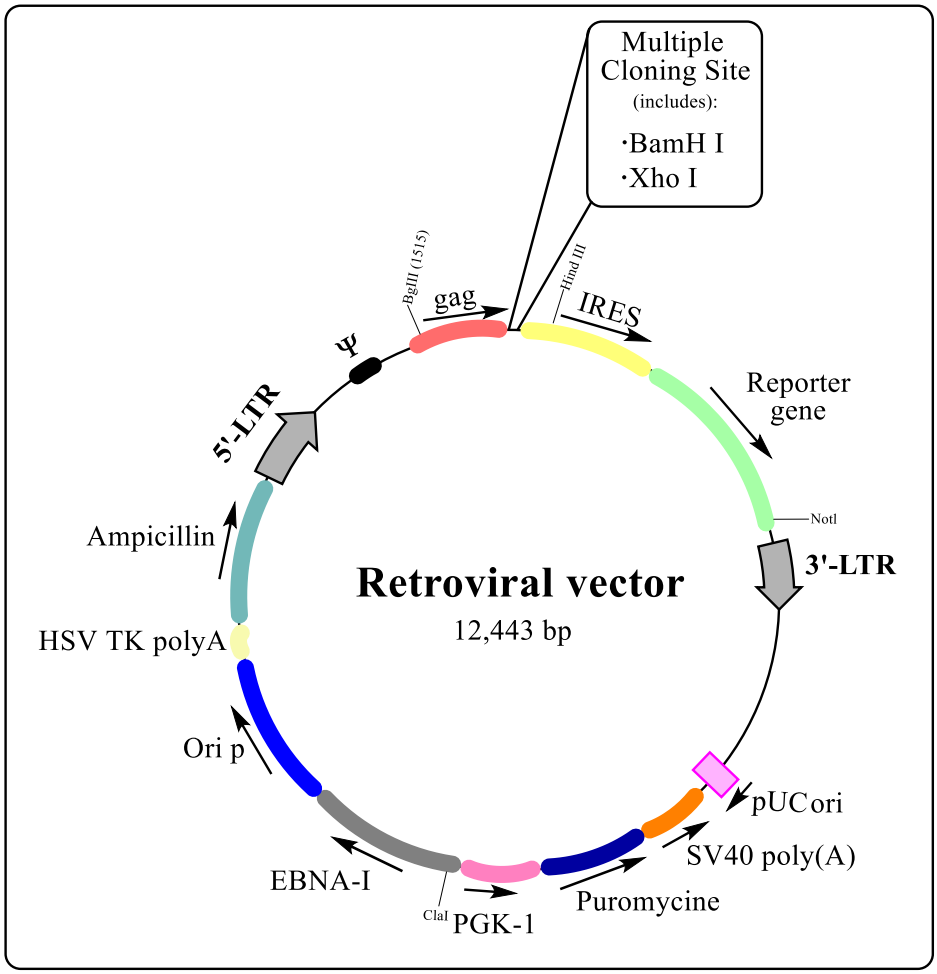

Figure 5-9. The retroviral vector pLZ-IRES-eGFP (pLZ). The multiple cloning site lies between two long terminal repeats (LTRs) which permits the permanent expression of the cloned gene. The packaging signal (Ψ) upstream of the cloning site allows the packaging of the plasmid into viral particles. The internal ribosomal entry site (IRES) upstream of eGFP permits the detection of cells transduced with the retroviral constructs. The ampicillin resistance gene and the puromycin resistance gene will be used for the selection of transformed bacteria and transfected phoenix cells, respectively.

In preparation for the cloning into the retroviral vector both plasmids, pLZRS-IRES-eGFP (pLZ) and pCR-Blunt II TOPO that contains the full-length TCR were digested with BamHI (NEB) and XhoI (NEB) enzymes in two separate reactions. Both reaction mixtures were left for 15 minutes at 37 °C. The digested fragments were purified in 0.7% agarose gel for 1 h 40 min at 100 V.

The linearized form of the retroviral vector (12.4 kb) and the insert (full-length TCR) (1.9 kb) were extracted from the gel and eluted in pre-warmed ddH_2O to improve the efficiency of the elution. The concentration of DNA in each sample was measured using the Nanodrop spectrophotometer.

The linearized fragments isolated were directionally ligated in a reaction at 20:1 insert to vector ratio, using 20 ng of the retroviral plasmid. To calculate the amount of insert to be added I have used the following formula:

$$x\ (ng\ insert) = \frac{20y\ (insert\ bp) \times 20\ (ng\ linearized\ retroviral\ vector)}{12443(retroviral\ vector\ bp)}$$

The ligation reaction was performed with the NEB Instant sticky-end Ligase Master Mix (M0370S). To the mixture of vector and insert, 5 µl of the Ligase master mix were added and mixed by thoroughly pipetting up and down 7-10 times, and placed on ice. Immediately after, the sample was ready for the transformation of the DH5α competent cells. The cells were incubated on ice for 30 min then heat shocked for 30 sec at 42 °C. The cells were then placed on ice for 2 min before addition of 250 µl LB broth medium (Invitrogen) and incubated at 30 ^{o}C in a shaking incubator for one 1 h.

The transformed cells were spread on LB Agar (Invitrogen) plates containing 100 µg/ml Ampicillin (Sigma) and incubated overnight at 37 ^{o}C. Single colonies of the positive transformants were cultured overnight at 37 ^{o}C in 10 ml of LB broth containing 100 µg/ml Ampicillin, and bulked up into 100 ml of LB broth containing ampicillin 100 µg/ml and the plasmid DNA was isolated. PCRs and/or restriction enzyme digests were performed on

plasmid DNA to characterize the transformants and to confirm the presence of the insert. The plasmids were sent to Sources Biosciences for sequencing using the pLZ-gag primer; 5'-TCTTGTCTGCTGCAGCATCG-3' and/or the primers complementary to the insert sequence.

5.3.3 CELL BIOLOGY

5.3.3.1 Isolation of thymocytes and lymphocytes from thymus and skin-draining lymph nodes.

C57BL/6 mouse thymus and skin-draining lymph nodes: brachial, inguinal and axillary, were removed and added into different tubes containing ice-cold Roswell Park Memorial Institute Medium (RPMI)-1640 (Invitrogen). Afterwards, the organs were crushed using a 5 ml plunger and strained through an 80 μm metal mesh (Sefar Ltd, UK) into appropriately labelled falcon tubes (15 ml). Fluorescence-activated cell sorting buffer (FACS buffer) (See Solutions section) was added to wash recover remaining cells from the strainer and obtain a single cell suspension. Cells were counted and stained for FACS analysis.

5.3.3.2 Isolation of splenocytes

C57BL/6 mouse spleens were removed and stored in ice-cold RPMI-1640 (Invitrogen). The organs were crushed and strained through an 80 μm metal mesh (Sefar Ltd, UK) into the respective labelled tubes (Falcon 15 ml). Immediately after, FACS buffer was added to recover all the cells from the strainer and obtain a single cell suspension. Cells were centrifuged at 1400 rpm at 4^{o} C for 5 minutes. The red blood cells were destroyed by lysis with 500 μl of ammonium-chloride potassium (ACK) lysis buffer (Invitrogen) incubated at 37 ^{o}C for 5 minutes. Afterwards, the cells were washed in two steps by centrifugation at 1400 rpm at 4 ^{o}C for 5 minutes with FACS buffer to eliminate any remaining debris of blood cells and wash out the lysis buffer.

5.3.3.3 Lymphocyte extraction from the dermis and epidermis

The extraction of the skin cells from the dermis and epidermis of the C57BL/6 involved the following steps. First, the ears were divided into dorsal and ventral sides. The separation was done mechanically using forceps. Each halve was then digested enzymatically in a process involving two steps. In the first step, 5 U/ml dispase I (BD) in phosphate buffer solution (PBS) for 90 min at 37°C to allow for epidermal and dermal separation. In the second step, 1 mg/ml collagenase D (Sigma-Aldrich) in PBS for 45 min at 37°C was added to release cells from the skin matrix. At last, the tissues were filtered through an 80-μm stainless steel mesh to obtain single-cell suspensions.

5.3.3.4 Isolation of γδ lymphocytes from adult thymus

Adult C57BL/6 mouse thymuses were obtained by dissection and re-suspended in plain fresh RPMI-1640 (Invitrogen). The thymuses were crushed with a pestle and strained using a 80 μm cell strainer (Sefar Ltd, UK). The cell suspensions were made up to 7 ml with RPMI and 500 μl of hybridoma supernatant was added (a mix of anti-CD4 and anti-CD8 antibodies IgM isotype for complement lysis). The cell suspensions were incubated at 37 °C for 10 min. 1 ml of resuspended complement (Cedar lane Laboratories) was added and mixed by inversion. Cell suspensions were then incubated with complement at 37 °C for 30 min. To separate live thymocytes, including DN cells, from dead complement-lysed thymocytes that were $CD4^+$ and/or $CD8^+$, lymphocyte separation medium (MP Biomedical) was layered underneath each cell suspension. Tubes were centrifuged for 20 min at 1,600 rpm at room temperature in a bench-top centrifuge with no brake. Live thymocytes were removed from the Ficoll interface by pipetting the interface out using a glass Pasteur pipette and transferred to a FACS tube. Lysed dead cells, i.e. cells that expressed CD4 and/or CD8, form a pellet at the

bottom of the tube. The cells were washed with FACS buffer before staining for analysis in the LSRII flow cytometer.

5.3.3.5 Phoenix (ØNX) Ecotropic Packaging Cell line

Phoenix Ecotropic (phoenix) cells were kindly provided by the Nolan Laboratory (www.stanford.edu/group/nolan/). The cells were cultured in Phoenix media (see solutions section) at 37 °C and 5% CO2. For healthy cells, cultures were split when cells reached 70-80% confluency. Cells were frozen in foetal calf serum (FCS) containing 10% DMSO (Sigma), and aliquots were stored at -80 ^{o}C.

5.3.3.6 Transfection of Phoenix cells

18-24 hours prior to transfections, approximately 1 x 10^6 phoenix cells were plated per 60 mm x 15 mm culture dish (Corning) in 7 ml of culture media, for 60% confluency at the time of transfection. 2 μg of plasmid DNA was used for transfection. Fugene-6 reagent (Roche) was used for transfections. A DNA-Fugene complex was prepared with a 3:1 ratio (μl Fugene: μg DNA) in DMEM with a total volume of 200 μl. The 200 μl transfection complex was added drop wise to cells and left to incubate for 48 h at 37 ^{o}C and 5% CO_2. Two days after transfection, the cells were removed from 60 mm x 15 mm plates containing Fugene and plated in T175 flasks (BD-Falcon) in 25 ml phoenix media with 2 μg/ml of Puromycin (Sigma). Puromycin selection allows for stable transfection of the packaging cell line. Cells were cultured at 37 °C, 5% CO_2 until they reached 70-80 % confluency, then split or harvested the retroviral supernatants. Cells transfected with pLZ vectors were visualised under the UV microscope to check GFP expression.

5.3.3.7 Harvesting Retroviruses

Removal of growth medium containing puromycin from cells was necessary for harvesting retroviral supernatants. 25 ml of filtered-sterilized DMEM with 20% HI-FCS was added to the cells. This media did not contain antibiotics. Cells were incubated overnight at 32 °C. The media on the cells or the supernatant contains the viral particles produced by the cell line. This retroviral supernatant was collected the following day and kept on ice. The supernatants were centrifuged for 3 minutes at 1,000 rpm using a bench top centrifuge to remove any cells; and then filtered using a 0.45 μm filter (Millipore). 1 ml of the filtered supernatant was aliquoted into 1.5 ml Eppendorf tubes. The retroviruses were concentrated by centrifuging the 1 ml aliquots at 13,000 rpm in a table-top micro centrifuge for 45 mins at 4 °C. The surface liquid was discarded and 125 μl of the retroviral "pellet" from 10 aliquots were pooled into one. Concentrated supernatants were frozen and stored at -80 ^{o}C until used for transduction.

5.3.3.8 Retroviral transduction of E15 thymocytes (Retronectin)

Immature E14 or E15 thymocytes were transduced with retroviruses in the presence of a surface-bound transduction enhancer Retronectin (RN-Takara Bio Inc). 35 mm x 10 mm tissue culture dishes (Corning) were coated with 12 μg/ml of RN in 1 ml PBS (Invitrogen). Dishes were incubated at room temperature for 2 h then blocked with 2% BSA (Sigma) for 30 mins before washing twice with 1 ml PBS. E15 embryos were dissected and their thymic lobes were extracted using Dumont forceps (Sigma-Aldrich) and a dissection microscope. The lobes were crushed in 1.5 ml Eppendorf tubes containing 250 μl FTOC media (See solutions section) using a conical tissue homogenizer and strained to make a single cell suspension. The E15 thymocytes were counted and made up to 1 ml in FTOC media. Each 1 ml ali-

quot of cells was then added to 1 ml of thawed, concentrated retroviral supernatant in a FACS tube and mixed. The retrovirus/ thymocyte mixture was added to RN coated plates and incubated at 37 °C for 5 h for transduction to take place.

5.3.3.9 Retroviral transduction of E15 thymocytes (Spinoculation)

1 hour prior to transfection a bench top centrifuged was equilibrated to 37 ºC by holding at 2000 x g. Immature E15 thymocytes were isolated from the thymus and counted in the haemocytometer. The thymocytes were aliquoted into several FACS tubes depending on the number of conditions and centrifuged 1500 rpm for 5 minutes. During the centrifugation the viral stocks was thawed in 37 ºC water bath. The media from the thymocytes was decanted and the cells were mixed with the neat virus stock produced in the protocol described above (See section 1.3.6). 200 µl/ well of 96 well U-bottom plates were aliquoted and then centrifuged at 1000 xg at 37 ºC for 2 hours. After the centrifugation, the plates were carefully removed from the centrifuge and incubated at 37 ºC with 5% CO_2 for 1 hour. Once the incubation was finished, the cells were washed three times (200 µL/ well each time) with room temperature PBS, re-suspend in OP9-DL1 media and incubated at 37 ºC with 5% CO_2 until the analysis by flow cytometry.

5.3.3.10 Foetal thymic organ culture (FTOC)

Mouse embryos were harvested from time-mated, pregnant female C57BL/6 mice at E15-days post-conception (E15) and separated from one another. The individual embryos were cut transversely using scissors and washed with 1X PBS. Using a dissecting microscope, thymic lobes were extracted with Dumont tweezers (Sigma-Aldrich) and transferred to a drop of 1X PBS on a petri dish. Up to 4 thymic lobes were placed on a nucleopore membrane filter (Whatman) in 3 ml-filtered FTOC media (See solution section) in 6 well plates. FTOCs were incubated at 37 ^{o}C in 5% CO_2 for 7-12 days (otherwise will be specified in the text). On the day of processing, thymic lobes were collected in 1.5 ml tubes, gently crushed using a pestle, and filtered through a 40 μm cell strainer to obtain a single-cell suspension. Subsequently, cells were counted using a haemocytometer and stained for FACS.

5.3.3.11 OP9-DL1 cultures

The OP9-DL1 cell line was kindly provided by the Zuniga-Pflucker laboratory. OP9-DL1 stromal cell line[264] is a bone-marrow derived preadipocyte cell line (OP9) that was retrovirally transduced to express Delta-like-1 (DL1), a Notch ligand, to support growth and differentiation of lymphocyte progenitors. DL1 is expressed from bicistronic vector that has GFP as reporter gene. OP9-DL1 cells were cultured in OP9-DL1 media (see solutions section, Table 5-9) at 37 °C and 5% CO_2. For healthy cells, cultures were split, using trypsin (Invitrogen) when cells reached 75% confluency, normally a 1:4 or 1:5 passage every two days. Cells were frozen in HI-FCS (Invitrogen) with 10% DMSO (Sigma), and aliquots were stored at -80 ^{o}C.

5.3.3.12 OP9-DL1 and thymocyte co-cultures

18-24 hours prior to transfections, a 75% confluent cells were transferred to 6 well plates in 4 ml of media for 75% confluency at the time of transfection. Following the 5 h transduction of E15 thymocytes, the cells were removed from the retronectin coated plates (see section 2.5) by repetitive pipetting. 1ml of cell suspension was pelleted by centrifugation at 2,500 rpm for 2 minutes in 1.5 ml tubes. The supernatant was removed and the second 1 ml of cell suspension was added to the pellet and centrifuged again. The retronectin plates were then washed with 1 ml OP9-DL1 media to ensure that all the cells had been collected. After the wash cells were re-suspend in 1 ml OP9-DL1 media and 5 ng/ml of Flt3 ligand and 1 ng/ml of IL-7 (both Miltenyi Biotech) were added to the media. 1 ml of media was removed from the OP9-DL1 cultures and 1 ml solution containing the thymocytes and the cytokines was added to the semi-confluent monolayer of OP9-DL1. Cultures were incubated for 6-7 days at 37 ^{o}C, 5% CO_2.

5.3.3.13 Analysis of cells in OP9-DL1 cultures

Thymocytes were removed from the monolayer of OP9-DL1 cells by vigorously and repetitive pipetting. The cell suspension was filtered using a 40 μm cell strainer into a 1.5 ml Eppendorf tube and then centrifuged for 5 minutes at 1,400 rpm on a bench-top centrifuge. The supernatant was removed and the cells were re-suspended in 100 μL of FACS buffer and stained for extracellular markers as described in section 1.7.14.1.

5.3.3.14 Staining protocols for FACS

5.3.3.14.1 Extracellular staining

Between 1 and 10 x 10^6 cells were filtered through a 40 μm strainer (BD) and transferred to a fresh FACS tube (Becton, Dickinson and Company, BD). The tubes were centrifuged and cells were re-suspended in 100 μl FACS buffer. All antibodies were used at 1:200 dilution, unless otherwise stated in the text, and samples were stained at room temperature in the dark for 45 minutes (Table 5-8). The viability reagent Zombie Aqua Fixable dye (1:200 dilution, Biolegend) was also included in the staining cocktail for dead cell exclusion. After staining, cells were washed with FACS buffer by centrifugation at 1400 rpm for 5 minutes at room temperature and then re-suspended in 200 μl of FACS buffer.

5.3.3.14.2 Mouse antibodies used in this project

Protein	Clone	Fluorochrome	Supplier
TCRδ	GL3	PerCp5.5	eBioscience
TCRδ	eBioGL3	APC	Invitrogen
TCRδ	GL3	Pe-Cy7	Biolegend
TCRβ	H57-597	PerCp5.5	eBioscience
CD24	M1/69	PB	eBioscience
MHC-II	M5/114.15.2	PeCy7	eBioscience
CD25	PC61	PeCy7	eBioscience
CD44	IM7	V500	eBioscience
CD45	30-F11	PE	Biolegend
CD8α	53-6.7	APCCy7	Biolegend
Vγ4	UC3-10A6	APC	eBioscience
Vγ1 (Vγ1.1)	2.11	PE	Biolegend
Vγ5 (Vγ3)	536	PE	Biolegend
CD45RB	C363-16A	APCCy7	Biolegend
Zombie Aqua	NA		Biolegend
TruStain fcX	93	NA	Biolegend

Table 5-8. Antibodies used in this thesis. The antibodies are anti-mouse and the clone and supplier are shown. APC, allophycocyanin; Cy, cyanine dye; PE, phycoerythrin; PerCP, peridinin chlorophyll protein; PB, pacific blue; TCR is T cell receptor, MHC-II, major histocompatibility complex II.

5.3.3.14.3 Compensation

Single colour controls were run before each experiment to set up the voltages and to be used to compensate for spillover in between the fluorochromes. The compensation was carried out semi-automatically with the FlowJo software. For the single colour control 15 µl of OneComp eBeads (eBioscience) were stained with 1 µl of antibody in 100 µl of FACS buffer.

5.3.3.14.4 Gating strategy

All lymphocytes were identified based on their size (Forward scatter, FSC) and granularity (Side scatter, SSC). Afterwards, doublets (FSC-area vs FSC-height and SSC-area vs SSC-height) and dead cells were gated out.

5.3.3.14.5 FACS acquisition

The acquisition of the flow cytometry data was done using a LSR-II Flow Cytometer (BD Bioscience) through FACSDIVA software (BD Bioscience).

5.3.3.14.6 FACS analysis

FACS data were analysed using the FlowJo software Version 10 (Tree star).

5.3.4 Mice

C57BL/6 (B6) mice were purchased from Charles River Laboratories. RAG-$2^{-/-}$ were bred in house. The embryos were obtained by setting up timed-pregnancies. All animals were bred and maintained in individually ventilated cages (IVC) at Barts and the London School of Medicine and Dentistry. All experiments involving animals were performed in compliance with relevant Home Office UK laws and institutional guidelines approved by a local ethics committee.

5.3.5 Solutions section

Solution	Composition
OP9-DL1 Medium	DMEM with Glutamax, 10% HI-FCS, 1% Pen/Strep, 1% NEAA, 50µM 2-mercaptoethanol (all Invitrogen)
FTOC media	RPMI, 1% Pen/strep, 2mM L-glutamine, 50µM 2-mercaptoethanol – (all Invitrogen), 10% FCS (Stem Cell Technologies)
FACS buffer	2% HI-FCS in PBS (both Invitrogen)
TAE (50x)	2M Tris pH8 (Sigma), 50 mM EDTA (Invitrogen), 1M glacial acetic acid (Sigma)
dNTP mix	2.5 mM dATP, 2.5 mM dTTP, 2.5 mM dGTP and 2.5 mM dCTP (Takara Bio-Clontech)

Table 5-9. Solutions used in this study.

5.4 RESULTS

5.4.1 Experimental approach

To evaluate the relationship between the molecular characteristics of TCRγδ and the acquisition of γδ effector function during thymic development of γδ T cells, we want to establish a system in which we could express a TCRγδ restricted to the IL-17 effector popula-

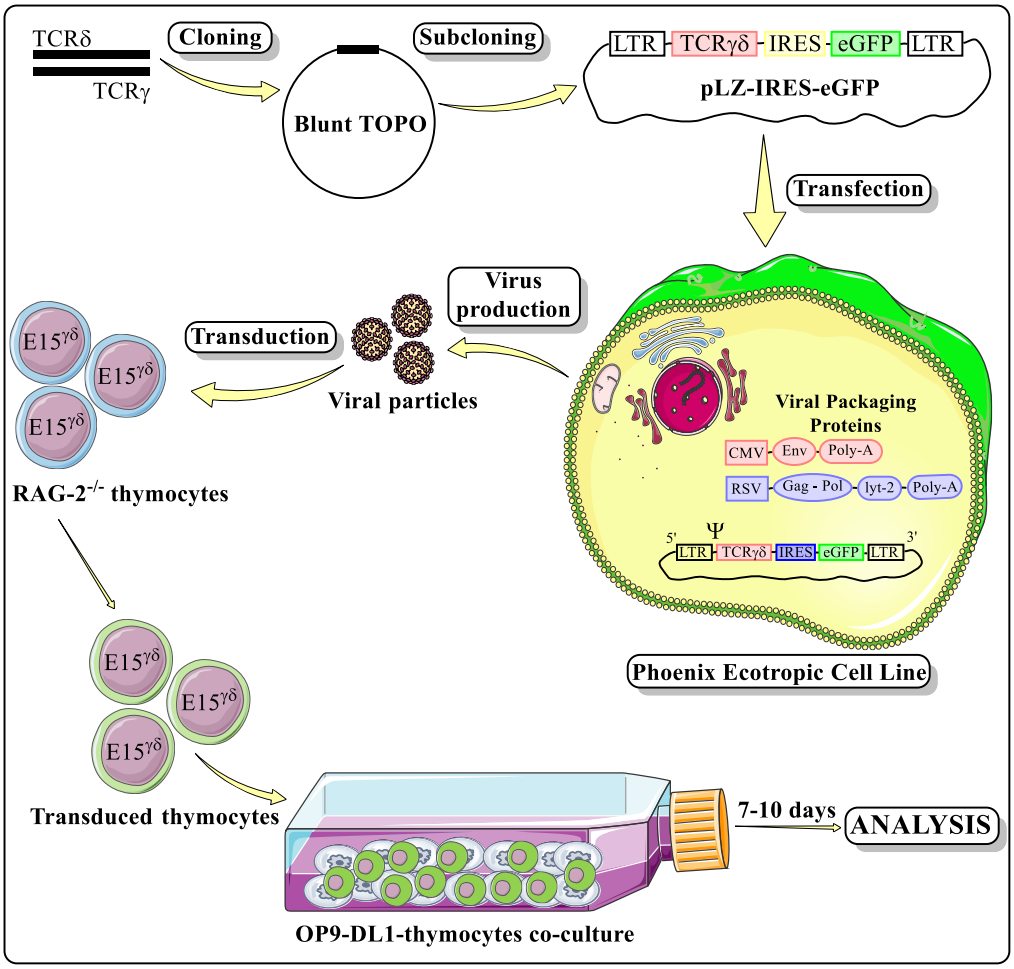

Figure 5-10. Graphic representation of the experimental plan. TCR chains were cloned into Blunt-TOPO vector and subcloned into the retroviral vector. This plasmid was transfected into the Phoenix ecotropic packaging cell line. Retroviral particles were collected and used to infect E15 RAG-2$^{-/-}$ thymocytes. The transduced cells were seeded onto a monolayer of OP9-DL1 cells and cultured for 7 to 14-days. LTR, long terminal repeat; eGFP, enhanced green fluorescent protein; IRES, internal ribosomal entry site; CMV, cytomegalovirus; env, envelope protein; RSV, Rous sarcoma virus; Gag, group antigens.

tion (TCRγδ$^{IL\text{-}17}$) in thymocytes from E15 Rag2$^{-/-}$ mice, that cannot rearrange and therefore express endogenous TCR chains.

Retroviral particles were generated to deliver the TCRγδ$^{IL\text{-}17}$ chains into γδ progenitors. The general approach is illustrated in Figure 5-10.

The retroviral vector[306] used in this study, pLZRS-IRES-eGFP (pLZ), possesses two long terminal repeats (LTRs) flanking the multiple cloning site (MCS). These LTRs mediate the integration of the cloned TCRγδ into the host genome and act as promoters for the transcription of the cloned receptor. In addition, between the LTRs but downstream of the multiple cloning site (See Figure 5-14), the retroviral plasmid contains an internal ribosomal entry site (IRES) sequence followed by the gene encoding the reporter enhanced green fluorescent protein (eGFP). The IRES sequence will allows the independent translation of the eGFP reporter alongside the cloned TCRγδ.

The retroviral vector was transfected into the Phoenix (ØNX) Ecotropic cell line[307]. The ØNX Phoenix cell line is a retrovirus producer system based on 293T cells. The cells contain constructs that allow the stable expression of viral proteins, i.e. gag, pol and env, derived from the Moloney Murine Leukemia Virus. The expression of the viral proteins is controlled by different promoters, reducing the chances of inter-recombination and production of the empty helper virus. The incorporation of the retroviral vector into the viral capsid is mediated by the packaging Psi (Ψ) sequence located in the 5-LTR of the retroviral plasmid.

Retroviruses collected from the supernatant of cultured ØNX phoenix cells were used to transduce E15 thymocytes. The transduction was performed with Retronectin (Clontech). Retronectin is a recombinant human fibronectin fragment (rFN-CH-296) that contains three

functional domains: the cell-binding domain, the heparin-binding domain, and the CS-1 sequence, which allow the enhancement of lentiviral- and retroviral-mediated gene transduction by aiding the co-localization of target cells and viral particles.

In addition to Retronectin, we also performed the transduction using the Spinoculation[308] method. It has been shown that retroviral infection can be substantially improved by centrifugal inoculation (spinoculation) although the underlying mechanism of enhancement is unclear[309].

The transduced thymocytes were then transferred to a monolayer of OP9-DL1 cells to allow for their development in culture from for 7 to 14-days post-transduction. After the incubation period, the cells were stained and analysed for the expression of the cloned TCRγδ by flow cytometry.

5.4.2 Cloning of the TCRγδ^{IL17} receptor.

As described above, we aimed to determine how a TCRγδ^{IL17} composed of a canonical Vγ4Jγ1 and a germline-rearranged Vδ5Dδ2Jδ1 chains restricted to CCR6^{+} CD27^{-} Vγ4^{+} T cells directs the development of Rag2$^{-/-}$ E14 fetal thymocytes towards a certain effector phenotype. Therefore, in the next sections the steps carried out to clone and assemble the TCRγδ^{IL17} are described.

5.4.3 Construction of the TCRγ chain

The primary structure i.e. amino acid sequence of the TCRVγ4 chain used in this study consisted of 330 residues and is represented in Figure 5-11. As mentioned in the Methods (Section 5.3.1.6) the construction of the TCRVγ4 chain was engineered by a procedure that involved three steps, illustrated in Figure 5-12.

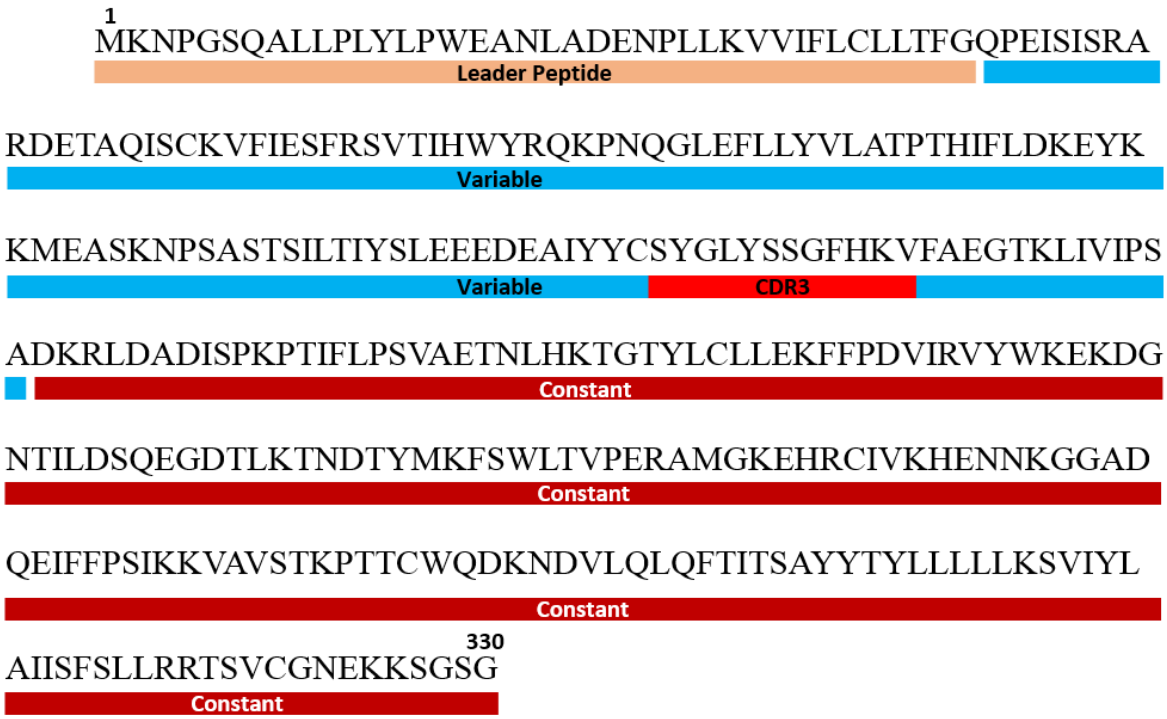

Figure 5-11. Schematic representation of the primary structure of TCRVγ4 chain. The line shows the aminoacid sequence of the Vγ4 chain that will be assembled. The different colours represent different regions of the TCRVγ4 chain; leader peptide in orange, variable region in blue, constant region in dark red. The CDR3 is highlighted in bright red.

Plasmids (obtained from Immo Prinz, Hanover Medical School) containing the Vγ4Jγ1 and the Cγ1-P2A sequence were linearized with the restriction enzymes AgeI-PacI and Mlul-PflMl (step not shown, see enzymes on Table 5-3). In the first step (see Figure 5-12, step 1), the linearized products were used as templates for two PCRs: reaction 1, PCR with primers Fp3γ/Rp4γ which generated product 7 (Vγ4Jγ1, 381 bp), and reaction 2, PCR with primers Fp1γ/Rp2γ which generated product 6 (Cγ1-P2A, 585 bp) (see Table 5-5) respectively. Of note, primer Rp4γ had an overhanging sequence of 33 bp that was complementary to the Cγ1-P2A fragment. The PCR products were purified in agarose gel and extracted (Figure 5-13 B). In the second step, (Figure 5-12, Step 2), both gel-extracted and purified products Vγ4Jγ1 (product 7) and Cγ1-P2A (product 6) were used as templates in the next PCR. After denaturation of the DNA fragments, the single strands of each fragment will be hybridized by their 33 bp overlapping end, and this region acts as a primer for the amplification of the annealed product. The amplification of the assembled fragments Vγ4Jγ1Cγ1-P2A (product 8) (933 bp) is driven by primers Fp3γ/Rp2γ. The PCR product was run in agarose gel and extracted (Figure 5-13 C). To evaluate the successful assembly of the fragments, product 8 was sequenced by Sources Biosciences. In the third step (Figure 5-12, step 3), the leader peptide sequence was added to product 8. The TCRVγ4 leader peptide sequence was obtained from the international ImMunoGeneTics information system (IMGT). The single strand oligonucleotide (117 bp) molecule was chemically synthetized by the Eurofins Company. In a similar approach, the single strand was used as a template for PCR to generate the double strand leader peptide (product 9) with primers Spfg1/Sprg2 (Figure 5-13 A). Of note, primer Sprg2 contains a 29 bp overhanging sequence that is complementary to product 8. An additional PCR was set up with product 9 and product 8 as templates to generate product 10

(LeaderVγ4Jγ1Cγ1-P2A, 1062 bp) (Figure 5-13 D). After denaturation, the single strands of product 8 and product 9 are hybridized via their 29 bp complementary sequence and this fragment acts as a primer in the amplification of the chains. The final amplification of the LeaderVγ4Jγ1Cγ1-P2A (product 10) is driven by primers Spfg1/Rp2γ.

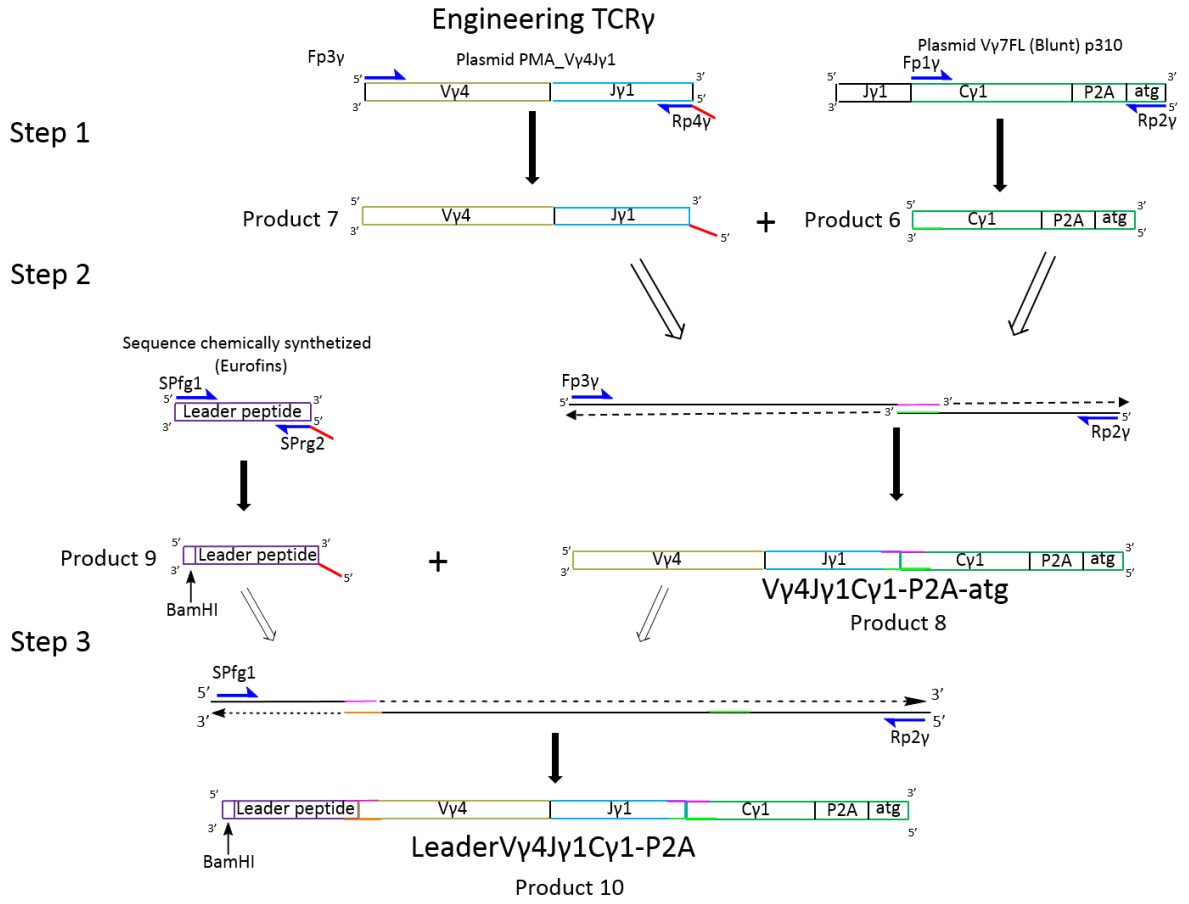

Figure 5-12. Experimental approach to engineer the construction of the TCRγ chain. Two plasmids containing the Vγ4Jγ1 and the Cγ1-P2A were used as initial templates. In the first step the linearized plasmids were used as templates in two PCRs to generate multiple copies of the Vγ4Jγ1 (product 7) and the Cγ1-P2A (product 6) fragments. The primer Rp4γ contains an overhanging sequence of 33 bp that is complementary to the first 33 bp of the product 6. In step 2, products 6 and 7 were denatured and used as templates for the PCR; the single strands hybridize via their 33bp overlap, and subsequent amplification was driven with the primers Fp3γ/Rp2γ to obtain the fragment Vγ4Jγ1Cγ1-P2A (product 8). In the last step, the leader peptide (product 9), that contains a 29 bp overhanging sequence complementary to the Vγ4 fragment was used together with product 8 as templates in a new PCR. After denaturation, the single strands hybridize via their 29 bp complementary sequence and the fragment is further amplified with the set of primers Spfg1/Rp2γ. The primers Spfg1 contain the restriction site for the BamHI that will be used for the cloning of the full construct into the vector.

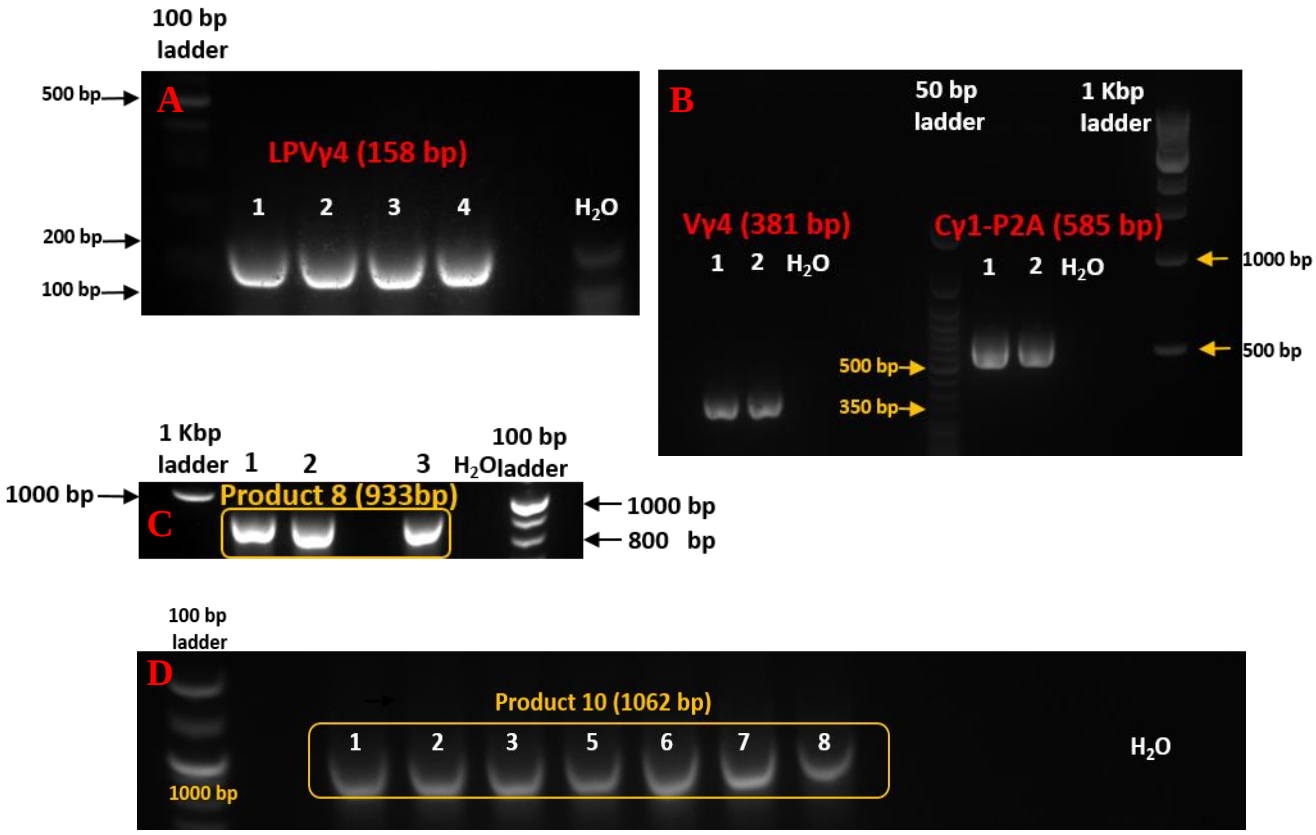

Figure 5-13 Agarose gels showing the PCR products generated in the construction of the TCRVγ4 chain. **A)** Leader peptide of the Vγ4 chain (LPVγ4) (Product 9) with molecular weight of 158bp. **B)** Fragments Vγ4 (381bp) that contains the sequence Vγ4Jγ1 (Product 7) and Cγ1-P2A with a molecular weight of 585bp (Product 6). **C)** Fragment Vγ4Jγ1Cγ1-P2A-atg of 933bp denominated Product 8. **D)** Fragment LeaderVγ4Jγ1Cγ1-P2A-atg (Product 10) with a molecular weight 1062bp represents the final product in the construction of the TCRVγ4 chain. The number of the products are indicated alongside with the size of the fragments. For each PCR the control negative (H_2O) is also indicated together with the molecular ladder. The number on top of the bands indicates the number of PCR replicas that were run to generate enough product for the next step.

5.4.4 Construction of the TCRδ chain

In a very similar approach to that described in the previous section, we tackled the synthesis of the TCRVδ5 chain. The primary structure is made of 292 aminoacid residues, which is represented with a one-letter code in Figure 5-14. The joining of the fragments for the construction of the TCRVδ5 chain was engineered also in three steps, similar to the procedure described in the section 5.3.1.7 and is illustrated in Figure 5-15.

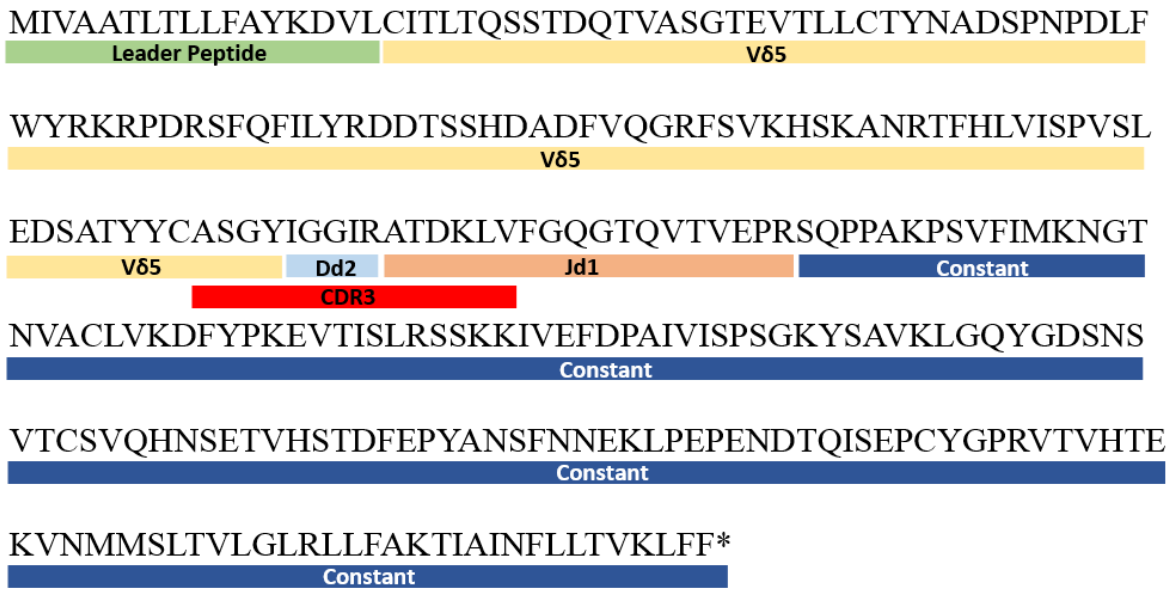

Figure 5-14. Schematic representation of the TCRVδ5 chain. The line shows the primary sequence of the TCRδ chain that will be assembled. The different colours represent the different regions of the TCRVδ5 chain; leader peptide in green, variable delta 5 in yellow, diversity region in light blue, joining region in pale red, and the constant region in dark blue. The CDR3 is highlighted in red.

The cloning of the TCRVδ5 chain was accomplished in three steps (Figure 5-15). Before step 1 the plasmids containing the Vδ5Dδ2Jδ1 and the Cδ1 sequence were linearized with the restriction enzymes AgeI-PacI and MluI-PvuI, respectively (Not shown, See Table 5-3). In the first step, the linear products were used as a template for two PCRs with primers Fp3δ/Rp4δ and Fp1δ/Rp2δ (See Table 5-6) to generate the fragments Vδ5Dδ2Jδ1 (product 2) and the Cδ1-vector (product 1), respectively (Figure 5-15, step 1). The primer Rp4δ contains an overhanging sequence of 23 bp that is complementary to the Cδ1 fragment. The PCR products were purified in agarose gel and extracted. The Vδ5Dδ2Jδ1 (product 2) is a fragment of 385 bp and the Cγ1-vector (product 1) of 585 bp (Figure 5-16 A). In the second step (Figure 5-15, step 2), both products Vδ5Dδ2Jδ1 and the Cδ1-vector were used as templates in the next PCR. After denaturation of the DNA fragments, the single strands of each fragment hybridize by their 23 bp overlapping ends, and this region acts as a primer for the amplification of the annealed sequence. The amplification of the assembled fragments Vδ5Dδ2Jδ1Cδ1-vector (Product 3) (877 bp) is driven by primers Fp3δ/Rp2δ (Figure 5-16 B). Before the third step, the leader peptide (Product 4) was amplified with primers Fp7δ/Rp6δ. Rp6δ contains an overhanging sequence of 27 bp that is complementary to Vδ5Dδ2Jδ1Cδ1-vector (product 3). The third step (Figure 5-15, step 3), was performed with Vδ5Dδ2Jδ1Cδ1-vector (Product 3) and leader peptide (Product 4) as templates. After denaturation, the fragments hybridize via their 27 bp complementary sequence and this fragment acts as a primer for the amplification of the chains. The final amplification of the LeaderVδ5Dδ2Jδ1Cδ1-vector (product 5) (Figure 5-16 C) is driven by the set of primers Fp7δ/Rp2δ. Importantly; the Fp7δ contains a 27 bp sequence that is complementary to the Cγ1-P2A fragment that will be used to engineer the assembly of both TCR chains illustrated in Figure 5-17. To evaluate

the successful assembly of product 5 the PCR fragment was sequenced by Sources Biosciences with 100% match between the expected and the synthetized sequences.

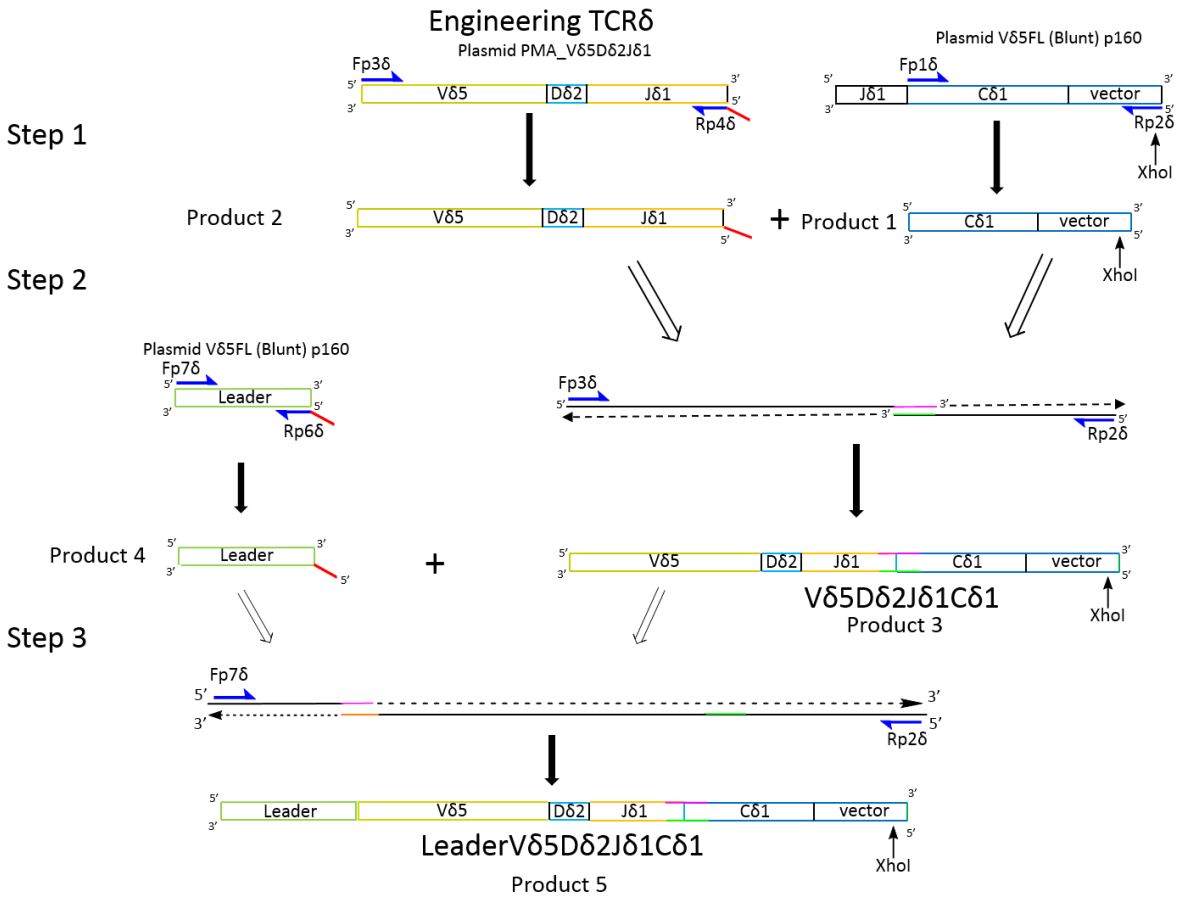

Figure 5-15. Experimental approach to engineer the TCRδ chain. Two plasmids containing the Vδ5Dδ2Jδ1 and the Cδ1, respectively were used as initial templates. In the first step the linearized plasmids were used as templates in two PCRs to generate multiple copies of the Vδ5Dδ2Jδ1 (product 2) and the Cδ1-vector (product 1) fragments. The primer Rp4δ contains an overhanging sequence of 23 bp that is complementary to the first 23 bp of the product 1. In the step 2, products 1 and 2 were denatured and used as templates for the PCR; the single strands hybridize via their 23bp overlap, and subsequent amplification was driven with the primers Fp3δ/Rp2δ to obtain the fragment Vδ5Dδ2Jδ1Cδ1-vector (product 3). In the last step, the leader peptide (product 4), that contains a 27 bp overhanging sequence complementary to the Vδ5 fragment was used together with product 3 as templates in a new PCR. After denaturation, the single strands hybridize via their 27 bp complementary sequence and the fragment is further amplified with primers Fp7δ/Rp2δ. The primers Rp2δ contain the restriction site for XhoI that will be used to clone the full construct into the vector.

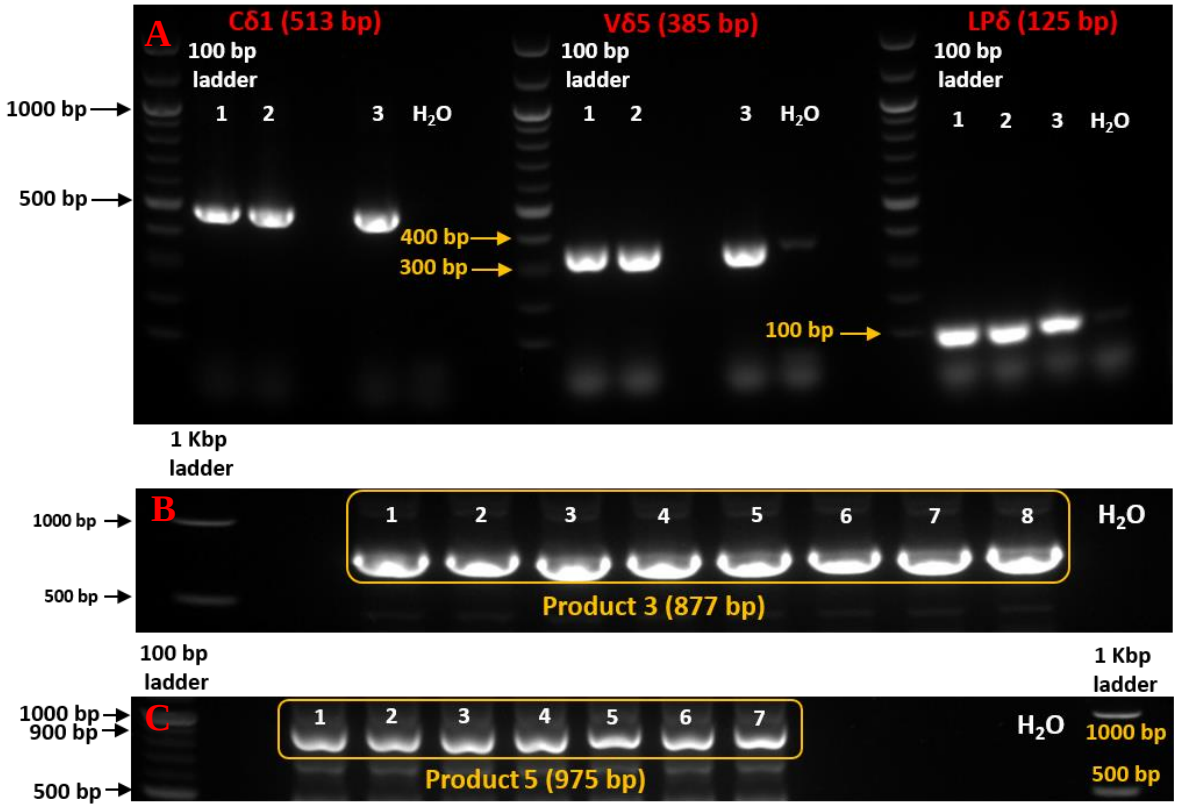

Figure 5-16 Agarose gels showing the PCR bands corresponding to the different fragments amplified for construction of the TCRVδ5 chain. **A)** In this panel (from left to right) is represented the bands corresponding to the fragment Cδ1 (513bp) (Product 1), Vδ5 (385bp) that enclosed the Vδ5Dδ2Jδ1 (Product 2), and LPδ (125bp) that represent the leader peptide (Product 4). **B)** This panel shows the eight bands corresponding to the fragment Vδ5Dδ2Jδ1Cδ1 (877bp) (Product 3). **C)** Panel showing the fragment LeaderVδ5Dδ2Jδ1Cδ1-vector (975bp) Product 5 and final fragment in the synthesis of the TCRVδ5 chain. The name of the product and the molecular weight of each fragment is indicated on the top of the bands. The negative control of each PCR (H_2O) is also shown as reference together with the molecular ladder. The figure on top of the bands indicates the number of the replica amount loaded in the gel.

5.4.5 Assembly of the TCRγ and TCRδ chains

The TCRγ-2A-TCRδ construct was generated following the same overlapping ends PCR methodology described above for the synthesis of the TCRγ and TCRδ chains (Figure 5-17. The fragment denominated LeaderVγ4Jγ1Cγ1-P2A (Product 10) and the amplicon called LeaderVδ5Dδ2Jδ1Cδ1-vector (Product 5) were used as templates in a new PCR. The product 5 contains an overhanging sequence of 27 bp that is complementary to the P2A sequence in Product 10, and will act as a primer for the assembly of the single strands of TCRγ and the TCRδ fragments upon denaturation. The final amplification of the annealed fragment will be driven by primers Spfg1 and Rp2δ, which contain the restriction sites for BamHI and XhoI, at the 5', and the 3' ends, respectively. These restriction sites are going to be used in the cloning of the TCRγ-2A-TCRδ construct into the retroviral vector pLZ-IRES-eGFP. To ascertain whether the joining of both fragments, Product 5 and Product 10, is correct, we designed the primer 5'-CTGCCTACTACACCTACCTT-3', called joining primer (see Figure 5-17). This primer will bind the Cγ1 sequence; specifically the region located 119 bp before the 2A motif and will allow the amplification of the stitching zone. The sequence data obtained from Source Biosciences demonstrated the joining of the LeaderVγ4Jγ1Cγ1-P2A (Product 10) and LeaderVδ5Dδ2Jδ1Cδ1-vector (Product 5) was achieved successfully and we have now generated the final construct TCRγ-2A-TCRδ (see Appendix).

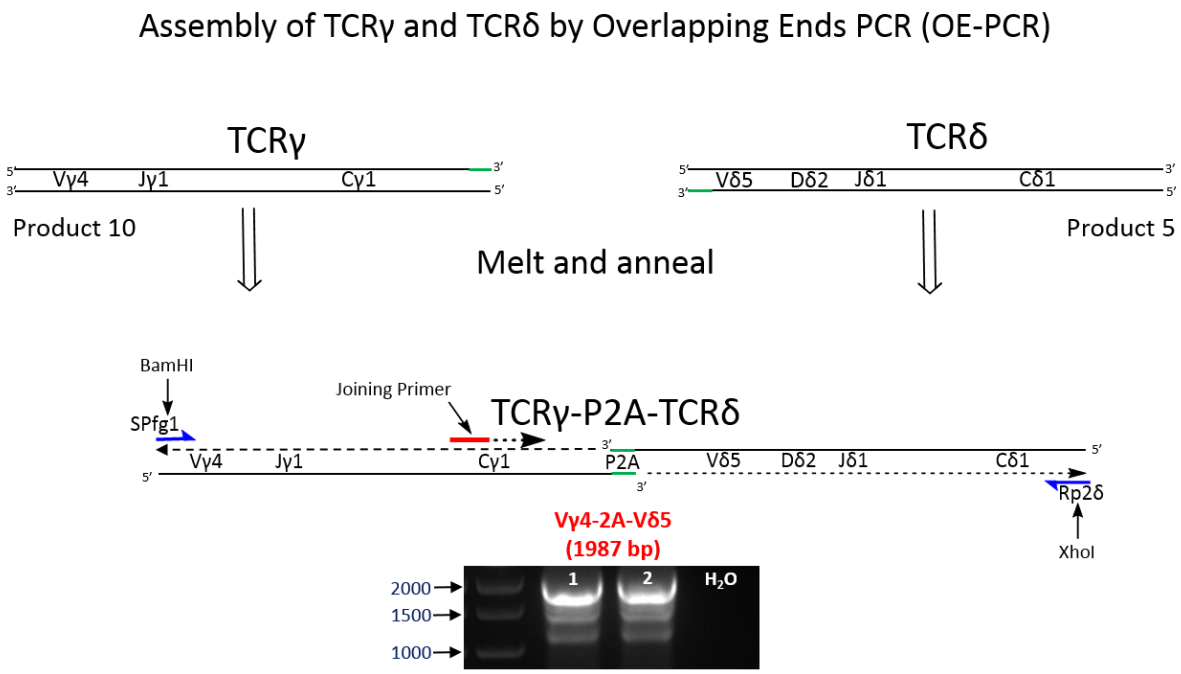

Figure 5-17. Scheme of the experimental approach used to engineer the final product TCRγ-2A-TCRδ. The TCRγ and TCRδ fragments were joined in one step overlapping ends PCR. The LeaderVγ4Jγ1Cγ1-P2A (Product 10) and LeaderVδ5Dδ2Jδ1Cδ1-vector (Product 5) were used as templates together with the SPfg1 (containing BamHI) as forward primer, and Rp2γ as reverse primer. Product 5 was engineered to contain a 27 bp complementary overhanging sequence to the P2A within the Product 10. The final product TCRγ-2A-TCRδ (1987 bp) includes restriction sites for BamHI and XhoI at the 5'and 3' ends, respectively. These two restriction sites were inserted by homology to primers Spfg1 and Rp2δ. The joining primer (shown as a red line) was used check the stitching of both fragments was successful. Agarose gel showing the final product Vγ4–2A-Vδ5 that contains the desired TCRγδ$^{IL\text{-}17}$ (1987bp) and the negative control (H_2O) (size of the fragment is indicated).

5.4.6 Cloning the Vγ4-2A-Vδ5 into BLUNT TOPO and pLZ-IRES-eGFP

The blunt ended Vγ4-2A-Vδ5 PCR fragment was cloned into the pCRII-Blunt-TOPO vector and transformed into the DH5α E-Coli strain. After isolation by Maxiprep, the plasmid was analysed for the presence of the Vγ4-2A-Vδ5 insert. For the analysis, we performed a double digestion of the TOPO plasmid with the restriction enzyme EcoRI, which was cut at each end of the Blunt PCR product (see Figure 5-8), releasing a linear fragment containing the Vγ4-2A-Vδ5 insert. The digested product was tested in a new PCR reaction with primers Spfg1/Rp2δ in a similar approach as described in the Section 5.4.5 and Figure 5-17. The analysis of the PCR reaction illustrated in Figure 5-18 A, revealed a band with a molecular weight near 2000 bp that is in agreement with the expected size of the Vγ4-2A-Vδ5 fragment (1987 bp). Moreover, we decided to double check whether the cloning reaction was successful by performing a double digestion of the pCRII-Blunt-TOPO vector containing the Vγ4-2A-Vδ5 with BamHI and XhoI. As mentioned in section 5.4.5, these two restriction sites were introduced into the sequence of the final construct Vγ4-2A-Vδ5 to facilitate its directional insertion during the cloning reaction into the retroviral backbone (see Figure 5-9). The theoretical analysis of the digestion products of the TOPO plasmid containing the Vγ4-2A-Vδ5 predicts two bands of 3519 and 1961 bp, corresponding to the linearized TOPO vector and the Vγ4-2A-Vδ5, respectively (see Methods, Figure 5-8). The analysis of the gel indeed revealed (Figure 5-18 B) two bands that co-localize near the ladder and correspond to the expected molecular weight of the fragments.

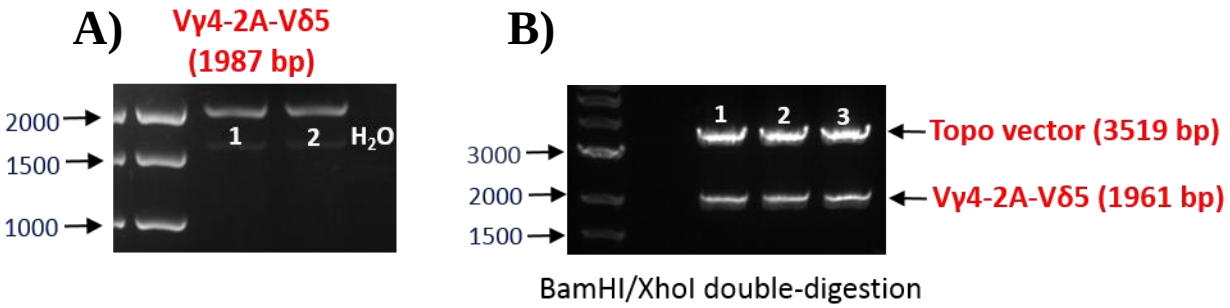

Figure 5-18. Agarose gel electrophoresis. **A)** Analysis of the product of the digestion reaction of pCRII-Blunt-TOPO vector containing the Vγ4-2A-Vδ5 construct with EcoRI. The two bands, corresponding to the same reaction co-localize near 2000 bp on the ladder, which is in agreement with the expected molecular weight of the Vγ4-2A-Vδ5 fragment (1987 bp). **B)** Double digestion of the pCRII-Blunt-TOPO vector containing the Vγ4-2A-Vδ5 with BamHI and XhoI. The gel shows two fragments with molecular weight in correspondence with the expected sizes of the product: linear TOPO vector (3519 bp) and full construct Vγ4-2A-Vδ5 (1961 bp). The negative control of each PCR (H_2O) is also shown as reference together with the molecular ladder. The figure on top/bottom of the bands indicates the number of lanes run in the gel.

Sequencing of the pCRII-Blunt-TOPO plasmid was performed by Sources Biosciences with a primer provided by the company (SP6). The analysis of the sequence confirmed the successful incorporation of the Vγ4-2A-Vδ5 fragment into the plasmid backbone (Data not shown).

To clone the TCR into the pLZ vector we digested the Blunt II Topo containing Vγ4-2A-Vδ5 and the pLZ-IRES-eGFP with BamHI-HF/XhoI in separate reactions (see Table 5-3). The digested products were run on agarose (0.7%) and the desired bands (1961 bp and 12443 bp) extracted and purified. To ligate Vγ4-2A-Vδ5 and pLZ we used the instant sticky-end Ligase Master Mix (Biolabs) with 20:1 insert to vector ratio. For the analysis of the insertion of the Vγ4-2A-Vδ5 fragment into the pLZ-IRES-eGFP retroviral vector, we carried out a PCR reaction using as templates the double digested retroviral plasmid with the BamHI and XhoI restriction enzymes. Furthermore, we also decided to test the reaction with un-digested (circular shape) retroviral plasmid. The primers used for the amplification were Spfg1/Rp4δ. The primers will amplify the sequence LeaderVγ4Jγ1Cγ1-P2A-LeaderVδ5Dδ2Jδ1 that will contain approximately 1496 bp. Figure 5-19 shows the bands for both digested and undigested plasmids.

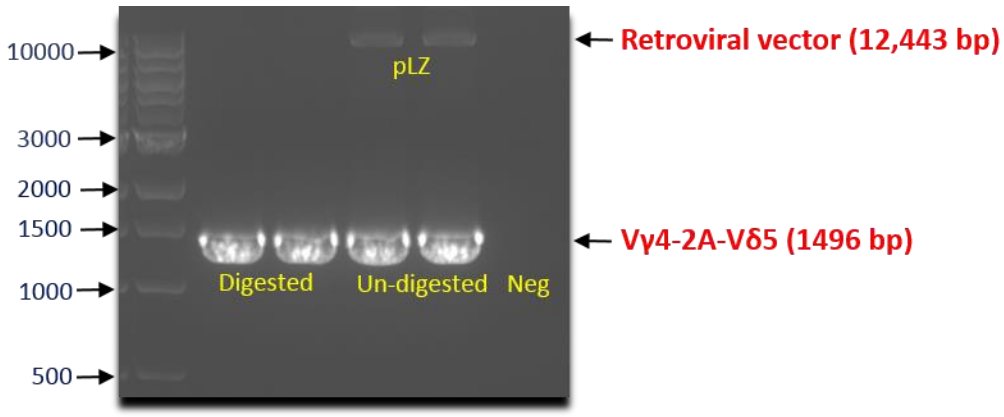

Figure 5-19. Agarose gel electrophoresis of un-digested and double digested (BamHI/XhoI) pLZ-Vγ4-2A-Vδ5-IRES-eGFP showing the two products: pLZ backbone (12,443 bp) and the amplified fragment (1496 bp) in the double digested plasmid and the 1496 bp fragment in the un-digested vector. The negative control (H_2O) is also shown together with the ladder as molecular weight reference.

The position of the fragments are slightly lower than 1500 bp on the ladder, which is in agreement with the expected size of the amplicon (1496 bp). In the lanes corresponding to the undigested plasmid, is it possible to observe as well two faint bands above 10 Kbp that we suspect corresponds to the retroviral backbone used as template.

In conclusion, the data presented in these sections suggest that the cloning of Vγ4-2A-Vδ5 ($TCR\gamma\delta^{IL\text{-}17}$) fragment into the pCRII-Blunt-TOPO and pLZ-IRES-eGFP retroviral plasmid was successfully achieved.

5.4.7 Monitoring the stability of the Phoenix Ecotropic packaging cell line (ϕNX)

The Phoenix Ecotropic cell line is the retrovirus producer line, based on 293T cells that our lab has extensively used for the transduction of mouse thymocytes. The line is a helper-free virus producer that can be easily monitored for the production of the viral packaging proteins, i.e. gag-pol and envelope proteins. Downstream of the gag-pol construct is an IRES-CD8 surface marker that can be monitored as an indirect reporter of the gag-pol production by flow cytometry. To assess the stability of our stock of phoenix cells we prepared three conditions (Figure 5-20): 1) un-transfected cells as a negative control, 2) cells transfected with the pLZ-Vγ4-2A-Vδ5 vector to evaluate the transfection protocol, 3) cells unstained as a negative reference for CD8 expression. Figure 5-20 shows that approximately 90% of phoenix cells expressed CD8 on the cell surface, regardless of whether they were transfected or un-transfected with our pLZ construct.

Summary

These results demonstrates that our retroviral system for the delivery of the TCRVγ4-2A-Vδ5 into the $Rag2^{-/-}$ thymocytes has been successfully tested for the production of the gag-pol viral packaging proteins and that the retroviral vector pLZ-Vγ4-2A-Vδ5 is effectively transfected in our conditions and leads to the production of GFP^{+} cells (by means of the IRES sequence).

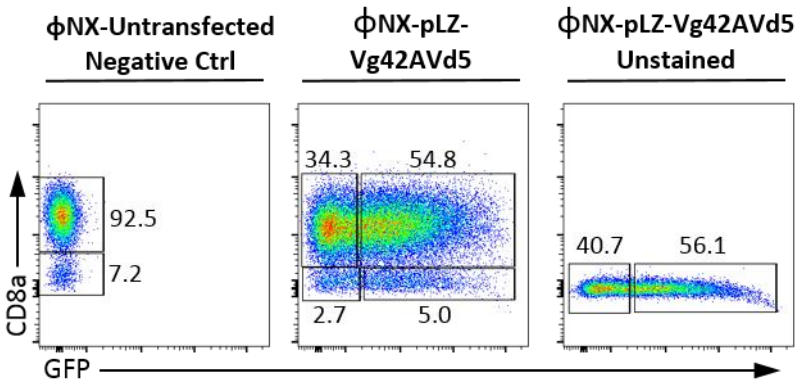

Figure 5-20. Transfected Phoenix cell line with the pLZ-Vγ4-2A-Vδ5 plasmid and Fugene 6 transfection reagent. Flow cytometry analysis of the transfected Phoenix cell line used in the packaging of the retroviral particles (left, untransfected; middle, transfected right, unstained). The transfected packaging cell line was analyzed for the expression of GFP and CD8a. CD, cluster of differentiation; ϕNX, phoenix cell line (n=1).

5.4.8 Assessing the efficiency of transfection of pLZ-Empty and pLZ-Vγ4-2A-Vδ5 into 293 T cells and the Phoenix Ecotropic cell line

To assess the transfection efficiency of the pLZ-Vγ4-2A-Vδ5 vector, both 293T and the Phoenix Ecotropic cell lines were transfected. As negative control we used non-transfected cells (see Figure 5-21 A and B). After transfection the cells were left resting in culture for 48 hours. The 293T cells were analysed by flow cytometry and fluorescence microscopy (Figure 5-21 A), whilst the Phoenix cells were evaluated solely for GFP expression by flow cytometry (Figure 5-21 B).

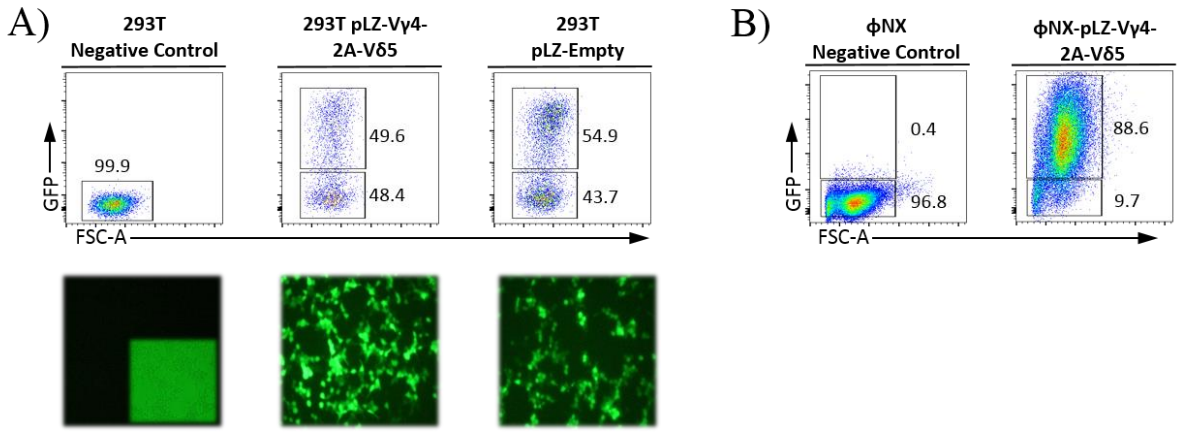

Figure 5-21. **Transfection of 293T and Phoenix cells with control plasmid (pLZ-Empty) and the TCRγδ containing plasmid (pLZ-Vγ4-2A-Vδ5) and Fugene 6 transfection reagent. A)** Flow cytometry results 48 hr post-transfection of 293T cells with the pLZ-Vγ4-2A-Vδ5 and pLZ-empty plasmids (middle and right panels). The results show the percentage of transfected cells, based on the expression of GFP. Untransfected (293T cells) were used as a negative control (left panel). Second Row: Cells analyzed by microscopy. Non-transfected cells are shown in the left panel (negative control) with an inset showing the bright field image. Middle and right plots represent 293T cells transfected with pLZ-Vγ4-2A-Vδ5 and pLZ-empty plasmids, respectively. **B)** Analysis of the transfection efficiency of phoenix cells with pLZ-Vγ4-2A-Vδ5 (right plot). Untransfected cells were used as negative control (left plot). GFP, Green fluorescent protein; ϕNX, phoenix cell line (n=1).

As the FACS plots show (Figure 5-21 A), near fifty percent of the total 293T cells in the culture were transfected with the pLZ-Vγ4-2A-Vδ5 vector and a good expression of GPF can be observed by microscopy. Similarly, the number of GFP^+ cells with the pLZ-empty vector is above fifty percent with a homogenous GFP pattern by microscopy. The transfection of the Phoenix Ecotropic cell line shows that almost ninety percent of the cells were GFP^+, therefore successfully transfected with the pLZ-Vγ4-2A-Vδ5 plasmid in the conditions tested in this experiment.

Summary

In conclusion, these data demonstrate that the pLZ-empty and pLZ-Vγ4-2A-Vδ5 vectors could drive expression of GFP when transfected into the 293T cell line, with a transfection efficiency of approximately fifty percent. In addition, we also show the transfection efficiency was near ninety percent in the Phoenix Ecotropic cell line, which is the system that will produce the retroviral particles.

5.4.9 Assessing the development of Rag2$^{-/-}$ and B6 WT embryonic thymocytes in the OP9DL1 system.

To investigate whether thymocytes could be successfully cultured using the OP9DL1 system, we cultured E14 Rag2$^{-/-}$ thymocytes for 9-days and E15 C57BL/6 wild type thymocytes for 7-days and assessed their development by flow cytometry (Figure 5-22).

The OP9DL1 cell line[264] is a bone marrow derived preadipocyte cell line, OP9[310] that was genetically manipulated to express the Notch ligand, Delta-like 1 (see Introduction 5.1.4). The key aspect of this cell line is that it is able to support growth and differentiation of thymocytes from progenitor cells, therefore has been extensively used in studies of T cell development in vitro[1, 264, 291].

E14 Rag2$^{-/-}$ thymocytes left in culture for 9 days developed successfully as demonstrated by the sizable fraction of live cells observed, i.e. around ninety percent (Figure 5-22 A). Further analysis showed that Rag2$^{-/-}$ thymocytes did not express TCRαβ nor TCRγδ, as expected. Moreover, the staining of the double negative population with CD44 and CD24, which are phenotypic markers of murine T cell precursors[2] allows the identification of three distinct populations: DN1, DN2 and DN3. These populations are characterized by the expression of CD44^{+}CD24^{-} (DN1), CD44^{+}CD24^{+} (DN2), and or CD44^{-}CD24^{+} (DN3). Most of the thymocytes were DN1 or DN3 cells (see Discussion 5.5.2.3). We did not observe progression beyond the DN3 stage. This is due to the inability of the thymocytes to rearrange any TCR, as signaling through the TCR is necessary for the progression to the DN4 stage[291].

The analysis of the E15 C57BL/6 thymocytes showed that cells survived and developed with development of both TCRαβ^{+} and TCRγδ^{+} cells (Figure 5-22). The double nega-

tive subset ($\alpha\beta^-$ $\gamma\delta^-$) was further analysed with CD44 and CD24 markers and we identified that most of the cells (ninety-seven percent of all $\alpha\beta^-$ $\gamma\delta^-$) are in the DN3 stage of development. A small fraction of thymocytes had progressed to the DN4 stage.

We next decided to analyse the developmental progression of the TCR$\gamma\delta^+$ subset based on the expression of CD24. Sumaria et al[1] have shown that E14 thymocytes show a developmental progression from $CD25^+CD24^+$ to $CD25^-CD24^+$ to $CD25^-CD24^-$, where $CD24^-$ thymocytes represent a mature stage in the thymus. Based on these data we performed a similar analysis and both $\gamma\delta^{24+}$ and $\gamma\delta^{24-}$ thymocytes were further subdivided by the expression of CD44 and CD45RB to identify the effector fate profile. As Figure 5-22 B shows, immature $\gamma\delta^{24+}$ have not yet entered any effector fate pathway and almost all the cells are $CD44^-$ $CD45RB^-$. By contrast, mature $\gamma\delta^{24-}$ cells have already entered one of the two pathways of development (IL-17, or IFNγ) as illustrated in the summary graph (Figure 5-22 C).

Summary

In summary, these data show that in our lab we can drive satisfactory development of both E14 $Rag2^{-/-}$ thymocytes and E15 C57BL/6 wild type thymocytes cultured on OP9DL1 cells.

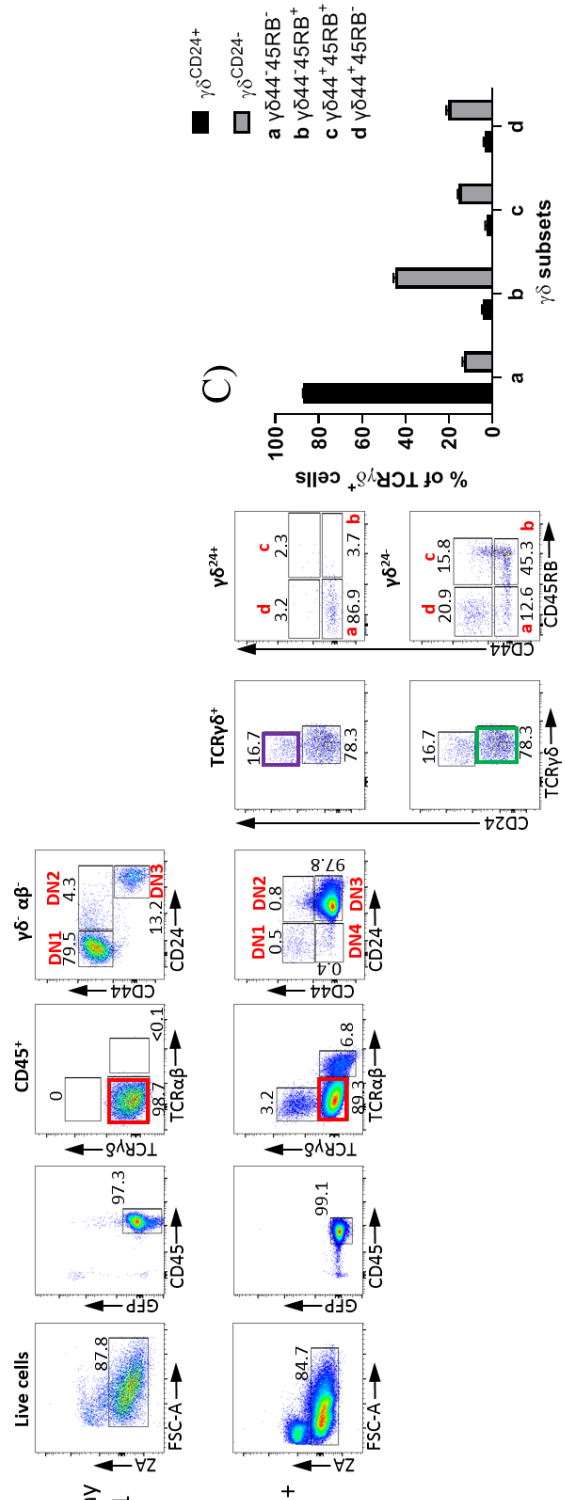

Figure 5-22. Assessing the development of Rag2$^{-/-}$ and B6 WT embryonic thymocytes in the OP9DL1 system. **(A)** Live CD45^{+} E14 Rag$^{-/-}$ thymocytes cultured in OP9DL1 for 9 days were analyzed for the expression of TCRαβ and TCRγδ. To assess the stages of development, the double negative population (red square) was further analyzed with the markers CD44 and CD24 to characterize the development of murine early T-lineage progenitors[2]. CD44^{+}CD24^{-} (DN1) represents the earlier T cell progenitor entering the thymus. CD44^{+}CD24^{+} characterize the DN2 stage. The thymocytes progress to the next stage DN3 characterized by CD44^{Lo} CD24^{+}. **(B)** B6 E15 thymocytes were analyzed following the same gating strategy as described in (A). By contrast, we observed expression of both TCRαβ/TCRγδ receptors. TCRγδ^{+} cells were was stained for CD24, CD44 and CD45RB to evaluate the development of TCRγδ^{+} thymocytes. The mature γδ^{24+} population (green square) was evaluated for the expression of CD44 and CD45RB to assess their effector fate commitment. Four populations were identified denominated "a" (CD44^{-} CD45RB^{-}), "b" (CD44^{-}CD45RB^{+}), "c" (CD44^{+}Cd45RB^{+}) and "d" (CD44^{+}CD45RB^{-}). The immature γδ^{24+} population (purple square) was analyzed in a similar way. **(C)** Summary graph of (B) showing the percentage of TCRγδ^{+} thymocytes within each effector fate pathway for γδ^{24-} and γδ^{24+} subsets, after 7 days culture on OP9DL1 cells. Numbers represent the percentage of cells. Representative plots. CD, cluster of differentiation; DN, double negative.

5.4.10 Retroviral transduction of E14 Rag2$^{-/-}$ thymocytes with retroviruses generated with the pLZ-empty and pLZ-Vγ4-2A-Vδ5 vectors

To analyze the effect of the Vγ4-2A-Vδ5 TCRγδ^{IL-17} on development and effector fate acquisition of γδ progenitors E14 Rag2$^{-/-}$ thymocytes were transduced with Vγ4-2A-Vδ5-expressing retroviruses. To ensure stoichiometric co-expression of the Vγ4 and Vδ5 TCR chains the 2A sequence of the Porcine teschovirus 1 (PTV-1) was placed between the two TCR sequences in the pLZ vector. Briefly, the 2A peptide sequence functions as a cis-acting hydrolase element to mediate cleavage between two proteins[311]. The 2A peptide sequence seems to abort the formation of a Glycine-Proline peptide bond at the end of the 2A sequence via a ribosomal skip mechanism[312]. We chose the PTV-1 2A sequence (22 amino acids long) due to its high cleavage efficiency (> 95%) and observations from previous studies showing successful stoichiometric expression of TCRαβ[312, 313].

E14 Rag2$^{-/-}$ thymocytes were transduced with pLZ-Vγ4-2A-Vδ5 or pLZ-empty retroviruses using Retronectin to enhance the binding of virions, and subsequently, co-cultured on OP9DL1 cells. After 9-days of culture, approximately 10% of the thymocytes transduced with the pLZ-empty were GFP^{+}, whilst the transduction efficiency for the pLZ-Vγ4-2A-Vδ5 was about 6% (Figure 5-23 A and B). The analysis of the GFP^{+} Rag2$^{-/-}$ thymocytes transduced with the pLZ-empty showed that these cells were unable to express any TCR on their cells surface, and consequently, the development of the Rag2$^{-/-}$ thymocytes was blocked at the DN3 stage as previously reported in the literature[267, 314] (Figure 5-23 A). In addition, the staining of the DN3 subset for CD44 and CD45RB shows a similar pattern to that of immature γδ^{24+} subset (see Figure 5-32 A). On the other hand, analysis of thymocytes transduced

with the pLZ-Vγ4-2A-Vδ5 showed that ~2.4% of the GFP^+ cells expressed TCRγδ and around 94% were double negative (Figure 5-23 A). Interestingly, analysis of the DN population revealed that 16% of the cells had progressed beyond the DN3 stage of development and become DN4 cells (see Discussion 5.5.2.1). Moreover, the analysis of the DN4 subset with CD44 and CD45RB showed that 44% of these cells had upregulated CD45RB. Although we observed these cells within the $TCR\gamma\delta^-$ ($TCR\alpha\beta^-$) population it is well established that progression to the DN4 stage is TCR-dependent. For example, it has been shown that TCR signal transduction by TCRγδ or the pre-TCR is indispensable for T cell development[278]. Moreover, the absence of some key components of the signal transduction machinery, e.g. LAT[315], ZAP-70[316]and Syk[317] halt the development of double negative cells at the DN3 stage.

As mentioned before, downregulation of CD24 correlate to γδ T cell maturation[1, 305]. The analysis of the $TCR\gamma\delta^+$ population (Figure 5-23 B) shows that 71% of the cells have downregulated CD24 expression whereas 25% of the cells express high levels of CD24. Interestingly, staining of the $\gamma\delta^{24-}$ thymocytes with CD44 and CD45RB showed that 100% of the $\gamma\delta^{CD24-}$population had upregulated CD45RB and CD44, suggesting commitment to IFN-γ production (Figure 5-23 B).

The analysis of the mean fluorescence intensity (MFI) of CD24 on the GFP^+ DN3 subset was observed to be higher on cells transduced with the pLZ-empty vector than in the thymocytes transduced with the pLZ-Vγ4-2A-Vδ5 vector (Figure 5-23 D).

The percentage of DN4 cells within the GFP^+ population revealed that around 16% of the thymocytes transduced with pLZ-Vγ4-2A-Vδ5 were able to progress beyond the DN3

stage whereas virtually no progression was observed for thymocytes transduced with the pLZ-empty vector (Figure 5-23 E).

Next, we analyzed the GFP^- population for thymocytes transduced with pLZ-empty and found that similar to the GFP^+ counterpart, there was no expression of TCR on the cell surface and the development of DN thymocytes was arrested at the DN3 stage (Figure 5-23 C). Interestingly, the analysis of GFP^- thymocytes transduced with the pLZ-Vγ4-2A-Vδ5 vector revealed that 10% of the thymocytes had progressed beyond the DN3 stage. This result suggests that the IRES is not thoroughly efficient in expressing GFP and in fact some transduced thymocytes may be GFP^-. The analysis of the GFP^-DN4 population for the expression of CD44 and CD45RB demonstrated that indeed 87% of the thymocytes had upregulated CD45RB (Figure 5-23 C), similar to the GFP^+DN4 subset (Figure 5-23 A).

Summary

Collectively, these data show that the transduction of $Rag2^{-/-}$ thymocytes with retroviruses containing pLZ-empty and pLZ-Vγ4-2A-Vδ5 was successful, although the transduction efficiency was lower than expected. Transduction with the pLZ-Vγ4-2A-Vδ5 vector can drive progression of $Rag2^{-/-}$ thymocytes into the DN4 stage of development and induce downregulation of CD24 levels in the $TCR\gamma\delta^+$ subset which has been associated with γδ T cell maturation. In addition, we observed that the IRES was not completely efficient as some GFP^- thymocytes progressed towards the DN4 stage of development. Interestingly, the analysis of the $TCR\gamma\delta^+$ thymocytes from progenitors transduced with pLZ-Vγ4-2A-Vδ5 revealed that $\gamma\delta^{24-}$ cells developed towards the IFNγ effector pathway (See Discussion 5.5.2.2).

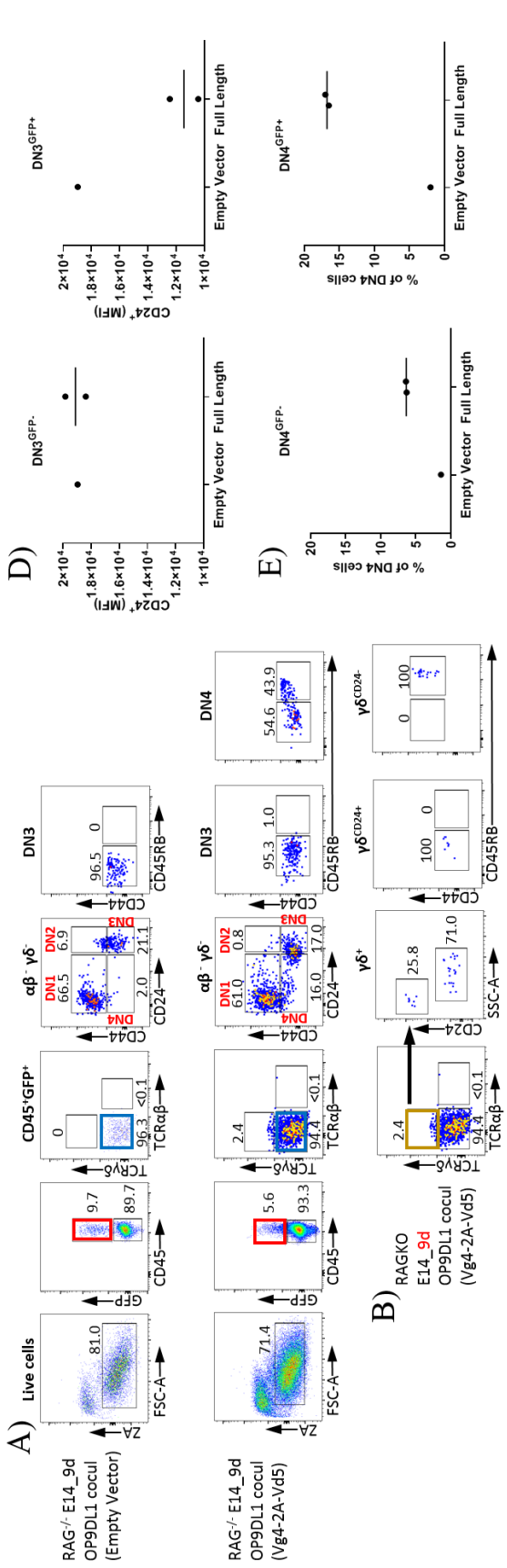

Figure 5-23. **Retroviral transduction of E14 Rag2$^{-/-}$ thymocytes with retroviruses expressing control (pLZ-empty) and pLZ-Vγ42AVδ5 constructs.** The cells were co-cultured with OP9DL1 cells for 9-days. **(A)** Transfected thymocytes (CD45^{+}GFP^{+}) (red squares) were analysed for the expression of TCRγδ, TCRαβ, CD24 and CD44/CD45RB. **(B)** The TCRγδ^{+} subset (brown square) was stained for CD24 to evaluate the development of the γδ^{+} thymocytes. The mature γδ^{24+} population and the immature population γδ^{24+} were double stained with CD44 and CD45RB to assess their effector fate commitment. **(C)** The CD45^{+}GFP^{-} thymocytes (green squares) were analysed following the same gating strategy shown in (A). **(D)** Summary graph showing the CD24 MFI of the DN3 population within the αβ^{-} γδ^{-} population for GFP^{+} and GFP^{-} thymocytes. **(E)** Summary graph showing the percentage of DN4 thymocytes within the αβ^{-} γδ^{-} subset gated for both GFP^{+} and GFP^{-} thymocytes. Numbers represent the percentage of cells. CD, cluster of differentiation; MFI, mean fluorescence intensity; DN, double negative. Representative plots (n=2).

5.4.11 Retroviral transduction of E15 Rag2$^{-/-}$ thymocytes with retroviruses generated with the pLZ-empty and pLZ-Vγ4-2A-Vδ5 vectors

As described in the previous section 5.4.10, the transduction efficiency of E14 Rag2$^{-/-}$ thymocytes was low, i.e. approximately 10% and 6% for pLZ-Empty and pLZ-Vγ4-2A-Vδ5, respectively. Our lab had previously noted that transduction of early progenitors such as E14 thymocytes can yield low transduction efficiency. Based on this observation, we decided to transduce E15 Rag2$^{-/-}$ thymocytes. Moreover, instead of transfecting the cells using Retronectin as a transfection enhancer, we used the spinoculation method[308].

The spinoculation method is based on centrifugal inoculation. The mechanism is not clear. However, some preliminary observations with HIV-1 suggest that modest G forces, e.g. 1200 g, can concentrate the viral particles close to target cells, thus improving transduction efficiency considerably[308].

After spinoculation, thymocytes were cultured for 9-days on OP9DL1 cells. As predicted, the transduction efficiency improved with approximately 37% of E15 Rag2$^{-/-}$ thymocytes transduced with the pLZ-Vγ4-2A-Vδ5 construct expressing GFP (Figure 5-24 A). By contrast, the transduction efficiency with pLZ-empty was lower with approximately 8% GFP^{+} cells observed (Figure 5-24 A). As expected, the GFP^{+} Rag2$^{-/-}$ thymocytes transduced with pLZ-empty did not express any TCR and consequently the development of these cells was blocked at the DN3 stage (Figure 5-24 A). By contrast, a sizable proportion of GFP^{+} cells from E15 Rag2$^{-/-}$ thymocytes transduced with pLZ-Vγ4-2A-Vδ5 retrovirus expressed TCRγδ on their cell surface (Figure 5-24 A). In order to be consistent, we analyzed the TCRγδ^{-} population, which revealed that 38% of the cells had progressed beyond the DN3

stage of development to become DN4. However, analysis of the DN4 subset with CD44 and CD45RB showed a decrease (6.7%) in the number of cells that upregulated CD45RB (Figure 5-24 A and E) compared to the 43.9% observed in the previous experiment (see Section 5.4.10, Figure 5-23 A).

As mentioned before, downregulation of CD24 has been reported as an indicator of γδ maturation[1, 305]. However, CD24 is not the only useful marker of γδ cell maturation. CD25 has also being described as a thymic determinant of γδ cell progression[1, 2]. Since the majority of mature γδ thymocytes do not express CD25, downregulation of CD25 can be used as an indicator of γδ cell maturation. Therefore, to assess the maturation of the γδ cells we analyzed the expression of CD25 and CD24 upon transduction of E15 Rag2$^{-/-}$ thymocytes with the pLZ-Vγ4-2A-Vδ5 construct.

The analysis of the TCRγδ^{+} population (Figure 5-24 B and D) showed that 55% of the cells were γδ^{24+25+}, whereas ~43% had downregulated CD25 and probably expressed lower levels of CD24. However, we found only 1% of γδ^{+} cells among the mature γδ^{24-25-} compartment. Further analysis with CD44 and CD45RB among γδ^{24+25+}, γδ^{24+25-}, and γδ^{24-25-} subsets showed that the immature populations, γδ^{24+25+} and γδ^{24+25-}, were double negative, whilst the γδ^{24-25-}subset showed upregulation of CD45RB, similarly to the γδ^{24-} thymocytes in Figure 5-23 B. The upregulation of CD45RB (Figure 5-24 D) suggests commitment to the IFNγ effector pathway; however, the scant number of cells found within this population makes any conclusions speculative at this stage.

Next, we analyzed the changes in the mean fluorescence intensity (MFI) of CD25 within the DN3 subset. Both, the GFP^{+} and GFP^{-} DN3 thymocytes among pLZ-empty and

pLZ-Vγ4-2A-Vδ5 were analyzed (Figure 5-24 C). We observed that among the GFP^- cells, the CD25 MFI for DN3 thymocytes transduced with pLZ-Vγ4-2A-Vδ5 was lower than the DN3 cells transduced with pLZ-Empty. However, when we looked at the GFP^+ population we found striking differences, with DN3 thymocytes transduced with pLZ-Vγ4-2A-Vδ5 showing almost a 3-fold decrease in CD25 MFI compared to GFP^+ DN3 thymocytes transduced with pLZ-Empty (Figure 5-24 C).

When assessing the GFP^- population, thymocytes transduced with pLZ-empty showed, as expected, lack of TCR expression and blocked development of thymocytes at DN3 stage (Figure 5-24 A and 5-25 A). Noticeably, the analysis of the DN subset among GFP^- thymocytes transduced with the pLZ-Vγ4-2A-Vδ5 vector showed that ~3% of the thymocytes had progressed beyond the DN3 stage. Further analysis of the GFP^- DN4 population for the expression of CD44 and CD45RB showed that 21% of the thymocytes had, in fact, upregulated CD45RB (Figure 5-25 A), similar to the GFP^+ DN4 subset (Figure 5-24 A, third row).

Finally, we assessed the percentage of DN4 thymocytes within the GFP^- and GFP^+ subsets for both pLZ-Empty and pLZ-Vγ4-2A-Vδ5 transductions (Figure 5-25 B). It is important to note that progression beyond the DN3 stage of development is TCR-dependent, therefore in $Rag2^{-/-}$ thymocytes treated with retroviruses containing pLZ-empty, no progression beyond the DN3 stage of development should be observed. By contrast, we observed that 2.6% of the GPF^- thymocytes were among the DN4 compartment in the pLZ-Vγ4-2A-Vδ5 condition.

Summary

In summary, the data demonstrate improvement in transduction efficiency with E15 $Rag2^{-/-}$ thymocytes. We observed a higher frequency of GFP^{+} thymocytes when we employed the spinoculation method. We showed that cells transduced with pLZ-Vγ4-2A-Vδ5 progressed to the DN4 stage of development, which suggests successful signaling through the TCR. Moreover, we recorded downregulation of CD25 levels in the DN3 subset, which is an indicator of maturation. In addition, we also showed that a fraction of GFP^{-} thymocytes progressed towards the DN4 stage of development, which reinforces the idea that the IRES is not completely efficient in promoting the translation of GFP. Interestingly, the analysis of $TCR\gamma\delta^{+}$ thymocytes with CD44 and CD45RB revealed that few cells in the $\gamma\delta^{24\text{-}25\text{-}}$ subset were $CD44^{-}CD45RB^{+}$, which suggests commitment to the IFNγ effector pathway (See Discussion 5.5.2.2).

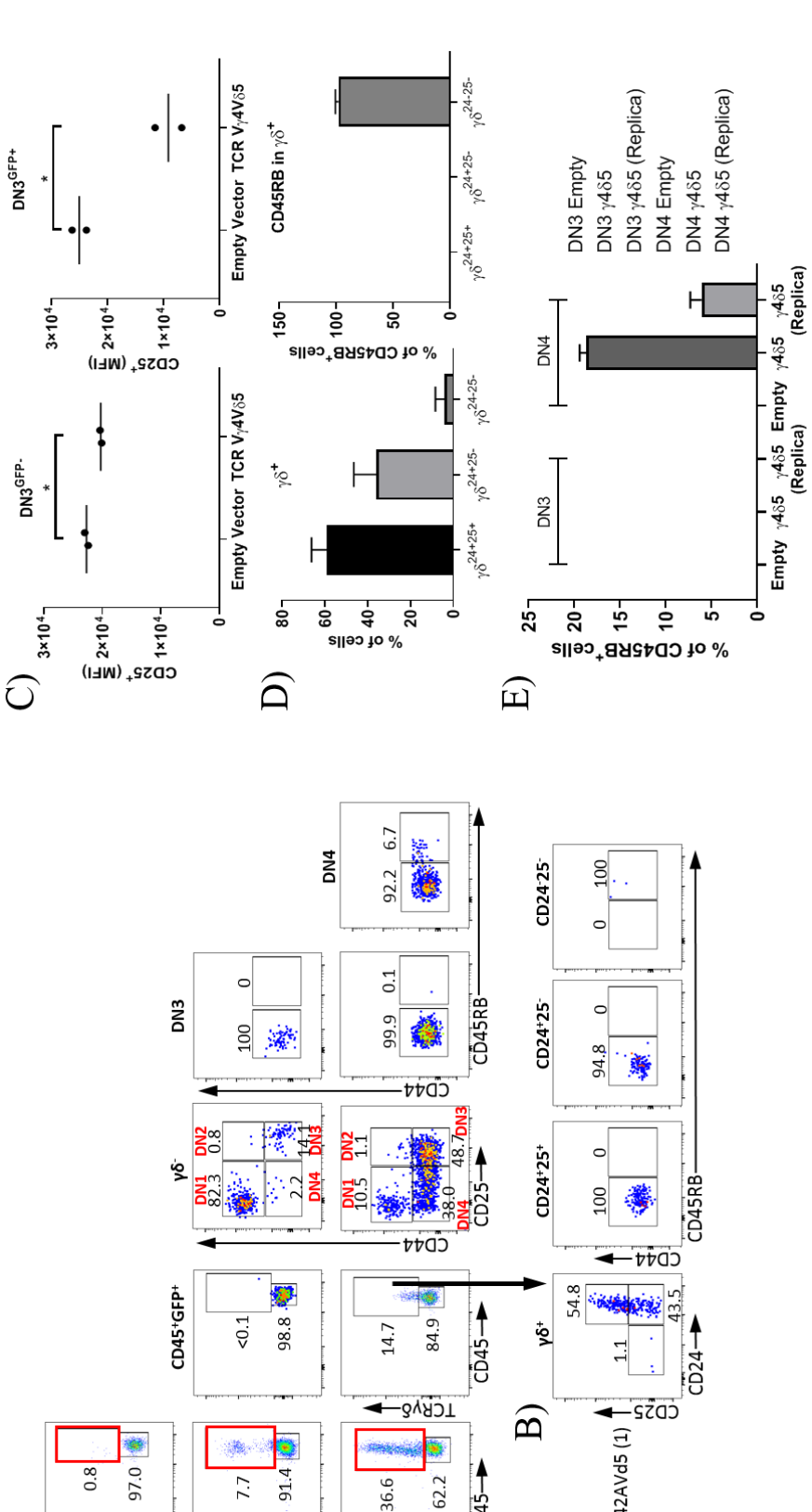

Figure 5-24. **Retroviral transduction of E15 Rag$^{-/-}$ thymocytes with retroviruses generated with the pLZ-empty and pLZ-Vγ42AVδ5 constructs.** Cells were co-cultured with OP9DL1 cells for 9-days. **(A)** Transfected thymocytes (CD45^{+}GFP^{+}) (red squares) were analysed for expression of TCRγδ, CD45, CD25 and CD44/CD45RB. **(B)** The TCRγδ^{+} subset was stained for CD24 and CD25 to evaluate the development of the γδ^{+} thymocytes. The three subsets γδ^{24+25+}, γδ^{24+25-}, and γδ^{24-25-}, were further stained with CD44 and CD45RB to assess their effector fate commitment. **(C)** Summary graph showing CD25 MFI of the DN3 population within the γδ^{-} population for GFP^{+} and GFP^{-} thymocytes. **(D)** Summary graph of (B) showing the percentage of γδ^{24+25+}, γδ^{24+25-}, and γδ^{24-25-} within the γδ^{+} subset gated in GFP^{+} thymocytes and expression of CD45RB within each subset. **(E)** Summary graph of (A) showing the percentage of CD45RB^{+} cells within the DN3 and DN4 stages of development for thymocytes transduced with the empty and the full-length construct. CD, cluster of differentiation; MFI, mean fluorescence intensity; DN, double negative. Representative plots (n=2).

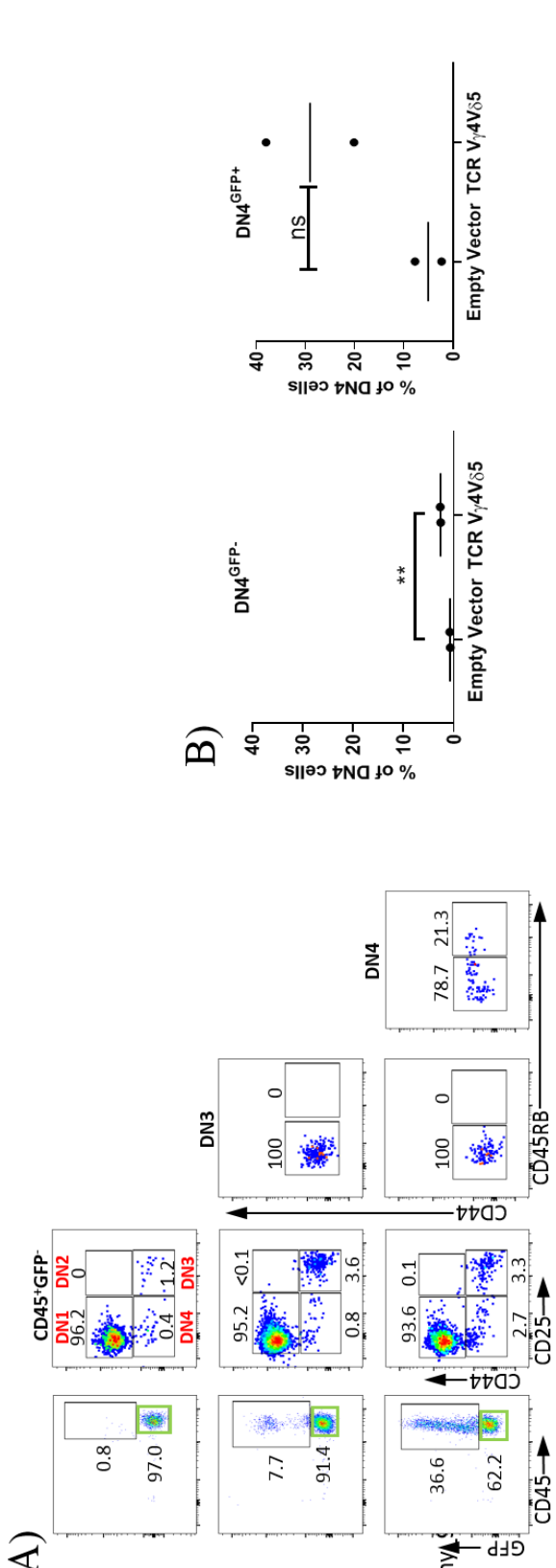

Figure 5-25. **Retroviral transduction of E15 Rag$^{-/-}$ thymocytes with retroviruses generated with the pLZ-empty and pLZ-Vγ42AVδ5 constructs.** Cells were co-cultured on OP9DL1 for 9-days. **(A)** Thymocytes (CD45^{+}GFP^{-}) (green squares) were analysed for the expression of CD44, CD25 and CD44/CD45RB to evaluate their stages of development. The DN3 and DN4 stages of development were further stained for CD44 and CD45RB. **(B)** Summary graph showing the percentage of DN4 thymocytes within the CD45^{+} GFP^{-} subset (A) and the γδ^{-} subset (Figure 5-24 A) for both, empty and the full-length construct. Numbers represent the percentage of cells. CD, cluster of differentiation; DN, double negative. Representative plots (n=2).

5.4.12 Evaluating the development of Rag2$^{-/-}$ embryonic thymocytes in FTOC and OP9DL1 systems

In the previous section, we demonstrated how the transduction of E15 Rag2$^{-/-}$ thymocytes seems to be more productive in terms of yield of transduction. Based on these results we asked ourselves whether leaving the thymocytes resting in FTOC for 2 days before isolation and transduction would also be translated into an enhanced transduction yield. Before proceeding with the transduction of thymocytes, we first decided to assess the development of E15 Rag2$^{-/-}$ thymocytes in two different experimental conditions. To this end, we set up an experiment where E15 Rag2$^{-/-}$ thymocytes were placed in two different culture systems (Figure 5-26): 1) cultured for 9 days in FTOC; 2) cultured in FTOC for 2 days and subsequently transferred to OP9DL1 cells for 7-days. After 9-days incubation the thymocytes were isolated and stained for analysis. Figure 5-26 A shows that from 9-day FTOC culture we recovered around 22.5% of E15 Rag$^{-/-}$ with 99.3% of the cells alive. Double staining with CD44 and CD25 was used to assess the development of double negative thymocytes. As Figure 5-26 A and B show, the majority of the thymocytes (76.4%) develop to the DN3 stage, and 14.4% of cells remain in the DN1 stage, with a low number of DN2 cells (3.2%) (see Discussion 5.5.2.3). As expected in Rag2$^{-/-}$ mice, there was no further development beyond DN3 stage.

By contrast, 2 day FTOC followed by 7-days on the OP9DL1 cell we only retrieved around 3.4% of E15 Rag2$^{-/-}$ thymocytes with 98% rate of survival. Assessment of development revealed that almost all the thymocytes (97%) remained in the DN1 compartment with no observed progression beyond this stage (See Discussion 5.5.2.4).

Summary

From this experiment, we can conclude that a 9-day FTOC, as expected, better supports proliferation, survival and development of $Rag2^{-/-}$ thymocytes. The results from the OP9DL1 system, when compared with the FTOC system, suggest limited proliferation and survival. In addition, the cells may need more than 7-days to develop beyond the DN1 stage. However, for the viral infection the thymocytes needs to be released from the thymic stroma and be accessible to virions, hence the requirement for the use of the OP9DL1 culture system.

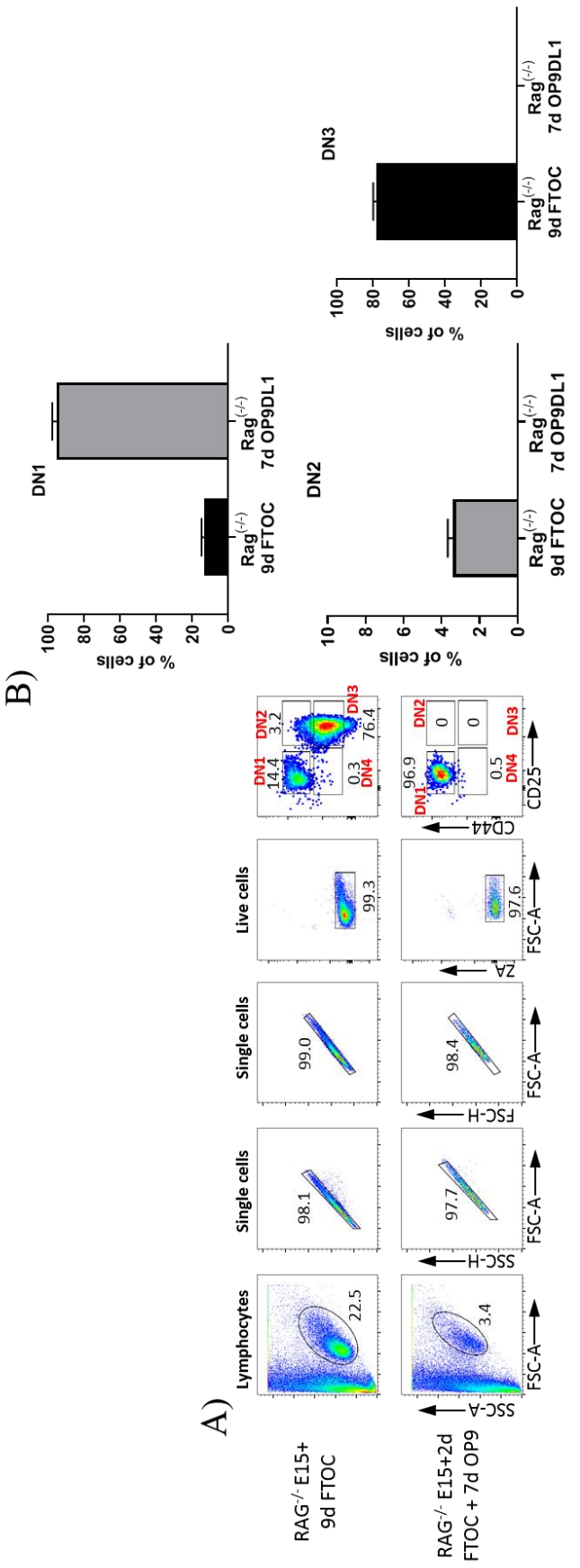

Figure 5-26. **Evaluating the development of Rag2$^{-/-}$ embryonic thymocytes in FTOC and OP9DL1 systems. (A)** Gating strategy followed to assess the development of the E15 Rag$^{-/-}$ thymocytes after 9 days FTOC or 2 days FTOC followed by 7 days culture on OP9DL1. Total lymphocytes were selected for analysis, and live cells were double stained with CD44 and CD25 to assess the stages of development. CD44^{+}CD25^{-} (DN1) represents the earliest T cell progenitor subset, CD44^{+}CD25^{+} characterize the DN2 population, cells progress to the next stage CD44^{-}CD25^{+}, denominated DN3. The last stage of development is denominated DN4 (CD44^{-}CD25^{-}) but Rag$^{-/-}$ thymocytes are unable to progress beyond the DN3 stage of development due to the inability to express any T cell receptor. **(B).** Summary graph of (A) showing the percentage of cells within DN1, DN2, and DN3 stages of development for both FTOC and OP9DL1 culture systems. Numbers represent the percentage of cells. CD, cluster of differentiation; FTOC, fetal thymic organ culture; DN, double negative. Representative plot (n=2).

5.4.13 Retroviral transduction of E15 Rag2$^{-/-}$ thymocytes and culture for 2d in FTOC and 7d in OP9DL1

As we have shown in section 5.4.11, transduction of E15 Rag2$^{-/-}$ thymocytes seems better than transduction of E14 Rag2$^{-/-}$ thymocytes. Thus, we decided to evaluate whether further maturation of embryonic day 15 thymocytes for 2 days in FTOC prior to infection with retroviruses would further enhance transduction efficiency. To this end, we isolated thymic lobes from E15 Rag2$^{-/-}$ mice and placed them in culture for 2 days. Afterwards, thymocytes were isolated, infected with retroviruses using the spinoculation method (See Methods 5.3.3.9) and transferred to a monolayer of OP9DL1 cells. After 7-days of culture, the cells were processed for analysis (Figure 5-27).

The analysis of the GFP$^+$ population (Figure 5-27 A) revealed that 2% and ~5% of the thymocytes were transfected with pLZ-Empty and pLZ-Vγ4-2A-Vδ5, respectively. However, developmental evaluation with CD44 and CD25 of the double negative thymocytes transduced with the pLZ-Empty showed 71% were DN1 (CD44$^+$CD25$^-$) while 25% of the cells were DN3 (CD44$^-$CD25$^+$) (Figure 5-27 A and C). No further development beyond DN3 was observed. Moreover, staining of the DN3 subset with CD44 and CD45RB did not reveal up-regulation of CD45RB, similar to the results described in previous sections 5.4.10 and 5.4.11. The development of the GFP$^+$ double negative thymocytes transfected with pLZ-Vγ4-2A-Vδ5 showed that 67.9% were DN1 (CD44$^+$CD25$^-$), 10.8% were DN3 (CD44$^-$CD25$^+$), and 19.1% of the thymocytes had matured further into the DN4 stage (CD44$^-$CD25$^-$) (Figure 5-27 A and D). Consistent with previous observations, the analysis of the DN3 subset with CD44 and CD45RB did not segregate this homogenous immature population. By contrast, the anal-

ysis of the DN4 compartment showed that ~45% of thymocytes had upregulated CD45RB (Figure 5-27 A and E).

Moreover, the comparison of the mean fluorescence intensity of the CD25 between the DN3 populations of both pLZ-Empty and pLZ-Vγ4-2A-Vδ5, revealed that the latter underwent a 2-fold decrease in CD25 MFI (Figure 5-27 C). This observation may suggest these thymocytes had started to downregulate CD25 stimulated by TCRγδ signaling, although we could not record any expression of surface receptor.

We went next to analyze the ~5% of GFP^+ thymocytes that expressed the TCRγδ on the surface (Figure 5-27 A orange square, and B). As mentioned previously (Section 5.4.11, paragraph 4) the maturation of γδ thymocytes can be assessed with the markers CD24 and CD25. The evaluation of the $TCR\gamma\delta^+$ subset revealed that ~45% of the thymocytes were $\gamma\delta^{24+25+}$, ~29% were $\gamma\delta^{24+25-}$, and ~21% had progressed to the mature $\gamma\delta^{24-25-}$ stage (Figure 5-27 B and F). Further analysis for the expression of CD44 and CD45RB (Figure 5-27 B and F) showed that while the immature subsets $\gamma\delta^{24+25+}$ and $\gamma\delta^{24+25-}$ did not express either of these two markers. The mature $\gamma\delta^{24-25-}$ population did upregulate both CD44 and CD45RB (~80%), which, as demonstrated by Sumaria et al[1] indicates commitment towards the IFNγ secretion effector pathway.

The analysis of the GFP^- thymocytes showed that the majority of thymocytes under all conditions, appeared to be arrested at the DN1 stage of development ($CD44^+CD25^-$) (Figure 5-27 G) with no progression towards the next stage of development (DN2) (See Discussion 5.5.2.3).

Summary

The data presented here suggest that culturing E15 Rag2$^{-/-}$ thymocytes for a further 2-days in FTOC followed by 7 days on OP9DL1 cells did not have a great impact on transduction efficiency. However, some of the results previously observed are repeated under these conditions. Interestingly, despite the drawback in the transduction yield, we observed a considerable increase in the percentage of γδ$^{24\text{-}25\text{-}}$ cells with upregulation of CD44 and CD45RB, suggesting commitment to the IFNγ effector pathway (See Discussion 5.5.2.1).

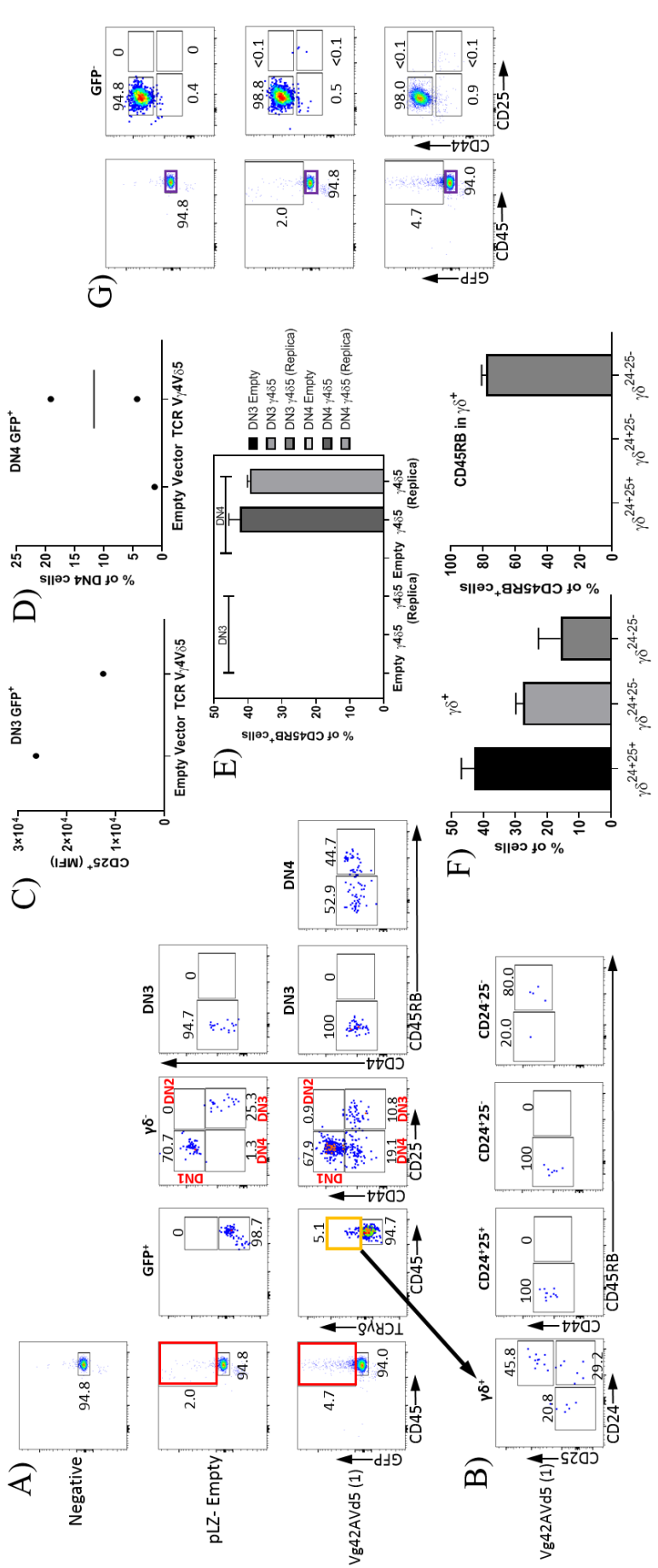

Figure 5-27. **Retroviral transduction of E15 Rag$^{-/-}$ thymocytes with retroviruses generated with the pLZ-empty and pLZ-Vγ42AVδ5 constructs.** The cells were left in FTOC for 2 days followed by 7 days co-culture on OP9DL1 cells. **(A)** Transfected thymocytes (CD45^{+}GFP^{+}) (red squares) were analysed for expression of TCRγδ, CD45, CD25 and CD44/CD45RB. **(B)** The TCRγδ^{+} subset was stained for CD24 and CD25 to evaluate the development of γδ^{+} thymocytes. The three subsets γδ^{24+25+}, γδ^{24+25-}, and γδ^{24-25-}, were further stained with CD44 and CD45RB to assess their effector fate commitment. **(C)** Summary graph of (A) showing the CD25 MFI of the DN3 population within the γδ^{-} population for GFP^{+} thymocytes. **(D)** Summary graph of (A) showing the percentage of DN4 thymocytes within the CD45^{+} GFP^{+} subset for both, empty and the full-length construct. **(E)** Summary graph of (A) showing the percentage of CD45RB^{+} cells within the DN3 and DN4 stages of development for thymocytes transduced with empty and full-length vectors. **(F)** Summary graph of (B) showing the percentage of γδ^{24+25+}, γδ^{24+25-}, and γδ^{24-25-} within the γδ^{+} subset (orange square) gated in GFP^{+} thymocytes and expression of CD45RB within each subset. **(G)** Transfected thymocytes (CD45^{+}GFP^{-}) (purple squares) were analysed for the expression of CD44/CD25 to evaluate their stages of development. Mainly all the cells are in the DN1 stage (CD44^{+}CD25^{-}). CD, cluster of differentiation; MFI, mean fluorescence intensity; DN, double negative. Representative plots (n=2).

5.5 DISCUSSION

5.5.1 Introduction

It is clear that in mice, γδ T cells are a heterogeneous group of lymphocytes that can be classified based on the usage of the Vγ variable chain[228], their tissue location[242] or their effector function[1]. In development, γδ and αβ T cells arise from a common double negative (DN) precursor[291]. Experimental evidence suggests that commitment into the γδ or αβ lineage occurs at some point between the DN2 and DN3 stages of development driven by the TCR[285]. Furthermore, it is well established that fully committed γδ T cells adopt subsequent effector function and in this process, the TCR plays a key role. For example, our lab has demonstrated that increasing the signal strength delivered by TCRγδ is deleterious for the development of the IL-17 effector subset, but enhances the development of IFNγ committed cells[1]. However, due to limited knowledge regarding the natural ligands of TCRγδ, it is not clear how these signals i.e. strong vs weak, are generated *in vivo*. Interestingly, some studies with truncated forms of TCRγδ, that lack the Vγ and Vδ domains (critical for ligand engagement) showed that truncated receptors were able to initiate signalling in DN thymocytes[291]. These observations suggest that TCRγδ itself, in a ligand independent-manner, might be critical in promoting development of γδ T cells towards certain effector fates. In fact, it has been shown that some gamma variable regions (Vγ) are predominantly represented in either the IL-17 effector pathway (Vγ4 and Vγ6) or the IFNγ effector pathway (Vγ5 and Vγ1).[318] Therefore, we decided to begin to address how characteristics of TCRγδ, for example the CDR3 regions, instructs γδ thymocyte progenitors towards the acquisition of one of the two major effector fates.

5.5.2 Summary of Results

To begin to evaluate the role of TCRγδ in the acquisition of γδ effector function we expressed a TCRγδ restricted to the IL-17 effector pathway (Vγ4Jγ1-Vδ5Dδ2Jδ1) in thymocytes isolated from fetal Rag-$2^{-/-}$ mice and assessed their effector commitment outcome. The points below summarize the major accomplishments of the second part of this thesis:

h) A Vγ4Vδ5 TCRγδ from an IL-17 secreting γδ T cell was successfully cloned into a retroviral vector for transduction of $Rag2^{-/-}$ thymocytes that themselves cannot express TCR chains.

i) Successful generation of infectious retroviral particles was achieved.

j) Successful transduction of WT and $Rag2^{-/-}$ early thymocytes progenitors was observed.

k) Productive development of early thymocytes was observed in culture on OP9DL1 cells.

l) Retroviral transfection of $Rag2^{-/-}$ embryonic thymocytes with TCR Vγ4Jγ1-Vδ5Dδ2Jδ1 allowed progression beyond the DN3 stage of development, suggesting that the TCR is signaling competent.

m) Thymocytes expressing the TCR Vγ4Jγ1-Vδ5Dδ2Jδ1, restricted to the IL-17 secretion pathway appear to develop along the CD45RB pathway, suggesting commitment towards an IFNγ secreting effector fate.

n) The OP9DL1 culture system is not as efficient, in our hands, for development of $Rag2^{-/-}$ thymocytes, when compared to conventional FTOC.

5.5.2.1 Retroviral transfection of Rag2$^{-/-}$ embryonic thymocytes with TCR Vγ4Jγ1-Vδ5Dδ2Jδ1 allows progression beyond the DN3 stage of development.

Rag2$^{-/-}$ thymocytes are an invaluable tool to understand the role of the TCR in the context of development due to their inability to rearrange their endogenous TCR genes. The lack of TCR and the absence of the concomitant signals produce a developmental arrest of thymocytes at the DN3 stage of development, also known as β-selection checkpoint. To overcome the arrest at the DN3 stage thymocytes need to receive a CD3-mediated signal[291]. Thus, the expression of a functional TCR that is able to initiate signaling can promote progression of Rag2$^{-/-}$ thymocytes beyond the DN3 stage. Indeed, it has been reported that expression of a truncated form of a TCR, lacking any variable domains, permits signal initiation in DN cells, and subsequent development to the DP stage[291].

Here, fetal Rag2$^{-/-}$ thymocytes were retrovirally transduced with TCR Vγ4Jγ1-Vδ5Dδ2Jδ1which was previously described as restricted to the IL-17 γδ T cell pathway. For those Rag2$^{-/-}$ that were transfected with TCRVγ4Vδ5 a fraction of GFP^{+} secreting restricted TCR Vγ4Jγ1-Vδ5Dδ2Jδ1, we found that a fraction of TCRγδ^{-} DN GFP^{+} DN cells progressed beyond the DN3 stage of development to the DN4 stage. Moreover, DN3 cells from the TCRVγ4Vδ5 cultures had much lower surface expression of CD25. Thus, these results suggest that the Vγ4Vδ5 TCR is capable of being expressed and is competent to signal in DN cells. To support this, we observed from CD44 vs CD45RB analysis that the DN4 population displayed a substantial upregulation of the CD45RB expression, a marker that is known to be upregulated after TCR signaling[319, 320].

Our experiments also demonstrated that within the GFP^{+} subset, a small of cells expressed the TCRγδ on the cell surface. To evaluate the signaling capacity of these TCRγδ we

double-stained with CD24 and CD25 to monitor γδ development. Our observations on the maturation within the γδ population clearly suggest that the TCRγδ is delivering signals that instruct γδ progenitors to first downregulate CD25 followed by CD24.

Analysis of the GFP^- subset showed maturation beyond the DN3 stage of development for those $Rag2^{-/-}$ infected with the retroviruses containing the $TCR^{IL\text{-}17}$. Control of gene expression of both the TCRγ and TCRδ chain is regulated by the retroviral promoter long terminal repeats (LTR). The LTRs contains all the signals required for gene expression: enhancer, promoter, transcription initiation, transcription termination and polyadenylation signal[321]. In contrast, eGFP translation is controlled by an internal ribosomal entry site that lies downstream of the $TCR^{IL\text{-}17}$ sequence. Thus, our observations suggest that a fraction of $Rag2^{-/-}$ thymocytes successfully transcribe and translate the $TCR^{IL\text{-}17}$ without translating eGFP. Based on the stochastic probability of this process we did not expect that one-hundred percent of TCR^+ thymocytes would be also $eGFP^+$. Therefore, we believe that a fraction of thymocytes were infected and expressed the $TCR^{IL\text{-}17}$-although undetectable on the cell surface by flow cytometry- but did not express GFP. Further evidence pointing towards the expression and signaling of the TCR within the GFP^- subset comes from looking at CD44 vs CD45RB expression, in which upregulation of CD45RB was observed.

In summary, our results demonstrate that a $TCR^{IL\text{-}17}$ was successfully transduced into $Rag2^{-/-}$ thymocytes. We could also demonstrate that only transduced thymocytes were able to progress beyond the DN3 stage of development to the DN4 stage, although we could not always observe TCR surface expression. We could also provide evidence that a fraction of the cells expressed a TCRγδ that was functional and capable to promote maturation within the γδ subset. In addition, we demonstrated that the efficiency of the internal ribosomal entry site

leading to the translation of GFP in infected thymocytes was not 100% efficient, as some GFP^- thymocytes were clearly infected and developed beyond the DN3 stage.

5.5.2.2 Foetal thymocytes expressing an IL-17 secreting γδ T cell-derived TCR Vγ4Jγ1-Vδ5Dδ2Jδ1, appears to drive commitment towards an IFNγ secreting effector fate, on OP9DL1 cells

Having established the successful delivery of the $TCR^{IL\text{-}17}$ construct into fetal $Rag2^{-/-}$ thymocytes, we went on to evaluate the development of γδ T cells and their acquisition of effector fate. We observed that $Rag2^{-/-}$ thymocytes that expressed the TCR were able to mature to become $\gamma\delta^{24-}$ cells. Importantly, when these $\gamma\delta^{24-}$were assessed for expression of CD44 and CD45RB, they uniformly displayed a $CD44^{+}CD45RB^{+}$ phenotype that is consistent with commitment to the IFNγ pathway. We did not record any evidence of development into the IL-17 pathway, which is the opposite to what we expected as we hypothesized that $TCR^{IL\text{-}17}$ would drive development of $Rag2^{-/-}$ towards the IL-17 pathway. This is an intriguing result and is the basis for the expansion and continuation of this project in the Pennington Lab. It may be that the development of thymocytes on OP9DL1 cells might not support entry into the γδ T cell IL-17 pathway. If the TCR has a critical role in the selection of thymocytes towards an IL-17 effector fate it is logical to think that some sort of ligand engagement might be important, one that the OP9DL1 cell culture system cannot provide. However, if this is the case, any such ligand is unlikely to be conventional, as it would need to reduce rather than promote signaling to induce an IL-17 secreting phenotype. Therefore, we suspect that OP9DL1 cells do not support the development of IL-17 secreting γδ T cells, and in turn, enhance (or do not affect) the development of the IFNγ effector subset.

5.5.2.3 The development of DN2 cells seems to be restricted on the OP9DL1 system

We observed a low number of thymocytes within the DN2 subset from E14 Rag2$^{-/-}$ and C57BL/6 mice background after 9-days of OP9DL1 culture with IL-7 and Flt3-ligand at 1 and 5ng/μl respectively. Similarly, Rag2$^{-/-}$ E15 thymocytes cultured for 2-days in FTOC and a further 7-days on OP9DL1 culture showed a marked reduction in the DN2 and DN3 populations, with many cells arrested at the DN1 stage. By contrast, Rag2$^{-/-}$ E15 thymocytes cultured for 9-days in FTOC developed to the DN3 stage, as expected, with a fraction of cells at the DN1 stage and a small percentage of DN2. We do not know why in our OP9DL1 cultures, the fraction of thymocytes at DN2 is so small compared with previous published data[322]. However, we suspect that the reduced number of Rag2$^{-/-}$ thymocytes at the DN2 stage might be the cause of our low efficiency in the transduction experiment. Retroviral transduction is only successful in dividing cells as retroviruses are only capable of entering the nucleus during the mitotic period when the nuclear envelope dissolves for cell division[323]. It has been shown that most proliferating cells among the double negative Rag2$^{-/-}$ thymocytes are DN2, with a lesser extent at the DN1 subset[322,324].

In addition, the absence of precursors at the DN2 stage of development might also explain the lack of development in IL-17 secreting γδ lymphocytes. Shibata et al[325] reported that IL-17 secreting γδ T cells develop from DN2 cells. In addition, they also observed that DN1 cells have also the potential to acquire IL-17 effector function, although with a lesser extent. Interestingly, they observed that IFNγ secreting γδ T cells were derived mainly from cells at DN3 stage of development. These results explain why we did not observe development of the IL-17 secreting γδ T cells, probably because we missed the DN2 cells when performing the transfection.

In summary, our experimental observations suggest that thymocyte development was not as efficient as it could be on OP9DL1 cells. Moreover, this decrease in the numbers of DN2 cells might be the cause of both, our low transduction efficiency and the absence of IL-17 secreting γδ T cells.

5.5.2.4 Possible reasons for inefficient development of thymocytes on OP9DL1 cells

The OP9DL1 co-culture system has been extensively used as an in-vitro model for T cell development[264]. In addition to the signal delivered by the Notch receptor, IL-7, Flt3 ligand and stem cell factor (SCF) are also critical for T cell development[326]. Flt3 ligand[327] and IL-7[328] were used in our culture system at concentrations of 5 ng/μl and 1 ng/μl, respectively. This resulted in inefficient thymocyte development when compared to $Rag2^{-/-}$ thymocytes cultured in conventional FTOC. A possible explanation for this could be that the concentration of IL-7 (1 ng/μl) in our OP9DL1 cultures was too high, in agreement with previous results showing failure of T cell differentiation from adult-derived lymphoid progenitors in an IL-7 dose-dependent manner[329]. However, Wang et al, using a similar system to ours, studied the effect of IL-7 and Flt3 ligand (both at 5 ng/μl) on T cell development in OP9DL1 culture. One of the conclusions of that study was that IL-7 is necessary for the differentiation of early T cell progenitors to later stages of development. In fact, the addition of a blocking IL-7 antibody arrested the development of 83% of the DN thymocytes at the DN1 stage[326]. Of note, they cultured the thymocytes with OP9DL1 cells for more than 15-days; this could explain why we do not see progression in our system, because we only left the thymocytes in culture for 9-days.

In conclusion, we observed slow progression of thymocyte development in 9-day cultures on OP9DL1cells with Flt3 ligand and IL-7 at 5 ng/μl and 1 ng/μl, respectively. We think, based on previous observations, that this might be a consequence of a short incubation period rather than a high concentration of IL-7. However, this is just a suggestion that needs to be further investigated, and a titration of IL-7 with WT E15 thymocyte culture is a logical next step.

5.5.3 Future Work

The aim of this project was to develop a system to begin to understand the role of TCRγδ on the acquisition of certain γδ T cell effector fates during the development of early thymocyte progenitors. The major, albeit preliminary, finding from this work will be the basis of the continuation of this project in the Pennington Lab. This finding suggests that in our OP9DL1 culture system expression of a cloned $TCR^{IL\text{-}17}$ in fetal $Rag2^{-/-}$ thymocytes does not drive commitment to an IL-17 secreting γδ T cell phenotype. Instead, γδ T cells committed to the IFNγ secreting pathway appear to be generated. This is presumably a consequence of culturing cells on OP9DL1 cells in our hands, and may signify the absence of a factor(s), which permits IL-17 secreting γδ T cell development. This may be a result of sub-optimal concentrations of IL-7, Flt3-l or SCF. Thus, titrations of these factors would be a first important step. It may also be that the choice of OP9DL1 cells is not the best for the study of this problem. We could attempt to directly infect intact thymic lobes in hanging drop cultures. In this E14/E15 thymic lobes will be suspended in 25 μl drops containing infectious retrovirus. It is hoped that progenitors will be transduced and the intact lobe will facilitate "normal" T cell development. Alternatively, we could try to reconstitute depleted thymic lobes (of thymocytes) with retrovirally-transduced E14/E15 $Rag2^{-/-}$ cells in hanging drops. After 2-days these reconstituted lobes would be transfer to filters for a further 7-days.

It is likely that an understanding of why this IL-17-specific TCRγδ does not drive development of IL-17-secreting γδ T cells on OP9DL1 cells will be of critical importance, it could suggest that a factor such as a IL-17-specific TCR-ligand could be missing. This factor presumably would reduce TCR signaling to permit IL-17 γδ development. The expression of Scart 1 and Scart 2, two potentially interacting partners for TCRγδ will be assessed on γδ

progenitors developing on OP9DL1 cells and compared to WT lobes. Scart 1 and Scart 2 are normally expressed on developing thymocytes and may dampen TCRγδ signaling when binding to stromal cells. This idea will be tested in future work.

6 CHAPTER 6

6.1 **FINAL CONCLUSIONS**

The integration of chemistry and biology has led to the development of the chemical-biology field that has proven very useful to answer biological questions that could not be solved by pure chemical or biological approaches alone. In this project, we have aimed to elucidate the mechanism of T cell receptor signaling using a chemical-biology approach, based on the synthesis of a maleimide-porphyrin aggregation reporter linked covalently to one of the transmembrane segments of the γδ T cell receptor and liposomes as model membranes (Chapters 2-4). In addition, we have also peformed functional studies in vitro with early thymocytes progenitors to understand the role of the TCRγδ receptor in the acquisition of effector function (Chapter 5).

The starting point of this study was the synthesis of the aggregation reporter - 5-(4-maleimide)-10, 15, 20 tris (4 - sulfonatophenyl) – porphyrin - denominated compound #5. In Chapter 2 we describe the synthetic pathway followed, which was based on previous work by Kochany et al[129]. Slight modifications were introduced ad hoc to improve the efficiency and the yield in some steps compared to the original protocol. The successful synthesis of Compound #5 was achieved and the product characterized by ^{1}H-NMR spectroscopy and mass spectrophotometry.

In Chapter 3 we investigated the conditions required to perform the labeling of some model thiols e.g. N-acetylcyteine, γ-gluthathion and 1-hexadecanethiol with Compound #5 prior to the work with the transmembrane peptide. We successfully achieved the model thiols labeling and determined that RP-HPLC was the best analytical technique to follow the reaction. As was demonstrated before, the labeling reaction only proceeds if the sulfhydryl group

is in the reduced state therefore we explored different reducing agents and whether or not the reduction was compatible with the labeling in a one-pot reaction. Our results suggested that TCEP and sodium dithionite, the reducing agents tested here, both cross-reacted with the maleimide group in compound #5. This indicated that reduction of the sulfhydryl group must be performed in a separate step.

In Chapter 4 we designed and studied some analytical methods to determine aggregation in model membranes. We successfully calculated the binding constant of compound #5 with phospholipids using an algorithm based on a 1:1 binding model. The Ka suggested that a fraction of unreacted Compound #5 was bound to the liposome membrane, which was confirmed by the experimental data. To remove the excess of unreacted porphyrin we determined that a GPC column combined with filtration using a concentrator was the best method. We also investigated the capacity of two reagents - p-Xylene –bis- (N-pyridinium bromide) (DPX) and 1,1′-diheptyl-4, 4′-bipyridinium dibromide (DPB) –to quench the fluorescence of Compound #5 and determined that DPB was the best quencher. The titration experiments with the peptides and lipids suggest that both peptides were inserted with the N-terminal facing the extra liposomal side. However, this result needs to be verified with further investigation. We successfully followed the reaction of the peptide control and the compound #5 by RP-HPLC.

In Chapter 5 we studied the role of the TCRγδ in the acquisition of effector fate phenotype during early thymocyte development. We successfully cloned the TCRVγ4Vδ5 restricted to the IL-17 secreting population into a retroviral vector. We achieved the generation of viral particles that successfully transduced the TCRγδ receptor to WT and $Rag2^{-/-}$ thymocyte. Our results show development of thymocyte beyond the DN3 stage, which effectively

demonstrate that the transduced receptor was able to transmit signaling, and interestingly our analysis revealed that thymocyte develops along the IFN-γ secreting pathway.

In summary, we have not obtained enough data to make firm conclusions regarding the ability of the TCRγδ transmembrane segment to aggregate when inserted in the model membrane. However, the results obtained here could serve as the basis for further study. On the other hand, we have demonstrated that the TCRγδ receptor that is restricted to the IL-17 secreting phenotype leads the development of the IFN-γ pathways, which suggests several conclusions. First, the development system (OP9DL1) does not support the development of the IL-17 effector subset. Second, some important signals might be missing that abrogate the development of the IL-17 effector thymocyte. This preliminary result will be followed up in our laboratory to further investigate the role of the TCRγδ in the acquisition of the γδ effector phenotype.

6.2 APPENDIX

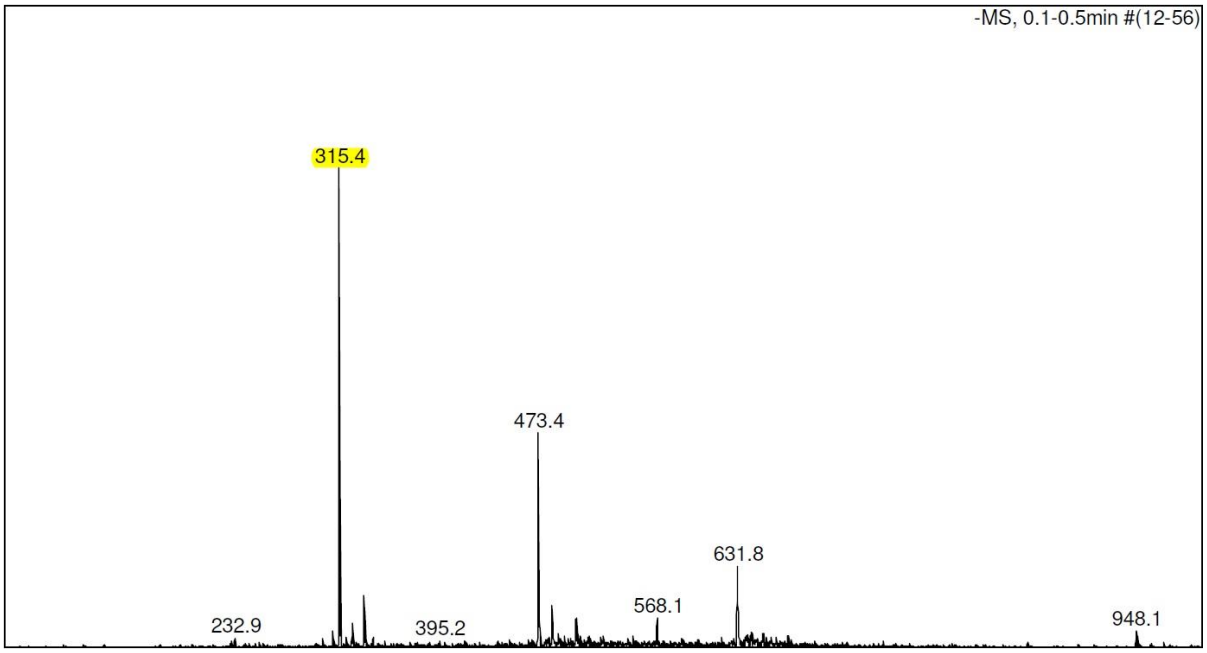

Figure 6-2. MALDI-TOF of compound #5 in the negative ion mode. As reference, the exact mass of the compound #5 is 946.10g/mol.

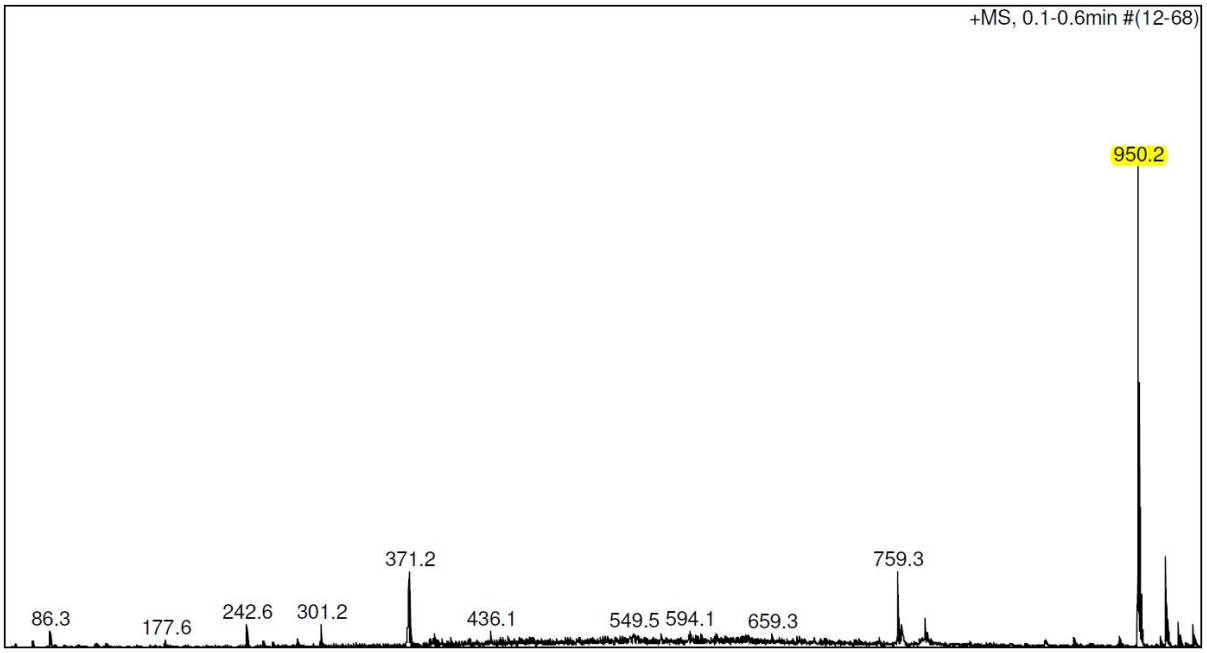

Figure 6-1. MALDI-TOF of compound #5 in the positive ion-mode. As reference, the exact mass of the compound #5 is 946.10g/mol.

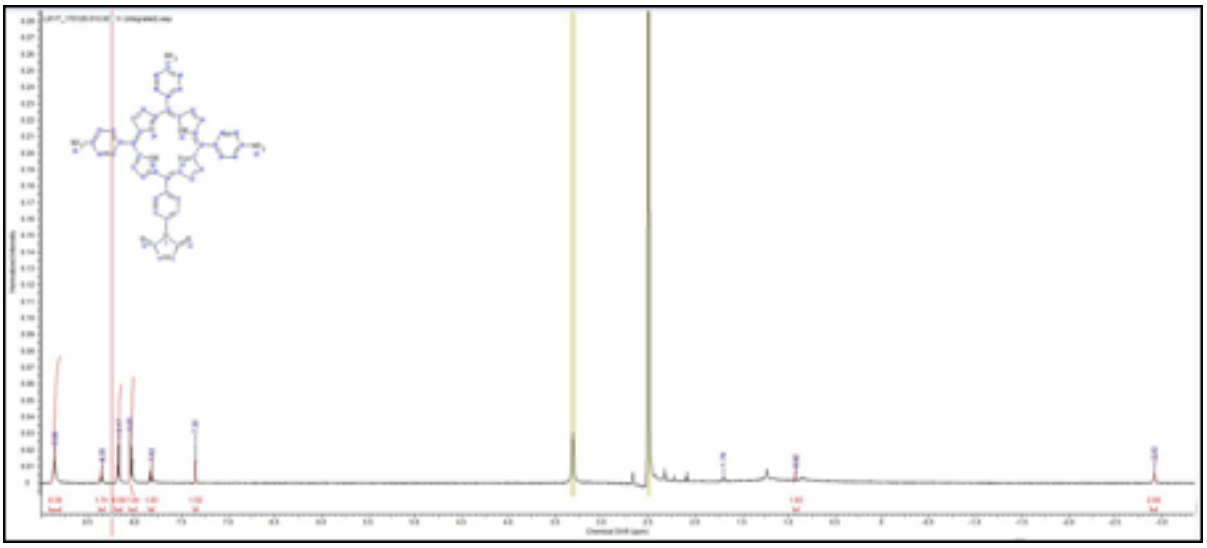

Figure 6-3. 1H NMR (400 MHz, DMSO-d6) spectrum of the maleimide sodium salt (close ring), (Pure Compound #5) at 25° C. recovered from the ion exchange chromatography.

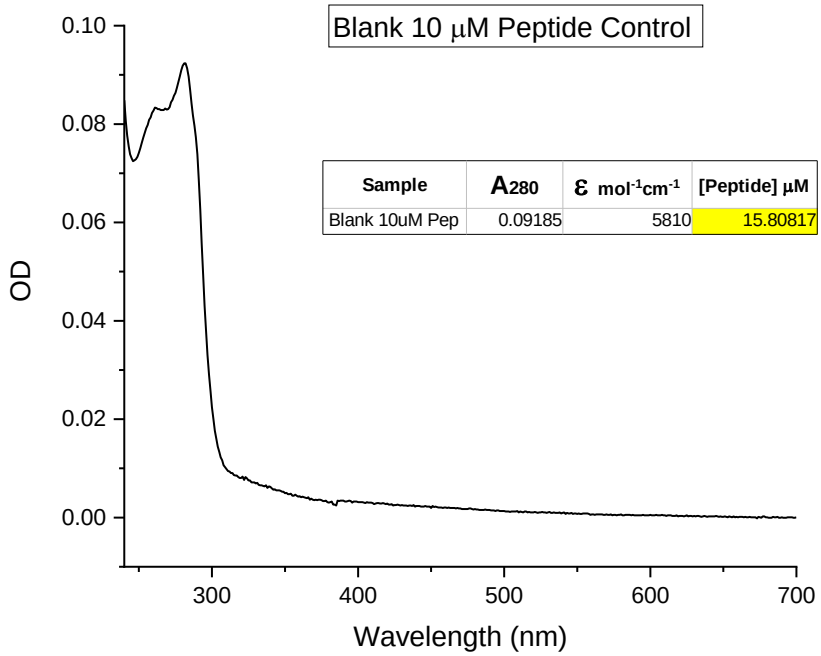

Figure 6-4. UV-vis spectrum of the control peptide sample. The inset table shows the concentration of the peptide based on the absorption of tryptophan at 280 nm.

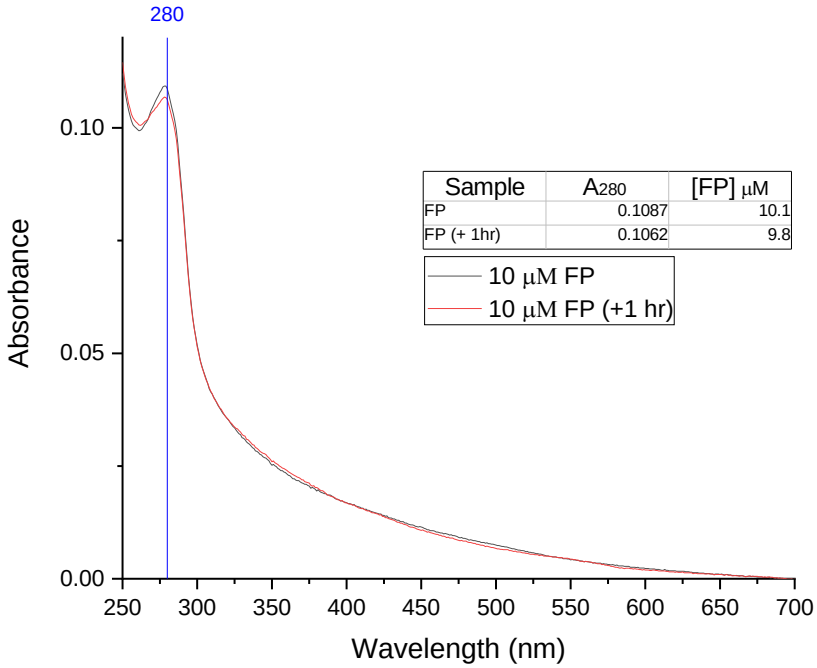

Figure 6-5. UV-vis spectra of two samples of full-length peptide recorded at time 0 and 1hr. The inset table shows the concentration of the peptide based on the absorption of tryptophan at 280 nm

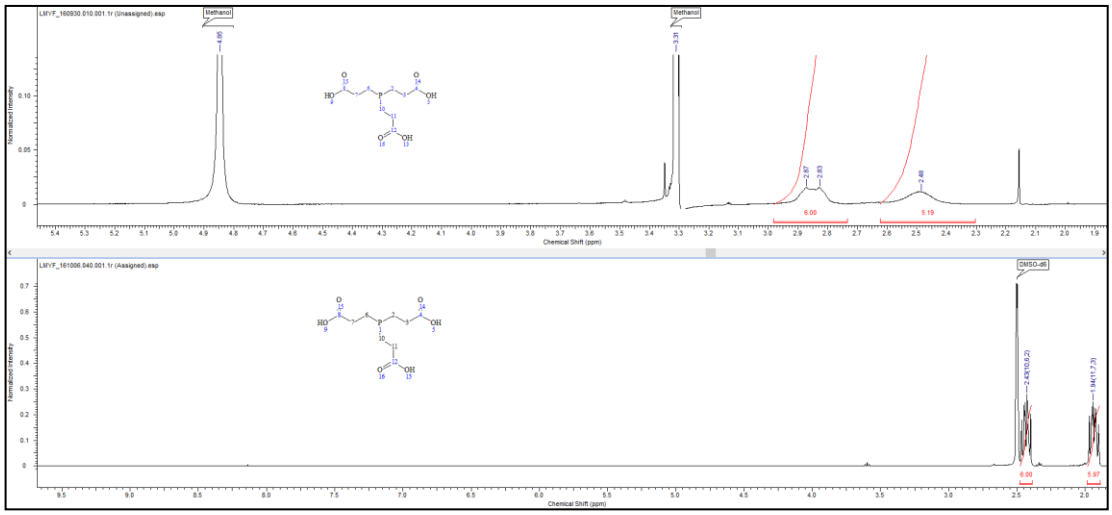

Figure 6-6. 1H NMR (400 MHz, MeOD and DMSO-d6) spectra of TCEP: A) 5 mM TCEP in MeOD; B) 5 mM TCEP DMSO.

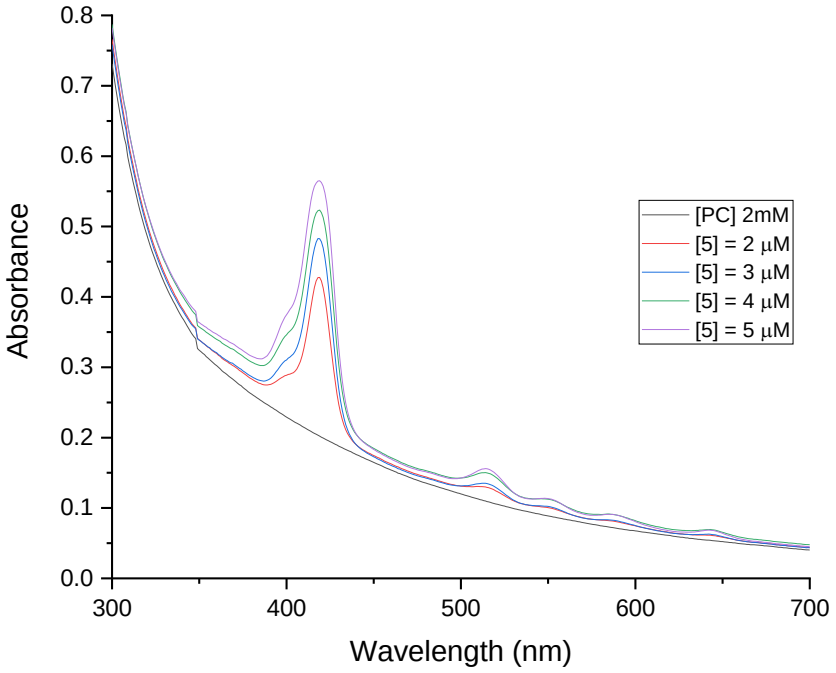

Figure 6-8. 2 mM solution of liposomes prepared with compound #5 at 2, 3, 4, and 5 μM.

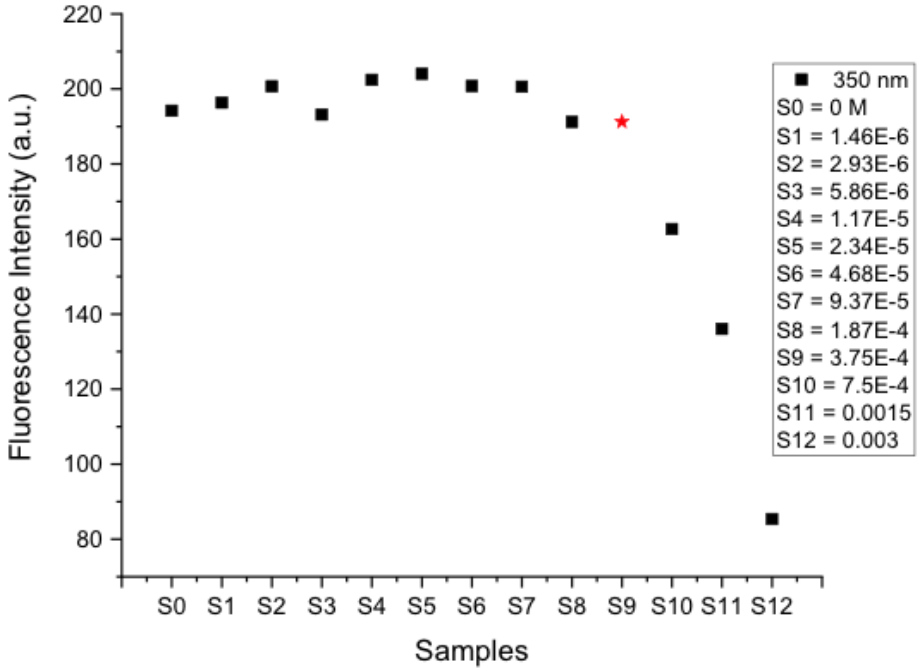

Figure 6-7. Plot showing the changes in the tryptophan fluorescence intensity at 350 nm at different concentrations of [PC]. The sample at 3.75 x 10^{-4} M (S9) marked with an arrow represents the concentration from which the fluorescence started to be quenched.

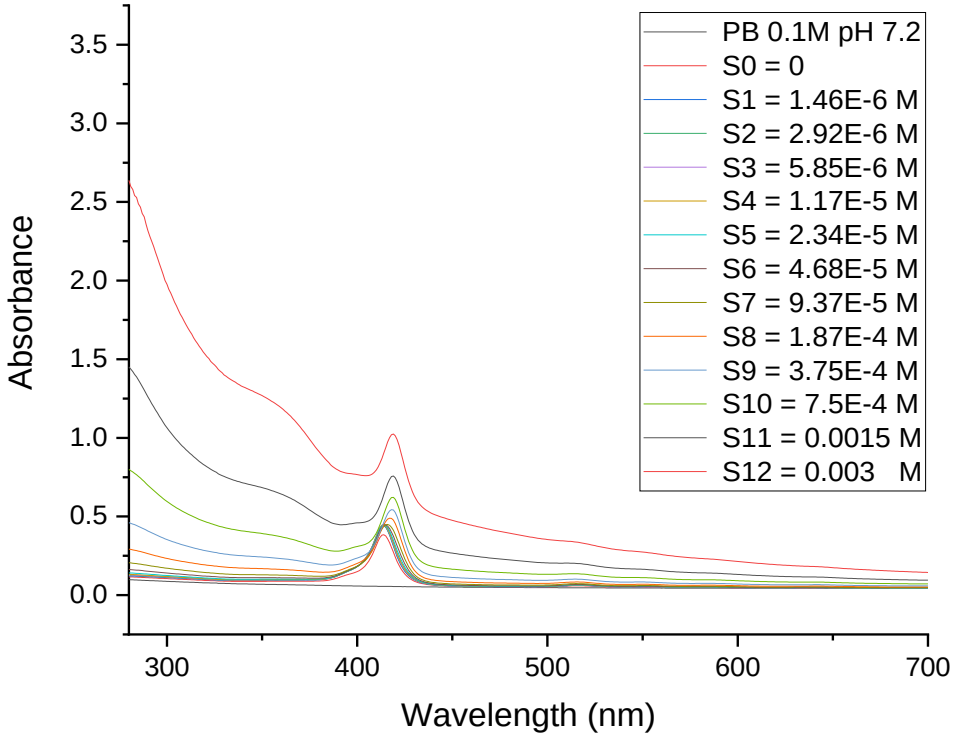

Figure 6-10. Raw UV-vis spectral data of the titration of compound #5 with twelve solutions of liposomes.

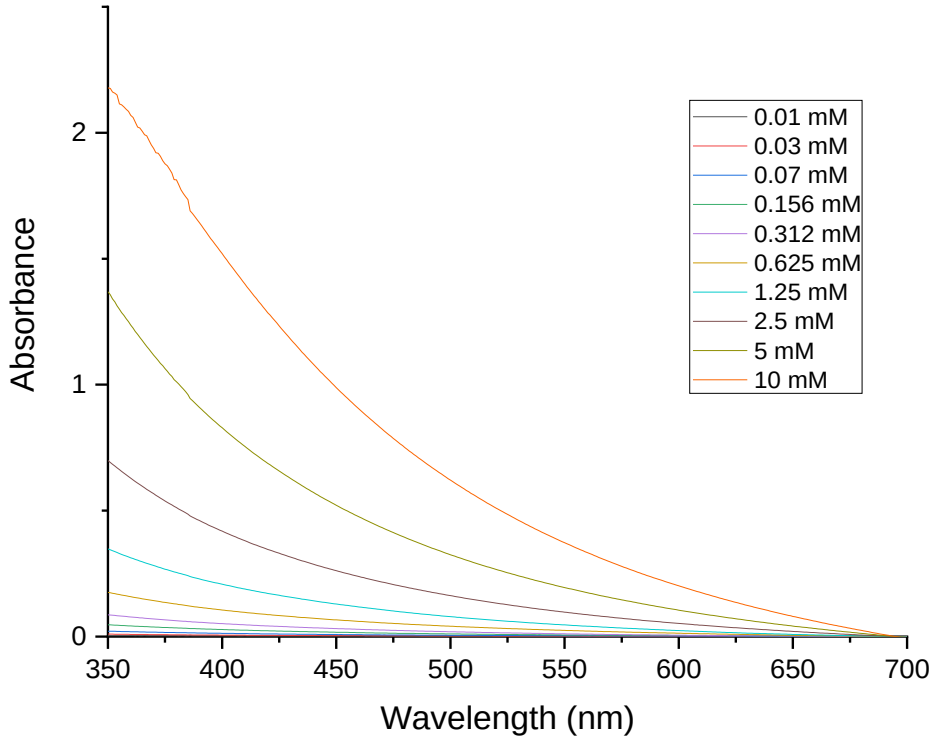

Figure 6-9. Raw UV-vis spectral data of light scattering of ten-solutions of liposome at increasing concentrations of phosphatidyl-choline.

Product 10 (LeaderVγ4Jγ1Cγ1-P2A, 1062bp) (5'-3')

ctcggatccactatgaagaaccctggctcacaagccctgcttccttttatatcttccctgggaagccaacctggcagatga
gaatccactcctgaaagtagtcattttcttatgcctcttgacatttggacaacctgaaatatcaatttccagagcaagag
atgagactgcacaaatatcctgtaaagttttcatcgaaagctttaggagtgtaaccatacactggtaccggcagaaacca
aaccaaggtttagagtttctattatatgtccttgcaacccctacccatattttcttagataaggagtacaagaaaatgga
ggcaagtaaaaatcctagtgcttctacatcgatattgacaatatattccttggaggaagaagacgaagctatctactact
gttcctacggcttatatagctcaggttttcacaaggtatttgcagaaggaactaagctcatagtaattccctctgcagac
aaaaggcttgatgcagacatttcccccaagcccactattttccttccttctgttgctgaaacaaatctccataagactgg
gacataccttttgtctccttgaaaagttctttccagatgttataagggtgtattggaaagaaaaggatggcaatactatcc
tggactcccaggaaggggatacgctgaagactaacgacacatacatgaagtttagctggcttacagtgcctgaaagggca
atggggaaagagcacagatgtattgtcaaacatgagaacaacaaaggaggagcagatcaagagattttctttccttcaat
aaagaaagttgctgtgagtaccaagcctacaacttgctggcaagataaaaatgatgtgctgcagctccagttcacgatca
cctctgcctactacacctaccttctcctgctcctcaagagtgtgatctacttggccatcatcagcttctctctgcttaga
agaacatctgtctgtggcaatgagaagaaatccggctccggagccacgaacttctctctgttaaagcaagcaggagacgt
ggaagaaaaccccggtcccatg

Product 5 (LeaderVδ5Dδ2Jδ1Cδ1-vector, 975bp) (5'-3')

cgagctcggatccactagtaacggccgccagtgtgctggaattcaggatgattgtt-
gccgcgacccttacccttctgtttgcctacaaggatgtgctgtgcatcac-
gctgacccagagctccactgaccagacagtggcaagcggcactgaagtaacactgctctg-
cacgtacaatgcggattctccaaacccagatttattttggtatcgcaaaaggccaga-
cagatccttccagttcatcctttatagggacgacactagttcccatgatgcagatttt-
gttcaaggtcgattttctgtgaagcacagcaaggccaacagaac-
cttccatctggtgatctctccagtgagccttgaagacagcgc-
tacttattactgtgcctcggggtatatcggagggatacgagctaccgacaaactcgtcttt-
ggacaaggaacccaagtgactgtggaaccaaggagccagcctccggccaaac-
catctgttttcatcatgaaaaatggaacaaatgttgcttgtctggtgaaagatttc-
taccctaaagaggtgactataagtctcagatcatccaagaagattgtggaattcgaccctgc-
tatagtcatctcccccagcgggaagtacagtgctgtcaagcttggtcagtatggagat-
tcgaattcagtgacatgttcagttcagcacaacagtgaaactgtgcactcgactgacttt-
gaaccatatgcaaattctttcaataatgaaaaactaccagaac-
ctgaaaatgacacacaaatttcagagccttgctatggcccaagagtcacagttcacactga-
gaaggtaaacatgatgtccctcacggtgctgggcctacgactgctgtttgccaagaccatt-
gccatcaattttctcttgactgttaagttattcttttaacctgaattctgcaga-
tatccatcacactggcggccgctcgagcatgcatctagag

TCRγ-2A-TCRδ (1987bp) (5'-3')

ctcggatccactatgaagaaccctggctcacaagccctgcttccctttatatcttccctgggaagccaacctggcagatga
gaatccactcctgaaagtagtcattttcttatgcctcttgacatttggacaacctgaaatatcaatttccagagcaagag
atgagactgcacaaatatcctgtaaagttttcatcgaaagctttaggagtgtaaccatacactggtaccggcagaaacca
aaccaaggtttagagtttctattatatgtccttgcaacccctacccatattttcttagataaggagtacaagaaaatgga
ggcaagtaaaaatcctagtgcttctacatcgatattgacaatatattccttggaggaagaagacgaagctatctactact
gttcctacggcttatatagctcaggttttcacaaggtatttgcagaaggaactaagctcatagtaattccctctgcagac
aaaaggcttgatgcagacatttcccccaagcccactattttccttccttctgttgctgaaacaaatctccataagactgg
gacataccttttgtctccttgaaaagttctttccagatgttataagggtgtattggaaagaaaaggatggcaatactatcc
tggactcccaggaaggggatacgctgaagactaacgacacatacatgaagtttagctggcttacagtgcctgaaagggca
atggggaaagagcacagatgtattgtcaaacatgagaacaacaaaggaggagcagatcaagagattttctttccttcaat
aaagaaagttgctgtgagtaccaagcctacaacttgctggcaagataaaaatgatgtgctgcagctccagttcacgatca
cctctgcctactacacctaccttctcctgctcctcaagagtgtgatctacttggccatcatcagcttctctctgcttaga
agaacatctgtctgtggcaatgagaagaaatccggctccggagccacgaacttctctctgttaaagcaagcaggagacgt
ggaagaaaaccccggtcccatgattgttgccgcgacccttacccttctgtttgcctacaaggatgtgctgtgcatcacgc
tgacccagagctccactgaccagacagtggcaagcggcactgaagtaacactgctctgcacgtacaatgcggattctcca
aacccagatttattttggtatcgcaaaaggccagacagatccttccagttcatcctttatagggacgacactagttccca
tgatgcagattttgttcaaggtcgattttctgtgaagcacagcaaggccaacagaaccttccatctggtgatctctccag
tgagccttgaagacagcgctacttattactgtgcctcggggtatatcggagggatacgagctaccgacaaactcgtcttt
ggacaaggaacccaagtgactgtggaaccaaggagccagcctccggccaaaccatctgttttcatcatgaaaaatggaac
aaatgttgcttgtctggtgaaagatttctaccctaaagaggtgactataagtctcagatcatccaagaagattgtggaat
tcgaccctgctatagtcatctcccccagcgggaagtacagtgctgtcaagcttggtcagtatggagattcgaattcagtg
acatgttcagttcagcacaacagtgaaactgtgcactcgactgactttgaaccatatgcaaattctttcaataatgaaaa
actaccagaacctgaaaatgacacacaaatttcagagccttgctatggcccaagagtcacagttcacactgagaaggtaa
acatgatgtccctcacggtgctgggcctacgactgctgtttgccaagaccattgccatcaattttctcttgactgttaag
ttattcttttaacctgaattctgcagatatccatcacactggcggccgctcgagcatgcatctagag

6.2.1.1 Distribution of Vγ4$^+$ γδ$^+$ lymphocytes in the mouse skin

To investigate the distribution of Vγ4$^+$ γδ T lymphocytes within the two compartments of the skin i.e. epidermis and dermis, we obtained single-cell suspensions from the epidermis and dermis of C57BL/6 ears. In agreement with previous observations[239] we found that almost all the CD3$^+$ cells residing in the epidermis are γδ cells, from which approximately 80% accounted for Vγ5$^+$, 4% for Vγ4$^+$ lymphocytes and 13% other Vγ usage lymphocytes (Figure 6-11 D). We identified a small fraction of CD3$^+$ lymphocytes (~1%) to be αβ T cells (Figure 6-11 B and C).

In the dermis, similarly, the majority of the CD3$^+$ cells were γδ lymphocytes (81%), however the percentage of the αβ cells homing to the dermis (5%) are higher compared with the epidermis (Figure 6-11 B and C). The analysis of the Vγ usage within the γδ subset shows that 75% are Vγ5$^+$ thymocytes, 2% represents the Vγ4$^+$ subset, and around 19% other Vγ receptors.

These results are at odds with previous observations in the mouse skin, that reported almost exclusively Vγ5$^+$ γδ cells homing in the epidermis, with scarce representation of other Vγ subsets[239], whereas in the dermis, in contrast, the proportion of the Vγ5$^+$ was significantly lower compared with the Vγ4$^+$ subset.

Summary

Collectively, these data indicate that the epidermis contains a residing population of $CD3^+$ cells that are predominantly $V\gamma5^+$ γδ cells with a minor representation of other Vγ subsets or αβ lymphocytes. On the other hand, for the dermis compartment, under our experimental conditions, we detect a sizable proportion of γδ cells, where $V\gamma5^+$ subset were the dominant subset, although a proportion of other subsets i.e. $V\gamma5^-V\gamma4^-$ were also found.

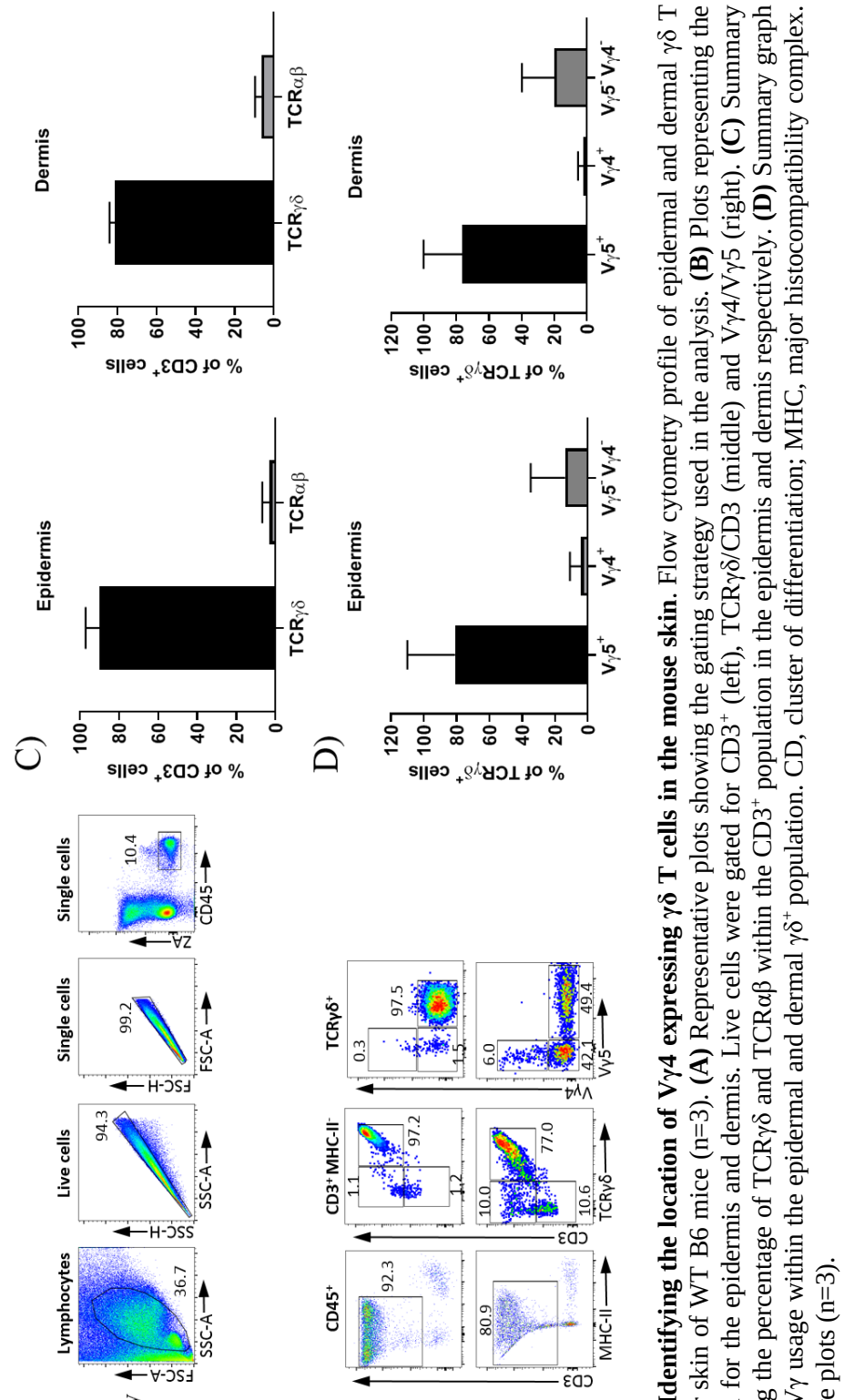

Figure 6-11. **Identifying the location of Vγ4 expressing γδ T cells in the mouse skin**. Flow cytometry profile of epidermal and dermal γδ T cells from ear skin of WT B6 mice (n=3). **(A)** Representative plots showing the gating strategy used in the analysis. **(B)** Plots representing the gate selection for the epidermis and dermis. Live cells were gated for $CD3^+$ (left), TCRγδ/CD3 (middle) and Vγ4/Vγ5 (right). **(C)** Summary graph showing the percentage of TCRγδ and TCRαβ within the $CD3^+$ population in the epidermis and dermis respectively. **(D)** Summary graph showing the Vγ usage within the epidermal and dermal $γδ^+$ population. CD, cluster of differentiation; MHC, major histocompatibility complex. Representative plots (n=3).

6.2.1.1 Representation of Vγ4$^+$ and Vγ1$^+$ γδ$^+$ lymphocytes in the mouse lymph nodes

After the examination of the skin, we decided to explore the distribution of Vγ4$^+$ and Vγ1$^+$ subsets of γδ cells within the lymph nodes. To this end, we isolated lymphocytes from the brachial, inguinal and axillary skin-draining lymph nodes from C57BL/6 mice and obtained a single-cell suspension (See section 5.3.3.1). Following the gating strategy shown in Figure 6-12 A we analysed the fraction of γδ$^+$ cells for the expression of both Vγ4$^+$ and Vγ1$^+$, and evaluated the representation of each Vγ subset within one of the two effector fate commitment pathways, following the methodology described in section 5.1.6.

The γδ$^+$ subset (~ 0.4%) was subdivided based on the expression of CD24, with a sizable proportion of γδ^{24-} (~80%) representation over the γδ^{24+} (~15%). The γδ^{24-} subset in the lymph nodes was composed of approximately 38% of Vγ1$^+$, 38% of Vγ4$^+$, and 16% of other subsets (Figure 6-12 C).

The Vγ1$^+$, Vγ4$^+$, and Vγ1$^-$ Vγ4$^-$ subsets were further analysed for the expression of CD44 and CD45RB (Figure 6-12 B). The summary graph presented in Figure 6-12 D, shows that around 20% of Vγ1$^+$ cells are CD44$^-$CD45RB$^+$ subset ("c"), which are committed to the secretion of IFN-γ, and nearly 10% are CD44$^+$CD45RB$^-$ ("d") and committed to the IL-17 pathway.

For the Vγ4$^+$ subset, we observed that approximately 25% of the cells are skewed towards the IL-17 effector pathway (CD44$^+$CD45RB$^-$) ("d"), whereas around 19% are CD44$^-$ CD45RB$^+$, thus committed to the IFN-γ secretion pathway.

The Vγ1^{-} Vγ4^{-} subset contains around 15% of γδ T cells engaged in both the IL-17 and the IFN-γ effector commitment pathways as illustrated in Figure 6-12 C.

Next, we decided to investigate the ability of the γδ^{+} lymphocytes to produce IFN-γ or IL-17 after 4 hours stimulation with PMA and ionomycin. As Figure 6-12 B shows, within population "c" (IFN-γ producers) around 5% of Vγ1^{+} and Vγ1^{-} Vγ4^{-} γδ^{+} lymphocytes readily produce IFN-γ, whereas this percentage is increased up to 18% for the Vγ4^{+} subset. The analysis of the population "d" shows that 6.7% of Vγ1^{+}, followed by 16.4% of Vγ1^{-} Vγ4^{-}, and around 60% of Vγ4^{+} subset produce IL-17. These results are in agreement with previously reported data for γδ^{+} lymphocytes from the lymph nodes, although they observed a significantly higher production of IFN-γ[1].

Summary

In conclusion, the data presented in this section suggest that in C57BL/6 adult, the skin draining lymph nodes harbour a population of γδ^{+} lymphocytes composed of Vγ1^{+}and Vγ4^{+} predominantly. We also observed that the Vγ1^{+} subset is almost two-fold increased in the IFN-γ effector pathway, whereas the Vγ4^{+} subset shows a preference towards the IL-17 effector fate. The pool of Vγ1^{-} Vγ4^{-} lymphocytes seems to contribute proportionally to each effector fate pathway.

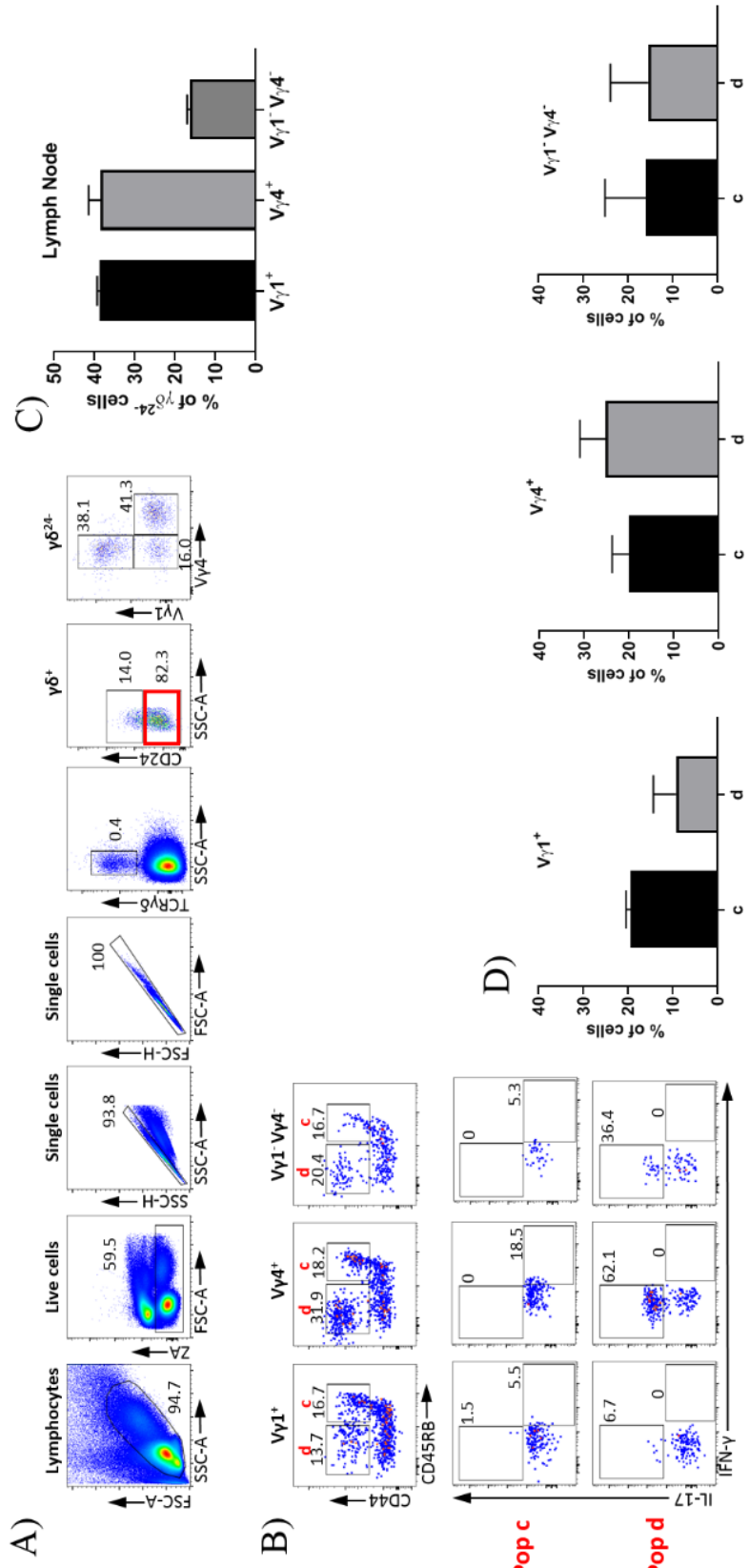

Figure 6-12. **Identification of Vγ1 and Vγ4 usage within the pool of γδ T lymphocytes populating the lymph nodes**. **(A)** Assessing the usage of Vγ1, Vγ4 and the effector phenotype in the γδ T cell population from the skin-draining lymph nodes (LNs) of C57BL/6 WT adult mice. Mature, $CD24^{-}$ γδ T cells (red square) were stained for Vγ1 and Vγ4 identifying three populations (first row, far right). **(B)** Each Vγ specific population was gated for the expression of CD44 and CD45RB. To assess the expression of IL-17/IFN-γ in the Vγ1, Vγ4, and other Vγ usage cells intracellular staining with IL-17 and IFN-γ antibodies was performed in both "c" and "d" subsets as shown in the second and third rows. **(C)** Summary graph showing the percentage of $Vγ1^{+}$, $Vγ4^{+}$, and $Vγ1^{-}$ $Vγ4^{-}$ within the mature $γδ^{CD24-}$ population. **(D)** Summary of (B) showing the percentage of cells within the c and d population for $Vγ1^{+}$, $Vγ4^{+}$, and $Vγ1^{-}$ $Vγ4^{-}$. Representative plots (n=3).

6.2.1.2 Characterization of the Vγ4$^+$ and Vγ1$^+$ γδ$^+$ lymphocytes repertoire in the mouse spleen

In a similar approach as the one described in section 5.4.7.5, we investigated the distribution of Vγ1$^+$ and Vγ4$^+$ γδ$^+$ lymphocytes in the spleen of adult C57BL/6 mice.

We observed that about 66% of the γδ$^+$ lymphocytes are within the γδ^{24-}, and they represent the mature population[1]. We went on to double stain for Vγ1$^+$ and Vγ4$^+$ to identify the representation of these receptors in the adult spleen (Figure 6-13 A). The analysis of the data shows that Vγ1$^+$ represents approximately 42 % of the γδ^{24-} splenocytes, the Vγ4$^+$ subset account for around 29% and the pool of Vγ1$^-$Vγ4$^-$ around 16% (Figure 6-13 C).

Then we decided to further investigate each particular subset with the staining method described previously, i.e. CD44 vs CD45RB, to visualize the commitment of the splenocytes towards the IFN-γ or IL-17 secretion pathway (Figure 6-13 B and D). We observed that 28% of the cells within the Vγ1$^+$ subset are CD44$^-$CD45RB$^+$ ("c"), whilst around 5% are committed to the IL-17 pathway (CD44$^+$CD45RB$^-$, "d"). Interestingly, around 33% of the Vγ4$^+$ splenocytes are engaged in the IFN-γ pathway ("c"), and nearly 22% of the cells enter the IL-17 secretion pathway ("d"). For the Vγ1$^-$Vγ4$^-$ γδ cells, the percentage of cells within each developmental pathway is similar, with 20% and 18% of splenocytes within "c" and "d" populations, respectively.

The capability of the cells to synthetize cytokines was also evaluated (Figure 6-13 B). Although the stimulation does not seems to be have worked as well it is possible to see that within the "d" population some of the cells are readily synthetizing IL-17A, especially the Vγ4$^+$ subset with approximately 23% of the cells. The cells within population "c" do not respond to the PMA and ionomycin stimulation as readily as we expected.

Summary

In the light of these results we can conclude that in the C57BL/6 adult spleen the $V\gamma1^+$ subset represents the majority of the mature splenocytes homing to the spleen, followed by the $V\gamma4^+$ subset, and some other $V\gamma$ subsets are also observed, although less abundantly. Importantly, we detected that most of the $V\gamma1^+$ splenocytes are biased towards the IFN-γ production, although the cells were less inclined to produce cytokine (IFN-γ) after stimulation. The $V\gamma4^+$ population, instead, shows an increment in the number of cells within the "d" compartment, although the majority of the cells found are engaged in the IFN-γ secretion pathway. Similar to the previous observation in the last section, the pool of $V\gamma1^-V\gamma4^-$ splenocytes seems to contribute equally to each effector fate pathway.

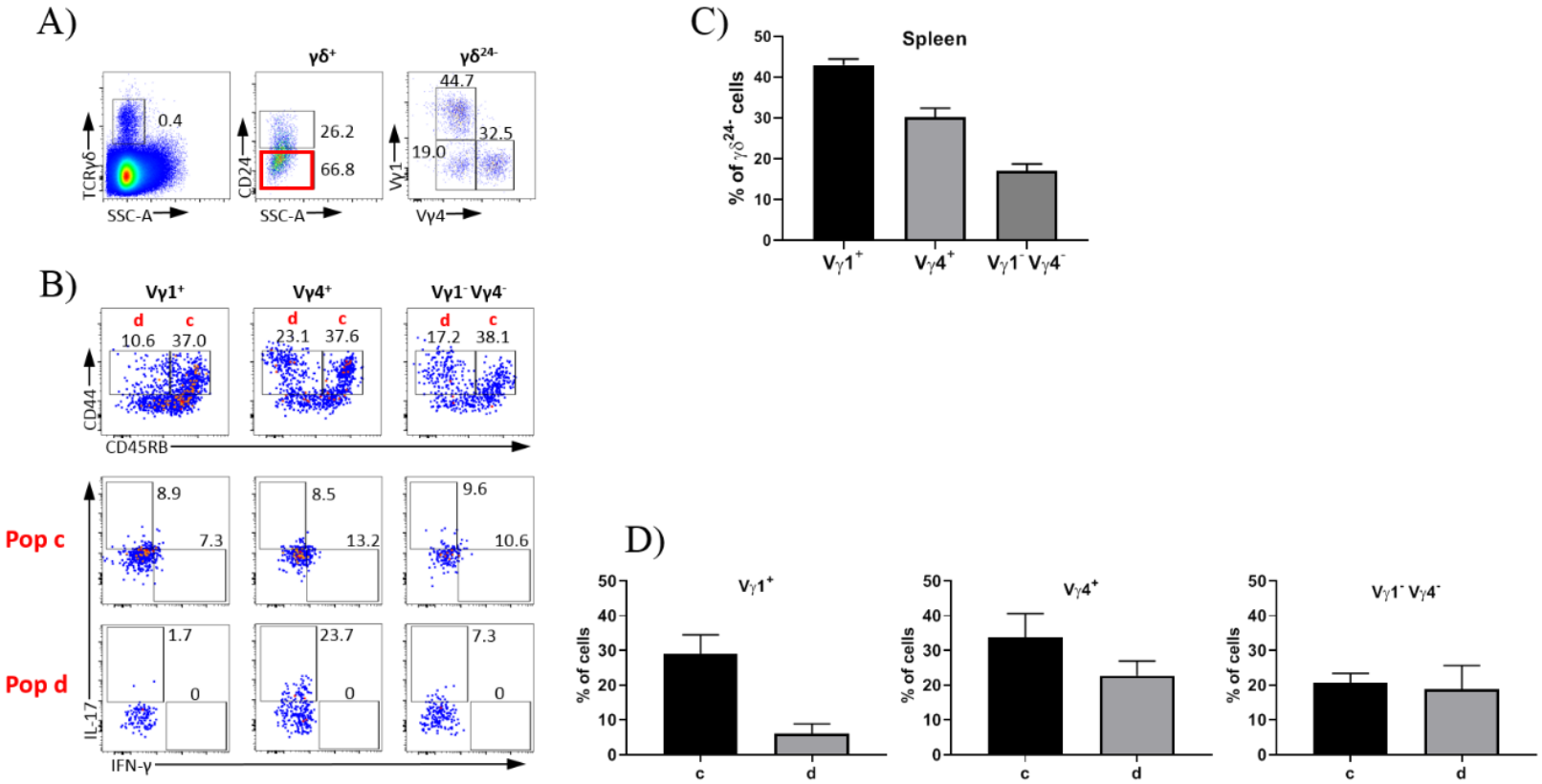

Figure 6-13. **Gating strategy to identify the frequency of Vγ1$^+$ and Vγ4$^+$ γδ cells within the splenocyte pool. (A)** γδ T cell profile from the spleen of a C57BL/6 adult mouse. Mature γδ^{CD24-} cells (top middle, within red square) were assessed for the expression of Vγ1$^+$ and Vγ4$^+$. **(B)** Vγ1$^+$, Vγ4$^+$, and Vγ1$^-$ Vγ4$^-$ populations are further subdivided with the markers CD44 and CD45RB. The synthesis of cytokines was evaluated by intracellular staining within the "c" (second row) and "d" (third row) populations for Vγ1$^+$, Vγ4$^+$, and Vγ1$^-$ Vγ4$^-$. **(C)** Summary plot of (A) showing the percentage of Vγ1$^+$, Vγ4$^+$, and Vγ1$^-$ Vγ4$^-$ within the mature subset γδ^{CD24-}. **(D)** Summary graphs of (B) showing the percentage of cells within each subset "c" and "d" for Vγ1$^+$, Vγ4$^+$, and Vγ1$^-$ Vγ4$^-$ subsets. Representative plots (n=3).

6.2.1.1 Repertoire of Vγ4$^+$ and Vγ1$^+$ γδ$^+$ lymphocytes in the mouse thymus

To study the repertoire of Vγ1$^+$ and Vγ4$^+$ γδ$^+$ lymphocytes in the thymus we harvested thymuses from adult C57BL/6 mice and obtained single-cell suspensions that were depleted of CD4$^+$ and CD8$^+$ cells but containing the γδ$^+$ subset.

The γδ$^+$ population was subdivided and analysed by the expression of CD24. As can be observed in Figure 6-14 A the γδ^{24+} subset represents the majority of the γδ$^+$ cells within the thymus. The double staining for Vγ1 and Vγ4 reveal that 50.0% of the γδ^{24+} are Vγ4$^+$, followed by 26.6% of Vγ1$^+$ and 16% for the Vγ1$^-$Vγ4$^-$ pool (Figure 6-14 C). The CD44 and CD45RB staining of γδ^{24+} thymocytes revealed that these cells had not matured enough yet to enter any route of differentiation towards the IFN-γ or the IL-17 effector pathway.

On the other hand, the γδ^{24-} population represents a small fraction of the γδ$^+$ subset (Figure 6-14 B). Unlike the γδ^{24+} subset, the staining for Vγ1 and Vγ4 shows that 56% of the cells are Vγ1$^+$, followed by 22% of Vγ4$^+$, and 12% of Vγ1$^-$Vγ4$^-$ subset (Figure 6-14 D). As Figure 6-14 E shows, the staining for CD44 and CD45RB segregates each particular Vγ subset into two populations, CD44$^-$CD45RB$^+$ ("c") and CD44$^+$CD45RB$^-$ ("d"), engaged towards the IFN-γ or IL-17 effector pathway, respectively. Moreover, we observed that within the Vγ1$^+$ subset, 70% of the cells were differentiated towards the IFN-γ producer (population "c"). Interestingly, the majority of the Vγ4$^+$ cells, around 82%, were biased towards the IL-17 effector phenotype. Similarly, the same trend was observed within the pool of Vγ1$^-$Vγ4$^-$ cells where 86% of the cells were found in the CD44$^+$CD45RB$^-$ gate (population "d"). These results, in fact, are in agreement with previous observations from Sumaria et al[1] described in the introduction section of this thesis.

Summary

Collectively, the data obtained from these experiments suggest the majority of the $\gamma\delta^{+}$ cells in the C57BL/6 adult thymus is represented by the immature $\gamma\delta^{24+}$ subset. In addition, we identified that within that subset the Vγ representation was $V\gamma4^{+} > V\gamma1^{+} > V\gamma1^{-}V\gamma4^{-}$. However, the staining for CD44 and CD45RB reveal that $\gamma\delta^{24+}$ thymocytes are double negative, thus their effector phenotype cannot be discriminated using this strategy at this early stage of development (data already published). Analysis of the mature $\gamma\delta^{24-}$ showed that this population were less abundant in the adult thymus compared to the $\gamma\delta^{24+}$. The evaluation of the Vγ repertoire shows a different picture with $V\gamma1^{+} > V\gamma4^{+} > V\gamma1^{-}V\gamma4^{-}$. The CD44 vs CD45RB staining strategy within the mature $\gamma\delta^{24-}$ subset allows the recognition of the two distinct effector committed subsets. Analysis of each subset revealed that $V\gamma1^{+}$ thymocytes are skewed towards the IFN-γ production, whilst the $V\gamma4^{+}$ and $V\gamma1^{-}V\gamma4^{-}$ cells are predominantly engaged in the IL-17 secreting pathway.

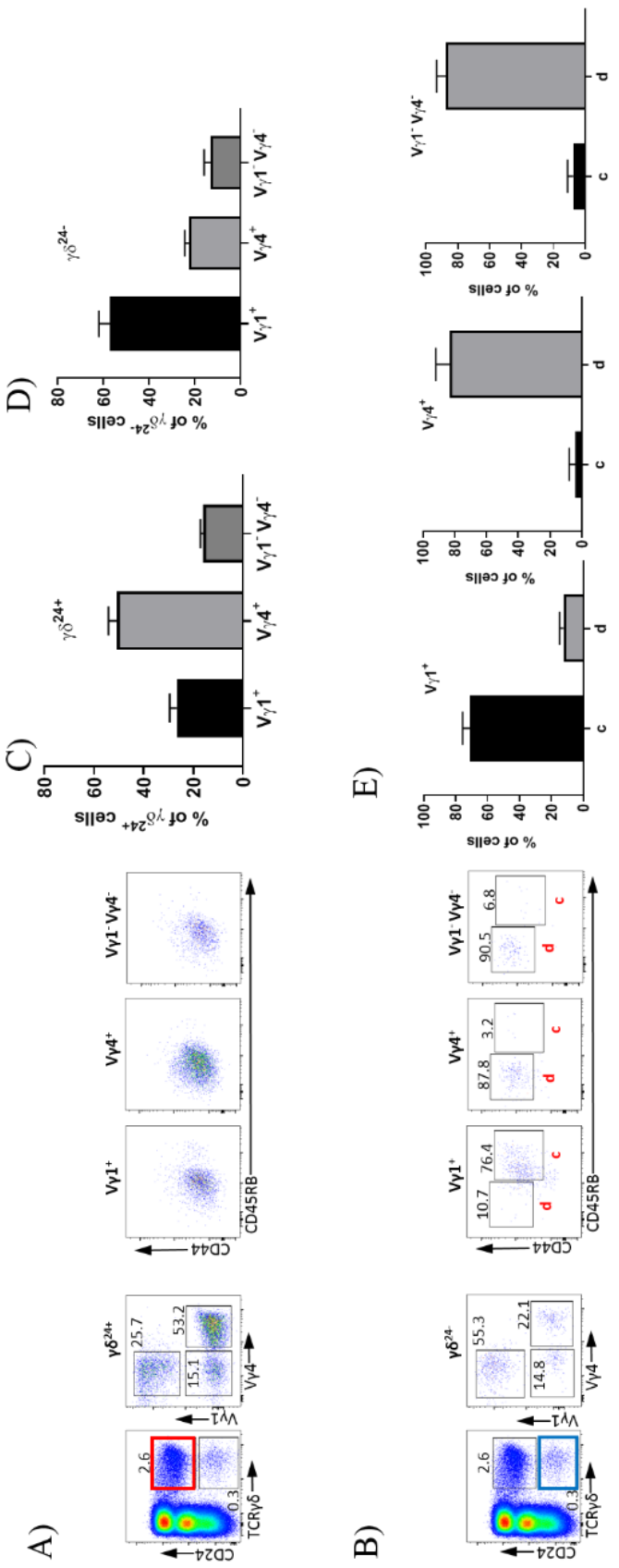

Figure 6-14. **Repertoire of Vγ1 and Vγ4 γδ thymocytes within the $\gamma\delta^{CD24-}$ and $\gamma\delta^{CD24+}$ subsets and evaluation of the effector fate commitment.** γδ T cells from the thymus of C57BL6 adult mice were assessed by the expression of TCRγδ and CD24. **(A)** Immature $\gamma\delta^{CD24+}$ thymocytes (red square) were assessed for the expression of Vγ1/Vγ4 chain receptor. The effector fate commitment of all three subsets were further analyzed by double staining with CD44 and CD45RB. **(B)** Selection of mature $\gamma\delta^{CD24-}$ thymocytes (blue square) for assessment of Vγ1/Vγ4 usage. **(C)** Summary plot of (A) showing the percentage of $V\gamma1^+$, $V\gamma4^+$, and $V\gamma1^-V\gamma4^-$ within the mature subset $\gamma\delta^{CD24+}$. **(D)** Summary plot of (B) showing the percentage of $V\gamma1^+$, $V\gamma4^+$, and $V\gamma1^-V\gamma4^-$ within the mature subset $\gamma\delta^{CD24-}$. **(E)** Summary graphs of (B) showing the percentage of cells within each subset "c" and "d" for $V\gamma1^+$, $V\gamma4^+$, and $V\gamma1^-V\gamma4^-$ subsets. Representative plots (n=3).

6.3 **BIBLIOGRAPHY**

1. Sumaria, N.; Grandjean, C. L.; Silva-Santos, B.; Pennington, D. J., Strong TCRgammadelta Signaling Prohibits Thymic Development of IL-17A-Secreting gammadelta T Cells. *Cell Rep* **2017,** *19* (12), 2469-2476.
2. Rothenberg, E. V.; Moore, J. E.; Yui, M. A., Launching the T-cell-lineage developmental programme. *Nat Rev Immunol* **2008,** *8* (1), 9-21.
3. Pereira, P.; Boucontet, L., Rates of recombination and chain pair biases greatly influence the primary gammadelta TCR repertoire in the thymus of adult mice. *J Immunol* **2004,** *173* (5), 3261-70.
4. Luckey, M., *Membrane Structural Biology*. 2008.
5. Kinoshita, T., Glycosylphosphatidylinositol (GPI) Anchors: Biochemistry and Cell Biology: Introduction to a Thematic Review Series. *J Lipid Res* **2016,** *57* (1), 4-5.
6. Stefanova, I.; Horejsi, V.; Ansotegui, I. J.; Knapp, W.; Stockinger, H., GPI-anchored cell-surface molecules complexed to protein tyrosine kinases. *Science* **1991,** *254* (5034), 1016-9.
7. Moran, M.; Miceli, M. C., Engagement of GPI-linked CD48 contributes to TCR signals and cytoskeletal reorganization: a role for lipid rafts in T cell activation. *Immunity* **1998,** *9* (6), 787-96.
8. Simons, K.; Toomre, D., Lipid rafts and signal transduction. *Nat Rev Mol Cell Biol* **2000,** *1* (1), 31-9.
9. Allen, J. A.; Halverson-Tamboli, R. A.; Rasenick, M. M., Lipid raft microdomains and neurotransmitter signalling. *Nat Rev Neurosci* **2007,** *8* (2), 128-40.
10. Munoz, P.; Mittelbrunn, M.; de la Fuente, H.; Perez-Martinez, M.; Garcia-Perez, A.; Ariza-Veguillas, A.; Malavasi, F.; Zubiaur, M.; Sanchez-Madrid, F.; Sancho, J., Antigen-induced clustering of surface CD38 and recruitment of intracellular CD38 to the immunologic synapse. *Blood* **2008,** *111* (7), 3653-64.
11. Tolar, P.; Hanna, J.; Krueger, P. D.; Pierce, S. K., The constant region of the membrane immunoglobulin mediates B cell-receptor clustering and signaling in response to membrane antigens. *Immunity* **2009,** *30* (1), 44-55.
12. Chichili, G. R.; Rodgers, W., Clustering of membrane raft proteins by the actin cytoskeleton. *J Biol Chem* **2007,** *282* (50), 36682-91.
13. Wang, H.; Bedford, F. K.; Brandon, N. J.; Moss, S. J.; Olsen, R. W., GABA(A)-receptor-associated protein links GABA(A) receptors and the cytoskeleton. *Nature* **1999,** *397* (6714), 69-72.
14. Calebiro, D.; Rieken, F.; Wagner, J.; Sungkaworn, T.; Zabel, U.; Borzi, A.; Cocucci, E.; Zurn, A.; Lohse, M. J., Single-molecule analysis of fluorescently labeled G-protein-coupled receptors reveals complexes with distinct dynamics and organization. *Proc Natl Acad Sci U S A* **2013,** *110* (2), 743-8.
15. Dorsch, S.; Klotz, K. N.; Engelhardt, S.; Lohse, M. J.; Bunemann, M., Analysis of receptor oligomerization by FRAP microscopy. *Nat Methods* **2009,** *6* (3), 225-30.
16. Renner, M.; Specht, C. G.; Triller, A., Molecular dynamics of postsynaptic receptors and scaffold proteins. *Curr Opin Neurobiol* **2008,** *18* (5), 532-40.
17. Grakoui, A.; Bromley, S. K.; Sumen, C.; Davis, M. M.; Shaw, A. S.; Allen, P. M.; Dustin, M. L., The immunological synapse: a molecular machine controlling T cell activation. *Science* **1999,** *285* (5425), 221-7.

18. Dustin, M. L.; Depoil, D., New insights into the T cell synapse from single molecule techniques. *Nat Rev Immunol* **2011,** *11* (10), 672-84.
19. Alarcon, B.; Mestre, D.; Martinez-Martin, N., The immunological synapse: a cause or consequence of T-cell receptor triggering? *Immunology* **2011,** *133* (4), 420-5.
20. Brown, D. A.; London, E., Functions of lipid rafts in biological membranes. *Annu Rev Cell Dev Biol* **1998,** *14*, 111-36.
21. Sankaram, M. B.; Thompson, T. E., Interaction of cholesterol with various glycerophospholipids and sphingomyelin. *Biochemistry* **1990,** *29* (47), 10670-5.
22. Schroeder, R.; London, E.; Brown, D., Interactions between saturated acyl chains confer detergent resistance on lipids and glycosylphosphatidylinositol (GPI)-anchored proteins: GPI-anchored proteins in liposomes and cells show similar behavior. *Proc Natl Acad Sci U S A* **1994,** *91* (25), 12130-4.
23. Simons, K.; Ikonen, E., Functional rafts in cell membranes. *Nature* **1997,** *387* (6633), 569-72.
24. Fridriksson, E. K.; Shipkova, P. A.; Sheets, E. D.; Holowka, D.; Baird, B.; McLafferty, F. W., Quantitative analysis of phospholipids in functionally important membrane domains from RBL-2H3 mast cells using tandem high-resolution mass spectrometry. *Biochemistry* **1999,** *38* (25), 8056-63.
25. Lingwood, D.; Simons, K., Lipid rafts as a membrane-organizing principle. *Science* **2010,** *327* (5961), 46-50.
26. Hunter, T., Signaling--2000 and beyond. *Cell* **2000,** *100* (1), 113-27.
27. Yethiraj, A.; Weisshaar, J. C., Why are lipid rafts not observed in vivo? *Biophys J* **2007,** *93* (9), 3113-9.
28. Baird, B.; Sheets, E. D.; Holowka, D., How does the plasma membrane participate in cellular signaling by receptors for immunoglobulin E? *Biophys Chem* **1999,** *82* (2-3), 109-19.
29. Sheets, E. D.; Holowka, D.; Baird, B., Critical role for cholesterol in Lyn-mediated tyrosine phosphorylation of FcepsilonRI and their association with detergent-resistant membranes. *J Cell Biol* **1999,** *145* (4), 877-87.
30. Field, K. A.; Holowka, D.; Baird, B., Fc epsilon RI-mediated recruitment of p53/56lyn to detergent-resistant membrane domains accompanies cellular signaling. *Proc Natl Acad Sci U S A* **1995,** *92* (20), 9201-5.
31. Roy, S.; Luetterforst, R.; Harding, A.; Apolloni, A.; Etheridge, M.; Stang, E.; Rolls, B.; Hancock, J. F.; Parton, R. G., Dominant-negative caveolin inhibits H-Ras function by disrupting cholesterol-rich plasma membrane domains. *Nat Cell Biol* **1999,** *1* (2), 98-105.
32. Bouvier, M., Oligomerization of G-protein-coupled transmitter receptors. *Nat Rev Neurosci* **2001,** *2* (4), 274-86.
33. Suryanarayana, S.; von Zastrow, M.; Kobilka, B. K., Identification of intramolecular interactions in adrenergic receptors. *J Biol Chem* **1992,** *267* (31), 21991-4.
34. Kaupmann, K.; Malitschek, B.; Schuler, V.; Heid, J.; Froestl, W.; Beck, P.; Mosbacher, J.; Bischoff, S.; Kulik, A.; Shigemoto, R.; Karschin, A.; Bettler, B., GABA(B)-receptor subtypes assemble into functional heteromeric complexes. *Nature* **1998,** *396* (6712), 683-7.
35. Kuner, R.; Kohr, G.; Grunewald, S.; Eisenhardt, G.; Bach, A.; Kornau, H. C., Role of heteromer formation in GABAB receptor function. *Science* **1999,** *283* (5398), 74-7.
36. Ng, G. Y.; Clark, J.; Coulombe, N.; Ethier, N.; Hebert, T. E.; Sullivan, R.; Kargman, S.; Chateauneuf, A.; Tsukamoto, N.; McDonald, T.; Whiting, P.; Mezey, E.;

Johnson, M. P.; Liu, Q.; Kolakowski, L. F., Jr.; Evans, J. F.; Bonner, T. I.; O'Neill, G. P., Identification of a GABAB receptor subunit, gb2, required for functional GABAB receptor activity. *J Biol Chem* **1999,** *274* (12), 7607-10.
37. Benkirane, M.; Jin, D. Y.; Chun, R. F.; Koup, R. A.; Jeang, K. T., Mechanism of transdominant inhibition of CCR5-mediated HIV-1 infection by ccr5delta32. *J Biol Chem* **1997,** *272* (49), 30603-6.
38. Musil, L. S.; Goodenough, D. A., Multisubunit assembly of an integral plasma membrane channel protein, gap junction connexin43, occurs after exit from the ER. *Cell* **1993,** *74* (6), 1065-77.
39. Bennett, M. V.; Barrio, L. C.; Bargiello, T. A.; Spray, D. C.; Hertzberg, E.; Saez, J. C., Gap junctions: new tools, new answers, new questions. *Neuron* **1991,** *6* (3), 305-20.
40. Goodenough, D. A.; Paul, D. L., Beyond the gap: functions of unpaired connexon channels. *Nat Rev Mol Cell Biol* **2003,** *4* (4), 285-94.
41. Bennett, M. V.; Goodenough, D. A., Gap junctions, electrotonic coupling, and intercellular communication. *Neurosci Res Program Bull* **1978,** *16* (3), 1-486.
42. Bennett, M. V.; Sandri, C.; Akert, K., Neuronal gap junctions and morphologically mixed synapses in the spinal cord of a teleost, Sternarchus albifrons (Gymnotoidei). *Brain Res* **1978,** *143* (1), 43-60.
43. Stock, A. M., A nonlinear stimulus-response relation in bacterial chemotaxis. *Proc Natl Acad Sci U S A* **1999,** *96* (20), 10945-7.
44. Parkinson, J. S., Signal transduction schemes of bacteria. *Cell* **1993,** *73* (5), 857-71.
45. Hazelbauer, G. L.; Berg, H. C.; Matsumura, P., Bacterial motility and signal transduction. *Cell* **1993,** *73* (1), 15-22.
46. Alon, U.; Camarena, L.; Surette, M. G.; Aguera y Arcas, B.; Liu, Y.; Leibler, S.; Stock, J. B., Response regulator output in bacterial chemotaxis. *EMBO J* **1998,** *17* (15), 4238-48.
47. Grebe, T. W.; Stock, J., Bacterial chemotaxis: the five sensors of a bacterium. *Curr Biol* **1998,** *8* (5), R154-7.
48. Barkai, N.; Leibler, S., Robustness in simple biochemical networks. *Nature* **1997,** *387* (6636), 913-7.
49. Gestwicki, J. E.; Strong, L. E.; Kiessling, L. L., Tuning chemotactic responses with synthetic multivalent ligands. *Chem Biol* **2000,** *7* (8), 583-91.
50. Brunsveld, L.; Kuhlmann, J.; Alexandrov, K.; Wittinghofer, A.; Goody, R. S.; Waldmann, H., Lipidated ras and rab peptides and proteins--synthesis, structure, and function. *Angew Chem Int Ed Engl* **2006,** *45* (40), 6622-46.
51. Weise, K.; Triola, G.; Koch, S.; Waldmann, H.; Winter, R., Interactions of Lipidated Ras Proteins With Raft Membranes Studied By Time-Lapse Atomic Force Microscopy. *Biophysical Journal* **2010,** *98* (3), 19a-20a.
52. Nicolini, C.; Baranski, J.; Schlummer, S.; Palomo, J.; Lumbierres-Burgues, M.; Kahms, M.; Kuhlmann, J.; Sanchez, S.; Gratton, E.; Waldmann, H.; Winter, R., Visualizing association of N-Ras in lipid microdomains: Influence of domain structure and interfacial adsorption. *J Am Chem Soc* **2006,** *128* (1), 192-201.
53. Weise, K.; Triola, G.; Janosch, S.; Waldmann, H.; Winter, R., Visualizing association of lipidated signaling proteins in heterogeneous membranes-Partitioning into subdomains, lipid sorting, interfacial adsorption, and protein association. *Bba-Biomembranes* **2010,** *1798* (7), 1409-1417.

54. Gerald, K., *Cell and Molecular Biology (4th ed.)*. 2002.
55. Han, J.; Pluhackova, K.; Bockmann, R. A., Exploring the Formation and the Structure of Synaptobrevin Oligomers in a Model Membrane. *Biophys J* **2016,** *110* (9), 2004-15.
56. Murray, D. H.; Tamm, L. K., Molecular mechanism of cholesterol- and polyphosphoinositide-mediated syntaxin clustering. *Biochemistry* **2011,** *50* (42), 9014-22.
57. Kroch, A. E.; Fleming, K. G., Alternate interfaces may mediate homomeric and heteromeric assembly in the transmembrane domains of SNARE proteins. *J Mol Biol* **2006,** *357* (1), 184-94.
58. Margittai, M.; Otto, H.; Jahn, R., A stable interaction between syntaxin 1a and synaptobrevin 2 mediated by their transmembrane domains. *FEBS Lett* **1999,** *446* (1), 40-4.
59. Rickman, C.; Hu, K.; Carroll, J.; Davletov, B., Self-assembly of SNARE fusion proteins into star-shaped oligomers. *Biochem J* **2005,** *388* (Pt 1), 75-9.
60. Chothia, C.; Jones, E. Y., The molecular structure of cell adhesion molecules. *Annu Rev Biochem* **1997,** *66*, 823-62.
61. Aricescu, A. R.; Jones, E. Y., Immunoglobulin superfamily cell adhesion molecules: zippers and signals. *Curr Opin Cell Biol* **2007,** *19* (5), 543-50.
62. Zhang, Y.; Sivasankar, S.; Nelson, W. J.; Chu, S., Resolving cadherin interactions and binding cooperativity at the single-molecule level. *Proc Natl Acad Sci U S A* **2009,** *106* (1), 109-14.
63. Wu, Y.; Jin, X.; Harrison, O.; Shapiro, L.; Honig, B. H.; Ben-Shaul, A., Cooperativity between trans and cis interactions in cadherin-mediated junction formation. *Proc Natl Acad Sci U S A* **2010,** *107* (41), 17592-7.
64. Sommers, C. L.; Menon, R. K.; Grinberg, A.; Zhang, W.; Samelson, L. E.; Love, P. E., Knock-in mutation of the distal four tyrosines of linker for activation of T cells blocks murine T cell development. *J Exp Med* **2001,** *194* (2), 135-42.
65. Abul K. Abbas, A. H. L., Shiv Pillai., *Cellular and Molecular Immunology*. 2012.
66. Garcia, K. C., Molecular interactions between extracellular components of the T-cell receptor signaling complex. *Immunol Rev* **1999,** *172*, 73-85.
67. Brenner, M. B.; McLean, J.; Dialynas, D. P.; Strominger, J. L.; Smith, J. A.; Owen, F. L.; Seidman, J. G.; Ip, S.; Rosen, F.; Krangel, M. S., Identification of a putative second T-cell receptor. *Nature* **1986,** *322* (6075), 145-9.
68. Kuhns, M. S.; Davis, M. M.; Garcia, K. C., Deconstructing the form and function of the TCR/CD3 complex. *Immunity* **2006,** *24* (2), 133-9.
69. Call, M. E.; Wucherpfennig, K. W., Common themes in the assembly and architecture of activating immune receptors. *Nat Rev Immunol* **2007,** *7* (11), 841-50.
70. Call, M. E. W., K. W, The T cell receptor: critical role of the membrane environment in receptor assembly and function. *Annu. Rev. Immunol.* **2005**, 23, 101–125.
71. Call, M. E., Pyrdol, J., Wiedmann, M. & Wucherpfennig, K. W., The organizing principle in the formation of the T cell receptor–CD3 complex. *Cell.* **2002**, 111, 967–979.
72. Xu, C., Call, M. E. & Wucherpfennig, K. W., A membrane-proximal tetracysteine motif contributes to assembly of CD3deltaalt epsilon and CD3gammaalt epsilon dimers with the T cell receptor. *J. Biol. Chem.* **2006**, 281, 36977–36984.
73. Schamel, W. W.; Arechaga, I.; Risueno, R. M.; van Santen, H. M.; Cabezas, P.; Risco, C.; Valpuesta, J. M.; Alarcon, B., Coexistence of multivalent and monovalent TCRs explains high sensitivity and wide range of response. *J Exp Med* **2005,** *202* (4), 493-503.

74. Varma, R.; Campi, G.; Yokosuka, T.; Saito, T.; Dustin, M. L., T cell receptor-proximal signals are sustained in peripheral microclusters and terminated in the central supramolecular activation cluster. *Immunity* **2006,** *25* (1), 117-27.
75. Lillemeier, B. F.; Mortelmaier, M. A.; Forstner, M. B.; Huppa, J. B.; Groves, J. T.; Davis, M. M., TCR and Lat are expressed on separate protein islands on T cell membranes and concatenate during activation. *Nat Immunol* **2010,** *11* (1), 90-6.
76. Punt, J. A.; Roberts, J. L.; Kearse, K. P.; Singer, A., Stoichiometry of the T cell antigen receptor (TCR) complex: each TCR/CD3 complex contains one TCR alpha, one TCR beta, and two CD3 epsilon chains. *J Exp Med* **1994,** *180* (2), 587-93.
77. Dunne, P. D.; Fernandes, R. A.; McColl, J.; Yoon, J. W.; James, J. R.; Davis, S. J.; Klenerman, D., DySCo: quantitating associations of membrane proteins using two-color single-molecule tracking. *Biophys J* **2009,** *97* (4), L5-7.
78. James, J. R.; White, S. S.; Clarke, R. W.; Johansen, A. M.; Dunne, P. D.; Sleep, D. L.; Fitzgerald, W. J.; Davis, S. J.; Klenerman, D., Single-molecule level analysis of the subunit composition of the T cell receptor on live T cells. *Proc Natl Acad Sci U S A* **2007,** *104* (45), 17662-7.
79. Appel, H.; Gauthier, L.; Pyrdol, J.; Wucherpfennig, K. W., Kinetics of T-cell receptor binding by bivalent HLA-DR. Peptide complexes that activate antigen-specific human T-cells. *J Biol Chem* **2000,** *275* (1), 312-21.
80. Krogsgaard, M.; Li, Q. J.; Sumen, C.; Huppa, J. B.; Huse, M.; Davis, M. M., Agonist/endogenous peptide-MHC heterodimers drive T cell activation and sensitivity. *Nature* **2005,** *434* (7030), 238-43.
81. Monks CRF, B. F., H Kupfer, N Sciaky, and A. Kupfer, Three dimensional segregation of supramolecular activation clusters in T cells. *Nature* **1998**.
82. Yokosuka, T.; Sakata-Sogawa, K.; Kobayashi, W.; Hiroshima, M.; Hashimoto-Tane, A.; Tokunaga, M.; Dustin, M. L.; Saito, T., Newly generated T cell receptor microclusters initiate and sustain T cell activation by recruitment of Zap70 and SLP-76. *Nat Immunol* **2005,** *6* (12), 1253-62.
83. Campi, G.; Varma, R.; Dustin, M. L., Actin and agonist MHC-peptide complex-dependent T cell receptor microclusters as scaffolds for signaling. *J Exp Med* **2005,** *202* (8), 1031-6.
84. James, J. R.; McColl, J.; Oliveira, M. I.; Dunne, P. D.; Huang, E.; Jansson, A.; Nilsson, P.; Sleep, D. L.; Goncalves, C. M.; Morgan, S. H.; Felce, J. H.; Mahen, R.; Fernandes, R. A.; Carmo, A. M.; Klenerman, D.; Davis, S. J., The T cell receptor triggering apparatus is composed of monovalent or monomeric proteins. *J Biol Chem* **2011,** *286* (37), 31993-2001.
85. Dushek, P. A. v. d. M. a. O., Mechanism for the T cell receptor triggering. *Nature Reviews* **2010**.
86. Nika, K.; Soldani, C.; Salek, M.; Paster, W.; Gray, A.; Etzensperger, R.; Fugger, L.; Polzella, P.; Cerundolo, V.; Dushek, O.; Hofer, T.; Viola, A.; Acuto, O., Constitutively active Lck kinase in T cells drives antigen receptor signal transduction. *Immunity* **2010,** *32* (6), 766-77.
87. Sykulev, Y.; Joo, M.; Vturina, I.; Tsomides, T. J.; Eisen, H. N., Evidence that a single peptide-MHC complex on a target cell can elicit a cytolytic T cell response. *Immunity* **1996,** *4* (6), 565-71.

88. Irvine, D. J.; Purbhoo, M. A.; Krogsgaard, M.; Davis, M. M., Direct observation of ligand recognition by T cells. *Nature* **2002,** *419* (6909), 845-9.
89. Daniel Pennington, B. S. S., PreTCR and TCRγδ signal initiation in Thymocyte progenitors does not require domains implicated in receptor oligomerization. *Science Signaling* **2011**, 182.
90. Kusumi, A.; Suzuki, K. G. N.; Kasai, R. S.; Ritchie, K.; Fujiwara, T. K., Hierarchical mesoscale domain organization of the plasma membrane. *Trends Biochem Sci* **2011,** *36* (11), 604-615.
91. Delves, P. J.; Roitt, I. M., *Encyclopedia of immunology*. 2nd ed ed.; Academic Press: San Diego, 1998.
92. Anjum, R. Analysis of the interplay between membrane curvature and lipid assembly using a pyranine derivative.

. Queen Mary University of London., London, 2017.
93. Lasic, D. D., Novel applications of liposomes. *Trends Biotechnol* **1998,** *16* (7), 307-21.
94. A. Laouini, C. J.-M., I. Limayem-Blouza, S. Sfar, C. Charcosset, and H. Fessi, Preparation, Characterization and Applications of Liposomes: State of the Art. *Journal of Colloid Science and Biotechnology* **2012,** *Vol. 1*, 147–168.
95. Van Rooijen, N.; Sanders, A., Kupffer cell depletion by liposome-delivered drugs: comparative activity of intracellular clodronate, propamidine, and ethylenediaminetetraacetic acid. *Hepatology* **1996,** *23* (5), 1239-43.
96. van Rooijen, N.; Sanders, A.; van den Berg, T. K., Apoptosis of macrophages induced by liposome-mediated intracellular delivery of clodronate and propamidine. *J Immunol Methods* **1996,** *193* (1), 93-9.
97. F. Bordi C. Cametti, a. S. S., Advances in Planar Lipid Bilayers and Liposomes. *Academic Press* **2006**, 281-230.
98. A. Bangham, J. D. G., and G. Greville, Osmotic properties and water permeability of phospholipid liquid crystals. *Chem. Phys. Lipids* **1967,** *1*, 225.
99. Mui, B.; Chow, L.; Hope, M. J., Extrusion technique to generate liposomes of defined size. *Methods Enzymol* **2003,** *367*, 3-14.
100. Olson, F.; Hunt, C. A.; Szoka, F. C.; Vail, W. J.; Papahadjopoulos, D., Preparation of liposomes of defined size distribution by extrusion through polycarbonate membranes. *Biochim Biophys Acta* **1979,** *557* (1), 9-23.
101. Lipids, A. P., Mini-Extruder Extrusion Technique Manual. 2019.
102. Bangham, A. D.; Glover, J. C.; Hollingshead, S.; Pethica, B. A., The surface properties of some neoplastic cells. *Biochem J* **1962,** *84*, 513-7.
103. Rowland, R. N.; Woodley, J. F., The stability of liposomes in vitro to pH, bile salts and pancreatic lipase. *Biochim Biophys Acta* **1980,** *620* (3), 400-9.
104. Dapergolas, G.; Gregoriadis, G., Hypoglycaemic effect of liposome-entrapped insulin administered intragastrically into rats. *Lancet* **1976,** *2* (7990), 824-7.
105. Alving, C. R., Liposomes as carriers of antigens and adjuvants. *J Immunol Methods* **1991,** *140* (1), 1-13.
106. Rao, M.; Wassef, N. M.; Alving, C. R.; Krzych, U., Intracellular processing of liposome-encapsulated antigens by macrophages depends upon the antigen. *Infect Immun* **1995,** *63* (7), 2396-402.

107. Loutan, L.; Bovier, P.; Althaus, B.; Gluck, R., Inactivated virosome hepatitis A vaccine. *Lancet* **1994,** *343* (8893), 322-4.
108. A. Tahibi, J. D. S., R. Mathur, and D. F. H. Wallach, *Proc. Symp. Contr. Rel. Bioact. Mat.* **1991,** *18*, 231.
109. Tomas, S.; Milanesi, L., Mutual modulation between membrane-embedded receptor clustering and ligand binding in lipid membranes. *Nat Chem* **2010,** *2* (12), 1077-83.
110. Tomas, S.; Milanesi, L., Mutual modulation between membrane-embedded receptor clustering and ligand binding in lipid membranes. *Nat Chem* **2010,** *2* (12), 1077-1083.
111. Lahiri, J.; Fate, G. D.; Ungashe, S. B.; Groves, J. T., Multi-heme self-assembly in phospholipid vesicles. *J Am Chem Soc* **1996,** *118* (10), 2347-2358.
112. De Poli, M.; Zawodny, W.; Quinonero, O.; Lorch, M.; Webb, S. J.; Clayden, J., Conformational photoswitching of a synthetic peptide foldamer bound within a phospholipid bilayer. *Science* **2016,** *352* (6285), 575-80.
113. Gellman, S. H., Minimal model systems for beta sheet secondary structure in proteins. *Curr Opin Chem Biol* **1998,** *2* (6), 717-25.
114. Bandara, H. M.; Burdette, S. C., Photoisomerization in different classes of azobenzene. *Chem Soc Rev* **2012,** *41* (5), 1809-25.
115. Lister, F. G. A.; Eccles, N.; Pike, S. J.; Brown, R. A.; Whitehead, G. F. S.; Raftery, J.; Webb, S. J.; Clayden, J., Bis-pyrene probes of foldamer conformation in solution and in phospholipid bilayers. *Chem Sci* **2018,** *9* (33), 6860-6870.
116. Tokumasu, F.; Jin, A. J.; Feigenson, G. W.; Dvorak, J. A., Nanoscopic lipid domain dynamics revealed by atomic force microscopy. *Biophys J* **2003,** *84* (4), 2609-18.
117. Fischer, H., Uber Porphyrine und ihre Synthesen. *Berichte der Deutschen Chemischen Gesellschaft* **1927**, 168-169.
118. Sun, Y.; Wang, Y.; Li, J.; Ding, C.; Lin, Y.; Sun, W.; Luo, C., An ultrasensitive chemiluminescence aptasensor for thrombin detection based on iron porphyrin catalyzing luminescence desorbed from chitosan modified magnetic oxide graphene composite. *Talanta* **2017**, 809-818.
119. Krishnakumar, B.; Balakrishna, A.; Nawabjan, S.; Pandiyan, V.; Aguiar, A.; Sobral, A., Solar and visible active amino porphyrin/SiO2-ZnO for the degradation of naphthol blue black. *Journal of Physics and Chemistry of Solids* **2017**, 364-371.
120. Prakash, K.; Manchanda, S.; Sudhakar, V.; Sharma, N.; Sankar, M.; Krishnamoorthy, K., Facile synthesis of beta-functionalized "push-pull" Zn(II) porphyrins for DSSC applications. *Dyes and Pigments* **2017**, 56-66.
121. Shin, S.; Choi, C.; Lee, G.; Son, A.; Kim, S.; Park, H.; Batinic-Haberle, I.; Park, W., Mechanism of the Antitumor and Radiosensitizing Effects of a Manganese Porphyrin, MnHex-2-PyP. *Antioxidants & Redox Signaling* **2017**, 1067-1082.
122. Linares, I.; Oliveira, d.; Perussi, J., Chlorin derivatives sterically-prevented from self-aggregation with high antitumor activity for photodynamic therapy. *Dyes and Pigments* **2017**, 518-527.
123. Rothemund, P., Formation of porphyrins from pyrrole and aldehydes. *Journal of the American Chemical Society* **1935**, 2010-2011.
124. Rothemund, P., Porphyrin Studies III. The Structure of the Porphine Ring System. *Journal of Americal Chemical Society* **1939,** *61*, 2912-2915.
125. Rothemund, P., Porphyrin studies IV. Synthesis of the α,β,γ,δ-tetraphenylporphin. *Journal of the American Chemical Society* **1941**, 267-270.

126. Schmidt. D, S. H., *European Patent Application* **1984**, 127.
127. Masayuki Endo, M. F., and Tetsuro Majima, Diaterochemically Controlled Porphyrin Dimer Formation on a DNA Duplex Scaffold. *Journal of Organic Chemistry* **2008**, 1106-1112.
128. Hasegawa, E.; Nemoto, J.; Kangyama, T.; Tsuchida, E., Syntheses and properties of vinyl monomers containing a meso-tetraphenylporphin ring and their copolymers. *European Polymer Journal* **1978,** *14*, 123.
129. Krupper J. W, C. T., Kochanny M,, Regiospecific Aryl Nitration of Meso-Substituted Tetraarylporphyrins: A simple Route to Bifunctional Porphyrins. *American Chemical Society* **1989**, 2753-2756.
130. Srivastava, T. S.; Tsutui, T., Analytical and preparative chromatography of metalloporphyrins on polyamide. *J Org Chem* **1973**, 2103.
131. Busby, C. A.; Dinello, R. K.; Dolphin, D., Alkene Epoxidation and Alkane Hydroxylation with Periodate Catalysed by Manganese(III) Porphyrin Supported on Poly(4-vinylpyridine). *Canadian Journal Chemistry* **1975**, 1554.
132. Tsuchida, E., Spontaneous reduction of hemin complexes in dimethylformamide solution. *Journal of Macromolecular Sciences* **1979**, 739-742.
133. Takeda, J.; Ohta, S.; Hirobe, M., Rate-enhancing effect of intramolecular linkage of flavin-porphyrin on reduction by 1,4-dihydropyridine. *Tetrahedron Letters* **1985**, 4509.
134. Tabushi, I.; Kugimiya, S., Porphyrin building blocks for modular construction of bioorganic model systems. *Journal of American Chemical Society* **1986**, 6926.
135. Rita L, M. M. P., Beatriz R, Selective Reduction of Nitroarenes with Silanes Catalyzed by Nickel N-Heterocyclic Carbene Complexes. *Chem Cat Chem* **2017,** *9* (15), 3073-3077.
136. J.B, K.; F.R, L., NIR luminescence of gadolinium porphyrin complexes. *Porphyrin Chemistry Advances* **1979**, 305.
137. Fuhrhop, J. H., *Porphyrins and Metalloporphyrins*. K.M. Smith, Elsevier Scientific: Liverpool, 1975.
138. Fuhrhop, J. H., *The Porphyrins*. E.D Academic Press: New York, 1978.
139. Treibs, A., Chlorophyll- und Häminderivate in bituminösen Gesteinen, Erdölen, Erdwachsen und Asphalten. Ein Beitrag zur Entstehung des Erdöls. *Justus Liebigs Ann. Chem* **1933**, 506.
140. El.Z, H. *Doctoral Thesis*; Univesidad de Barcelona: Barcelona, 2002.
141. Rodriguez, C. E. *Homoasociacion de Porfirinas Sulfonadas*; Universidad de Barcelona: Barcelona, 2007.
142. Friedamnn. E, M. D. H., Simon-Reuss. I, Sulphydril Addition Compounds of Some Quinones and Related Substances in their Action on the Growth of Normal Cells. *Brit. J. Pharmacol* **1948**, 335.
143. Gregory, J. D., The Stability of N-Ethylmaleimide and its Reaction tion with Sulfhydryl Groups *Journal of Ame Chem Soc* **1955**, 3922.
144. Derek G. Smyth, A. N., Joseph S. Fruton, Some Reactions of N-Ethylmaleimide. *JACS* **1960**, 4600.
145. Smyth, D. G., Reactions of N-Ethylmaleimide with Peptides and Amino Acids. *Biochem Journal* **1963**, 589.
146. Hermanson, G. T., *Bioconjugate Techniques, Third Edition*. Elevier: 2013.

147. Masayuki Endo, M. F., and Tetsuro Majima, Diaterochemically Controlled Porphyrin Dimer Formation on a DNA Duplex Scaffold. *J Org Chem* **2008**, 1106-1112.
148. Kruper, W. J.; Chamberlin, T. A.; Kochanny, M., Regiospecific Aryl Nitration of Meso-Substituted Tetraarylporphyrins - a Simple Route to Bifunctional Porphyrins. *Journal of Organic Chemistry* **1989,** *54* (11), 2753-2756.
149. Tomas, S.; Milanesi, L., Hydrophobically Self-Assembled Nanoparticles as Molecular Receptors in Water. *J Am Chem Soc* **2009,** *131* (18), 6618-6623.
150. Milanesi, L.; Hunter, C. A.; Tzokova, N.; Waltho, J. P.; Tomas, S., Versatile Low-Molecular-Weight Hydrogelators: Achieving Multiresponsiveness through a Modular Design. *Chemistry-a European Journal* **2011,** *17* (35), 9753-9761.
151. Bauman. W. C, S. J. R., Osmun. R. H A New High Capacity Cation Exchange Resin *Industrial and Engineering Chemistry* **1948,** *40* (8), 5.
152. Ellman, G. L., Tissue sulfhydryl groups. *Arch Biochem Biophys* **1959,** *82* (1), 70-7.
153. Riddles, P. W.; Blakeley, R. L.; Zerner, B., Reassessment of Ellman's reagent. *Methods Enzymol* **1983,** *91*, 49-60.
154. Brocklehurst, K.; Kierstan, M.; Little, G., The reaction of papain with Ellman's reagent (5,5'-dithiobis- (2-nitrobenzoate) dianion). *Biochem J* **1972,** *128* (4), 811-6.
155. Hansen, R. E.; Ostergaard, H.; Norgaard, P.; Winther, J. R., Quantification of protein thiols and dithiols in the picomolar range using sodium borohydride and 4,4'-dithiodipyridine. *Anal Biochem* **2007,** *363* (1), 77-82.
156. Hansen, R. E.; Winther, J. R., An introduction to methods for analyzing thiols and disulfides: Reactions, reagents, and practical considerations. *Anal Biochem* **2009,** *394* (2), 147-158.
157. Han, J. C.; Han, G. Y., A procedure for quantitative determination of tris(2-carboxyethyl)phosphine, an odorless reducing agent more stable and effective than dithiothreitol. *Anal Biochem* **1994,** *220* (1), 5-10.
158. Schilter, D., A slippery slope. *Nat Rev Chem* **2017,** *1* (2).
159. Nair, D. P.; Podgorski, M.; Chatani, S.; Gong, T.; Xi, W. X.; Fenoli, C. R.; Bowman, C. N., The Thiol-Michael Addition Click Reaction: A Powerful and Widely Used Tool in Materials Chemistry. *Chem Mater* **2014,** *26* (1), 724-744.
160. Tsuruta, Y. T., Y., Some chemical and biological characteristics of showdomycin. *J. Antibiot* **1974,** *27*, 956–962.
161. Chen, Y.; Tsao, K.; De Francesco, E.; Keillor, J. W., Ring Substituent Effects on the Thiol Addition and Hydrolysis Reactions of N-Arylmaleimides. *J Org Chem* **2015,** *80* (24), 12182-92.
162. Knight, P., Hydrolysis of p-N, N0-phenylenebismaleimide and its adducts with cysteine: implications for cross-linking of proteins. *Biochem. J.* **1979,** *179*, 191-197.
163. Baldwin, A. D.; Kiick, K. L., Reversible maleimide-thiol adducts yield glutathione-sensitive poly(ethylene glycol)-heparin hydrogels. *Polym Chem* **2013,** *4* (1), 133-143.
164. Beutler, E.; Srivastava, S. K.; West, C., The reversibility of N-ethylmaleimide (NEM) alkylation of red cell glutathione. *Biochem Biophys Res Commun* **1970,** *38* (2), 341-7.
165. Guidotti, G., The rates of reaction of the sulfhydryl groups of human hemoglobin. *J Biol Chem* **1965,** *240* (10), 3924-7.
166. Rogers, L. K.; Leinweber, B. L.; Smith, C. V., Detection of reversible protein thiol modifications in tissues. *Anal Biochem* **2006,** *358* (2), 171-84.

167. Milanesi, L.; Jelinska, C.; Hunter, C. A.; Hounslow, A. M.; Staniforth, R. A.; Waltho, J. P., A method for the reversible trapping of proteins in non-native conformations. *Biochemistry* **2008,** *47* (51), 13620-34.
168. Milanesi, L.; Waltho, J. P.; Hunter, C. A.; Shaw, D. J.; Beddard, G. S.; Reid, G. D.; Dev, S.; Volk, M., Measurement of energy landscape roughness of folded and unfolded proteins. *Proc Natl Acad Sci U S A* **2012,** *109* (48), 19563-8.
169. Current opinion in clinical nutrition and metabolic care. *Curr Opin Clin Nutr Metab Care* **2008,** *11* (5), 671-81.
170. DEMPSEY, S., **1979**.
171. Meister, A.; Anderson, M. E., Glutathione. *Annu Rev Biochem* **1983,** *52*, 711-60.
172. Roberts, J. C.; Francetic, D. J., The importance of sample preparation and storage in glutathione analysis. *Anal Biochem* **1993,** *211* (2), 183-7.
173. WHITESIDES, R. I. a. G., *The chemistry of sulphur-containing functional groups.* 1993.
174. Bains, G. K.; Kim, S. H.; Sorin, E. J.; Narayanaswami, V., The extent of pyrene excimer fluorescence emission is a reflector of distance and flexibility: analysis of the segment linking the LDL receptor-binding and tetramerization domains of apolipoprotein E3. *Biochemistry* **2012,** *51* (31), 6207-19.
175. Getz, E. B.; Xiao, M.; Chakrabarty, T.; Cooke, R.; Selvin, P. R., A comparison between the sulfhydryl reductants tris(2-carboxyethyl)phosphine and dithiothreitol for use in protein biochemistry. *Anal Biochem* **1999,** *273* (1), 73-80.
176. Braakman, I.; Helenius, J.; Helenius, A., Manipulating disulfide bond formation and protein folding in the endoplasmic reticulum. *EMBO J* **1992,** *11* (5), 1717-22.
177. Cline, D. J.; Redding, S. E.; Brohawn, S. G.; Psathas, J. N.; Schneider, J. P.; Thorpe, C., New water-soluble phosphines as reductants of peptide and protein disulfide bonds: reactivity and membrane permeability. *Biochemistry* **2004,** *43* (48), 15195-203.
178. Ruegg, U. T.; Rudinger, J., Reductive cleavage of cystine disulfides with tributylphosphine. *Methods Enzymol* **1977,** *47*, 111-6.
179. Duchardt, F.; Ruttekolk, I. R.; Verdurmen, W. P.; Lortat-Jacob, H.; Burck, J.; Hufnagel, H.; Fischer, R.; van den Heuvel, M.; Lowik, D. W.; Vuister, G. W.; Ulrich, A.; de Waard, M.; Brock, R., A cell-penetrating peptide derived from human lactoferrin with conformation-dependent uptake efficiency. *J Biol Chem* **2009,** *284* (52), 36099-108.
180. Buecheler, J. W.; Winzer, M.; Tonillo, J.; Weber, C.; Gieseler, H., Impact of Payload Hydrophobicity on the Stability of Antibody-Drug Conjugates. *Mol Pharm* **2018,** *15* (7), 2656-2664.
181. Scales, C. W.; Convertine, A. J.; McCormick, C. L., Fluorescent labeling of RAFT-generated poly(N-isopropylacrylamide) via a facile maleimide-thiol coupling reaction. *Biomacromolecules* **2006,** *7* (5), 1389-92.
182. Chan, J. W.; Hoyle, C. E.; Lowe, A. B.; Bowman, M., Nucleophile-Initiated Thiol-Michael Reactions: Effect of Organocatalyst, Thiol, and Ene. *Macromolecules* **2010,** *43* (15), 6381-6388.
183. O'Donnell, M. E.; Williams, C. H., Jr., Proton stoichiometry in the reduction of the FAD and disulfide of Escherichia coli thioredoxin reductase. Evidence for a base at the active site. *J Biol Chem* **1983,** *258* (22), 13795-805.
184. Scaife, C. W. J.; Wilkins, R. G., Kinetics of the Reduction of Hexacyanoferrate(Iii) Ion by Dithionite Ion. *Inorg Chem* **1980,** *19* (11), 3244-3247.

185. Scaife, C. W. J.; Wilkins, R. G., Kinetics of Ferricyanide Reduction by Dithionite. *Abstr Pap Am Chem S* **1979,** (Sep), 112-112.
186. Cox, R. P.; Hollaway, M. R., Reduction by Dithionite of Fe(Iii) Myoglobin Derivatives with Different Ligands Attached to Iron Atom - Study by Rapid-Wavelength-Scanning Stopped-Flow Spectrophotometry. *Eur J Biochem* **1977,** *74* (3), 575-587.
187. Moreno, M. J.; Estronca, L. M.; Vaz, W. L., Translocation of phospholipids and dithionite permeability in liquid-ordered and liquid-disordered membranes. *Biophys J* **2006,** *91* (3), 873-81.
188. Tang, R. Y.; Zhong, P.; Lin, Q. L., A convenient conversion of pyrazolyl disulfide to sulfides by sodium dithionite and synthesis of sulfoxides. *J Fluorine Chem* **2006,** *127* (7), 948-953.
189. Vivian, J. T.; Callis, P. R., Mechanisms of tryptophan fluorescence shifts in proteins. *Biophys J* **2001,** *80* (5), 2093-109.
190. Pahlke, D. M.; Diederichsen, U., Synthesis and characterization of beta-peptide helices as transmembrane domains in lipid model membranes. *J Pept Sci* **2016,** *22* (10), 636-641.
191. Friesen, B. A. An Investigation of Porphyrin Aggregattion using Espectroscopic and Microscopic Methods. Washington State University, Washington, 2011.
192. Kantner, T.; Watts, A. G., Characterization of Reactions between Water-Soluble Trialkylphosphines and Thiol Alkylating Reagents: Implications for Protein-Conjugation Reactions. *Bioconjug Chem* **2016,** *27* (10), 2400-2406.
193. Neves, J. F. P. d. T cell development: determining factors for the differentiation & selection of thymocytes. Coimbra University, Portugal, 2011.
194. Call, M. E.; Wucherpfennig, K. W., The T cell receptor: critical role of the membrane environment in receptor assembly and function. *Annu Rev Immunol* **2005,** *23*, 101-25.
195. Heijne, G. V., Membrane-protein topolgy. *Nature Reviews Molecular Cell Biology* **2006,** *7* (December 2006), 909-918.
196. Andrade, S. M.; Costa, S. M., Spectroscopic studies on the interaction of a water soluble porphyrin and two drug carrier proteins. *Biophys J* **2002,** *82* (3), 1607-19.
197. Palazolo, G.; Rodriguez, F.; Farruggia, B.; Pico, G.; Delorenzi, N., Heat treatment of beta-lactoglobulin: Structural changes studied by partitioning and fluorescence. *J Agr Food Chem* **2000,** *48* (9), 3817-3822.
198. Kyte, J.; Doolittle, R. F., A simple method for displaying the hydropathic character of a protein. *J Mol Biol* **1982,** *157* (1), 105-32.
199. Baeza-Delgado, C.; Marti-Renom, M. A.; Mingarro, I., Structure-based statistical analysis of transmembrane helices. *Eur Biophys J* **2013,** *42* (2-3), 199-207.
200. Lew, S.; Ren, J.; London, E., The effects of polar and/or ionizable residues in the core and flanking regions of hydrophobic helices on transmembrane conformation and oligomerization. *Biochemistry* **2000,** *39* (32), 9632-40.
201. Ren, J.; Lew, S.; Wang, Z.; London, E., Transmembrane orientation of hydrophobic alpha-helices is regulated both by the relationship of helix length to bilayer thickness and by the cholesterol concentration. *Biochemistry* **1997,** *36* (33), 10213-20.
202. Ren, J.; Lew, S.; Wang, J.; London, E., Control of the transmembrane orientation and interhelical interactions within membranes by hydrophobic helix length. *Biochemistry* **1999,** *38* (18), 5905-12.

203. De Kroon, A. I.; Soekarjo, M. W.; De Gier, J.; De Kruijff, B., The role of charge and hydrophobicity in peptide-lipid interaction: a comparative study based on tryptophan fluorescence measurements combined with the use of aqueous and hydrophobic quenchers. *Biochemistry* **1990,** *29* (36), 8229-40.
204. Butterfield, S. M.; Lashuel, H. A., Amyloidogenic protein-membrane interactions: mechanistic insight from model systems. *Angew Chem Int Ed Engl* **2010,** *49* (33), 5628-54.
205. Thordarson, P., Determining association constants from titration experiments in supramolecular chemistry. *Chem Soc Rev* **2011,** *40* (3), 1305-23.
206. Galdiero, S.; Falanga, A.; Cantisani, M.; Vitiello, M.; Morelli, G.; Galdiero, M., Peptide-lipid interactions: experiments and applications. *Int J Mol Sci* **2013,** *14* (9), 18758-89.
207. Lokappa, S. B.; Nagaraj, R., Interaction of peptides spanning the transmembrane domain of caveolin-1 with model membranes. *J Pept Sci* **2012,** *18* (11), 696-703.
208. Gill, S. C.; von Hippel, P. H., Calculation of protein extinction coefficients from amino acid sequence data. *Anal Biochem* **1989,** *182* (2), 319-26.
209. de Planque, M. R.; Kruijtzer, J. A.; Liskamp, R. M.; Marsh, D.; Greathouse, D. V.; Koeppe, R. E., 2nd; de Kruijff, B.; Killian, J. A., Different membrane anchoring positions of tryptophan and lysine in synthetic transmembrane alpha-helical peptides. *J Biol Chem* **1999,** *274* (30), 20839-46.
210. Sparr, E.; Ash, W. L.; Nazarov, P. V.; Rijkers, D. T.; Hemminga, M. A.; Tieleman, D. P.; Killian, J. A., Self-association of transmembrane alpha-helices in model membranes: importance of helix orientation and role of hydrophobic mismatch. *J Biol Chem* **2005,** *280* (47), 39324-31.
211. Scheiner, S.; Kar, T.; Gu, Y., Strength of the Calpha H..O hydrogen bond of amino acid residues. *J Biol Chem* **2001,** *276* (13), 9832-7.
212. Hamai, S., Complex formation of hematoporphyrin with cyclodextrins and 1,1 '-diheptyl-4,4 '-bipyridinium dibromide in aqueous solutions. *Supramol Chem* **2004,** *16* (2), 113-120.
213. Ribo, J. M.; Crusats, J.; Farrera, J. A.; Valero, M. L., Aggregation in Water Solutions of Tetrasodium Diprotonated Meso-Tetrakis(4-Sulfonatophenyl)Porphyrin. *J Chem Soc Chem Comm* **1994,** (6), 681-682.
214. Luo, D.; Carter, K. A.; Razi, A.; Geng, J.; Shao, S.; Lin, C.; Ortega, J.; Lovell, J. F., Porphyrin-phospholipid liposomes with tunable leakiness. *J Control Release* **2015,** *220* (Pt A), 484-494.
215. Lum, W.; Bruzas, I.; Gorunmez, Z.; Unser, S.; Beck, T.; Sagle, L., Novel Liposome-Based Surface-Enhanced Raman Spectroscopy (SERS) Substrate. *J Phys Chem Lett* **2017,** *8* (12), 2639-2646.
216. Tomas, S.; Milanesi, L., Hydrophobically self-assembled nanoparticles as molecular receptors in water. *J Am Chem Soc* **2009,** *131* (18), 6618-23.
217. Helenius, A.; Simons, K., Solubilization of membranes by detergents. *Biochim Biophys Acta* **1975,** *415* (1), 29-79.
218. Dennis, E. A., Formation and characterization of mixed micelles of the nonionic surfactant Triton X-100 with egg, dipalmitoyl, and dimyristoyl phosphatidylcholines. *Arch Biochem Biophys* **1974,** *165* (2), 764-73.

219. Sudbrack, T. P.; Archilha, N. L.; Itri, R.; Riske, K. A., Observing the solubilization of lipid bilayers by detergents with optical microscopy of GUVs. *J Phys Chem B* **2011,** *115* (2), 269-77.
220. Fan, H. Y.; Das, D.; Heerklotz, H., "Staying Out" Rather than "Cracking In": Asymmetric Membrane Insertion of 12:0 Lysophosphocholine. *Langmuir* **2016,** *32* (44), 11655-11663.
221. Lichtenberg, D.; Ahyayauch, H.; Goni, F. M., The mechanism of detergent solubilization of lipid bilayers. *Biophys J* **2013,** *105* (2), 289-99.
222. Schnitzer, E.; Lichtenberg, D.; Kozlov, M. M., Temperature-dependence of the solubilization of dipalmitoylphosphatidylcholine (DPPC) by the non-ionic surfactant Triton X-100, kinetic and structural aspects. *Chem Phys Lipids* **2003,** *126* (1), 55-76.
223. Mattei, B.; Franca, A. D.; Riske, K. A., Solubilization of binary lipid mixtures by the detergent Triton X-100: the role of cholesterol. *Langmuir* **2015,** *31* (1), 378-86.
224. Medzhitov, R.; Janeway, C., Jr., Innate immunity. *N Engl J Med* **2000,** *343* (5), 338-44.
225. Akira, S.; Uematsu, S.; Takeuchi, O., Pathogen recognition and innate immunity. *Cell* **2006,** *124* (4), 783-801.
226. Silverstein, A. M., Cellular versus humoral immunology: a century-long dispute. *Nat Immunol* **2003,** *4* (5), 425-8.
227. Anderson, G.; Moore, N. C.; Owen, J. J.; Jenkinson, E. J., Cellular interactions in thymocyte development. *Annu Rev Immunol* **1996,** *14*, 73-99.
228. Hayday, A. C., [gamma][delta] cells: a right time and a right place for a conserved third way of protection. *Annu Rev Immunol* **2000,** *18*, 975-1026.
229. Saito, H.; Kranz, D. M.; Takagaki, Y.; Hayday, A. C.; Eisen, H. N.; Tonegawa, S., Complete primary structure of a heterodimeric T-cell receptor deduced from cDNA sequences. *Nature* **1984,** *309* (5971), 757-62.
230. Grusby, M. J.; Auchincloss, H., Jr.; Lee, R.; Johnson, R. S.; Spencer, J. P.; Zijlstra, M.; Jaenisch, R.; Papaioannou, V. E.; Glimcher, L. H., Mice lacking major histocompatibility complex class I and class II molecules. *Proc Natl Acad Sci U S A* **1993,** *90* (9), 3913-7.
231. Correa, I.; Bix, M.; Liao, N. S.; Zijlstra, M.; Jaenisch, R.; Raulet, D., Most gamma delta T cells develop normally in beta 2-microglobulin-deficient mice. *Proc Natl Acad Sci U S A* **1992,** *89* (2), 653-7.
232. Strid, J.; Roberts, S. J.; Filler, R. B.; Lewis, J. M.; Kwong, B. Y.; Schpero, W.; Kaplan, D. H.; Hayday, A. C.; Girardi, M., Acute upregulation of an NKG2D ligand promotes rapid reorganization of a local immune compartment with pleiotropic effects on carcinogenesis. *Nat Immunol* **2008,** *9* (2), 146-54.
233. Carding, S. R.; Egan, P. J., Gammadelta T cells: functional plasticity and heterogeneity. *Nat Rev Immunol* **2002,** *2* (5), 336-45.
234. Bonneville, M.; O'Brien, R. L.; Born, W. K., Gammadelta T cell effector functions: a blend of innate programming and acquired plasticity. *Nat Rev Immunol* **2010,** *10* (7), 467-78.
235. Jameson, J.; Havran, W. L., Skin gammadelta T-cell functions in homeostasis and wound healing. *Immunol Rev* **2007,** *215*, 114-22.
236. Itohara, S.; Farr, A. G.; Lafaille, J. J.; Bonneville, M.; Takagaki, Y.; Haas, W.; Tonegawa, S., Homing of a gamma delta thymocyte subset with homogeneous T-cell receptors to mucosal epithelia. *Nature* **1990,** *343* (6260), 754-7.

237. Sim, G. K.; Rajaserkar, R.; Dessing, M.; Augustin, A., Homing and in situ differentiation of resident pulmonary lymphocytes. *Int Immunol* **1994,** *6* (9), 1287-95.
238. Hamada, S.; Umemura, M.; Shiono, T.; Tanaka, K.; Yahagi, A.; Begum, M. D.; Oshiro, K.; Okamoto, Y.; Watanabe, H.; Kawakami, K.; Roark, C.; Born, W. K.; O'Brien, R.; Ikuta, K.; Ishikawa, H.; Nakae, S.; Iwakura, Y.; Ohta, T.; Matsuzaki, G., IL-17A produced by gammadelta T cells plays a critical role in innate immunity against listeria monocytogenes infection in the liver. *J Immunol* **2008,** *181* (5), 3456-63.
239. Sumaria, N.; Roediger, B.; Ng, L. G.; Qin, J.; Pinto, R.; Cavanagh, L. L.; Shklovskaya, E.; Fazekas de St Groth, B.; Triccas, J. A.; Weninger, W., Cutaneous immunosurveillance by self-renewing dermal gammadelta T cells. *J Exp Med* **2011,** *208* (3), 505-18.
240. Azuara, V.; Levraud, J. P.; Lembezat, M. P.; Pereira, P., A novel subset of adult gamma delta thymocytes that secretes a distinct pattern of cytokines and expresses a very restricted T cell receptor repertoire. *Eur J Immunol* **1997,** *27* (2), 544-53.
241. Gerber, D. J.; Azuara, V.; Levraud, J. P.; Huang, S. Y.; Lembezat, M. P.; Pereira, P., IL-4-producing gamma delta T cells that express a very restricted TCR repertoire are preferentially localized in liver and spleen. *J Immunol* **1999,** *163* (6), 3076-82.
242. Prinz, I.; Silva-Santos, B.; Pennington, D. J., Functional development of gammadelta T cells. *Eur J Immunol* **2013,** *43* (8), 1988-94.
243. Martin, B.; Hirota, K.; Cua, D. J.; Stockinger, B.; Veldhoen, M., Interleukin-17-producing gammadelta T cells selectively expand in response to pathogen products and environmental signals. *Immunity* **2009,** *31* (2), 321-30.
244. Ribot, J. C.; deBarros, A.; Pang, D. J.; Neves, J. F.; Peperzak, V.; Roberts, S. J.; Girardi, M.; Borst, J.; Hayday, A. C.; Pennington, D. J.; Silva-Santos, B., CD27 is a thymic determinant of the balance between interferon-gamma- and interleukin 17-producing gammadelta T cell subsets. *Nat Immunol* **2009,** *10* (4), 427-36.
245. Heilig, J. S.; Tonegawa, S., Diversity of murine gamma genes and expression in fetal and adult T lymphocytes. *Nature* **1986,** *322* (6082), 836-40.
246. Hayday, A. C.; Saito, H.; Gillies, S. D.; Kranz, D. M.; Tanigawa, G.; Eisen, H. N.; Tonegawa, S., Structure, organization, and somatic rearrangement of T cell gamma genes. *Cell* **1985,** *40* (2), 259-69.
247. Lefranc, M. P.; Pommie, C.; Kaas, Q.; Duprat, E.; Bosc, N.; Guiraudou, D.; Jean, C.; Ruiz, M.; Da Piedade, I.; Rouard, M.; Foulquier, E.; Thouvenin, V.; Lefranc, G., IMGT unique numbering for immunoglobulin and T cell receptor constant domains and Ig superfamily C-like domains. *Dev Comp Immunol* **2005,** *29* (3), 185-203.
248. Pang, D. J.; Neves, J. F.; Sumaria, N.; Pennington, D. J., Understanding the complexity of gamma delta T-cell subsets in mouse and human. *Immunology* **2012,** *136* (3), 283-290.
249. Asarnow, D. M.; Kuziel, W. A.; Bonyhadi, M.; Tigelaar, R. E.; Tucker, P. W.; Allison, J. P., Limited diversity of gamma delta antigen receptor genes of Thy-1+ dendritic epidermal cells. *Cell* **1988,** *55* (5), 837-47.
250. Strid, J.; Sobolev, O.; Zafirova, B.; Polic, B.; Hayday, A., The intraepithelial T cell response to NKG2D-ligands links lymphoid stress surveillance to atopy. *Science* **2011,** *334* (6060), 1293-7.

251. Gibbons, D. L.; Haque, S. F.; Silberzahn, T.; Hamilton, K.; Langford, C.; Ellis, P.; Carr, R.; Hayday, A. C., Neonates harbour highly active gammadelta T cells with selective impairments in preterm infants. *Eur J Immunol* **2009,** *39* (7), 1794-806.
252. Vermijlen, D.; Brouwer, M.; Donner, C.; Liesnard, C.; Tackoen, M.; Van Rysselberge, M.; Twite, N.; Goldman, M.; Marchant, A.; Willems, F., Human cytomegalovirus elicits fetal gammadelta T cell responses in utero. *J Exp Med* **2010,** *207* (4), 807-21.
253. Gao, Y.; Yang, W.; Pan, M.; Scully, E.; Girardi, M.; Augenlicht, L. H.; Craft, J.; Yin, Z., Gamma delta T cells provide an early source of interferon gamma in tumor immunity. *J Exp Med* **2003,** *198* (3), 433-42.
254. Kolls, J. K.; Linden, A., Interleukin-17 family members and inflammation. *Immunity* **2004,** *21* (4), 467-76.
255. King, D. P.; Hyde, D. M.; Jackson, K. A.; Novosad, D. M.; Ellis, T. N.; Putney, L.; Stovall, M. Y.; Van Winkle, L. S.; Beaman, B. L.; Ferrick, D. A., Cutting edge: protective response to pulmonary injury requires gamma delta T lymphocytes. *J Immunol* **1999,** *162* (9), 5033-6.
256. Umemura, M.; Yahagi, A.; Hamada, S.; Begum, M. D.; Watanabe, H.; Kawakami, K.; Suda, T.; Sudo, K.; Nakae, S.; Iwakura, Y.; Matsuzaki, G., IL-17-mediated regulation of innate and acquired immune response against pulmonary Mycobacterium bovis bacille Calmette-Guerin infection. *J Immunol* **2007,** *178* (6), 3786-96.
257. Shibata, K.; Yamada, H.; Hara, H.; Kishihara, K.; Yoshikai, Y., Resident Vdelta1+ gammadelta T cells control early infiltration of neutrophils after Escherichia coli infection via IL-17 production. *J Immunol* **2007,** *178* (7), 4466-72.
258. Kashani, E.; Fohse, L.; Raha, S.; Sandrock, I.; Oberdorfer, L.; Koenecke, C.; Suerbaum, S.; Weiss, S.; Prinz, I., A clonotypic Vgamma4Jgamma1/Vdelta5Ddelta2Jdelta1 innate gammadelta T-cell population restricted to the CCR6(+)CD27(-) subset. *Nat Commun* **2015,** *6*, 6477.
259. Gray, E. E.; Suzuki, K.; Cyster, J. G., Cutting edge: Identification of a motile IL-17-producing gammadelta T cell population in the dermis. *J Immunol* **2011,** *186* (11), 6091-5.
260. Godfrey, D. I.; Kennedy, J.; Suda, T.; Zlotnik, A., A developmental pathway involving four phenotypically and functionally distinct subsets of CD3-CD4-CD8- triple-negative adult mouse thymocytes defined by CD44 and CD25 expression. *J Immunol* **1993,** *150* (10), 4244-52.
261. Schlenner, S. M.; Rodewald, H. R., Early T cell development and the pitfalls of potential. *Trends Immunol* **2010,** *31* (8), 303-10.
262. Radtke, F.; Wilson, A.; Stark, G.; Bauer, M.; van Meerwijk, J.; MacDonald, H. R.; Aguet, M., Deficient T cell fate specification in mice with an induced inactivation of Notch1. *Immunity* **1999,** *10* (5), 547-58.
263. Pui, J. C.; Allman, D.; Xu, L.; DeRocco, S.; Karnell, F. G.; Bakkour, S.; Lee, J. Y.; Kadesch, T.; Hardy, R. R.; Aster, J. C.; Pear, W. S., Notch1 expression in early lymphopoiesis influences B versus T lineage determination. *Immunity* **1999,** *11* (3), 299-308.
264. Schmitt, T. M.; Zuniga-Pflucker, J. C., Induction of T cell development from hematopoietic progenitor cells by delta-like-1 in vitro. *Immunity* **2002,** *17* (6), 749-56.
265. Kawamoto, H.; Ohmura, K.; Fujimoto, S.; Lu, M.; Ikawa, T.; Katsura, Y., Extensive proliferation of T cell lineage-restricted progenitors in the thymus: an essential

process for clonal expression of diverse T cell receptor beta chains. *Eur J Immunol* **2003,** *33* (3), 606-15.
266. Molina, T. J.; Kishihara, K.; Siderovski, D. P.; van Ewijk, W.; Narendran, A.; Timms, E.; Wakeham, A.; Paige, C. J.; Hartmann, K. U.; Veillette, A.; et al., Profound block in thymocyte development in mice lacking p56lck. *Nature* **1992,** *357* (6374), 161-4.
267. Mombaerts, P.; Iacomini, J.; Johnson, R. S.; Herrup, K.; Tonegawa, S.; Papaioannou, V. E., RAG-1-deficient mice have no mature B and T lymphocytes. *Cell* **1992,** *68* (5), 869-77.
268. Wu, L.; Li, C. L.; Shortman, K., Thymic dendritic cell precursors: relationship to the T lymphocyte lineage and phenotype of the dendritic cell progeny. *J Exp Med* **1996,** *184* (3), 903-11.
269. Fehling, H. J.; Krotkova, A.; Saint-Ruf, C.; von Boehmer, H., Crucial role of the pre-T-cell receptor alpha gene in development of alpha beta but not gamma delta T cells. *Nature* **1995,** *375* (6534), 795-8.
270. Hoffman, E. S.; Passoni, L.; Crompton, T.; Leu, T. M.; Schatz, D. G.; Koff, A.; Owen, M. J.; Hayday, A. C., Productive T-cell receptor beta-chain gene rearrangement: coincident regulation of cell cycle and clonality during development in vivo. *Genes Dev* **1996,** *10* (8), 948-62.
271. Schweighoffer, E.; Fowlkes, B. J., Positive selection is not required for thymic maturation of transgenic gamma delta T cells. *J Exp Med* **1996,** *183* (5), 2033-41.
272. Miyazaki, T., Two distinct steps during thymocyte maturation from CD4-CD8- to CD4+CD8+ distinguished in the early growth response (Egr)-1 transgenic mice with a recombinase-activating gene-deficient background. *J Exp Med* **1997,** *186* (6), 877-85.
273. Mombaerts, P.; Clarke, A. R.; Rudnicki, M. A.; Iacomini, J.; Itohara, S.; Lafaille, J. J.; Wang, L.; Ichikawa, Y.; Jaenisch, R.; Hooper, M. L.; et al., Mutations in T-cell antigen receptor genes alpha and beta block thymocyte development at different stages. *Nature* **1992,** *360* (6401), 225-31.
274. Kappler, J. W.; Roehm, N.; Marrack, P., T cell tolerance by clonal elimination in the thymus. *Cell* **1987,** *49* (2), 273-80.
275. Xiong, N.; Baker, J. E.; Kang, C.; Raulet, D. H., The genomic arrangement of T cell receptor variable genes is a determinant of the developmental rearrangement pattern. *Proc Natl Acad Sci U S A* **2004,** *101* (1), 260-5.
276. Ciofani, M.; Knowles, G. C.; Wiest, D. L.; von Boehmer, H.; Zuniga-Pflucker, J. C., Stage-specific and differential notch dependency at the alphabeta and gammadelta T lineage bifurcation. *Immunity* **2006,** *25* (1), 105-16.
277. Pardoll, D. M.; Fowlkes, B. J.; Bluestone, J. A.; Kruisbeek, A.; Maloy, W. L.; Coligan, J. E.; Schwartz, R. H., Differential expression of two distinct T-cell receptors during thymocyte development. *Nature* **1987,** *326* (6108), 79-81.
278. Saint-Ruf, C.; Ungewiss, K.; Groettrup, M.; Bruno, L.; Fehling, H. J.; von Boehmer, H., Analysis and expression of a cloned pre-T cell receptor gene. *Science* **1994,** *266* (5188), 1208-12.
279. Kang, J.; Volkmann, A.; Raulet, D. H., Evidence that gammadelta versus alphabeta T cell fate determination is initiated independently of T cell receptor signaling. *J Exp Med* **2001,** *193* (6), 689-98.

280. Kreslavsky, T.; Garbe, A. I.; Krueger, A.; von Boehmer, H., T cell receptor-instructed alphabeta versus gammadelta lineage commitment revealed by single-cell analysis. *J Exp Med* **2008,** *205* (5), 1173-86.
281. Livak, F.; Petrie, H. T.; Crispe, I. N.; Schatz, D. G., In-frame TCR delta gene rearrangements play a critical role in the alpha beta/gamma delta T cell lineage decision. *Immunity* **1995,** *2* (6), 617-27.
282. Bruno, L.; Fehling, H. J.; von Boehmer, H., The alpha beta T cell receptor can replace the gamma delta receptor in the development of gamma delta lineage cells. *Immunity* **1996,** *5* (4), 343-52.
283. Melichar, H. J.; Narayan, K.; Der, S. D.; Hiraoka, Y.; Gardiol, N.; Jeannet, G.; Held, W.; Chambers, C. A.; Kang, J., Regulation of gammadelta versus alphabeta T lymphocyte differentiation by the transcription factor SOX13. *Science* **2007,** *315* (5809), 230-3.
284. Gray, E. E.; Ramirez-Valle, F.; Xu, Y.; Wu, S.; Wu, Z.; Karjalainen, K. E.; Cyster, J. G., Deficiency in IL-17-committed Vgamma4(+) gammadelta T cells in a spontaneous Sox13-mutant CD45.1(+) congenic mouse substrain provides protection from dermatitis. *Nat Immunol* **2013,** *14* (6), 584-92.
285. Hayes, S. M.; Li, L.; Love, P. E., TCR signal strength influences alphabeta/gammadelta lineage fate. *Immunity* **2005,** *22* (5), 583-93.
286. Love, P. E.; Shores, E. W.; Johnson, M. D.; Tremblay, M. L.; Lee, E. J.; Grinberg, A.; Huang, S. P.; Singer, A.; Westphal, H., T cell development in mice that lack the zeta chain of the T cell antigen receptor complex. *Science* **1993,** *261* (5123), 918-21.
287. Zarin, P.; Wong, G. W.; Mohtashami, M.; Wiest, D. L.; Zuniga-Pflucker, J. C., Enforcement of gammadelta-lineage commitment by the pre-T-cell receptor in precursors with weak gammadelta-TCR signals. *Proc Natl Acad Sci U S A* **2014,** *111* (15), 5658-63.
288. Prinz, I.; Sansoni, A.; Kissenpfennig, A.; Ardouin, L.; Malissen, M.; Malissen, B., Visualization of the earliest steps of gammadelta T cell development in the adult thymus. *Nat Immunol* **2006,** *7* (9), 995-1003.
289. Cosgrove, D.; Gray, D.; Dierich, A.; Kaufman, J.; Lemeur, M.; Benoist, C.; Mathis, D., Mice Lacking Mhc Class-Ii Molecules. *Cell* **1991,** *66* (5), 1051-1066.
290. Jensen, K. D.; Su, X.; Shin, S.; Li, L.; Youssef, S.; Yamasaki, S.; Steinman, L.; Saito, T.; Locksley, R. M.; Davis, M. M.; Baumgarth, N.; Chien, Y. H., Thymic selection determines gammadelta T cell effector fate: antigen-naive cells make interleukin-17 and antigen-experienced cells make interferon gamma. *Immunity* **2008,** *29* (1), 90-100.
291. Mahtani-Patching, J.; Neves, J. F.; Pang, D. J.; Stoenchev, K. V.; Aguirre-Blanco, A. M.; Silva-Santos, B.; Pennington, D. J., PreTCR and TCRgammadelta signal initiation in thymocyte progenitors does not require domains implicated in receptor oligomerization. *Sci Signal* **2011,** *4* (182), ra47.
292. Lewis, J. M.; Girardi, M.; Roberts, S. J.; Barbee, S. D.; Hayday, A. C.; Tigelaar, R. E., Selection of the cutaneous intraepithelial gammadelta+ T cell repertoire by a thymic stromal determinant. *Nat Immunol* **2006,** *7* (8), 843-50.
293. Barbee, S. D.; Woodward, M. J.; Turchinovich, G.; Mention, J. J.; Lewis, J. M.; Boyden, L. M.; Lifton, R. P.; Tigelaar, R.; Hayday, A. C., Skint-1 is a highly specific, unique selecting component for epidermal T cells. *Proc Natl Acad Sci U S A* **2011,** *108* (8), 3330-5.

294. Boyden, L. M.; Lewis, J. M.; Barbee, S. D.; Bas, A.; Girardi, M.; Hayday, A. C.; Tigelaar, R. E.; Lifton, R. P., Skint1, the prototype of a newly identified immunoglobulin superfamily gene cluster, positively selects epidermal gammadelta T cells. *Nat Genet* **2008,** *40* (5), 656-62.
295. Chien, Y. H.; Konigshofer, Y., Antigen recognition by gammadelta T cells. *Immunol Rev* **2007,** *215*, 46-58.
296. Ito, K.; Van Kaer, L.; Bonneville, M.; Hsu, S.; Murphy, D. B.; Tonegawa, S., Recognition of the product of a novel MHC TL region gene (27b) by a mouse gamma delta T cell receptor. *Cell* **1990,** *62* (3), 549-61.
297. Crowley, M. P.; Reich, Z.; Mavaddat, N.; Altman, J. D.; Chien, Y., The recognition of the nonclassical major histocompatibility complex (MHC) class I molecule, T10, by the gammadelta T cell, G8. *J Exp Med* **1997,** *185* (7), 1223-30.
298. Bonneville, M.; Itohara, S.; Krecko, E. G.; Mombaerts, P.; Ishida, I.; Katsuki, M.; Berns, A.; Farr, A. G.; Janeway, C. A., Jr.; Tonegawa, S., Transgenic mice demonstrate that epithelial homing of gamma/delta T cells is determined by cell lineages independent of T cell receptor specificity. *J Exp Med* **1990,** *171* (4), 1015-26.
299. Dent, A. L.; Matis, L. A.; Hooshmand, F.; Widacki, S. M.; Bluestone, J. A.; Hedrick, S. M., Self-reactive gamma delta T cells are eliminated in the thymus. *Nature* **1990,** *343* (6260), 714-9.
300. Pereira, P.; Zijlstra, M.; McMaster, J.; Loring, J. M.; Jaenisch, R.; Tonegawa, S., Blockade of transgenic gamma delta T cell development in beta 2-microglobulin deficient mice. *EMBO J* **1992,** *11* (1), 25-31.
301. Tarakhovsky, A.; Kanner, S. B.; Hombach, J.; Ledbetter, J. A.; Muller, W.; Killeen, N.; Rajewsky, K., A role for CD5 in TCR-mediated signal transduction and thymocyte selection. *Science* **1995,** *269* (5223), 535-7.
302. Azzam, H. S.; Grinberg, A.; Lui, K.; Shen, H.; Shores, E. W.; Love, P. E., CD5 expression is developmentally regulated by T cell receptor (TCR) signals and TCR avidity. *J Exp Med* **1998,** *188* (12), 2301-11.
303. Turchinovich, G.; Hayday, A. C., Skint-1 identifies a common molecular mechanism for the development of interferon-gamma-secreting versus interleukin-17-secreting gammadelta T cells. *Immunity* **2011,** *35* (1), 59-68.
304. Coffey, F.; Lee, S. Y.; Buus, T. B.; Lauritsen, J. P.; Wong, G. W.; Joachims, M. L.; Thompson, L. F.; Zuniga-Pflucker, J. C.; Kappes, D. J.; Wiest, D. L., The TCR ligand-inducible expression of CD73 marks gammadelta lineage commitment and a metastable intermediate in effector specification. *J Exp Med* **2014,** *211* (2), 329-43.
305. Haks, M. C.; Lefebvre, J. M.; Lauritsen, J. P.; Carleton, M.; Rhodes, M.; Miyazaki, T.; Kappes, D. J.; Wiest, D. L., Attenuation of gammadeltaTCR signaling efficiently diverts thymocytes to the alphabeta lineage. *Immunity* **2005,** *22* (5), 595-606.
306. Heemskerk, M. H.; Blom, B.; Nolan, G.; Stegmann, A. P.; Bakker, A. Q.; Weijer, K.; Res, P. C.; Spits, H., Inhibition of T cell and promotion of natural killer cell development by the dominant negative helix loop helix factor Id3. *J Exp Med* **1997,** *186* (9), 1597-602.
307. Dr. Garry Nolan, P. D. https://web.stanford.edu/group/nolan/_OldWebsite/index.html.
308. O'Doherty, U.; Swiggard, W. J.; Malim, M. H., Human immunodeficiency virus type 1 spinoculation enhances infection through virus binding. *J Virol* **2000,** *74* (21), 10074-80.

309. Hughes, J. H., Physical and chemical methods for enhancing rapid detection of viruses and other agents. *Clin Microbiol Rev* **1993,** *6* (2), 150-75.
310. Kodama, H.; Nose, M.; Niida, S.; Nishikawa, S.; Nishikawa, S., Involvement of the c-kit receptor in the adhesion of hematopoietic stem cells to stromal cells. *Exp Hematol* **1994,** *22* (10), 979-84.
311. de Felipe, P.; Hughes, L. E.; Ryan, M. D.; Brown, J. D., Co-translational, intraribosomal cleavage of polypeptides by the foot-and-mouth disease virus 2A peptide. *J Biol Chem* **2003,** *278* (13), 11441-8.
312. Donnelly, M. L.; Hughes, L. E.; Luke, G.; Mendoza, H.; ten Dam, E.; Gani, D.; Ryan, M. D., The 'cleavage' activities of foot-and-mouth disease virus 2A site-directed mutants and naturally occurring '2A-like' sequences. *J Gen Virol* **2001,** *82* (Pt 5), 1027-41.
313. Holst, J.; Szymczak-Workman, A. L.; Vignali, K. M.; Burton, A. R.; Workman, C. J.; Vignali, D. A., Generation of T-cell receptor retrogenic mice. *Nat Protoc* **2006,** *1* (1), 406-17.
314. Shinkai, Y.; Rathbun, G.; Lam, K. P.; Oltz, E. M.; Stewart, V.; Mendelsohn, M.; Charron, J.; Datta, M.; Young, F.; Stall, A. M.; et al., RAG-2-deficient mice lack mature lymphocytes owing to inability to initiate V(D)J rearrangement. *Cell* **1992,** *68* (5), 855-67.
315. Zhang, W.; Sommers, C. L.; Burshtyn, D. N.; Stebbins, C. C.; DeJarnette, J. B.; Trible, R. P.; Grinberg, A.; Tsay, H. C.; Jacobs, H. M.; Kessler, C. M.; Long, E. O.; Love, P. E.; Samelson, L. E., Essential role of LAT in T cell development. *Immunity* **1999,** *10* (3), 323-32.
316. Pivniouk, V.; Tsitsikov, E.; Swinton, P.; Rathbun, G.; Alt, F. W.; Geha, R. S., Impaired viability and profound block in thymocyte development in mice lacking the adaptor protein SLP-76. *Cell* **1998,** *94* (2), 229-38.
317. Cheng, A. M.; Negishi, I.; Anderson, S. J.; Chan, A. C.; Bolen, J.; Loh, D. Y.; Pawson, T., The Syk and ZAP-70 SH2-containing tyrosine kinases are implicated in pre-T cell receptor signaling. *Proc Natl Acad Sci U S A* **1997,** *94* (18), 9797-801.
318. Turchinovich, G.; Pennington, D. J., T cell receptor signalling in gammadelta cell development: strength isn't everything. *Trends Immunol* **2011,** *32* (12), 567-73.
319. Byth, K. F.; Conroy, L. A.; Howlett, S.; Smith, A. J.; May, J.; Alexander, D. R.; Holmes, N., CD45-null transgenic mice reveal a positive regulatory role for CD45 in early thymocyte development, in the selection of CD4+CD8+ thymocytes, and B cell maturation. *J Exp Med* **1996,** *183* (4), 1707-18.
320. Ogilvy, S.; Louis-Dit-Sully, C.; Cooper, J.; Cassady, R. L.; Alexander, D. R.; Holmes, N., Either of the CD45RB and CD45RO isoforms are effective in restoring T cell, but not B cell, development and function in CD45-null mice. *J Immunol* **2003,** *171* (4), 1792-800.
321. Thompson, P. J.; Macfarlan, T. S.; Lorincz, M. C., Long Terminal Repeats: From Parasitic Elements to Building Blocks of the Transcriptional Regulatory Repertoire. *Mol Cell* **2016,** *62* (5), 766-76.
322. Livak, F.; Tourigny, M.; Schatz, D. G.; Petrie, H. T., Characterization of TCR gene rearrangements during adult murine T cell development. *J Immunol* **1999,** *162* (5), 2575-80.
323. Matreyek, K. A.; Engelman, A., Viral and cellular requirements for the nuclear entry of retroviral preintegration nucleoprotein complexes. *Viruses* **2013,** *5* (10), 2483-511.

324. Gratzner, H. G., Monoclonal-Antibody to 5-Bromodeoxyuridine and 5-Iododeoxyuridine - a New Reagent for Detection of DNA-Replication. *Science* **1982,** *218* (4571), 474-475.
325. Shibata, K.; Yamada, H.; Nakamura, M.; Hatano, S.; Katsuragi, Y.; Kominami, R.; Yoshikai, Y., IFN-gamma-producing and IL-17-producing gammadelta T cells differentiate at distinct developmental stages in murine fetal thymus. *J Immunol* **2014,** *192* (5), 2210-8.
326. Wang, H.; Pierce, L. J.; Spangrude, G. J., Distinct roles of IL-7 and stem cell factor in the OP9-DL1 T-cell differentiation culture system. *Exp Hematol* **2006,** *34* (12), 1730-40.
327. Moore, T. A.; Zlotnik, A., Differential effects of Flk-2/Flt-3 ligand and stem cell factor on murine thymic progenitor cells. *J Immunol* **1997,** *158* (9), 4187-92.
328. Maki, K.; Sunaga, S.; Komagata, Y.; Kodaira, Y.; Mabuchi, A.; Karasuyama, H.; Yokomuro, K.; Miyazaki, J. I.; Ikuta, K., Interleukin 7 receptor-deficient mice lack gammadelta T cells. *Proc Natl Acad Sci U S A* **1996,** *93* (14), 7172-7.
329. Huang, J.; Garrett, K. P.; Pelayo, R.; Zuniga-Pflucker, J. C.; Petrie, H. T.; Kincade, P. W., Propensity of adult lymphoid progenitors to progress to DN2/3 stage thymocytes with Notch receptor ligation. *J Immunol* **2005,** *175* (8), 4858-65.